

AD-A154 714

VISIBILITY AND VERTICAL STRUCTURE MEASUREMENTS IN
SOUTHERN GERMANY(U) FRAUNHOFER-INST FUER
ATMOSPHAERISCHE UMWELTFORSCHUNG GARMISCH.

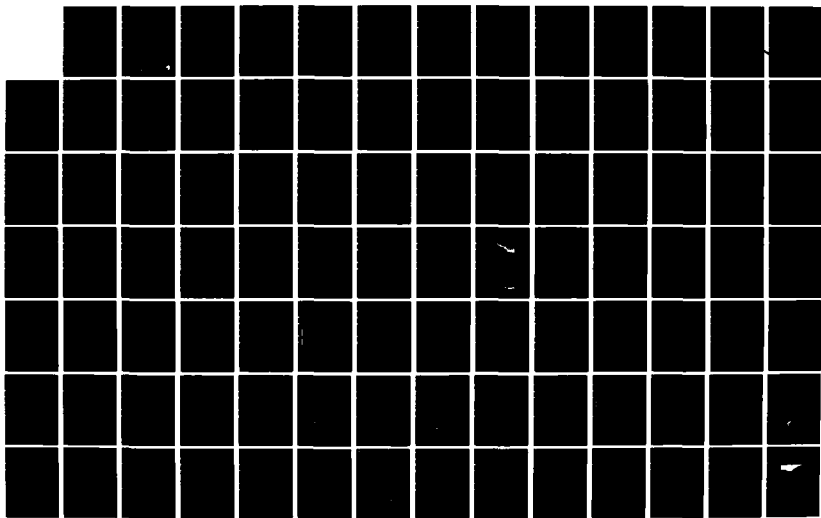
1/3

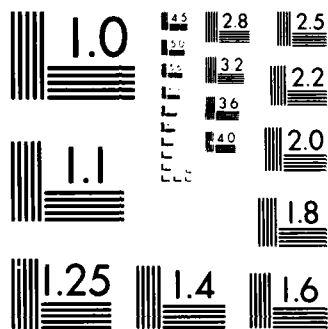
UNCLASSIFIED

R REITER ET AL. DEC 84 DAJA45-83-C-0023

F/G 4/2

NL





MICROCOPY RESOLUTION TEST CHART
NATIONAL BUREAU OF STANDARDS-1963-A

AD _____

VISIBILITY AND VERTICAL STRUCTURE MEASUREMENTS
IN SOUTHERN GERMANY

AD-A154 714

Final Technical Report

by

REINHOLD REITER

WALTER CARNUTH

WERNER FUNK

December 1984

EUROPEAN RESEARCH OFFICE

United States Army

London

England

GRANT NUMBER DAJA45-83-C-0023

Fraunhofer-Institut für Atmosphärische

Umweltforschung

Kreuzeckbahnstrasse 19

D-8100 Garmisch-Partenkirchen

DTIC FILE COPY

Approved for Public Release; distribution unlimited

DTIC
ELECTE

JUN 8

E

05 10 000

AD

VISIBILITY AND VERTICAL STRUCTURE MEASUREMENTS IN SOUTHERN GERMANY

Final Technical Report

by

REINHOLD REITER

WALTER CARNUTH

WERNER FUNK

December 1984

EUROPEAN RESEARCH OFFICE

United States Army

London England

GRANT NUMBER DAJA45-83-C-0023

Fraunhofer-Institut für Atmosphärische
Umweltforschung
Kreuzeckbahnstrasse 19
D-8100 Garmisch-Partenkirchen

Accession For	
NTIS GRA&I	<input checked="" type="checkbox"/>
DTIC TAB	<input type="checkbox"/>
Unannounced	<input type="checkbox"/>
Justification	
By	
Distribution/	
Availability Codes	
Dist	Avail and/or Special
A/	

Approved for Public Release; distribution unlimited



REPORT DOCUMENTATION PAGE		READ INSTRUCTIONS BEFORE COMPLETING FORM
1. REPORT NUMBER	2. GOVT ACCESSION NO.	3. RECIPIENT'S CATALOG NUMBER
	DD - 115414	
4. TITLE (and Subtitle)		5. TYPE OF REPORT & PERIOD COVERED
VISIBILITY AND VERTICAL STRUCTURE MEASUREMENTS IN SOUTHERN GERMANY		Final Technical Report Dec 82 - Dec 84
		6. PERFORMING ORG. REPORT NUMBER
7. AUTHOR(s)		8. CONTRACT OR GRANT NUMBER(s)
Reinhold Reiter, Walter Carnuth, Werner Funk		DAJA45-83-C-0023
9. PERFORMING ORGANIZATION NAME AND ADDRESS		10. PROGRAM ELEMENT, PROJECT, TASK AREA & WORK UNIT NUMBERS
Fraunhofer-Institut für Atmosphärische Umweltforschung D-8100 Garmisch-Partenkirchen, West Germany		61102AIT161102-BH57-01
11. CONTROLLING OFFICE NAME AND ADDRESS		12. REPORT DATE
USARDSG-UK BOX 65, FPO NY 09510		December 1984
		13. NUMBER OF PAGES
		44 + figures (322)
14. MONITORING AGENCY NAME & ADDRESS (if different from Controlling Office)		15. SECURITY CLASS. (of this report)
		unclassified
		15a. DECLASSIFICATION/DOWNGRADING SCHEDULE
16. DISTRIBUTION STATEMENT (of this Report)		
Approved for public release; distribution unlimited		
17. DISTRIBUTION STATEMENT (of the abstract entered in Block 20, if different from Report)		
Vertical profiles; atmospheric extinction; lidar; low visibility; fog; haze; clouds; cloud ceiling; aerosols; synoptic meteorology; extinction coefficient; backscatter profiles.		
18. SUPPLEMENTARY NOTES		
19. KEY WORDS (Continue on reverse side if necessary and identify by block number)		
20. ABSTRACT (Continue on reverse side if necessary and identify by block number)		
<p>The objective was to obtain a body of data describing the vertical profile of the extinction coefficient of the lower atmosphere under a broad range of atmospheric conditions in Southern Germany. The lidar system used included both a ruby and neodymium-glass laser, both used with and without frequency doubling, allowing alternate measurements in wavelengths 347, 530, and 1060 nm. The received backscattered signals were recorded in such a way that</p> <p style="text-align: right;">continued +++</p>		

20. almost-real time corrections for background luminosity, squared range, laser output, and input sensitivity could be made. Klett's inversion method was mainly used for the evaluation of the profiles. Conventional meteorological data were obtained in parallel, including aerosol characterization with Knollenberg counters. The report included graphic presentations of a number of data sets.

unclassified

Table of Contents

1	Introduction.....	1
2	Description of the lidar system.....	2
3	Further relevant equipment available.....	4
3.1	Broadband transmissometer system.....	4
3.2	Aerosol spectrometers and visibility recorders.....	4
3.3	Radiosondes.....	5
4	Listing of the lidar data.....	5
5	Evaluation technique.....	9
6	Examples for evaluated lidar profiles.....	18
6.1	Low optical depth.....	18
6.2	High optical depth.....	23
7	Extinction coefficient profiles from clouds and fog.....	30
8	Conclusions.....	41
9	References.....	43

1 Introduction

The objective of the research is the application of the lidar technique to measure vertical profiles of the extinction coefficient under various types of low visibility conditions such as highly concentrated dry aerosol, wet haze, fog, and clouds. Klett's evaluation method /1/ for lidar backscatter profiles should be applied and the reliability of the results examined. For this purpose the lidar measurements are supported by other data like aerosol particle size spectra, radiosonde ascents, transmissometer measurements, and others.

2 Description of the lidar system

A mobile lidar system is used containing a ruby and a neodymium-glass laser, both used with and without frequency doubling, allowing alternating measurements in the wavelengths 347, 530, 694 and 1060nm. The output energy is about 1 Joule in the fundamental and 20mJ in the first harmonics, the shot frequency 3 per minute. The receiving telescope is a 30cm Cassegrainian with 2.3m focal length. A large-area pin-diode with two-stage amplifier is used for the detection of the 694 and 1060nm signals and a bialkali photomultiplier tube (EMI 9813) for 347 and 530nm. Complete

beam overlap is achieved after 100m range in 694 and 1060nm and after 300m in the two other wavelengths, the difference being due to the detector geometries. The receiver FOV is variable by an iris stop. However, it is normally set to fixed values of 4 mrad for the photomultiplier and 10 mrad for the diode detector, in order to get a non-overlap range as short as possible. The reduced FOV for the photomultiplier tube is used for background reduction. Interference filters with 3nm spectral bandwidth (FWHM) for 347 and 530nm, mounted in a filter wheel, serve the same purpose. Since background luminosity is no problem with the diode detector, this is used without interference filters. However, neutral filters with 50 and 25% transmissivity are available to reduce strong backscatter signals from clouds and fog if necessary. Moreover, the amplifier gain may be reduced by a factor of 10.

The received signals are recorded by a Biomation 8100 transient digitizer with 8 bit amplitude resolution, 10ns minimum sample interval and 2k bytes memory capacity. Immediately after each measurement the data are transferred to an on-line minicomputer with 32k core memory. This computer allows the almost real-time display of backscatter profiles which are corrected for background luminosity, square range, laser output power and input sensitivity, on

a display tube and an x-y chart recorder. Furthermore, automatic programming of the transient digitizer and change of the detectors is done by the computer. For final evaluation on a larger computer the signals are stored, together with all housekeeping data, on floppy discs.

3 Further relevant equipment available

3.1 Broadband transmissometer system

Between the institute and a neighboring mountain peak (Kreuzeck, 1650m above MSL) a slant transmission path with 19 deg. inclination angle and 2.7km length is operated. Along this path the atmospheric transmissivity in the visible range (.35-.9 μ m) and in the 3-5 (since summer 1983) and 8-12 μ m IR ranges is measured.

3.2 Aerosol spectrometers and visibility recorders

Optical particle counters (Knollenberg classical scattering aerosol spectrometers) are used at the institute and at the source end of the transmission path (Kreuzeck) for continuous recording of the aerosol size distribution. The visibility is measured at the same sites by AEG-Ruppersberg integrating nephelometers.

3.3 Radiosondes

Profiles of temperature, humidity and wind speed and direction are recorded by balloon-borne radiosondes, the first two parameters also by cable car sondes.

4 Listing of the lidar data

In table 4.1 all the lidar data assessed under low visibility conditions are listed. The first three columns contain the date, time and number of profiles per day (n), respectively, the latter without regard of the wavelength used. Column 4 (tr) indicates whether transmissometer data are available (yes/no), and column 5 lists the visibility range (v) at ground level during the measuring period, recorded by the integrating nephelometer. The last column, finally, gives a short description of the current weather situation or atmospheric conditions. Measurements during extremely high visibility with predominant Rayleigh backscatter, which can serve for the calibration of the lidar (6 days total), are not included in the table.

All measurements except the last three were performed at the institute, located near Garmisch-Partenkirchen in an alpine valley in southern Bavaria. For the last three measurement

series a site in a flat fen area, about 20km to the north and outside the mountains, was selected, where the probability for the occurrence of ground-based fog and low-altitude stratus is higher than at the institute.

Table 4.1: Listing of the lidar data

date	time	n	tr	v	weather situation
82-08-11	07.53-16.00	36	yes	5-20	fair weather, ground-based dust layer up to 170 m
82-10-29	07.46-16.16	13	no	1-27	at first ground-based fog, then dry aerosol
82-11-10	09.18-11.13	12	no	>40	stratocumulus(Sc) clouds above 200 m
82-12-14	09.20-17.23	25	yes	2-40	Cu med and Cu fra, snowfall, ground fog in the evening
83-01-19	14.20-16.50	6	yes	>40	snowfall, frequently Cu fra occurring
83-01-27	08.30-17.30	28	yes	2-27	dust from the Sahara desert, rain in the afternoon
83-02-10	09.00-17.30	24	yes	8-21	stratus and stratocumulus clouds above 400 m
83-03-16	08.40-10.40	14	no	2-3	St cloud at 270 m, strong dust below
83-03-17	08.36-18.00	33	yes	3-5	extreme dust layer up to 600 m, weaker above; St 800 m
83-06-29	07.13-13.10	19	no	10-22	Cu fra and Sc 500 m, wet haze below
83-07-14	07.00-15.03	19	no	6-10	Cu fra and Sc, wet haze below, at times light rain
83-10-20	16.15-16.55	14	no	23-26	multi-layered Sc cover 550 m, moderate dust below
83-10-21	09.00-09.22	4	no	16	Sc cover at 100 m, inhomogeneous, wet haze below
83-10-25	07.56-08.30	8	no	3-7	ground fog before start, then shallow ground dust layer
83-11-18	08.50-16.40	31	yes	4-11	dust layer with increasing thickness, St 100 m
83-12-29	10.00-15.12	13	yes	4-40	Sc at 600 m, at times ground-based fog
84-02-28	11.00-18.00	28	yes	10-22	homogenizing intense dust up to 800 m; Cu fra 800 m
84-03-01	07.56-17.53	60	yes	4-7	intense ground fog in the morning, lifting off ground
84-03-02	09.13-16.07	24	yes	5-18	strong dust layer with increasing thickness from 250 m
84-03-15	08.40-18.00	34	yes	6-12	inflowing dust layer with increasing intensity
84-03-19	08.26-17.33	44	yes	2-9	situation similar to previous case, at times St fra
84-03-27	10.30-14.30	16	yes	>40	Cu fra at 700 m, clear air below
84-04-04	13.27-14.50	16	no	23-27	Cu fra, cloud base ascending from 750 to 1100 m
84-04-11	13.04-14.08	25	no	5-8	St/Sc cover at 200 m, wet haze below
84-04-13	08.55-09.04	6	no	15	multi-layered Sc cover above 250 m

Table 4.1: Listing of the lidar data(contd.)

date	time	n	tr	v	weather situation
84-08-27	07.10-13.40	24	no	.7-9	at first ground-based fog, then cloud base ascending
84-08-28	07.09-08.34	12	no	4-11	fair weather with ground-based wet haze
84-08-29	08.13-08.23	4	no	10	Sc layer at 1200 m, strong, homogeneous dust below
84-10-05	09.20-11.20	4	no	23-40	multi-layered St at 150 m
84-12-11	15.10-17.31	21	no	8-13	St at 200-230 m, moderate haze below
84-10-12	08.10-14.50	38	no	5-16	wet haze at ground level, at 100-200m St, Sc and Cu fra
84-11-07	09.03-09.11	6	no	4.7	St at 150 m, homogeneous haze below
84-11-16	10.44-12.44	32	no	-----	ground-based fog, dissolving during measurement
84-12-03	11.00-13.08	38	no	-----	Sc,Cu fra at 200m, 2nd Sc layer at 600m
84-12-04	11.00-15.40	71	no	-----	St between 100 and 400m

in base units and b) an extinction coefficient profile derived from this lidar return, e.g. by Klett's method with an experimental boundary value as described formerly in this subsection. We used backscatter profiles from an extremely clear atmosphere, where dominating molecular backscatter could be assumed, for the derivation of lidar calibration factors. This procedure is somewhat uncertain in the wavelength 1060nm, where Rayleigh scattering is smallest and the presence of aerosol scattering can be excluded with least security. However, it avoids the error sources associated with the calculation of backscatter coefficients from experimental aerosol data by the Mie theory. Using these calibration factors, we derived C constants from lidar profiles which were obtained on March 15 and 19, 1984 and evaluated by Klett's method as described above. For the wavelengths 530, 694 and 1060nm we obtained for March 15 the C ratios .030, .023 and .0105, respectively, from 8 profiles each with standard deviations amounting to about .006. For March 19, we obtained .023, .020 and .0112, respectively, from 8 profiles per wavelength and standard deviations around .004. The data from the two days differ up to 20%. The aerosol at the two days was dry and well mixed by eddy diffusion. 15 lidar profiles from atmospheres containing clouds or fog are treated in the same manner. C ratios with much larger scattering are obtained. We evaluated a few

inhomogeneous atmosphere with moderate optical thickness. The profile was combined from two profiles taken with different receiver sensitivities in order to improve the dynamic range. Otherwise the amplitude of the original, non-range-normalized profile would have dropped below the 8 bit resolution limit of the transient digitizer. Fig. 6 presents a sigma profile calculated by Klett's method, again with an experimental extinction coefficient as boundary value. From this profile the amplitude at the lowest utilisable range was now used as boundary value for the forward inversion method, and the profile Fig. 7 was obtained. The curve is obviously nearly identical to the Klett profile Fig. 6, thus demonstrating that the standard method, eq. (4), may deliver correct results if the optical thickness of the range interval is small or moderate and if a realistic boundary value is available.

As already mentioned above, the derivation of the boundary value from a calibrated lidar return itself requires the knowledge of the β - σ ratio or the constant C in (1). This ratio depends on the size distribution, refractive index, and shape of the scattering particles and is thus not constant. Mulders /6/, for instance, reports on strong variations of this ratio even within one day. It is possible to determine the constant C from a) a lidar return

catabatic wind which commonly occurs in mountain valleys. In the late afternoon the layer increased in concentration and became homogeneous, but did not fill the transmission path completely. Fig. 4 shows spatially averaged extinction coefficients derived from the lidar profiles in the four wavelengths versus time, and the transmissometer derived extinction coefficients. All curves show the ascending tendency which is expected from the development of the aerosol layer, especially toward the end of the measuring period. The transmissometer values are expected to agree best with the 530nm lidar extinction data, but we see that the former ones are distinctly smaller. We then derived the extinction coefficients from the integrating nephelometer data, i.e. data delivered by the visibility meter, and calculated again sigma profiles by Klett's method from the 530 nm lidar profiles. These data agree better with the transmissometer derived extinction data than those where the Knollenberg spectrometer was used. Obviously the direct measurement by the nephelometer gives better results than the indirect method used in the particle spectrometer.

As final examples in this section we present a comparison between sigma profiles obtained by the backward (Klett) and forward inversion method, eq. (4). Both methods were applied to a backscatter profile, shown in Fig. 5, from an

valid for the aerosol models introduced by Shettle and Fenn (10). From the visibility meter data the same coefficients can be recalculated by Koschmieder's formula, however only non-monochromatic for the visible range.

Fig. 1 shows a range-adjusted backscatter profile in the wavelength 530nm, which is close to the center of the visible transmission window. No clouds or fog were present in the lidar path, the ground level visual range was 13km. From the CSAS data at the path end .173/km was derived as attenuation coefficient. With this figure as boundary value Klett's method results in a $\sigma(r)$ profile shown in Fig. 2. The smooth curve presents the integration over σ or the optical depth which is .42 at the path end. The optical depth derived from the visible transmission, δ_{tr} , is also included in the figure. The latter value (.44) is slightly larger than the first one, but the agreement is still acceptable.

Fig. 3 shows a series of sigma profiles, in this case in 1060nm wavelength, from a more inhomogeneous, but still cloud-free atmosphere, again derived by Klett's method. The abscissa is now the extinction coefficient and the ordinate the altitude above ground level. The profiles show the influx of a ground based aerosol layer, initiated by the

for B follows then a boundary value

$$\sigma_2(r_c) = \frac{C_1 \frac{1}{k_1}}{C_2 \frac{1}{k_2}} \cdot \sigma_1(r_c) \quad (10)$$

for the interval $(0, r_c)$. It should be noted that the requirement of the ratio of the C values in (7) introduces an additional source of uncertainty into the evaluation, and it is thus not sure that the two-step integration results in a real improvement compared to the assumption of constant k 's and C's. In section 6 a lidar profile will be evaluated by both methods and the resulting σ near ground level compared with nephelometer data.

6 Examples for evaluated lidar profiles

6.1 Low optical depth

In the previous section we mentioned that we have the possibility to calculate extinction coefficients to be used as Klett boundary values from aerosol data at a remote point, namely, at the far end of the transmission path. From aerosol particle size spectra measured by a Knollenberg classical scattering aerosol spectrometer (CSAS) we calculate wavelength-dependent extinction coefficients using Van de Hulst's approximation /9/ and refractive indices

sometimes within a few hours. However, he also observed completely scattered β - σ diagrams.

(1) is certainly not valid in cases where different types of scatterers are present either simultaneously (for instance if particulate and molecular scattering is comparable in magnitude) or spatially separated (e.g., clouds and dry aerosol underneath). In such cases erroneous extinction data may be obtained if the analytical solution (4) or (6) is still used /7/. Fernald et al. /8/ applied Klett's backward inversion technique to a numerical algorithm to solve the 'lidar equation for atmospheric conditions where molecular backscatter cannot be neglected against particulate backscatter. On the other hand, if backscatter profiles from two sufficiently separated scattering media (e.g., dust and clouds) are to be evaluated (for example, dry aerosol from $r=0$ to r_c and fog from r_c to r_m), it is imaginable to integrate Klett's formula (6) in two steps, namely, first from $r=r_c$ to $r=r_m$, and then from $r=r_0$ or 0 to $r=r_c$. The first step would then deliver the boundary value for the second one, provided the k value and the constant C in (1) are known for both media. If (1) is valid with C_1 and k_1 from r_c to r_m and with C_2 and k_2 below r_c , the application of Klett's formula (6) to the interval (r_c, r_m) delivers a value $\sigma_i(r_c)$. From the condition of steadiness

$$\sigma(r) = \frac{[P(r) \cdot r^2]^{\frac{1}{k}}}{[P(r_m) \cdot r_m^2]^{\frac{1}{k}} / \sigma_m + \frac{2}{k} (1-F) \int_r^{r_m} [P(x) \cdot x^2]^{\frac{1}{k}} dx} \quad (9)$$

This kind of simplified multiple scattering correction is utilized e.g. by Evans /13/. It should at least be feasible for an estimation of the influence of multiple scattering upon the inverted lidar profiles. In the following section some extinction coefficient profiles calculated using the modified Klett formula (9) will be presented.

The second objection concerns the validity of the backscatter-to-extinction relationship (1). It is surely approximately valid if the type of the scattering medium does not change along the range interval considered. Fitzgerald /5/, for example, calculated backscatter and extinction coefficients as function of relative humidity of the surrounding air, for aerosols with varying chemical composition (soot content). He found a relation like (1) with k values ranging from .98 to 1.28 for humidities between 90 and 99%, and from .3 and .84 between 50 and 90%. This applies under the assumption that the dry aerosol characteristics do not vary along the path. Mulders /6/ found the relation (1) to be fulfilled on certain days, although with constants and k values varying with time,

treatment of this process requires the solution of the radiative transfer equation under appropriate boundary conditions and is therefore very complex. Several authors tried a treatment of the problem by the Monte Carlo method or numerically under restriction to double scattering /3/. Weinman /11/ and Tam /4/ found exact analytical expressions for the backscattered power using the small-angle approximation for the scattering phase function. For radiative fog and a receiver FOV of 2 mrad Tam found that the multiple backscattered power exceeds the single backscattered power already at an optical depth of 2. Weinman /11/ describes the multiple scattering effect using a correction function $F(r)$ for the extinction term in the lidar equation:

$$P(r) = G \cdot Q \cdot \beta \cdot r^{-2} \cdot \exp \left(-2 \int_0^r \sigma(x) [1 - F(x)] dx \right) \quad (8)$$

Monte Carlo analyses by Kunkel and Weinman /12/ now showed that this correction Function is approximately constant for optical depths greater than about one and for given constant extinction coefficients. With a constant F , however, the modified lidar equation (8) is as easily to be solved as the single scattering equation (2). The factor $2/k$ in front of the integral in the denominator of (4) and (6) is just to be replaced by $2(1-F)/k$:

calculation of experimental extinction coefficients and use them as boundary values for Klett's method. The resulting optical thickness of the range interval can directly be compared with the transmissometer data and so the validity of the lidar inversion be tested. Examples will be presented in the next section.

Although Klett's inversion algorithm delivers results which are stable especially at high optical depths, there are two major objections against the applicability of eq. (1) and (2). The first one is the neglect of multiple scattering in the lidar equation (2). The single scattering assumption means that each photon which is removed out of the laser beam path either by absorption or scattering has no chance at all to reach the receiver. However, in reality a part of the scattered photons can enter the beam path again due to further scattering processes and so increase the power received by the detector. Furthermore, all photons which are scattered in the near-forward direction into the cone of the laser beam don't leave this beam at all. The contribution of multiple scattering increases with optical depth, with the average size of the scattering particles relative to the laser wavelength, and with the transmitter and receiver FOV. Its neglect leads to an underestimation of the true extinction coefficient. The theoretical

still definitely above the noise or error level. Otherwise any signal errors, which are multiplied by r^2 in the solution formula, get an increasing influence upon the result. In this respect we have to note that the choice of r_m in the first evaluation example in the interim report from February 10, 1983 (Figs. 2 and 3) was not the best one.

With decreasing optical thickness of the range interval the influence of the boundary value upon the resulting σ -profile becomes more and more significant, and a σ_m more close to reality must be found. Here the superiority of Klett's method decreases considerably, and in cases where a realistic σ_0 value is available the standard or forward inversion method (4) may even deliver better results /2/, although the dependence of the resulting average attenuation coefficient or optical depth upon the boundary still remains smaller for Klett's formula (6). Furthermore it should again be noted here that the boundary value in the forward inversion formula (4) can be deduced from the lidar return itself only if the backscatter-to-extinction ratio is known. This condition involves an additional uncertainty in the application of (4). We have the opportunity to take advantage of our aerosol and visibility data from the Kreuzeck station at the end of the transmission path for the

The fundamental distinction to (4) is that in (6) the denominator is a sum instead of a difference and so those instabilities are avoided. The application of (6), however, requires the knowledge or assumption of the attenuation coefficient σ_m at the remote end r_m of the range interval, which in general cannot be deduced from the lidar signal itself. However, it can be shown that the influence of the boundary value upon the result decreases strongly with the optical depth between r and r_m . If we again name the terms in the denominator A and B, respectively, we get similar to (5):

$$(A+B)/A = \exp(2\delta/k) \quad (7)$$

from which we easily see that for instance within clouds with extinction coefficients $>10/\text{km}$ the term A solely containing the boundary value drops below 10% from B already after about 100m distance from r_m . For strongly turbid atmospheres, therefore, it is not difficult to find a boundary value which results in reasonable extinction coefficient profiles. In case of doubt a larger boundary value should be preferred. The reference range r_m should be sufficiently large in order to keep the influence of the boundary value low, but the received signal at r_m should be

the denominator in (4) becomes a small difference of two large terms with increasing optical depth. Since the numerator in (4) is proportional to the first derivative of the denominator, (4) can be integrated analytically and so the denominator be expressed in terms of the optical depth δ . If for brevity the two terms are named A and B, respectively, their relative difference becomes

$$(A-B)/A = \exp(-2\delta/k) \quad (5)$$

where δ is the optical thickness of the range interval from r_0 to r . It is easy to see that at high optical depths (5) can become zero or even negative for example if the boundary value contained in the term A is chosen slightly too small. Another reason for the denominator in (4) to become negative even if an absolutely correct boundary value is chosen may be the influence of multiple scattering. In this case the range-corrected signal amplitude may decrease not fast enough and the integral in (4) become too large.

If Klett's backward inversion method is applied to eq. (3), a solution form apparently only slightly different from (4) is found:

$$G(r) = \frac{[P(r) r^2]^{\frac{1}{k}}}{[P(r_m) \cdot r_m^2]^{\frac{1}{k}} / \sigma_m + \frac{2}{k} \int_r^{r_m} [P(x) \cdot x^2]^{\frac{1}{k}} dx} \quad (6)$$

into this differential equation:

$$\frac{d}{dr} [\ln(P r^2)] = \frac{k}{\sigma} \cdot \frac{d\sigma}{dr} - 2\sigma \quad (3)$$

which has the following analytical solution:

$$\sigma(r) = \frac{[P(r) \cdot r^2]^{\frac{1}{k}}}{[P(r_0) r_0^2]^{\frac{1}{k}} / \sigma_0 - \frac{2}{k} \int_{r_0}^r [P(x) \cdot x^2]^{\frac{1}{k}} dx} \quad (4)$$

σ_0 , the extinction coefficient at the reference range r_0 , is the required integration constant or boundary value. If r_0 is chosen sufficiently small the transmission loss between $r=0$ and $r=r_0$ can be neglected or estimated and the boundary value derived from the extinction coefficient at the lidar site itself (the choice $r_0=0$ is impossible because of the lidar overlap function, which has been omitted in (2)). This extinction coefficient in turn can be found by different ways, e.g. by absolute calibration of the lidar system, if the constants C and k in (1) are known or realistic assumptions are possible on them, by the slope method applied to horizontal or nearly horizontal backscatter profiles if the atmosphere is sufficiently homogeneous [2], or from data delivered by any visibility meter like an integrating nephelometer.

The instabilities mentioned above arise from the fact that

5 Evaluation technique

Since the beginning of lidar remote sensing research it is known that most methods for the inversion of the lidar equation, which relates the range-dependent received power to the optical parameters of the atmosphere, tend to be instable with respect to measurement errors and to errors in the required boundary value or calibration factor. Klett [1] published an inversion method which avoids such instabilities. His basic idea is to integrate the lidar equation not in the forward, but in the backward direction. The method is demonstrated using the analytical solution of the single scattering lidar equation, which exists if the backscatter and extinction coefficients, β and σ , respectively, can be related according to this power law:

$$\beta = C \cdot \sigma^k \quad (1)$$

The single scattering lidar equation

$$P(r) = G \cdot Q \cdot \beta \cdot r^{-2} \cdot \exp\left(-2 \int_0^r \sigma(x) dx\right) \quad (2)$$

where $P(r)$ is the received power from range r , Q the transmitted laser energy and G a constant including the efficiency of the receiving system, can then be transformed

cloud profiles and found β/σ ratios ranging from about .01 to .05, in accordance with the results of Mulders /6/. These variations contribute without doubt considerably to the uncertainties associated with the application of the forward inversion method (4).

6.2 High optical depth

High optical depth conditions we call those where clouds and fog are present within the lidar beam path. At first we consider the case where ground-based fog with meteorological ranges of several hundred meters surrounds the lidar site. Fig. 8 shows a range-corrected backscatter profile obtained during such a situation. We see that the signal amplitude drops to zero before complete overlap of transmitter beam and receiver FOV is reached. It is, therefore, impossible with our lidar configuration to make quantitative measurements within fog. For such applications a much smaller receiver telescope or an open detector without any collecting optics would be required.

$\sigma(r)$ profiles from an elevated stratocumulus cloud are presented in Figs. 9A to 12B, obtained by Klett's method in all four laser wavelengths available. In the diagrams the abscissae present the extinction coefficients in a

logarithmic scale, the ordinates the altitudes, measured vertically above ground level. The lidar elevation angle was 19.2 degrees. Reference ranges were chosen around 2.5km, just before the signal amplitudes dropped below the resolution level. As boundary value 10/km was used in Figs. 9A to 12A, and 30/km in 9B to 12B. It is clearly to see that the profiles differ remarkably only in the last 50m altitude (or 150m range). Below that level, especially in the cloud-free space, the profiles are very stable with respect to the boundary value.

It is now the question whether the resulting extinction coefficients are realistic, since the assumption of the same relation (1), especially the same C value, for both the cloud and dry aerosol regimes is surely not true. By the visibility meter 21km meteorological range was recorded near ground level at the time of the lidar measurements, resulting in an extinction coefficient of .186/km. The lidar profiles, on the other hand, deliver ground level attenuations which decrease with wavelength, as expected. For the wavelength closest to the visible region, 530nm, .11/km is obtained, that is distinctly less than the nephelometer value. This deviation may be attributed to the different $\beta/\sigma(C)$ ratios for both types of scattering media. From the Mie theory follow .044 and .024 for clouds and dry

aerosol, respectively, with typical size distributions. We may now apply Klett's inversion method in two steps, as pointed out in the previous section. The transition between the dust and cloud regimes can be located at 2190m slant range or 720m altitude. At this range the amplitude of the profile Fig. 9B is .15/km. Together with the steadiness condition (9) and the two C values mentioned above we get .275/km as boundary value for the lower part of the signal, if for simplicity $k=1$ is assumed to be valid within both regimes. From the resulting $\sigma(r)$ profile, which is shown in Fig. 13, follows now a ground level value of .16/km, which is in fact closer to the measured extinction coefficient.

On the other hand, a similar result is obtained by the one-step integration, if k is set to 1.15 instead of 1.0, as shown in Fig. 14. This method has the further advantage to be applicable also in cases where the transition between dust and cloud is less sharp defined, like in the profile Fig. 15. It was obtained on the same day as the formerly discussed profiles, but at a later hour. The ground level visual range was then 10.5km, resulting in an extinction coefficient of .37/km. This value obviously agrees with the lidar value (also .37/km) already for $k=1$. The diagram Fig. 26 shows a correlation between further extinction coefficients measured by the nephelometer about 15m above

ground level (abscissae) and extinction coefficients which are derived from lidar returns from clouds and fog by Klett's method (extrapolation to ground level, ordinates). In the heading are given the correlation coefficient R , the correlation factor CF (i.e. the slope of the regression line), the intersection point B of the regression line with the ordinate axis and the number of cases N . $CF < 1$ indicates that the average lidar extinction data are somewhat smaller than the nephelometer values, but the deviations do not exceed the general scatter of the data.

We can thus state that Klett's method results in stable extinction data for turbid atmospheres if reference range and boundary value are chosen as mentioned. They are not very far from reality in spite of the single scattering assumption and the restriction to the C ratio expressed in the relationship (1).

We will now discuss briefly the applicability of the forward inversion or standard method, eq. (4). On November 4, 1984, a stratocumulus layer was present at about 300m altitude, and well mixed dust with 4.7km visual range below. We made some lidar measurements at 20 deg. elevation angle, and one at 5 deg. elevation, in both 530 and 1060nm wavelength. To the latter profiles the slope method was

applicable resulting in extinction coefficients of about 1.04/km and .68/km, respectively. From the visual range follow .83/km. The 20 deg. elevation profiles were evaluated by Klett's method as discussed above, with boundary values 30/km and $k=1$. Examples are shown in Figs. 16A and 16B for 530 and 1060nm, respectively. The lowermost σ amplitudes are .6 and .25/km for the two wavelengths. The 530nm value, .6/km, agrees fairly well with the nephelometer value, (.83/km), but the slope coefficient (1.04) is distinctly larger. A similar deviation is observed in 1060nm between the slope and Klett data. Multiple scattering cannot be responsible for these discrepancies since it would produce deviations in opposite direction. However, the 1060nm profile seems to indicate the presence of a ground-based layer of increased aerosol concentration, with a thickness of about 30m. Because of the longer non-overlap range this layer does not show up in the 530nm profile.

We now applied the forward inversion method using the above-mentioned ground level data as boundary values. Figs. 17A and 17B show the results for the slope values. In both profiles singularities occur within the cloud region, i.e. the denominator in (4) becomes zero and then negative. If the boundary values are taken from the Klett curves (.6 and

.25/km, respectively), the singularities are shifted more towards the end of the range interval (Figs. 18A and 18B), but they are still present. Of course it is possible to adjust the boundary value such that no singularity occurs, but this procedure is actually already equivalent to the backward inversion technique.

We want to point out that the transition layer between clouds and the cloud-free space underneath shows considerable differences in thickness as well as in structure from case to case. We have already seen two examples for different thicknesses of that layer (Figs. 10 and 15). A still sharper transition is evident in the profile Fig. 19. In this case the near-ground visual range was $>40\text{km}$. Obviously the thickness of the transition layer increases with the aerosol concentration below. Due to water vapor absorption with increasing humidity, the particles may grow and give rise to increased backscatter already below the real cloud base. Sometimes we see, finally, a multi-layered structure of the cloud base (Fig. 20). This structure often changes rapidly with time. More detailed examples will be presented in section 7.

Concluding this section we present application examples for the Klett formula with simplified multiple scattering

correction (9). Fig. 21 shows a ~~6~~-profile from a low-level stratus cloud, calculated by the single scattering formula (6), i.e. with the correction factor F in (8) set to zero, as indicated in the heading of the Figure. For a receiver FOV of 10 milliradians, like in our system, and for a cumulus cloud (Deirmendjian's /14/ type C-1) Kunkel and Weinman /12/ found a value of about .3 for the correction function F . If (9) is applied to the same lidar return with this F value, the profile shown in Fig. 22 results. The difference to the profile Fig. 21 is just that the extinction coefficient is enlarged by the factor $1/(1-F)=1.43$. For simplicity, the total profile Fig. 22 was calculated with $F=.3$, including also the lower, cloud-free part, where single scattering conditions are more probable. An improvement of the evaluation should be possible by a two-step procedure, i.e. by application of the formula (6) between the reference range 537m and the range 290m, and the single-scattering formula (6) to the interval from zero to 290m, the cloud-free space. As boundary value for the second step the extinction coefficient resulting from the first step for $r=290m$ is to be used. Fig. 23 shows the result of this procedure for the lower range interval. Again no dramatic changes are observed.

If the multiple scattering correction formula (8) is applied to the previously discussed profile Fig. 10B, we get the profile shown in Fig. 24. Again the profile amplitude is raised by the factor 1.43. If the cloud-filled and cloud-free regimes are treated separately in the same manner as shown in Figs. 22 and 23, the profile Fig. 25 is obtained for the lower interval up to 2190m slant range or 720m altitude. The near-ground extinction coefficients resulting from both profiles, Fig. 24 and 25, agree better with the nephelometer value, .186/km, than that from the profile calculated by the single scattering formula (6).

7 Extinction coefficient profiles from clouds and fog

During the course of this project several hundreds of backscatter profiles from cloudy and foggy atmospheres have been obtained. We have seen in the previous sections that such profiles can be evaluated by Klett's method in a nearly straight-forward manner. The range just before the lidar return drops below the resolution limit should be chosen as reference range, and a large number greater than about 10/km may be used as boundary value, which is uncritical in such cases. We thus developed an automatic program which is able to calculate σ -profiles from a selected set of lidar returns. That range where the signal amplitude, seen from

the rear end of the interval, reaches first the digital value 6 (2.3 is chosen as reference range, and 20/km as boundary value). The exponent k is set to unity, since there is no cogent reason to choose any other value. The altitude ranges are selected automatically among the values 100, 200, 300m and so forth, according to the vertical altitude of the reference point. None of the corrections for multiple scattering etc. mentioned above are applied, since this would involve an individual treatment of each signal and would furthermore not come up with dramatic changes of the resulting profiles. For each diagram a heading is created containing first a figure number, 7.1 and so forth, where the part after the period is incremented automatically. It follow then the label "Klett- profile", the wavelength used, the lidar elevation angle, date (year, month, day) and time interval (Central European Time, CET) of the measurement, the reference range RM, and boundary value SM and exponent K (here 20/km and 1.0, respectively, throughout). A total of 303 diagrams have been created in this way. After plotting they were inspected critically and some of them, where the automatic procedure to find RM did obviously not work, recalculated manually. Other profiles were cancelled completely, and so some figure numbers are missing.

It is known that the amplitude of the lidar return signal is

reduced below a certain minimum range by incomplete crossover of laser beam and receiver FOV and in cases also due to overloading of the transient recorder. Since it is impossible to find this minimum range automatically, the profiles were always formally calculated up to zero range. Whereas this non-correct part of the profiles is easily recognized in cases where overloading occurred (that part of the curves increasing smoothly proportional to the log of range or altitude), this is more difficult in other cases. The minimum range was marked, therefore, by a small circle in a part of the diagrams.

Since backscatter from clouds in general changes rapidly within a minute or less, most of the presented profiles are single shots in order to show the momentary cloud structure. The above-mentioned method to increase the amplitude resolution by combining profiles obtained with different input ranges is not applicable, therefore, for cloud signals. So in some diagrams unavoidable digitization errors show up. Another source of errors are the rapid amplitude fluctuations which occur sometimes in cloud returns. They cause the occasional negative overshoots which are unavoidable in spite of careful design of the amplifiers. In some cases this effect causes small breaks in the calculated Klett profiles, where the amplitudes drop

to zero.

The remaining cloud extinction profiles are presented in the appendix, Figs. 7.1 to 7.303. We give now short descriptions of the weather situations during the measuring dates and some remarks on the presented profiles.

82-11-10, Figs. 7.1-7.12

After rainfall during nighttime stratocumulus banks were observed at the mountain slopes under a closed Sc cover. The air in the cloud-free space was extremely clear so that here the extinction coefficients remain only in 347nm wavelength within the presented range. The striking sharp cloud boundaries are to be noted.

82-12-14, Figs. 7.13-7.27

Occasional light snow showers, Cu fra and Sc at the slopes, lower boundaries between 250 and 720m altitude. Their structure shows heavy fluctuations causing negative overshoots of the signals.

83-01-19, Figs. 7.28-7.29

Cu fra clouds occurred at the end of the range interval at 830m altitude. The signal fluctuations below come from light snowfall, which is obviously very inhomogeneous.

83-02-10, Figs. 7.30-7.58

Two layers of Stratus/Stratocumulus were observed at 450 and 630m, respectively. The lower layer was temporarily transparent. In the afternoon only one layer remained at 600m. The aerosol concentration below the clouds was higher than in the previous cases, and a more smooth transition of the extinction coefficient was found. The thickness of the transition layer varied between 80 and 200m.

83-03-16, Figs. 7.61-7.65

Intense, moist haze near ground level was covered by an opaque stratus layer (advection fog) at about 200m altitude. Note the very smooth transition between the two layers.

83-06-29, Figs. 7.66-7.73

Cu fra clouds occurred at 620m altitude and temporarily at 620m. The haze layer below was rather moist in the morning and showed a remarkable structure due to precondensation effects. Later on the humidity decreased, the ground visual range increased from 10 to 22km and the structures disappeared. Again the cloud extinction shows a strong spatial structure.

83-07-19, Figs. 7.74-7.81

After a thundershower in the early morning Cu fra clouds were observed at 400-600m altitude, sometimes with multi-layered structure. Relatively sharp cloud boundaries were noted in this case in spite of the not small aerosol concentration below. An excellent agreement was found between visibility-derived extinction coefficients (6.1/km) and near-ground values of 530nm lidar profiles (6.0/km).

83-10-20, Figs. 7.82-7.84

Underneath a multi-layered stratocumulus at 700-800m fairly homogeneous dust with visibilities from 23 to 26km was recorded. The thickness of the cloud transition layer was 30m.

83-11-16, Figs. 7.85-7.87

A low-level opaque stratus layer (advection fog) was recorded at 300m altitude, and intense moist haze below (vis. range 7km). The lidar profiles show remarkable vertical structure.

84-02-28, Figs. 7.88-7.90

As remainder of a closed Sc layer, dissolving banks of Sc and Cu fra occurred at the mountain slopes at 700m. The cloud signals show considerable multilayer structure. The

profile Fig. 7.88 has already been discussed in detail in the previous section.

84-03-01, Figs. 7.91-7.122

In the morning a ground based layer of advection fog was present, which lifted slowly in the course of the day, i.e. the lower boundary ascended up to 200m in the afternoon. Correspondingly the visual range at ground level increased from .4 to 7km. Useful lidar returns could not be obtained before noon, when the lower cloud boundary had arrived at 90m altitude. Then the profiles show at first some multilayer structure, which vanished toward the evening. Finally a very smooth and continuous transition between cloud and cloud-free space is observed.

84-03-27, Figs. 7.123-7.125

At the clones at 600m Cu fra clouds occurred. The atmosphere below was extremely clear after a rain front, the extinction coefficients here remained below the limits of the diagram. Again a very thin transition layer was recorded (thickness below 10m).

FIG. 9A, 840228, 11:08
347NM, SM=10/KM, K=1

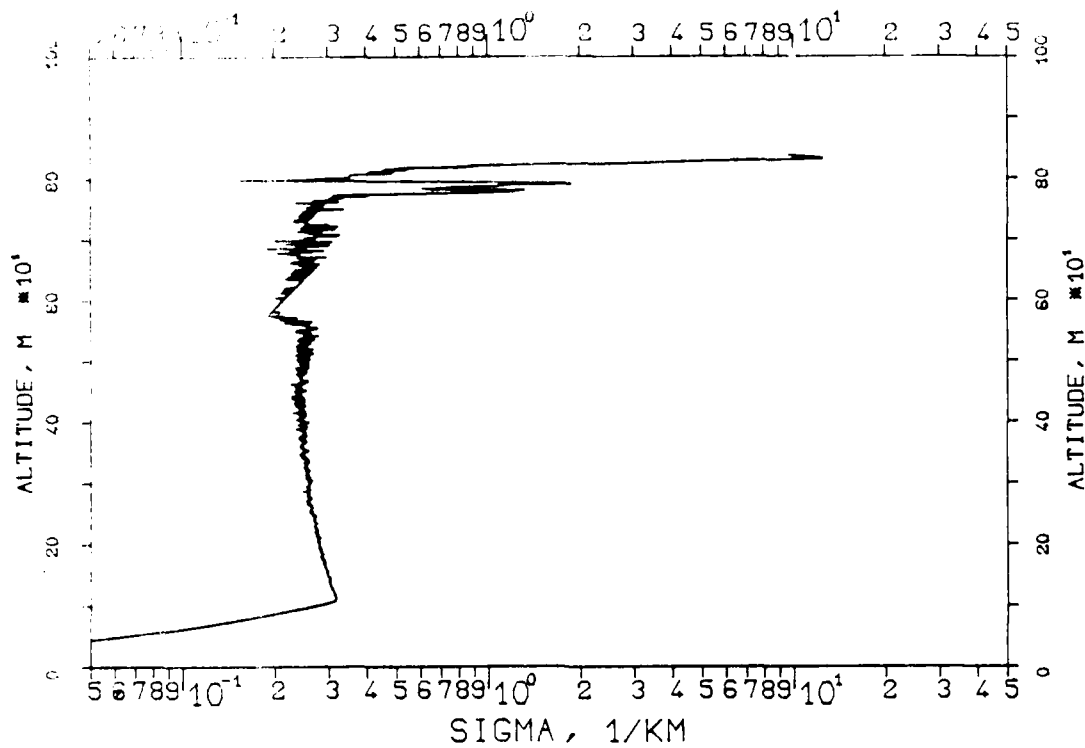
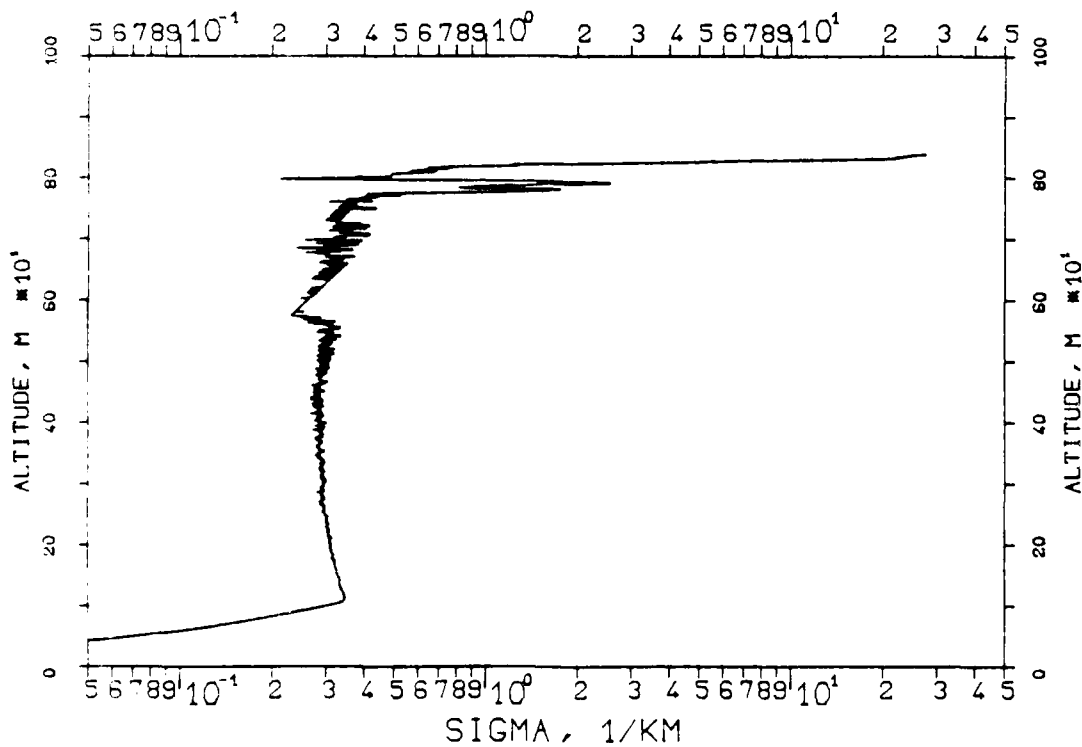


FIG. 9B, 840228, 11:08
347NM, SM=30/KM, K=1



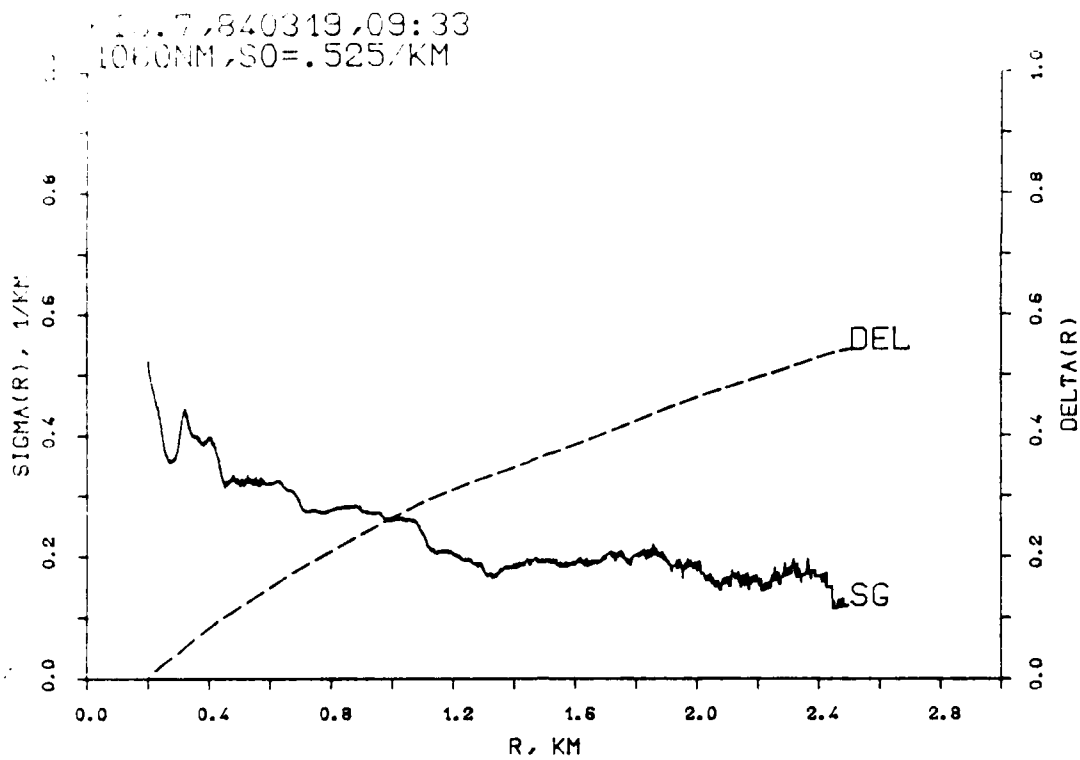


FIG. 8
RANGE-NORM. BACKSCATTER PROFILE, LIN.
841116, 10:44-10:44,CET
1060NM,EL.10DG00MN

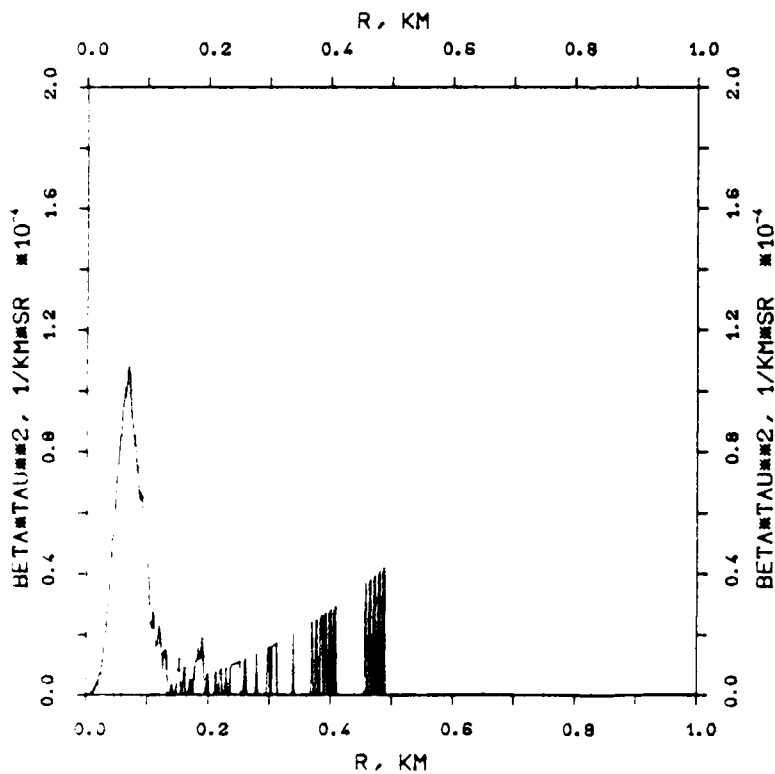


FIG. 5
 RANGE-NORM. BACKSCATTER PROFILE, LIN.
 840319, 09:32-09:35, CET
 1060NM, EL. 19DG12MN

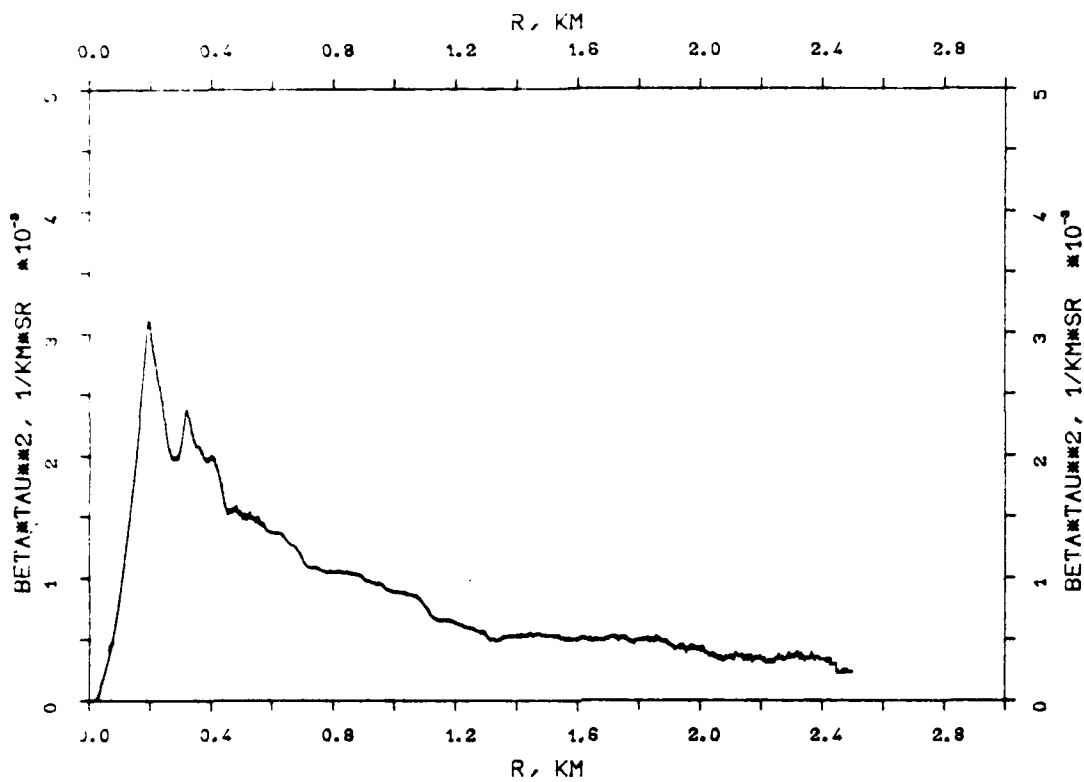


FIG. 6, 840319, 09:33
 1060NM, SM = .126/KM

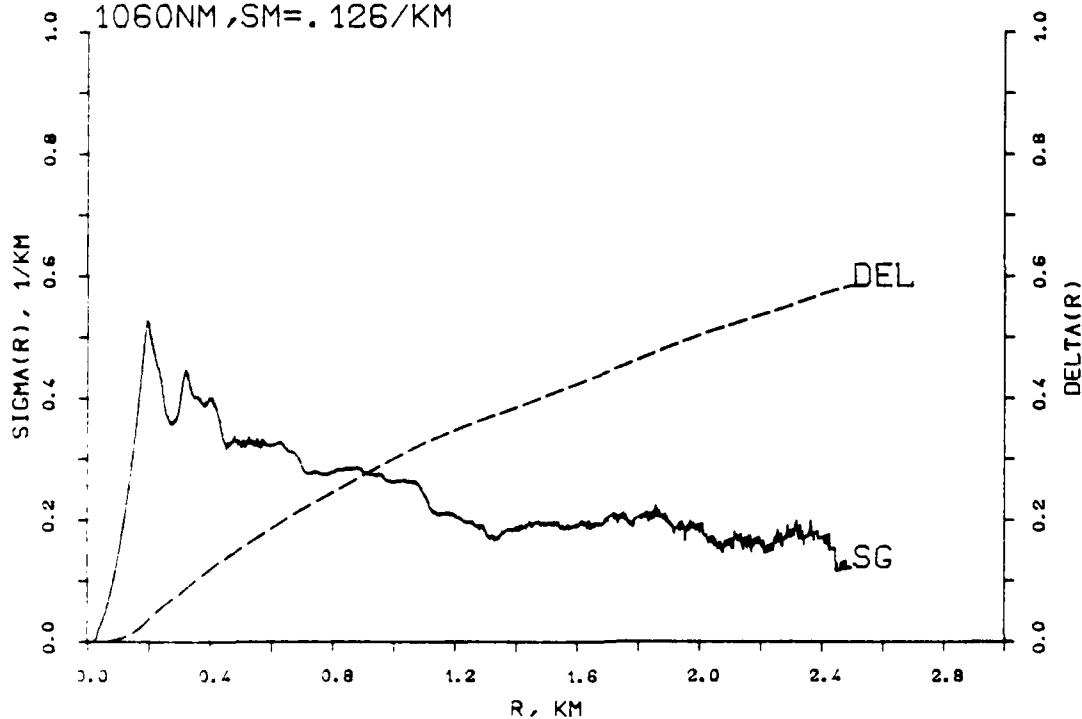


FIG.4: EXTINCTION DATA COMPARISON
LIDAR-Transm. VIS, 840315

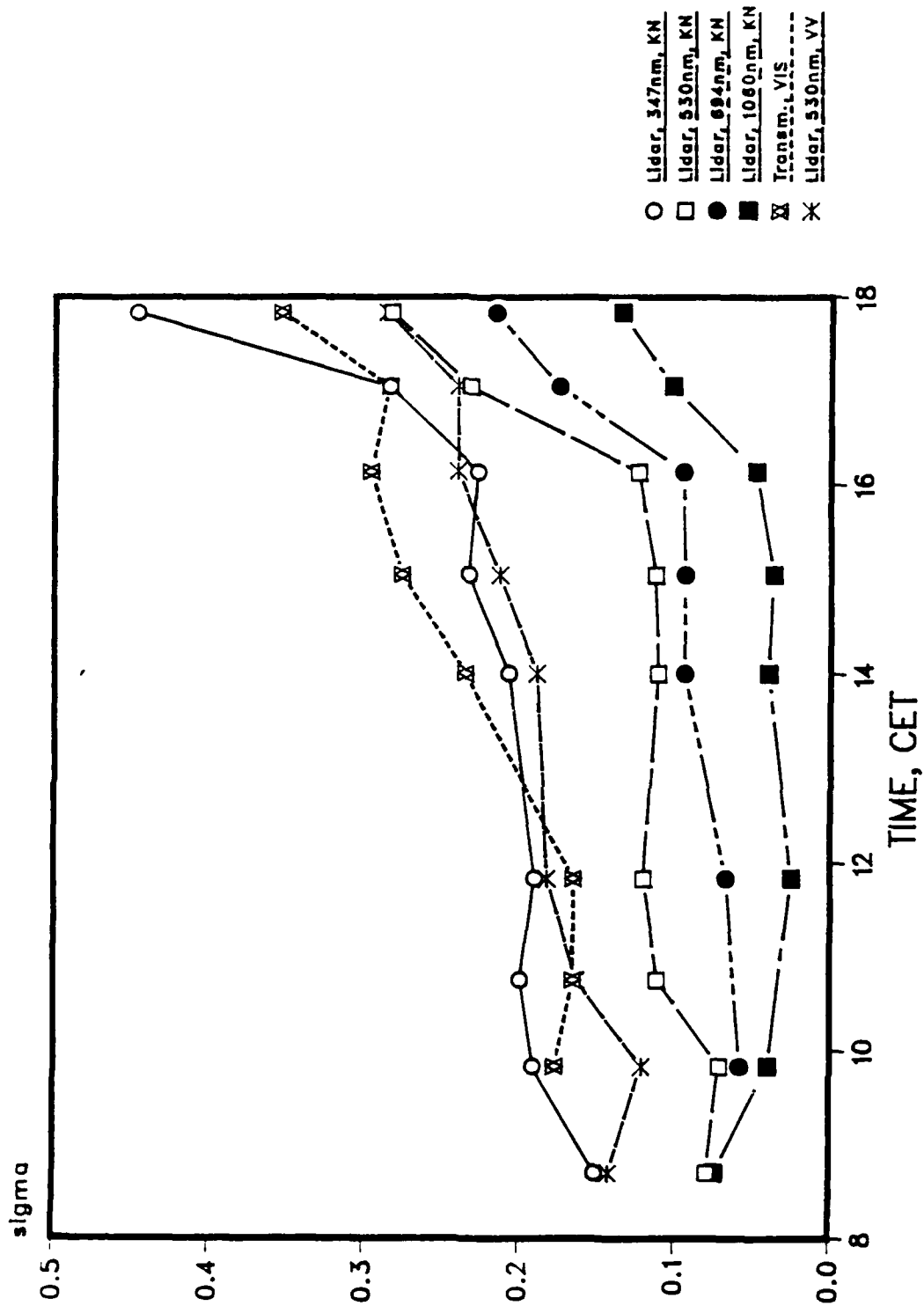
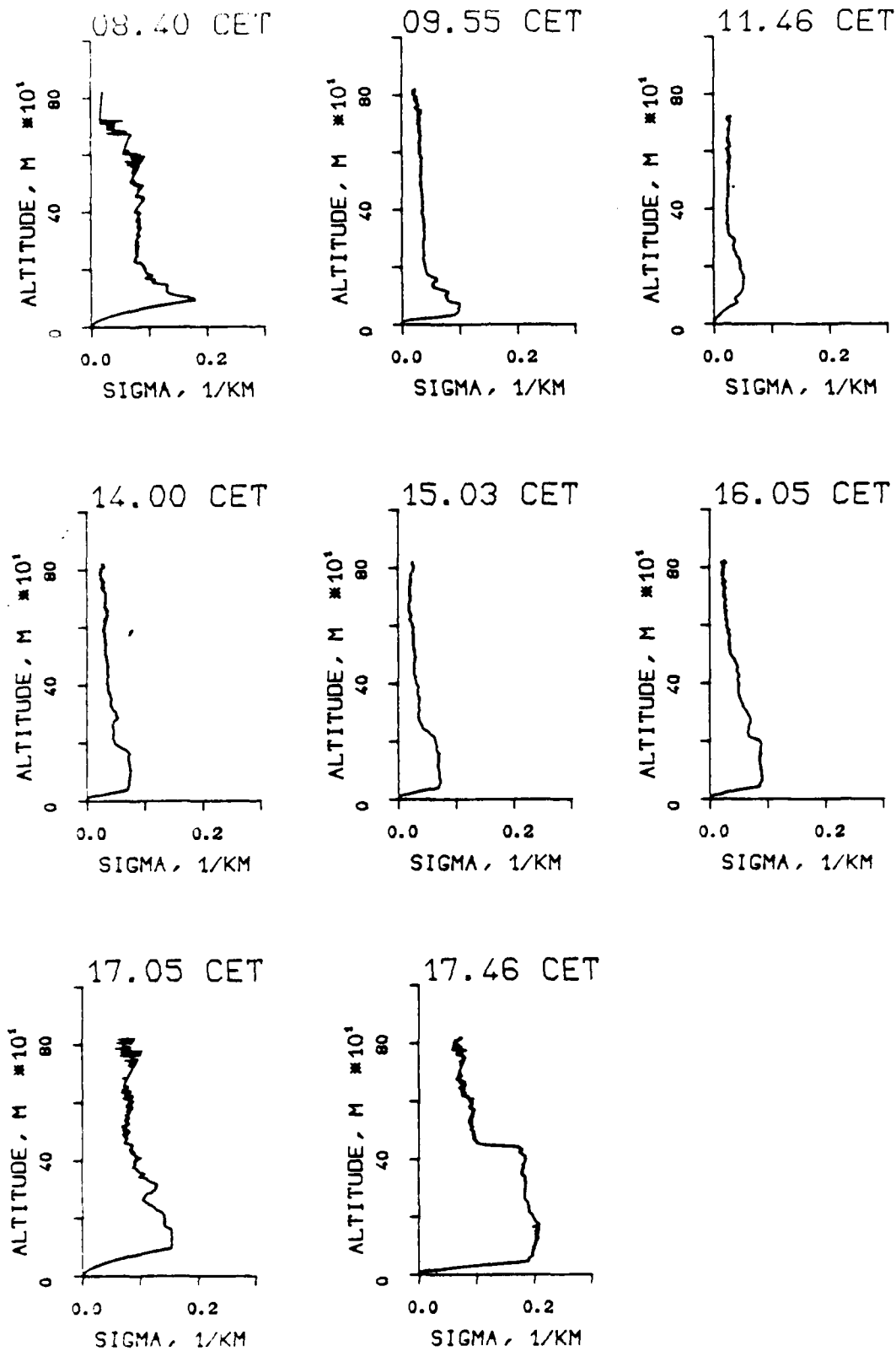


Fig. 3



REPRODUCED AT GOVERNMENT EXPENSE
 FIG. 1
 RANGE NORM. BACKSCATTER PROFILE, LIN.
 820811, 12:51-12:53, CET
 0530NM, EL. 19DG 12MN

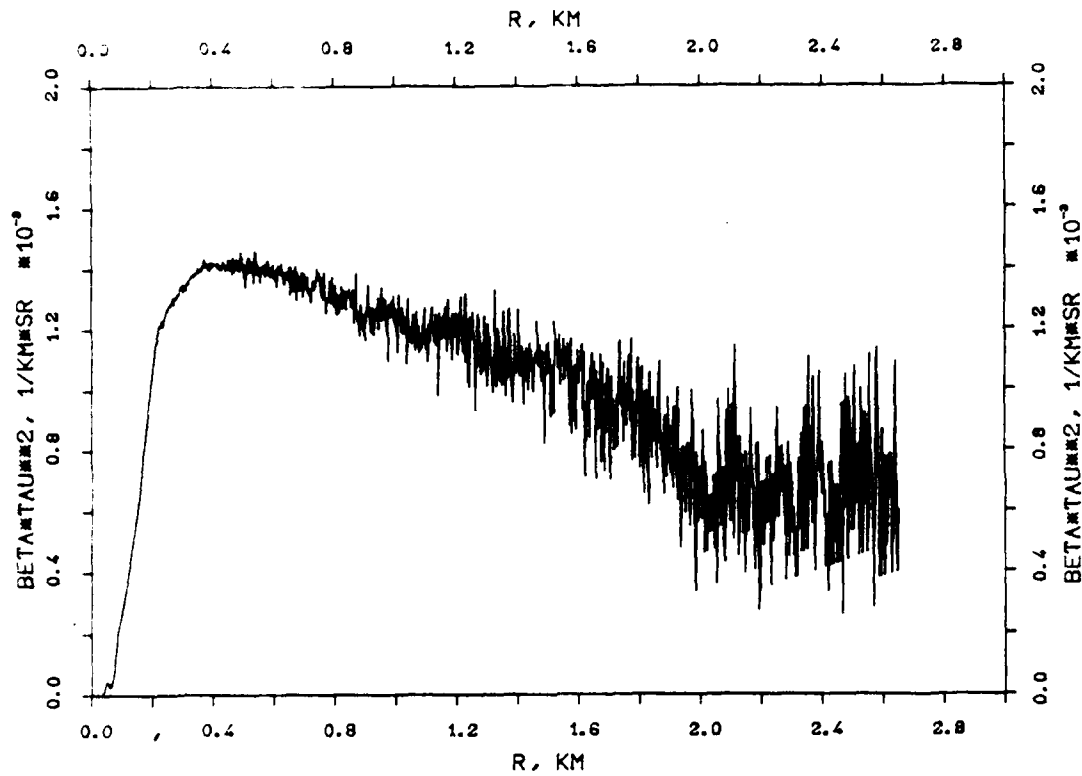
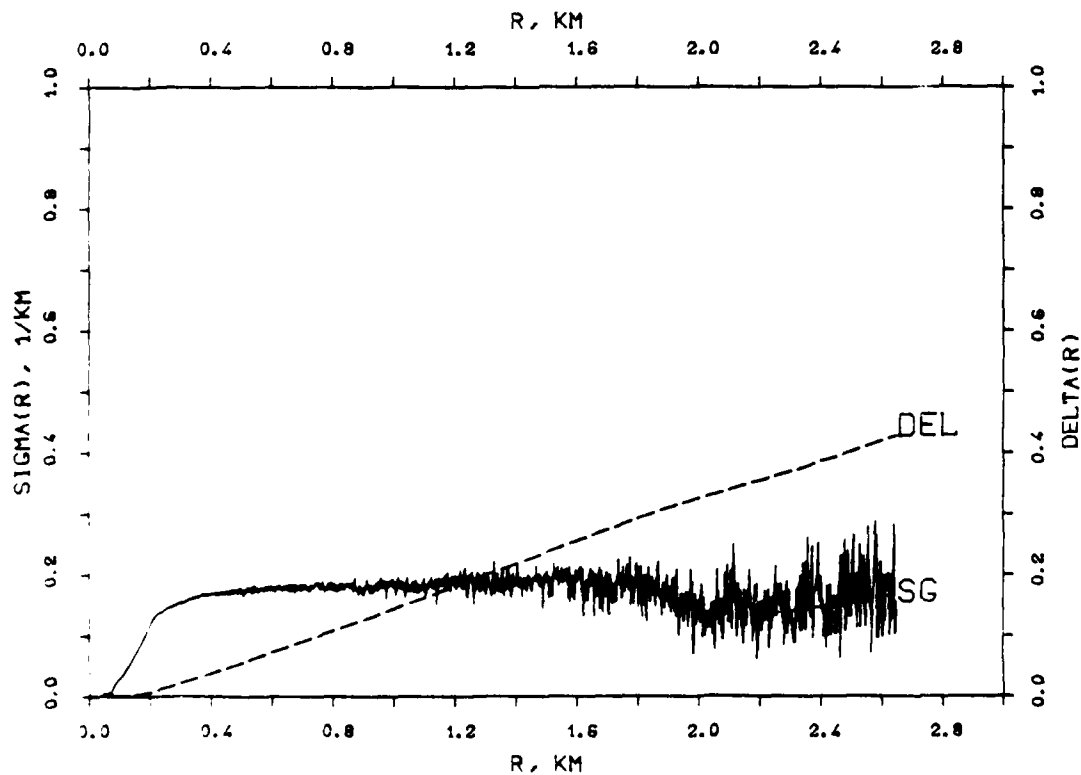


FIG. 2
 KLETT-PROFILE, 0530NM, EL. 19DG 12MN
 820811, 12:51-12:53, CET
 RM=2.650KM, SM= 0.1730/KM, K=1.000



APPENDIX

Figures 1 - 26

to Section 6

Figures 7.1. - 7.303

to Section 7

9 References

- /1/ J.D.Klett, "Stable Analytical Inversion Solution for Processing Lidar Returns," Appl.Opt.20, 211(1981)
- /2/ G.J.Kunz, "Vertical Atmospheric Profiles Measured with Lidar", Appl.Opt.22, 1955(1983)
- /3/ E.D.Hinkley ed., "Laser Monitoring of the Atmosphere," Springer, New York 1976
- /4/ W.G.Tam, "Aerosol Backscattering of a Laser Beam," Appl.Opt.22, 2965(1983)
- /5/ J.W.Fitzgerald, "Effect of Relative Humidity on the Aerosol Backscattering Coefficient at 0.694 and 10.6-um Wavelength," Appl.Opt.23, 411(1984)
- /6/ J.M.Mulders, "Algorithm for Inverting Lidar Returns: Comment," Appl.Opt.23, 2855(1984)
- /7/ J.H.Richter, RSG8 Meeting at FfO, Tübingen, 1984
- /8/ F.G.Fernald, "Analysis of Atmospheric Lidar Observations: some Comments", Appl.Opt.23, 652(1984)
- /9/ U.Halavee and A.Kohnle, "Fast Computer Code to Fit Aerosol Size Distributions and to Calculate Optical/IR Propagation Coefficients", Report FfO 1981/128
- /10/ E.P.Shettle and R.W.Fenn, "Models for the Aerosols of the Lower Atmosphere and the Effects of Humidity Variations on their Optical Properties," AFGL-TR-0214
- /11/ J.A.Weinman, "Effects of Multiple Scattering on Light Pulses Reflected by Turbid Atmospheres," J.Atmos.Sci.33, 1763(1976)
- /12/ K.E.Kunkel and J.A.Weinman, "Monte Carlo Analysis of Multiply Scattered Lidar Returns", J.Atmos.Sci.33, 1772(1976)
- /13/ B.T.N.Evans, "On the Inversion of the Lidar Equation," Defense Research Establishment Valcartier Report 4343/84
- /14/ D.Deirmendjian, Appl.Opt.3, 187(1964)

Under moderate optical depth conditions, on the other hand, Klett's method delivers results which agree with transmissometer data as long as realistic boundary values are available. If not, the forward inversion method can be applied, but a more precise boundary value is then required. It can be derived from the backscatter profile itself if the lidar is calibrated absolutely and the B/σ ratio is known, or, since it is difficult to keep the calibration status constant over long time periods, from data delivered by some visibility meter like an integrating nephelometer. Such a comparably simple and low-cost instrument may easily be operated close to the lidar.

set to 10 and 15 degrees only. The profiles thus present not only vertical structures. Considerable inhomogeneities were recorded throughout the period, but the temporal variations slowed down somewhat in the afternoon.

8 Conclusions

From the hitherto gained experiences with the evaluation of lidar returns we may conclude that Klett's backward inversion method provides extinction coefficients versus range which are very stable with respect to measurement errors and errors in the choice of the boundary value. In cases of high optical thickness of the range interval, i.e. especially when the lidar signal vanishes in clouds or fog, the resulting $\sigma(r)$ profiles depend only to a small extent upon the boundary value if the reference range is chosen properly. Furthermore, the profiles are in general not far from reality if the exponent k in the β - σ relation (1) is set to values around 1, in spite of the single scattering assumption in the lidar equation (2) and to the restrictions introduced by the assumption of the validity of (1). Thus the lidar, together with Klett's evaluation method, is an excellent tool for vertical structure measurements under low visibility conditions, especially for the study of the fine structure of cloud bases.

few minutes.

84-12-03, Figs. 7.232-7.256

This day two stratocumulus layers occurred at 200 and 600m, respectively. The upper layer covered the complete sky, the lower one only about half of it and disappeared completely during the two hours measurement time. Laser shots were fired in short time intervals down to a minute in order to show the rapid temporal fluctuations of the observed structures. At the end of the interval all structures below 500m had disappeared, and a smooth transition to the upper cloud layer was recorded. The oscillations showing up in some profiles are caused by occasional amplifier ringing and are thus not real.

84-12-04, Figs. 7.257-7.303

This final series at the fen area was extended over more than 4 hours, and from the totally obtained 71 lidar returns 47 were selected as useful for the presentation of the atmospheric structure and its temporal variations. The sky was completely overcast by a stratus layer with slowly descending base at about 100m above ground level. By eye observations from one of our mountain stations the upper boundary of this layer was located at 300m above ground. Because of the low cloud base the lidar elevation angle was

84-10-12, Figs. 7.208-7.209

Again a stratus cloud at 160m above dense and moist ground-based haze occurred at the measurement site. Since the lidar was fired at only 5 degr. elevation angle, the cloud was not recorded before 1.8km range and so the signal shows some considerable digitization errors.

84-11-04, Figs. 7.210-7.215

Between an St/Sc layer at 230m altitude and ground level dense and moist haze was observed another time. Some lidar returns were obtained at different elevation angles, showing a two-fold cloud base. The ground-level extinction data resulting from the Klett inversion have already been discussed in section 6 (Figs. 16-18).

84-11-16, Figs. 7.217-7.227

This and the remaining two measurement series were obtained at the selected site outside of the mountain area, where ground-based fog and low-level stratus occur more frequently. A shallow fog layer was transported up through the valley between the measurement site and the institute by the catabatic valley wind. Outside the mountains the fog layer base was somewhat elevated at 50m above ground. During noon time the fog dissolved. The profiles show considerable inhomogeneities which varied rapidly within a

84-08-27, Figs. 7.163-7.192

A ground-based fog layer with visibilities fluctuating between .5 and 2km ascended slowly and dissolved in the early afternoon. The ground visual range increased up to 9km. The first profiles at 10 degrees elevation again should represent in the first place horizontal structures. However a multilayer structure of the cloud base remains throughout the measurement period. In spite of the only moderate visual range at ground level a quite sharp transition between cloud and haze is recorded finally. Maybe the visibility was mainly reduced by high humidity and not by a high concentration of dry aerosol material.

84-08-29, Figs. 7.193-7.194

The two profiles indicate an Sc layer at 1100m altitude. The aerosol underneath is fairly homogeneous and moderately concentrated (visual range 10km). The transition layer is 30m in this case and thus relatively thick.

84-10-08, Figs. 7.195-7.197

Initially a fog layer at 60m was observed, which became transparent two hours later. A second cloud layer at 600m became thus visible through the remainders of the fog.

84-04-04, Figs. 7.126-7.137

The lidar returns were obtained from a cumulus cloud, with base at first at 700, then at 1200m. Between 500m and the cloud base a region with increased, irregular backscatter is observed, originating from light snowfall.

84-04-11, Figs. 7.138-7.156

A low-level stratus cover with base at 200-300m was present, and strong, moist haze underneath. Again a multilayer structure was observed in the beginning, which was later on replaced by a smooth transition between haze and cloud. It is interesting to note that profiles obtained at 7.5deg. elevation angle show more fine structure than those at 15 degrees. Obviously the observed inhomogeneities extend more in the horizontal than in the vertical direction.

84-04-18, Figs. 7.157-7.162

A stratocumulus layer is found at 500m altitude, with strong multilayer structure at the base. Also the aerosol below with 15km vis. range shows considerable inhomogeneity, probably due to precondensation effects.

FIG. 10A, 840228, 11:00
530NM, SM=10/KM, K=1

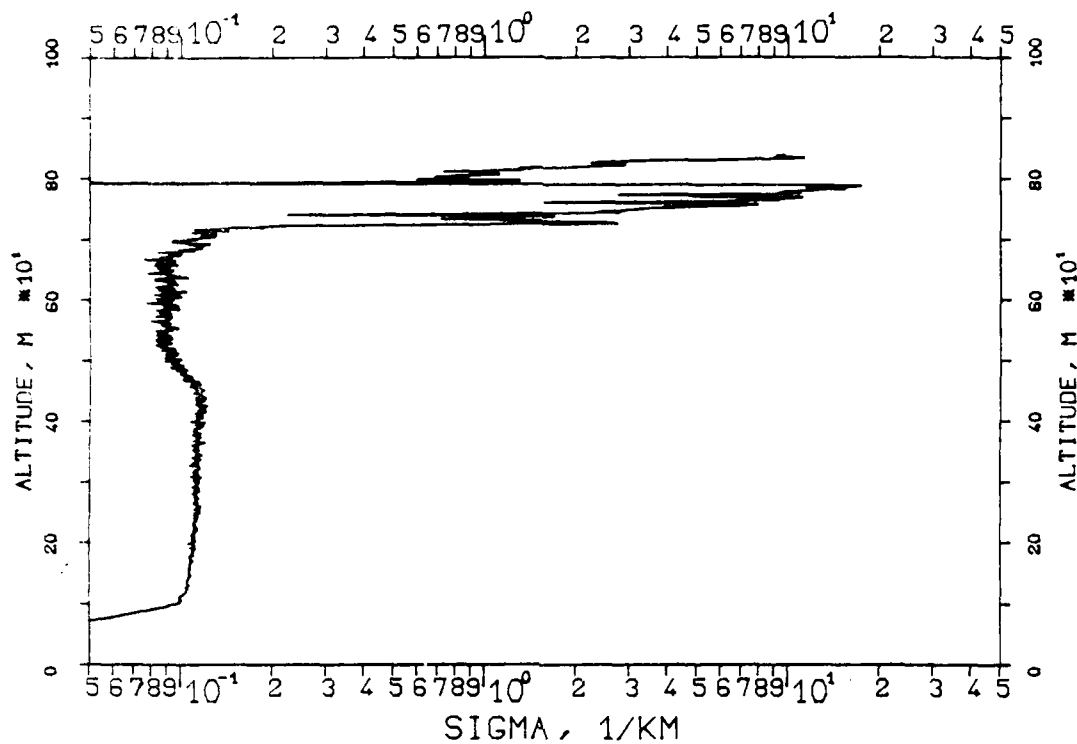


FIG. 10B, 840228, 11:00
530NM, SM=30/KM, K=1

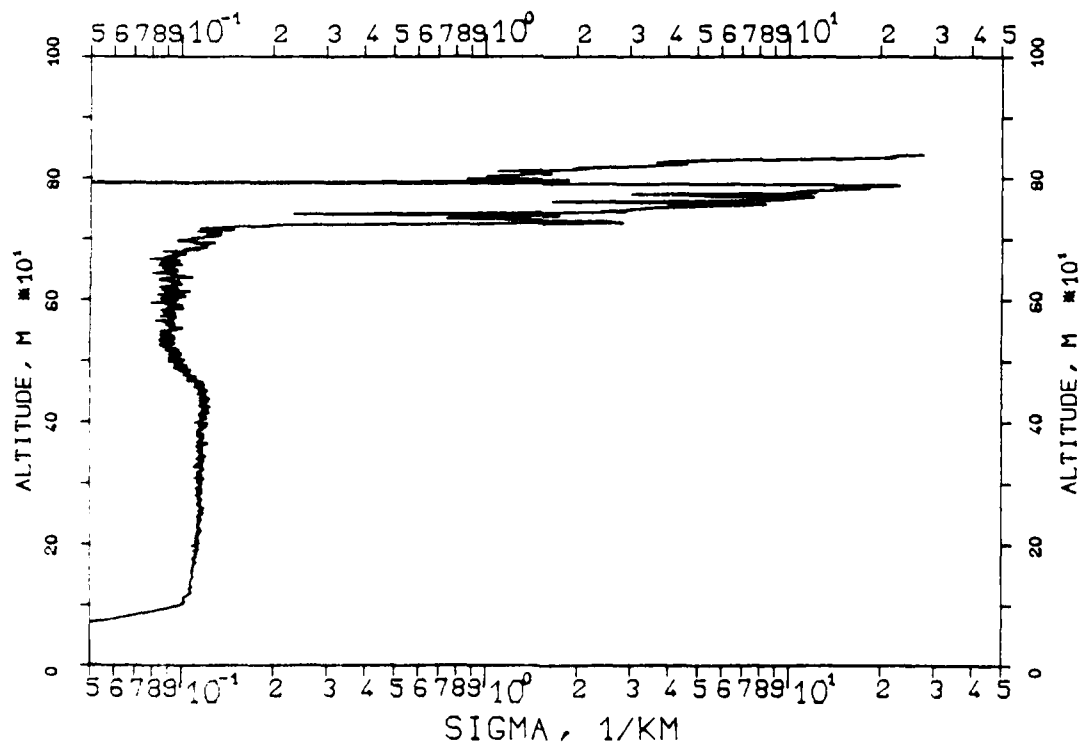


FIG. 11A, 840228, 11:05
694NM, SM=10/KM, K=1

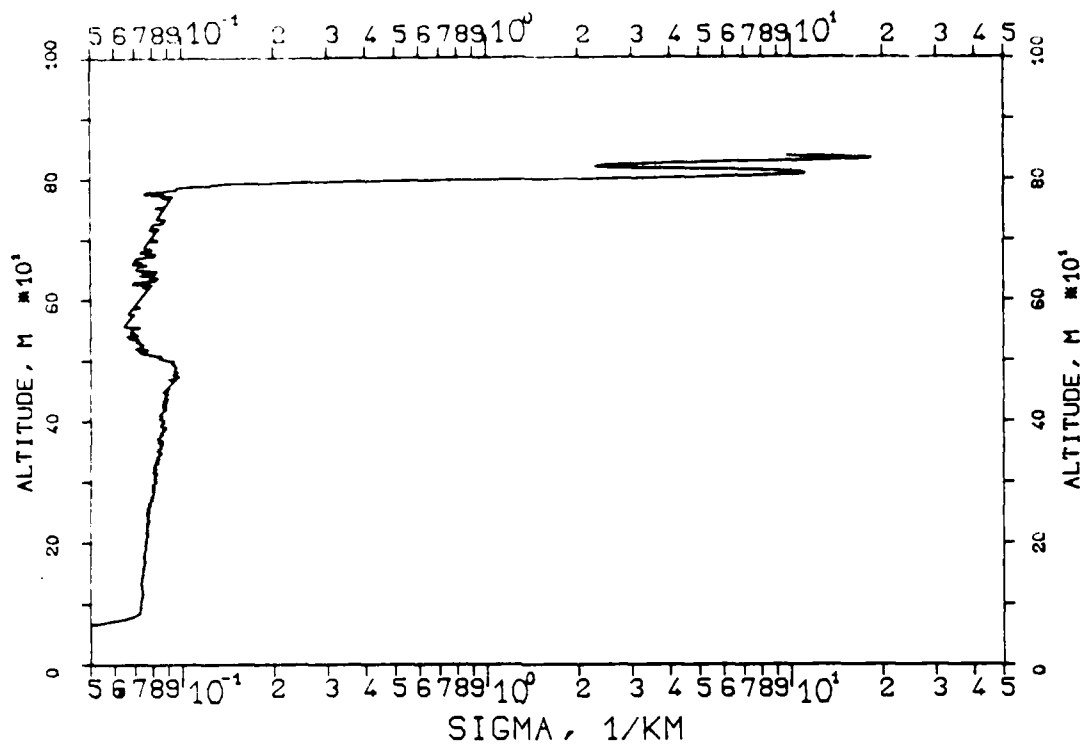


FIG. 11B, 840228, 11:05
694NM, SM=30/KM, K=1

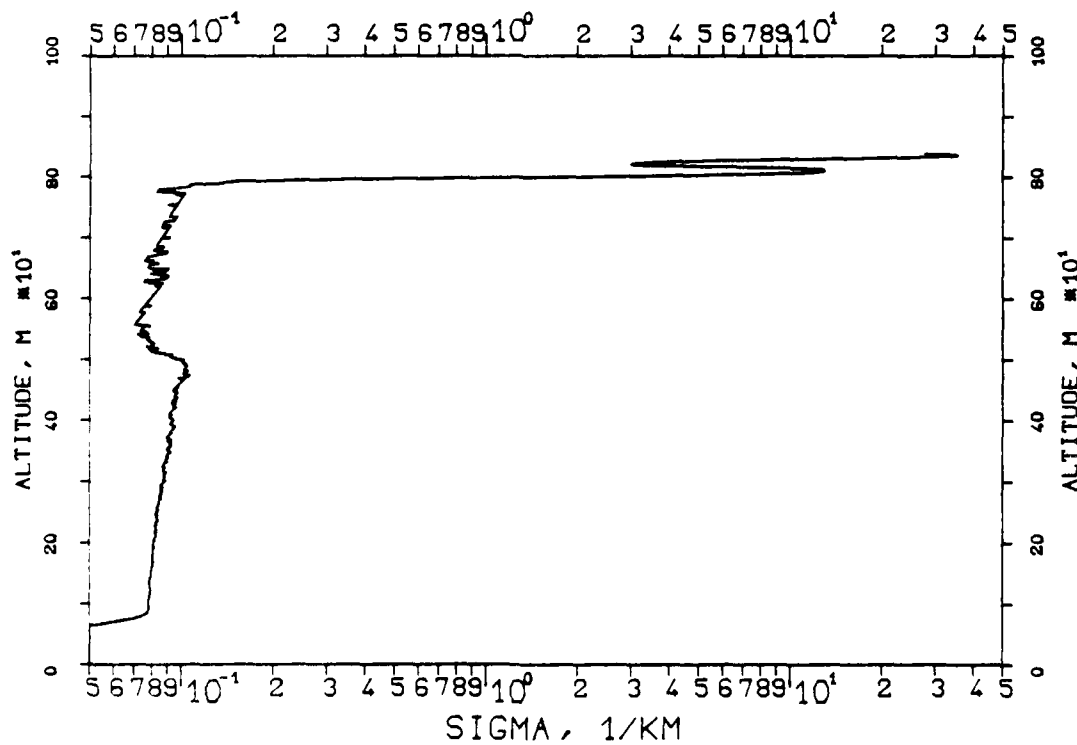


FIG. 12A, 840228, 11:03
1060NM, SM=10/KM, K=1

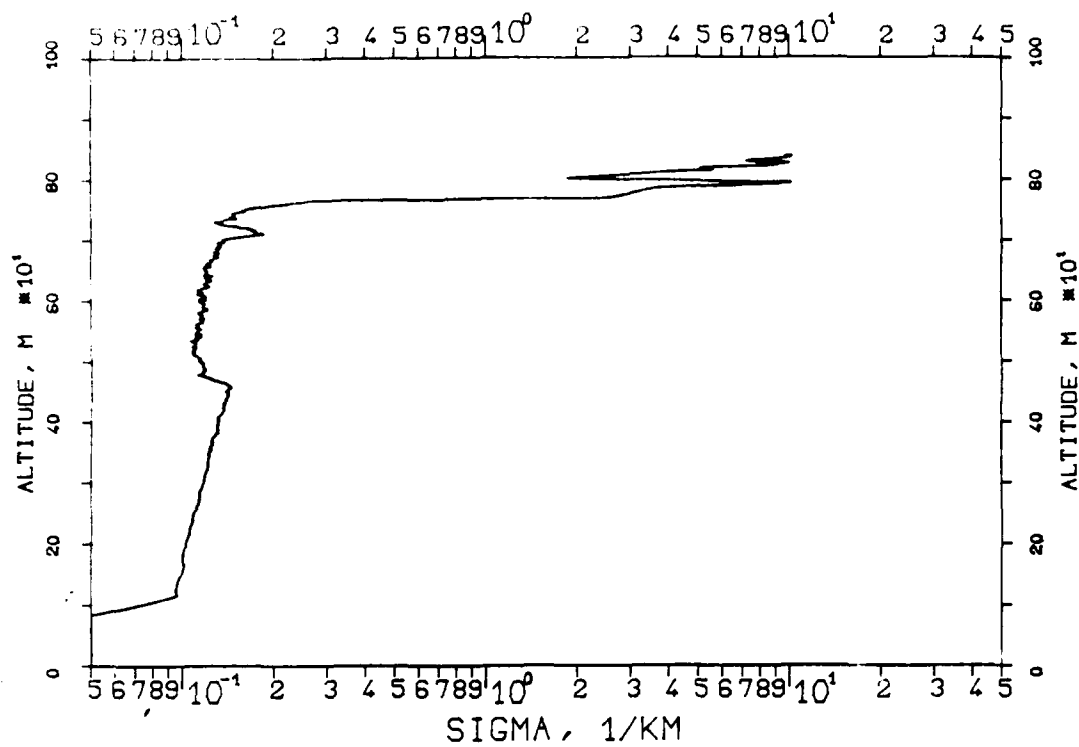


FIG. 12B, 840228, 11:03
1060NM, SM=30/KM, K=1

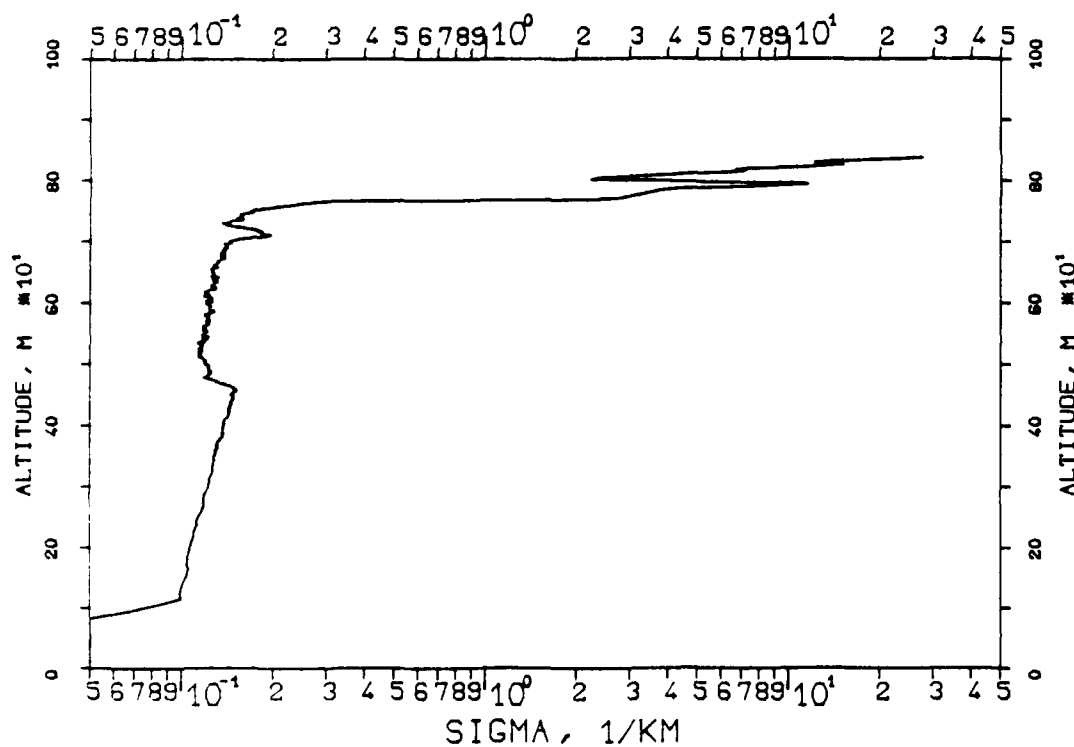


FIG. 13, 840228, 11:00
530NM, SM=.275/KM, K=1

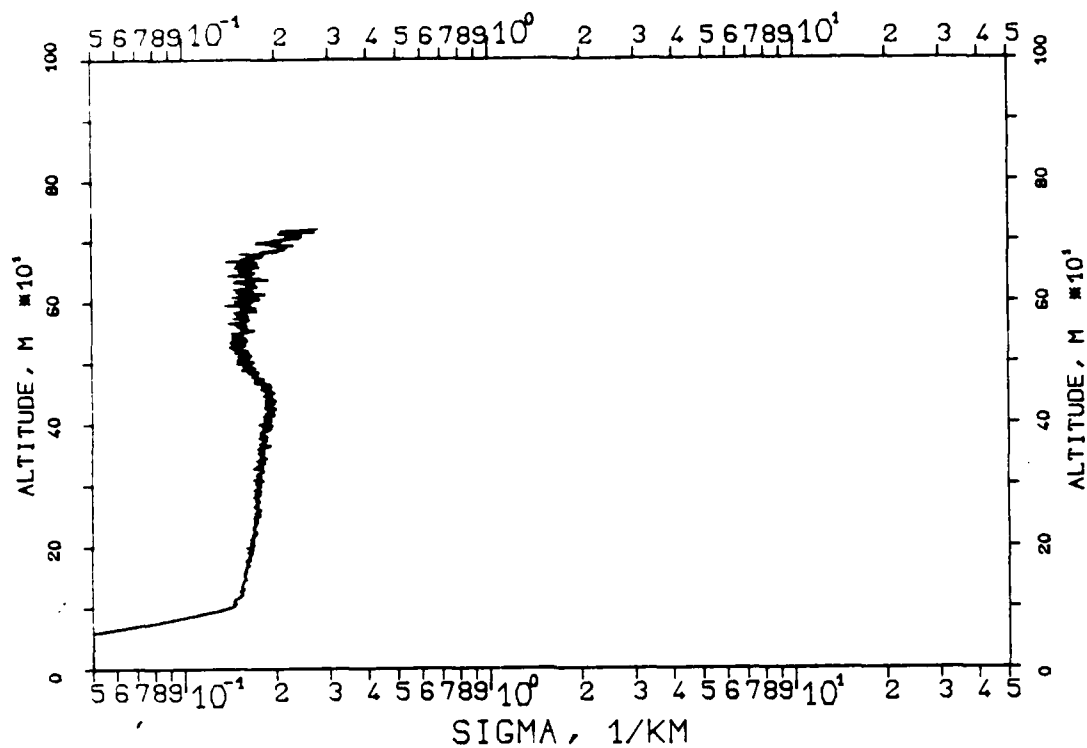


FIG. 14, 840228, 11:00
530NM, K=1.15

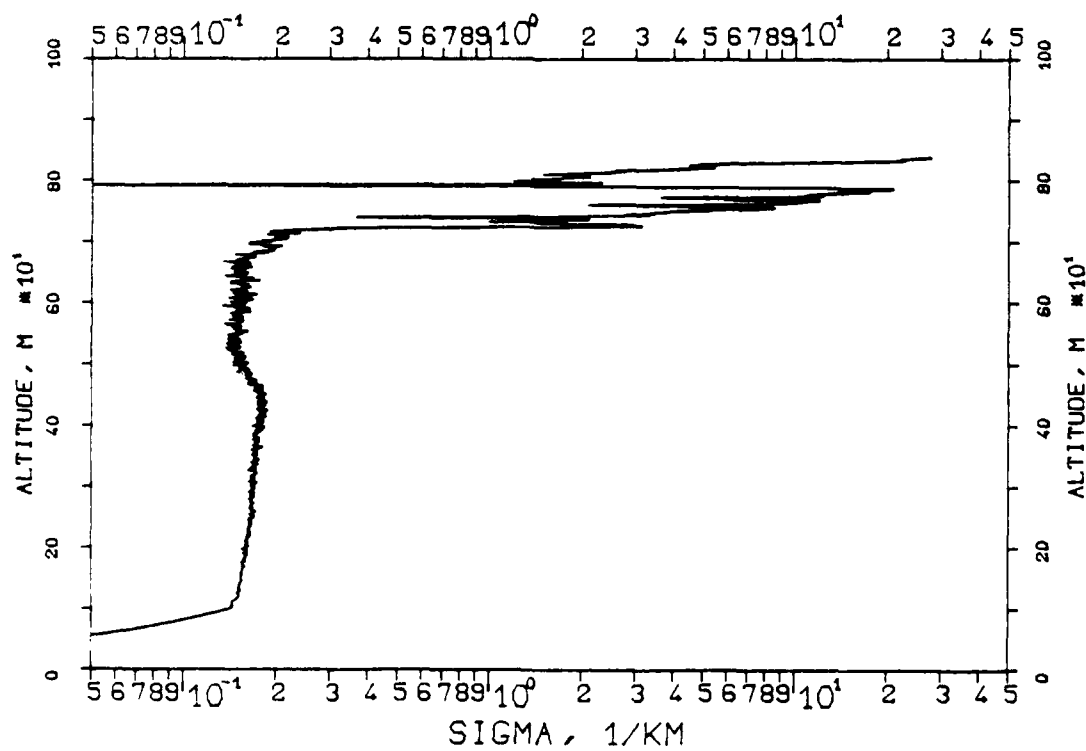


FIG. 15, 840228, 17:40
530NM, SM=30/KM, K=1

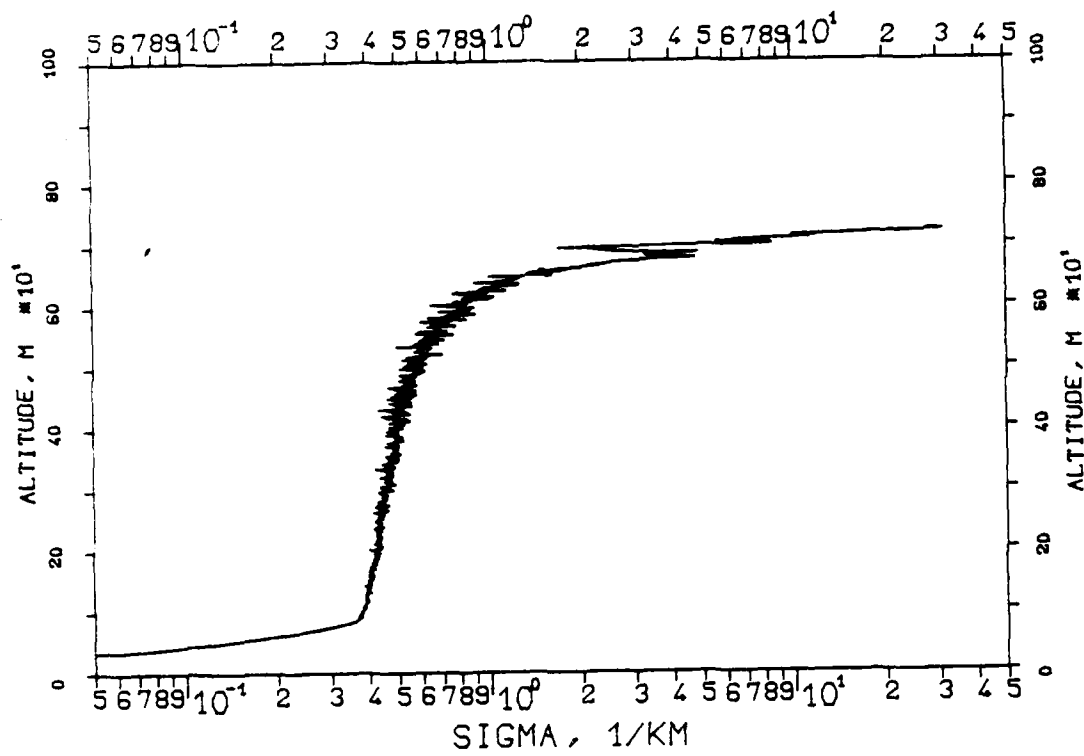


FIG. 16A, 841104, 9:08
530NM, SM=30, KM, K=1

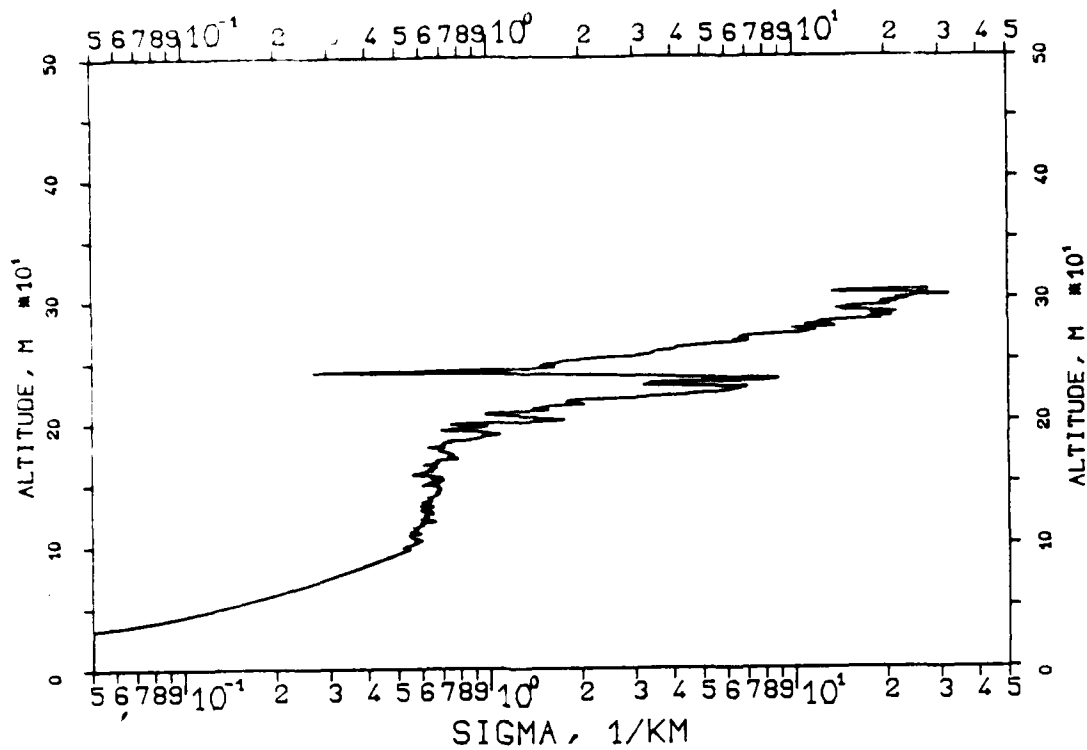


FIG. 16B, 841104, 9:09
1060NM, SM=30/KM, K=1

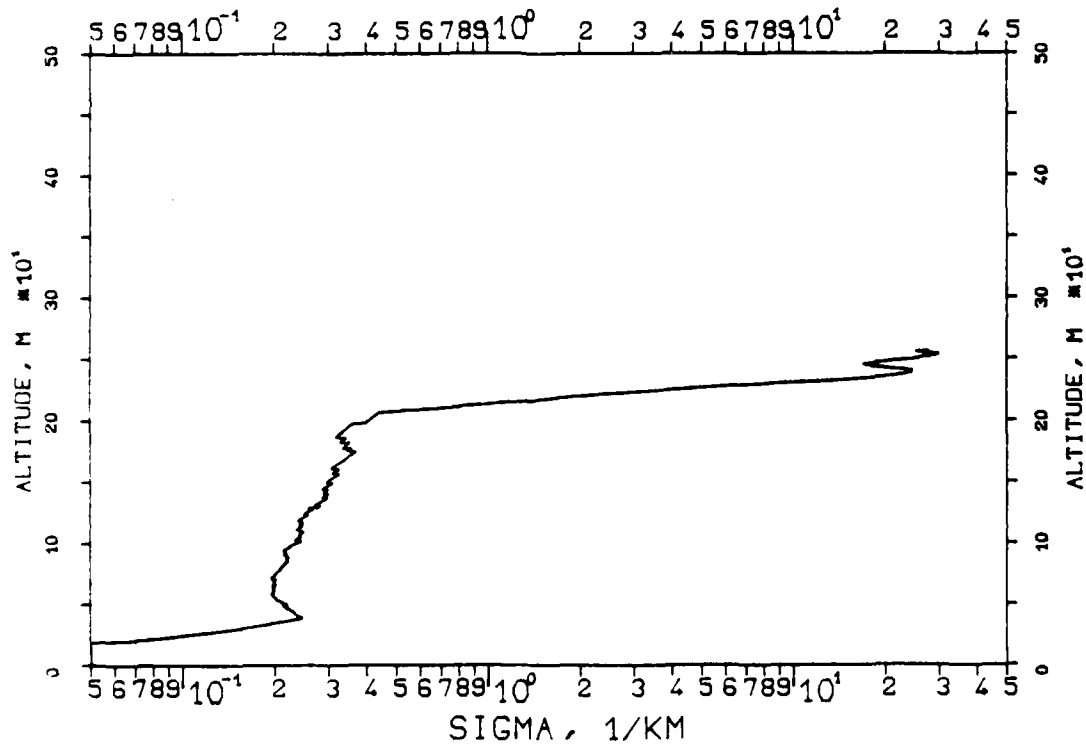


FIG. 17A, 841104, 9:08
530NM, $S_0=1.04/\text{KM}$, $K=1$

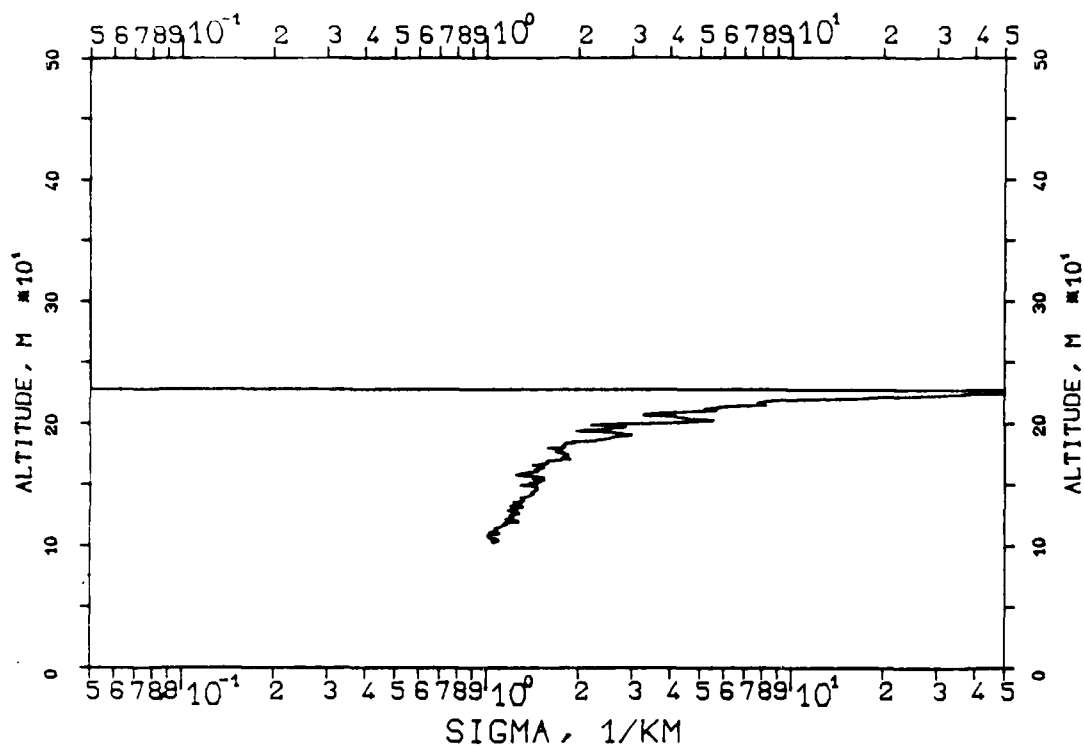


FIG. 17B, 841104, 9:09
1060NM, $S_0=.68/\text{KM}$, $K=1$

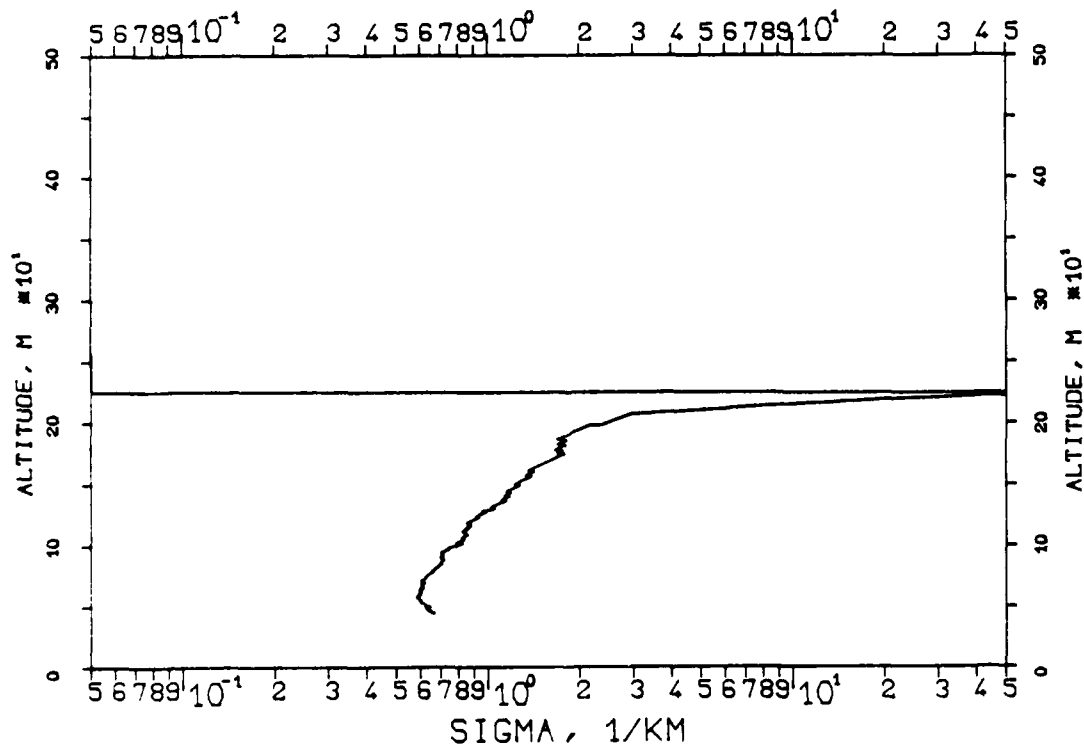


FIG. 18A, 841104, 9:08
530NM, $S_0 = .6/\text{KM}$, $K=1$

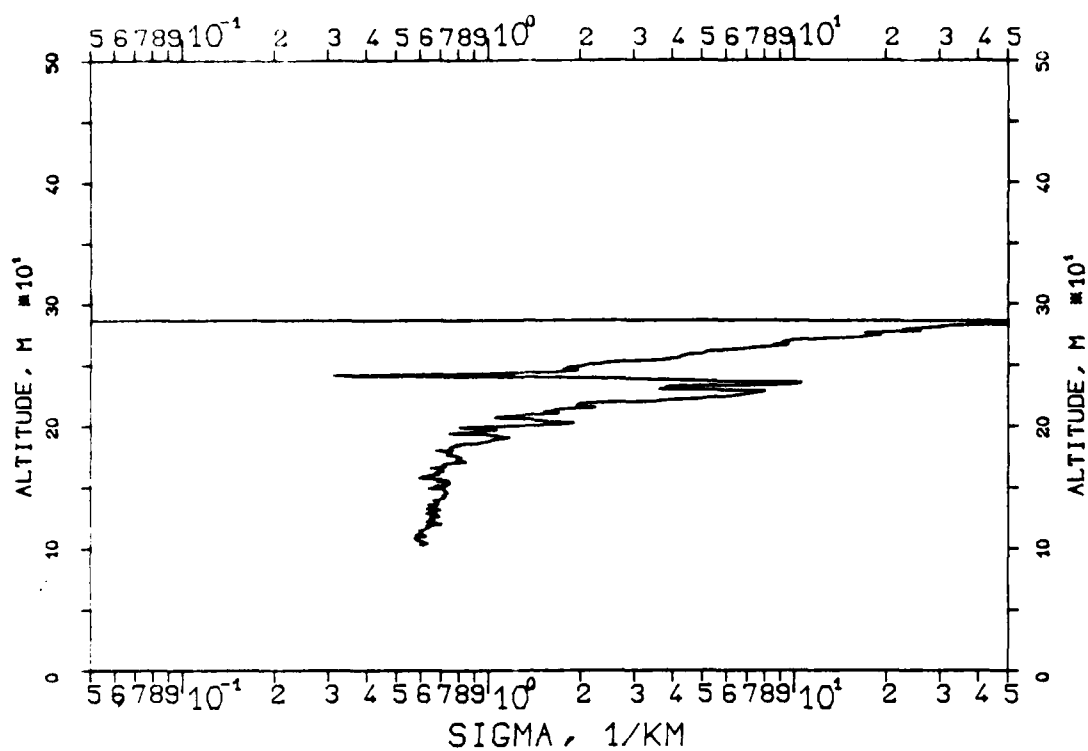
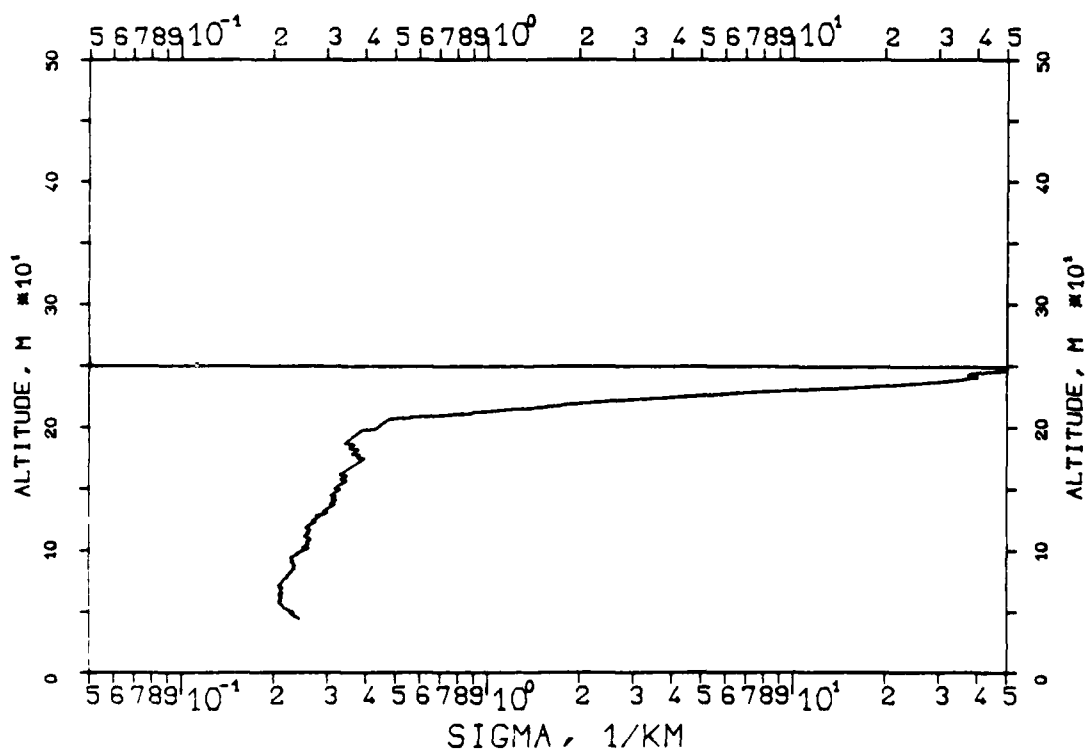


FIG. 18B, 841104, 9:09
1060NM, $S_0 = .25/\text{KM}$, $K=1$



110.10,821110,09:18
530NM,SM=30/KM,K=1

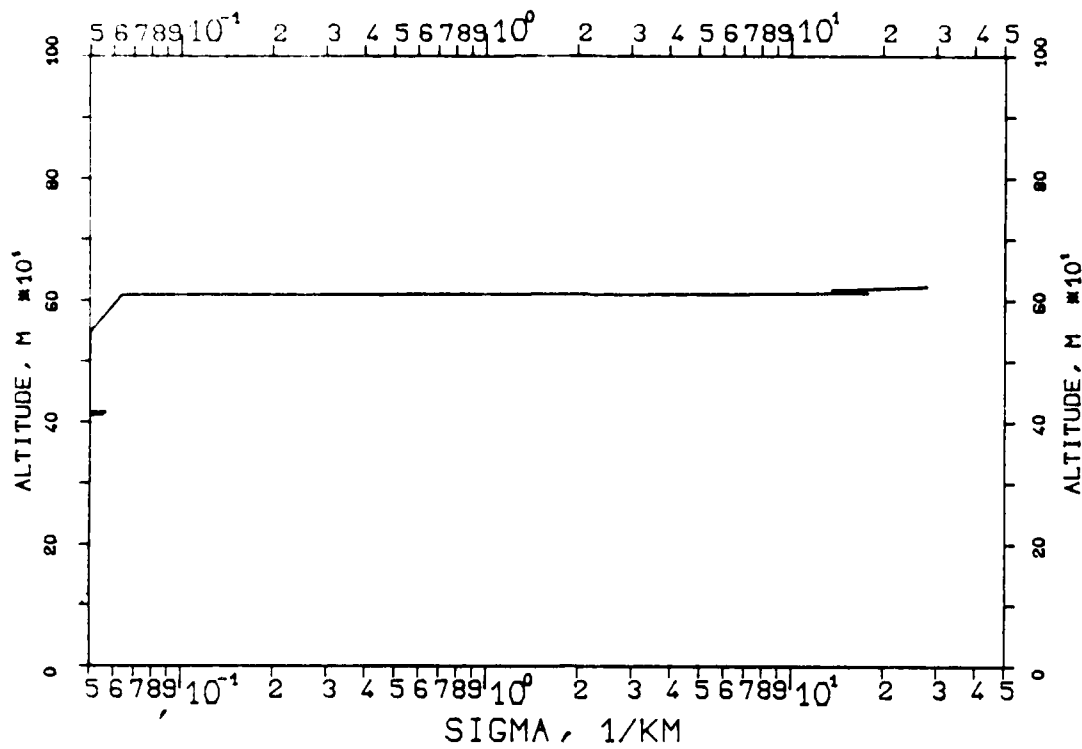


FIG. 20,840418,08:54
1060NM,SM=30/KM,K=1

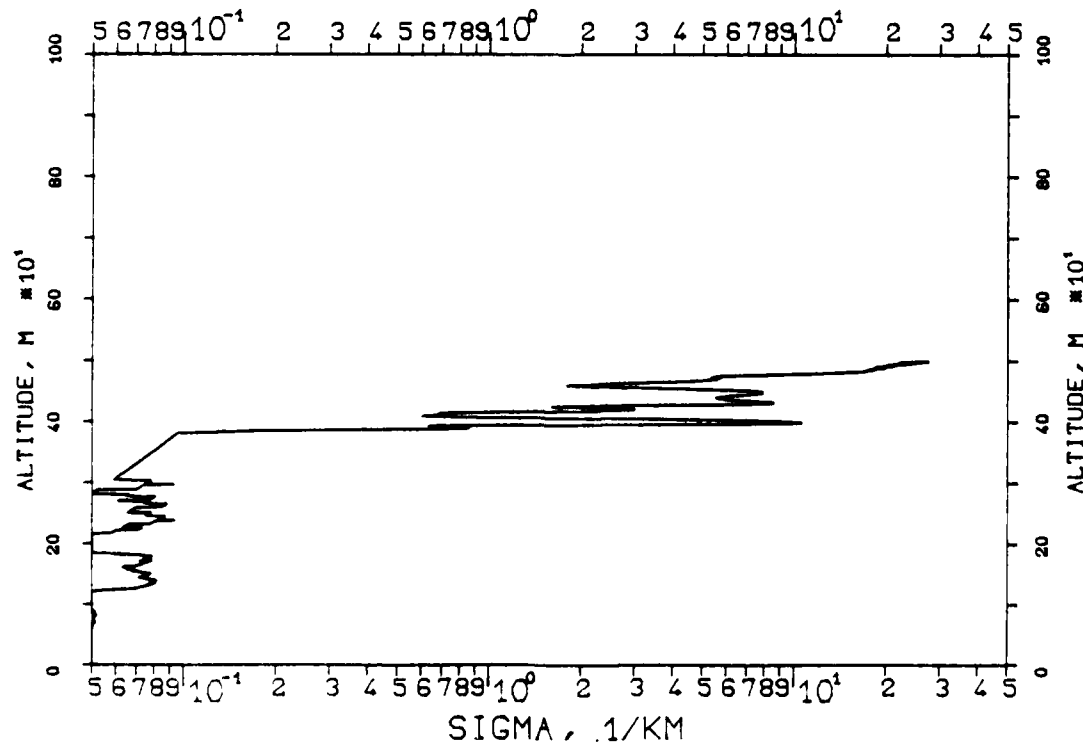


FIG. 21, F=0.0
KLETT-PROFILE, 0694NM, EL. 15DG00MN
841204, 14:30-14:30, CET
RM=0.537KM, SM=20.0000/KM, K=1.000

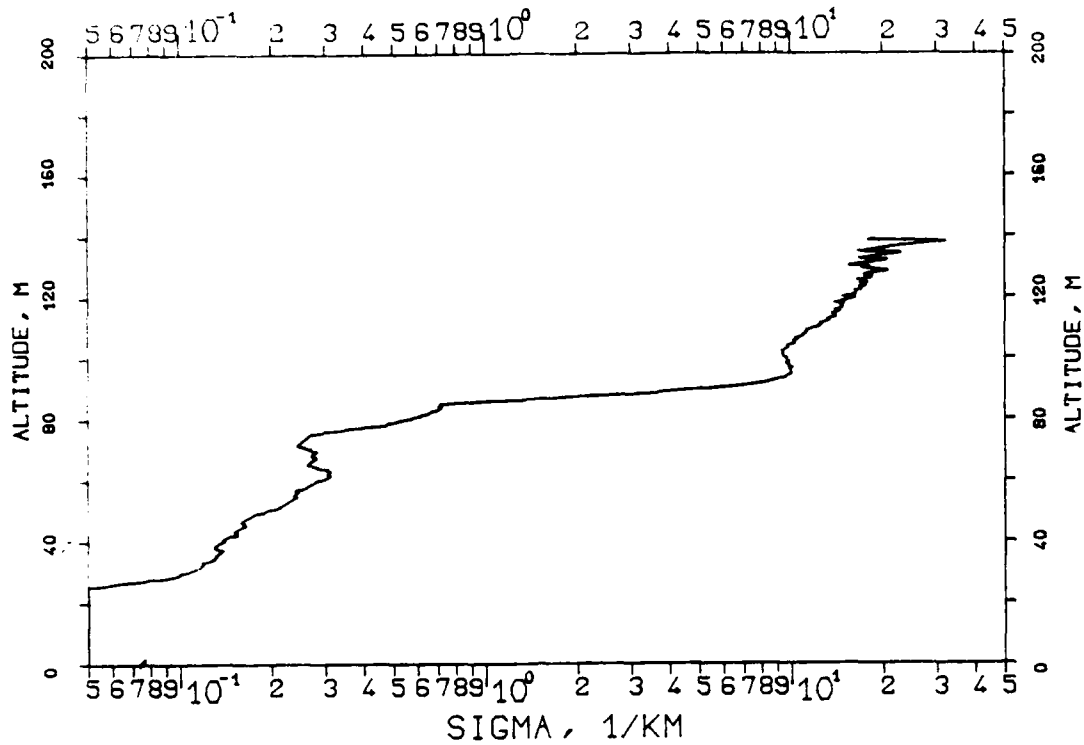


FIG. 22, F=0.3
KLETT-PROFILE, 0694NM, EL. 15DG00MN
841204, 14:30-14:30, CET
RM=0.537KM, SM=20.0000/KM, K=1.000

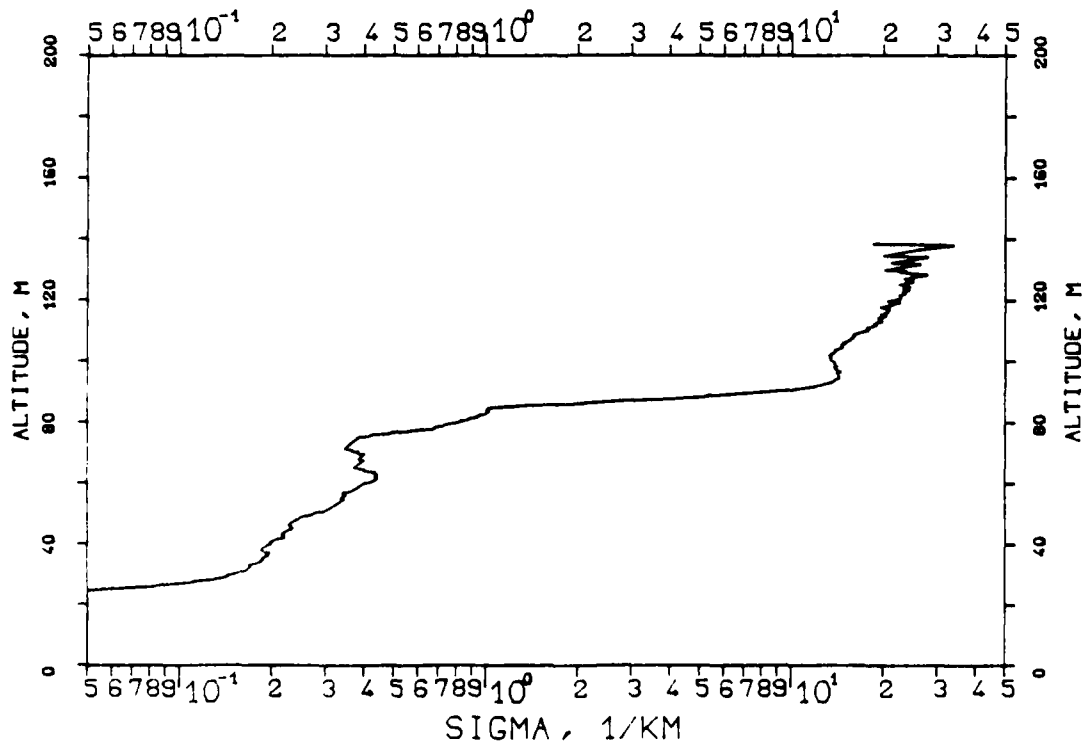
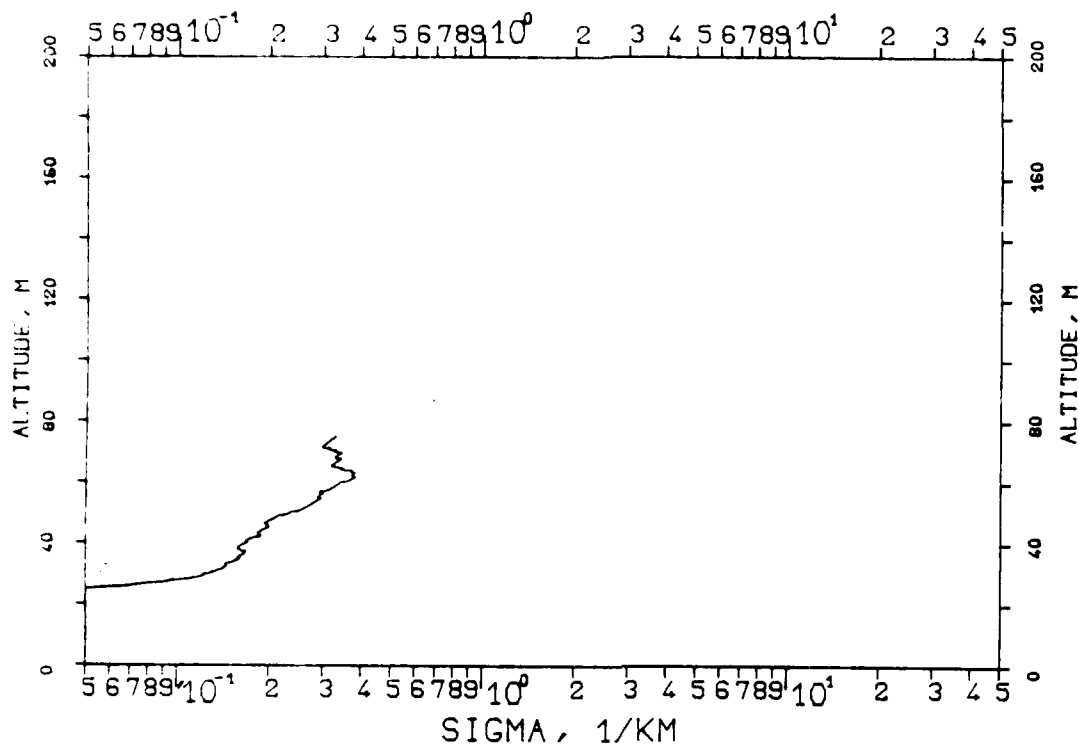


FIG. 23, $F=0.0$

KLETT-PROFILE, 0694NM, EL. 150G00MN

841204, 14:30-14:30, CET

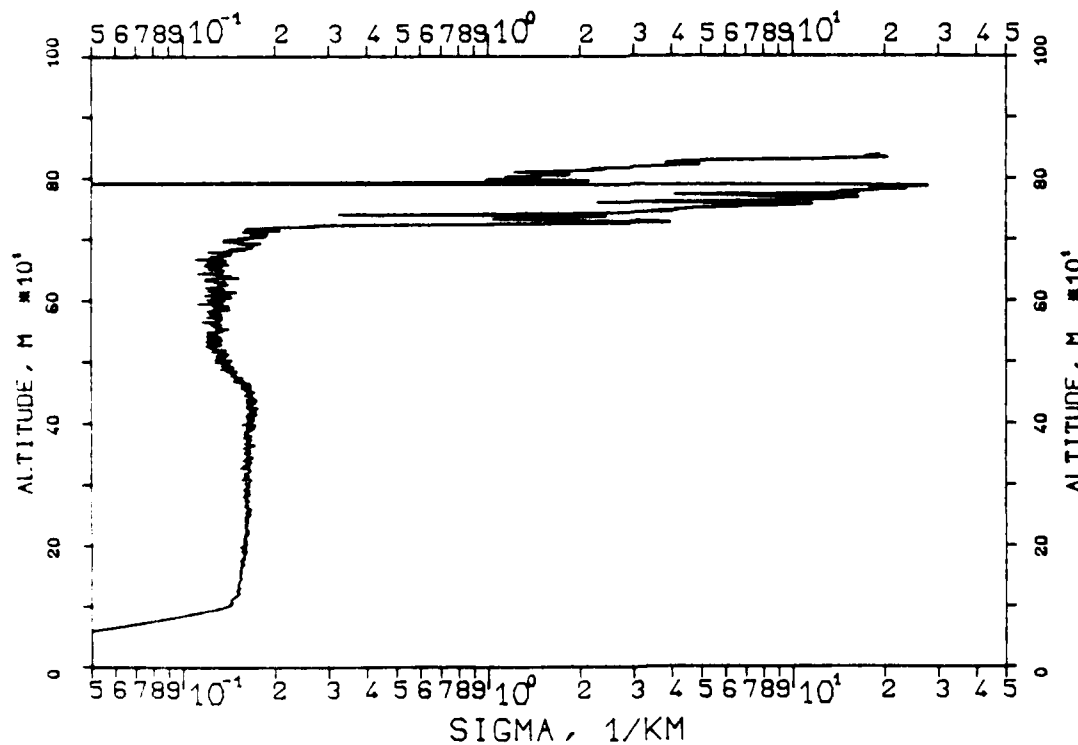
RM=0.290KM, SM= 0.3300/KM, K=1.000


FIG. 24, $F=0.3$

KLETT-PROFILE, 0530NM, EL. 19DG12MN

840228, 11:00-11:01, CET

RM=2.550KM, SM=20.0000/KM, K=1.000



KLETT-PR. 840228, 11:00-11:01, CET
 RM=2.190KM, SM= 0.1760/KM, K=1.000

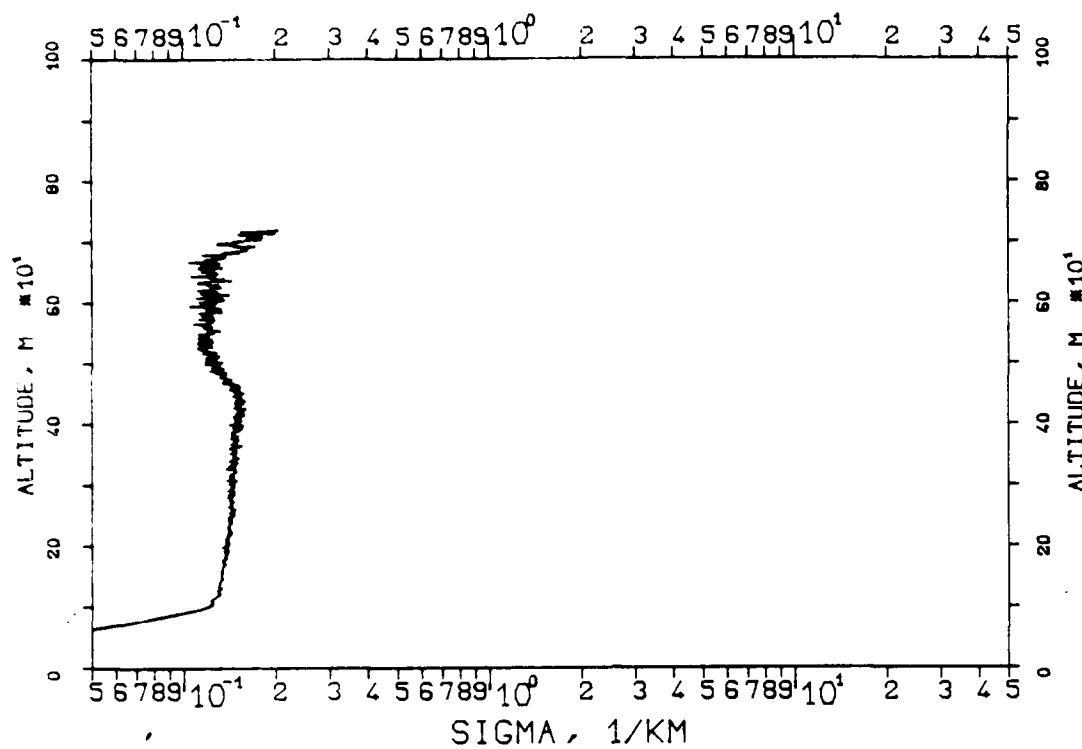


FIG. 26

R=0.8661
 CF=0.863
 B=0.001
 N=29

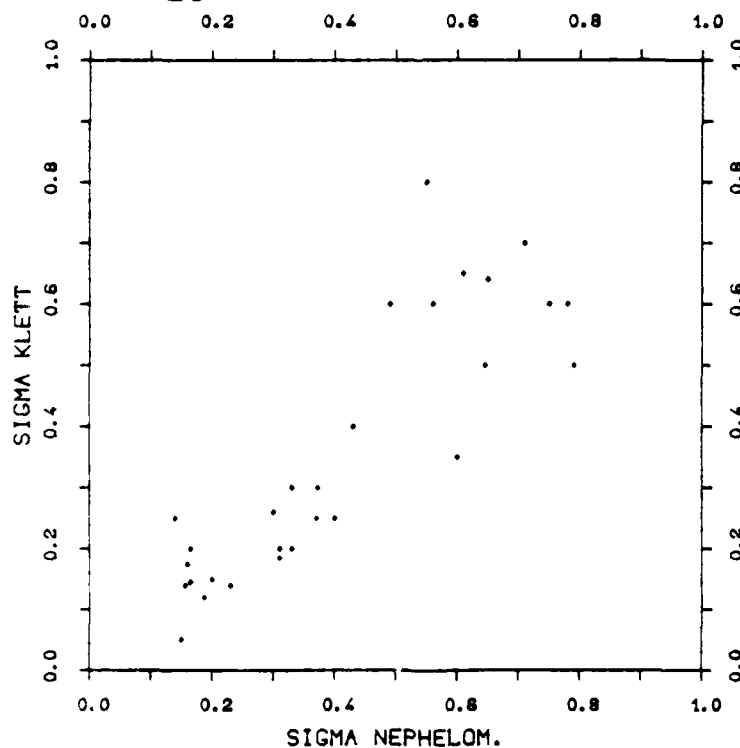


FIG. 7.1
KLETT-PROFILE, 0530NM, EL. 19DG12MN
821110, 09:18-09:18, CET
RM=2.050KM, SM=20.0000/KM, K=1.000

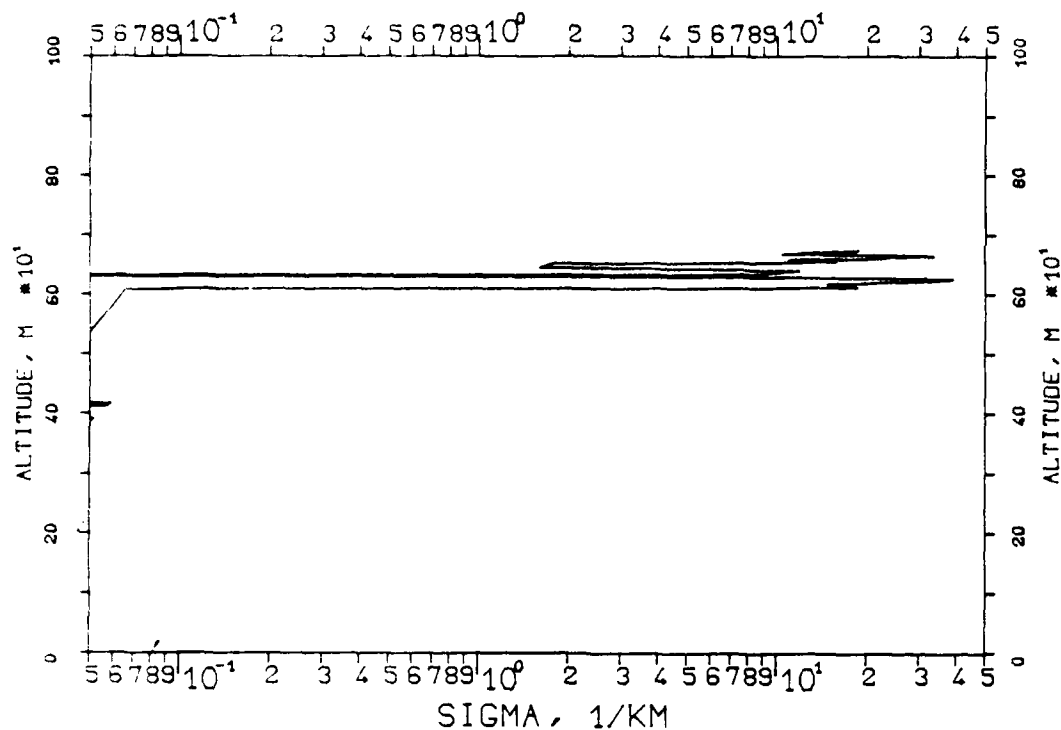
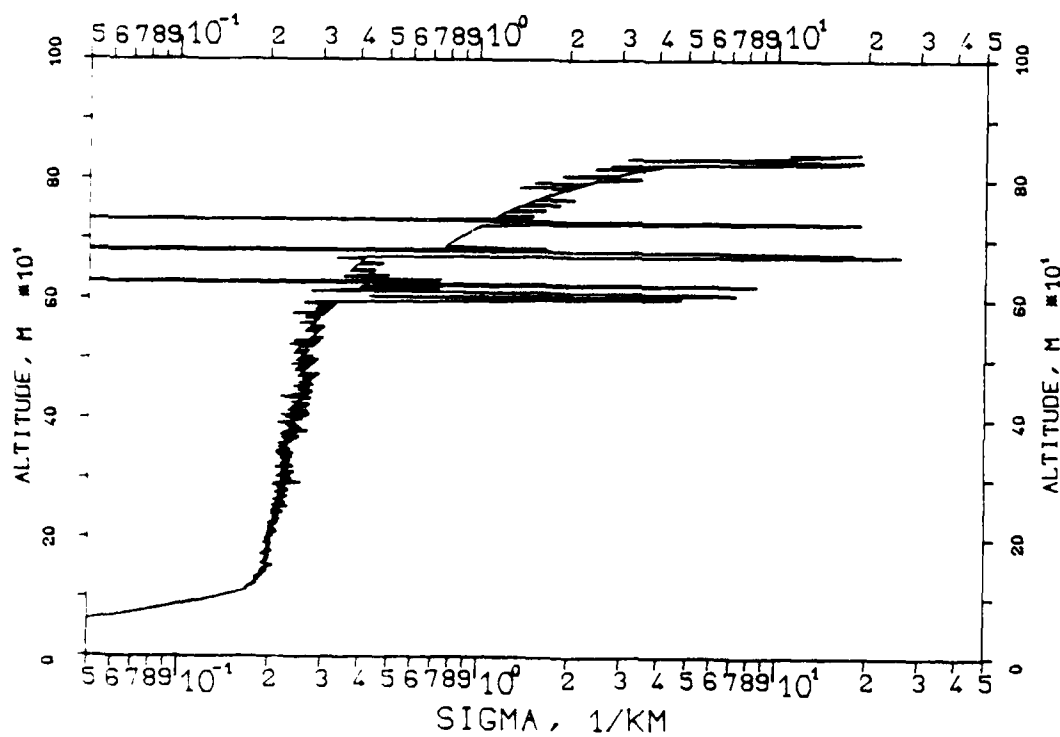


FIG. 7.2
KLETT-PROFILE, 0347NM, EL. 19DG12MN
821110, 09:20-09:20, CET
RM=2.566KM, SM=20.0000/KM, K=1.000



KLETT PROFILE, 0694NM, EL. 19DG12MN
 821110, 09:23-09:23, CET
 RM=1.858KM, SM=20.0000/KM, K=1.000

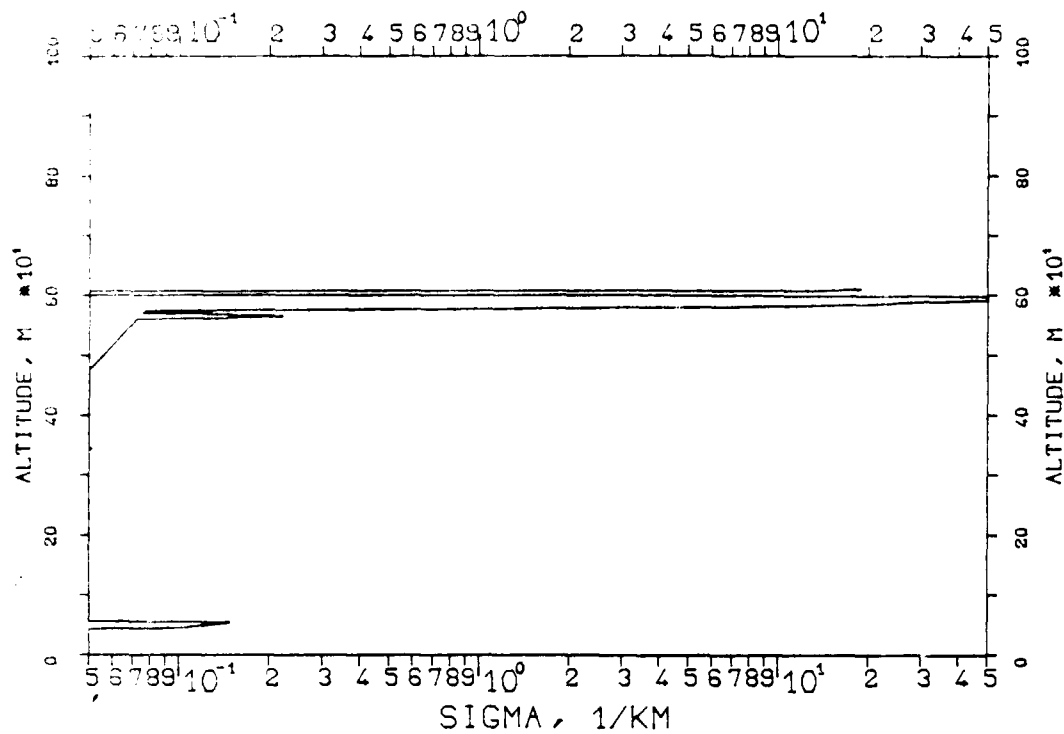


FIG. 7.4
 KLETT-PROFILE, 1060NM, EL. 19DG12MN
 821110, 09:26-09:26, CET
 RM=1.915KM, SM=20.0000/KM, K=1.000

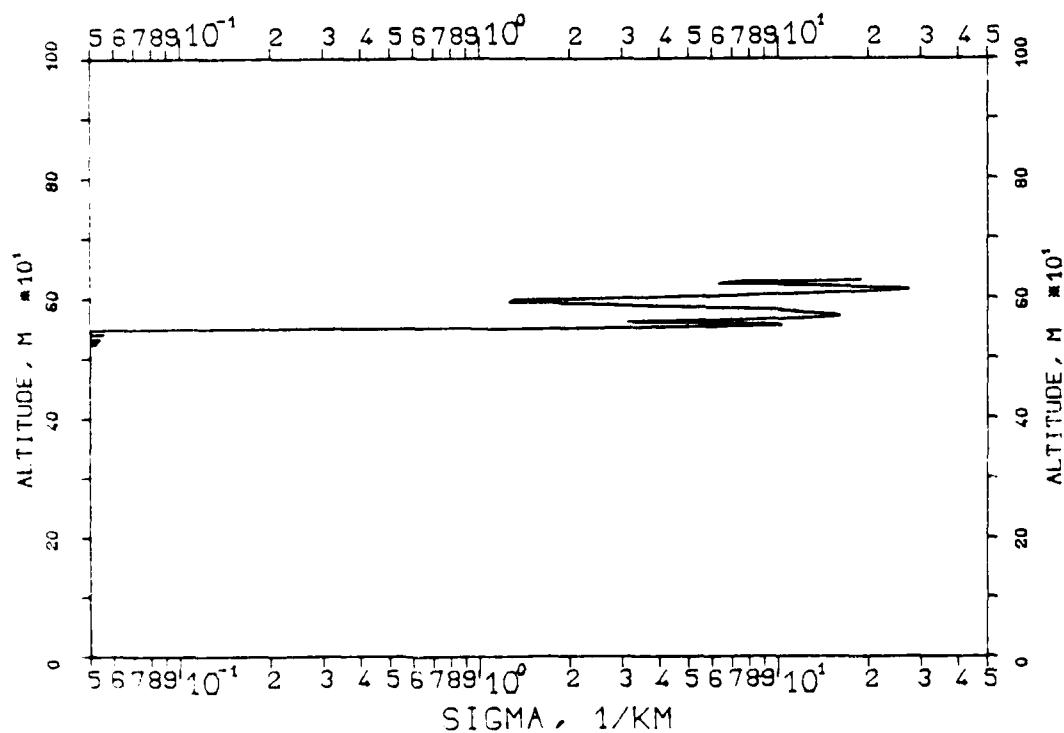


FIG. 7.31

KLETT-PROFILE, 0530NM, EL. 19DG12MN

830210, 09:28-09:29, CET

RM=1.717/KM, SM=20.0000/KM, K=1.000

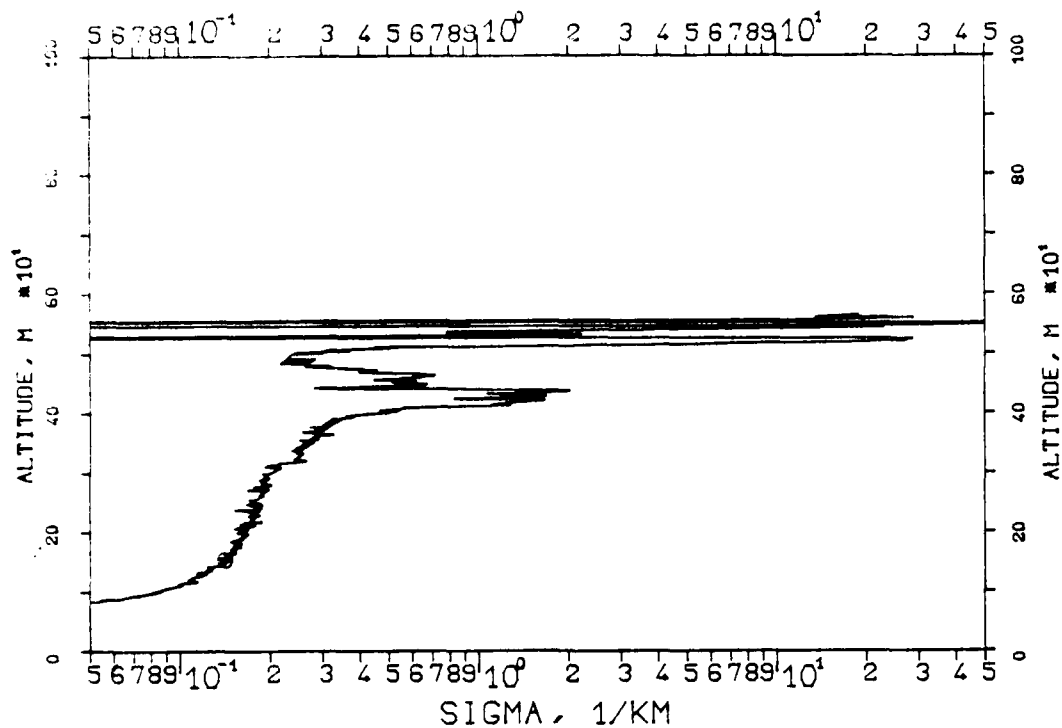


FIG. 7.32

KLETT-PROFILE, 0347NM, EL. 19DG12MN

830210, 09:34-09:34, CET

RM=2.626KM, SM=20.0000/KM, K=1.000

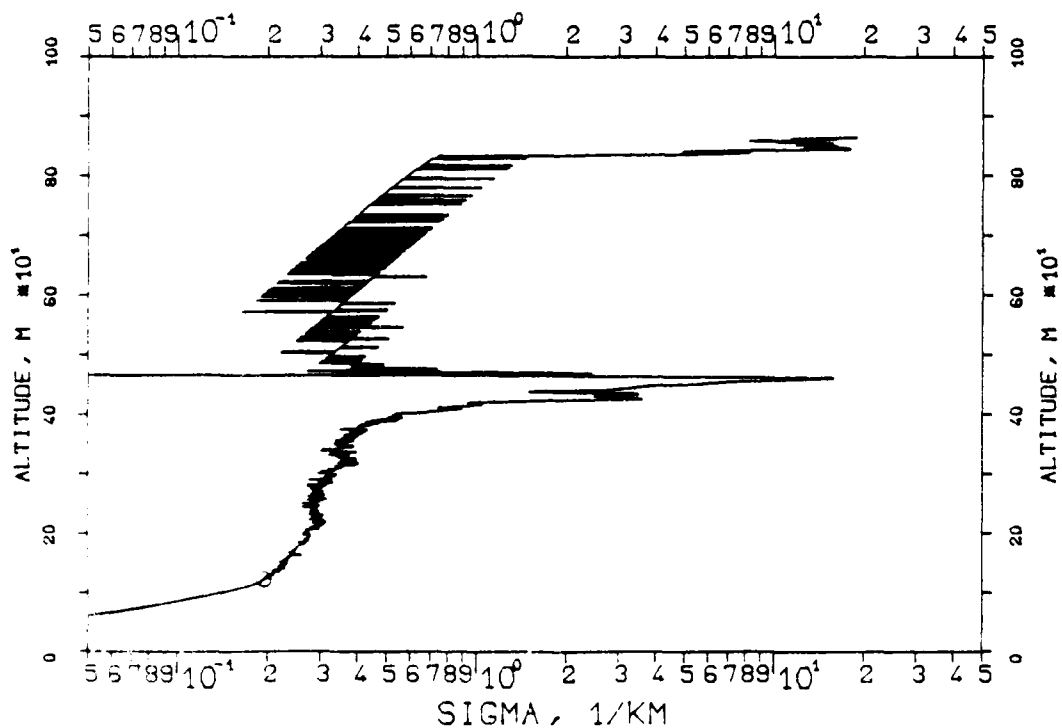


FIG. 7.29
KLETT-PROFILE, 1060NM, EL. 19DG 12MN
830119, 16:50-16:50, CET
RM=2.670KM, SM=20.0000/KM, K=1.000

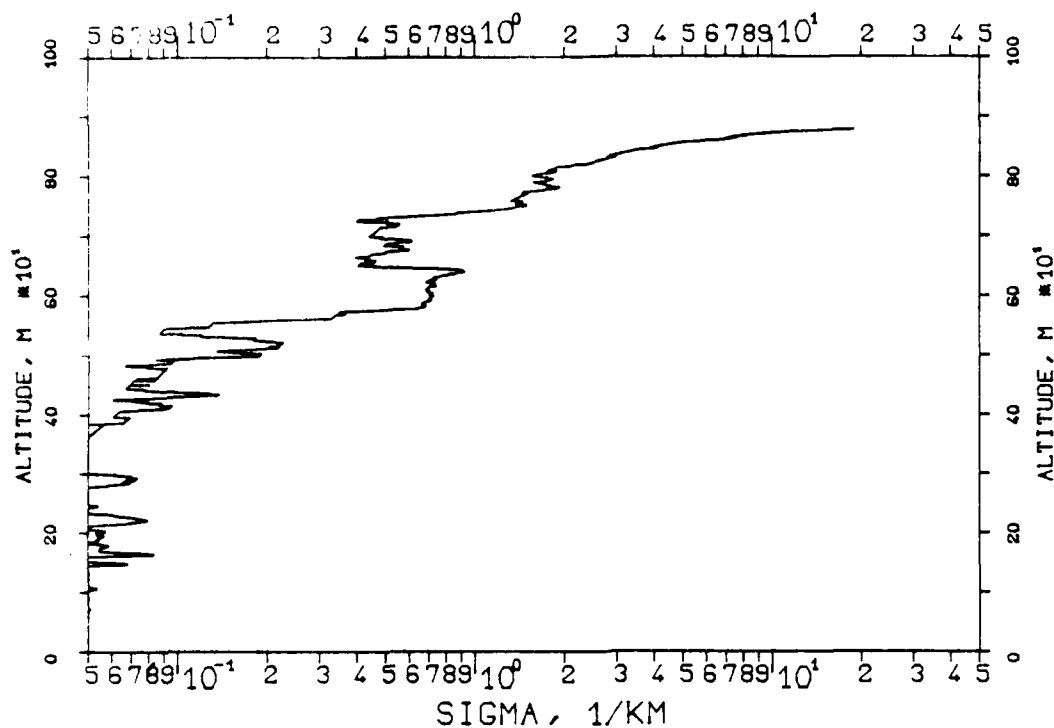


FIG. 7.30
KLETT-PROFILE, 0694NM, EL. 19DG 12MN
830210, 08:55-08:56, CET
RM=1.489KM, SM=20.0000/KM, K=1.000

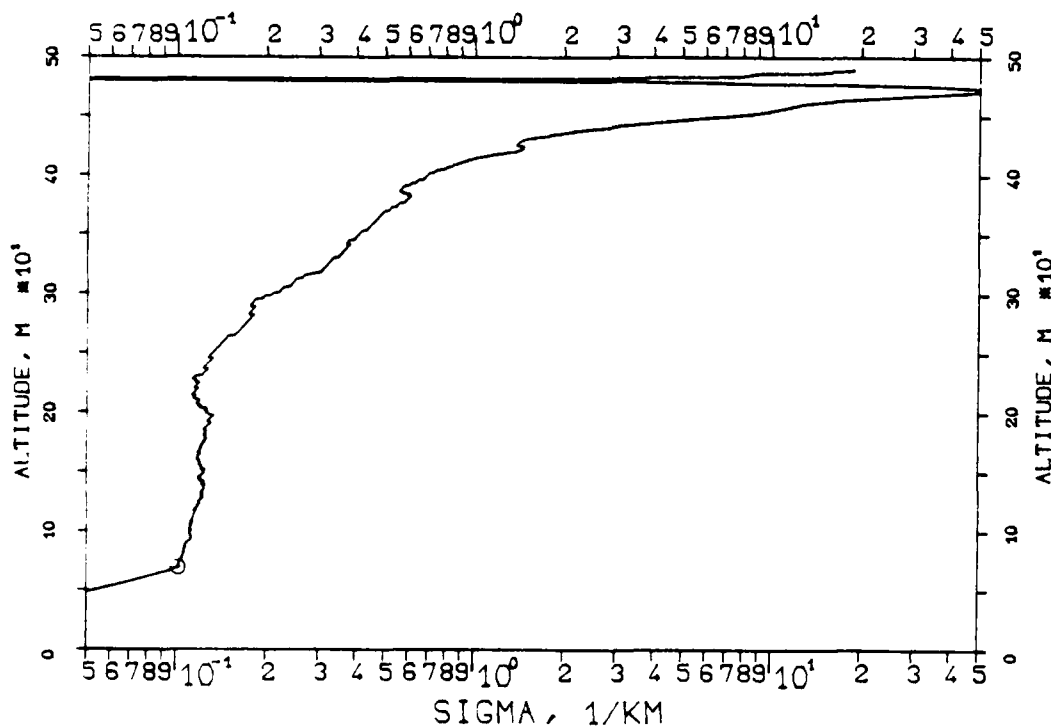


FIG. 7.27
KLETT PROFILE, 0530NM, EL. 19DG12MN
830114, 17:23-17:23, CET
RM=0.907KM, SM=20.0000/KM, K=1.000

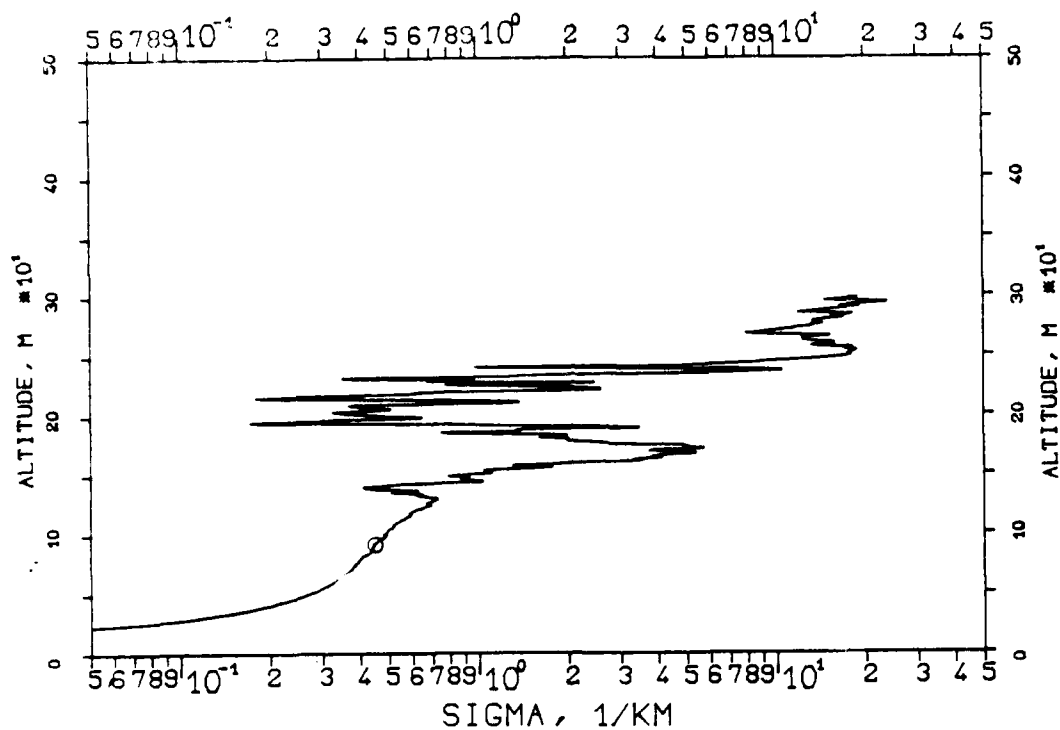


FIG. 7.28
KLETT-PROFILE, 1060NM, EL. 19DG12MN
830119, 16:05-16:05, CET
RM=2.670KM, SM=20.0000/KM, K=1.000

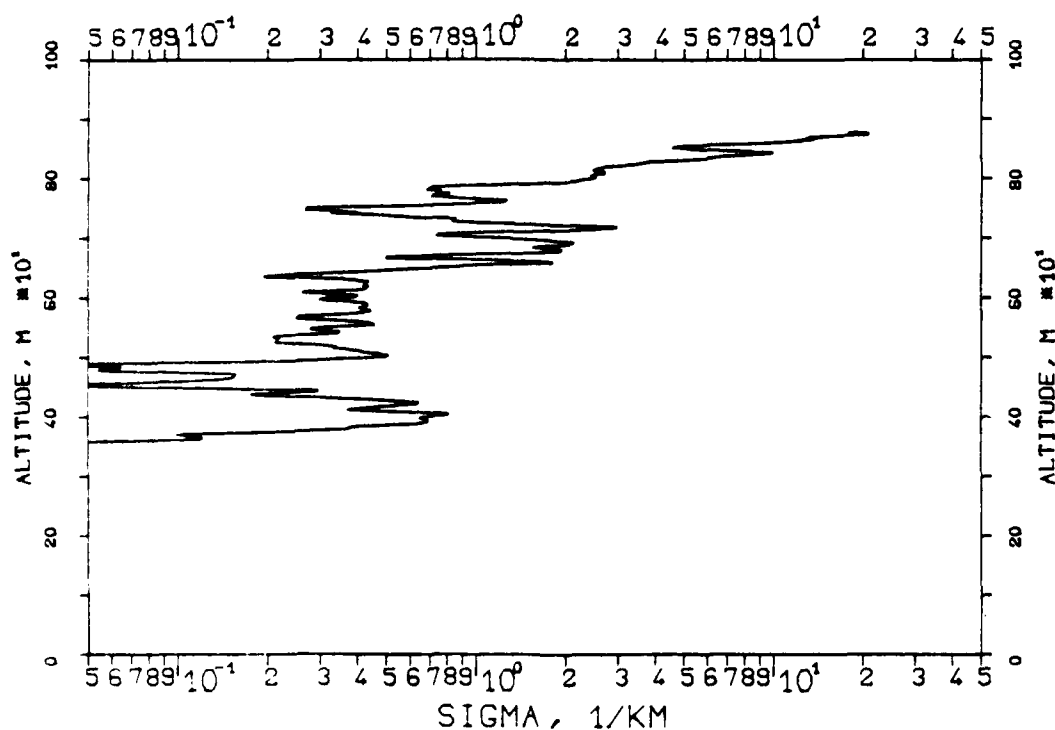


FIG. 7.25

KLETT-PROFILE, 0694NM, EL. 19DG12MN

821214, 17:09-17:09, CET

RM=1.257KM, SM=20.0000/KM, K=1.000

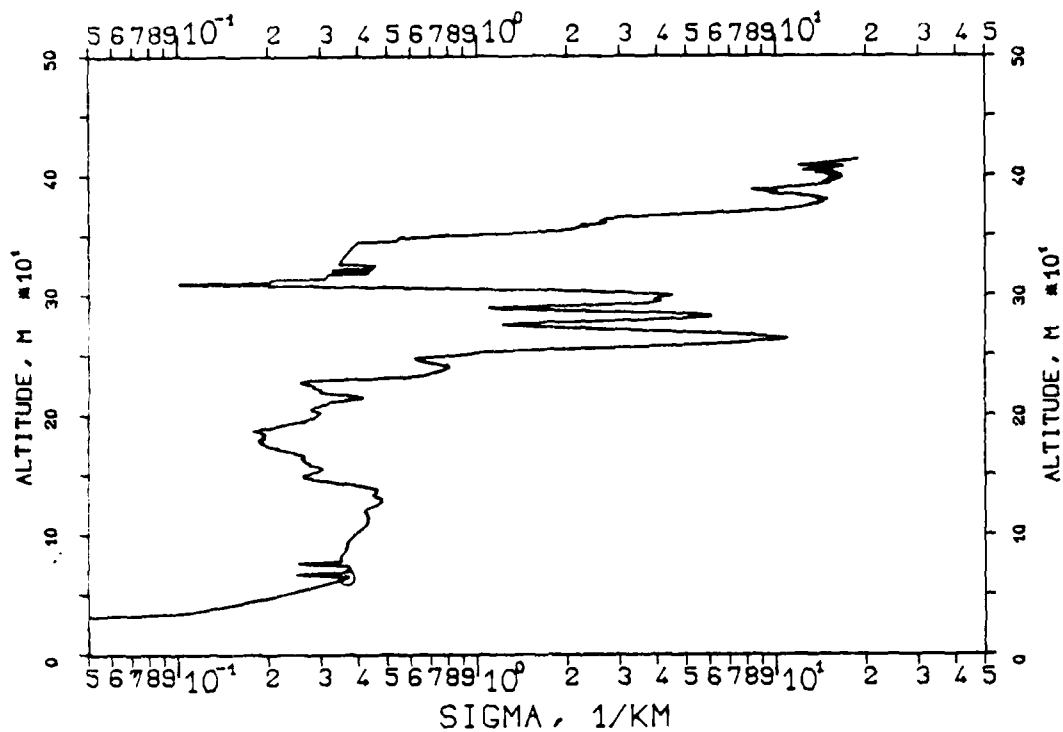


FIG. 7.26

KLETT-PROFILE, 1060NM, EL. 19DG12MN

821214, 17:14-17:15, CET

RM=1.035KM, SM=20.0000/KM, K=1.000

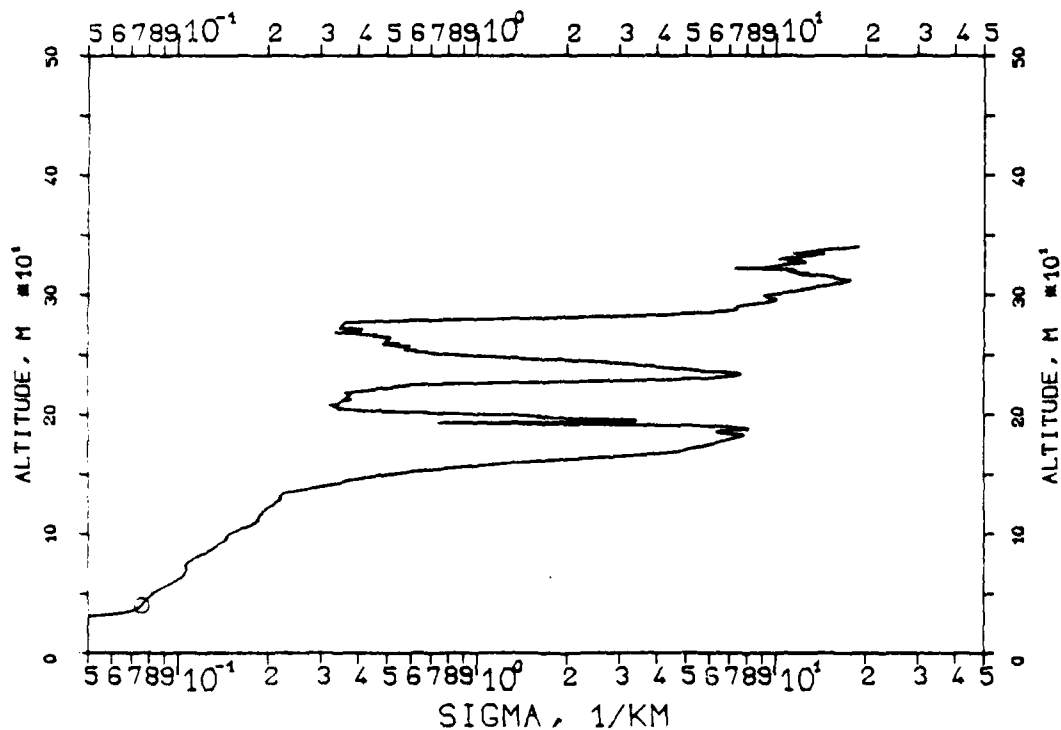


FIG. 7.23

KLETT-PROFILE, 1060NM, EL. 19DG12MN

821214, 16:45-16:46, CET

RM=1.846KM, SM=20.0000/KM, K=1.000

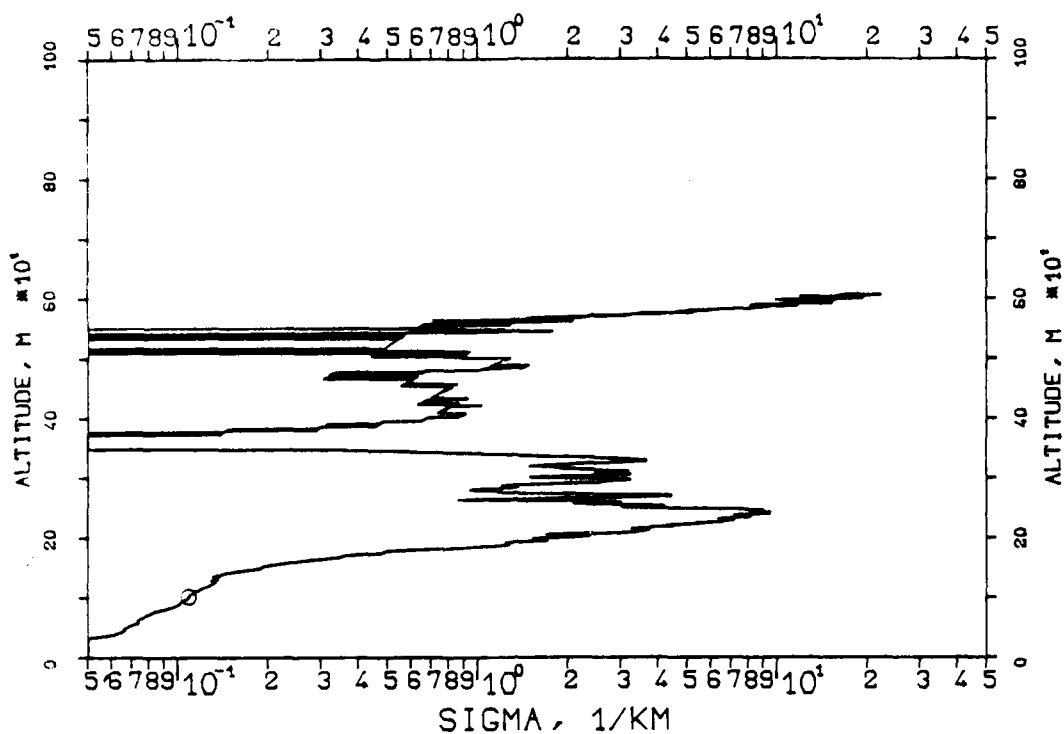


FIG. 7.24

KLETT-PROFILE, 0694NM, EL. 19DG12MN

821214, 16:47-16:48, CET

RM=0.942KM, SM=20.0000/KM, K=1.000

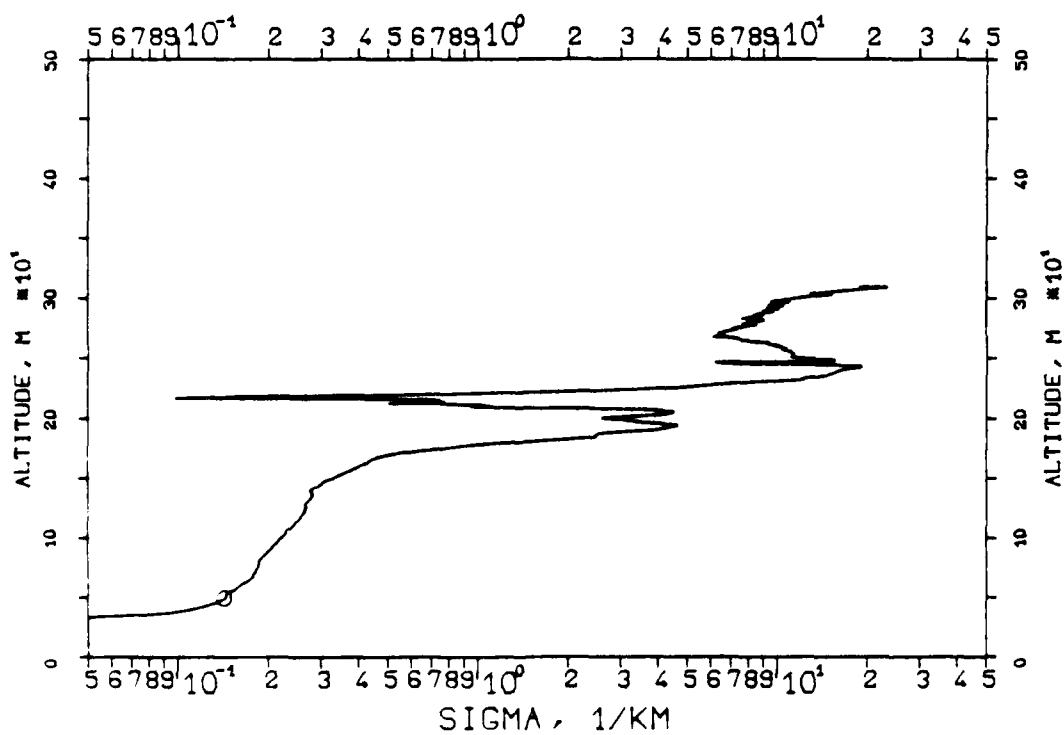


FIG. 7.21

KLETT-PROFILE, 0530NM, EL. 19DG 12MN

821214, 16:06-16:07, CET

RM=1.819KM, SM=20.0000/KM, K=1.000

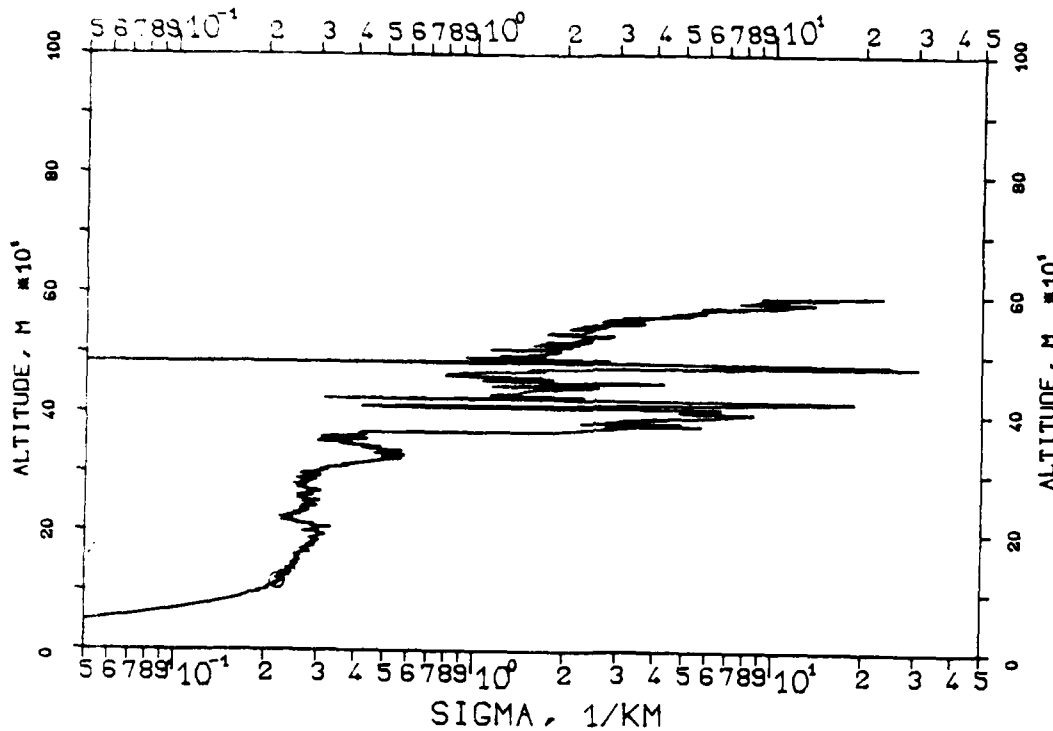


FIG. 7.22

KLETT-PROFILE, 0530NM, EL. 19DG 12MN

821214, 16:41-16:42, CET

RM=1.182KM, SM=20.0000/KM, K=1.000

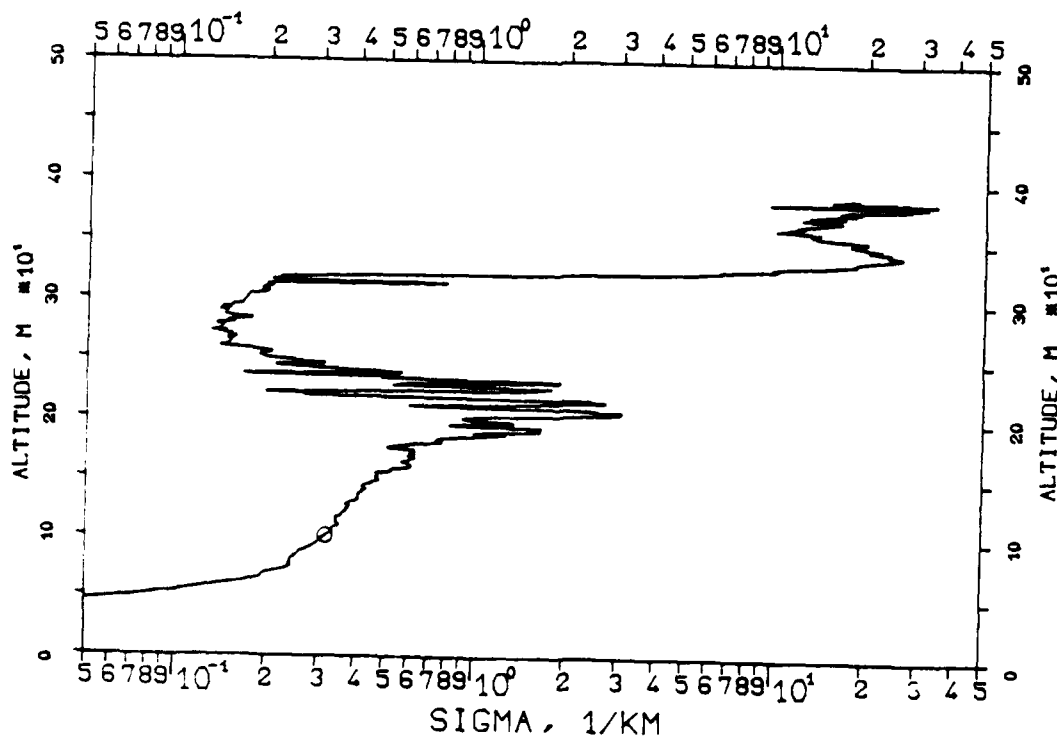


FIG. 7.19

KLETT PROFILE, 1060NM, EL. 19DG12MN

821214, 15:09-15:10, CET

RM=2.650KM, SM=20.0000/KM, K=1.000

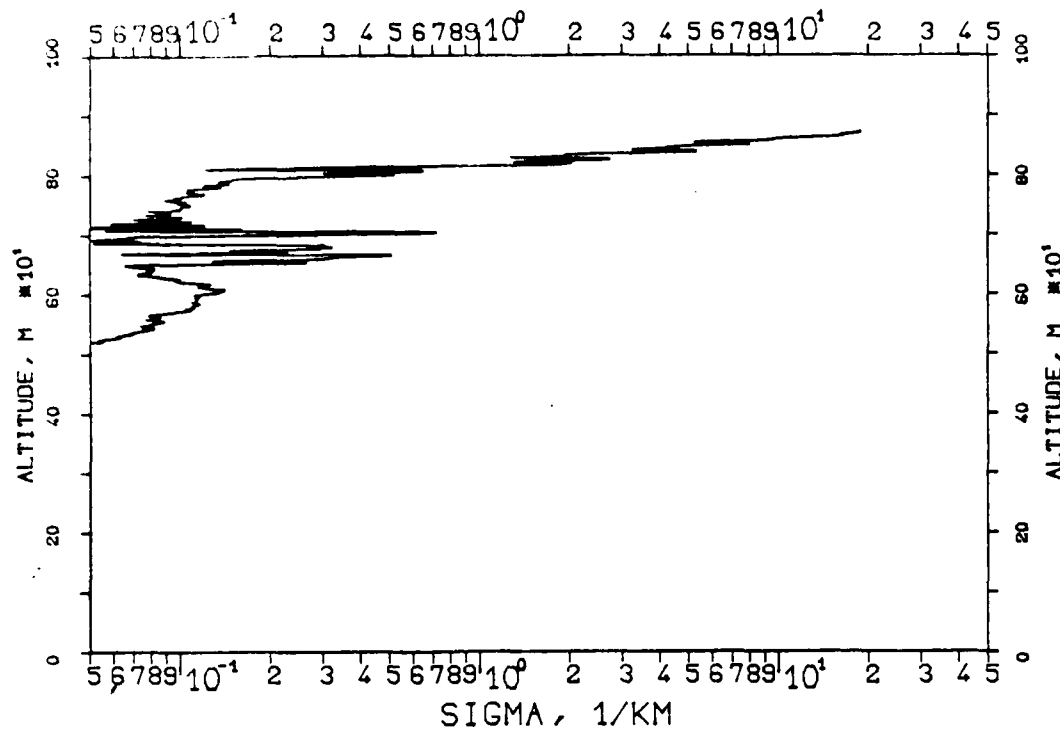
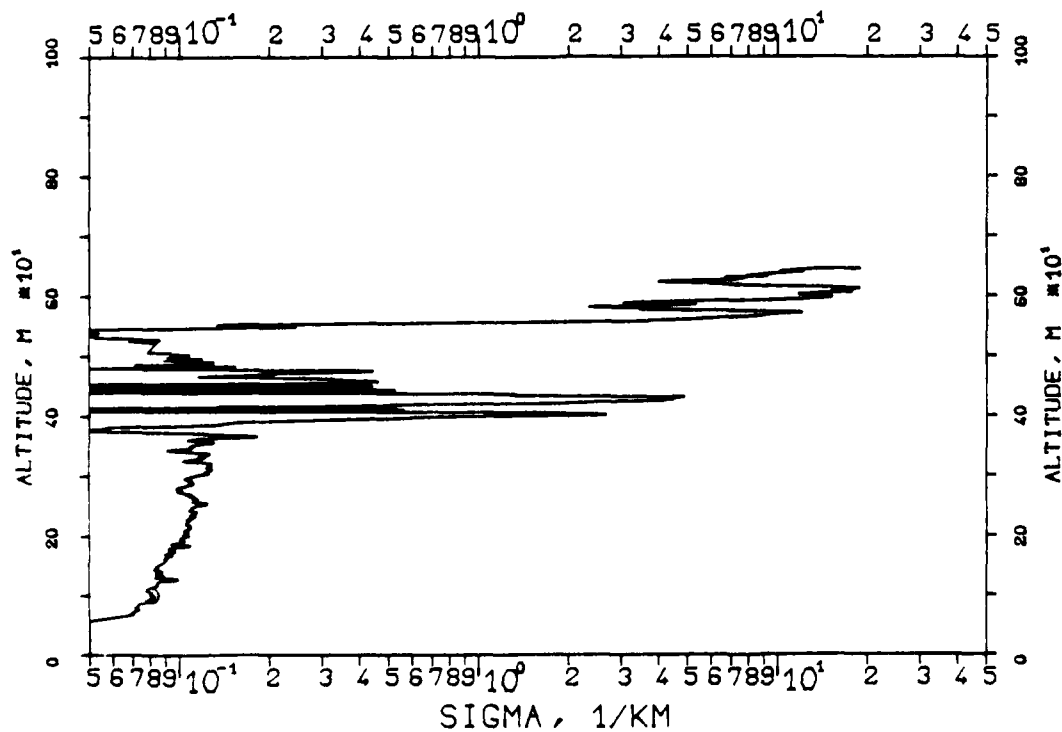


FIG. 7.20

KLETT-PROFILE, 0694NM, EL. 19DG12MN

821214, 15:59-15:59, CET

RM=1.965KM, SM=20.0000/KM, K=1.000



REPRODUCED AT GOVERNMENT EXPENSE
 11:13:17.1
 KLETT PROFILE, 0530NM, EL. 19DG12MN
 821214, 11:14-11:14, CET
 RM=2.511KM, SM=20.0000/KM, K=1.000

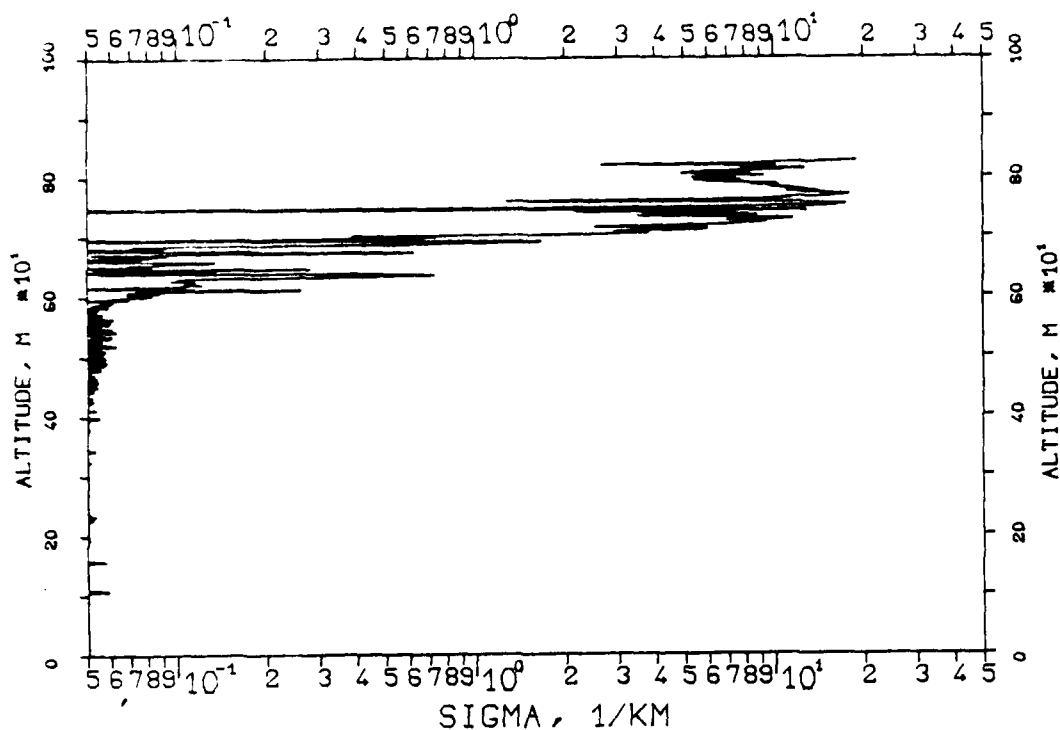


FIG. 7.18
 KLETT-PROFILE, 1060NM, EL. 19DG12MN
 821214, 11:17-11:18, CET
 RM=2.200KM, SM=20.0000/KM, K=1.000

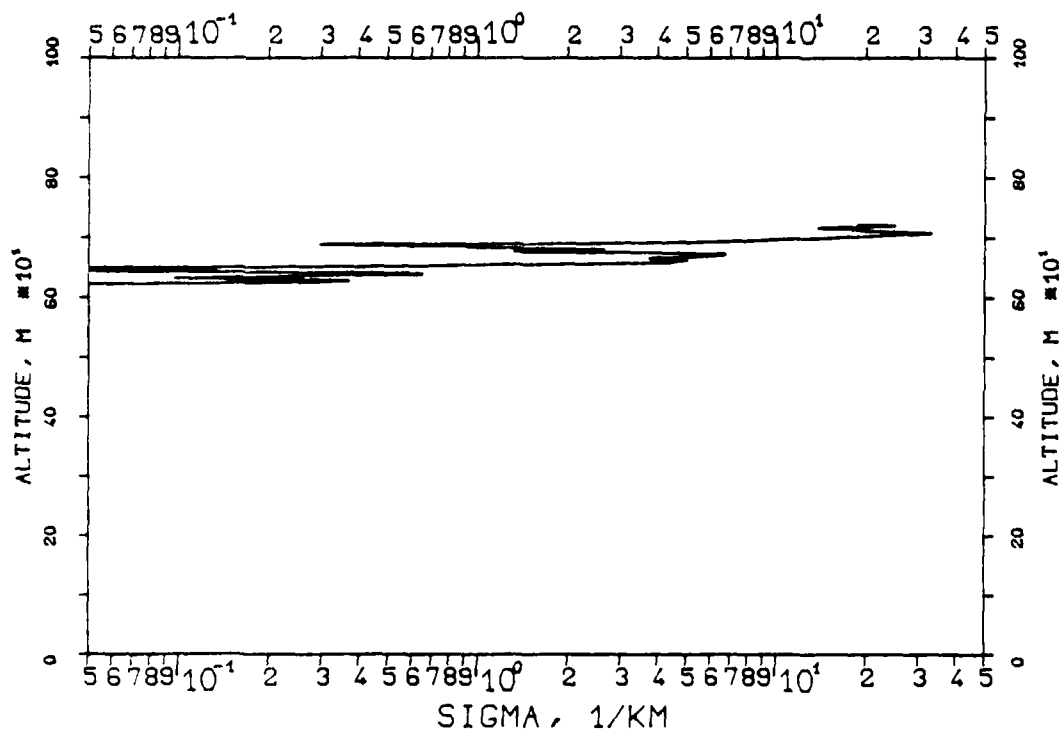


FIG. 7.15
KLETT PROFILE, 1060NM, EL. 19DG12MN
821014, 10:07-10:08, CET
RM=2.640KM, SM=20.0000/KM, K=1.000

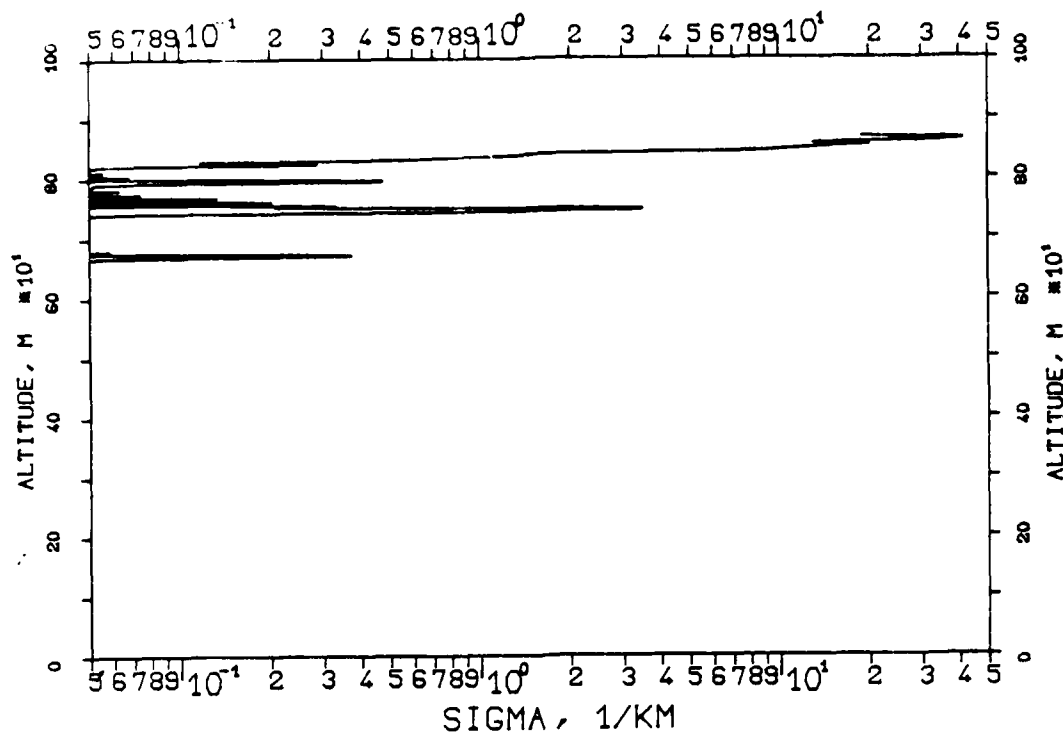


FIG. 7.16
KLETT-PROFILE, 0530NM, EL. 19DG12MN
821214, 10:10-10:11, CET
RM=2.670KM, SM=20.0000/KM, K=1.000

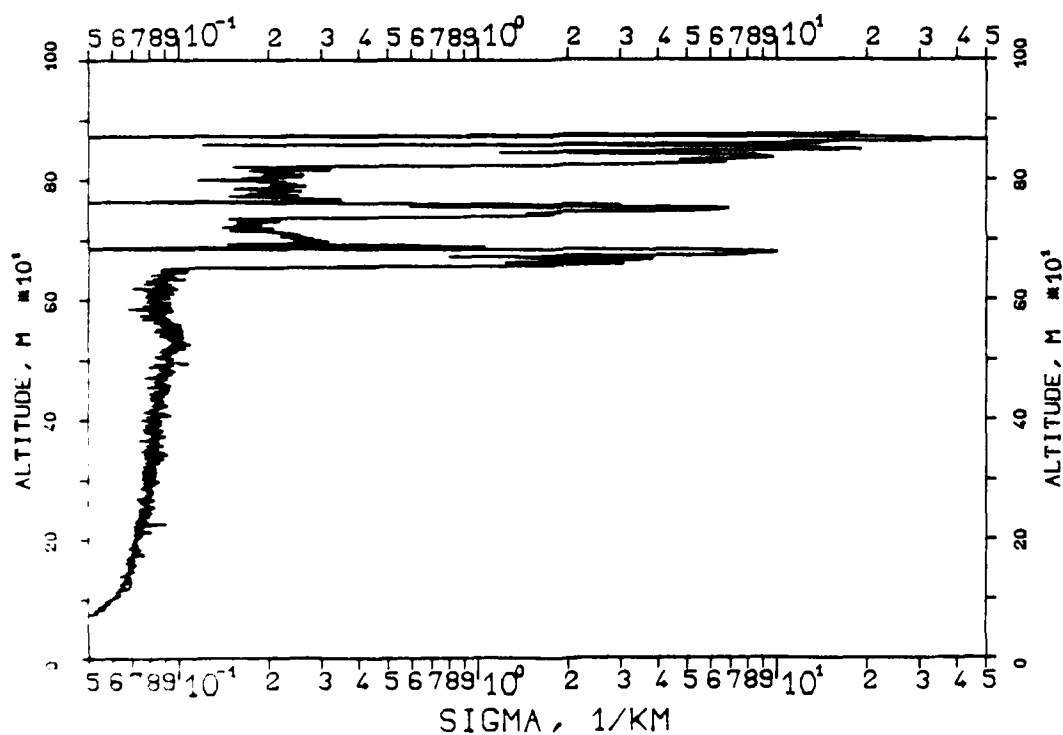


FIG. 7.13
KLETT-PROFILE, 0530NM, EL. 19DG12MN
821214, 09:27-09:27, CET
RM=2.670KM, SM=20.0000/KM, K=1.000

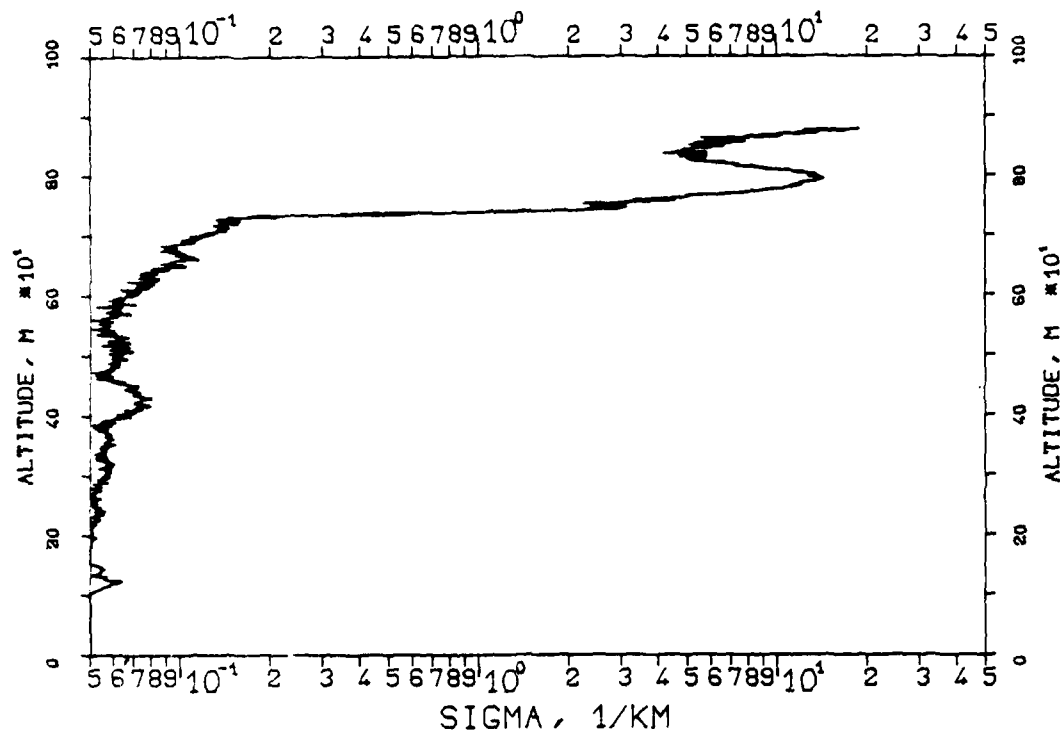


FIG. 7.14
KLETT-PROFILE, 1060NM, EL. 19DG12MN
821214, 09:30-09:31, CET
RM=2.670KM, SM=20.0000/KM, K=1.000

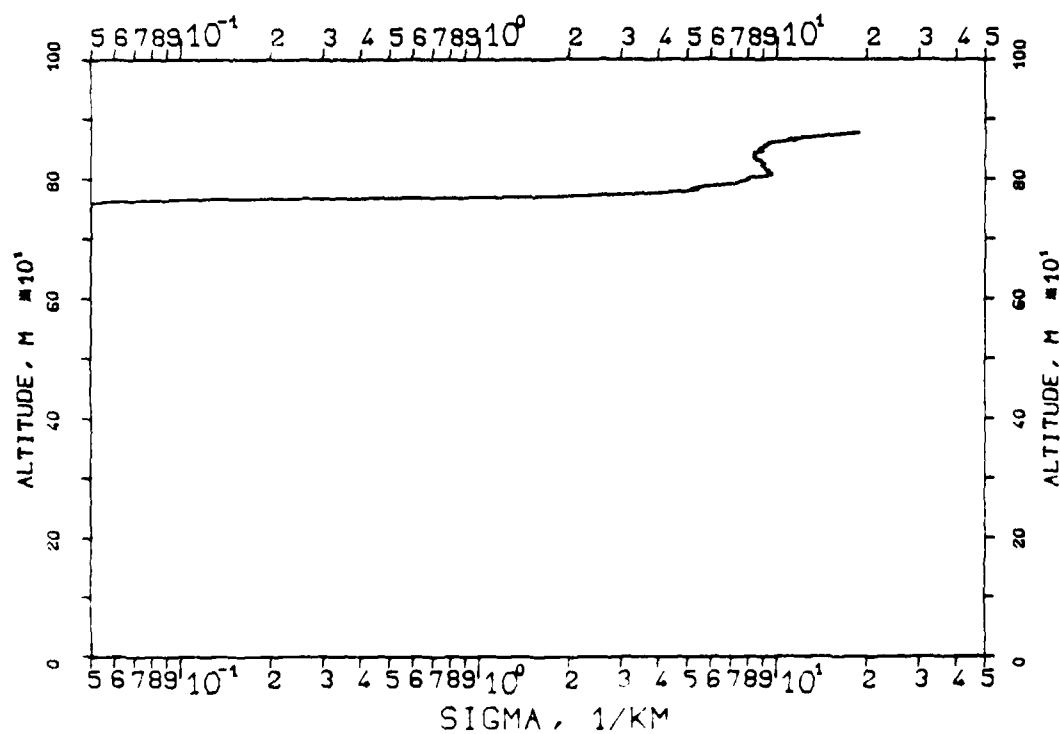


FIG. 7.11
 KLETT-PROFILE, 0347NM, EL. 19DG12MN
 821110, 11:08-11:08, CET
 RM=1.700KM, SM=20.0000/KM, K=1.000

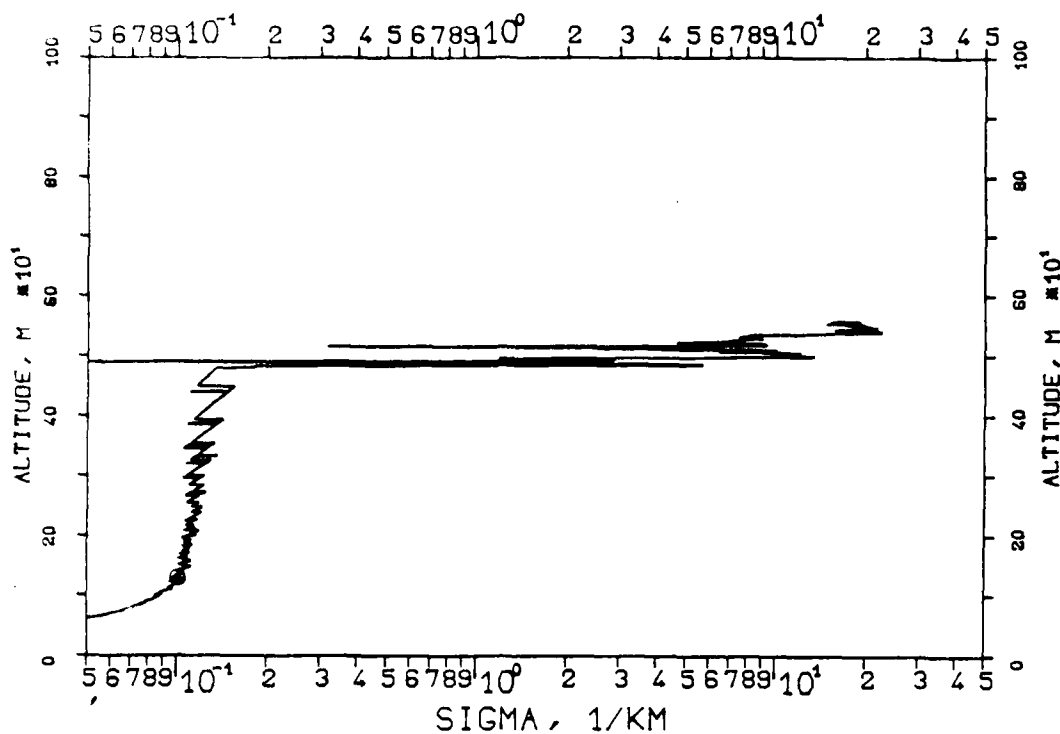


FIG. 7.12
 KLETT-PROFILE, 1060NM, EL. 19DG12MN
 821110, 11:13-11:13, CET
 RM=1.809KM, SM=20.0000/KM, K=1.000

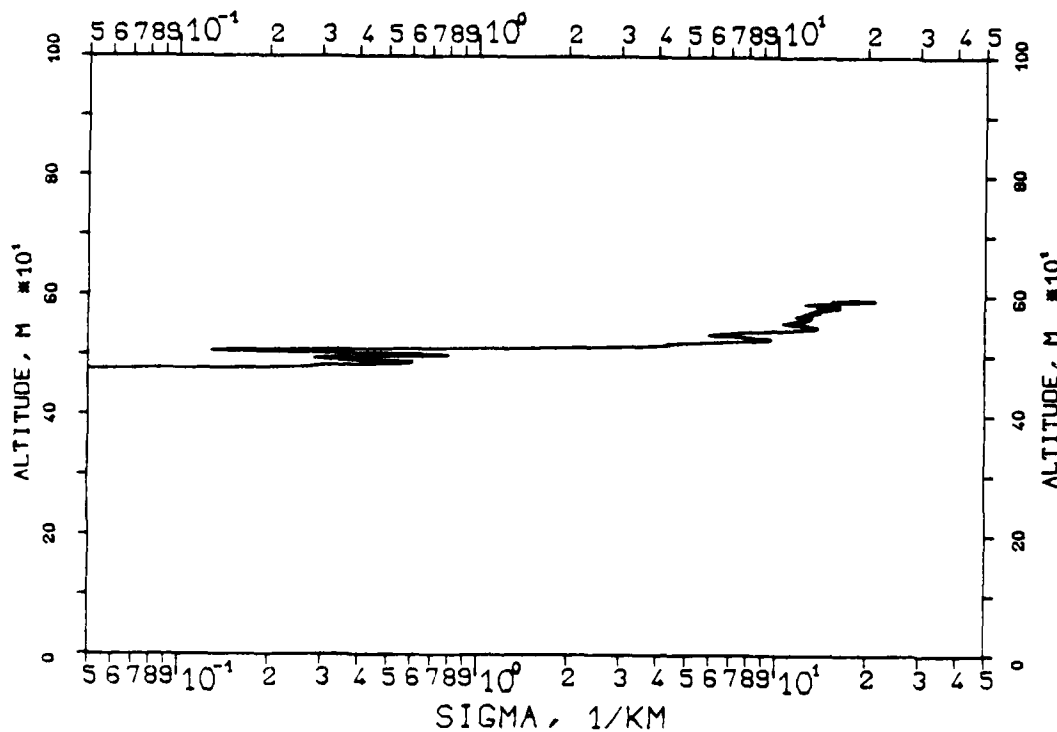


FIG. 7.9
KLETT PROFILE, 0530NM, EL. 19DG12MN
821110, 11:05-11:05, CET
RM=1.561KM, SM=20.0000/KM, K=1.000

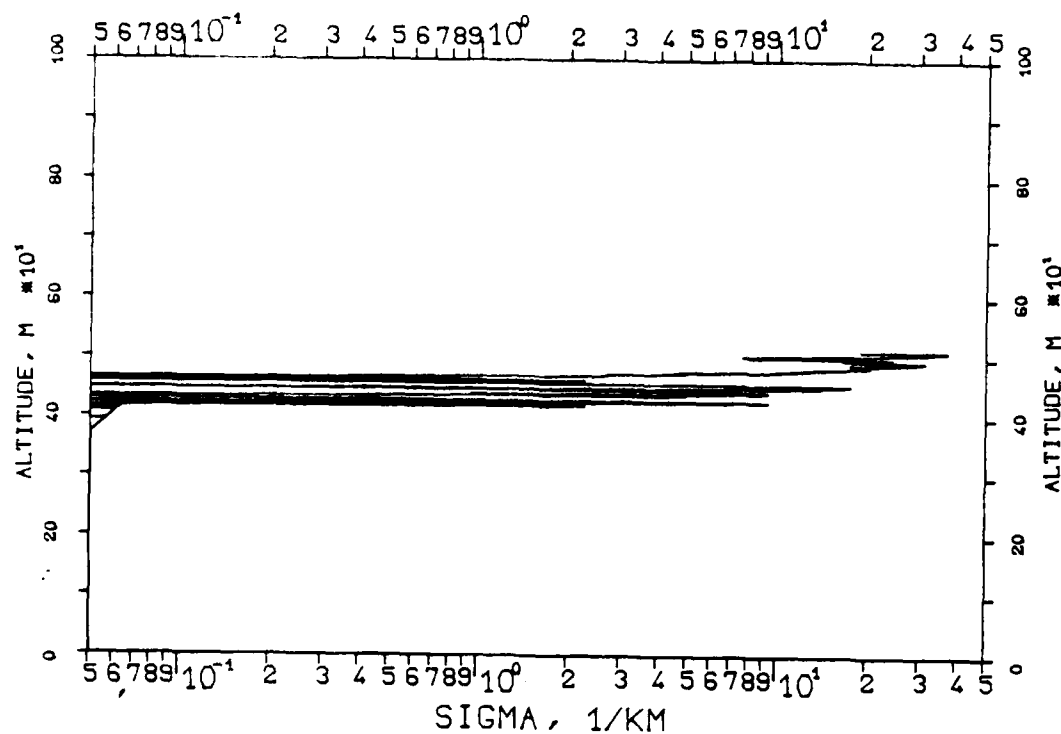


FIG. 7.10
KLETT-PROFILE, 0694NM, EL. 19DG12MN
821110, 11:10-11:10, CET
RM=1.794KM, SM=20.0000/KM, K=1.000

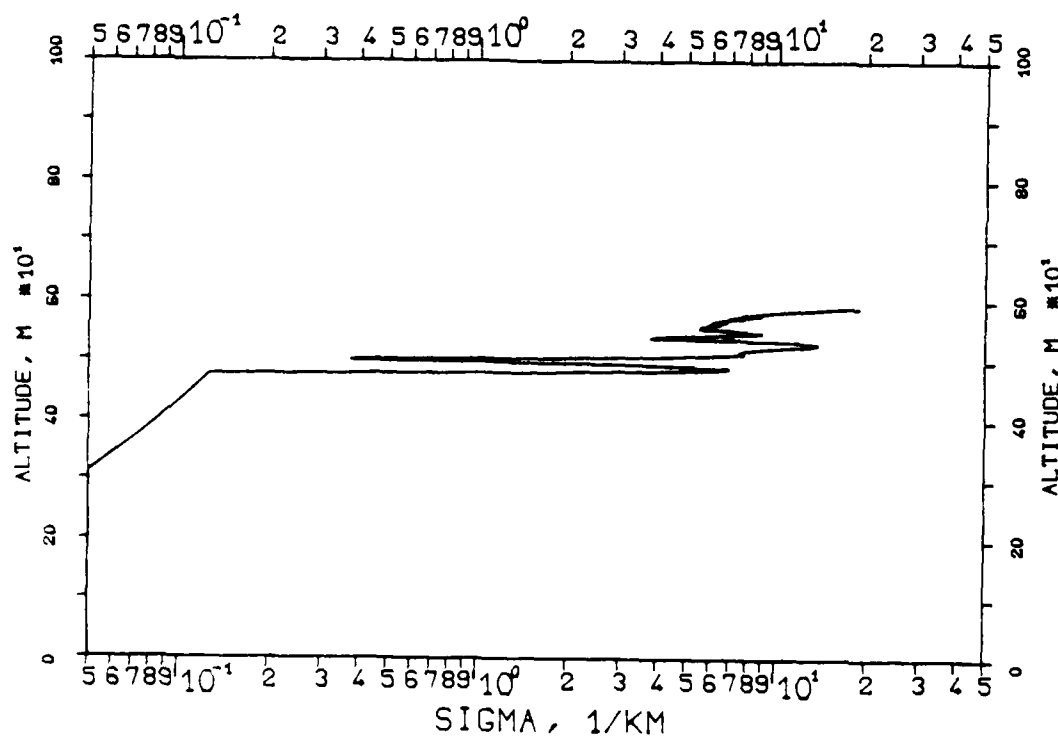


FIG. 7.7

KLETT-PROFILE ,0347NM,EL. 19DG12MN

821110, 10:04-10:04,CET

RM=1.843KM,SM=20.0000/KM,K=1.000

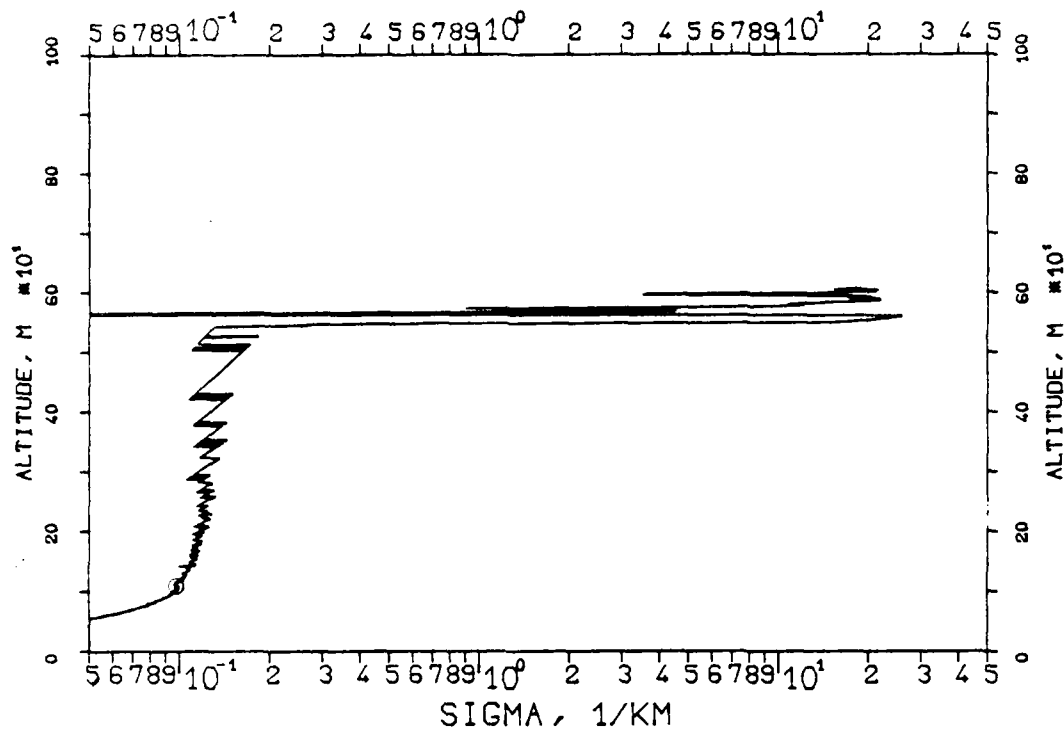


FIG. 7.8

KLETT-PROFILE ,0530NM,EL. 19DG12MN

821110, 10:08-10:09,CET

RM=1.824KM,SM=20.0000/KM,K=1.000

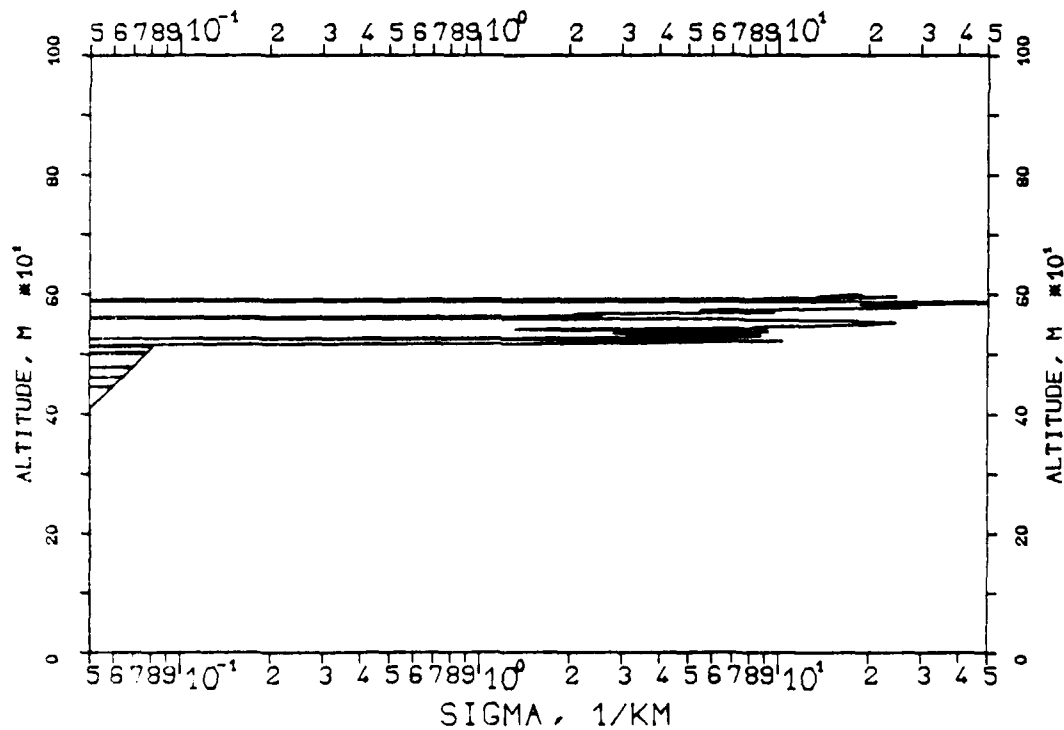


FIG. 7.5
KLETT-PROFILE, 1060NM, EL. 19DG12MN
821110, 09:58-09:58, CET
RM=2.646KM, SM=20.0000/KM, K=1.000

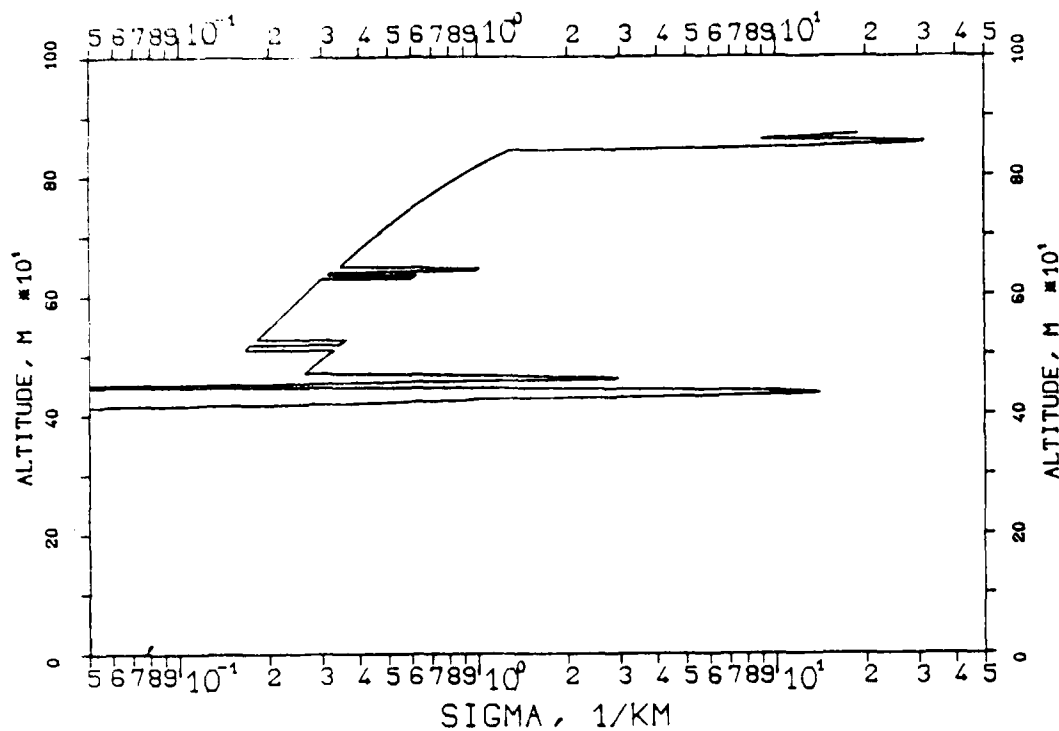
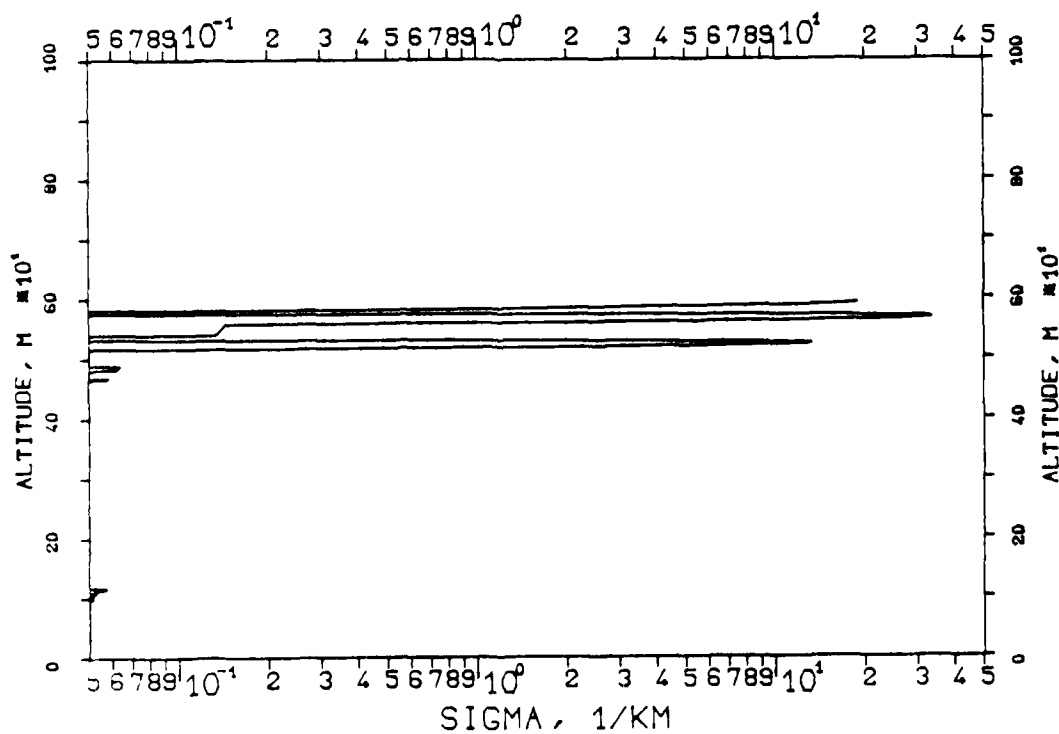


FIG. 7.6
KLETT-PROFILE, 0694NM, EL. 19DG12MN
821110, 10:00-10:00, CET
RM=1.800KM, SM=20.0000/KM, K=1.000



KLETT PROFILE, 0694NM, EL. 19DG12MN
830210, 09:38-09:38, CET
RM=2.646KM, SM=20.0000/KM, K=1.000

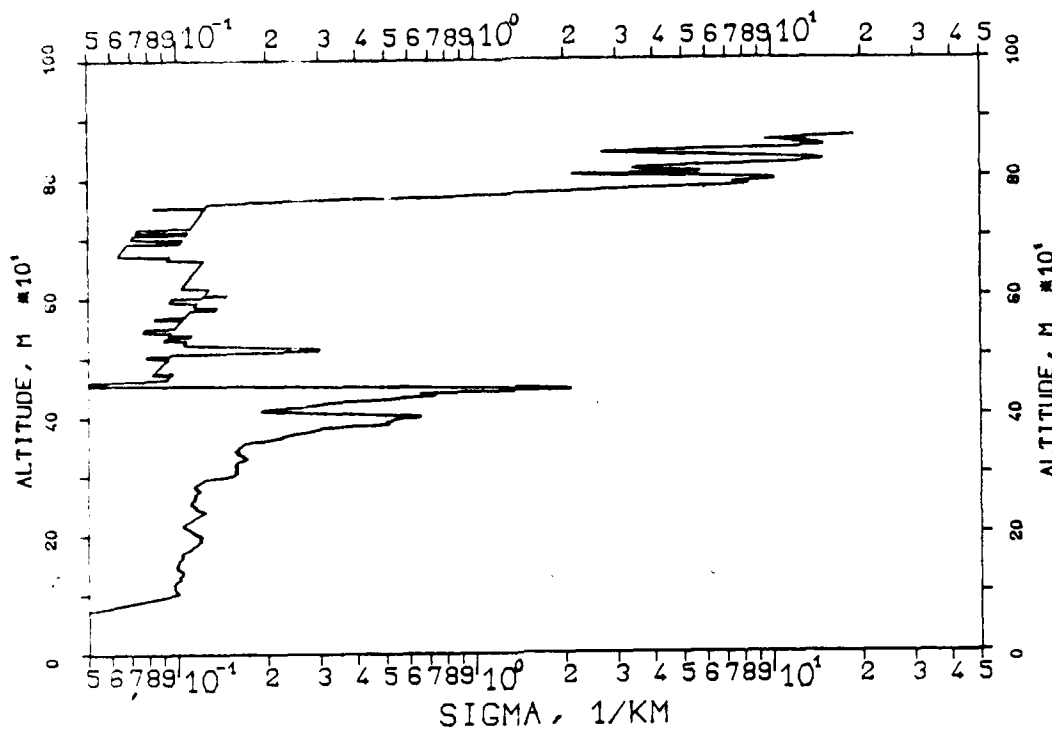


FIG. 7.34
KLETT-PROFILE, 1060NM, EL. 19DG12MN
830210, 09:42-09:43, CET
RM=2.670KM, SM=20.0000/KM, K=1.000

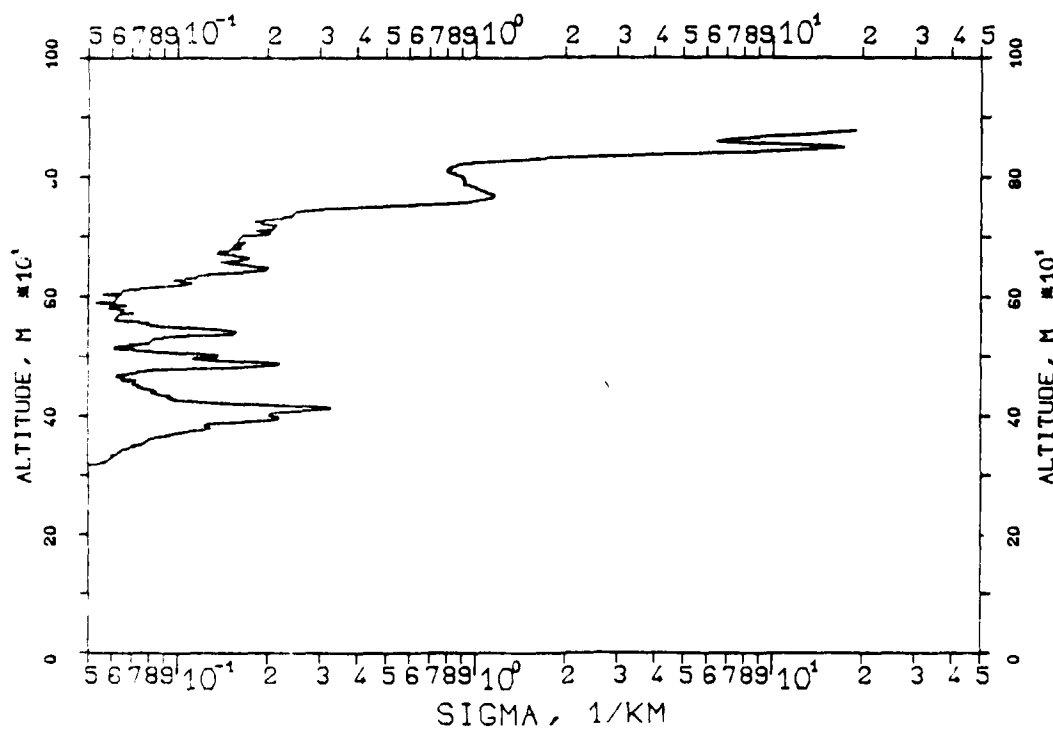


FIG. 7.35

KLETT-PROFILE, 1060NM, EL. 19DG12MN

830210, 10:31-10:31, CET

RM=2.670KM, SM=20.0000/KM, K=1.000

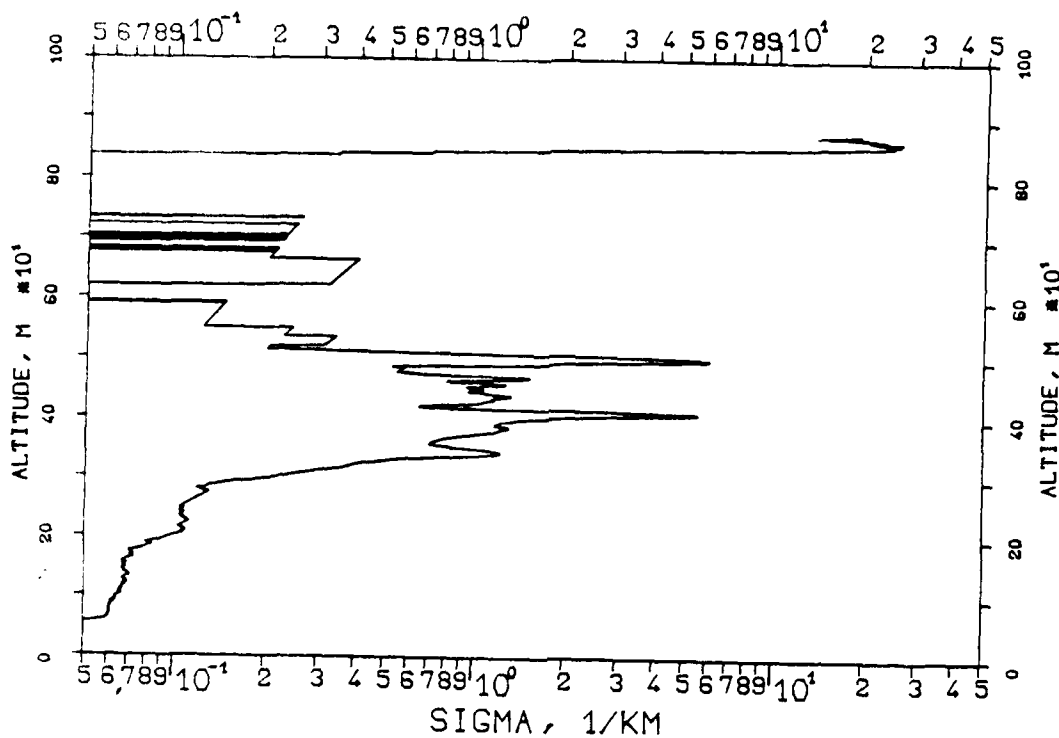


FIG. 7.36

KLETT-PROFILE, 0694NM, EL. 19DG12MN

830210, 10:34-10:34, CET

RM=1.525KM, SM=20.0000/KM, K=1.000

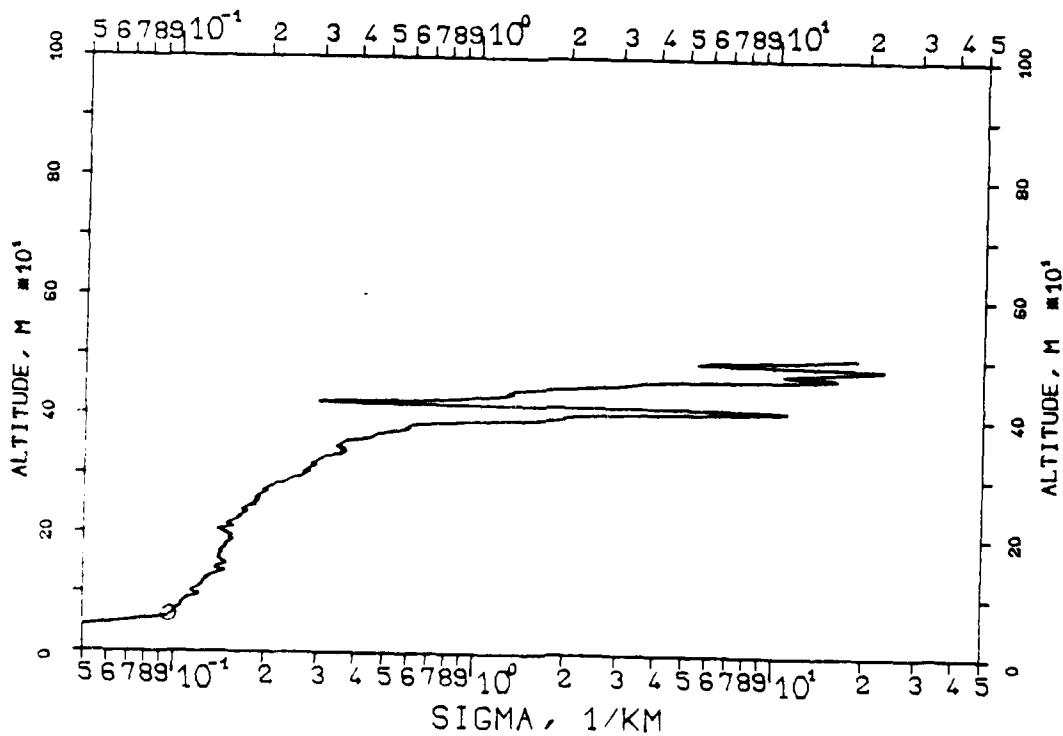


FIG. 7.37
KLETT-PROFILE, 0347NM, EL. 19DG12MN
830210, 10:41-10:41, CET
RM=1.471KM, SM=20.0000/KM, K=1.000

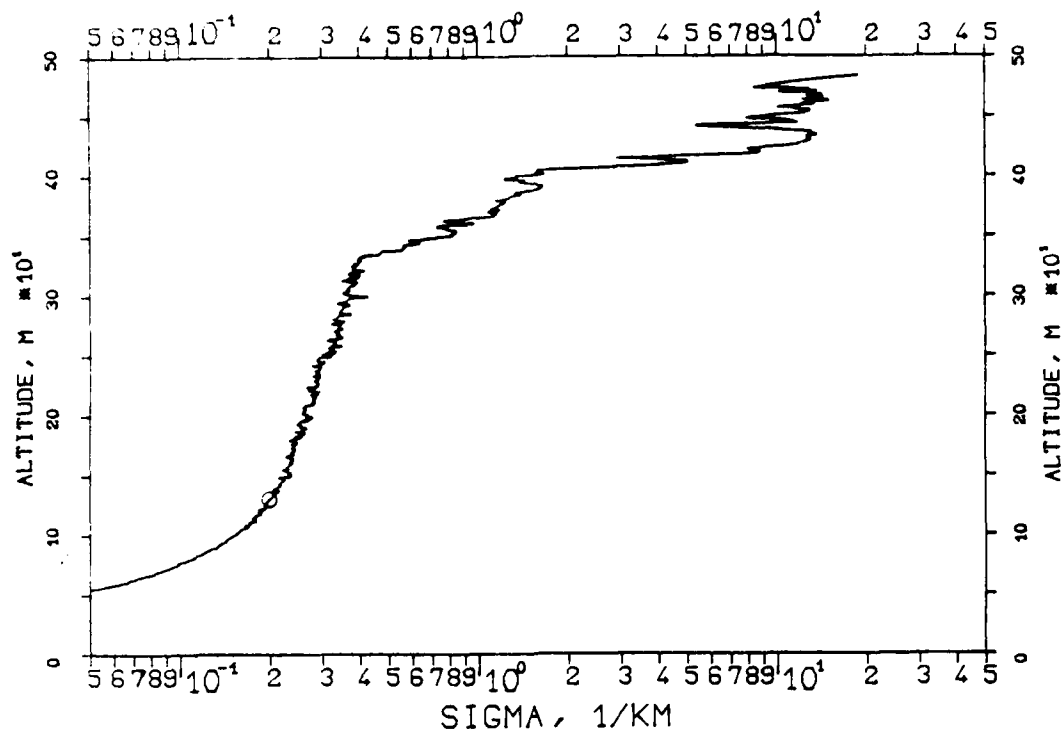


FIG. 7.38
KLETT-PROFILE, 0530NM, EL. 19DG12MN
830210, 10:45-10:46, CET
RM=1.632KM, SM=20.0000/KM, K=1.000

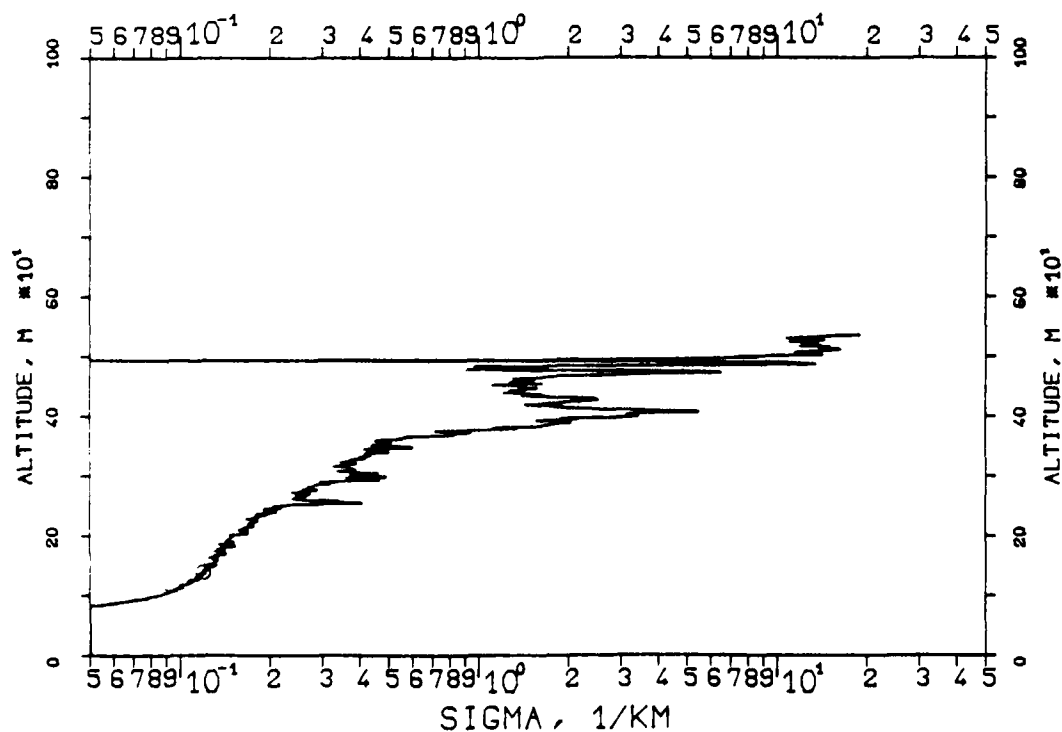


FIG. 7.39

KLETT-PROFILE ,0530NM,EL. 19DG12MN

830010, 11:40-11:40,CET

RM=2.193KM,SM=20.0000/KM,K=1.000

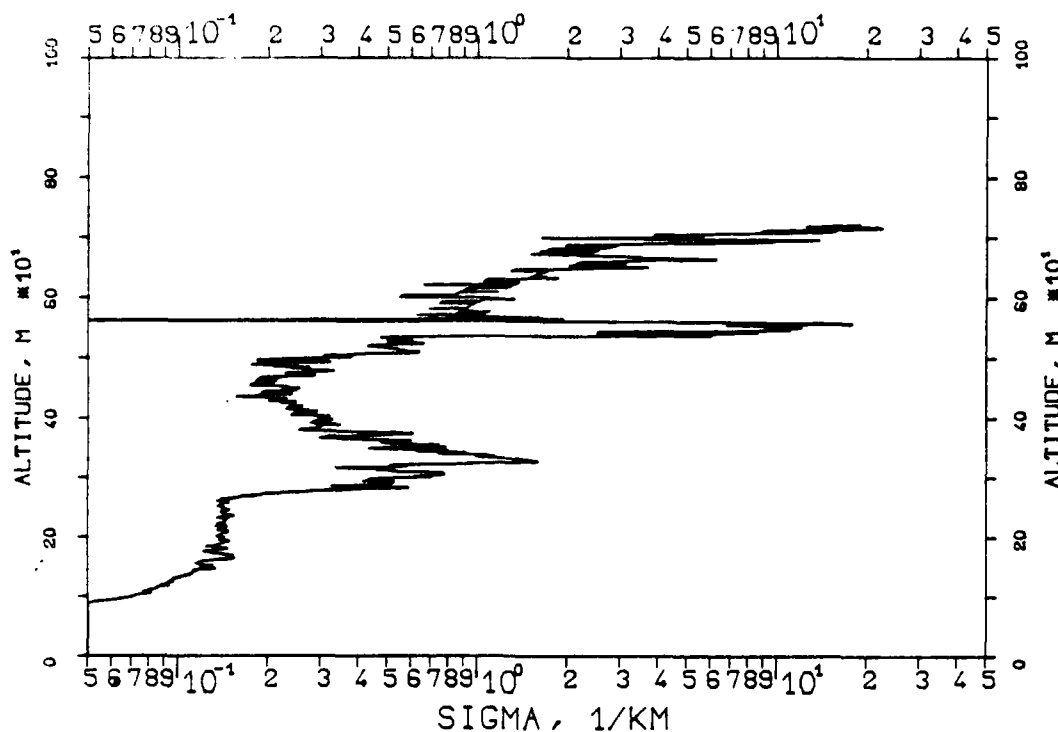


FIG. 7.40

KLETT-PROFILE ,0347NM,EL. 19DG12MN

830210, 11:42-11:43,CET

RM=2.218KM,SM=20.0000/KM,K=1.000

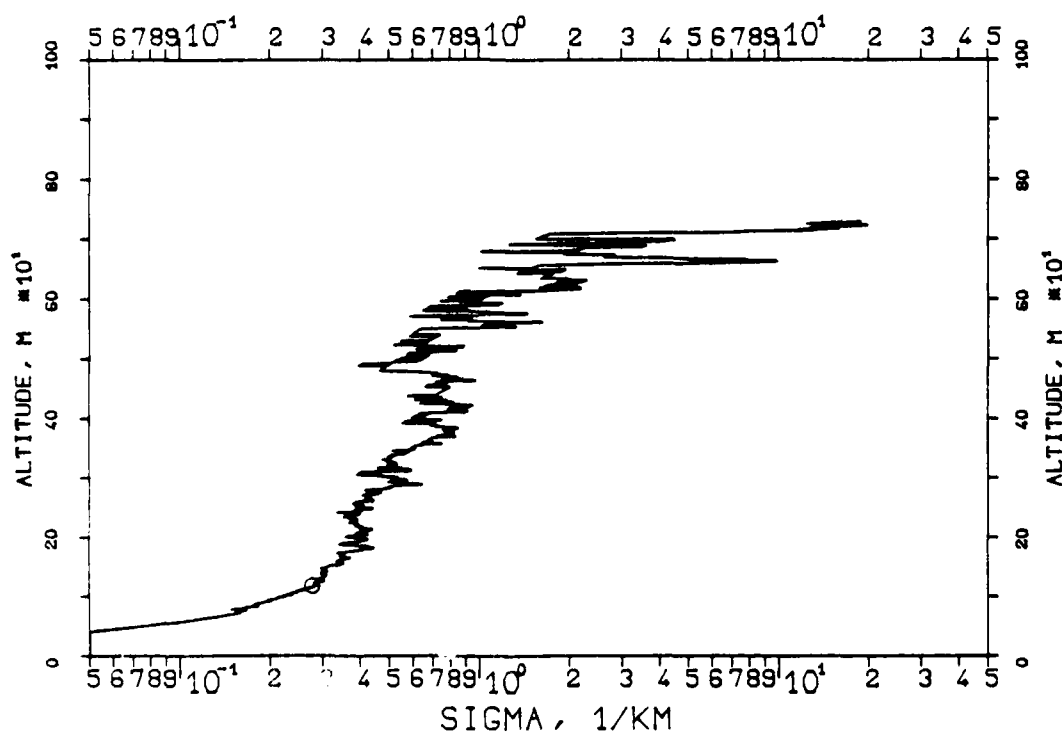


FIG. 7.41
KLETT-PROFILE, 0694NM, EL. 19DG12MN
830210, 11:45-11:45, CET
RM=2.203KM, SM=20.0000/KM, K=1.000

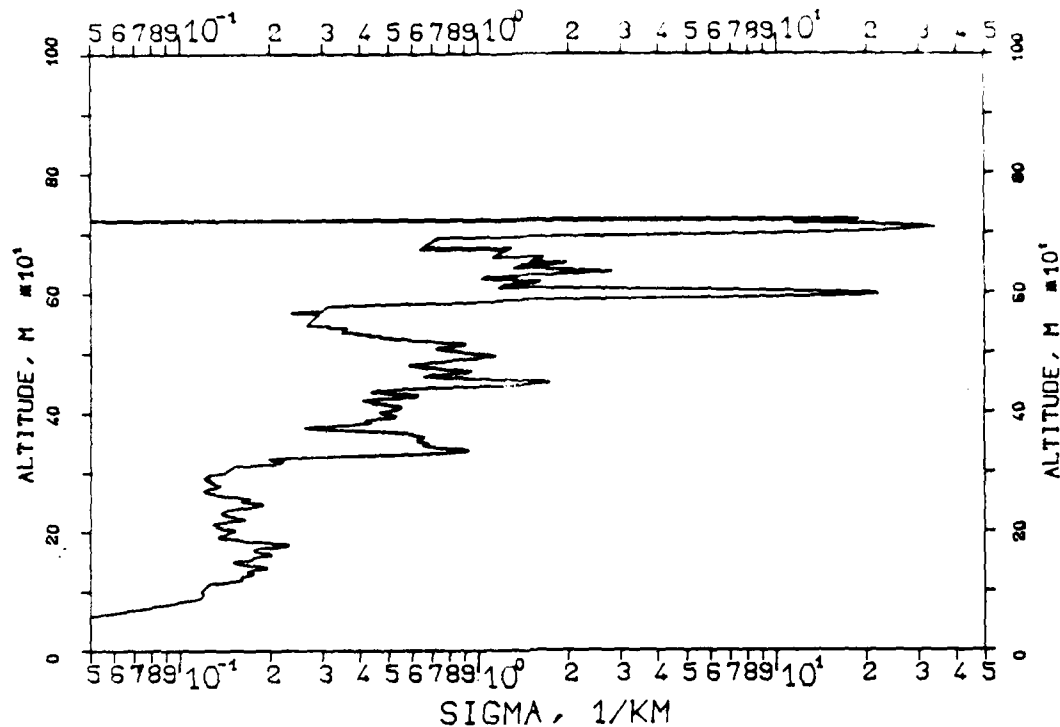


FIG. 7.42
KLETT-PROFILE, 1060NM, EL. 19DG12MN
830210, 11:49-11:49, CET
RM=2.548KM, SM=20.0000/KM, K=1.000

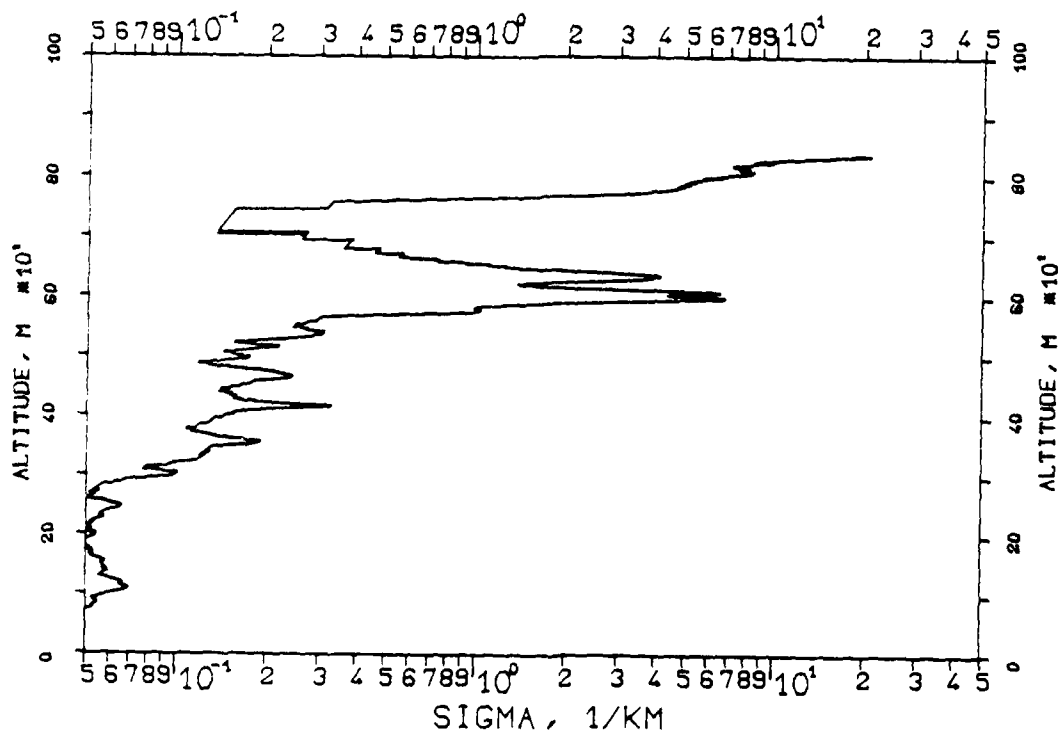


FIG. 7.43
KLETT PROFILE, 1060NM, EL. 19DG12MN
830210, 14:10-14:11, CET
RM=1.849KM, SM=20.0000/KM, K=1.000

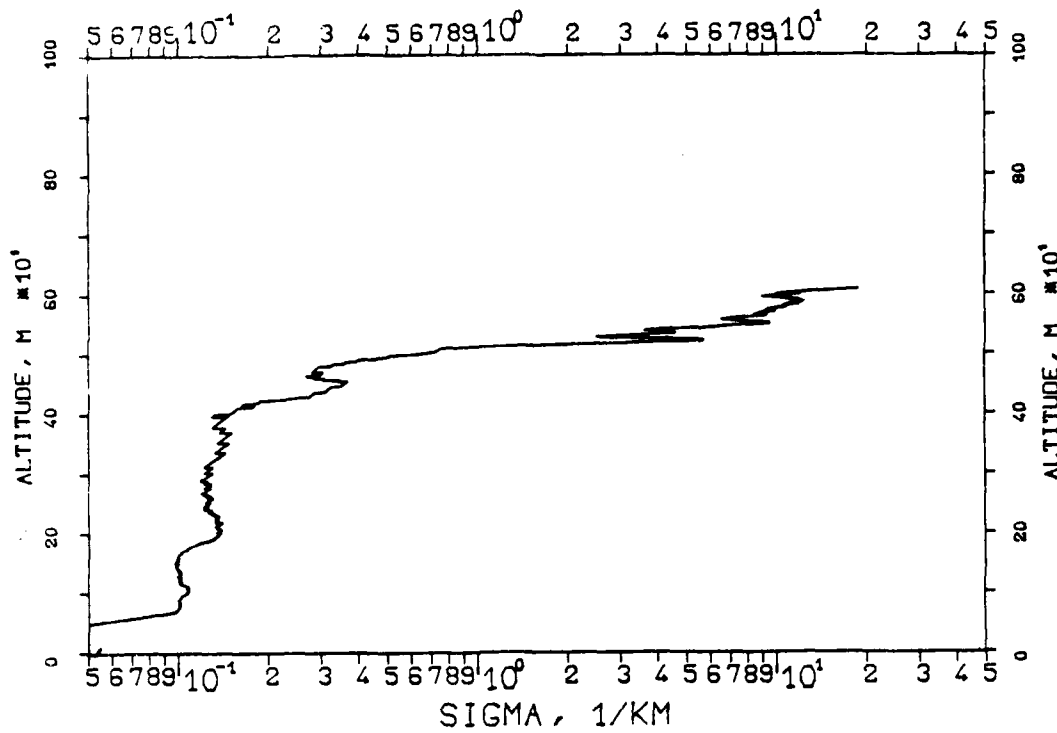


FIG. 7.44
KLETT-PROFILE, 0694NM, EL. 19DG12MN
830210, 14:12-14:12, CET
RM=1.750KM, SM=20.0000/KM, K=1.000

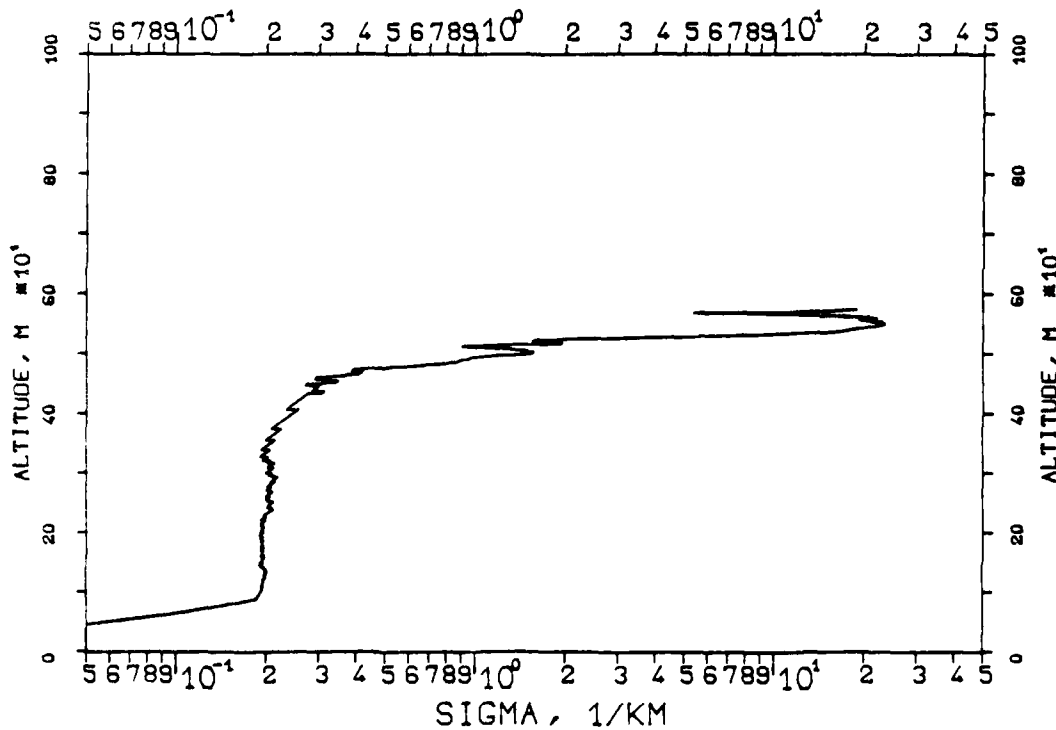


FIG. 7.45
KLETT-PROFILE, 0347NM, EL. 19DG12MN
830210, 14:14-14:15, CET
RM=1.702KM, SM=20.0000/KM, K=1.000

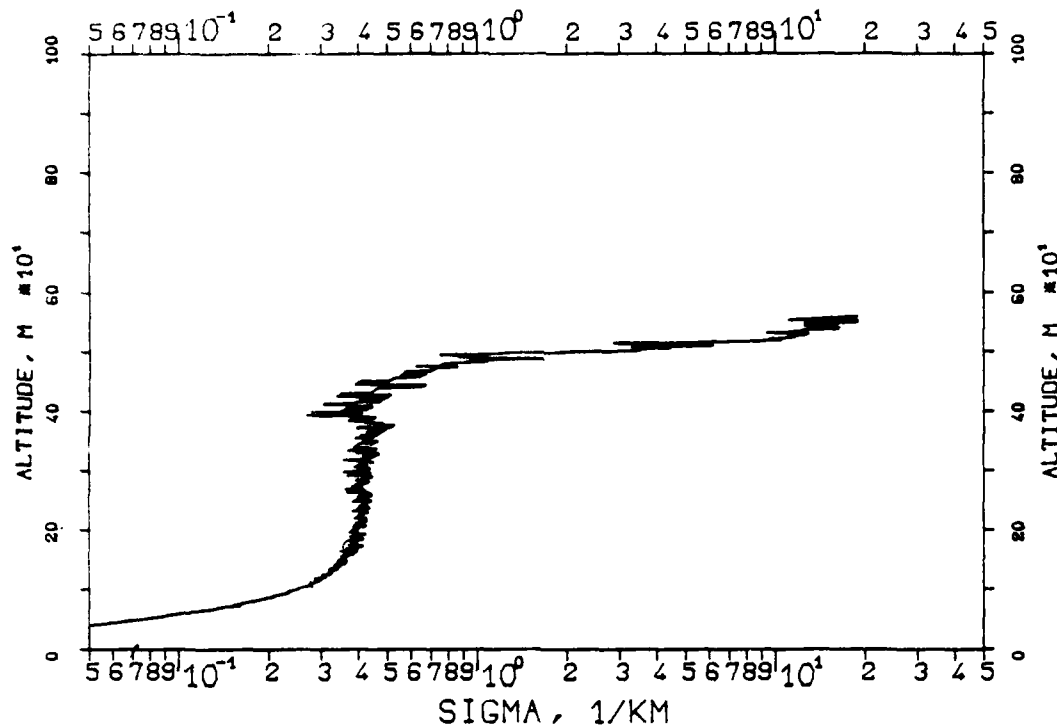


FIG. 7.46
KLETT-PROFILE, 0530NM, EL. 19DG12MN
830210, 14:16-14:17, CET
RM=1.762KM, SM=20.0000/KM, K=1.000

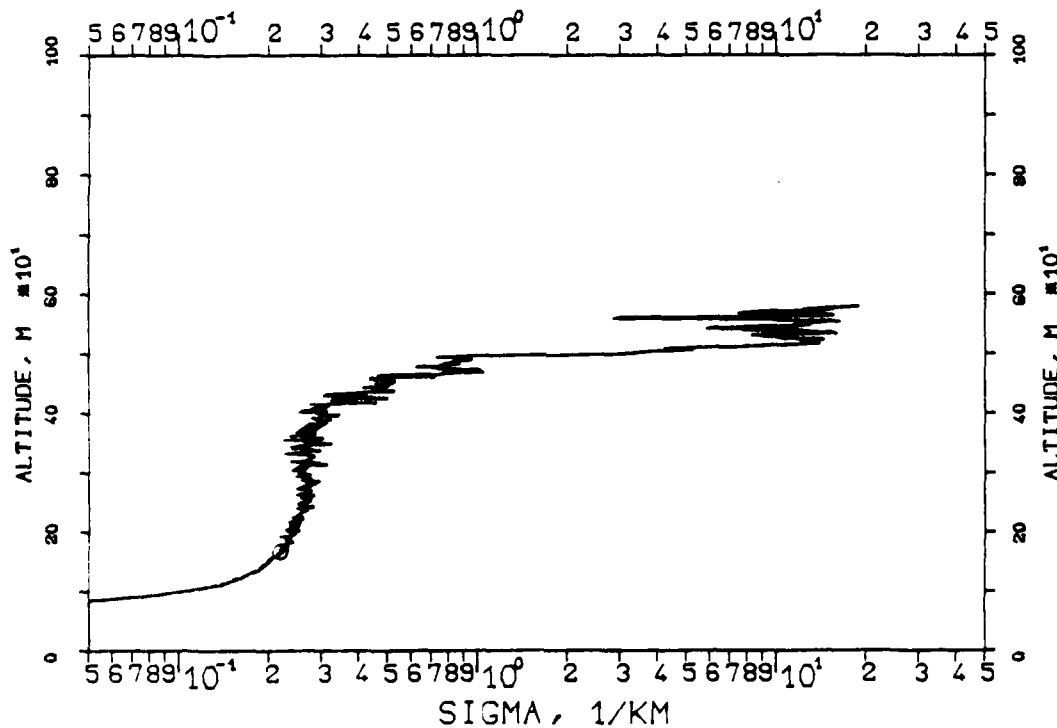


FIG. 7.47
 KLETT-PROFILE, 0530NM, EL. 19DG12MN
 830210, 15:09-15:09, CET
 RM=1.705KM, SM=20.0000/KM, K=1.000

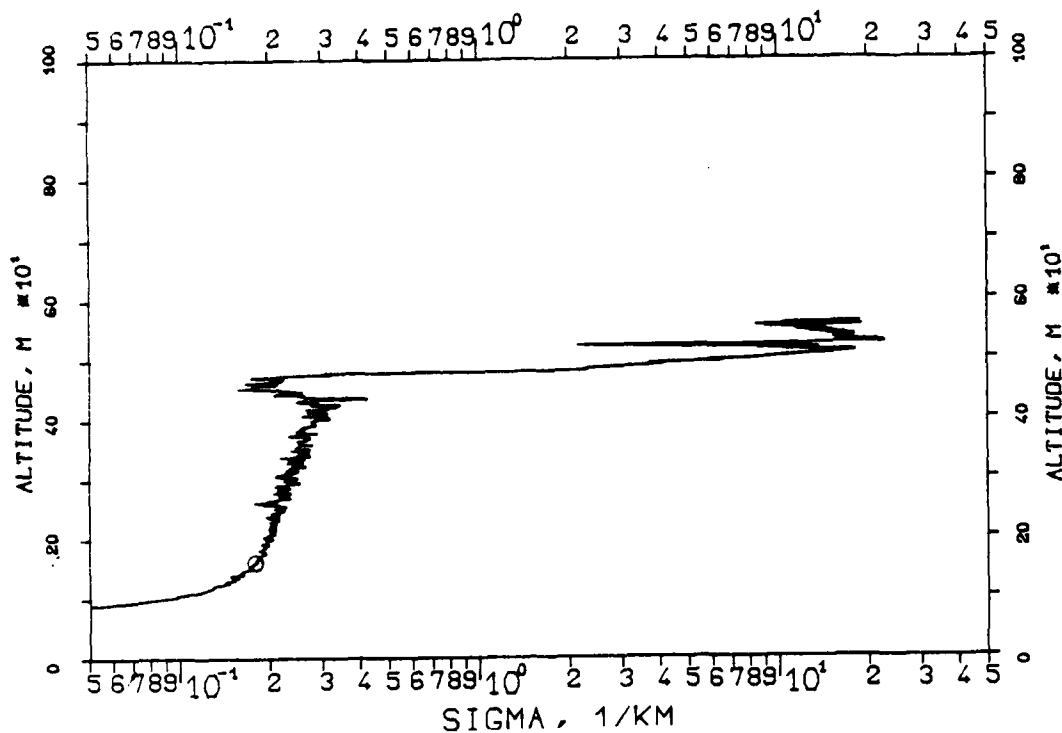


FIG. 7.48
 KLETT-PROFILE, 0347NM, EL. 19DG12MN
 830210, 15:12-15:12, CET
 RM=1.873KM, SM=20.0000/KM, K=1.000

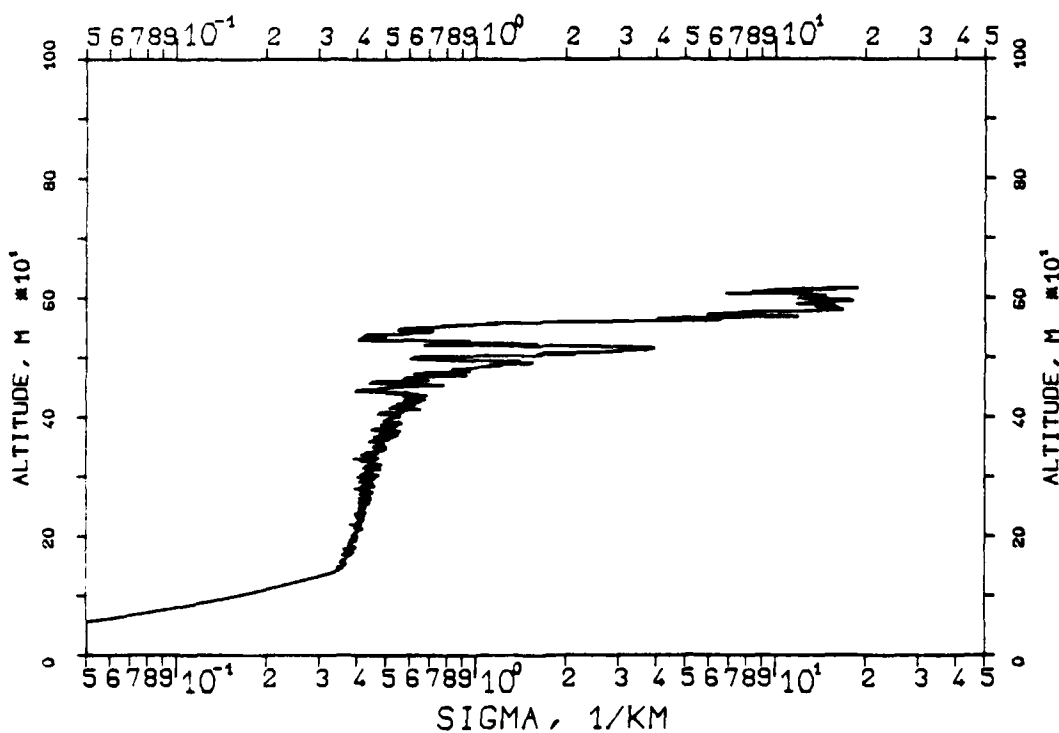


FIG. 7.49
KLETT-PROFILE, 0694NM, EL. 19DG12MN
830210, 15:14-15:14, CET
RM=1.851KM, SM=20.0000/KM, K=1.000

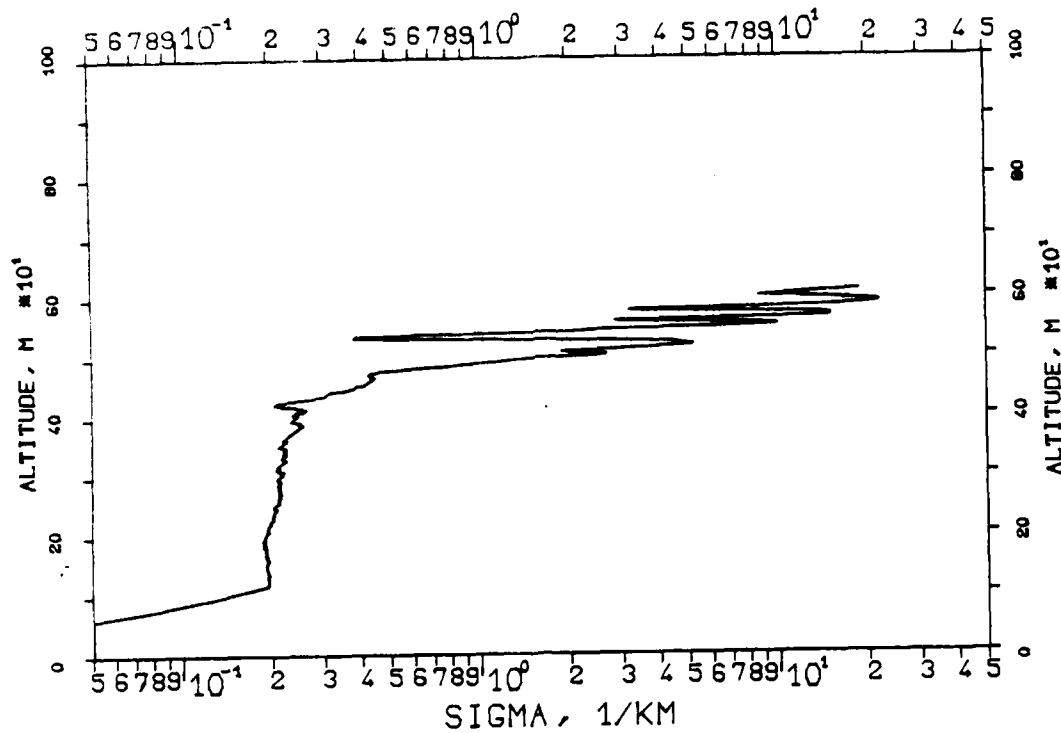


FIG. 7.50
KLETT-PROFILE, 1060NM, EL. 19DG12MN
830210, 15:17-15:17, CET
RM=2.023KM, SM=20.0000/KM, K=1.000

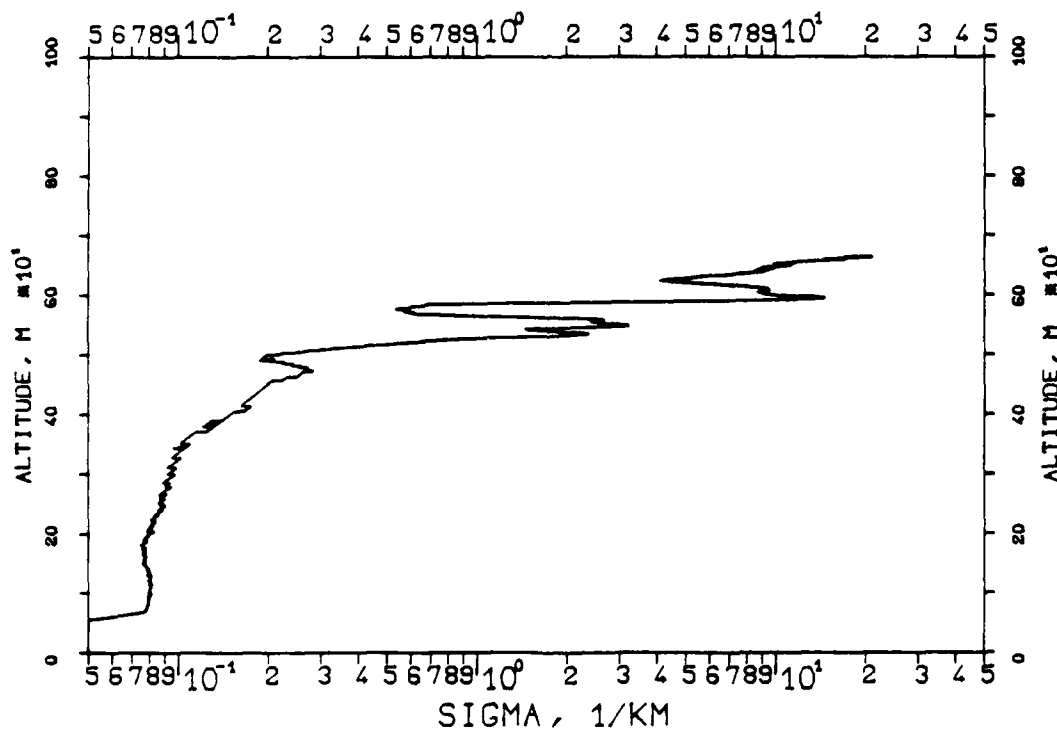


FIG. 7.51
KLETT-PROFILE, 1060NM, EL. 19DG12MN
830210, 16:19-16:19, CET
RM=1.989KM, SM=20.0000/KM, K=1.000

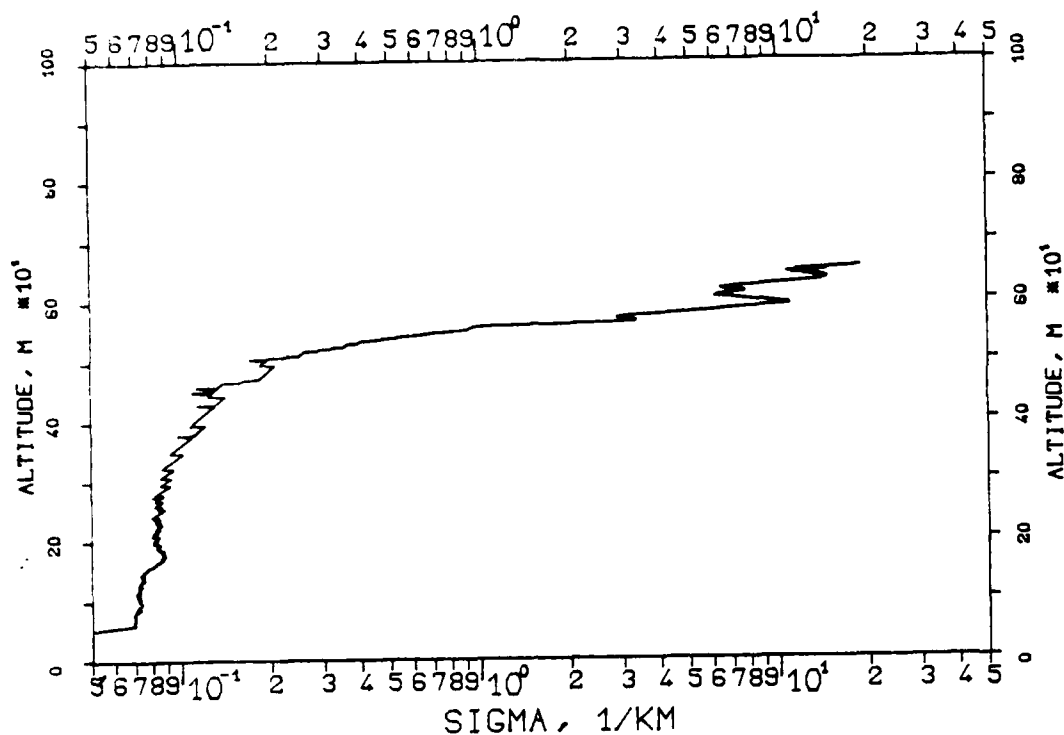


FIG. 7.52
KLETT-PROFILE, 0694NM, EL. 19DG12MN
830210, 16:22-16:22, CET
RM=1.896KM, SM=20.0000/KM, K=1.000

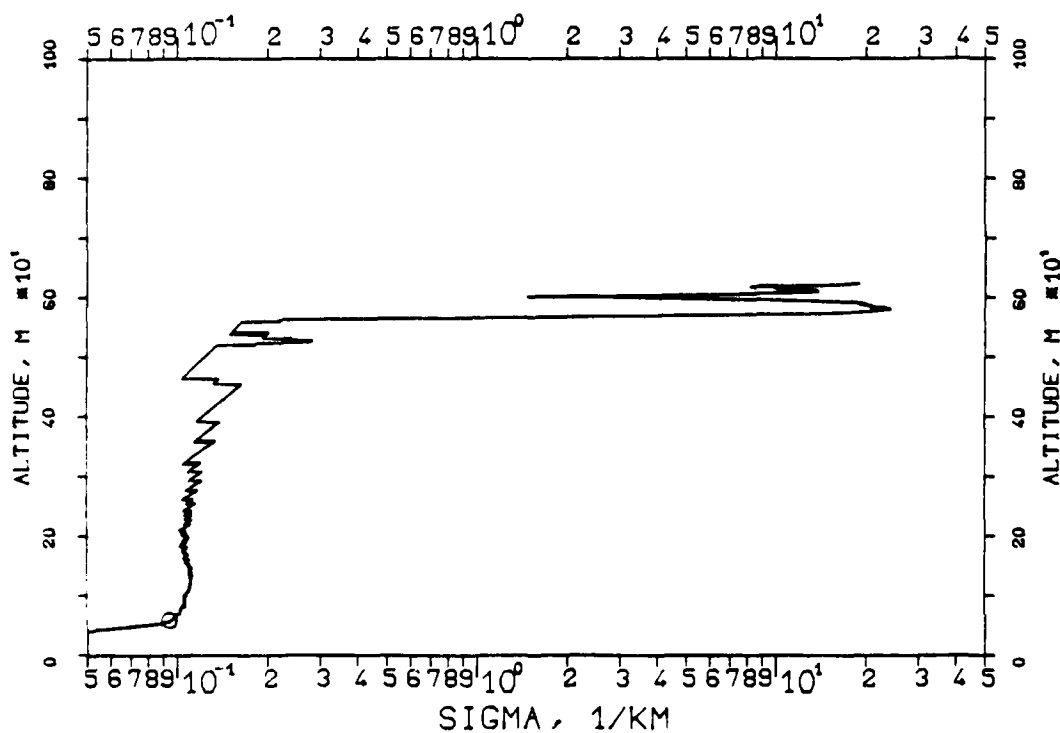


FIG. 7.53

KLETT-PROFILE, 0347NM, EL. 19DG 12MN
830210, 16:26-16:26, CET
RM=1.974KM, SM=20.0000/KM, K=1.000

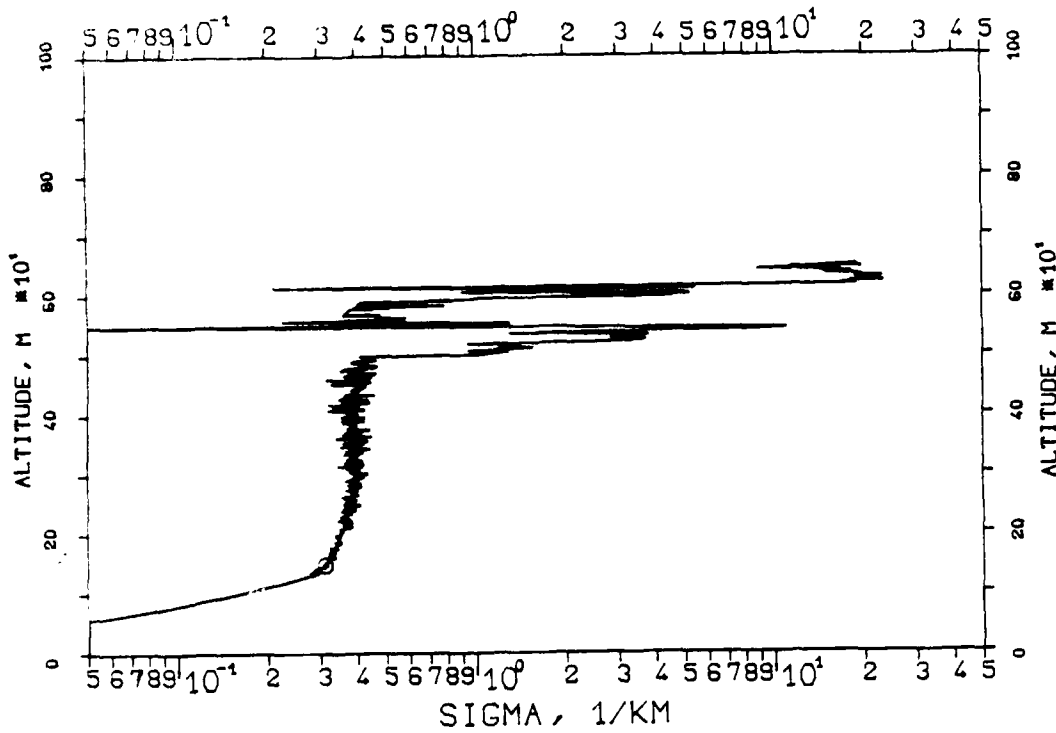


FIG. 7.54

KLETT-PROFILE, 0530NM, EL. 19DG 12MN
830210, 16:34-16:35, CET
RM=1.830KM, SM=20.0000/KM, K=1.000

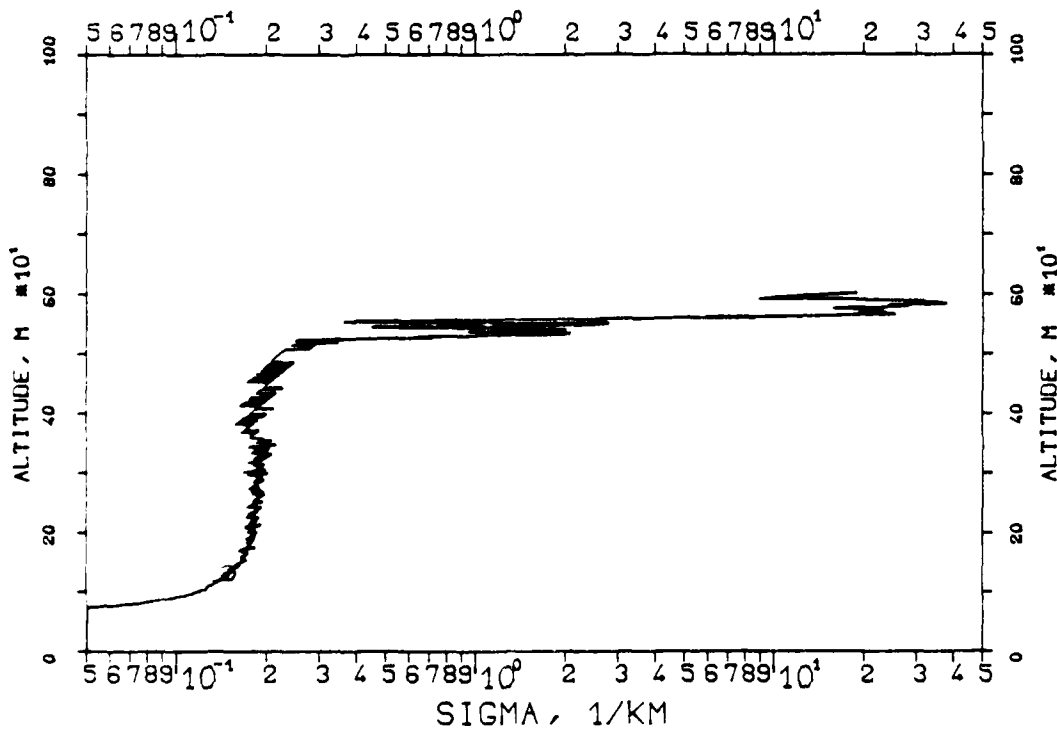


FIG. 7.55
KLETT-PROFILE, 0530NM, EL. 19DG12MN
830210, 17:15-17:15, CET
RM=1.774KM, SM=20.0000/KM, K=1.000

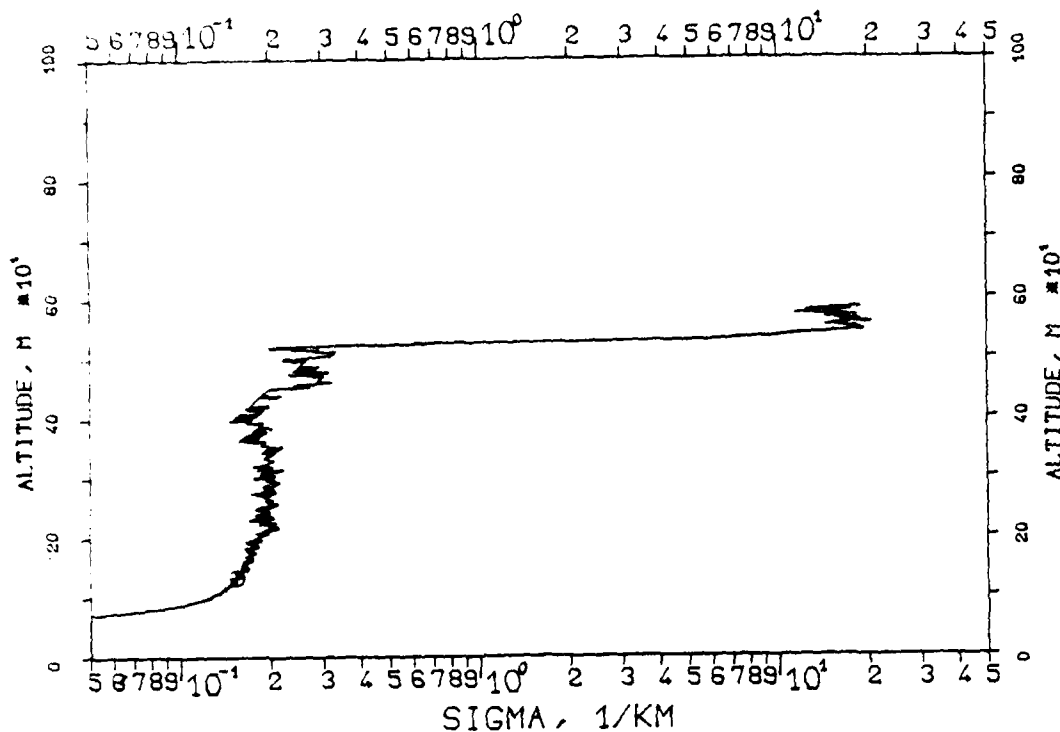


FIG. 7.56
KLETT-PROFILE, 0347NM, EL. 19DG12MN
830210, 17:18-17:18, CET
RM=1.851KM, SM=20.0000/KM, K=1.000

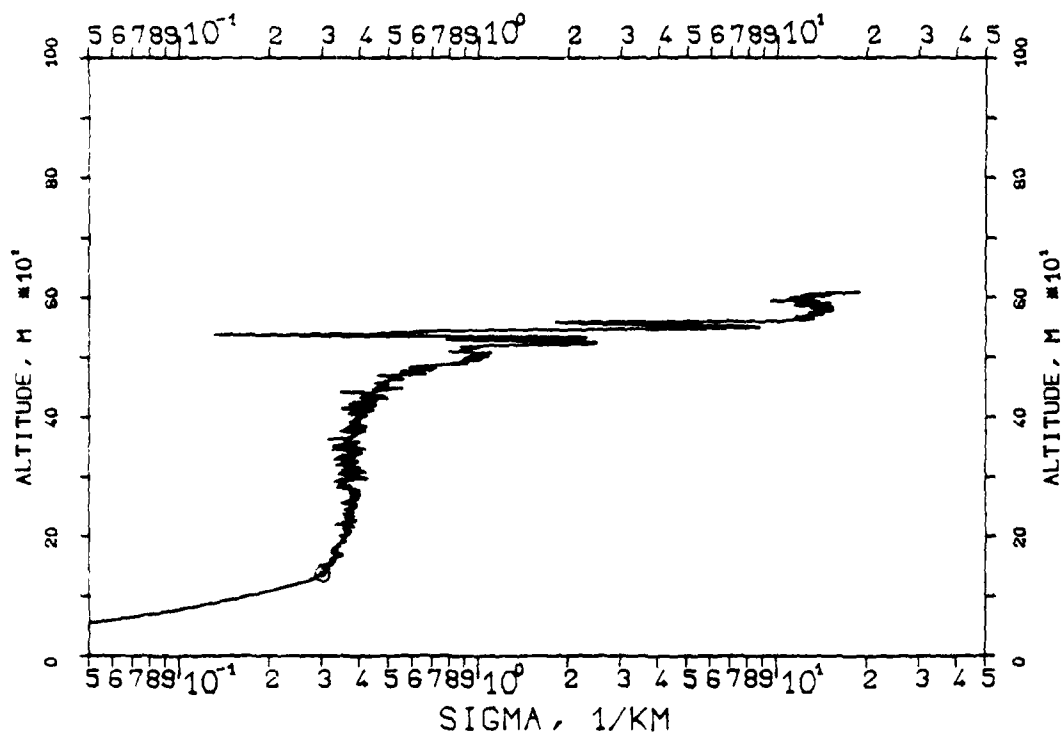


FIG. 7.57

KLETT-PROFILE, 0694NM, EL. 19DG 12MN

830210, 17:22-17:23, CET

RM=1.885KM, SM=20.0000/KM, K=1.000

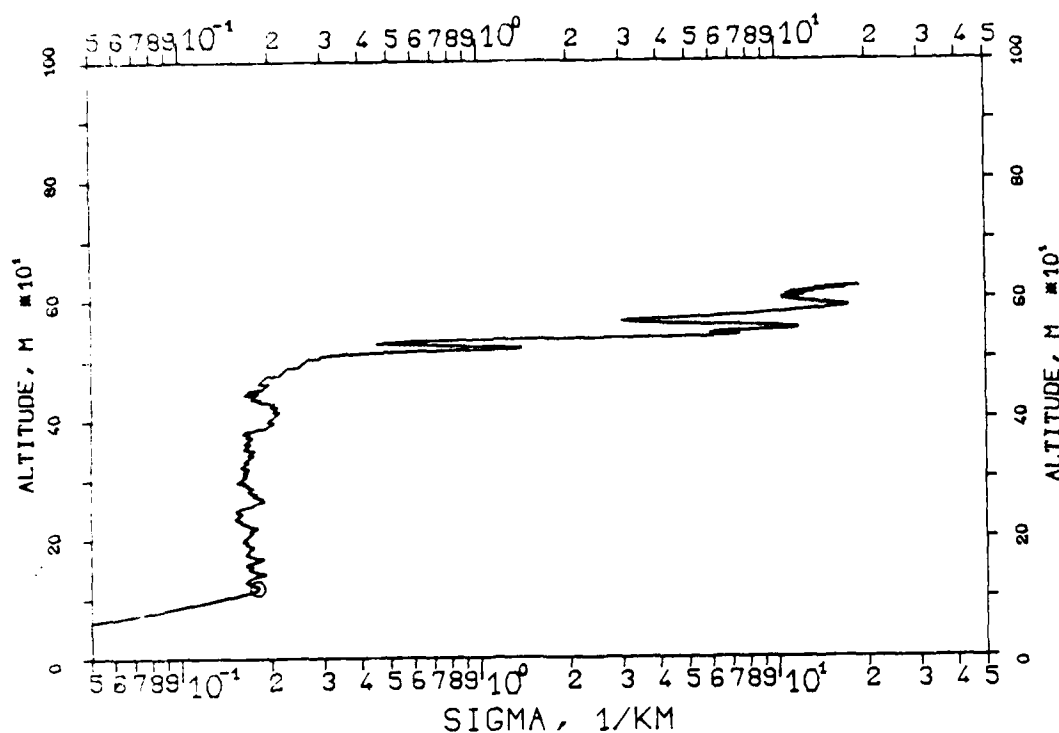
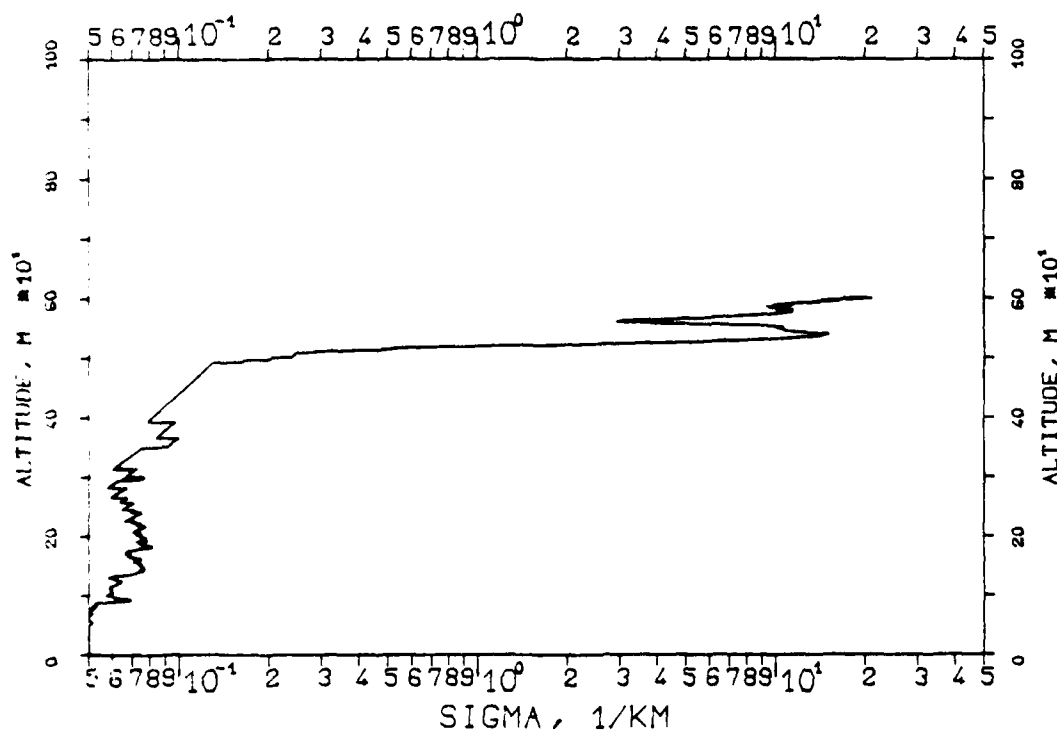


FIG. 7.58

KLETT-PROFILE, 1060NM, EL. 19DG 12MN

830210, 17:27-17:27, CET

RM=1.830KM, SM=20.0000/KM, K=1.000



FILE 7.61

KLETT PROFILE, 0530NM, EL. 19DG12MN

830316, 08:57-08:58, CET

RM=1.795KM, SM=20.0000/KM, K=1.000

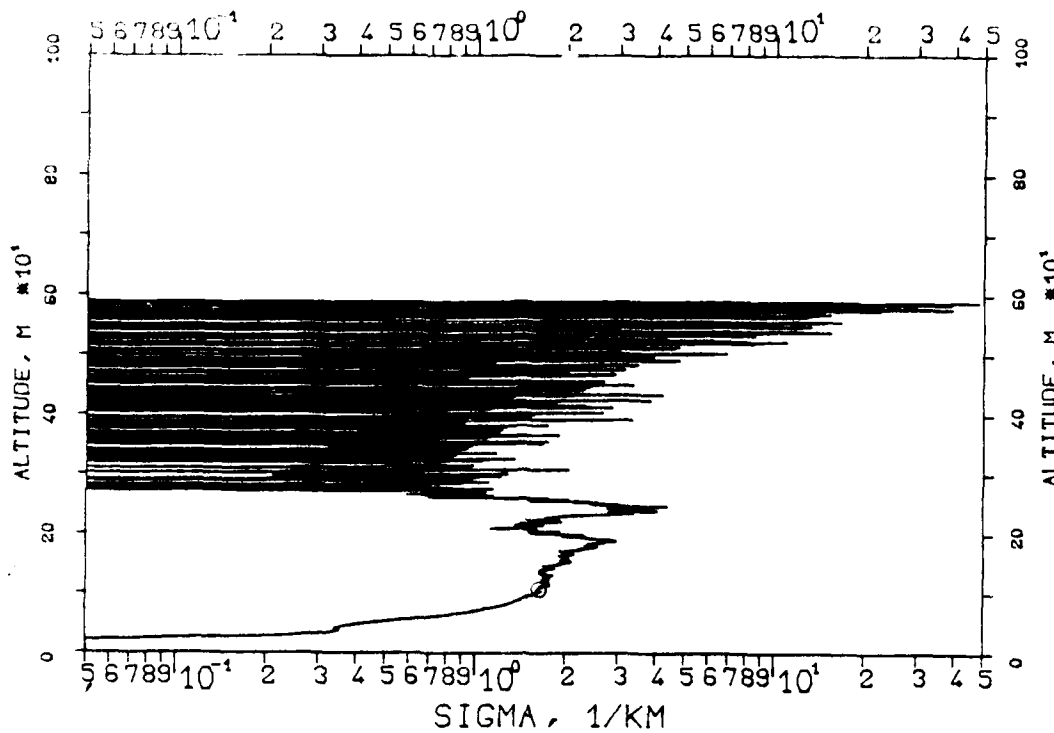
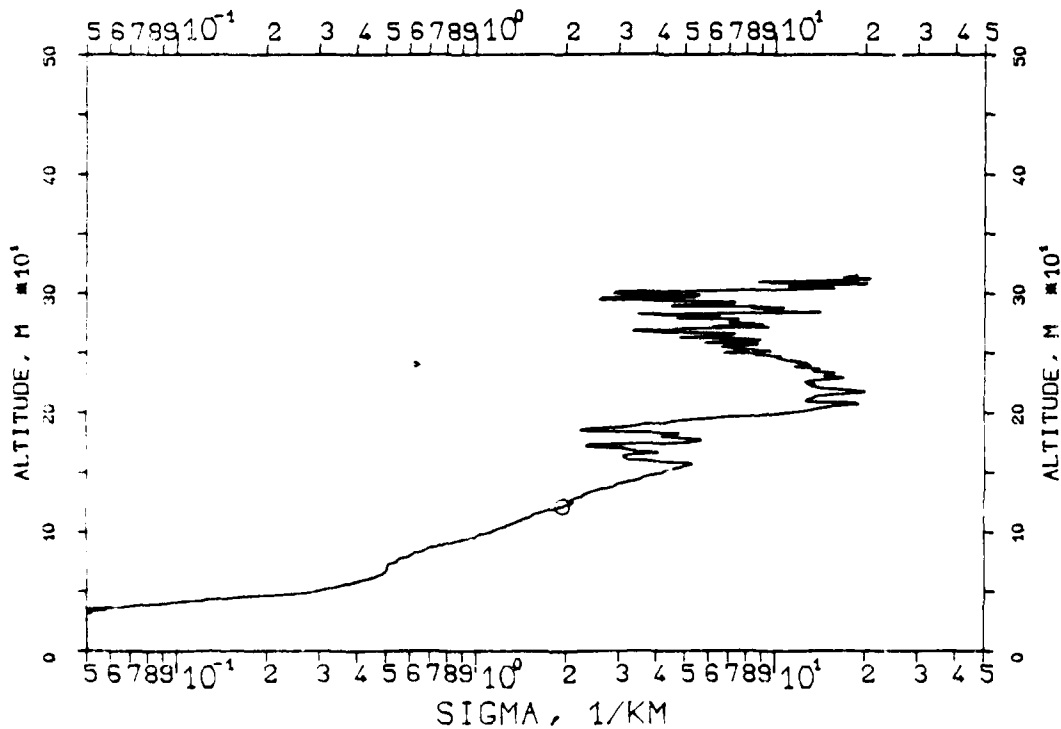


FIG. 7.61

KLETT-PROFILE, 0530NM, EL. 35DG00MN

830316, 09:09-09:09, CET

RM=0.550KM, SM=20.0000/KM, K=1.000



AD-A154 714

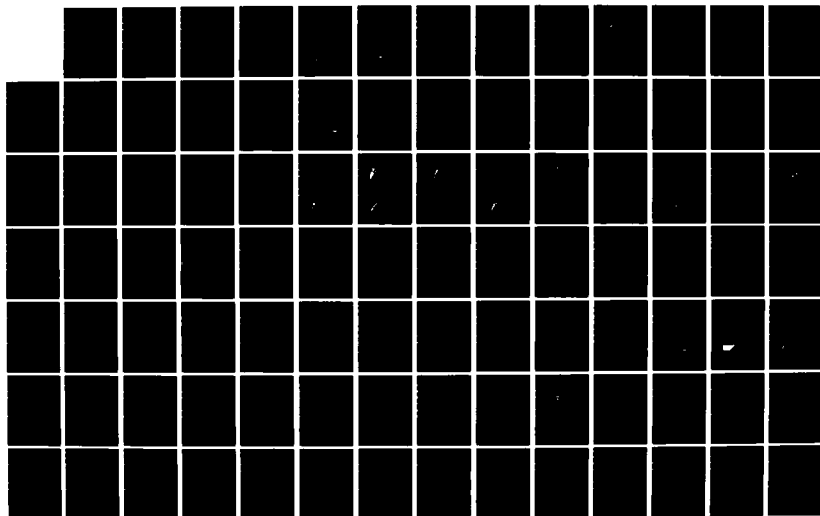
VISIBILITY AND VERTICAL STRUCTURE MEASUREMENTS IN
SOUTHERN GERMANY(U) FRAUNHOFER-INST FUER
ATMOSPHAERISCHE UMWELTFORSCHUNG GARMISCH.
R REITER ET AL. DEC 84 DAJA45-83-C-0023

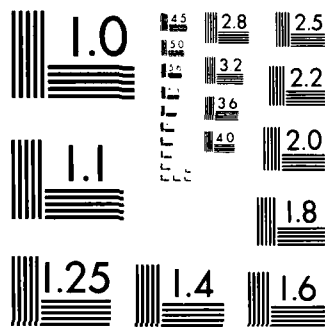
2/3

UNCLASSIFIED

F/G 4/2

NL





MICROCOPY RESOLUTION TEST CHART
NATIONAL BUREAU OF STANDARDS 1963-A

FIG. 7.62
KLETT-PROFILE, 0530NM, EL. 35DG00MN
830316, 09:11-09:11, CET
RM=0.400KM, SM=20.0000/KM, K=1.000

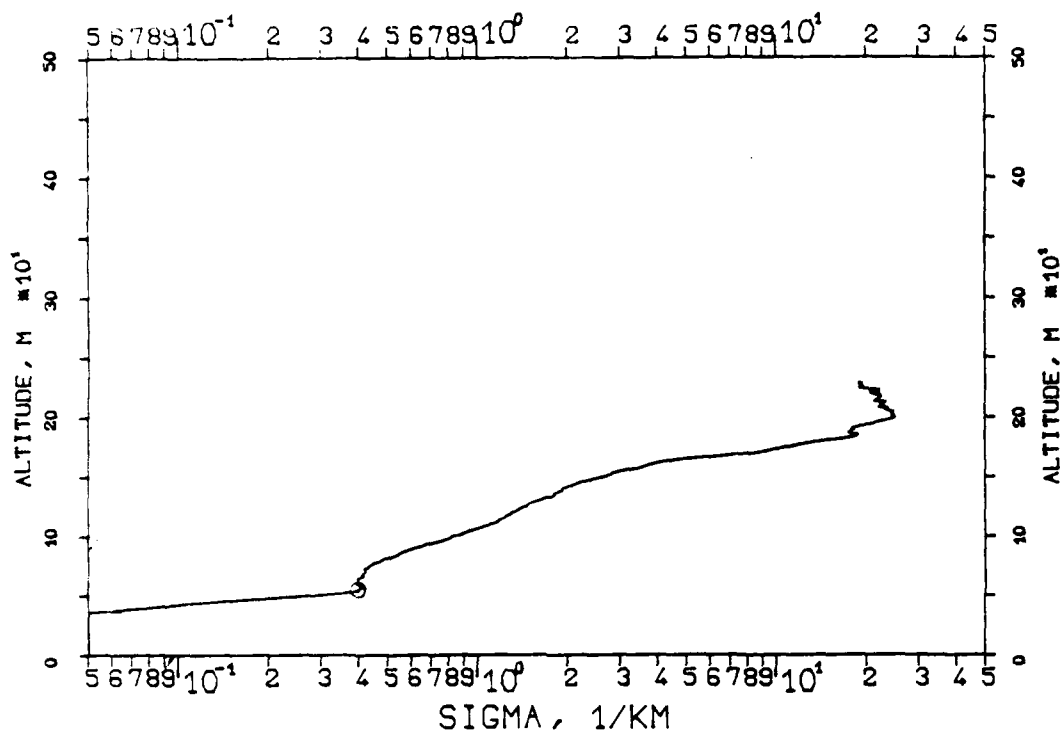


FIG. 7.63
KLETT-PROFILE, 1060NM, EL. 35DG00MN
830316, 09:16-09:17, CET
RM=0.460KM, SM=20.0000/KM, K=1.000

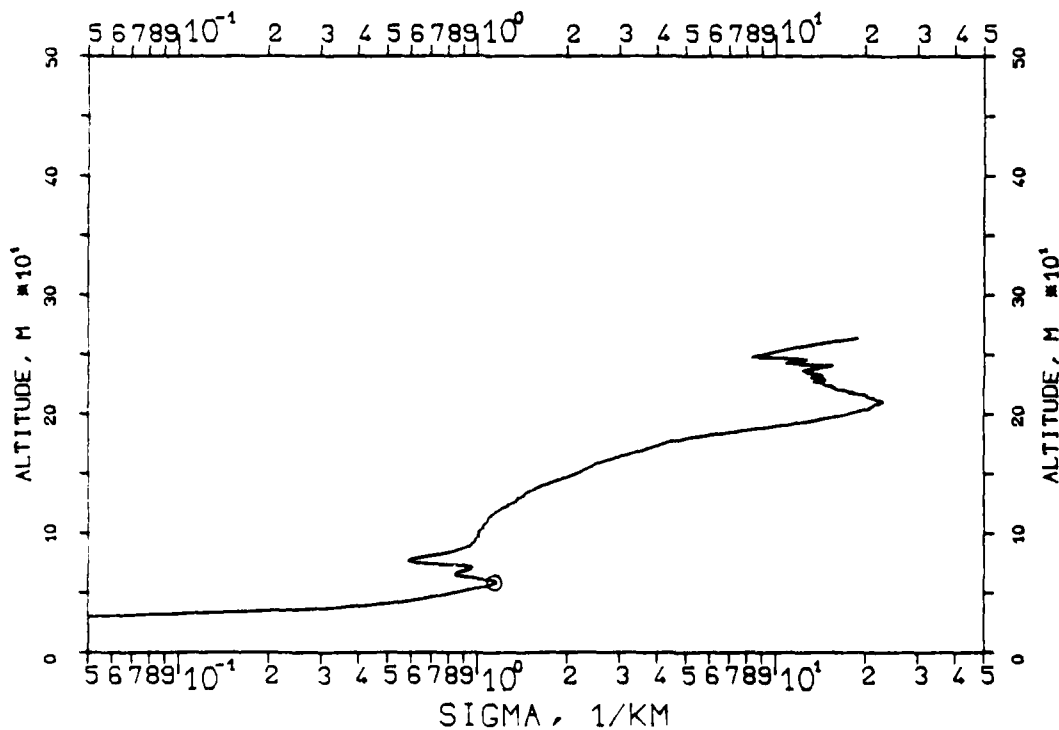


FIG. 7.64
KLETT-PROFILE, 1060NM, EL. 35DG00MN
830316, 09:19-09:20, CET
RM=0.450KM, SM=20.0000/KM, K=1.000

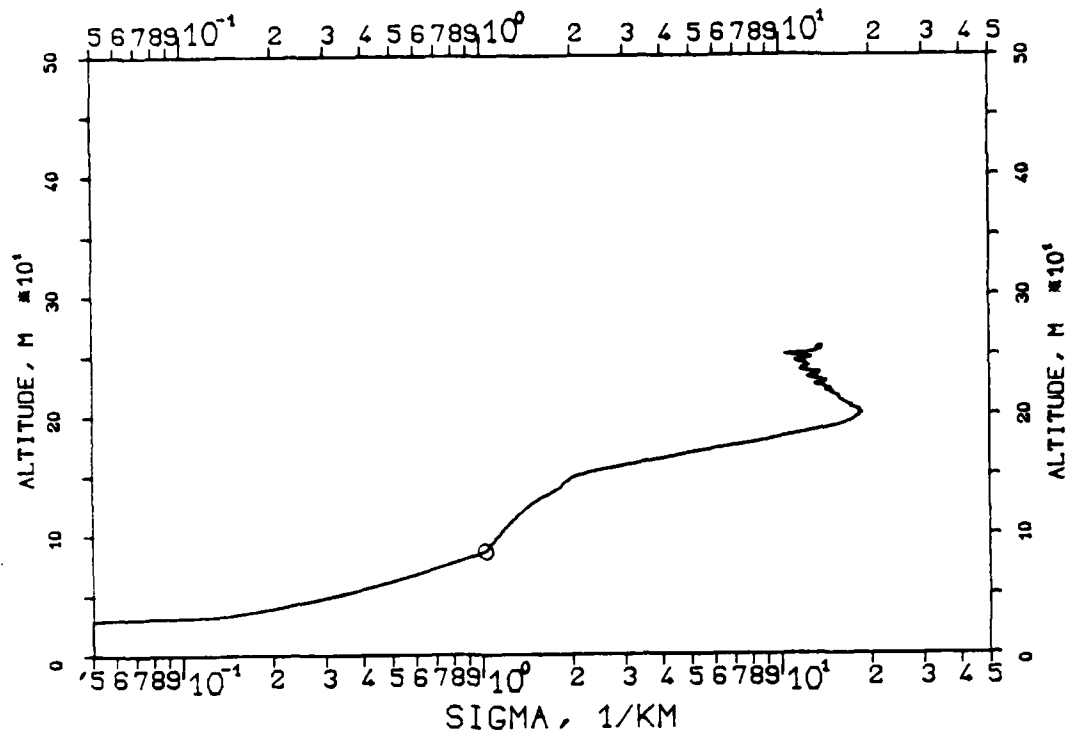


FIG. 7.65
KLETT-PROFILE, 0694NM, EL. 35DG00MN
830316, 09:22-09:23, CET
RM=0.450KM, SM=20.0000/KM, K=1.000

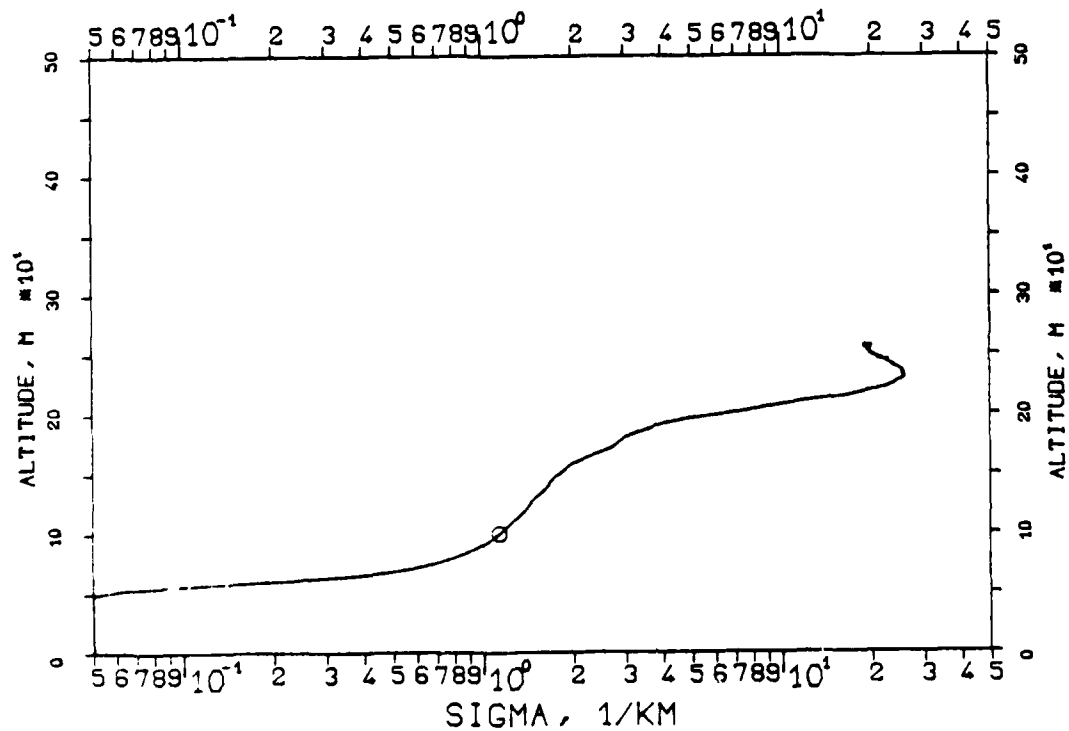


FIG. 7.66
 KLETT-PROFILE, 1060NM, EL. 19DG12MN
 830629, 07:13-07:13, CET
 RM=2.319KM, SM=20.0000/KM, K=1.000

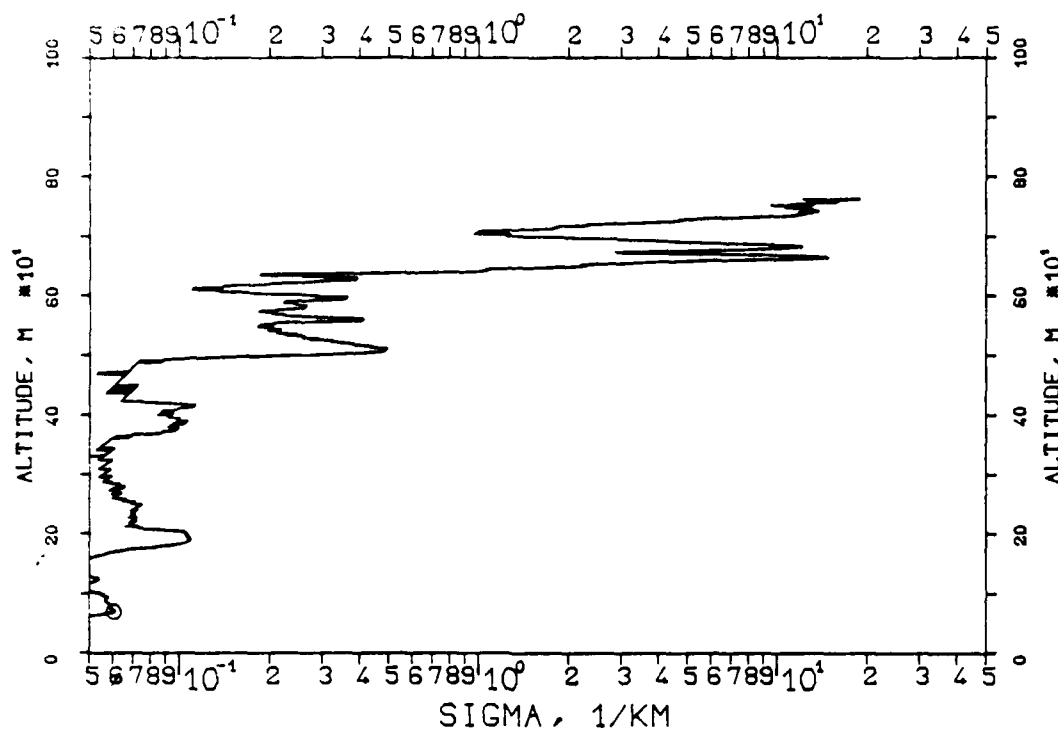


FIG. 7.67
 KLETT-PROFILE, 0694NM, EL. 19DG12MN
 830629, 07:17-07:17, CET
 RM=2.235KM, SM=20.0000/KM, K=1.000

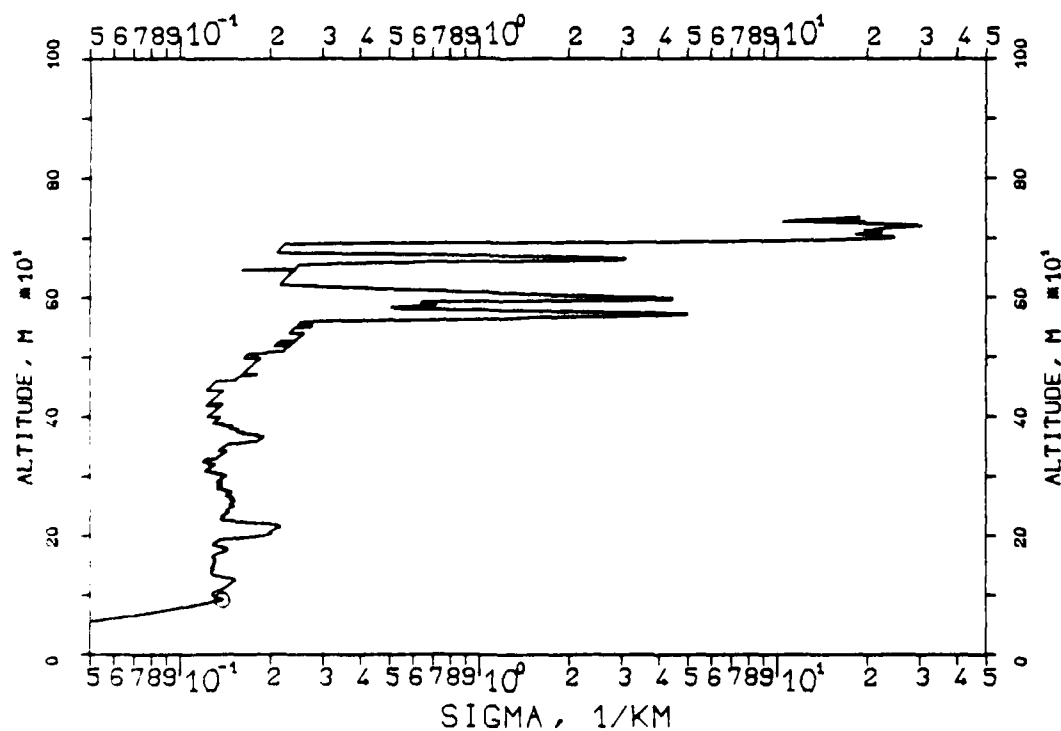


FIG. 7.68
KLETT-PROFILE ,0347NM,EL. 19DG12MN
830629, 07:20-07:20,CET
RM=2.004KM,SM=20.0000/KM,K=1.000

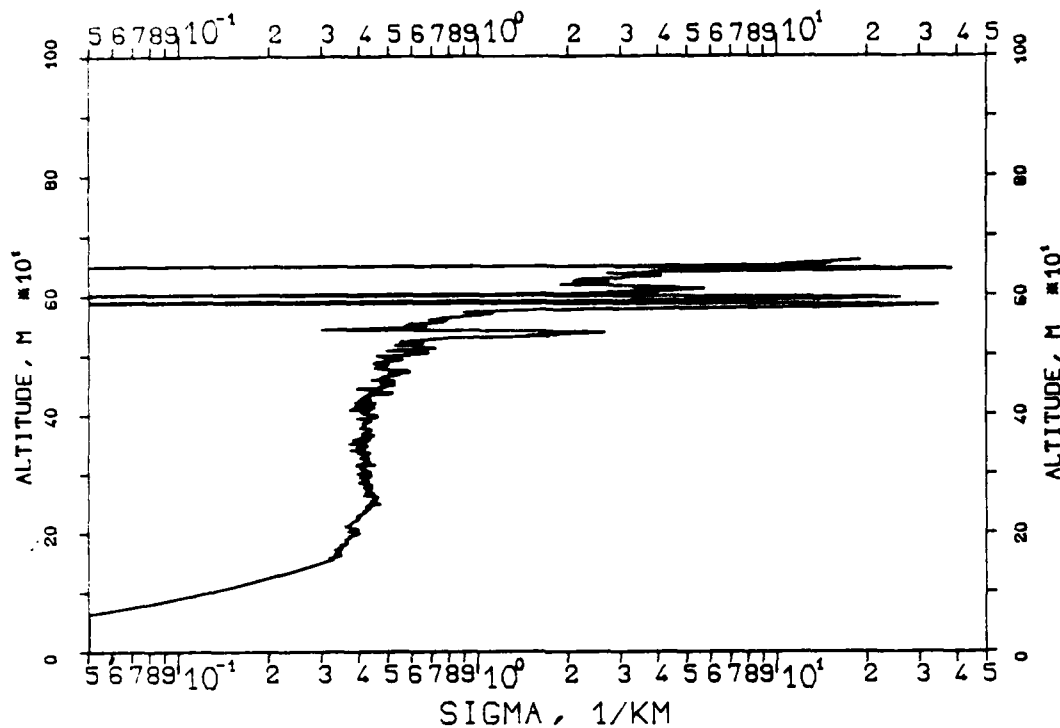


FIG. 7.69
KLETT-PROFILE ,0530NM,EL. 19DG12MN
830629, 07:22-07:22,CET
RM=1.849KM,SM=20.0000/KM,K=1.000

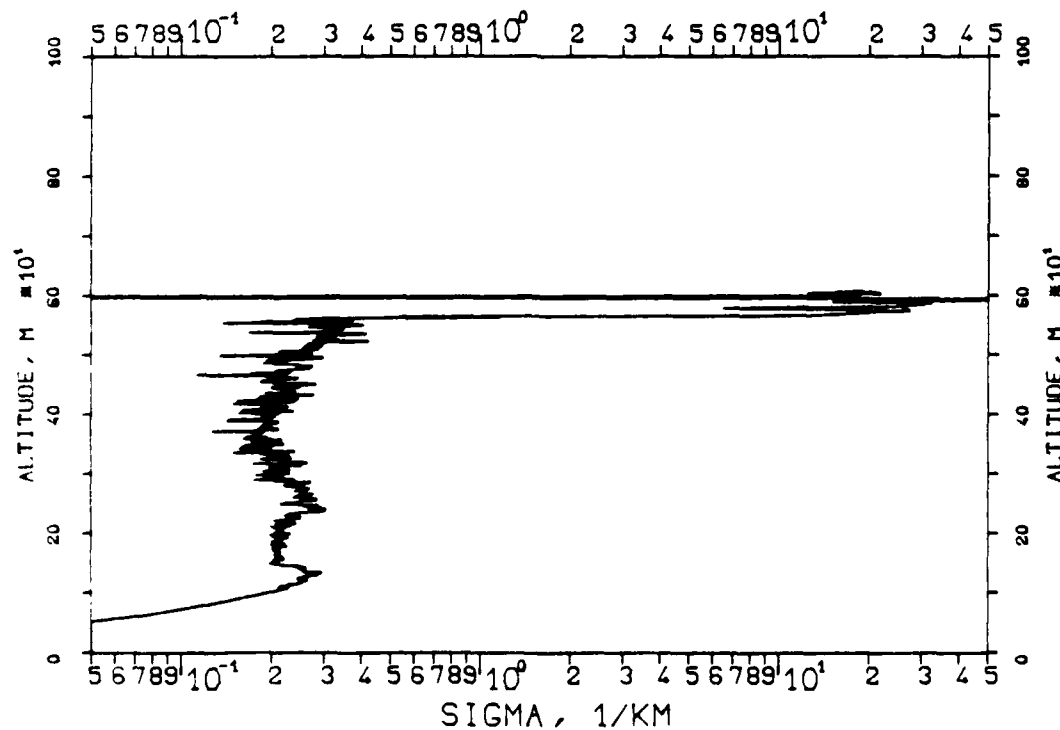


FIG. 7.70

KLETT-PROFILE, 0530NM, EL. 19DG12MN

830629, 08:03-08:04, CET

RM=2.300KM, SM=20.0000/KM, K=1.000

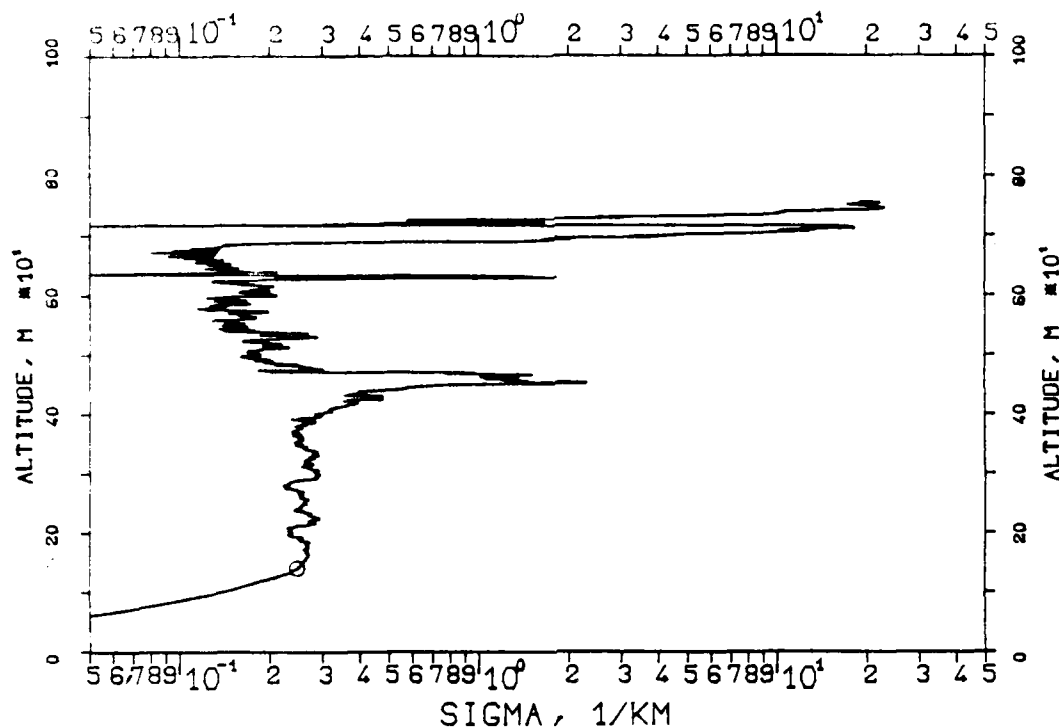


FIG. 7.71

KLETT-PROFILE, 0347NM, EL. 19DG12MN

830629, 08:06-08:06, CET

RM=2.025KM, SM=20.0000/KM, K=1.000

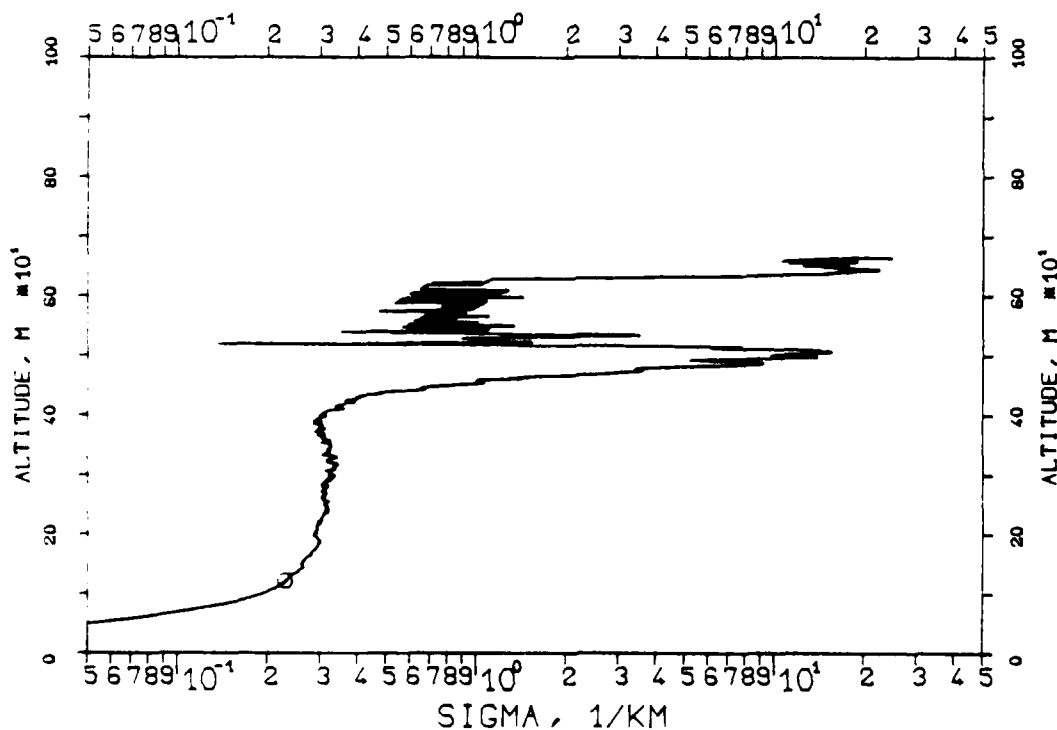


FIG. 7.72

KLETT-PROFILE, 0694NM, EL. 19DG12MN

830629, 08:10-08:10, CET

RM=1.918KM, SM=20.0000/KM, K=1.000

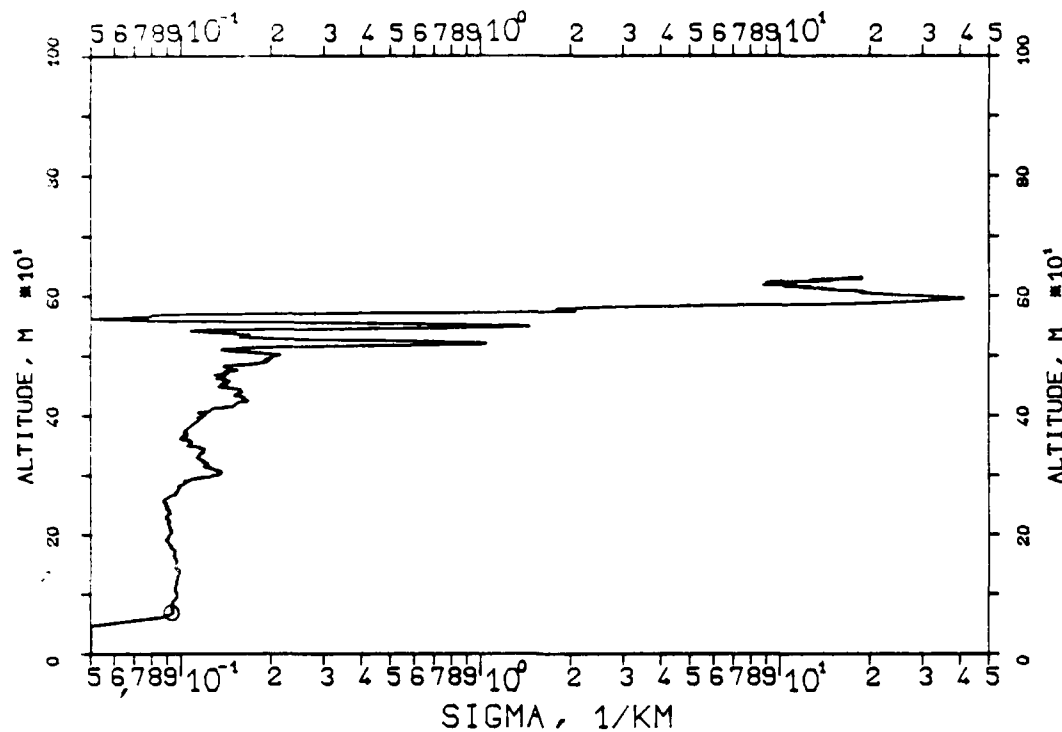


FIG. 7.73

KLETT-PROFILE, 1060NM, EL. 19DG12MN

830629, 08:12-08:13, CET

RM=1.711KM, SM=20.0000/KM, K=1.000

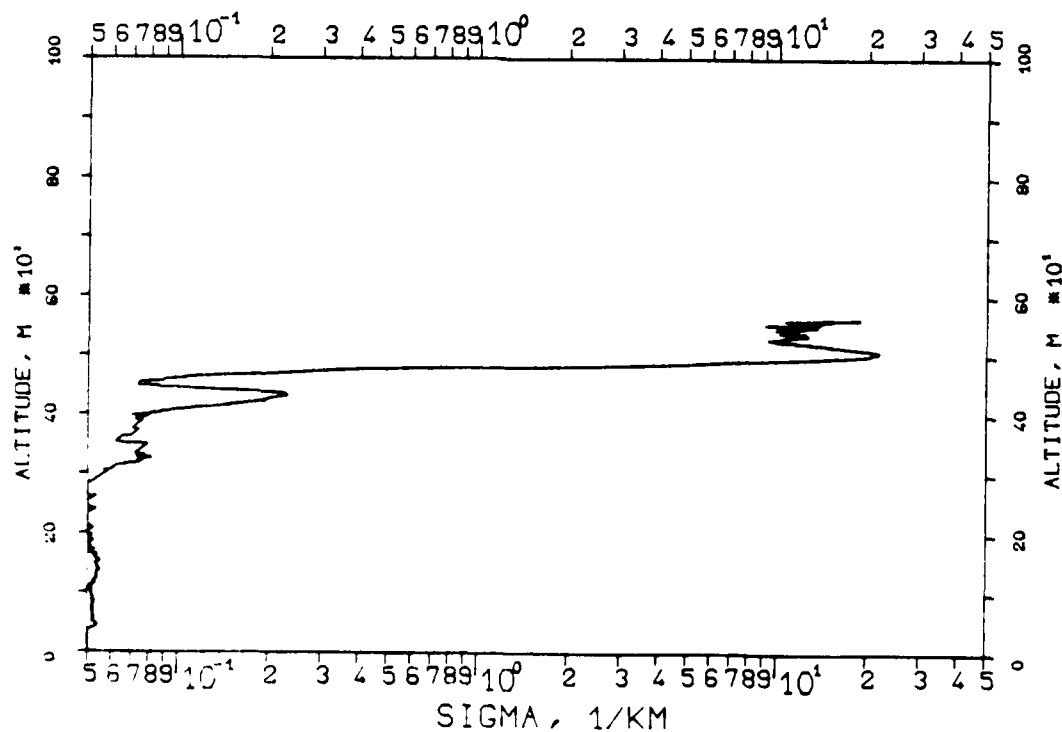


FIG. 7.74
KLETT-PROFILE, 1060NM, EL. 19DG12MN
830714, 07:33-07:34, CET
RM=1.570KM, SM=20.0000/KM, K=1.000

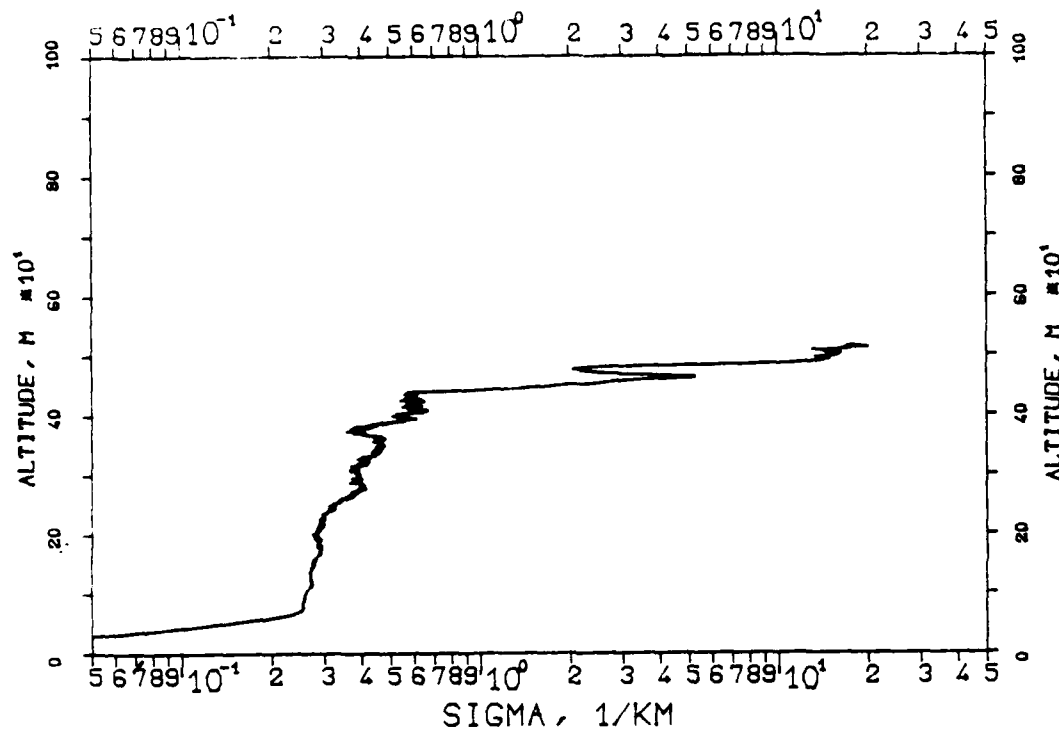


FIG. 7.75
KLETT-PROFILE, 1060NM, EL. 19DG12MN
830714, 07:37-07:38, CET
RM=1.570KM, SM=20.0000/KM, K=1.000

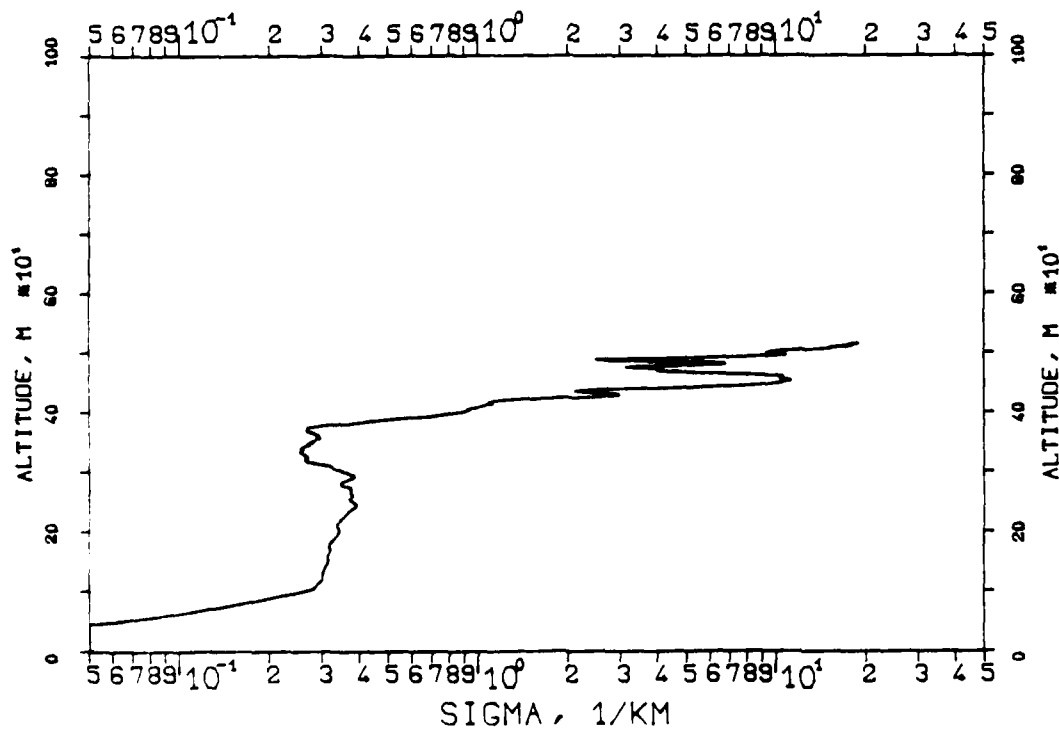


FIG. 7.76
 KLETT-PROFILE, 0694NM, EL. 19DG12MN
 830714, 07:40-07:41, CET
 RM=1.752KM, SM=20.0000/KM, K=1.000

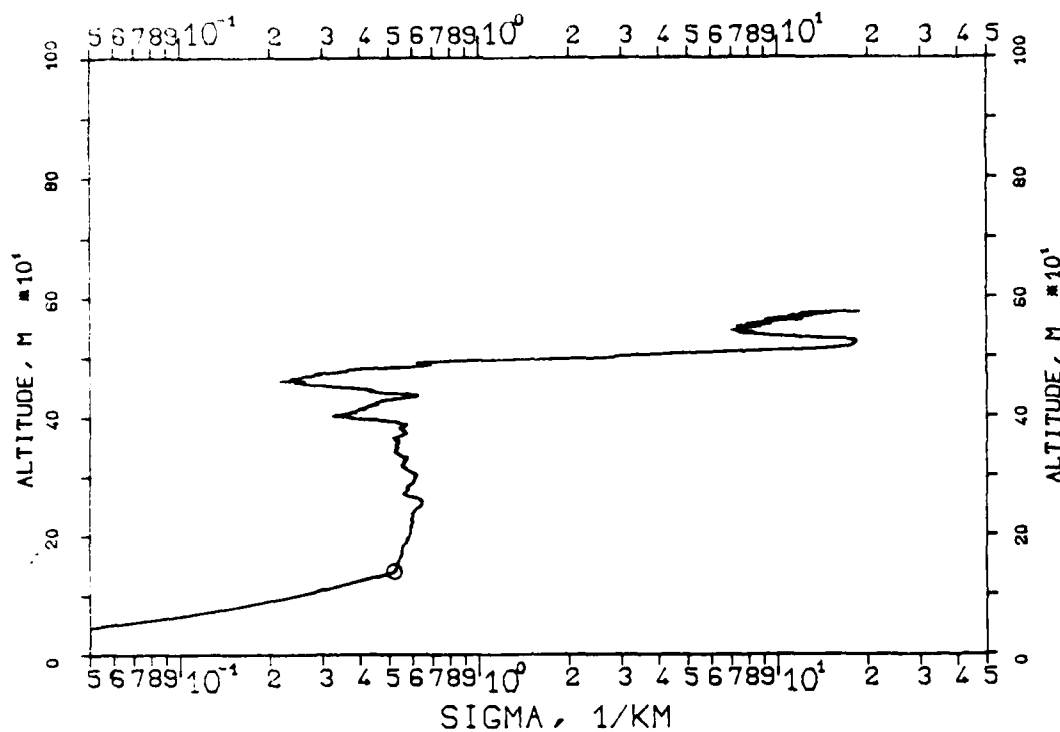


FIG. 7.77
 KLETT-PROFILE, 0694NM, EL. 19DG12MN
 830714, 07:42-07:43, CET
 RM=1.560KM, SM=20.0000/KM, K=1.000

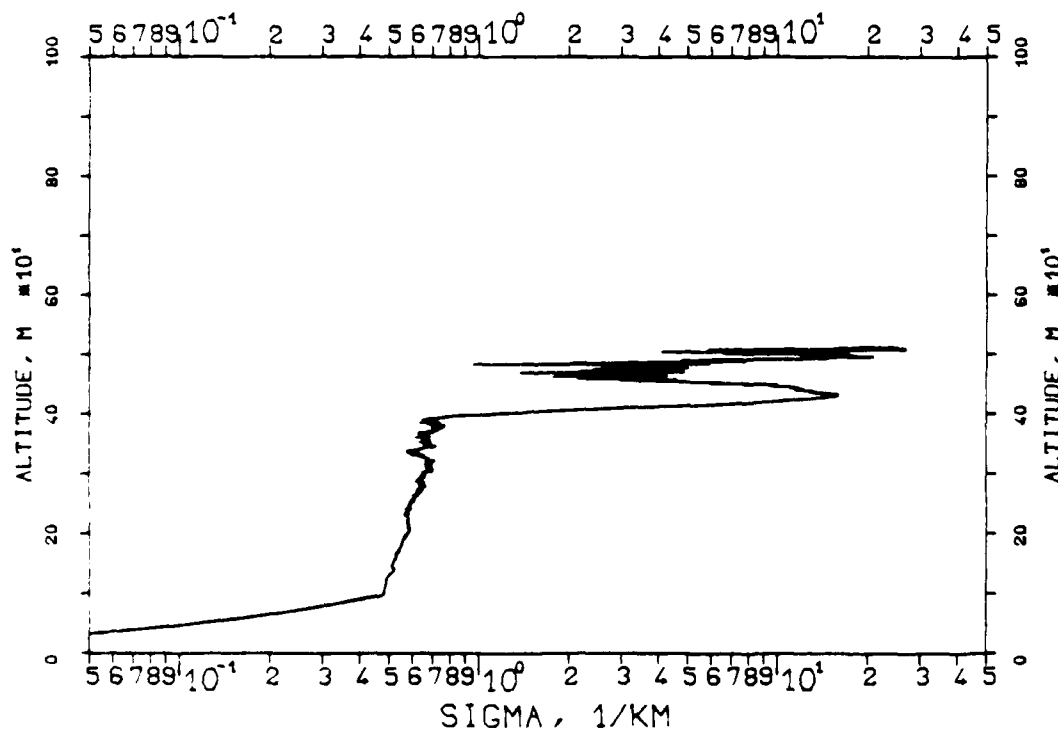


FIG. 7.78
KLETT-PROFILE, 0694NM, EL. 19DG12MN
830714, 08:13-08:14, CET
RM=1.770KM, SM=20.0000/KM, K=1.000

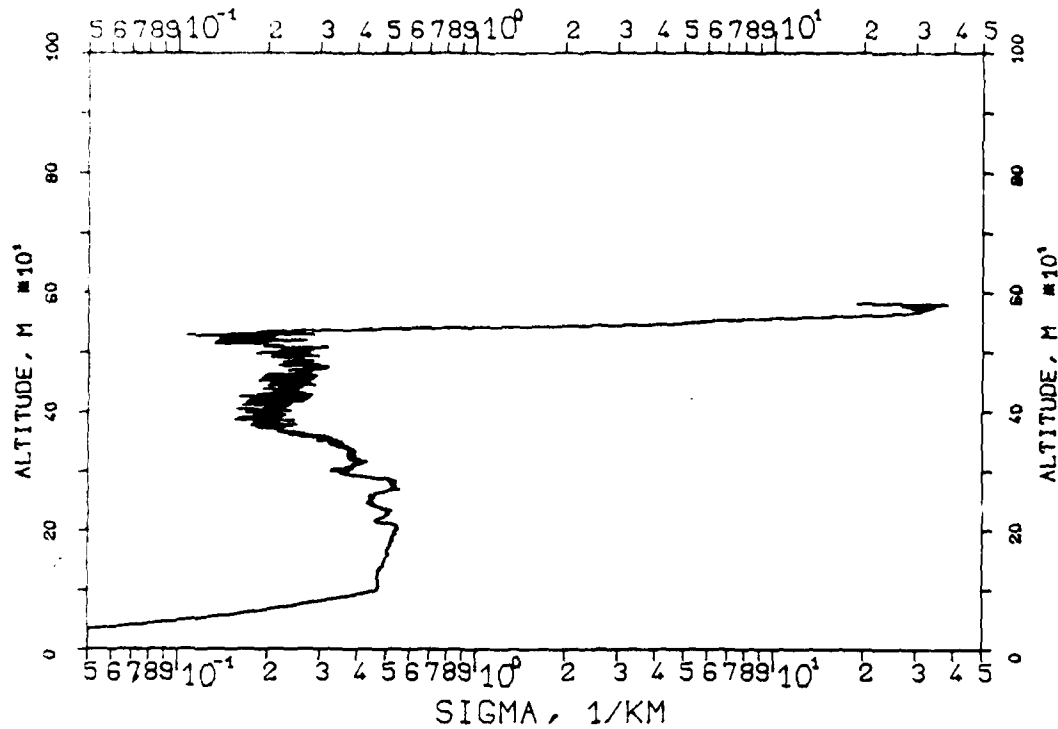
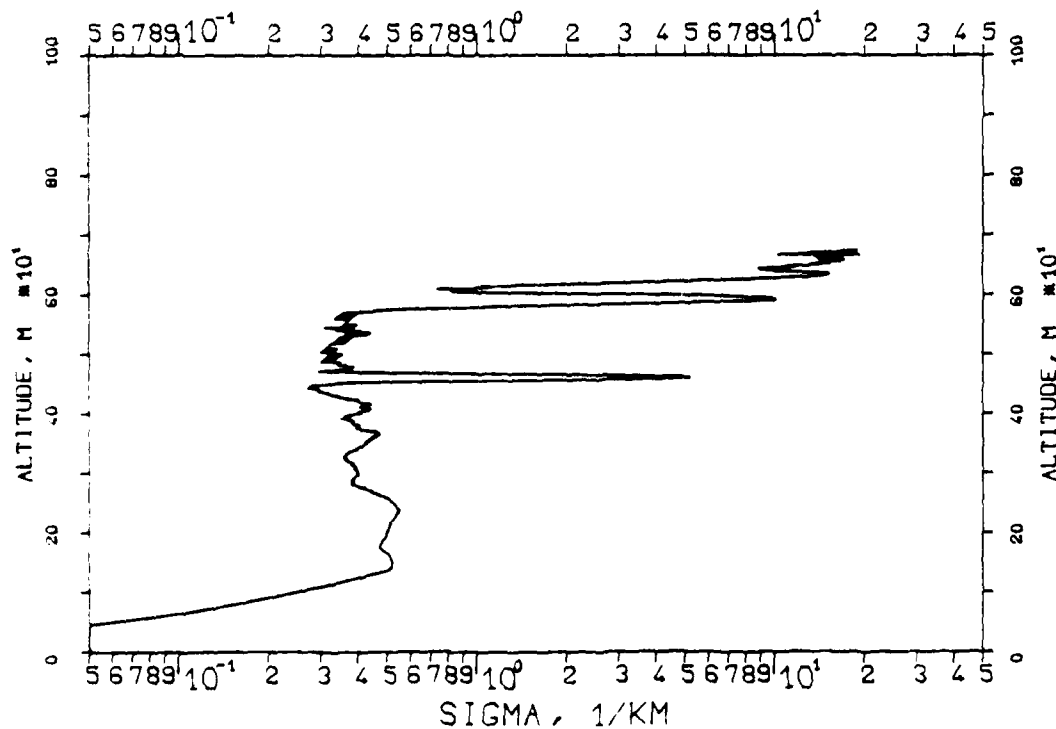


FIG. 7.79
KLETT-PROFILE, 0694NM, EL. 19DG12MN
830714, 08:17-08:18, CET
RM=2.047KM, SM=20.0000/KM, K=1.000



REPRODUCED AT GOVERNMENT EXPENSE

FIG. 7.80
KLETT-PROFILE, 1060NM, EL. 19DG12MN
830714, 08:22-08:23, CET
RM=1.957KM, SM=20.0000/KM, K=1.000

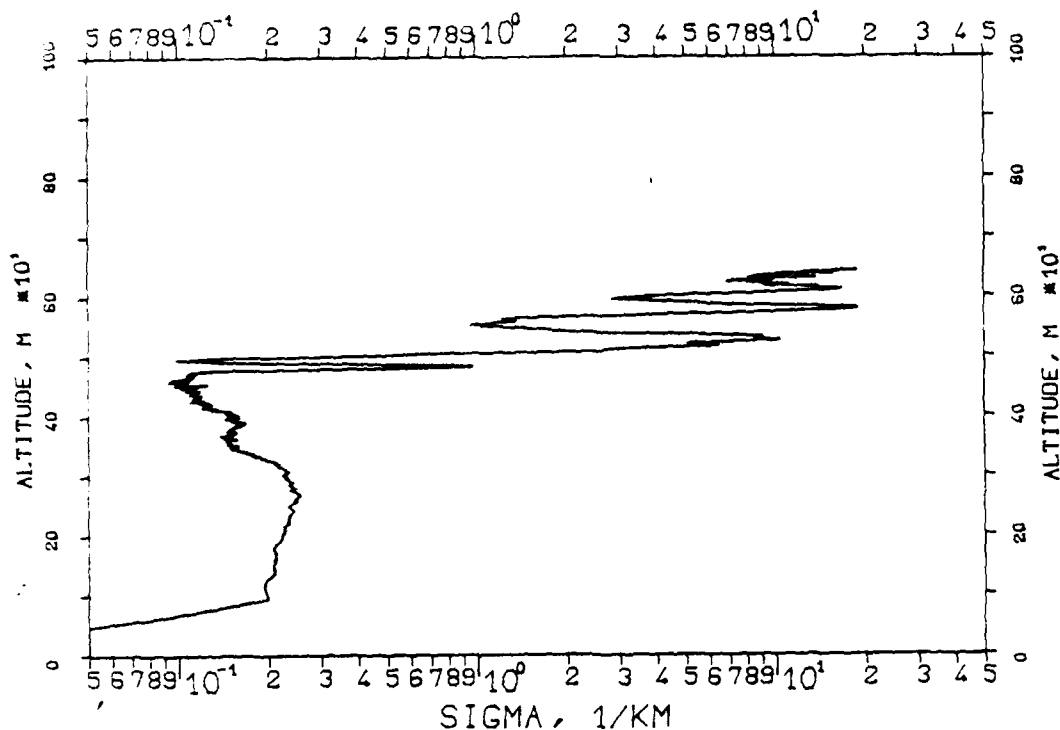
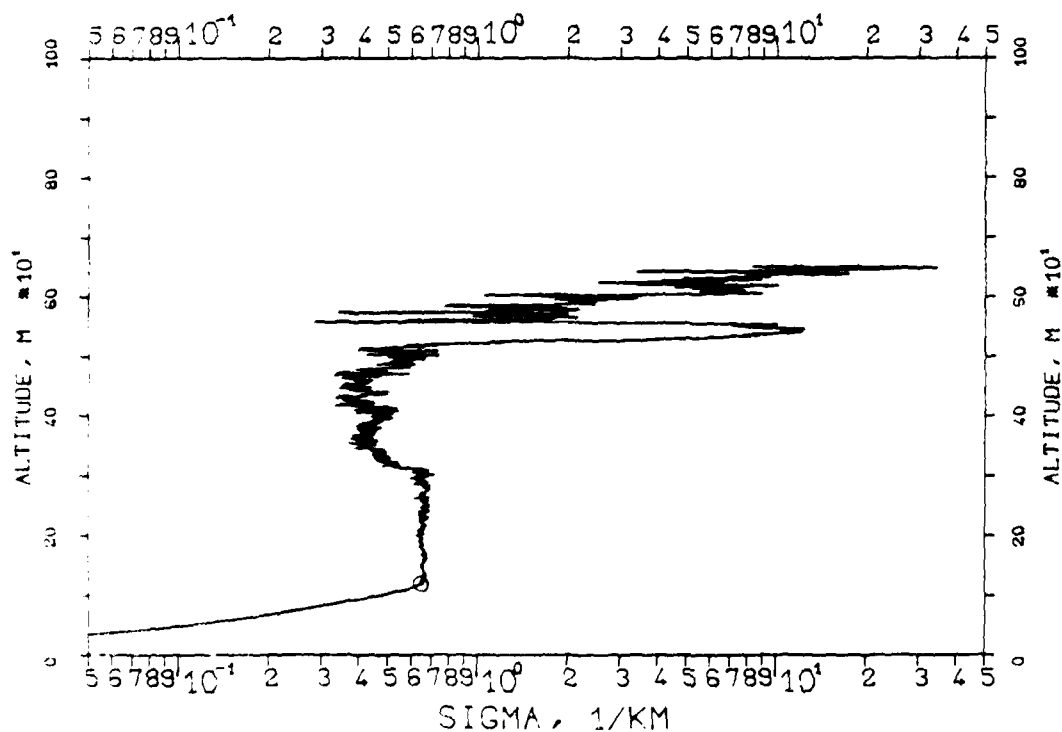


FIG. 7.81
KLETT-PROFILE, 0530NM, EL. 19DG12MN
830714, 08:34-08:36, CET
RM=1.981KM, SM=20.0000/KM, K=1.000



831000, 16:18-16:19, CET
 RM=2.570KM, SM=20.0000/KM, K=1.000

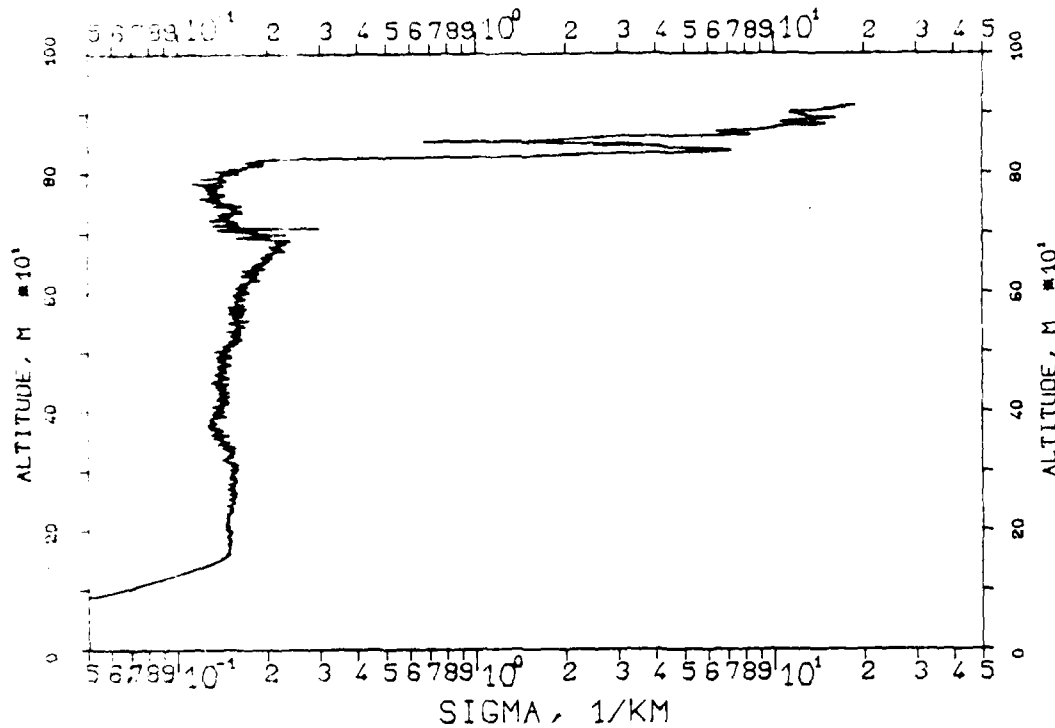


FIG. 7.83
 KLETT-PROFILE, 0530NM, EL. 30DG00MN
 831020, 16:21-16:22, CET
 RM=1.550KM, SM=20.0000/KM, K=1.000

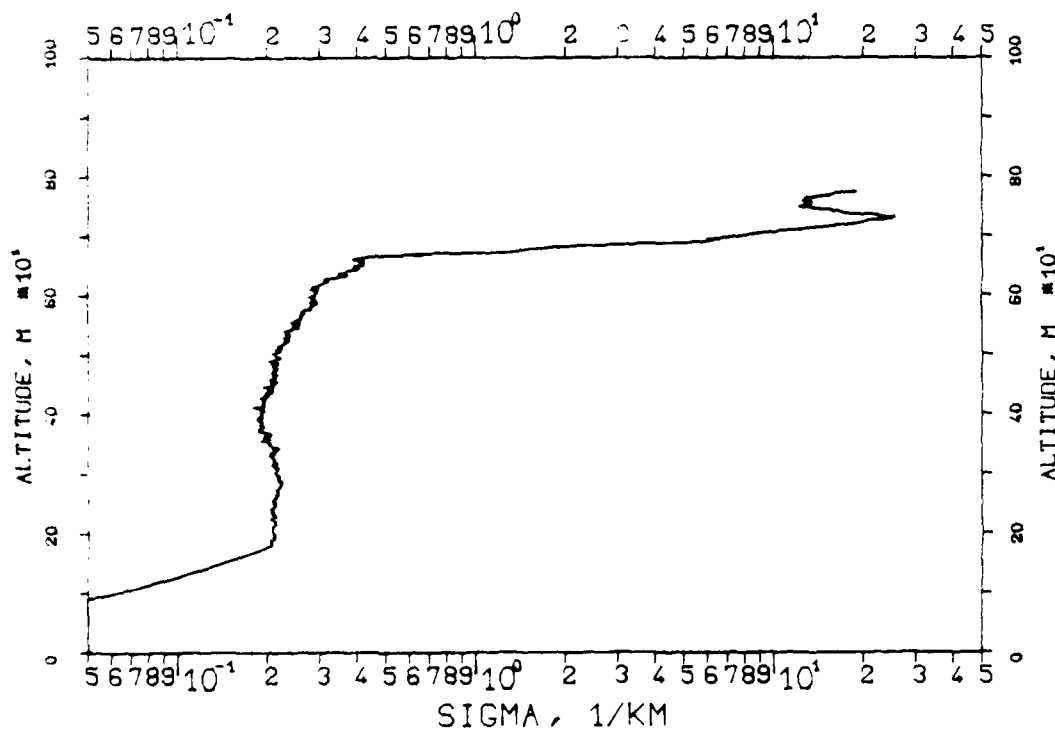


FIG. 7.84
 KLETT-PROFILE, 1060NM, EL. 20DG00MN
 831000, 16:53-16:53, CET
 RM=2.568KM, SM=20.0000/KM, K=1.000

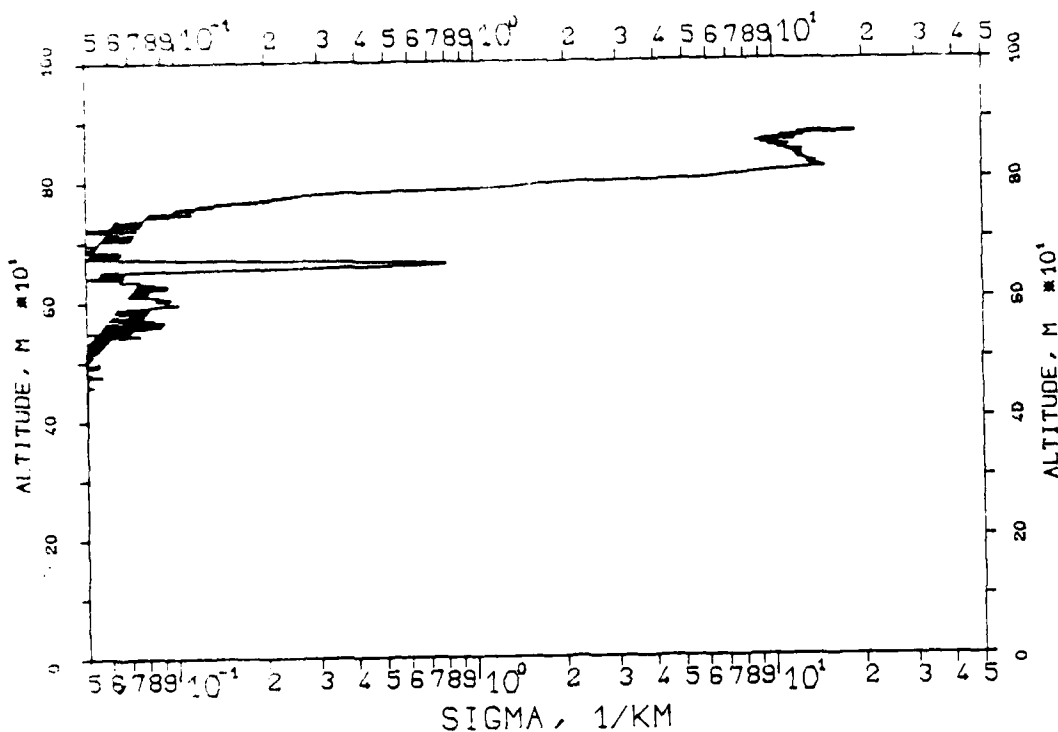


FIG. 7.85
 KLETT-PROFILE, 1060NM, EL. 19DG12MN
 831118, 13:40-13:41, CET
 RM=0.675KM, SM=20.0000/KM, K=1.000

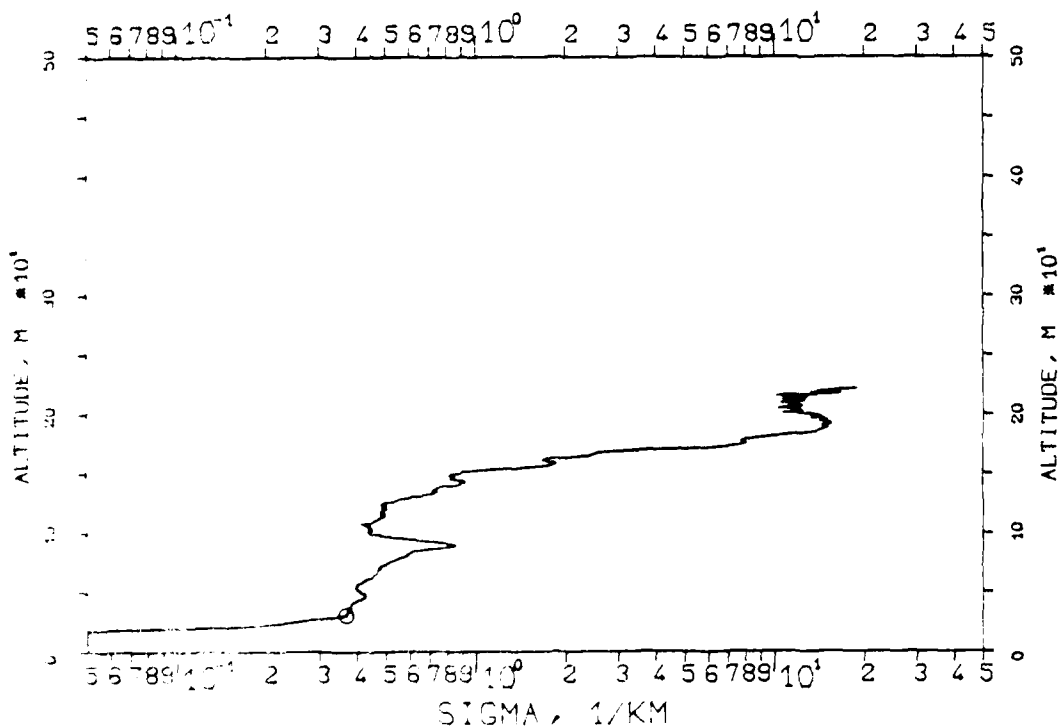


FIG. 7.112
KLETT PROFILE, 1060NM, EL. 20DG00MN
840301, 15:36-15:36, CET
RM=0.769KM, SM=20.0000/KM, K=1.000

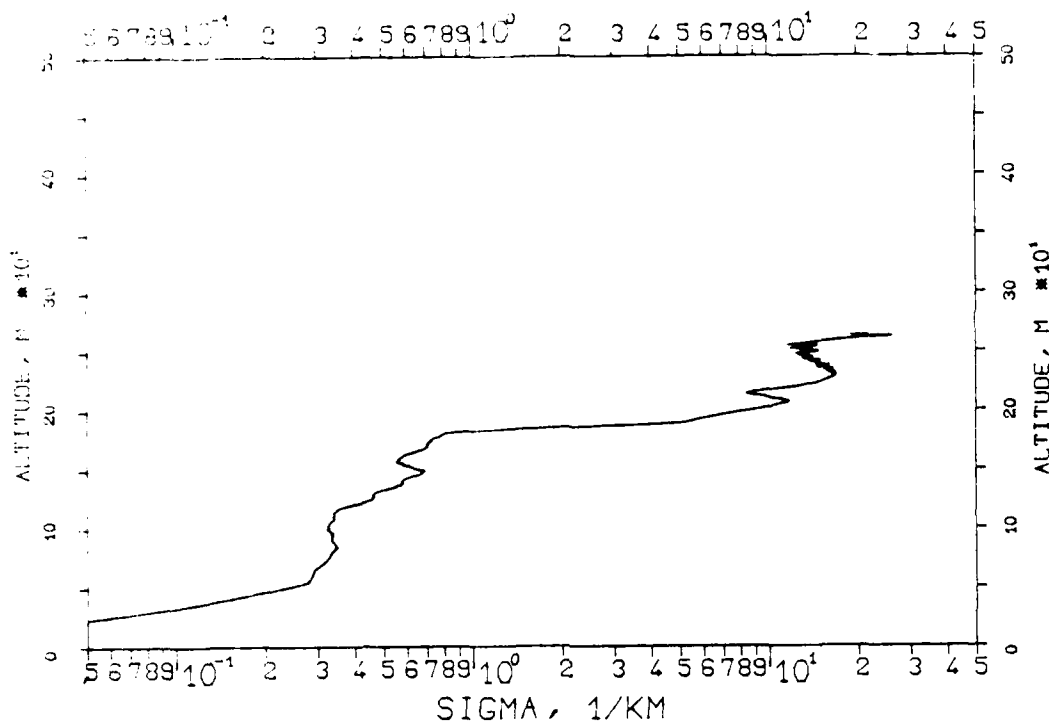


FIG. 7.113
KLETT-PROFILE, 1060NM, EL. 20DG00MN
840301, 15:36-15:37, CET
RM=0.762KM, SM=20.0000/KM, K=1.000

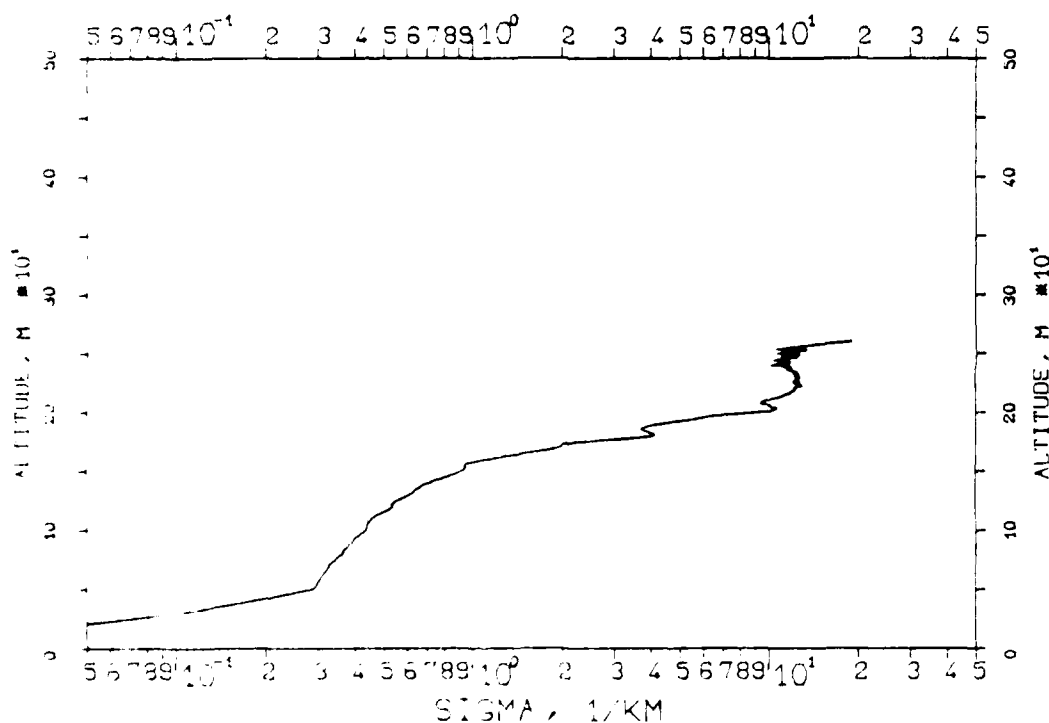


FIG. 7.110
 XLETT-PROFILE, 1060NM, EL. 20DG00MN
 840301, 15:35-15:35, CET
 RM=0.754KM, SM=20.0000/KM, K=1.000

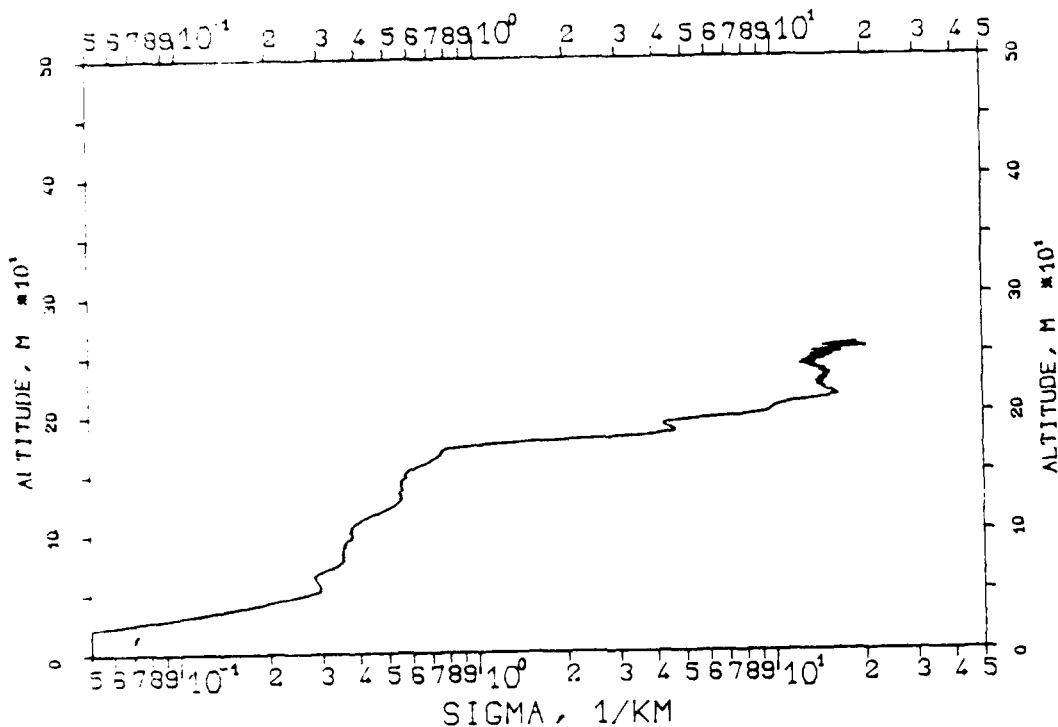


FIG. 7.111
 XLETT-PROFILE, 1060NM, EL. 20DG00MN
 840301, 15:36-15:36, CET
 RM=0.753KM, SM=20.0000/KM, K=1.000

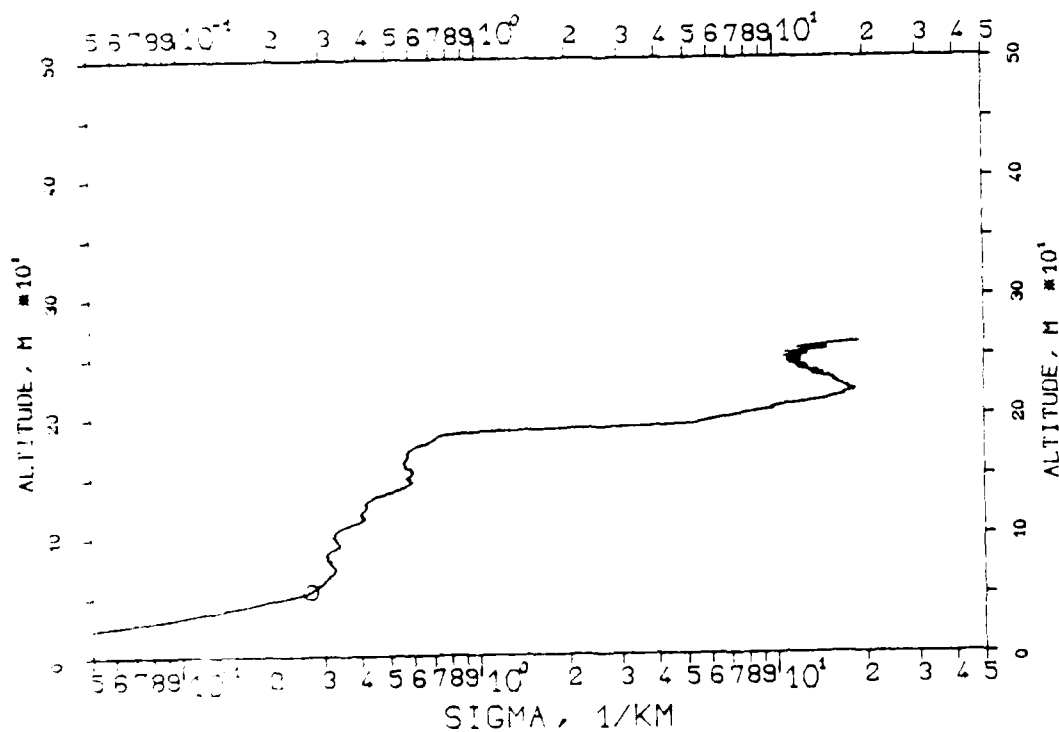


FIG. 7.108
KLETT-PROFILE, 1060NM, EL. 20DG00MN
840301, 15:35-15:35, CET
RM=0.777KM, SM=20.0000/KM, K=1.000

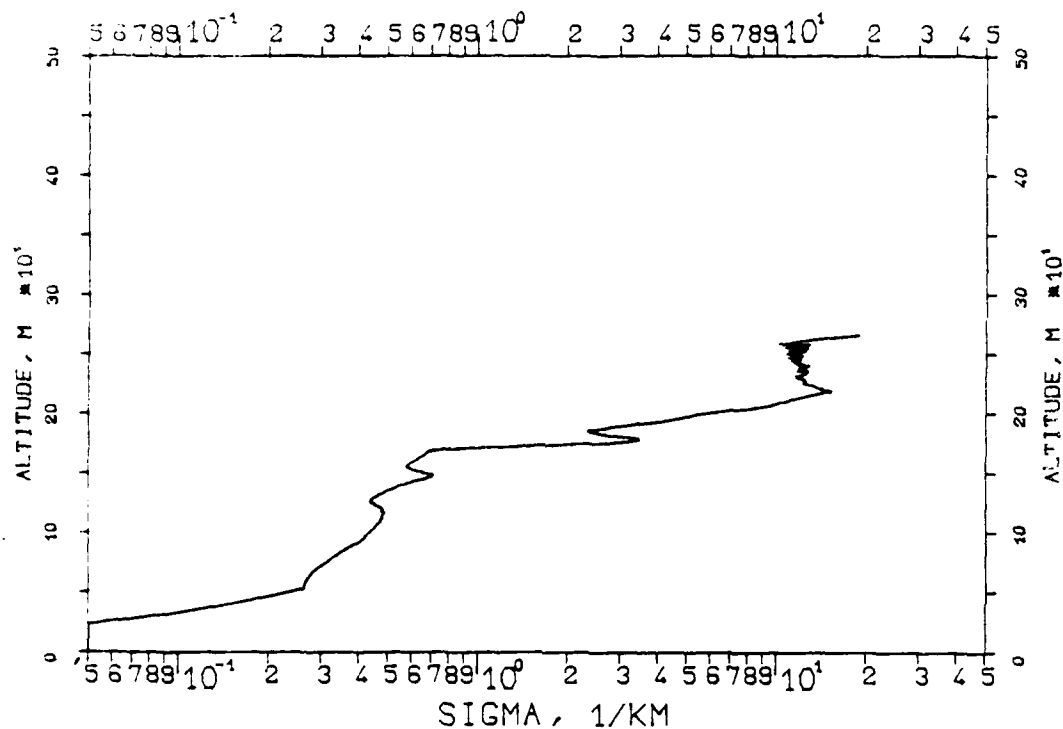


FIG. 7.109
KLETT-PROFILE, 1060NM, EL. 20DG00MN
840301, 15:35-15:35, CET
RM=0.777KM, SM=20.0000/KM, K=1.000

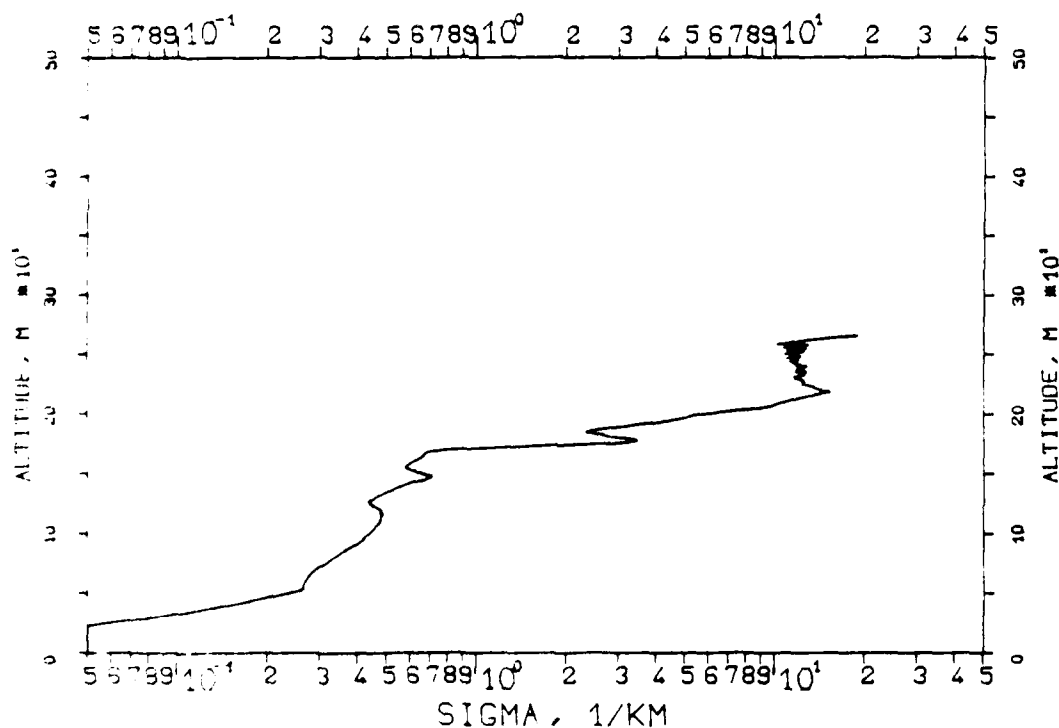


FIG. 7.106
 KLETT-PROFILE, 1060NM, EL. 20DG00MN
 840301, 15:34-15:34, CET
 RM=0.777KM, SM=20.0000/KM, K=1.000

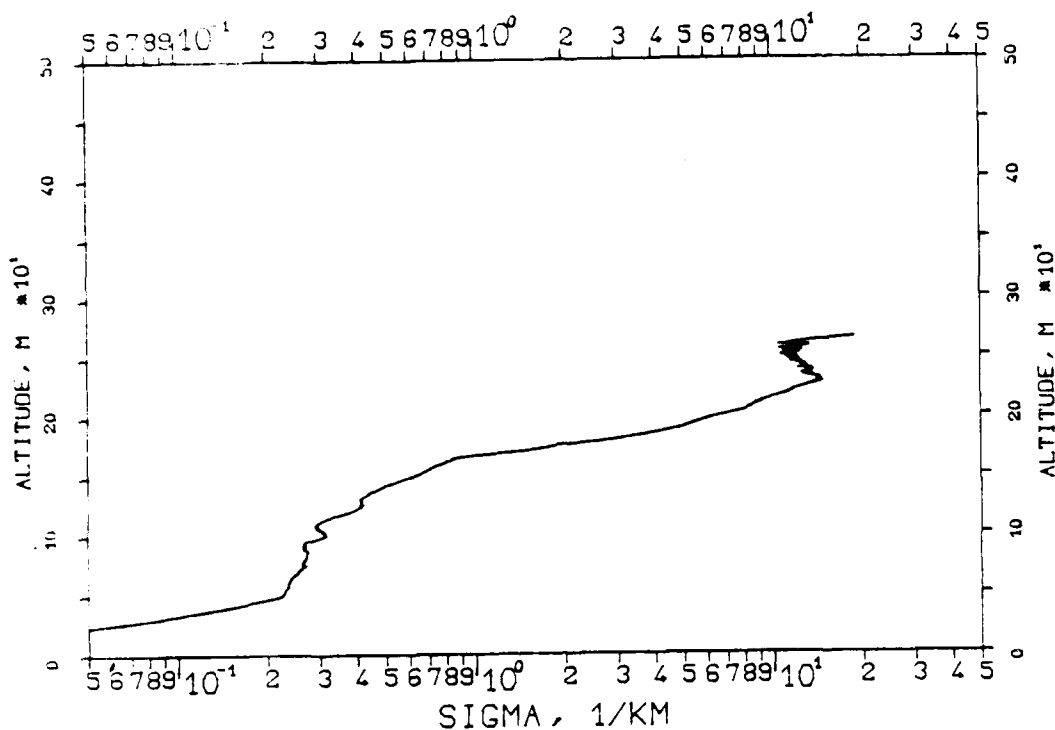


FIG. 7.107
 KLETT-PROFILE, 1060NM, EL. 20DG00MN
 840301, 15:35-15:35, CET
 RM=0.775KM, SM=20.0000/KM, K=1.000

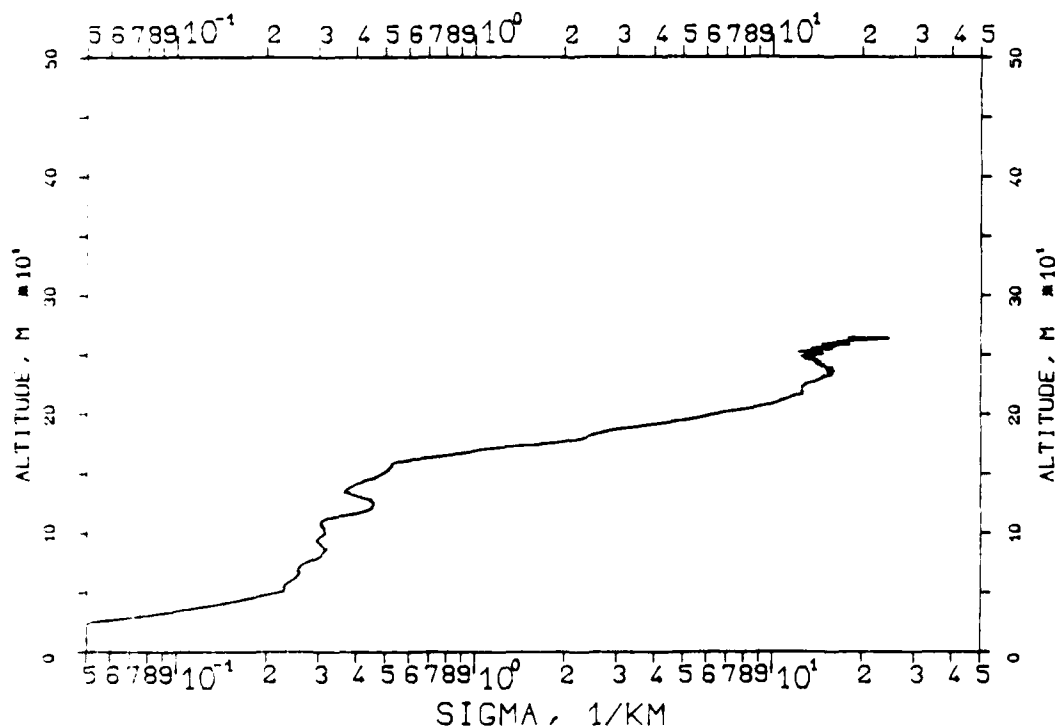


FIG. 7.104
 KLETT PROFILE, 1060NM, EL. 200G00MN
 840301, 15:30-15:30, CET
 RM=0.720KM, SM=20.0000/KM, K=1.000

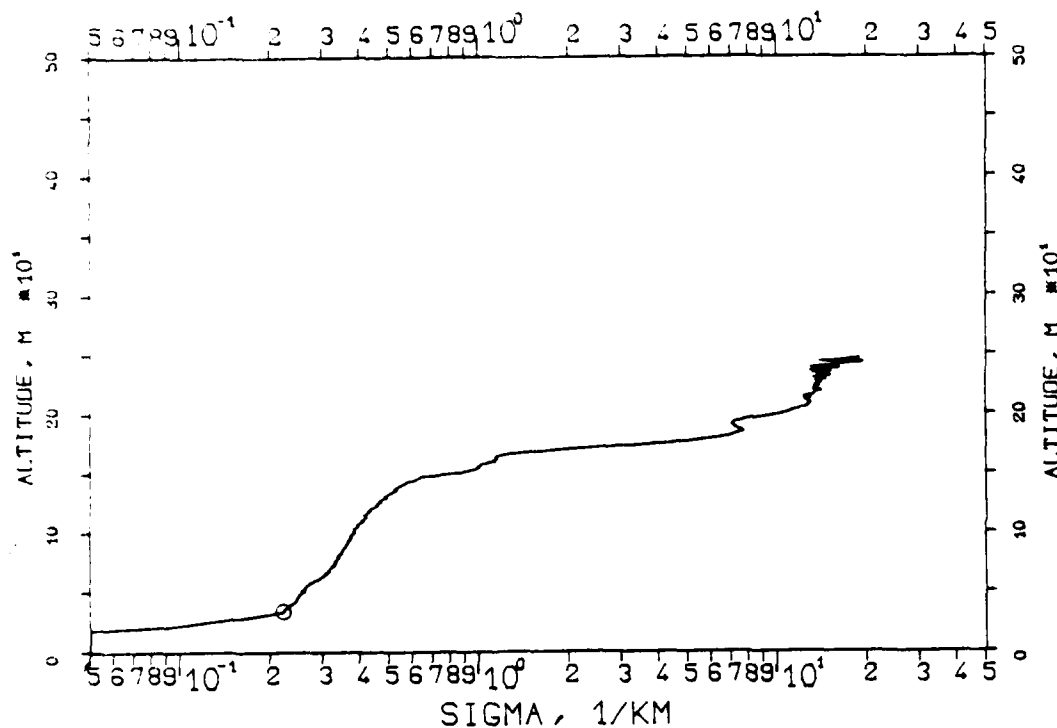


FIG. 7.105
 KLETT-PROFILE, 1060NM, EL. 200G00MN
 840301, 15:34-15:34, CET
 RM=0.771KM, SM=20.0000/KM, K=1.000

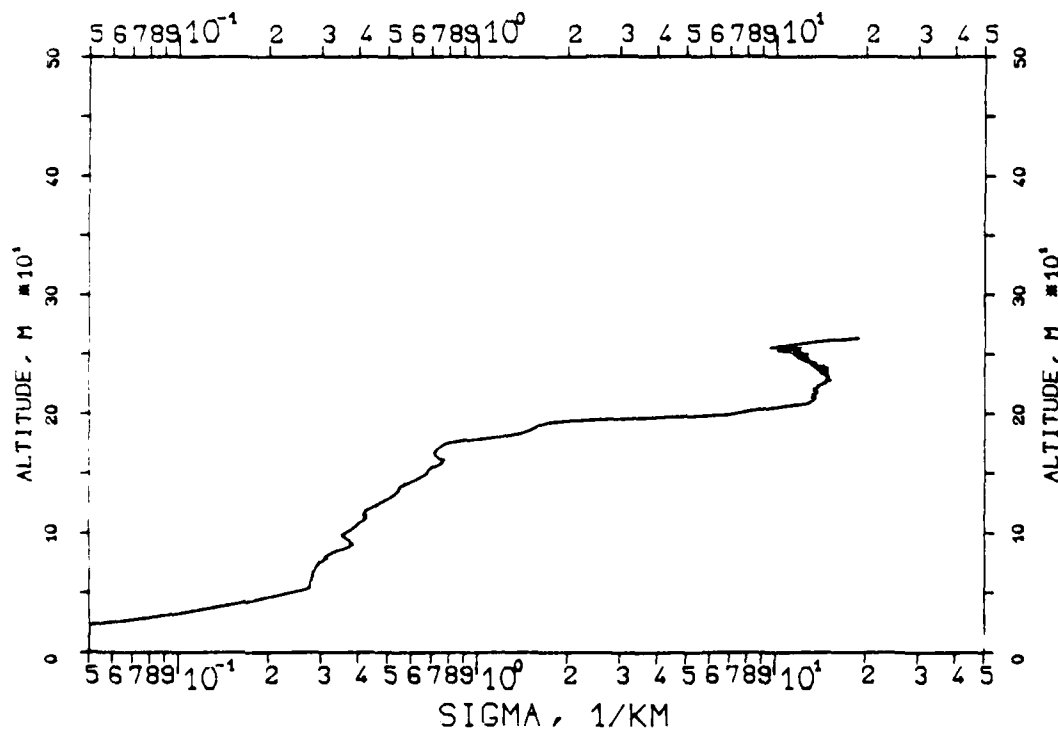


FIG. 7.102
KLETT-PROFILE, 1060NM, EL. 20DG00MN
840301, 15:26-15:27, CET
RM=0.732KM, SM=20.0000/KM, K=1.000

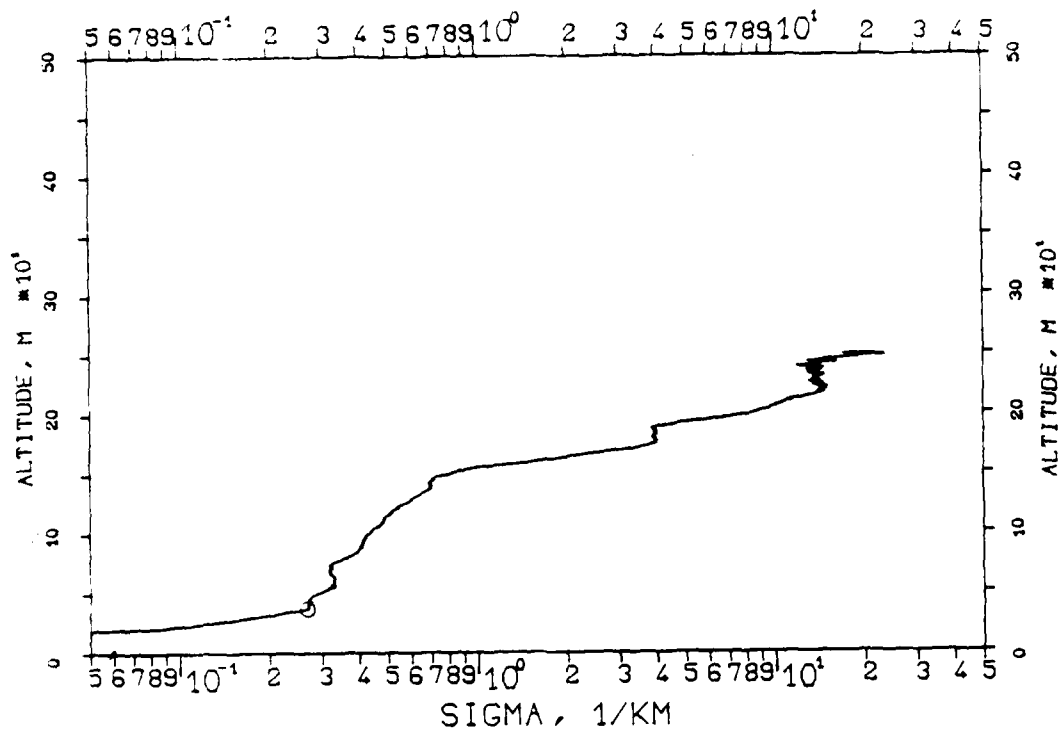


FIG. 7.103
KLETT-PROFILE, 1060NM, EL. 20DG00MN
840301, 15:27-15:27, CET
RM=0.730KM, SM=20.0000/KM, K=1.000

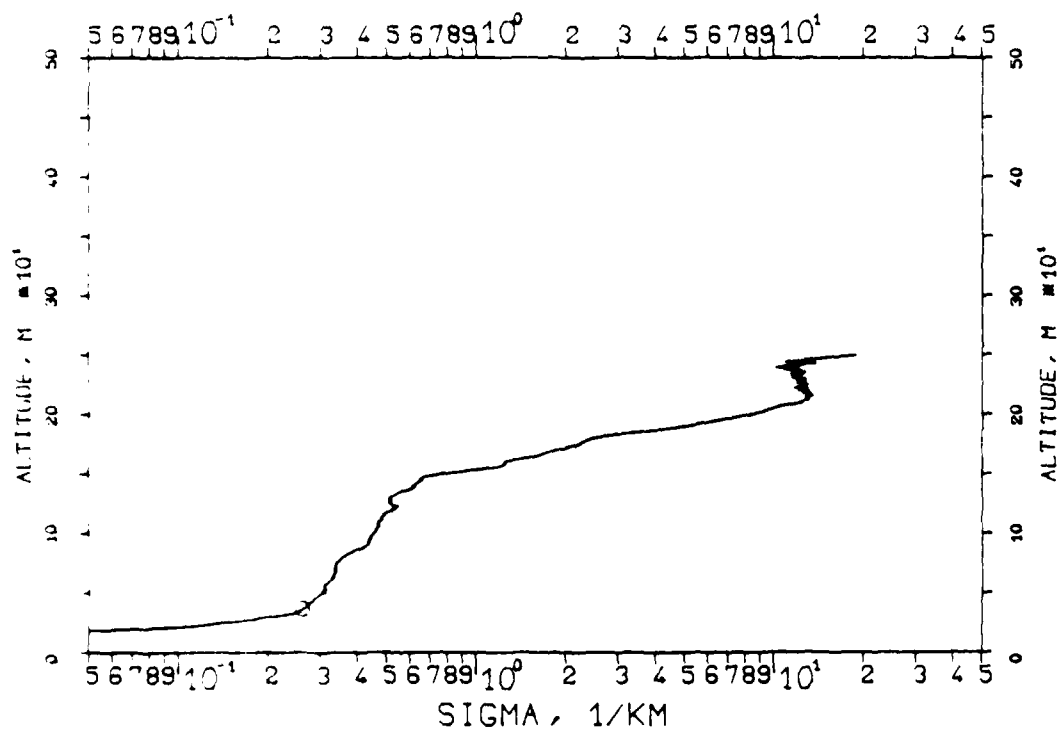


FIG. 7.100
KLETT-PROFILE, 1060NM, EL. 20DG00MN
840301, 15:24-15:24, CET
RM=0.733KM, SM=20.0000/KM, K=1.000

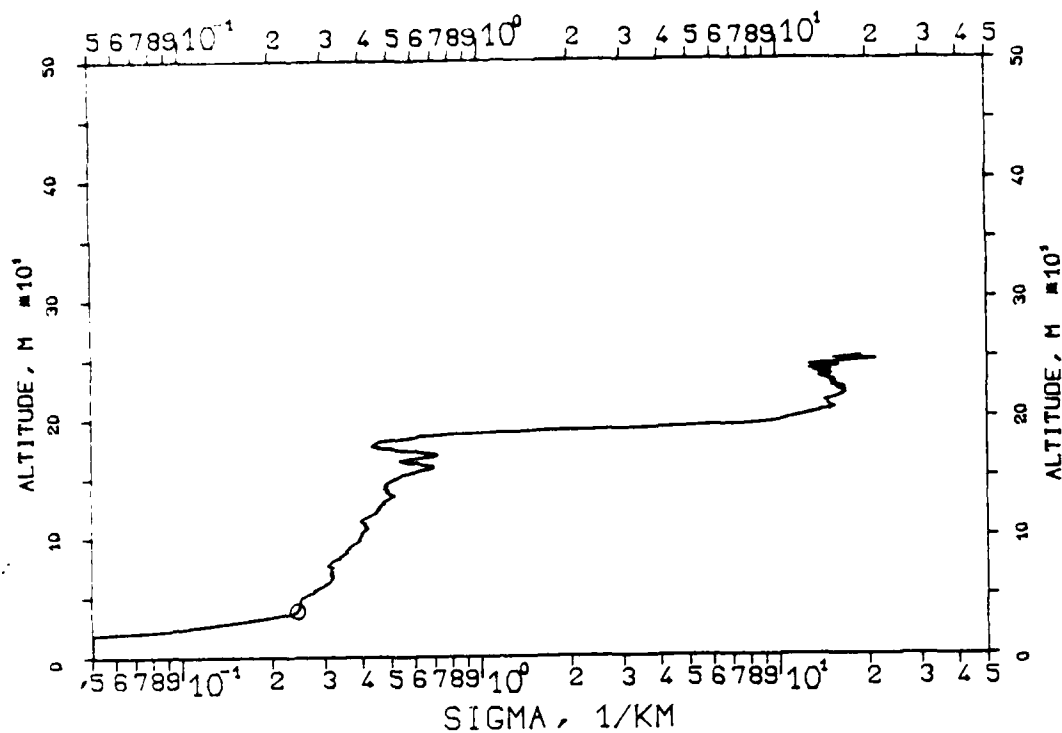


FIG. 7.101
KLETT-PROFILE, 1060NM, EL. 20DG00MN
840301, 15:25-15:25, CET
RM=0.739KM, SM=20.0000/KM, K=1.000

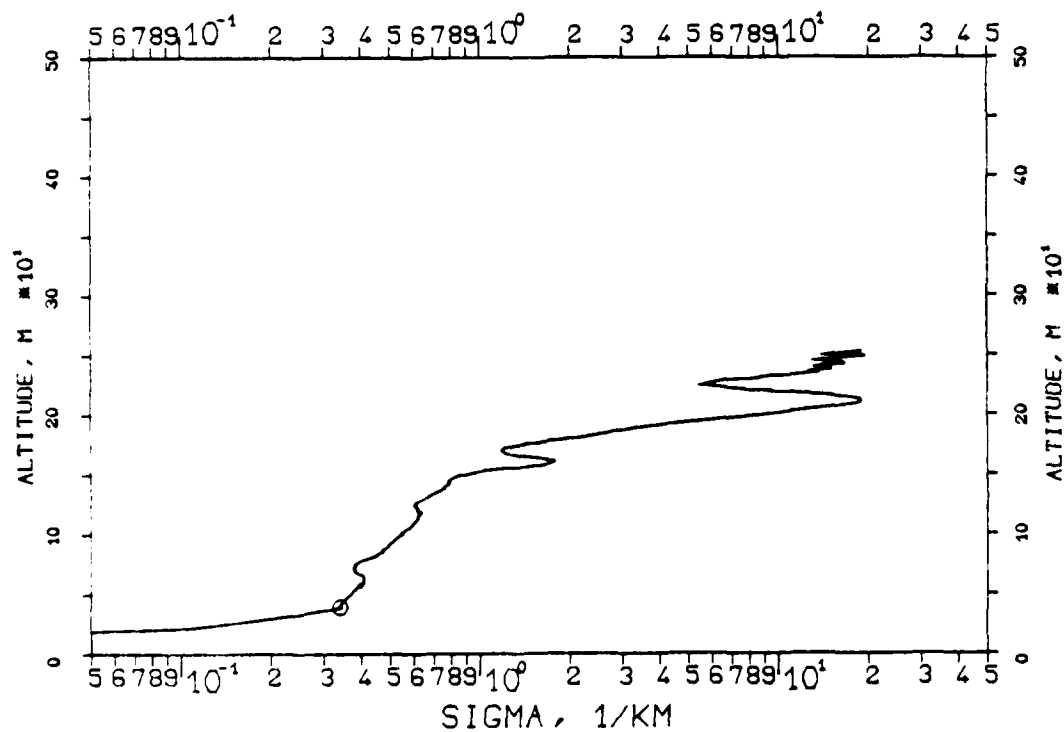


FIG. 7.98
KLETT-PROFILE, 0530NM, EL. 20DG00MN
840301, 14:22-14:23, CET
RM=0.841KM, SM=20.0000/KM, K=1.000

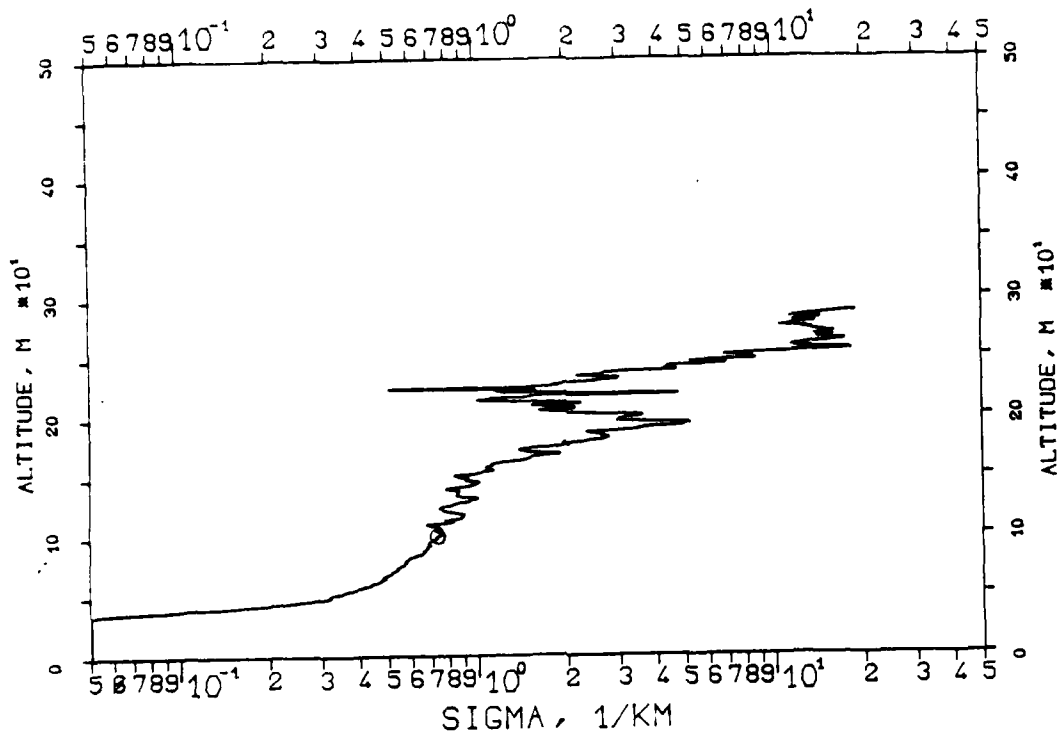


FIG. 7.99
KLETT-PROFILE, 1060NM, EL. 20DG00MN
840301, 14:24-14:24, CET
RM=0.711KM, SM=20.0000/KM, K=1.000

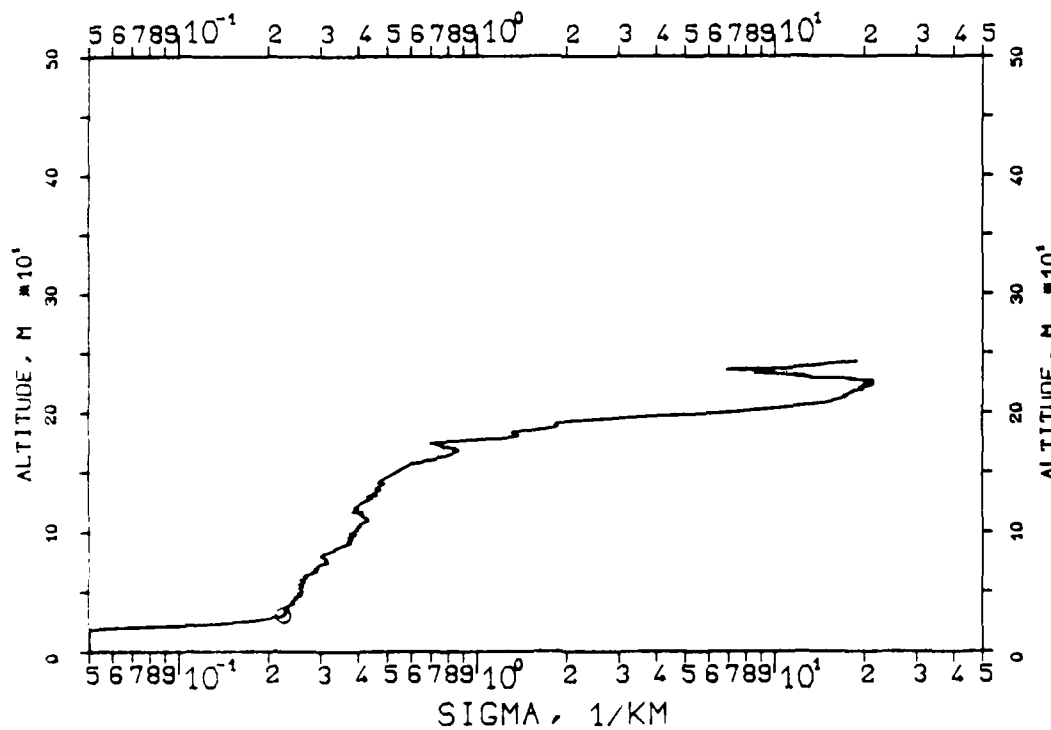


FIG. 7.96
KLETT-PROFILE, 1060NM, EL. 30DG00MN
840301, 12:14-12:15, CET
RM=0.421KM, SM=20.0000/KM, K=1.000

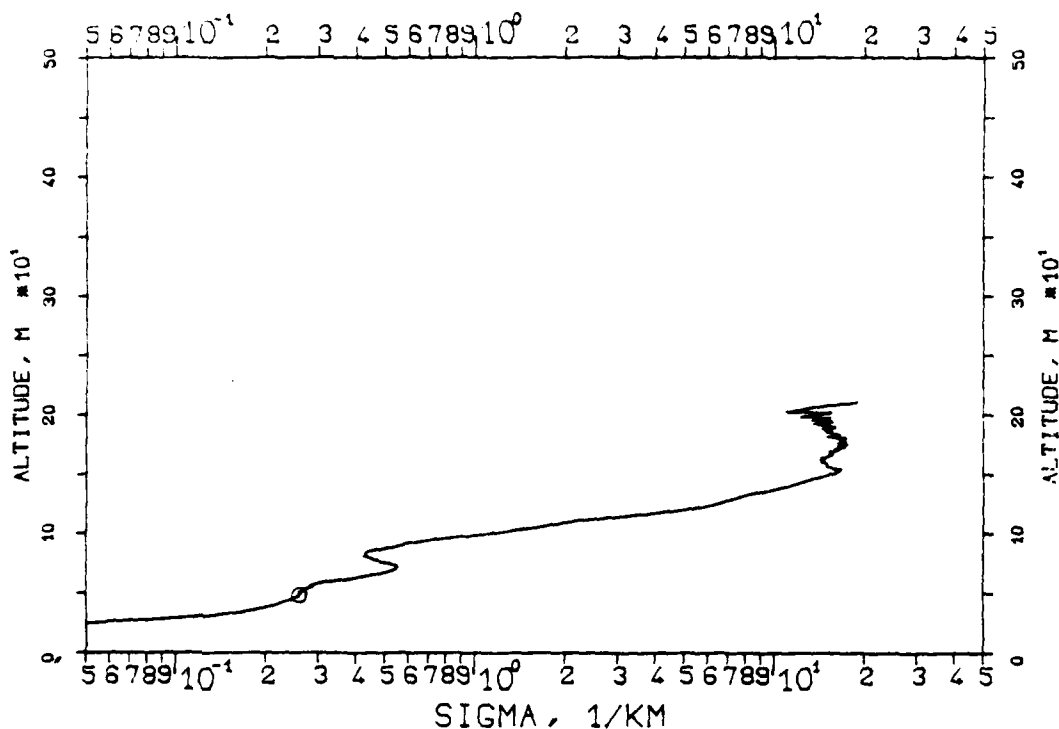


FIG. 7.97
KLETT-PROFILE, 0694NM, EL. 20DG00MN
840301, 14:18-14:18, CET
RM=0.855KM, SM=20.0000/KM, K=1.000

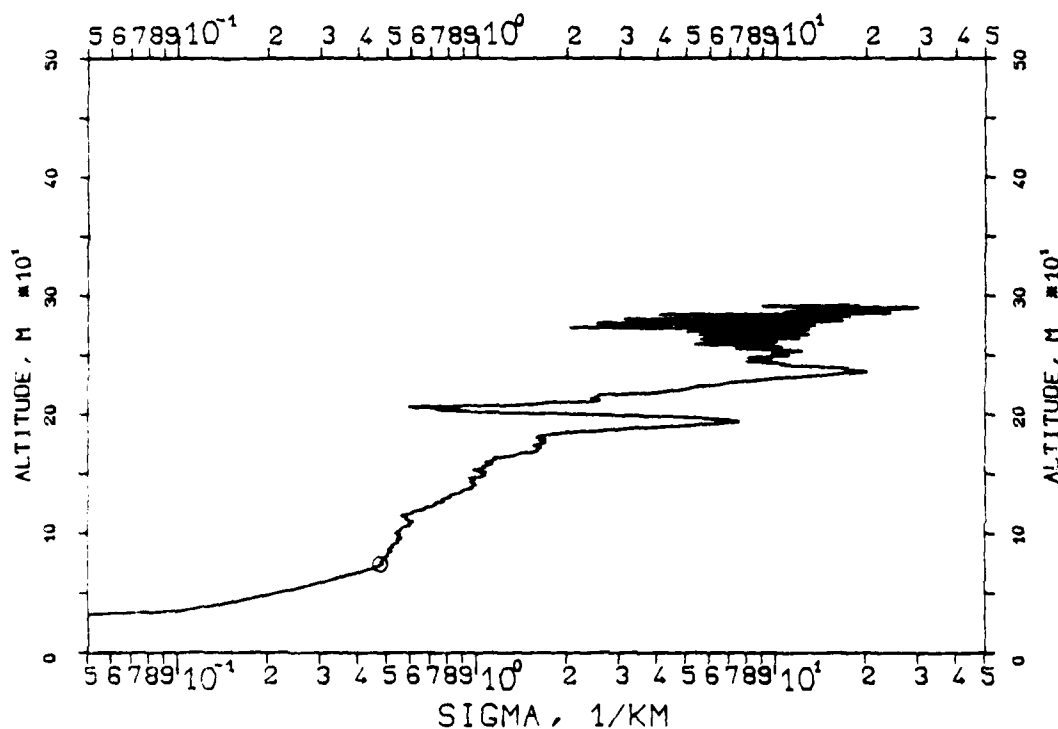


FIG. 7.94
KLETT-PROFILE, 0694NM, EL. 30DG00MN
840301, 12:09-12:09, CET
RM=0.430KM, SM=20.0000/KM, K=1.000

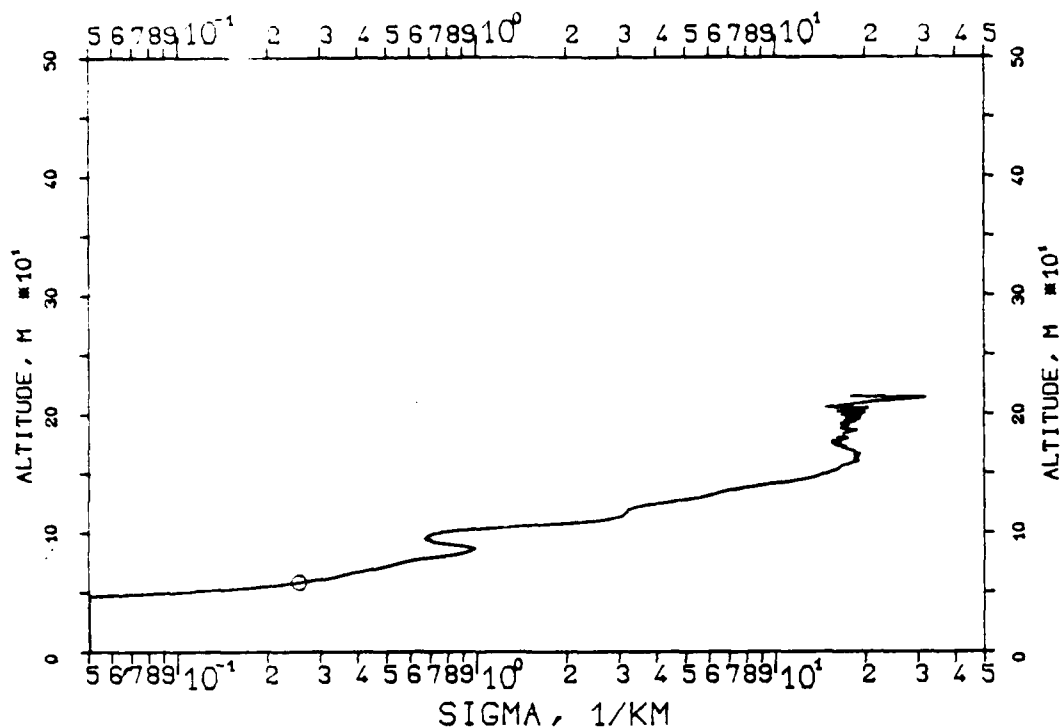


FIG. 7.95
KLETT-PROFILE, 0530NM, EL. 30DG00MN
840301, 12:13-12:13, CET
RM=0.429KM, SM=20.0000/KM, K=1.000

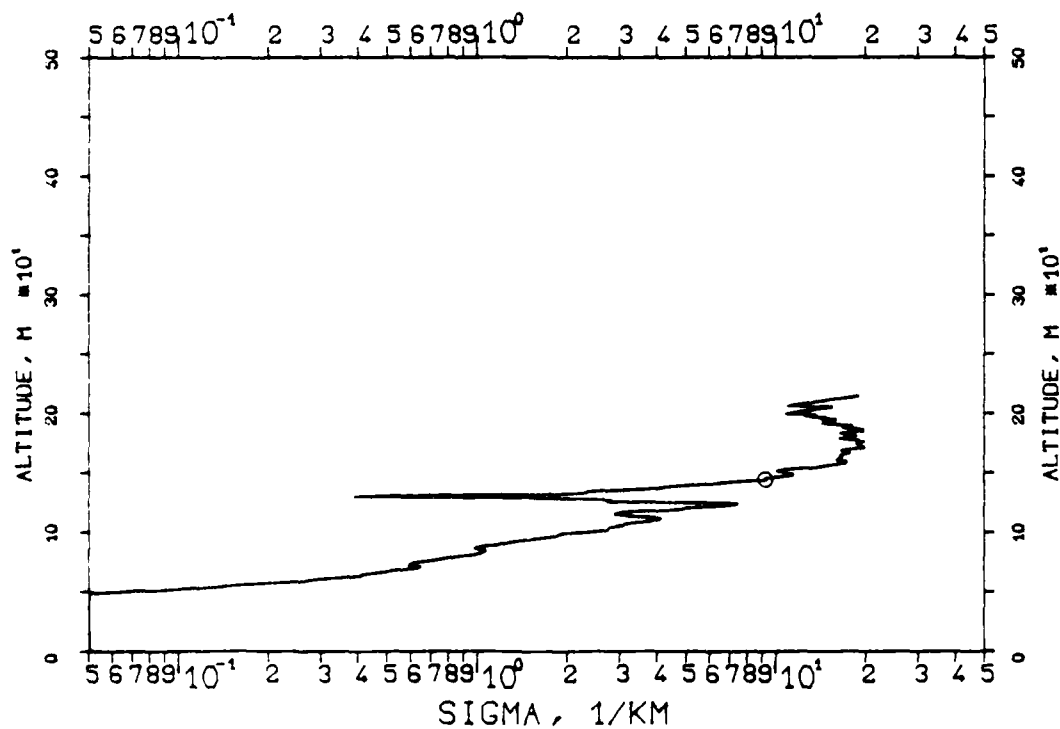


FIG. 7.92
 KLETT-PROFILE, 0530NM, EL. 10DG00MN
 840301, 12:03-12:03, CET
 RM=0.678KM, SM=20.0000/KM, K=1.000

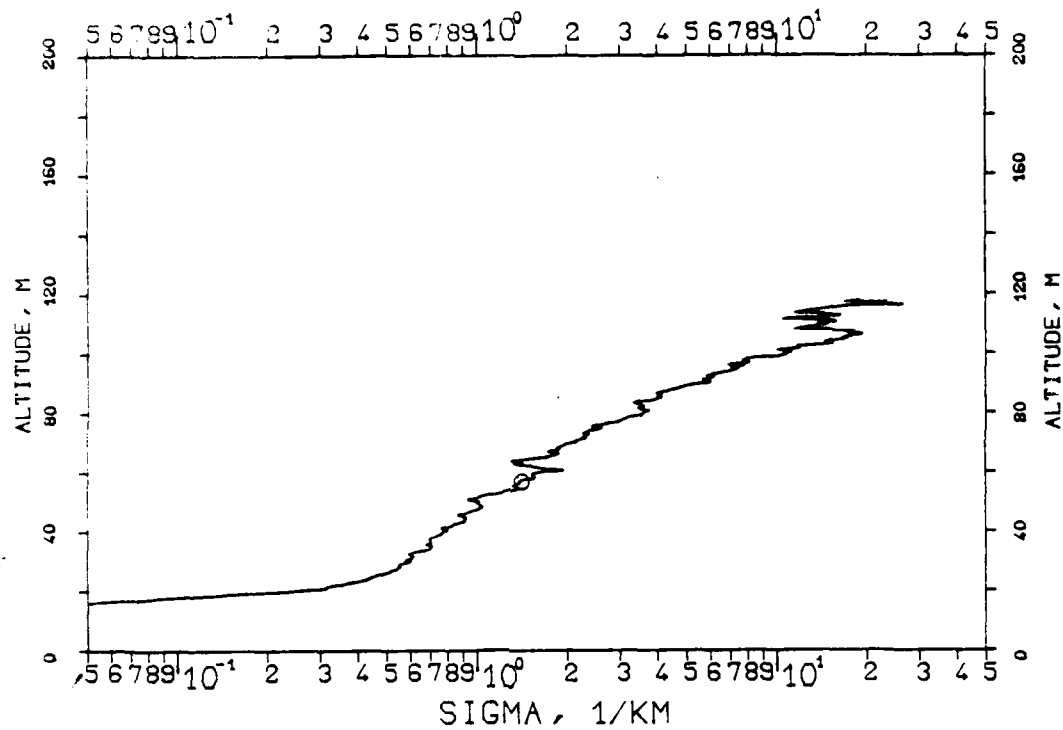
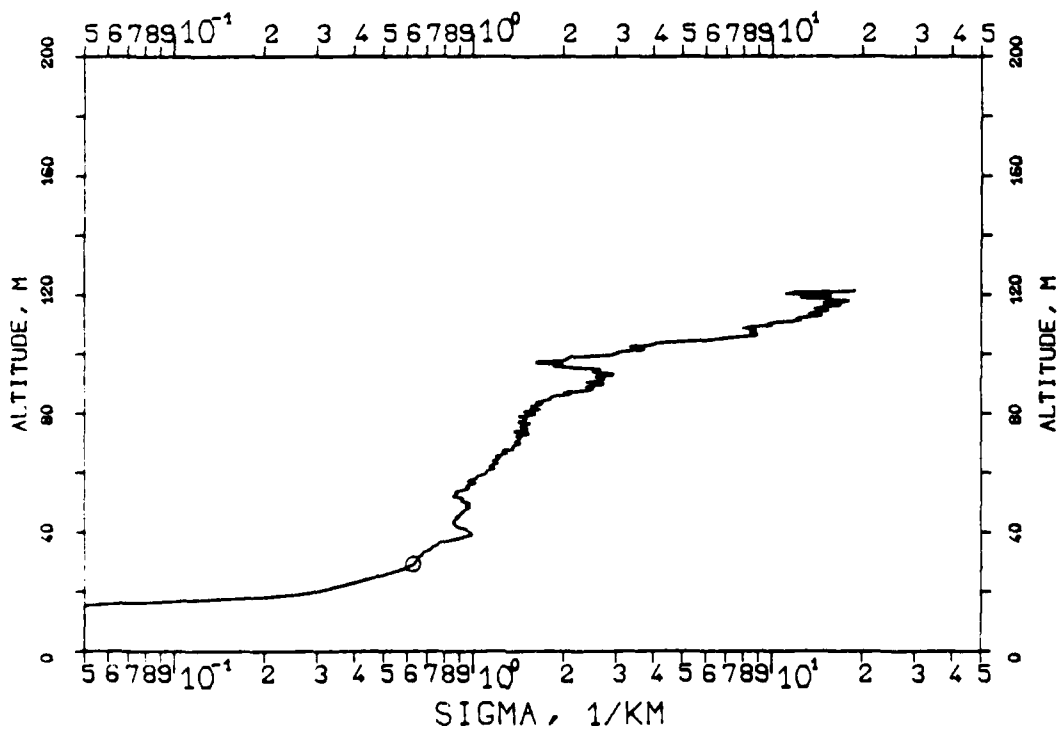


FIG. 7.93
 KLETT-PROFILE, 0694NM, EL. 10DG00MN
 840301, 12:07-12:07, CET
 RM=0.700KM, SM=20.0000/KM, K=1.000



1100 7.90
 KLETT PROFILE, 0694NM, EL. 19DG 12MN
 840028, 11:05-11:06, CET
 RM=2.670KM, SM=20.0000/KM, K=1.000

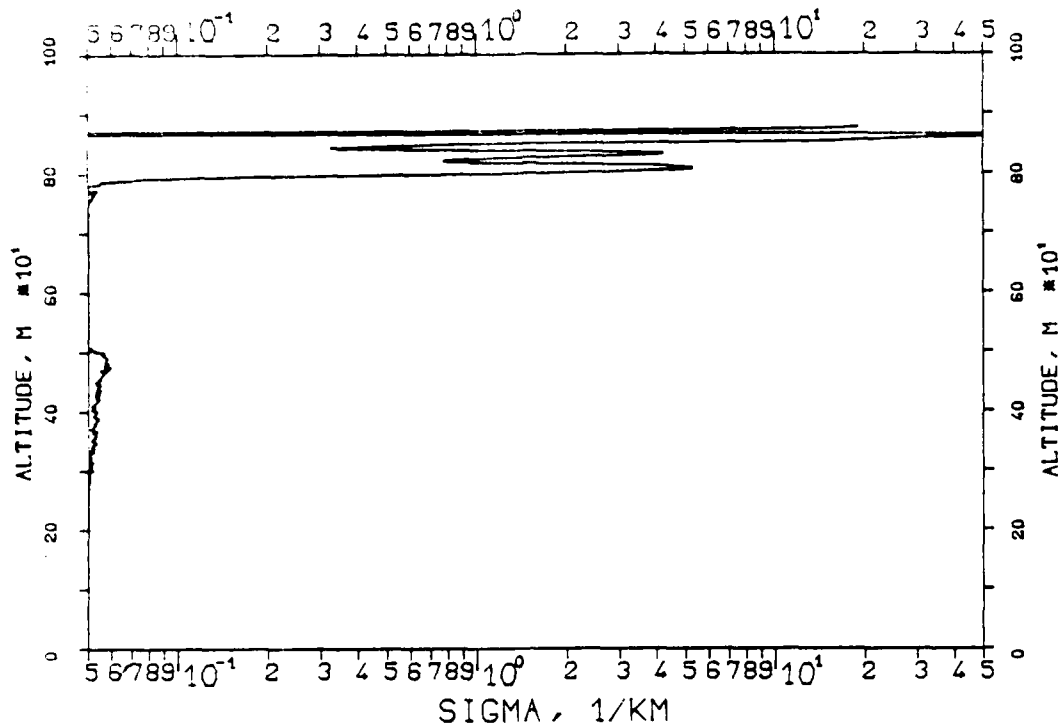


FIG. 7.91
 KLETT-PROFILE, 1060NM, EL. 10DG00MN
 840301, 12:01-12:01, CET
 RM=0.697KM, SM=20.0000/KM, K=1.000

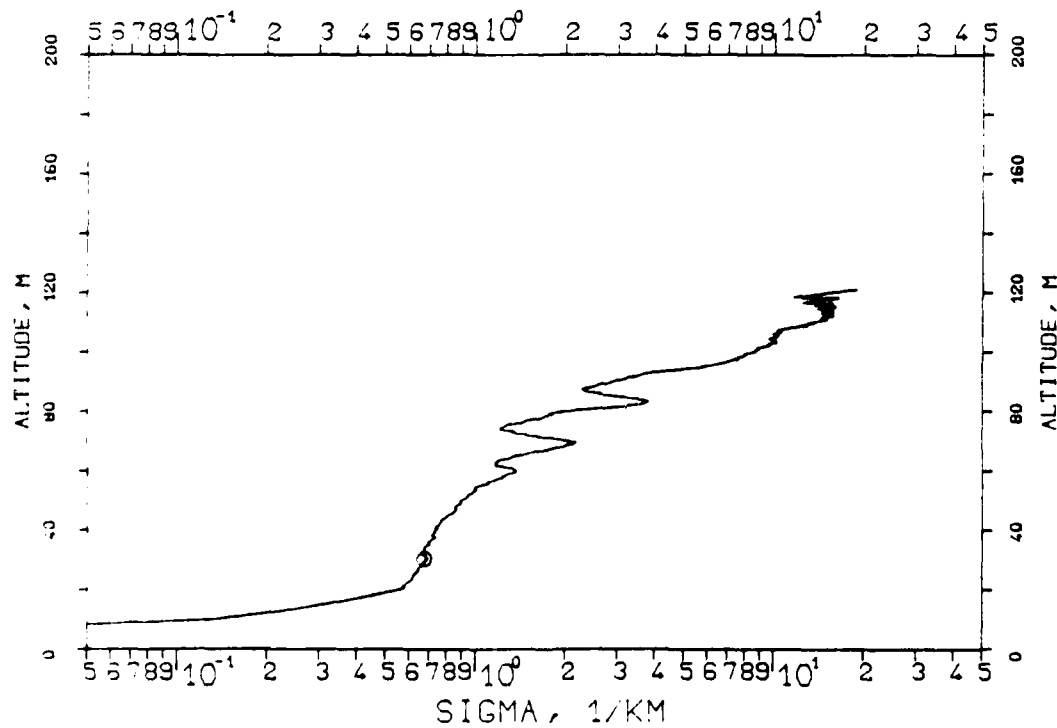


FIG. 7.88
KLETT-PROFILE, 0530NM, EL. 19DG12MN
840228, 11:00-11:01, CET
RM=2.400KM, SM=20.0000/KM, K=1.000

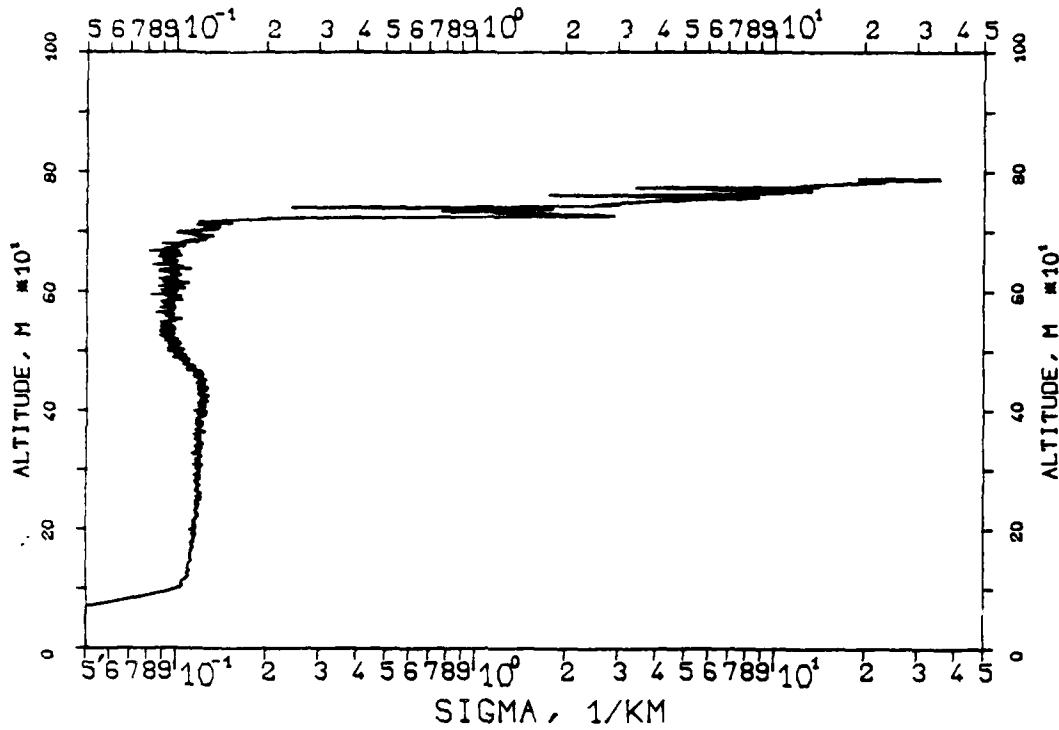


FIG. 7.89
KLETT-PROFILE, 1060NM, EL. 19DG12MN
840228, 11:03-11:04, CET
RM=2.670KM, SM=20.0000/KM, K=1.000

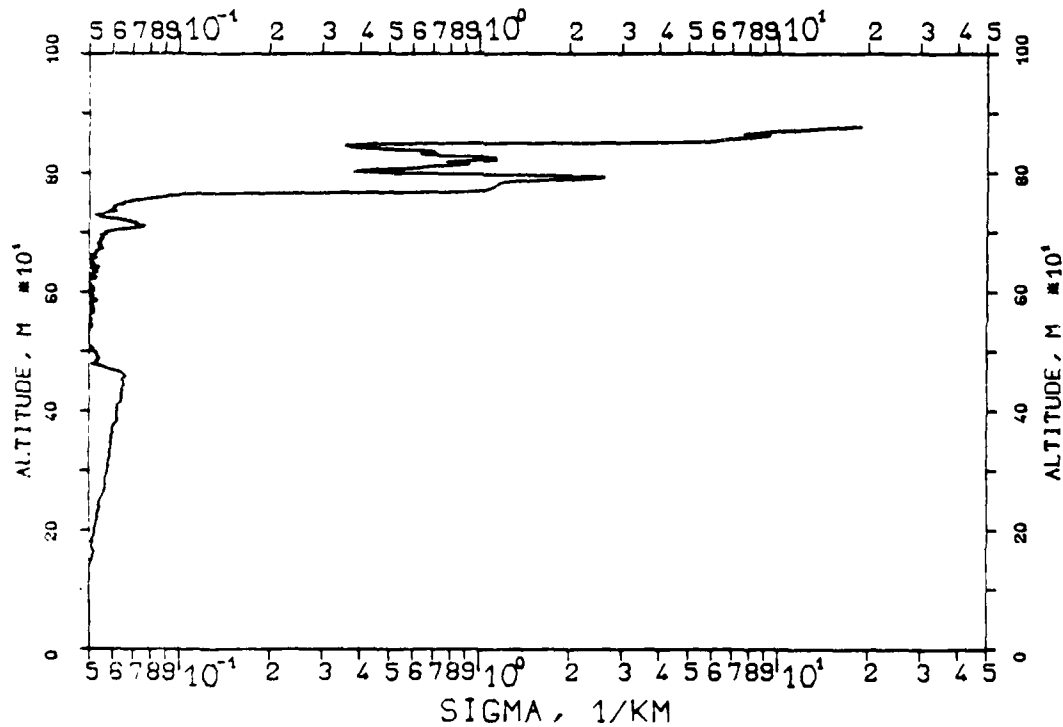


FIG. 7.86
KLETT-PROFILE ,0347NM,EL. 19DG12MN
831118, 13:49-13:49,CET
RM=0.640KM,SM=20.0000/KM,K=1.000

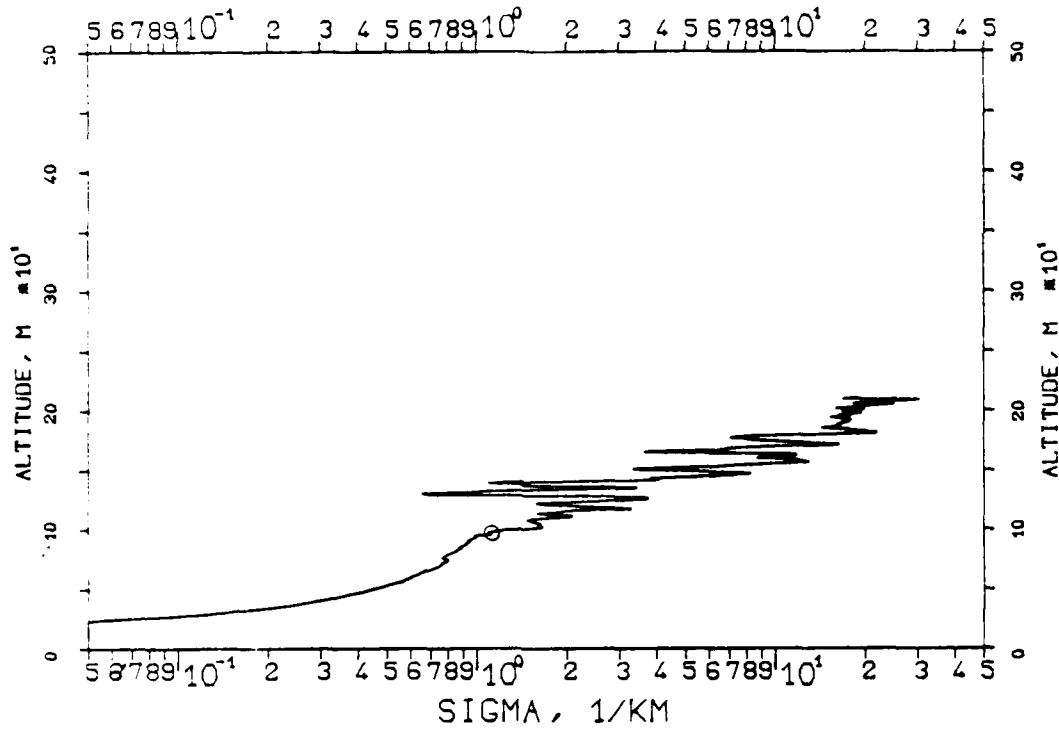


FIG. 7.87
KLETT-PROFILE ,0530NM,EL. 19DG12MN
831118, 13:54-13:55,CET
RM=0.660KM,SM=20.0000/KM,K=1.000

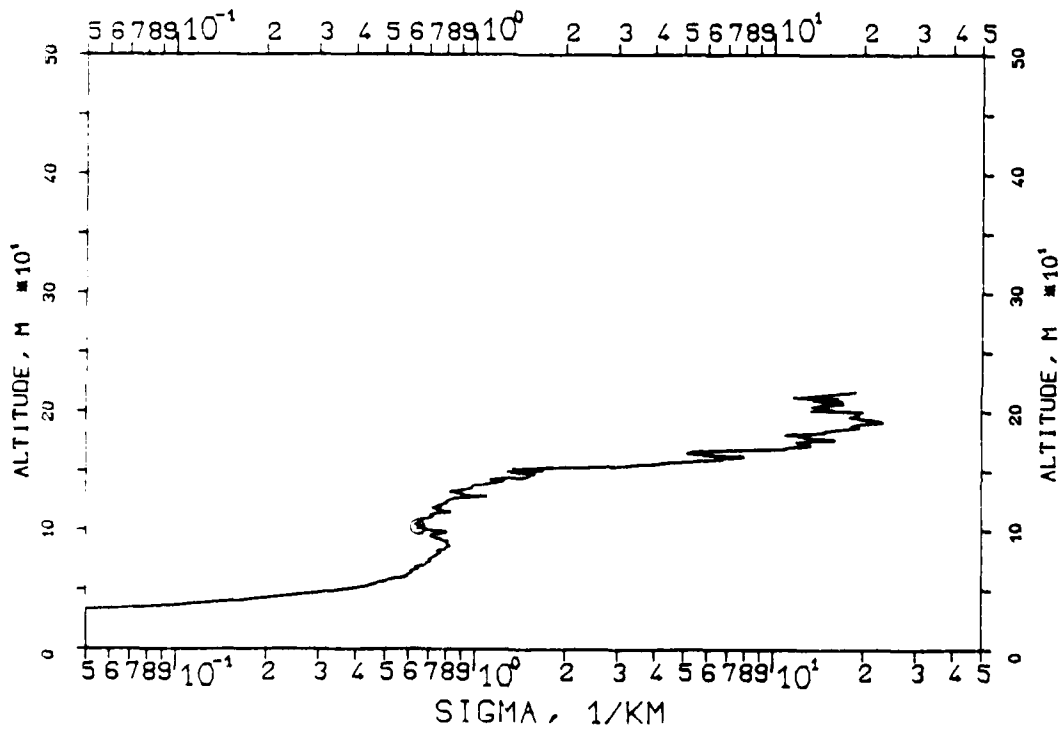


FIG. 7.114
 KLETT-PROFILE, 1060NM, EL. 10DG00MN
 840301, 16:36-16:37, CET
 RM=1.393KM, SM=20.0000/KM, K=1.000

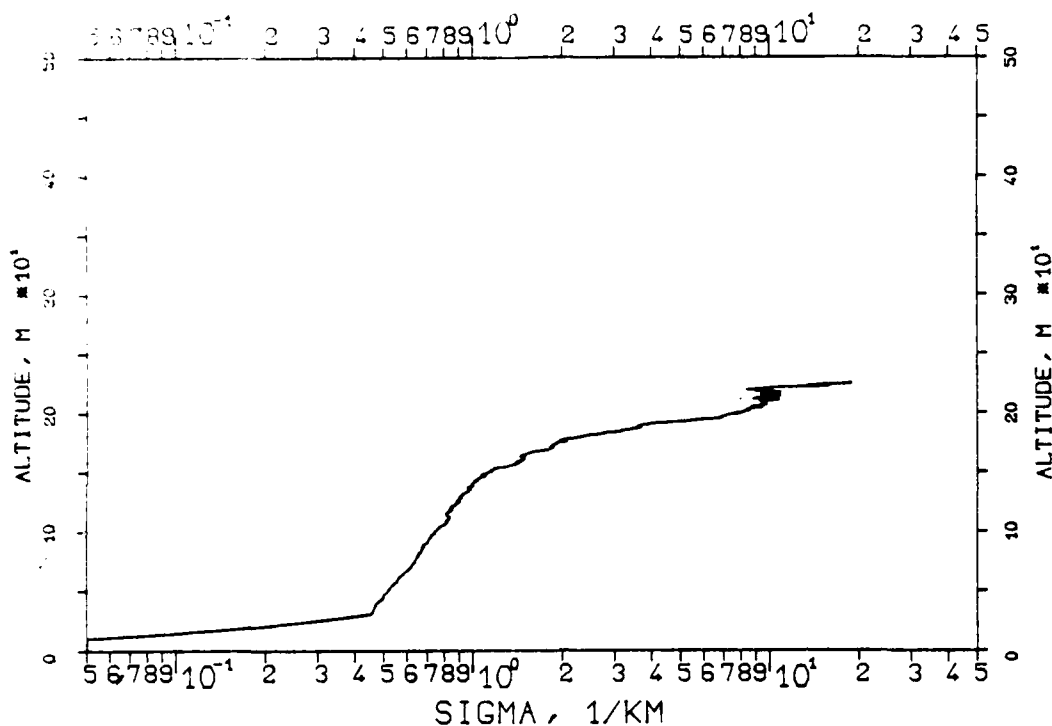


FIG. 7.115
 KLETT-PROFILE, 0530NM, EL. 10DG00MN
 840301, 16:39-16:40, CET
 RM=1.566KM, SM=20.0000/KM, K=1.000

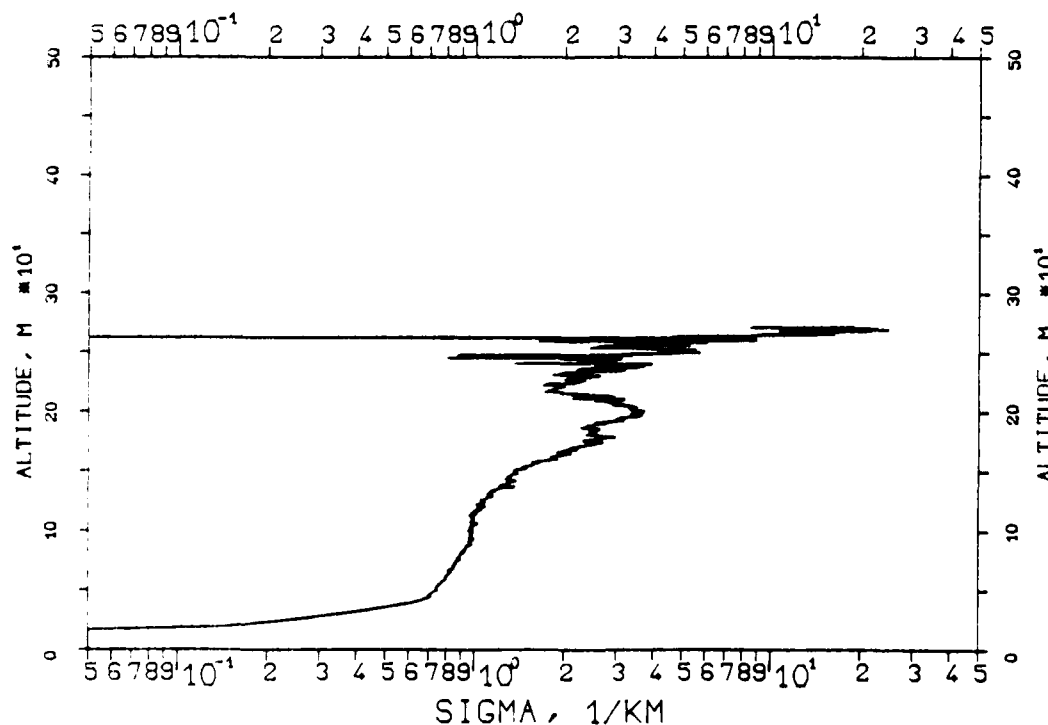


FIG. 7.116
KLETT-PROFILE, 0694NM, EL. 10DG00MN
840301, 16:43-16:44, CET
RM=1.250KM, SM=20.0000/KM, K=1.000

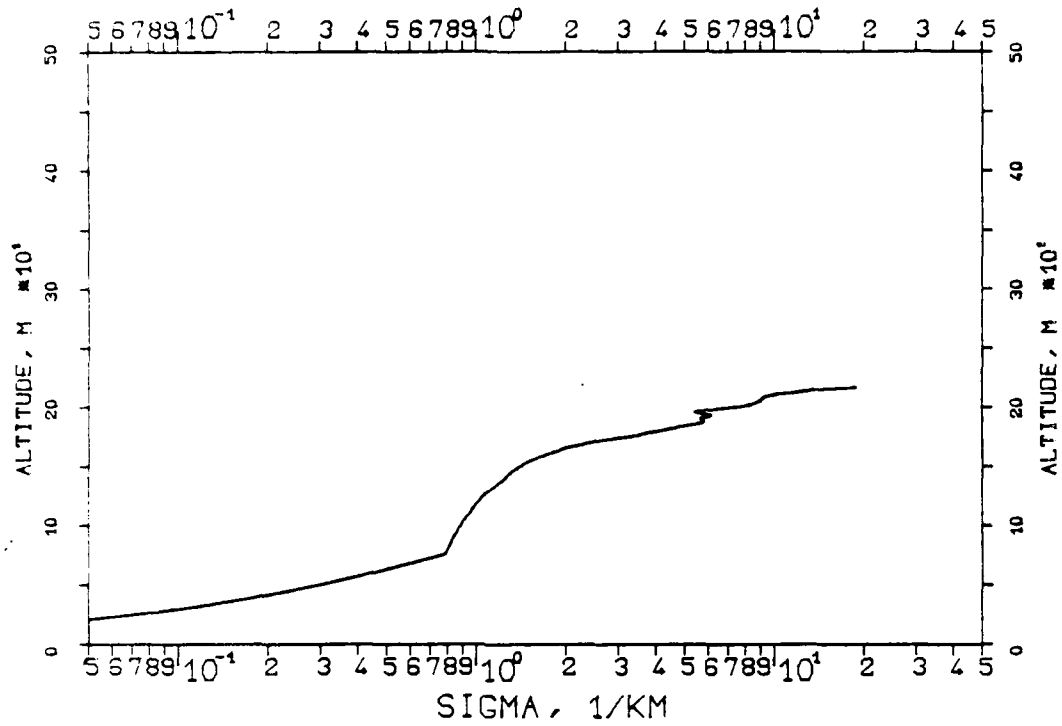


FIG. 7.117
KLETT-PROFILE, 0694NM, EL. 20DG00MN
840301, 16:45-16:46, CET
RM=0.750KM, SM=20.0000/KM, K=1.000

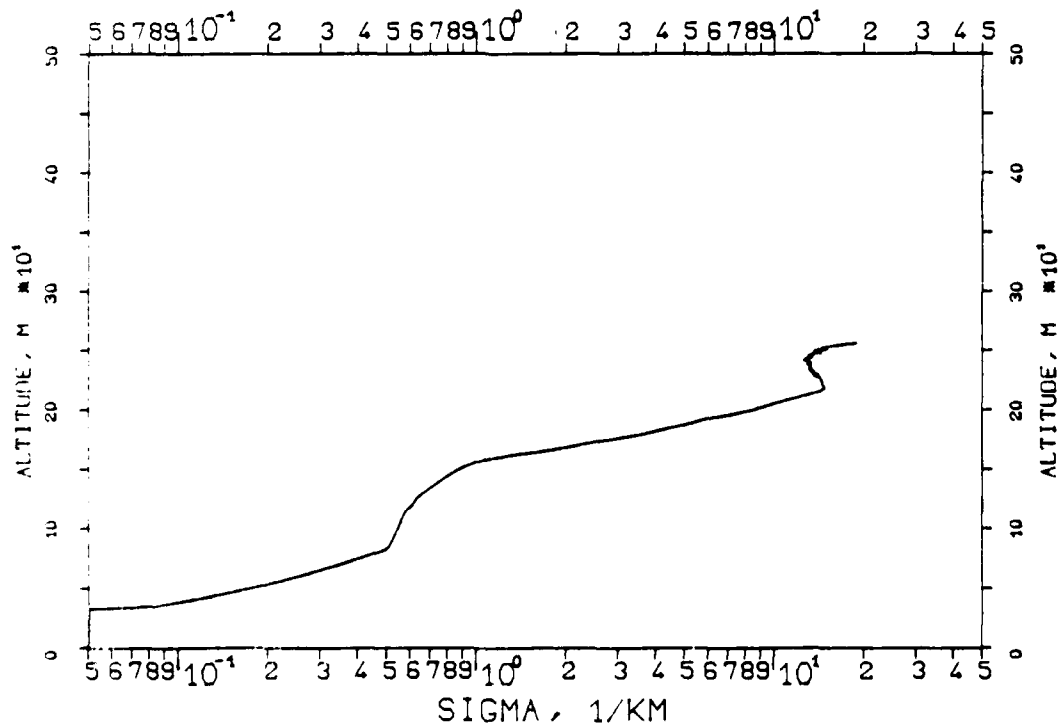


FIG. 7.118
 KLETT-PROFILE, 0530NM, EL. 20DG00MN
 840301, 16:50-16:51, CET
 RM=0.700KM, SM=20.0000/KM, K=1.000

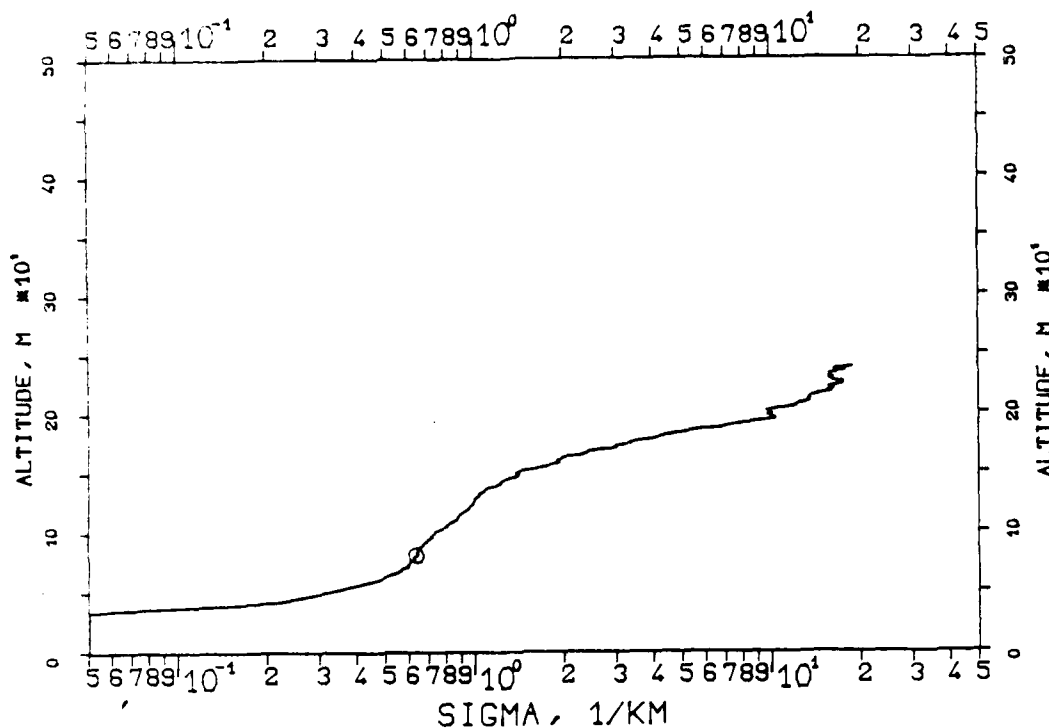


FIG. 7.119
 KLETT-PROFILE, 1060NM, EL. 20DG00MN
 840301, 16:52-16:53, CET
 RM=0.700KM, SM=20.0000/KM, K=1.000

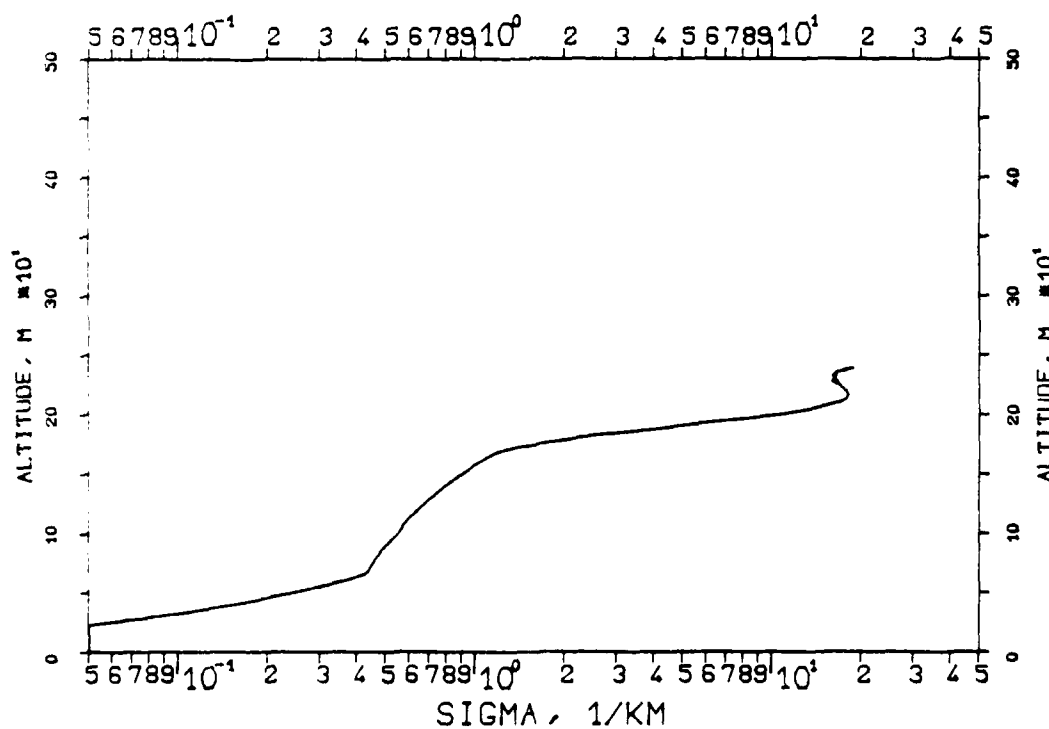


FIG. 7.120
 KLETT-PROFILE, 1060NM, EL. 20DG00MN
 840301, 17:32-17:33, CET
 RM=0.750KM, SM=20.0000/KM, K=1.000

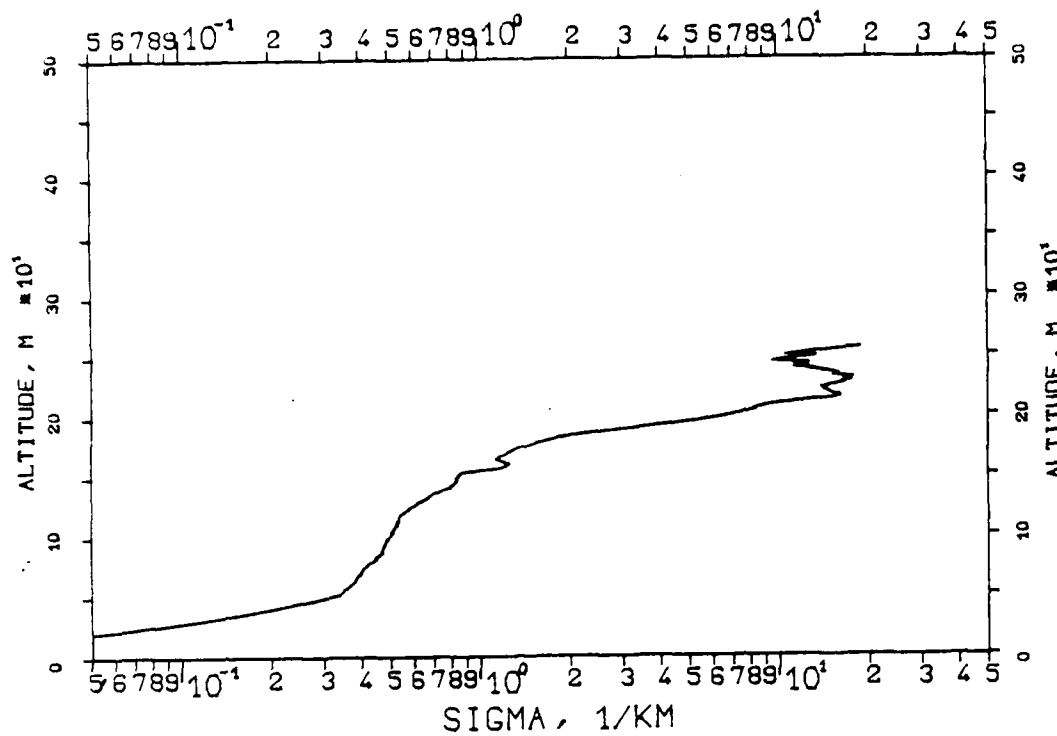


FIG. 7.121
 KLETT-PROFILE, 0530NM, EL. 20DG00MN
 840301, 17:34-17:35, CET
 RM=0.700KM, SM=20.0000/KM, K=1.000

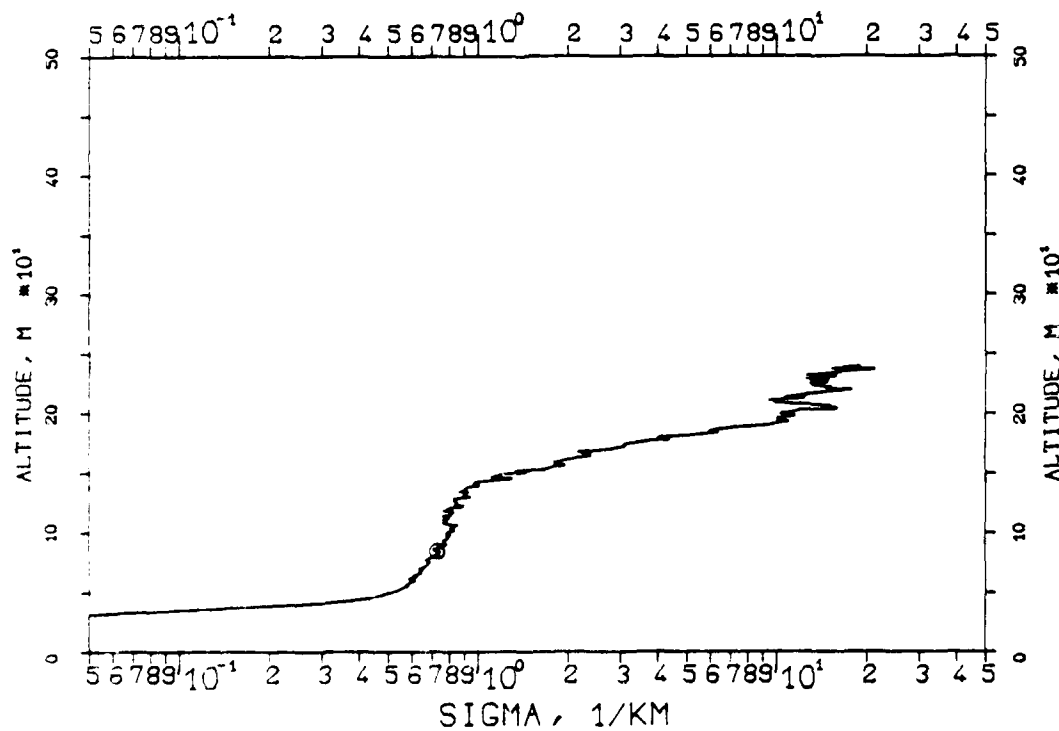


FIG. 7.122
 KLETT-PROFILE, 0694NM, EL. 20DG00MN
 840301, 17:37-17:38, CET
 RM=0.727KM, SM=20.0000/KM, K=1.000

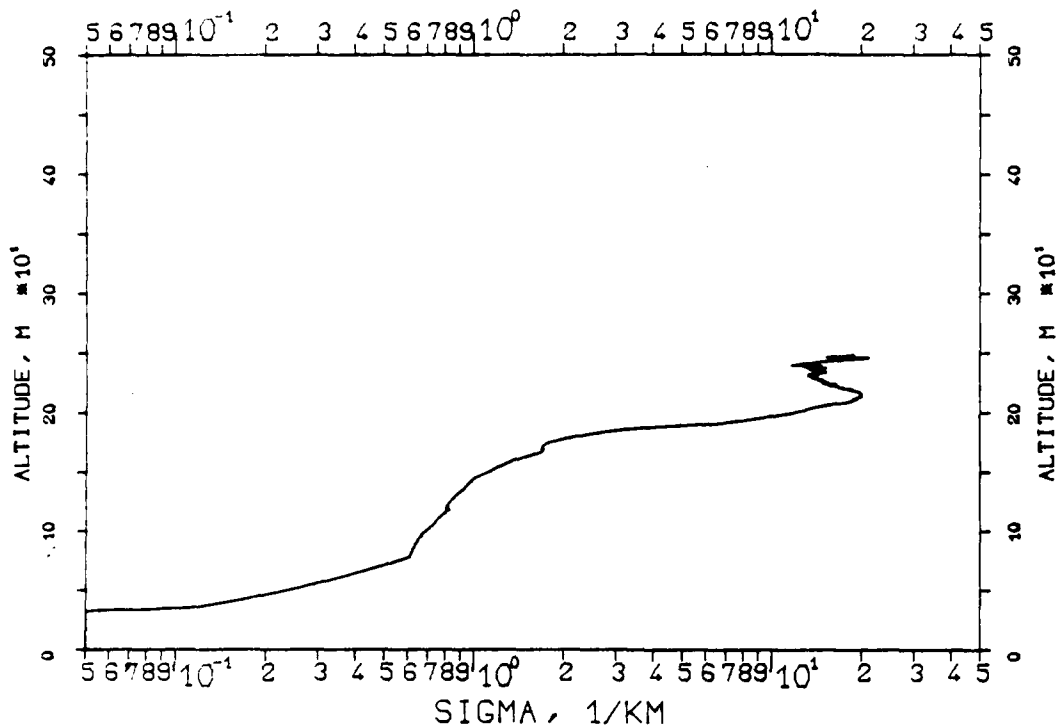


FIG. 7.123
 KLETT-PROFILE, 0694NM, EL. 19DG12MN
 840327, 10:41-10:41, CET
 RM=1.987KM, SM=20.0000/KM, K=1.000

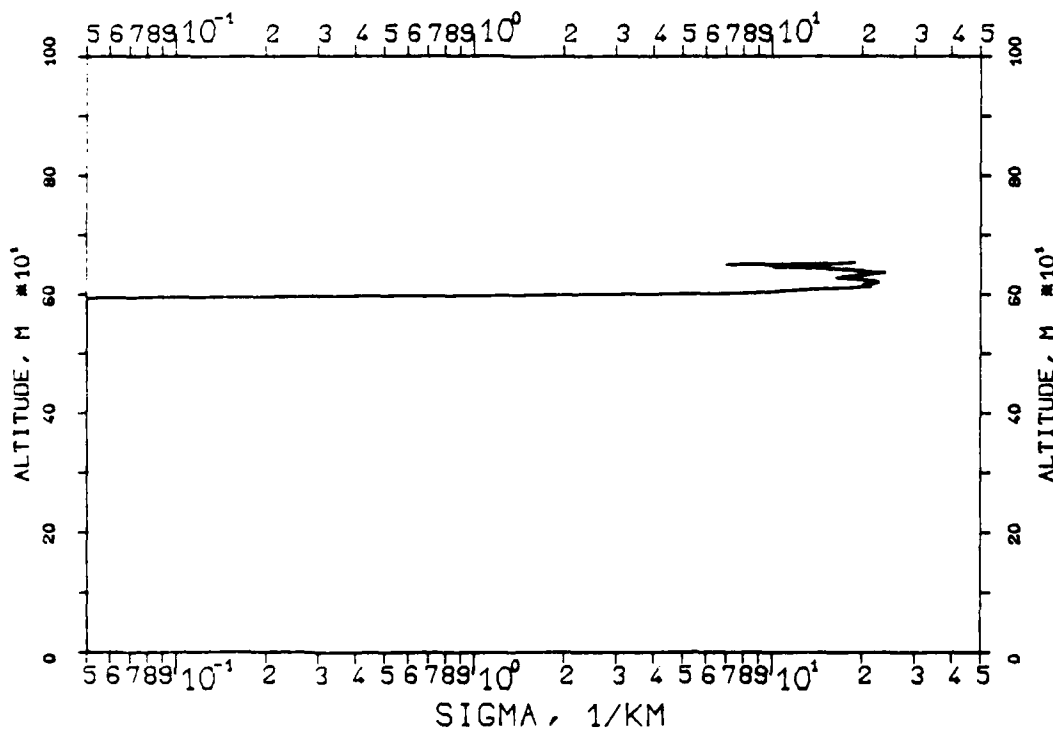


FIG. 7.124
 KLETT-PROFILE, 1060NM, EL. 19DG12MN
 840327, 10:42-10:42, CET
 RM=2.107KM, SM=20.0000/KM, K=1.000

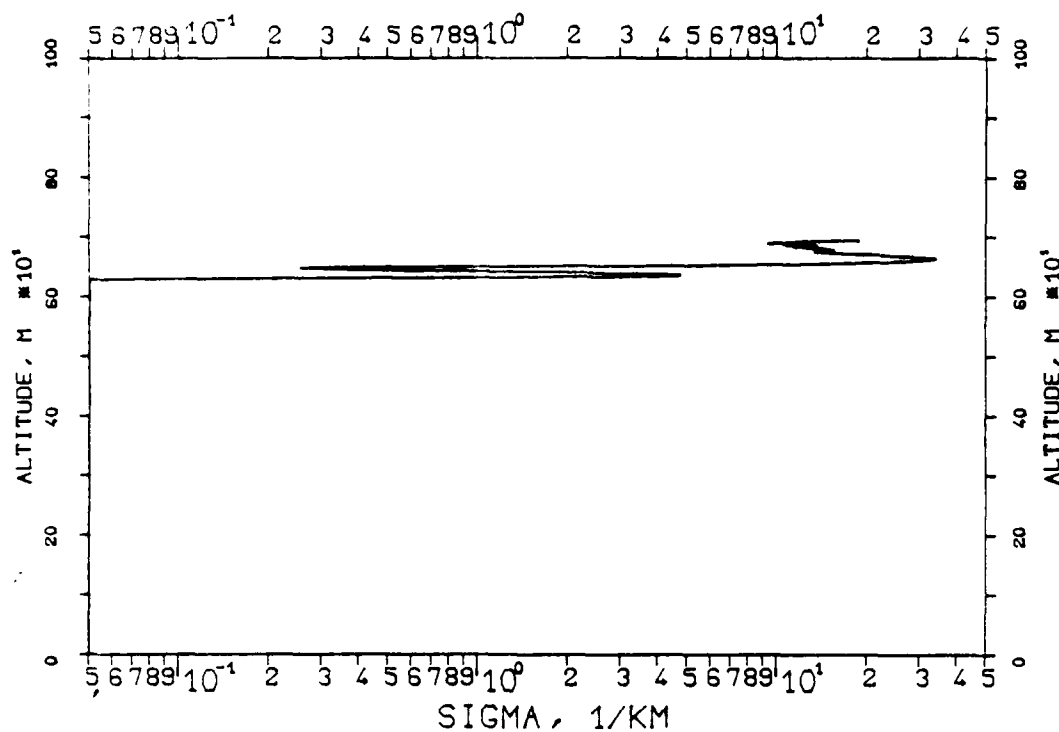


FIG. 7.125
 KLETT-PROFILE, 0530NM, EL. 19DG12MN
 840327, 10:43-10:44, CET
 RM=2.163KM, SM=20.0000/KM, K=1.000

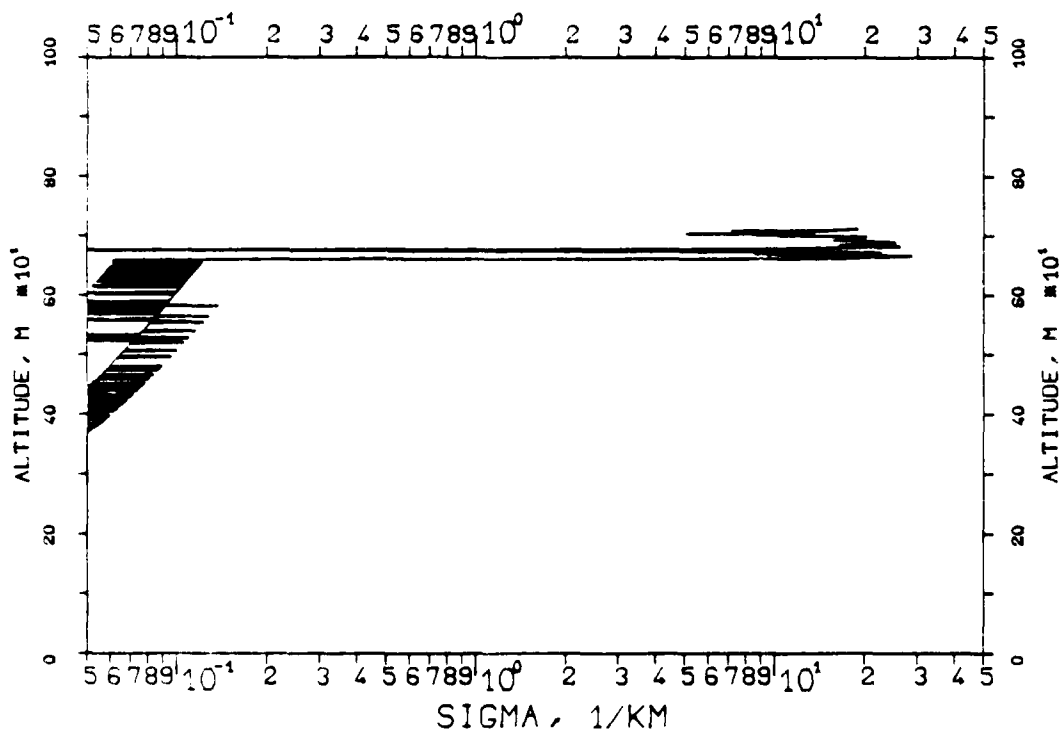


FIG. 7.128

KLETT-PROFILE, 0694NM, EL. 20DG00MN
840404, 13:34-13:35, CET
RM=2.317KM, SM=20.0000/KM, K=1.000

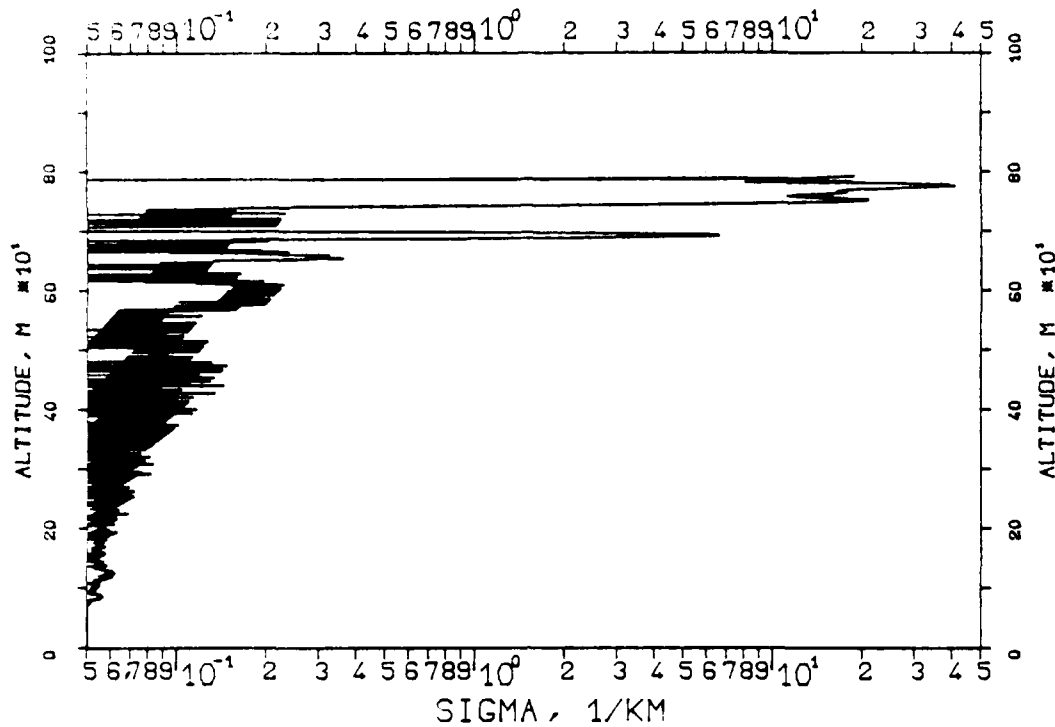


FIG. 7.129

KLETT-PROFILE, 0694NM, EL. 20DG00MN
840404, 13:40-13:40, CET
RM=2.086KM, SM=20.0000/KM, K=1.000

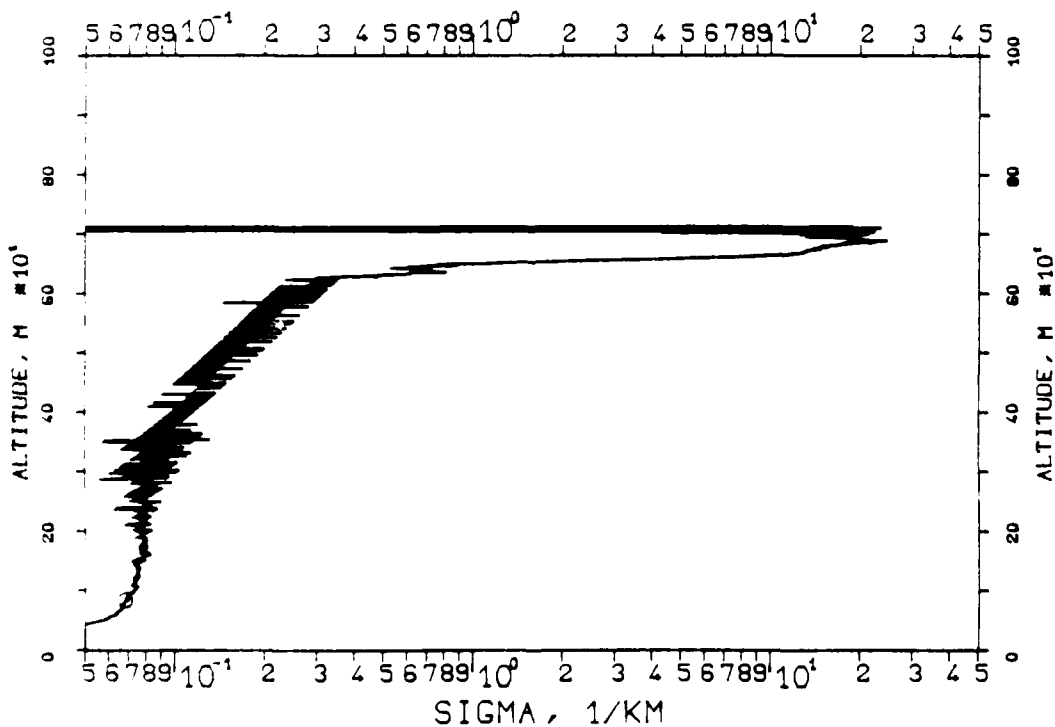


FIG. 7.126

KLETT-PROFILE, 0530NM, EL. 20DG00MN

840404, 13:27-13:28, CET

RM=2.257KM, SM=20.0000/KM, K=1.000

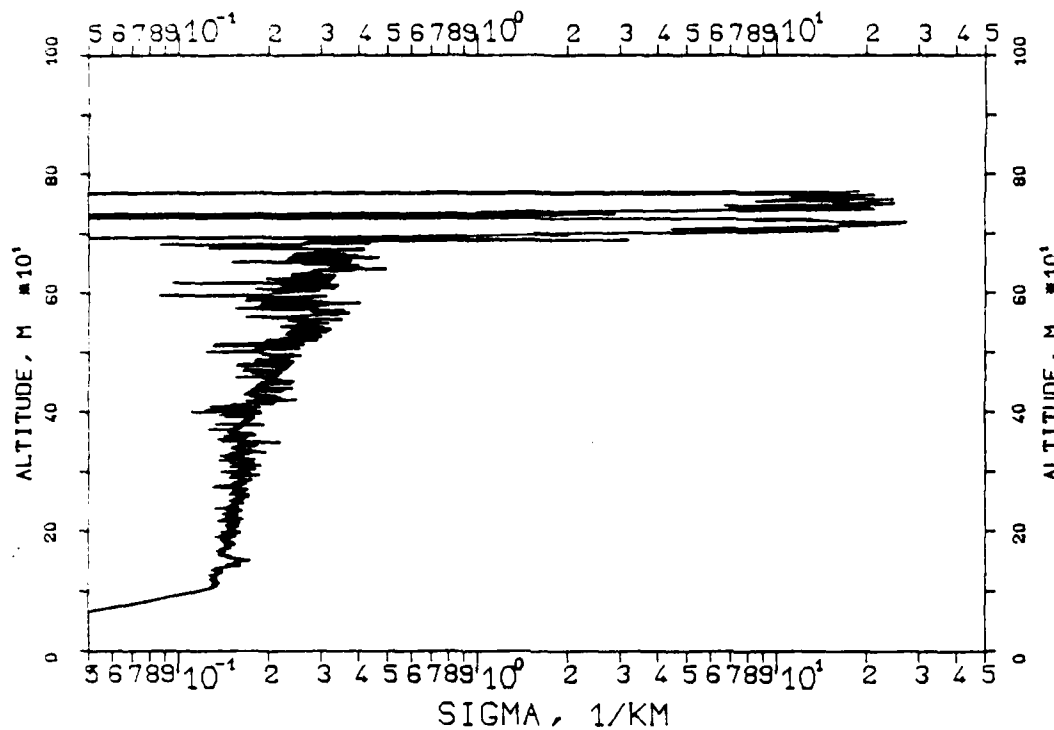


FIG. 7.127

KLETT-PROFILE, 1060NM, EL. 20DG00MN

840404, 13:33-13:33, CET

RM=2.439KM, SM=20.0000/KM, K=1.000

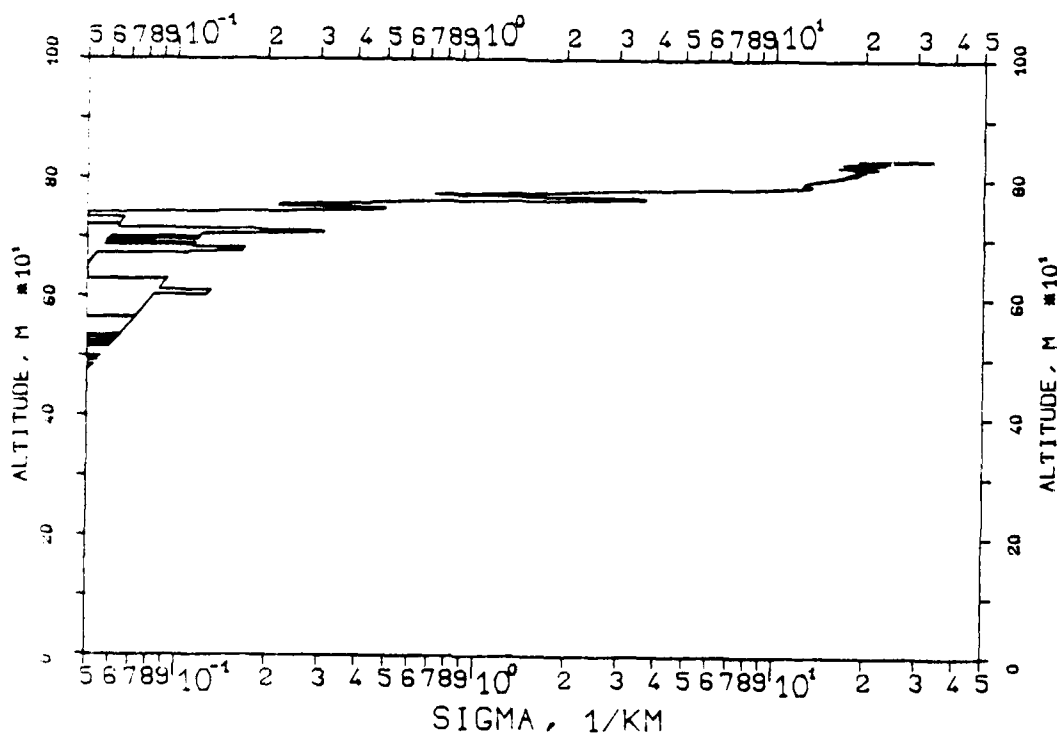


FIG. 7.130
 KLETT-PROFILE, 1060NM, EL. 20DG00MN
 840404, 13:43-13:43, CET
 RM=2.335KM, SM=20.0000/KM, K=1.000

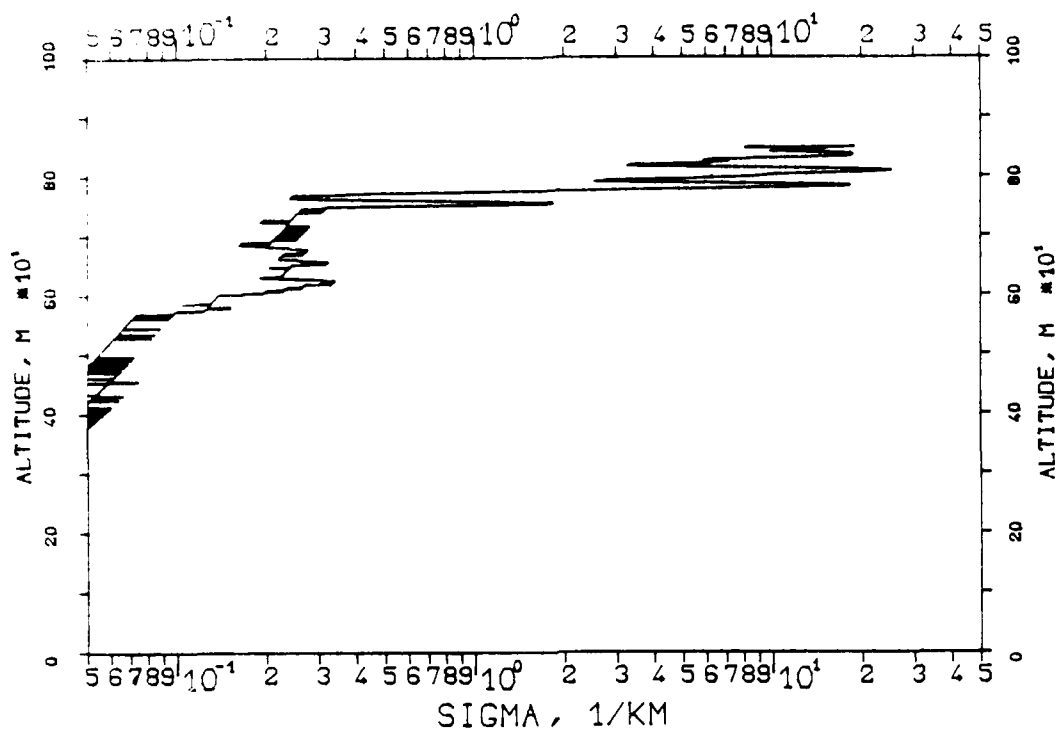


FIG. 7.131
 KLETT-PROFILE, 0530NM, EL. 20DG00MN
 840404, 13:44-13:45, CET
 RM=2.020KM, SM=20.0000/KM, K=1.000

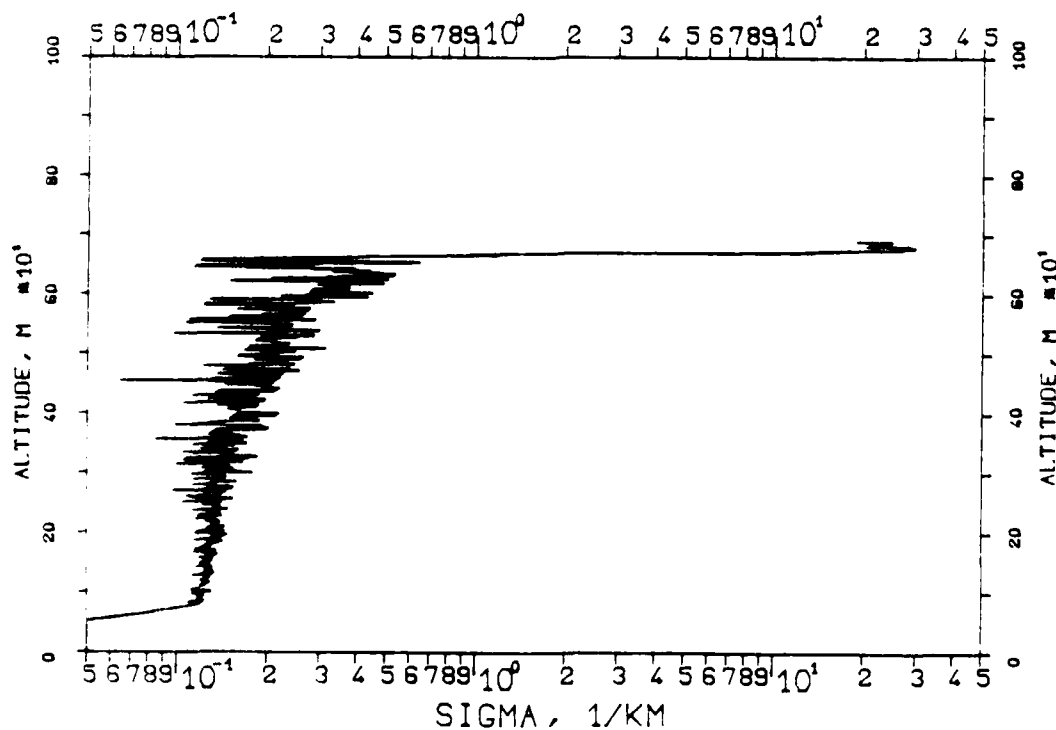


FIG. 7.132
KLETT-PROFILE, 0530NM, EL. 20DG00MN
840404, 14:35-14:36, CET
RM=2.643KM, SM=20.0000/KM, K=1.000

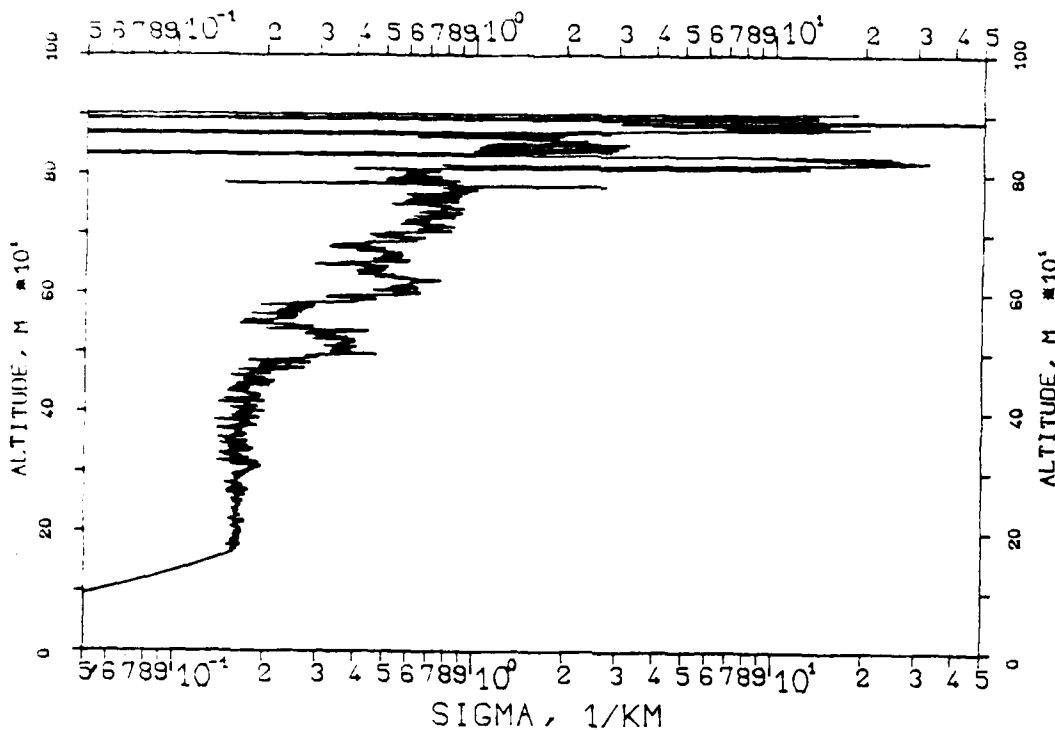


FIG. 7.133
KLETT-PROFILE, 1060NM, EL. 20DG00MN
840404, 14:38-14:38, CET
RM=2.569KM, SM=20.0000/KM, K=1.000

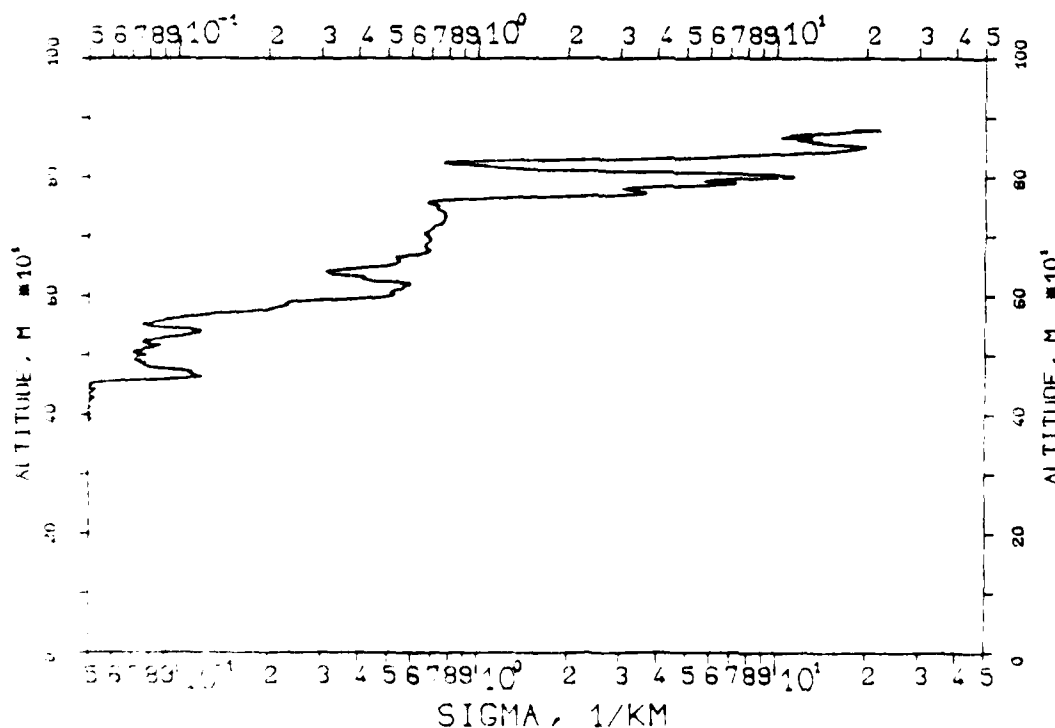


FIG. 7.134
KLETT-PROFILE, 0694NM, EL. 20DG00MN
840404, 14:39-14:40, CET
RM=2.608KM, SM=20.0000/KM, K=1.000

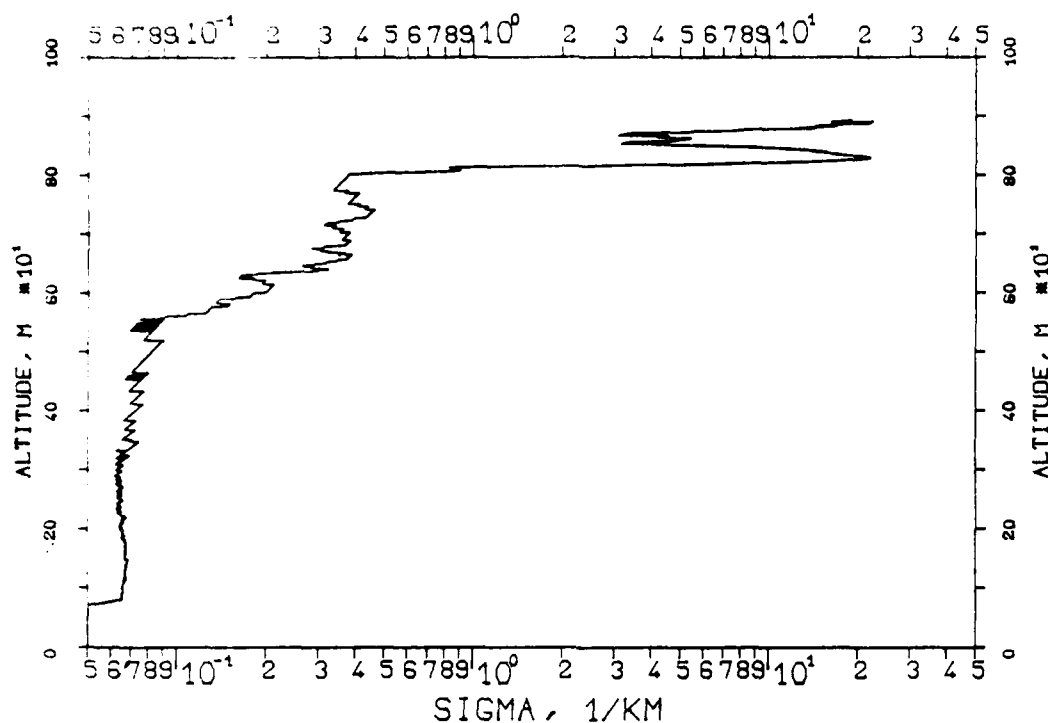


FIG. 7.135
KLETT-PROFILE, 0694NM, EL. 27DG00MN
840404, 14:45-14:45, CET
RM=2.600KM, SM=20.0000/KM, K=1.000

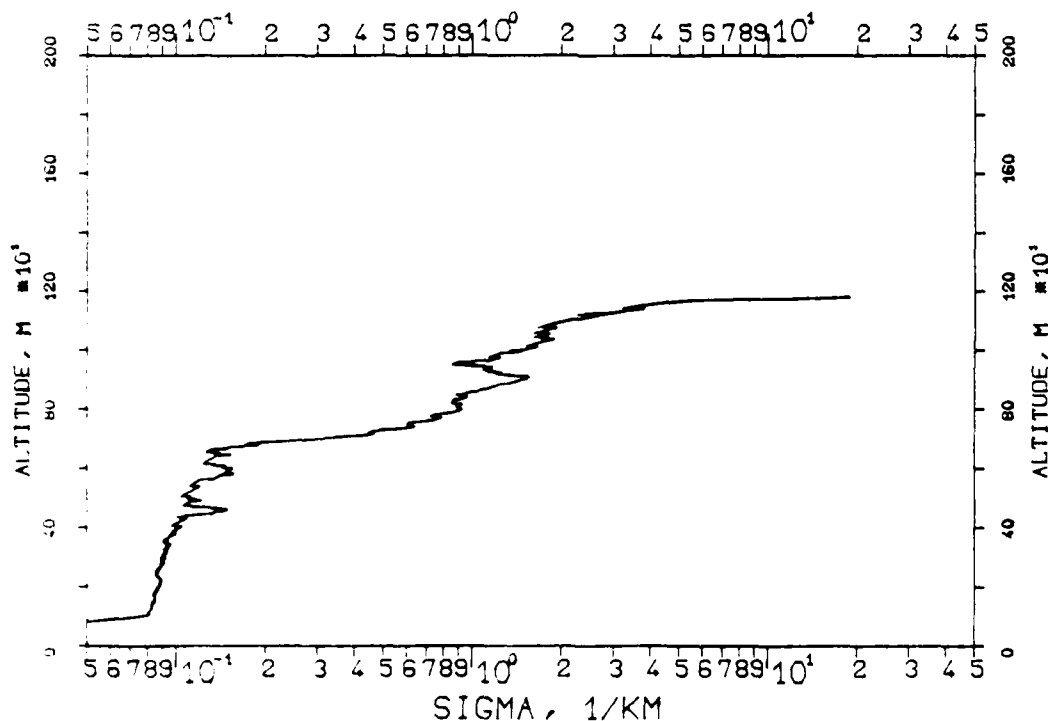


FIG. 7.136
 KLETT PROFILE, 1060NM, EL. 27DG00MN
 840404, 14:47-14:47, CET
 RM=2.630KM, SM=20.0000/KM, K=1.000

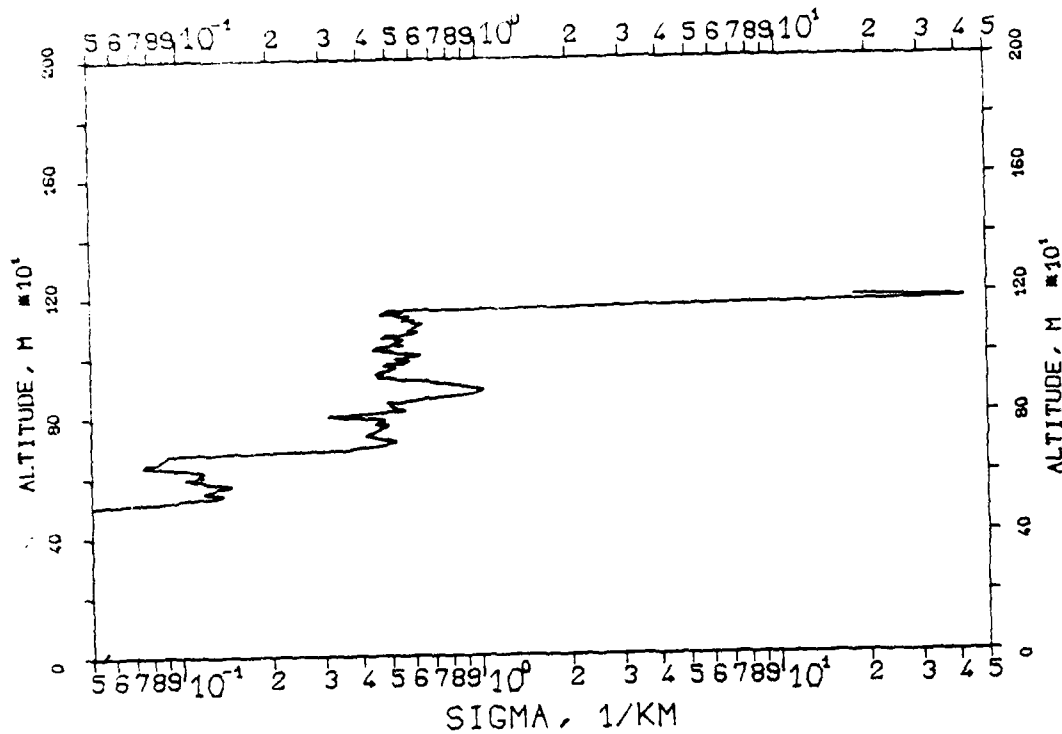


FIG. 7.137
 KLETT PROFILE, 0530NM, EL. 27DG00MN
 840404, 14:49-14:49, CET
 RM=2.550KM, SM=20.0000/KM, K=1.000

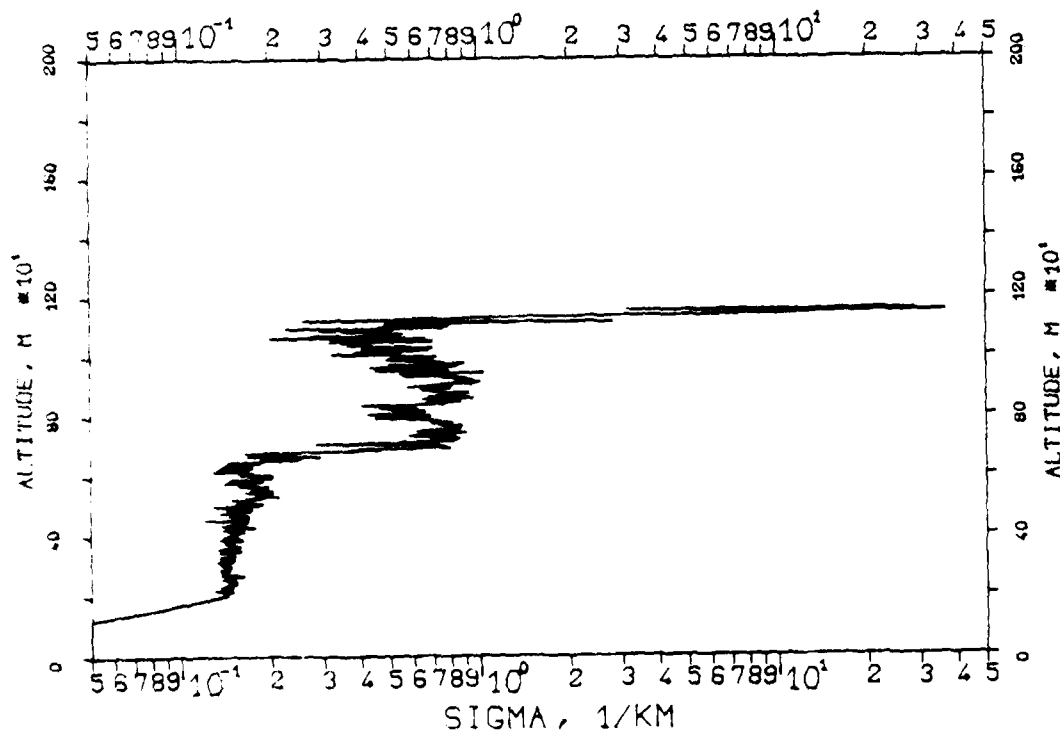


FIG. 7.138

KLETT-PROFILE, 0694NM, EL. 07DG30MN

840411, 13:04-13:04, CET

RM=0.388KM, SM=20.0000/KM, K=1.000

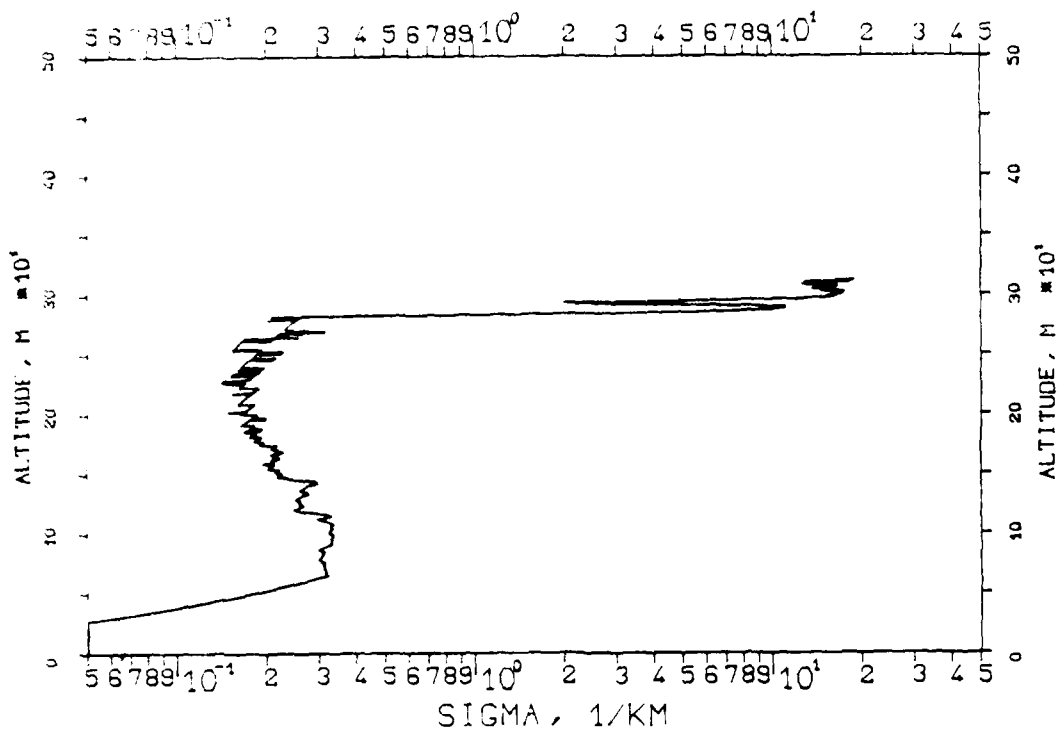


FIG. 7.139

KLETT-PROFILE, 1060NM, EL. 07DG30MN

840411, 13:10-13:10, CET

RM=2.436KM, SM=20.0000/KM, K=1.000

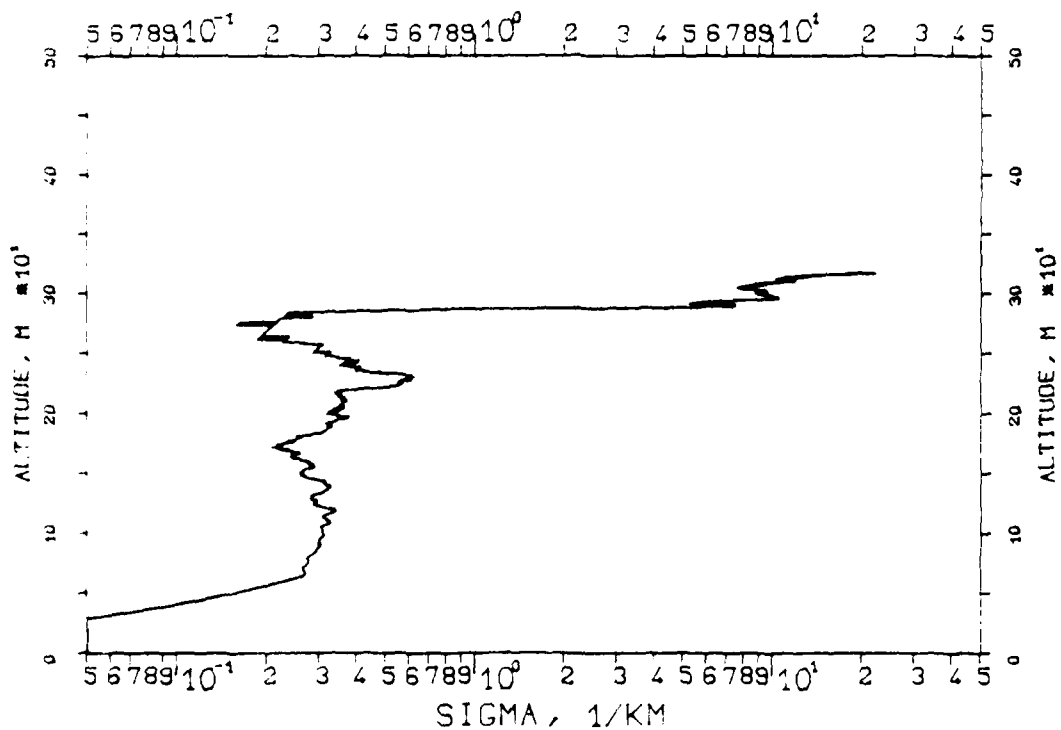


FIG. 7.140
 KLETT-PROFILE, 0530NM, EL. 07DG30MN
 840411, 13:12-13:13, CET
 RM=2.334KM, SM=20.0000/KM, K=1.000

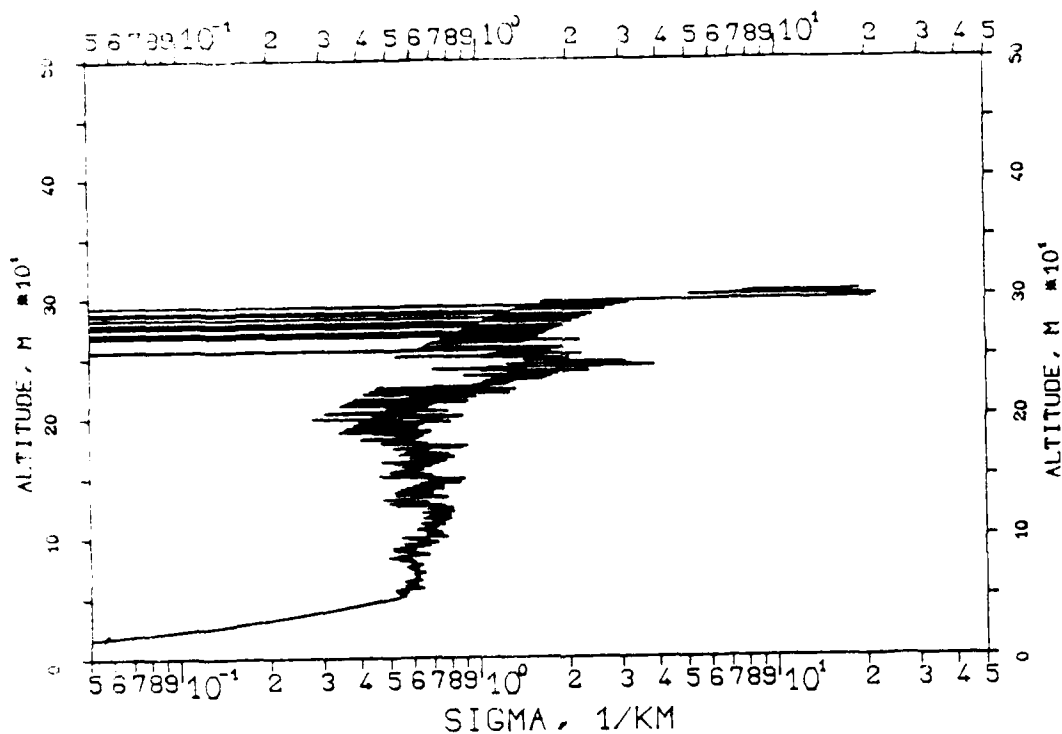


FIG. 7.141
 KLETT-PROFILE, 0694NM, EL. 1SDG00MN
 840411, 13:19-13:19, CET
 RM=1.026KM, SM=20.0000/KM, K=1.000

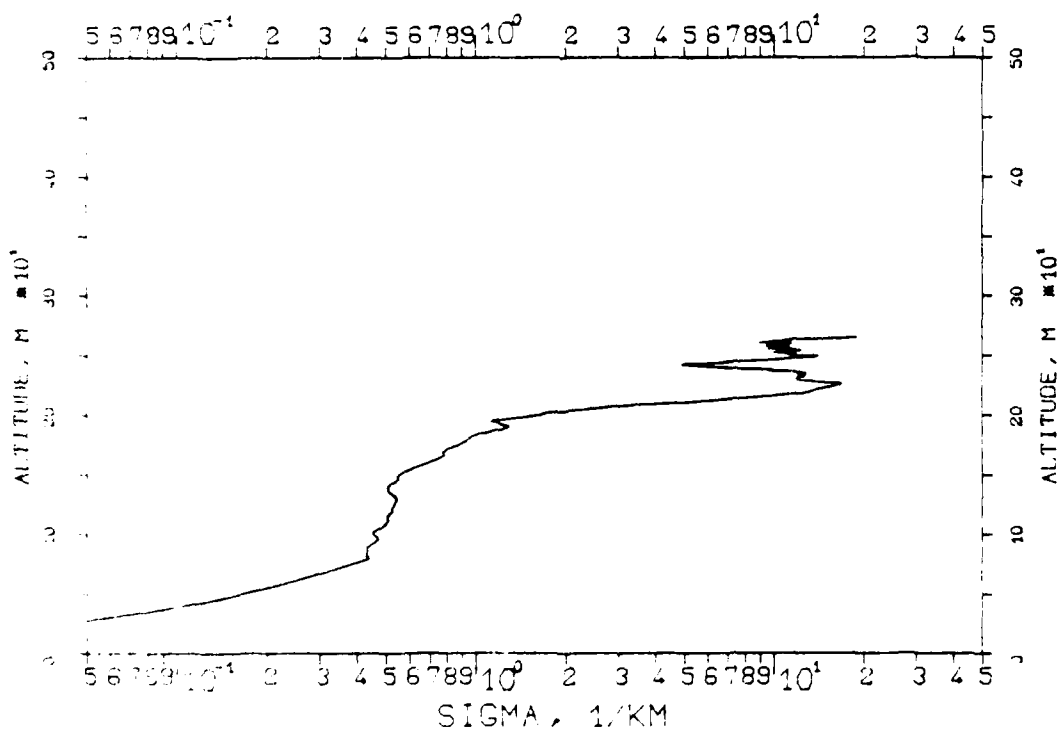


FIG. 7.168
KLETT-PROFILE, 1060NM, EL. 20DG00MN
840827, 08:56-08:56, CET
RM=0.59KM, SM=20.0000/KM, K=1.000

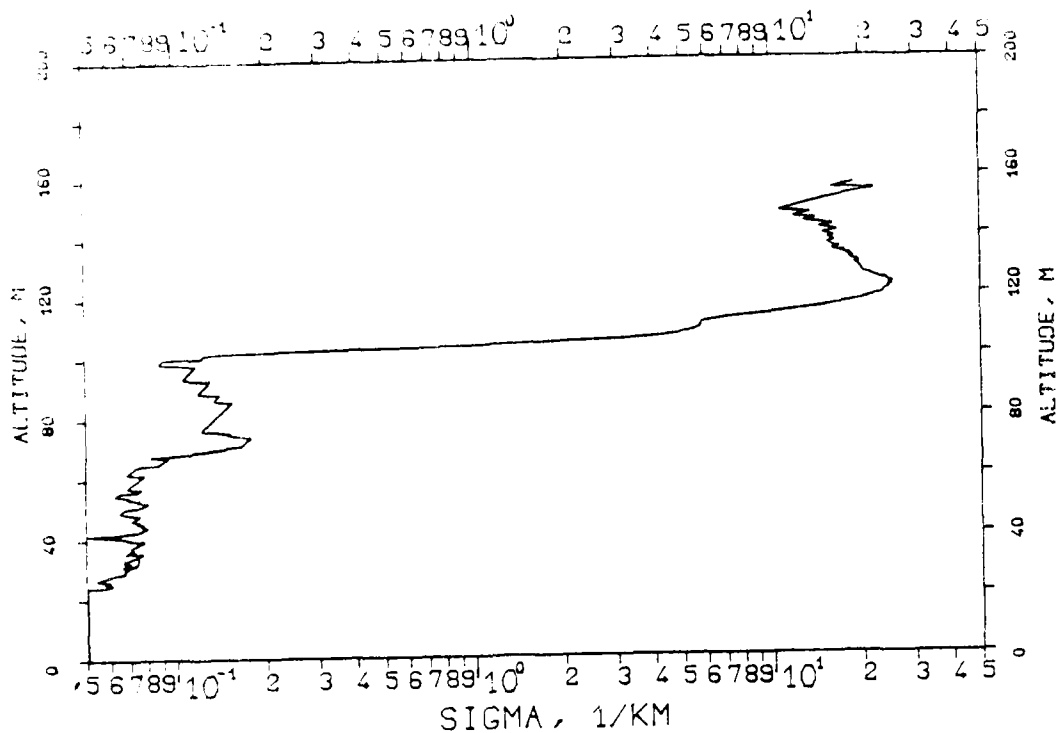


FIG. 7.169
KLETT-PROFILE, 1060NM, EL. 20DG00MN
840827, 08:57-08:57, CET
RM=0.468KM, SM=20.0000/KM, K=1.000

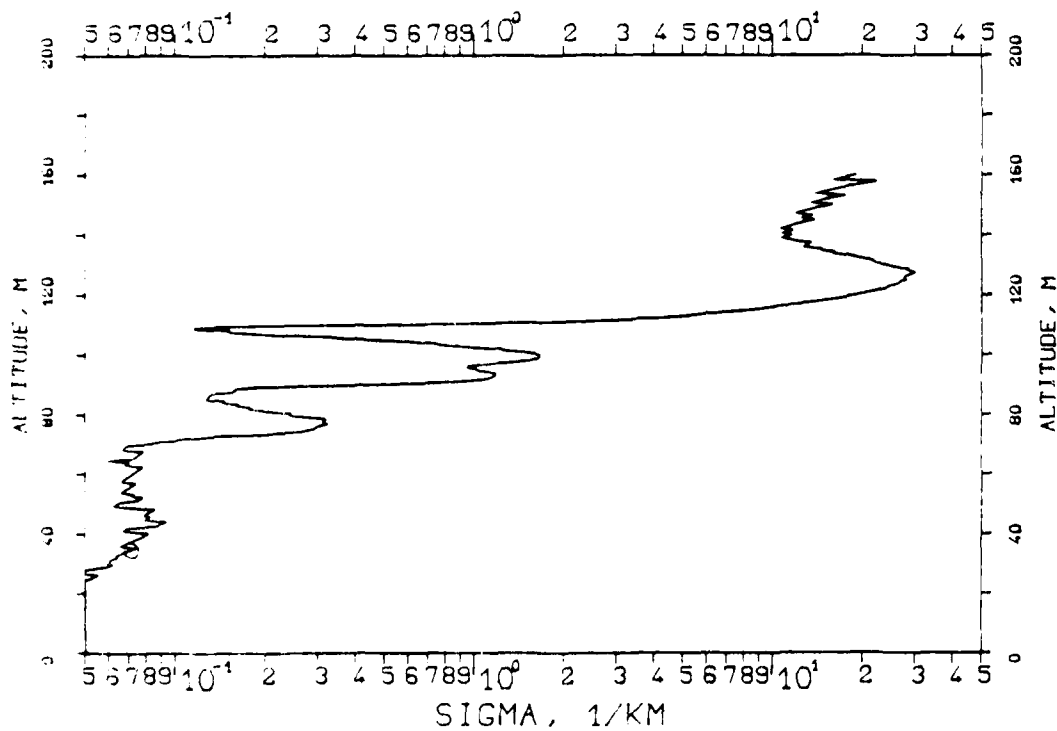


FIG. 7.166
KLETT-PROFILE, 1060NM, EL. 10DG00MN
8.0827, 07:15-07:15, CET
RM=0.354KM, SM=20.0000/KM, K=1.000

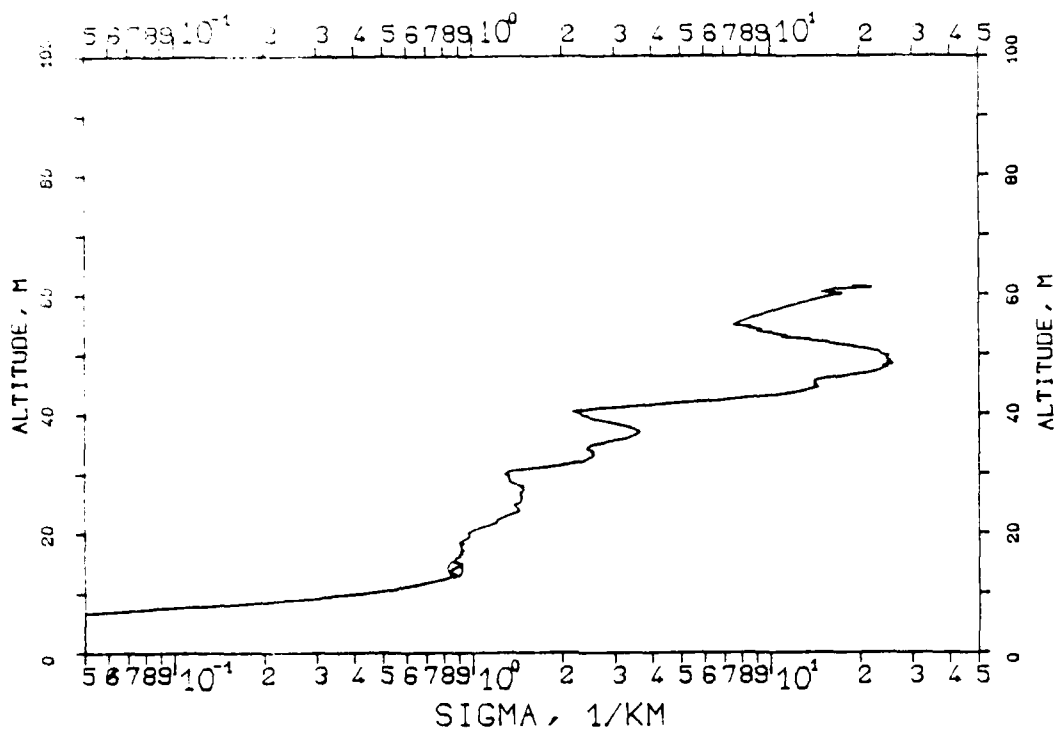


FIG. 7.167
KLETT-PROFILE, 1060NM, EL. 10DG00MN
840827, 07:16-07:16, CET
RM=0.352KM, SM=20.0000/KM, K=1.000

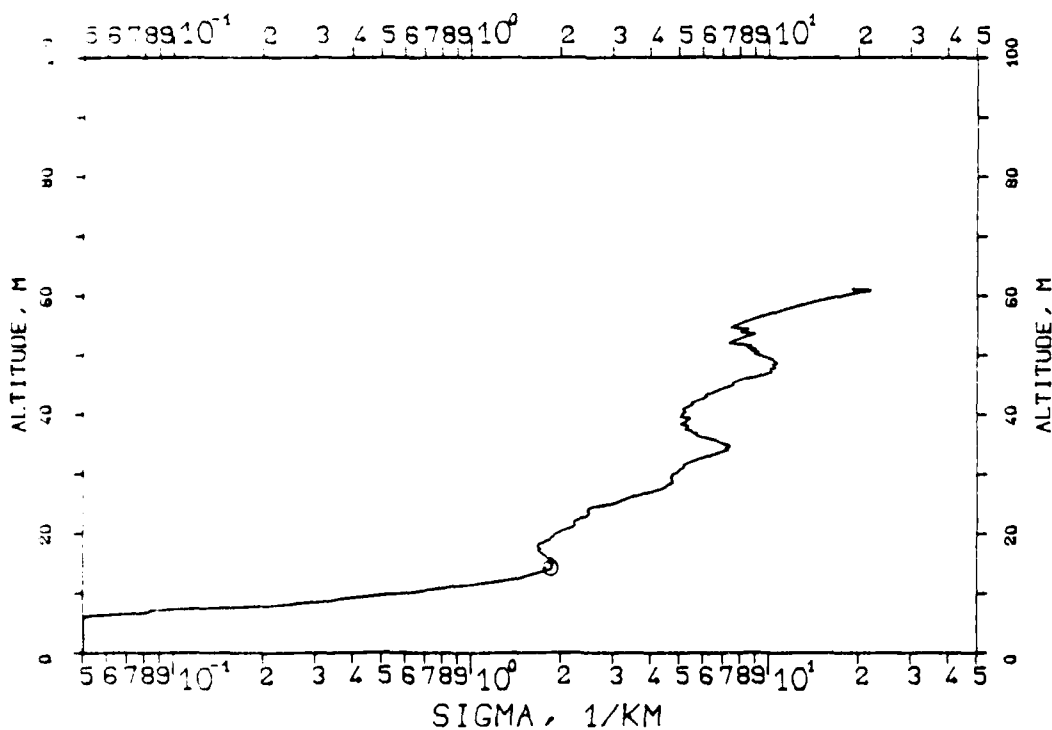


FIG. 7.164

KLETT PROFILE, 1060NM, EL. 10DG00MN

840827, 07:12-07:13, CET

RM=0.168KM, SM=20.0000/KM, K=1.000

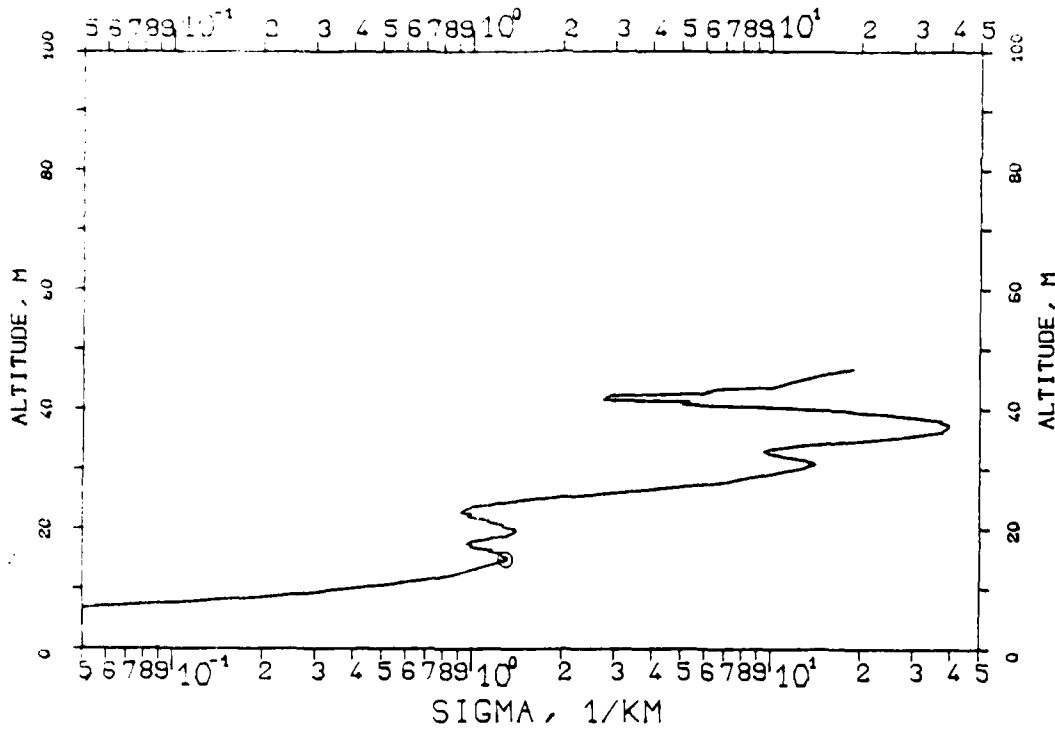


FIG. 7.165

KLETT-PROFILE, 1060NM, EL. 10DG00MN

840827, 07:13-07:14, CET

RM=0.315KM, SM=20.0000/KM, K=1.000

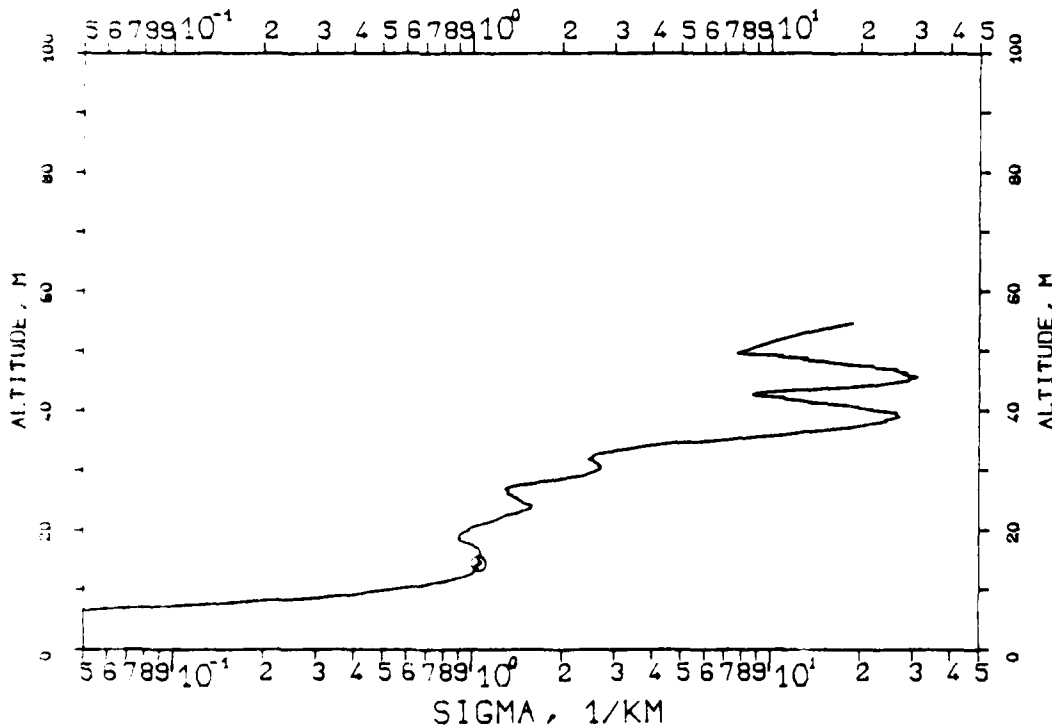


FIG. 7.162

KLETT-PROFILE, 0530NM, EL. 19DG12MN

840119, 09:03-09:04, CET

RM=1.436KM, SM=20.0000/KM, K=1.000

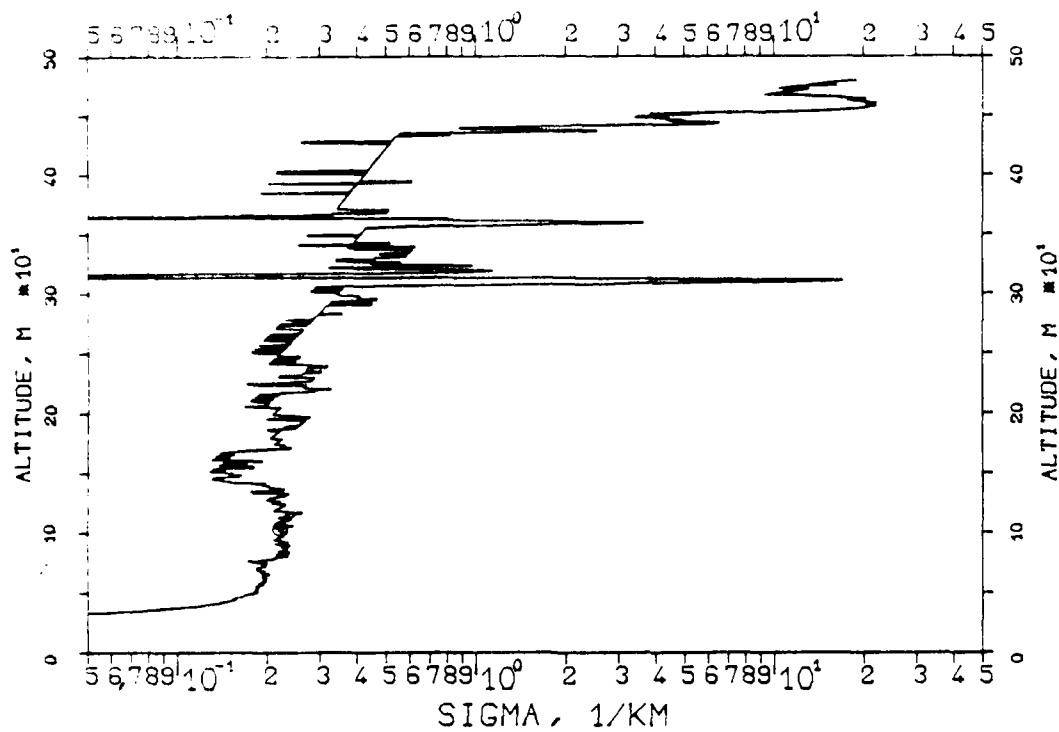


FIG. 7.163

KLETT-PROFILE, 1060NM, EL. 10DG00MN

840827, 07:10-07:10, CET

RM=0.247KM, SM=20.0000/KM, K=1.000

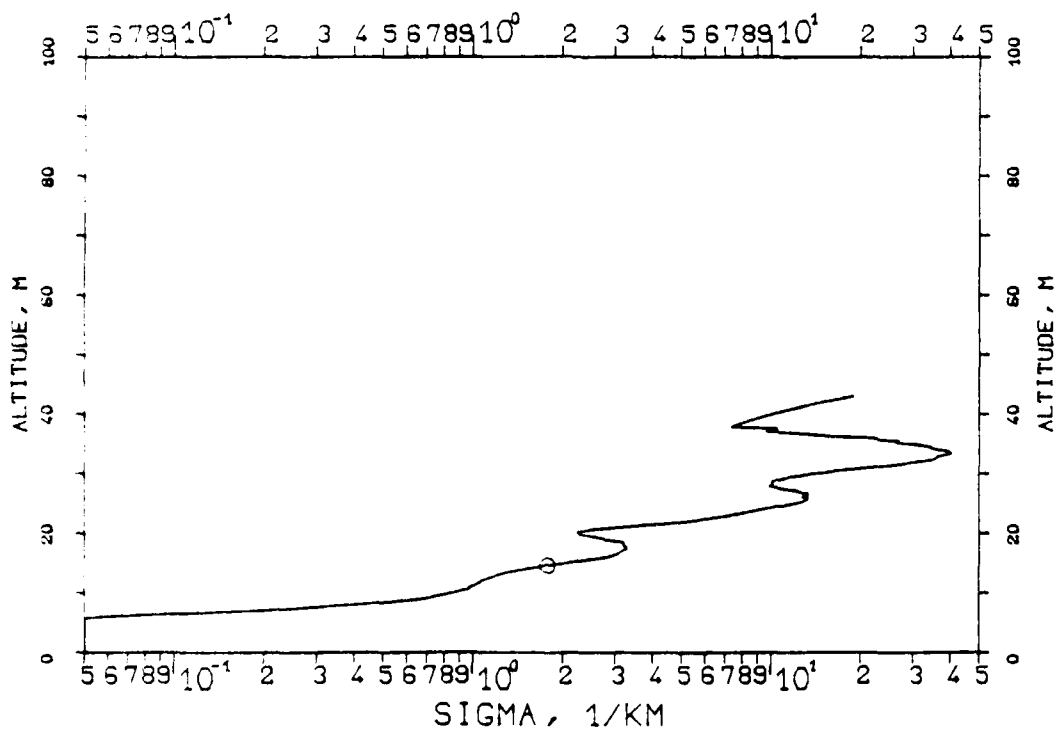


FIG. 7.160
KLETT PROFILE, 0530NM, EL. 19DG12MN
840418, 09:01-09:01, CET
RM=1.240KM, SM=20.0000/KM, K=1.000

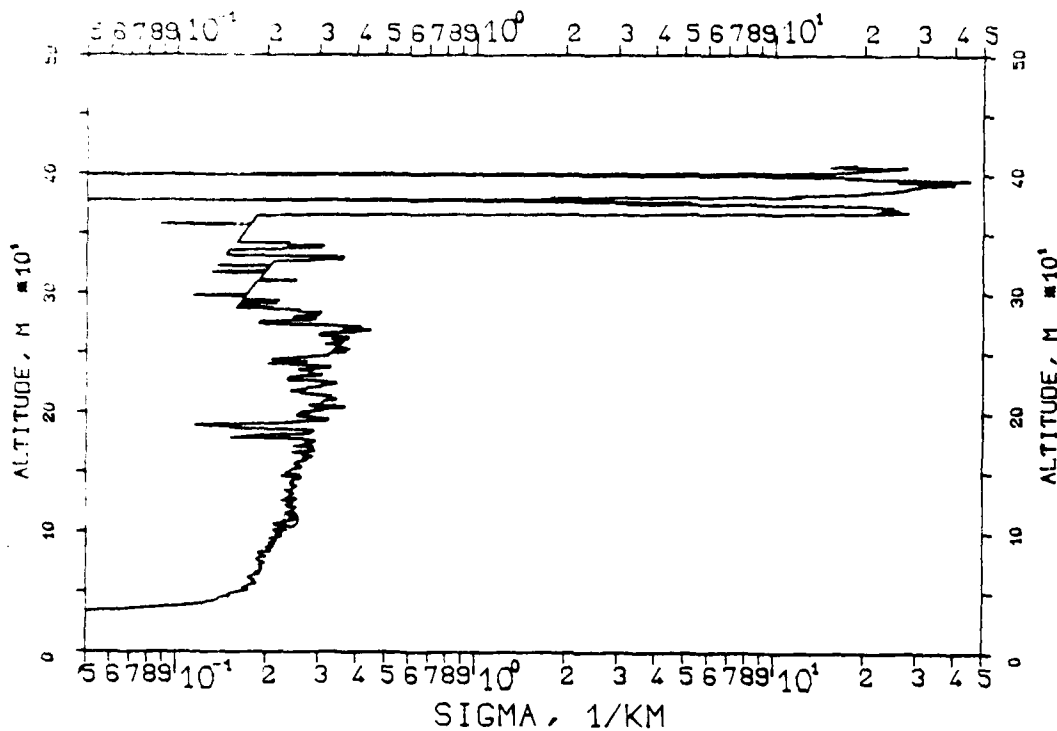


FIG. 7.161
KLETT PROFILE, 0530NM, EL. 19DG12MN
840418, 09:02-09:02, CET
RM=1.483KM, SM=20.0000/KM, K=1.000

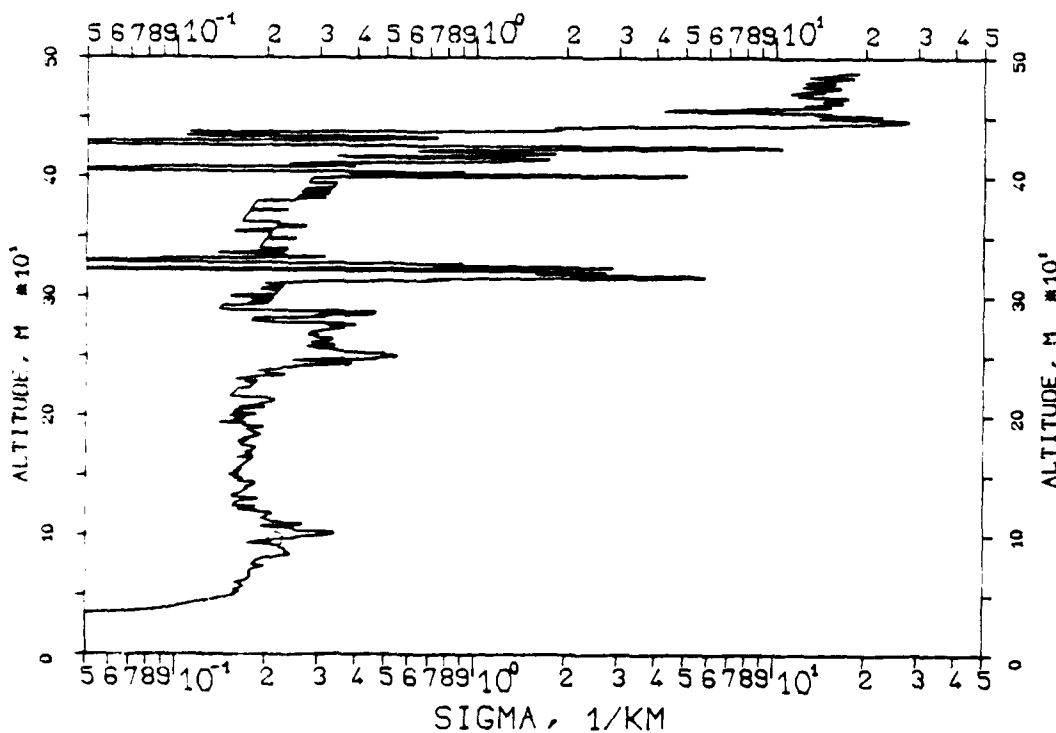


FIG. 7.158
KLETT-PROFILE, 1060NM, EL. 19DG12MN
840418, 08:54-08:55, CET
RM=1.548KM, SM=20.0000/KM, K=1.000

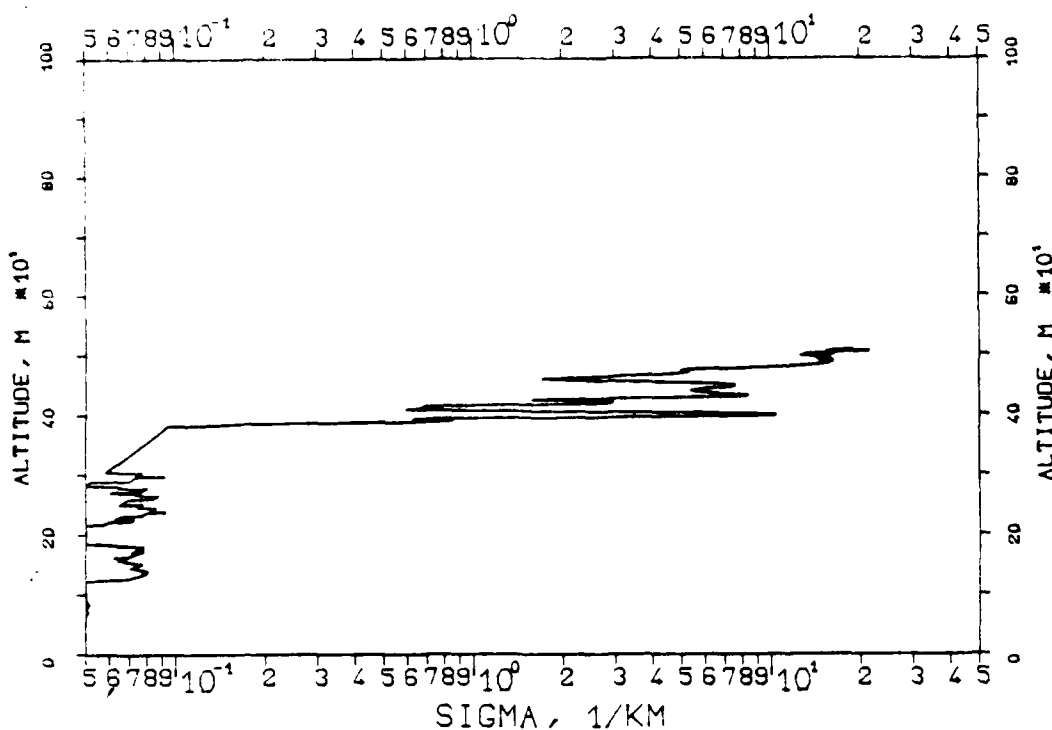


FIG. 7.159
KLETT-PROFILE, 1060NM, EL. 19DG12MN
840418, 08:56-08:56, CET
RM=1.566KM, SM=20.0000/KM, K=1.000

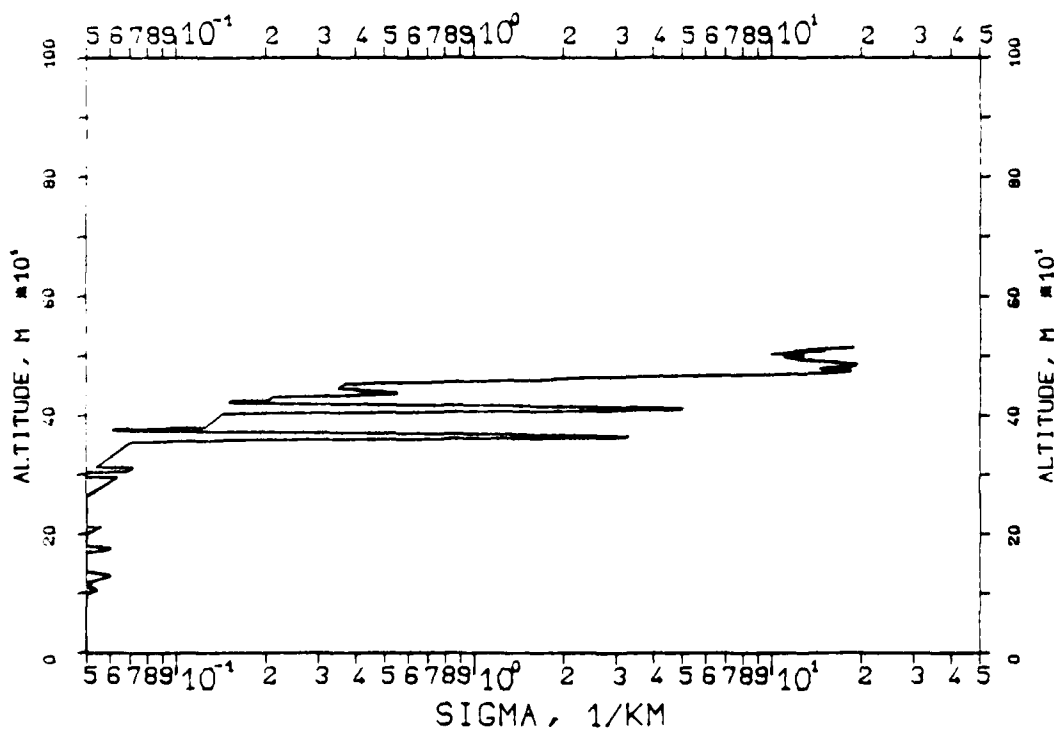


FIG. 7.156
KLETT-PROFILE, 0694NM, EL. 150600MN
840411, 14:08-14:08, CET
RM=0.810KM, SM=20.0000/KM, K=1.000

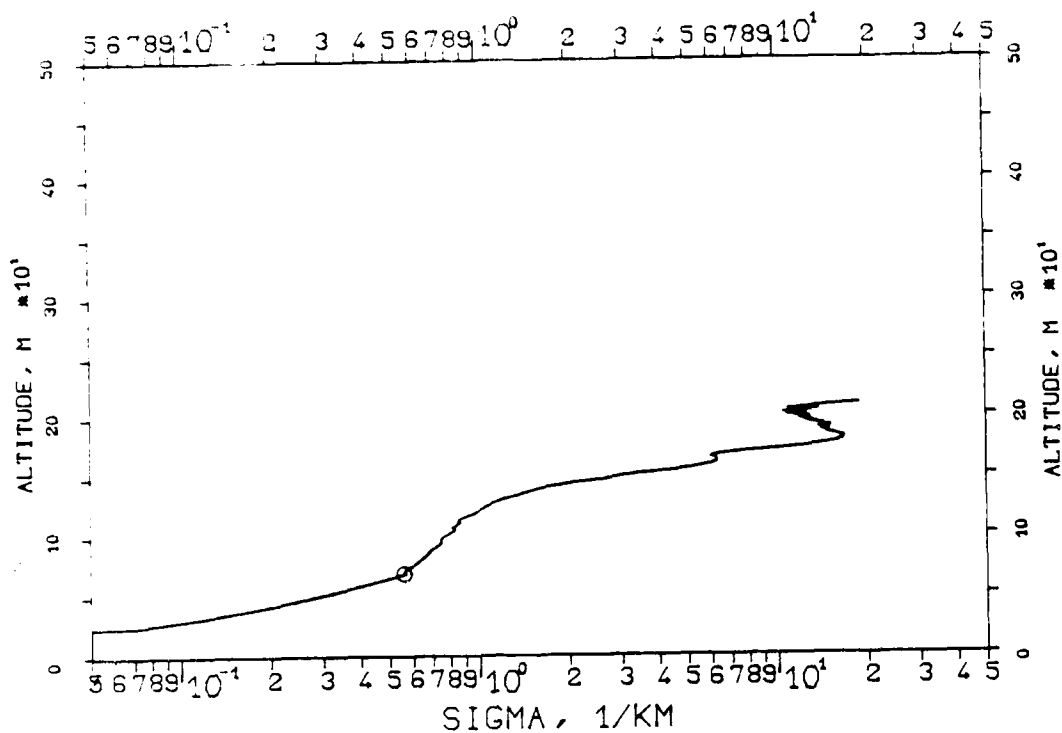


FIG. 7.157
KLETT-PROFILE, 1060NM, EL. 190612MN
840418, 08:53-08:53, CET
RM=1.528KM, SM=20.0000/KM, K=1.000

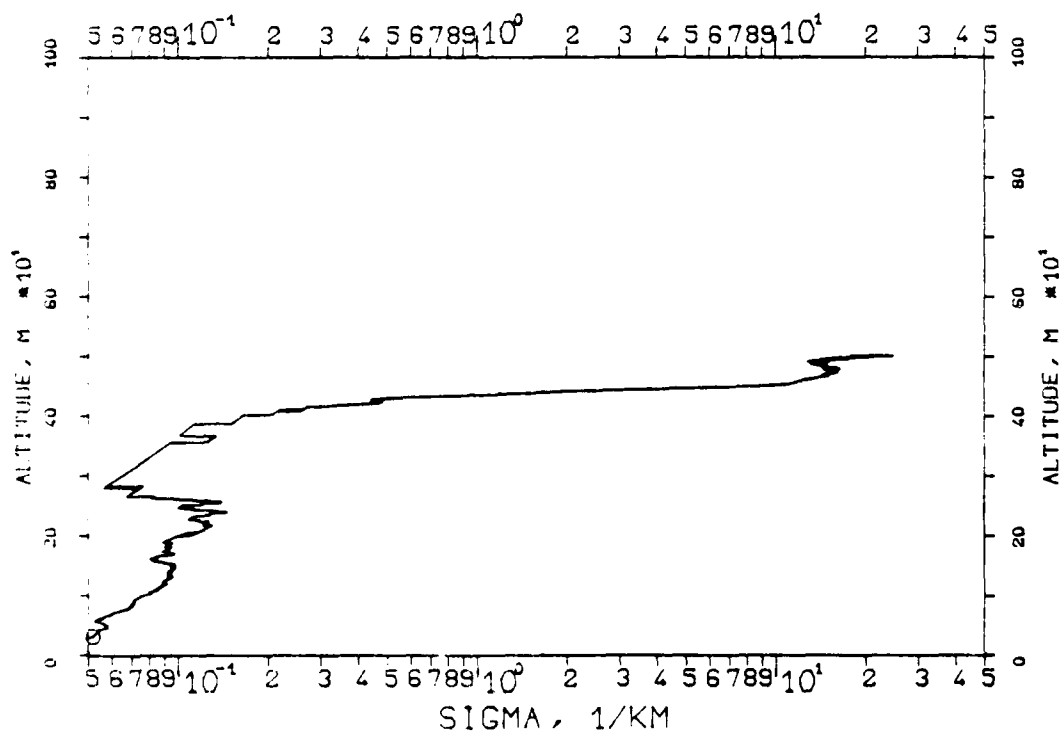


FIG. 7.154
 KLETT-PROFILE, 0694NM, EL. 15DG00MN
 340411, 14:06-14:06, CET
 RM=0.814KM, SM=20.0000/KM, K=1.000

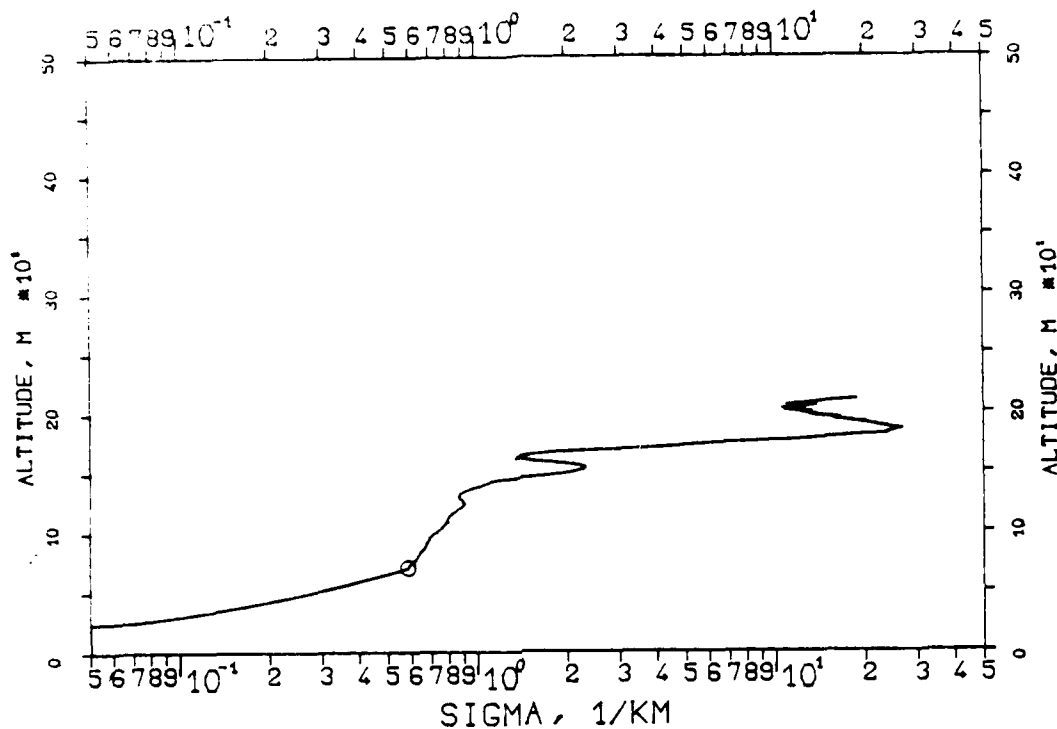


FIG. 7.155
 KLETT-PROFILE, 0694NM, EL. 15DG00MN
 840411, 14:07-14:07, CET
 RM=0.835KM, SM=20.0000/KM, K=1.000

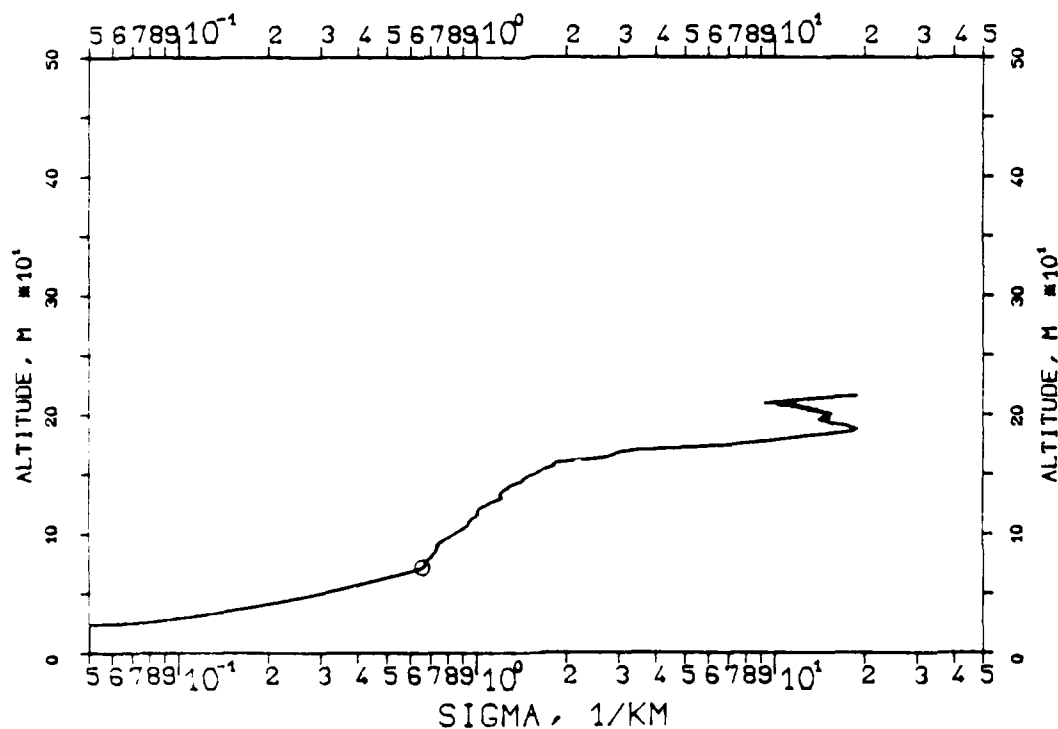


FIG. 7.152
 KLETT-PROFILE, 0694NM, EL. 15DG00MN
 840411, 14:04-14:04, CET
 RM=0.885KM, SM=20.0000/KM, K=1.000

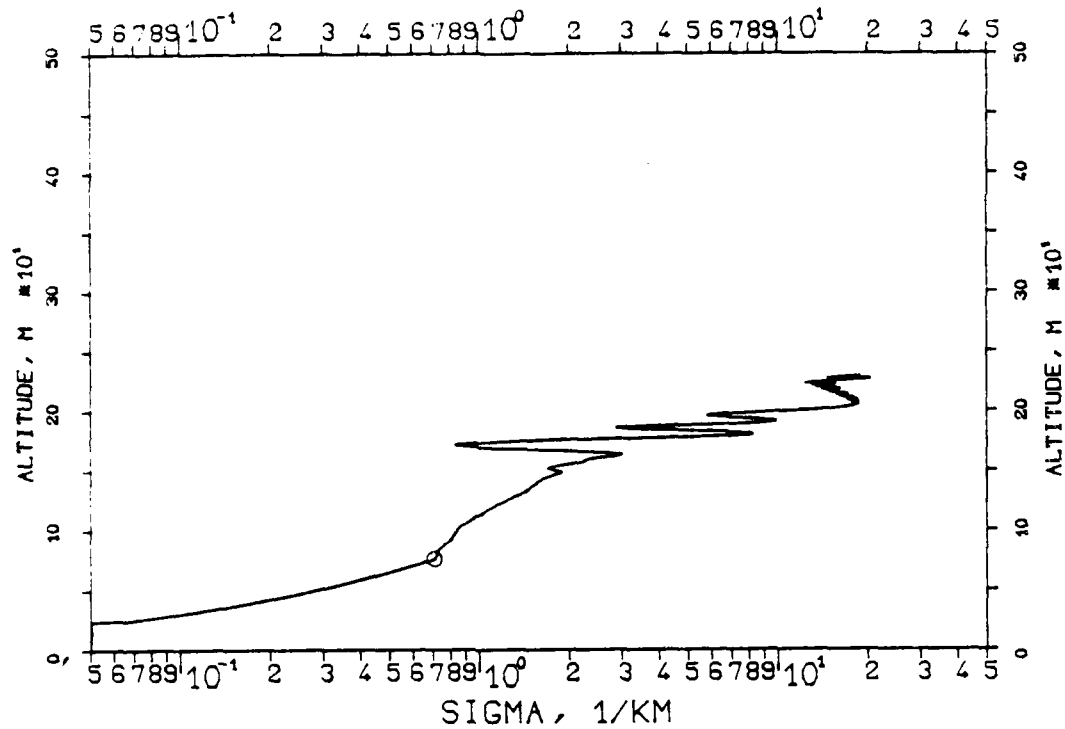


FIG. 7.153
 KLETT-PROFILE, 0694NM, EL. 15DG00MN
 840411, 14:05-14:05, CET
 RM=0.795KM, SM=20.0000/KM, K=1.000

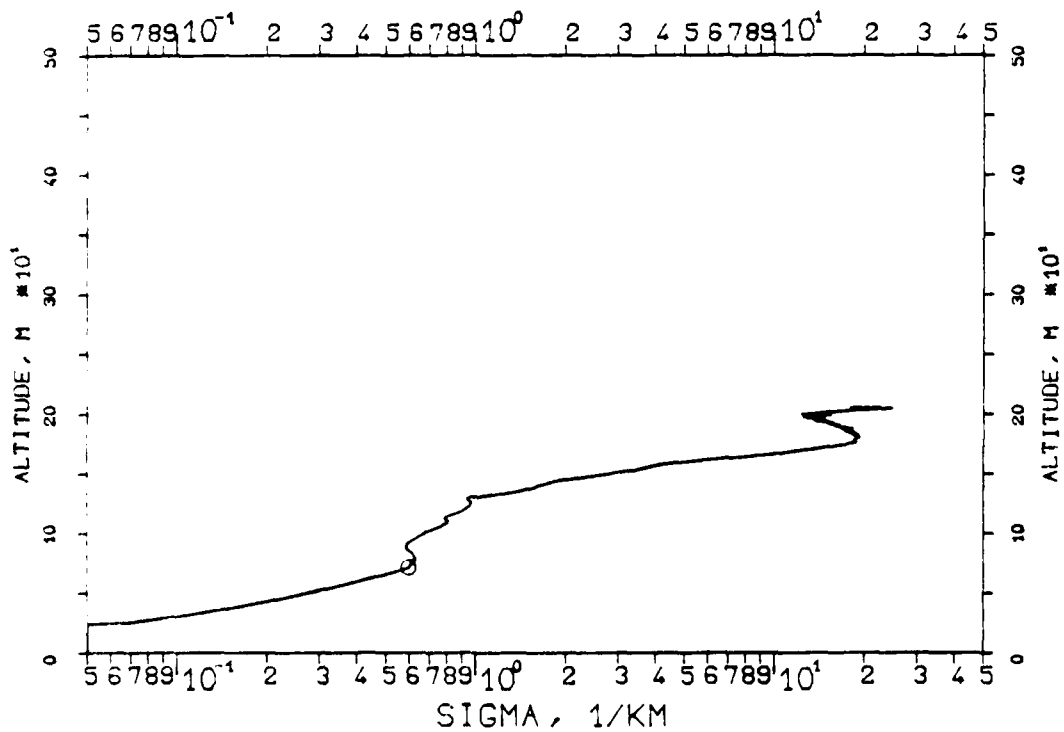


FIG. 7.150
KLETT-PROFILE, 0694NM, EL. 15DG00MN
840411, 13:59-13:59, CET
RM=0.870KM, SM=20.0000/KM, K=1.000

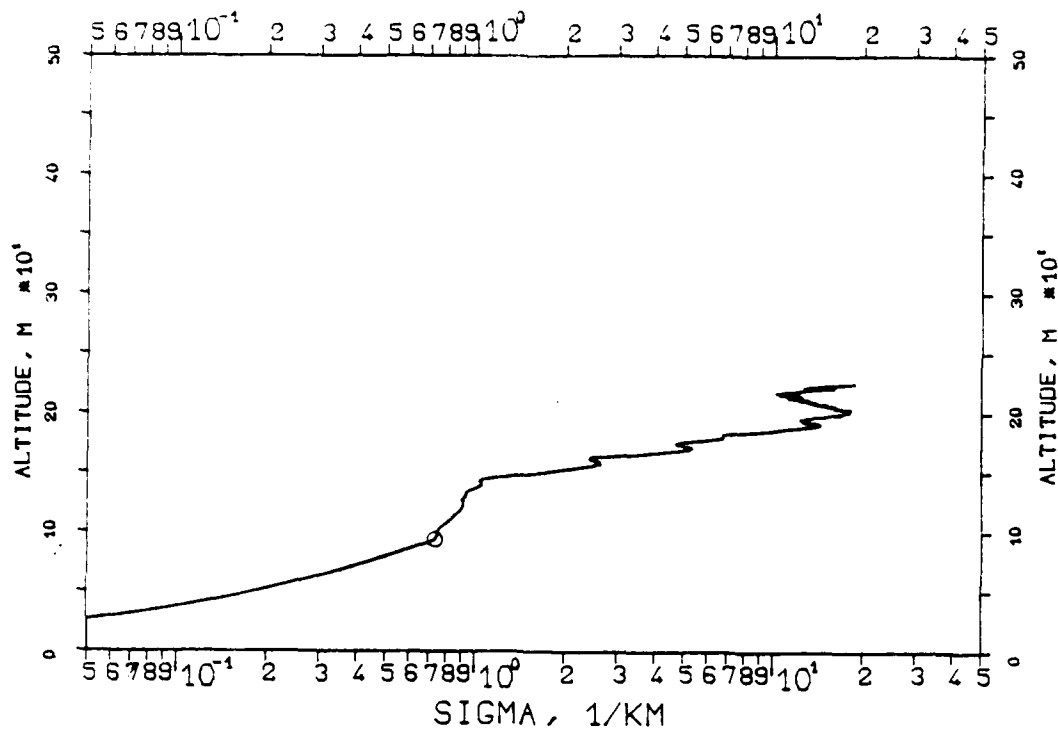


FIG. 7.151
KLETT-PROFILE, 1060NM, EL. 15DG00MN
840411, 14:01-14:01, CET
RM=0.817KM, SM=20.0000/KM, K=1.000

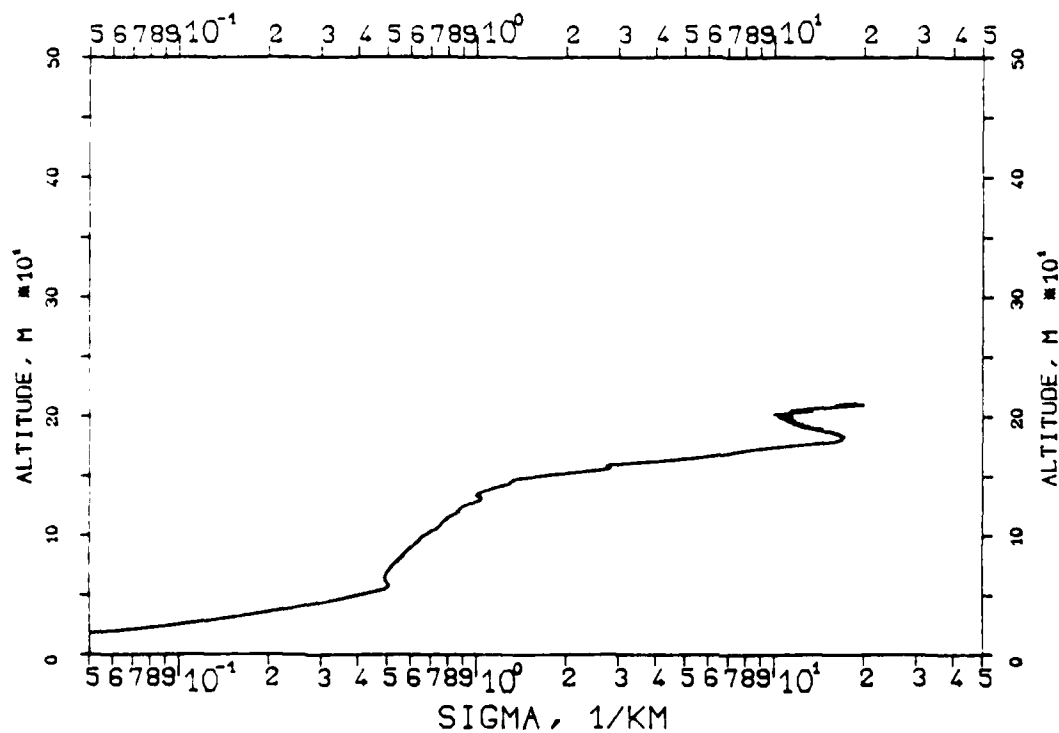


FIG. 7.148
KLETT-PROFILE, 1060NM, EL. 10DG00MN
840411, 13:31-13:31, CET
RM=1.501KM, SM=20.0000/KM, K=1.000

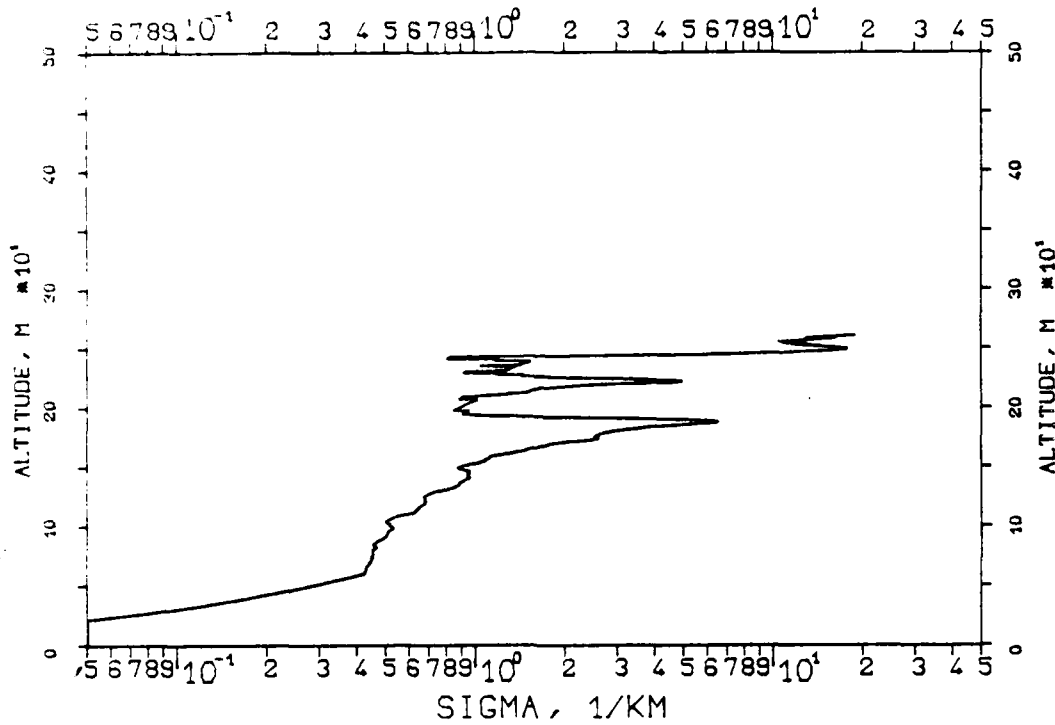


FIG. 7.149
KLETT-PROFILE, 1060NM, EL. 10DG00MN
840411, 13:32-13:32, CET
RM=1.308KM, SM=20.0000/KM, K=1.000

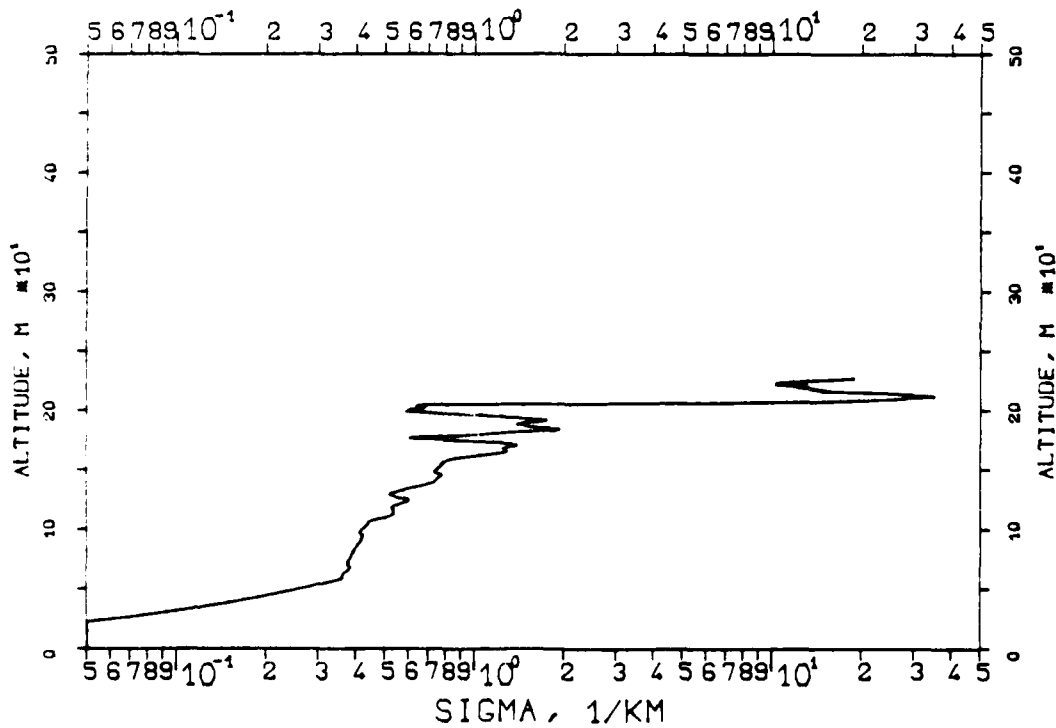


FIG. 7.146
KLETT-PROFILE, 1060NM, EL. 10DG00MN
840411, 13:29-13:29, CET
RM=1.434KM, SM=20.0000/KM, K=1.000

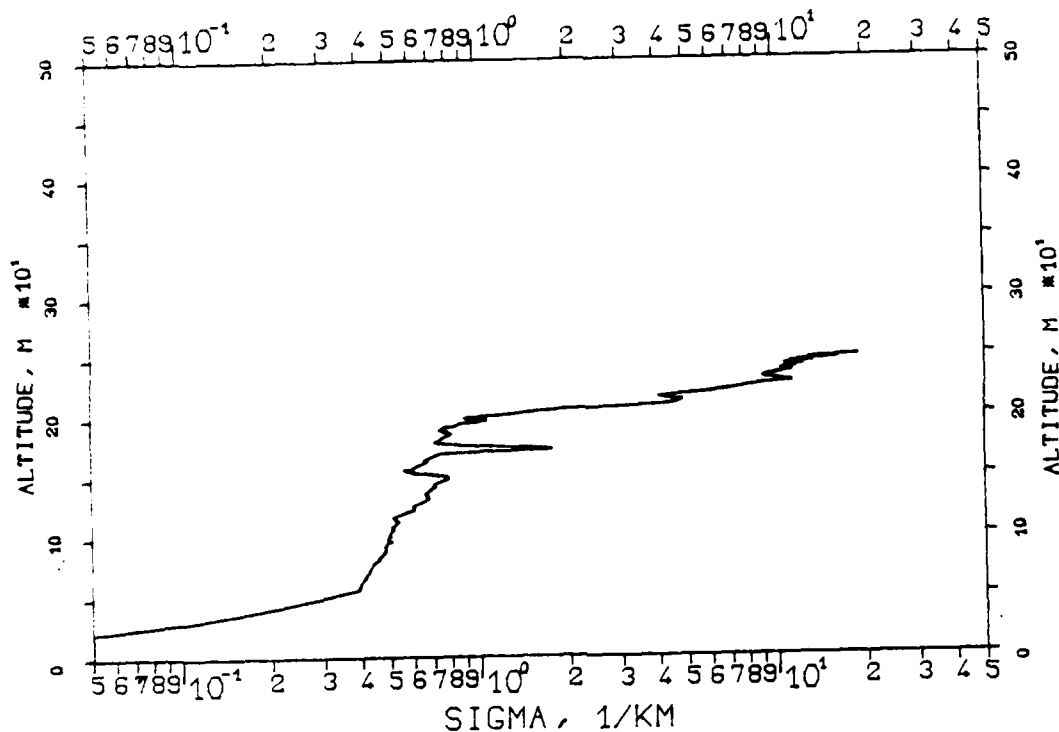


FIG. 7.147
KLETT-PROFILE, 1060NM, EL. 10DG00MN
840411, 13:30-13:30, CET
RM=1.474KM, SM=20.0000/KM, K=1.000

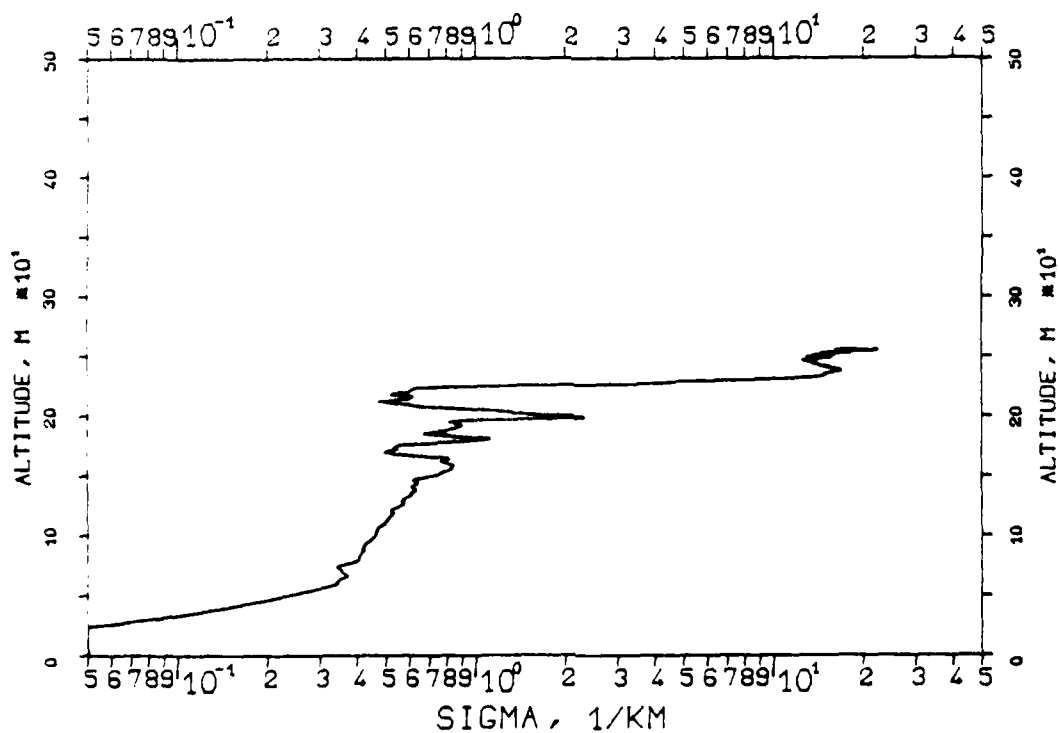


FIG. 7.144

KLETT-PROFILE, 1060NM, EL. 10DG00MN

840411, 13:25-13:25, CET

RM=1.452KM, SM=20.0000/KM, K=1.000

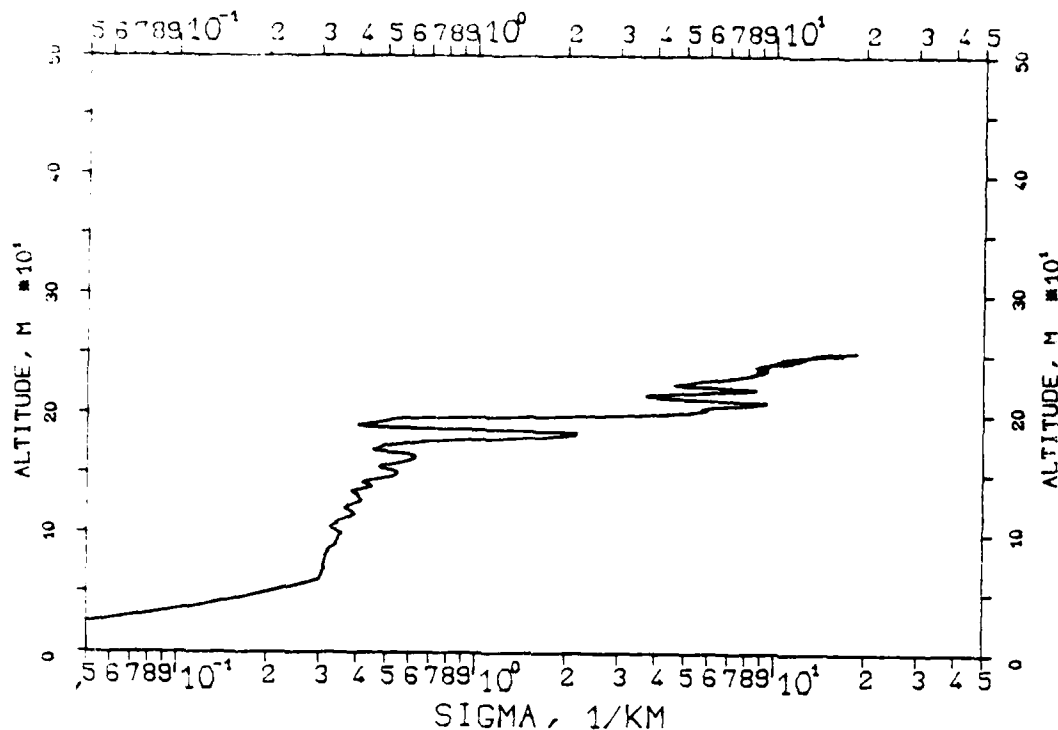


FIG. 7.145

KLETT-PROFILE, 1060NM, EL. 10DG00MN

840411, 13:26-13:27, CET

RM=1.558KM, SM=20.0000/KM, K=1.000

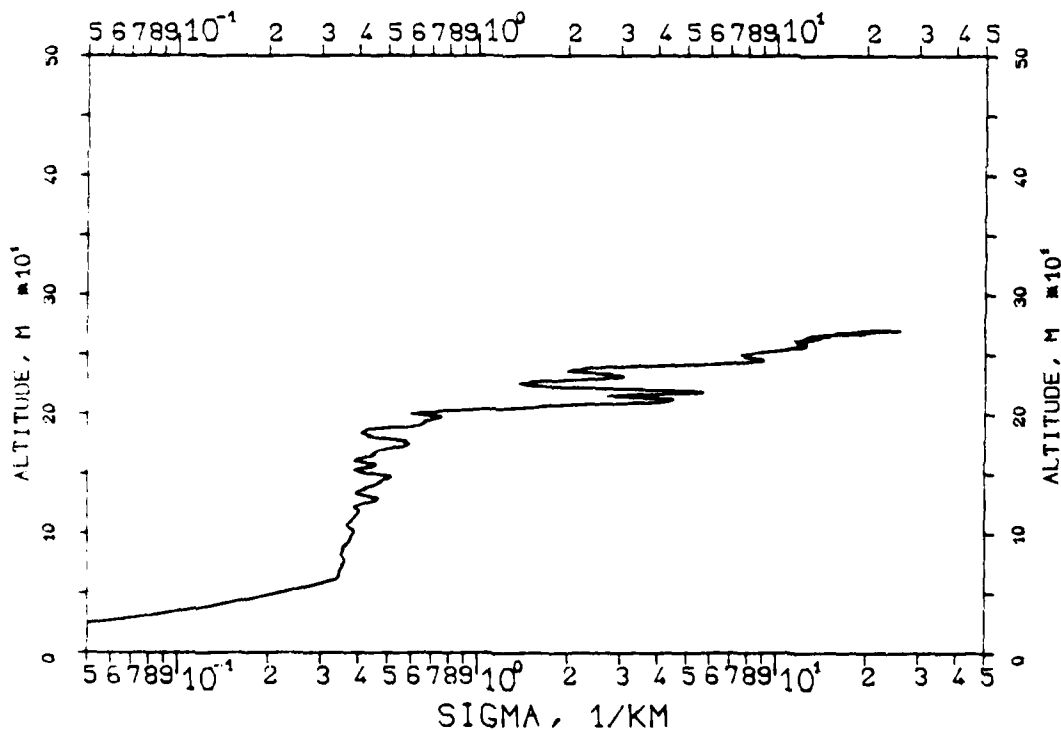


FIG. 7.142
KLETT-PROFILE, 1060NM, EL. 15DG00MN
840411, 13:21-13:21, CET
RM=1.003KM, SM=20.0000/KM, K=1.000

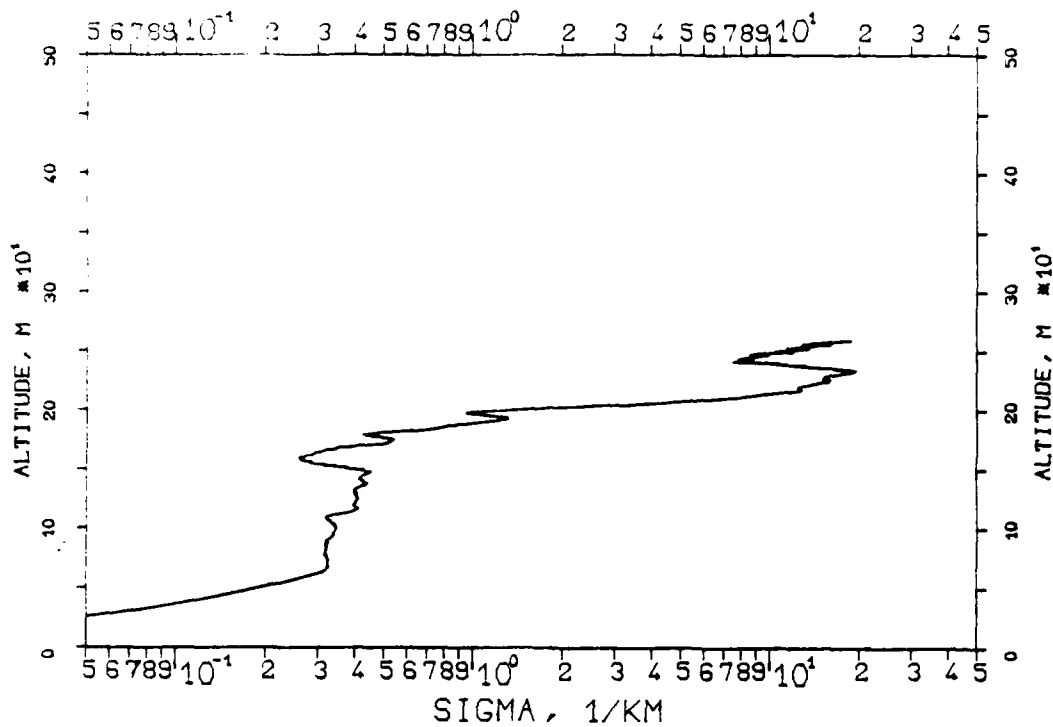


FIG. 7.143
KLETT-PROFILE, 0530NM, EL. 15DG00MN
840411, 13:22-13:23, CET
RM=1.063KM, SM=20.0000/KM, K=1.000

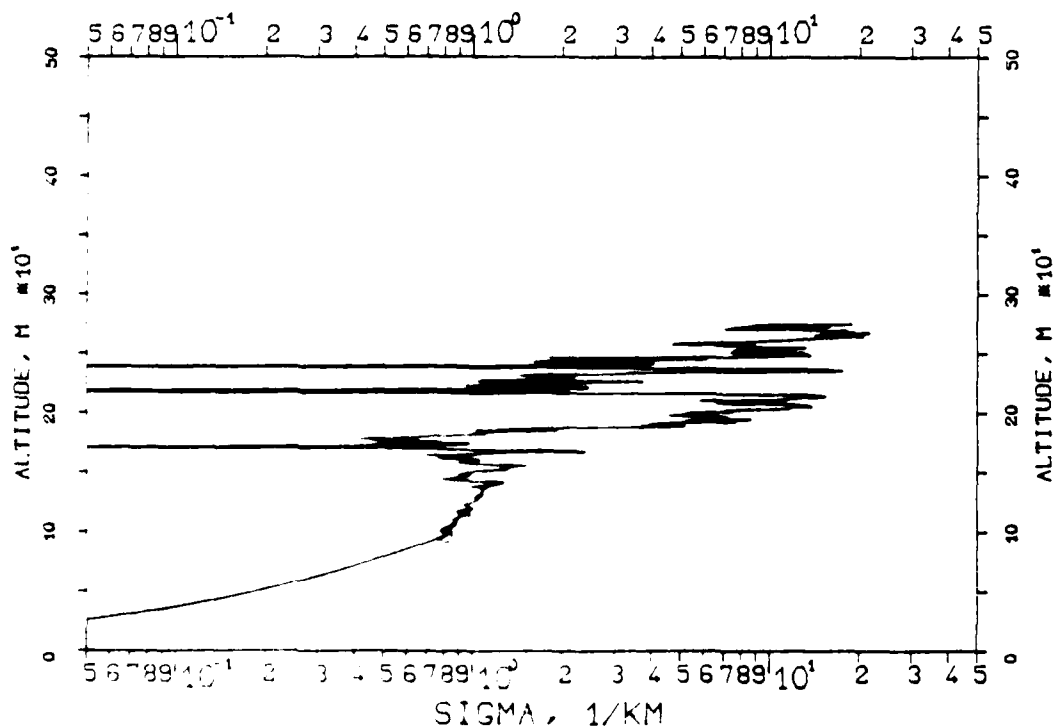


FIG. 7.170
 KLETT-PROFILE, 1060NM, EL. 20DG00MN
 840827, 08:58-08:58, CET
 RM=0.468KM, SM=20.0000/KM, K=1.000

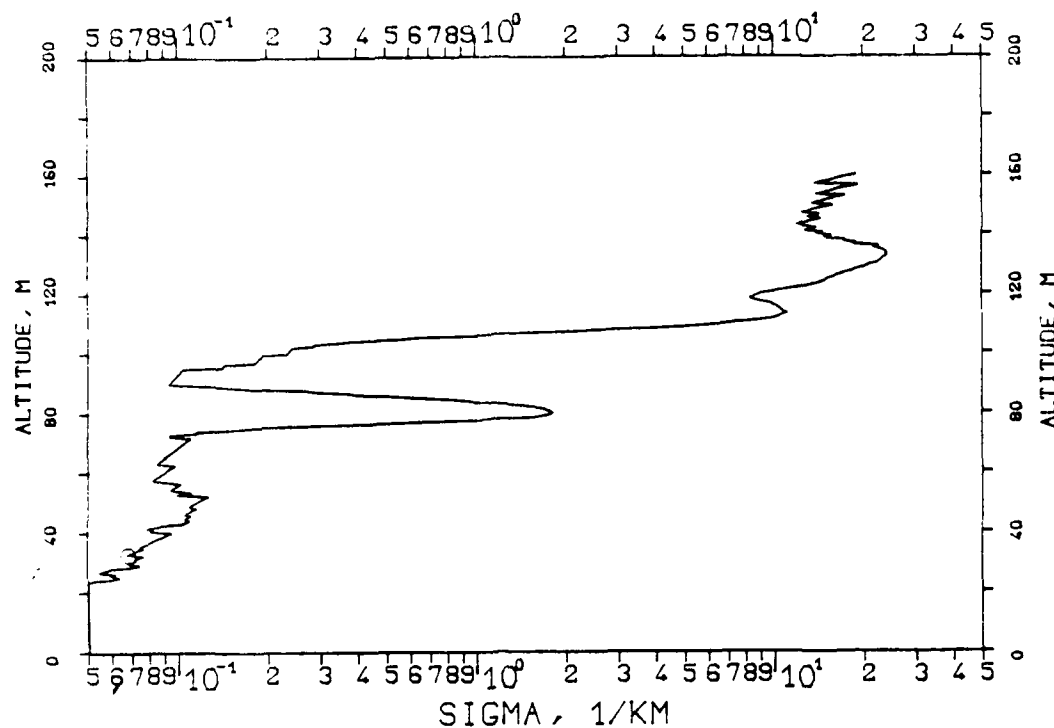


FIG. 7.171
 KLETT-PROFILE, 1060NM, EL. 20DG00MN
 840827, 08:59-08:59, CET
 RM=0.490KM, SM=20.0000/KM, K=1.000

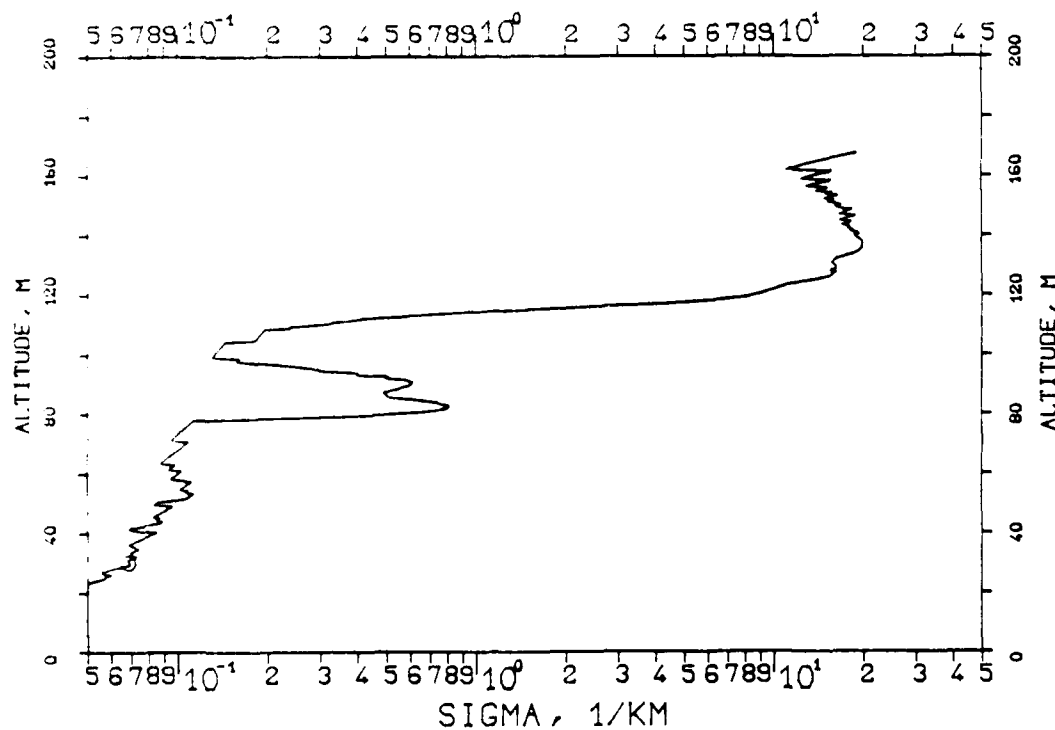


FIG. 7.172
KLETT-PROFILE, 1060NM, EL. 20DG00MN
840827, 09:00-09:00, CET
RM=0.462KM, SM=20.0000/KM, K=1.000

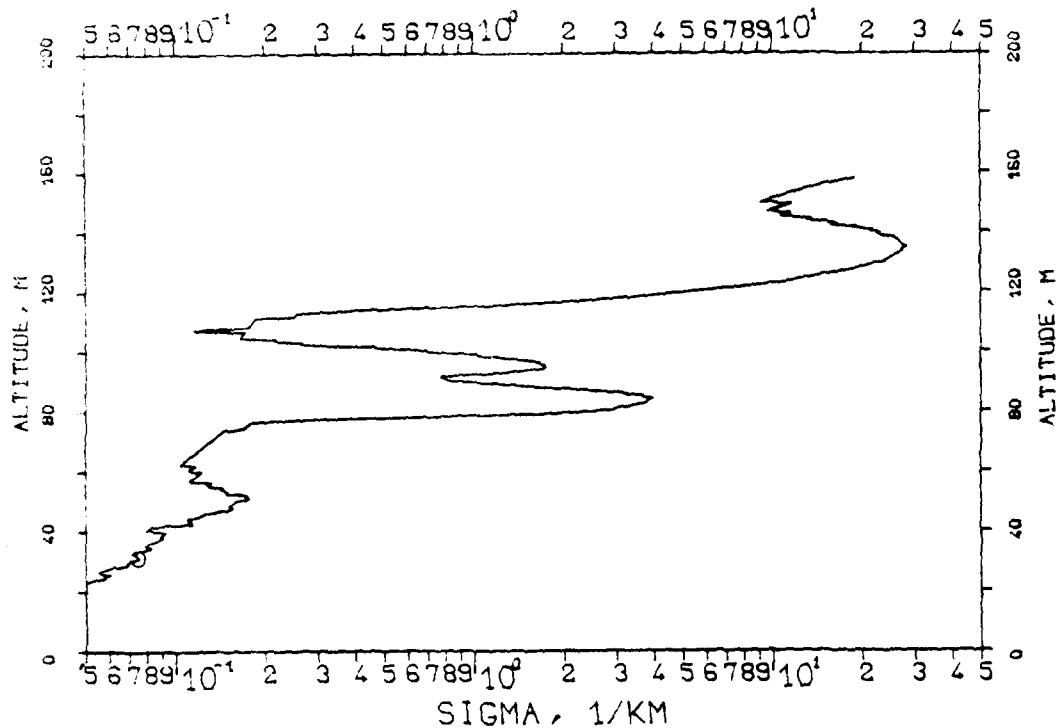


FIG. 7.173
KLETT-PROFILE, 1060NM, EL. 20DG00MN
840827, 09:01-09:01, CET
RM=0.477KM, SM=20.0000/KM, K=1.000

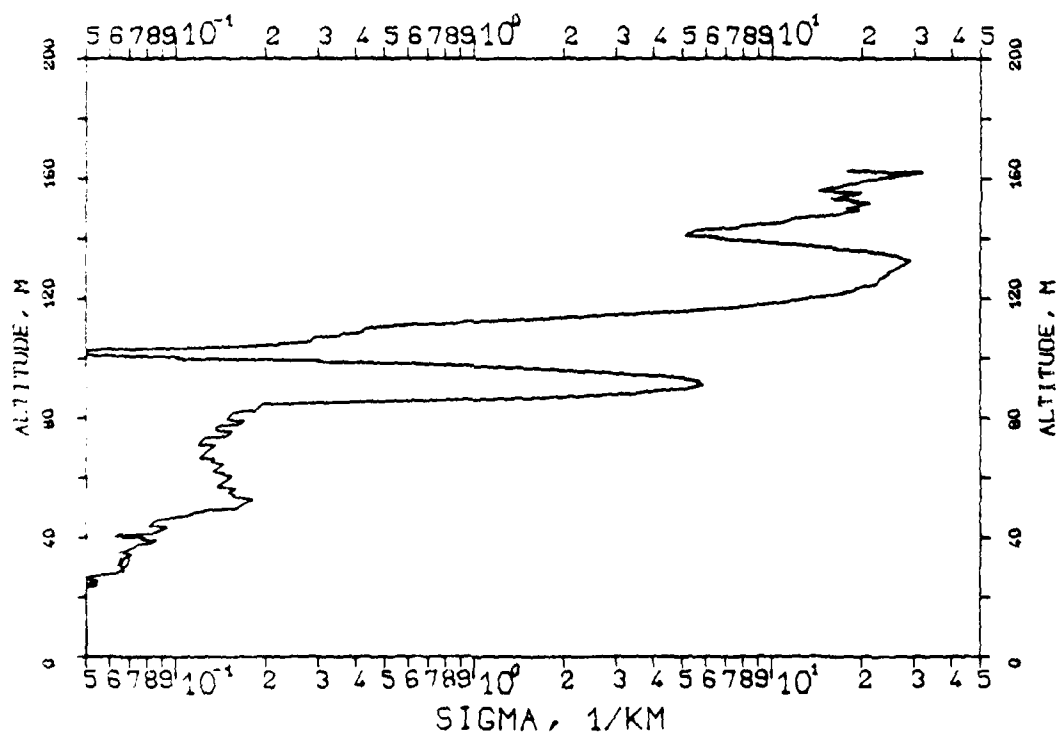


FIG. 7.174
 KLETT-PROFILE, 1060NM, EL. 20DG00MN
 840827, 09:03-09:03, CET
 RM=0.442KM, SM=20.0000/KM, K=1.000

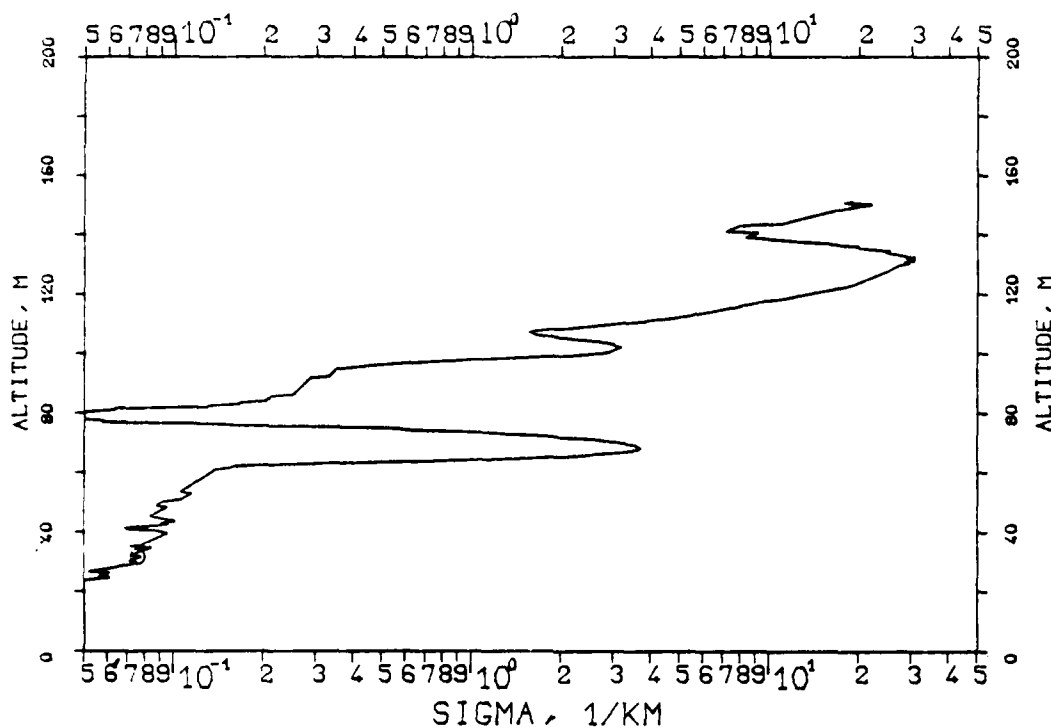


FIG. 7.175
 KLETT-PROFILE, 1060NM, EL. 20DG00MN
 840827, 09:05-09:05, CET
 RM=0.445KM, SM=20.0000/KM, K=1.000

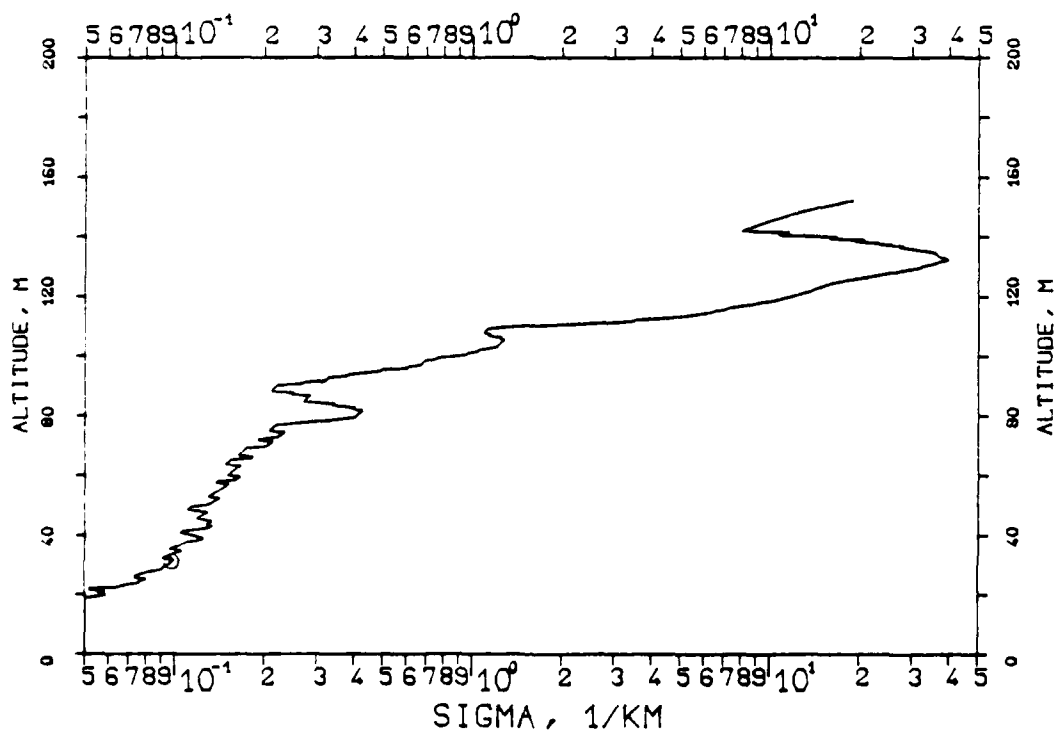


FIG. 7.176
KLETT-PROFILE, 0530NM, EL. 20DG00MN
840827, 09:06-09:08, CET
RM=0.436KM, SM=20.0000/KM, K=1.000

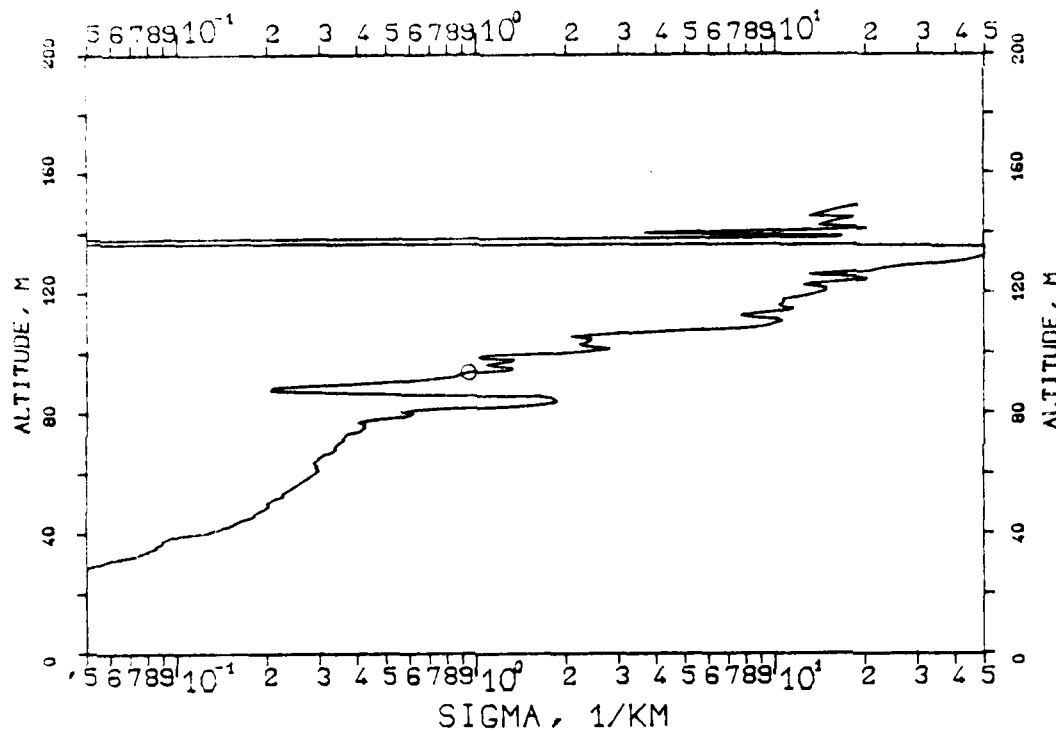


FIG. 7.177
KLETT-PROFILE, 0530NM, EL. 20DG00MN
840827, 09:07-09:08, CET
RM=0.463KM, SM=20.0000/KM, K=1.000

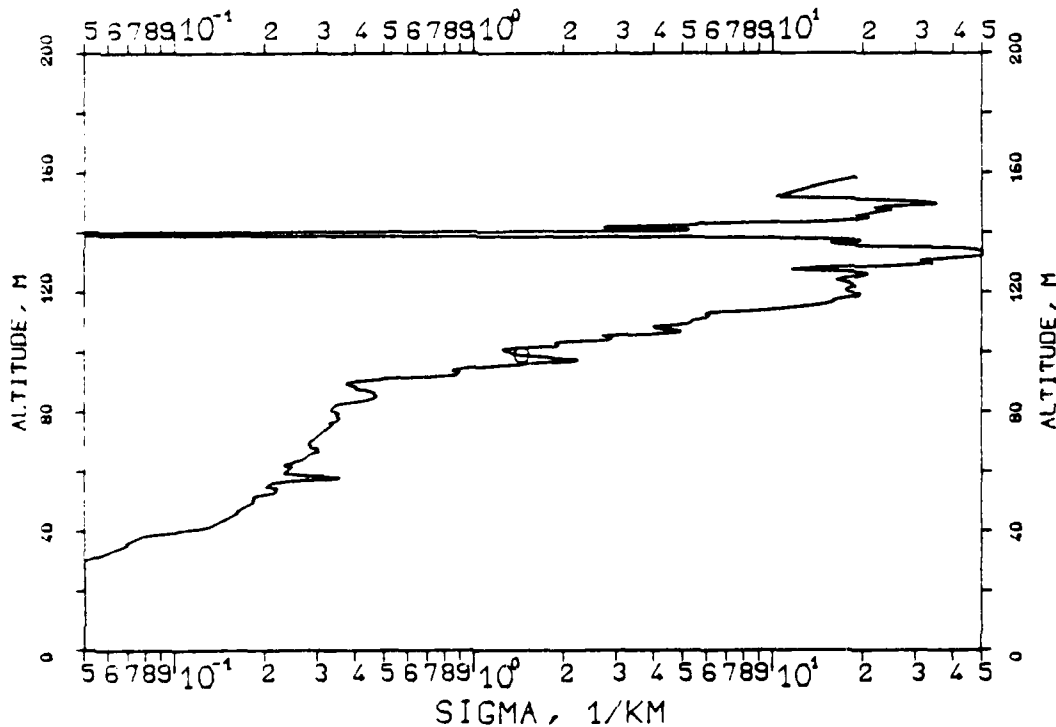


FIG. 7.178
KLETT-PROFILE, 0530NM, EL. 20DG00MN
840827, 09:08-09:09, CET
RM=0.456KM, SM=20.0000/KM, K=1.000

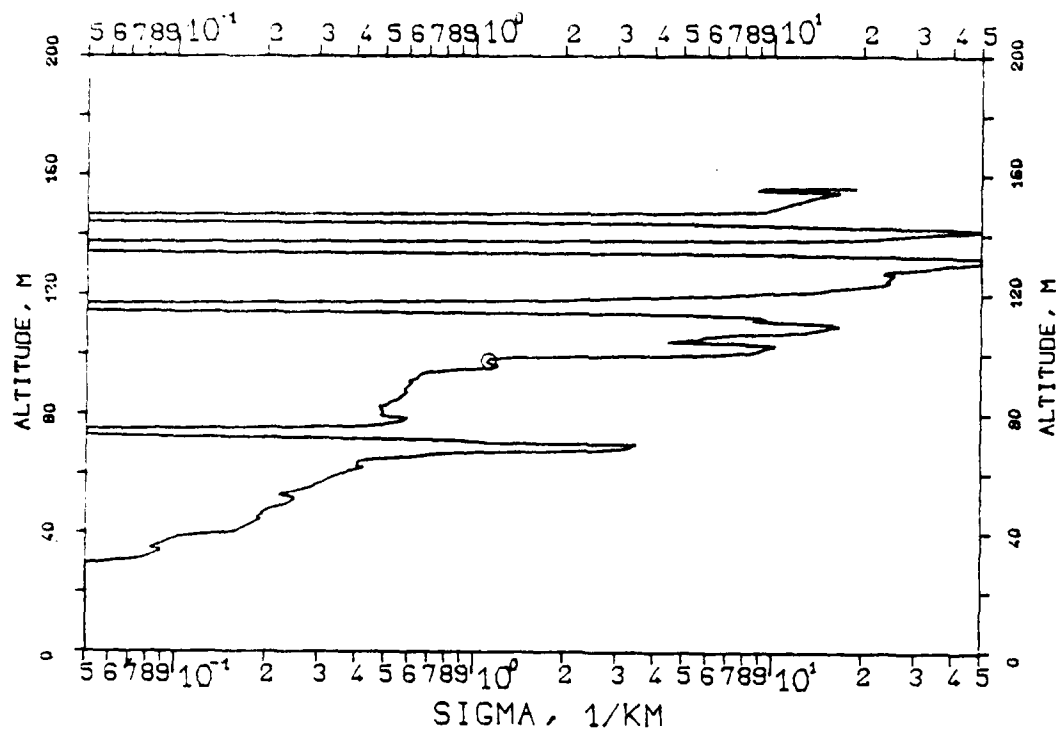


FIG. 7.179
KLETT-PROFILE, 0530NM, EL. 20DG00MN
840827, 09:09-09:10, CET
RM=0.460KM, SM=20.0000/KM, K=1.000

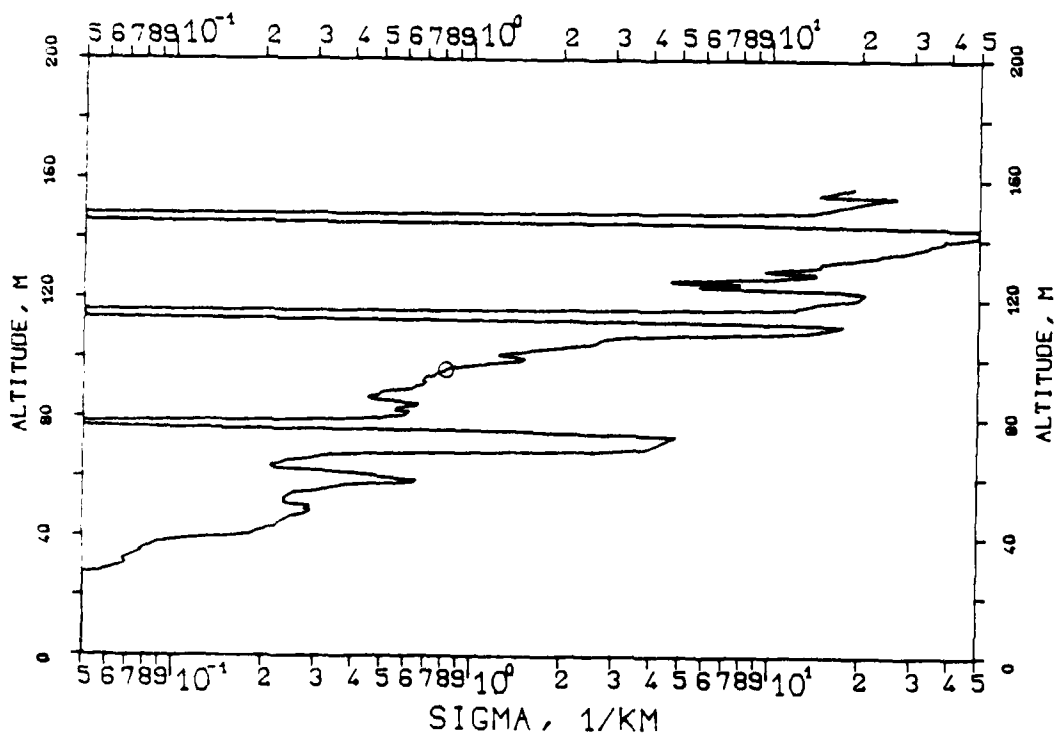


FIG. 7.180
 KLETT PROFILE, 0530NM, EL. 20DG00MN
 840827, 09:10-09:11, CET
 RM=0.454KM, SM=20.0000/KM, K=1.000

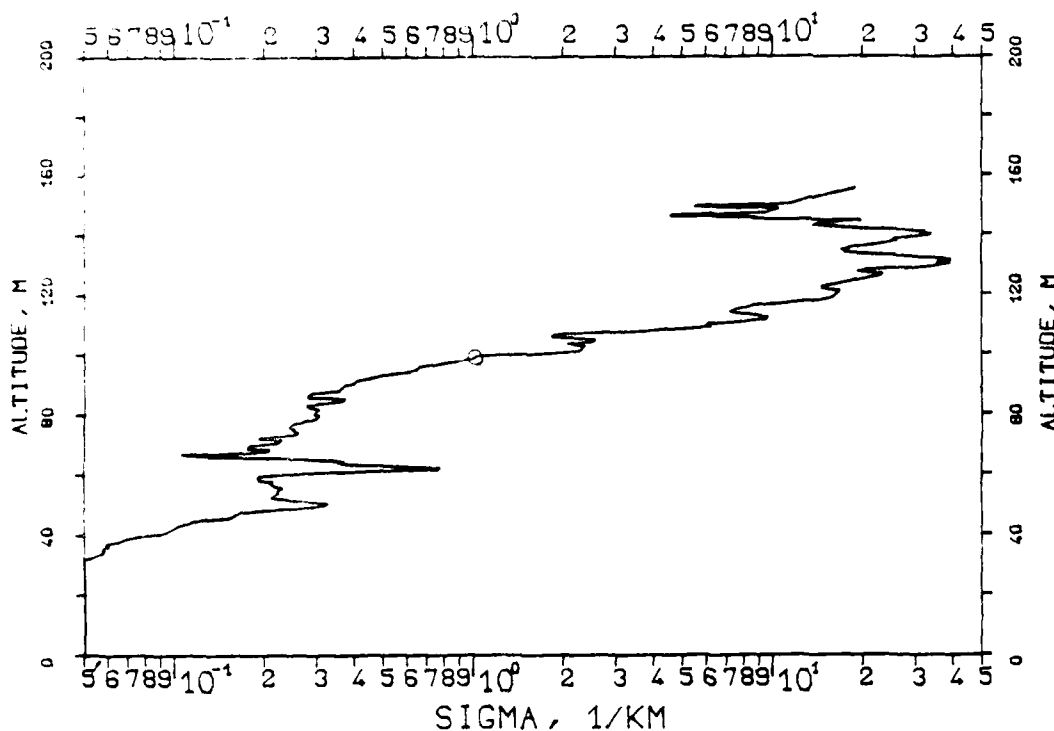


FIG. 7.181
 KLETT-PROFILE, 0530NM, EL. 20DG00MN
 840827, 09:11-09:12, CET
 RM=0.561KM, SM=20.0000/KM, K=1.000

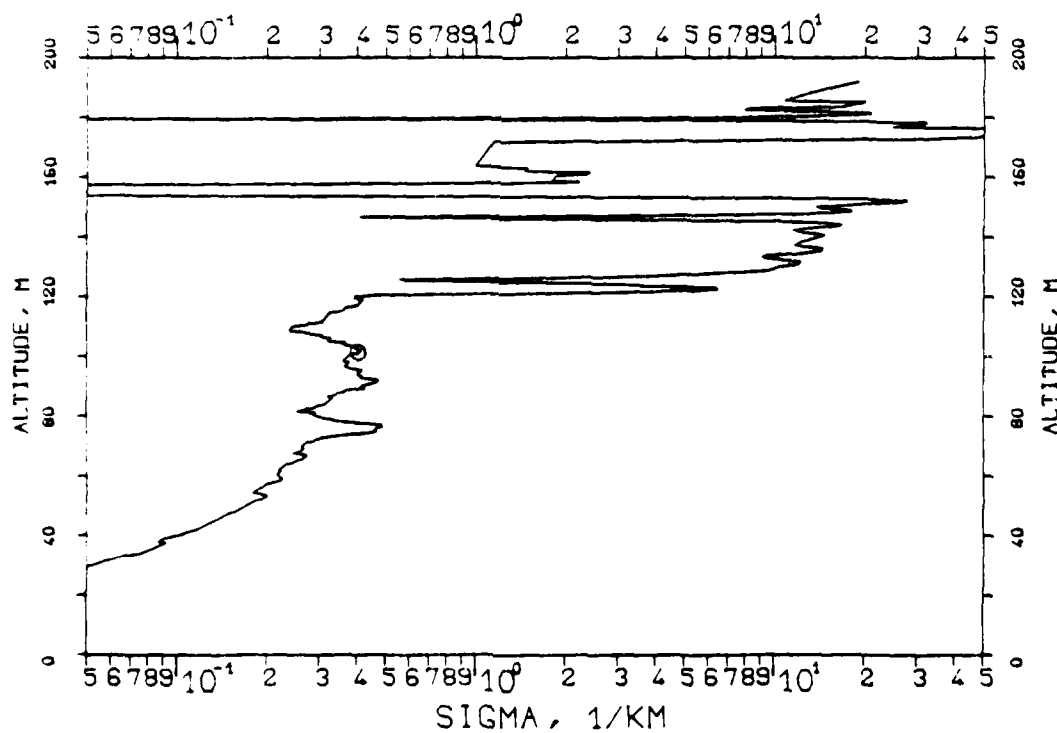


FIG. 7.183

KLETT-PROFILE, 0530NM, EL. 20DG00MN

840827, 11:00-11:01, CET

RM=0.756KM, SM=20.0000/KM, K=1.000

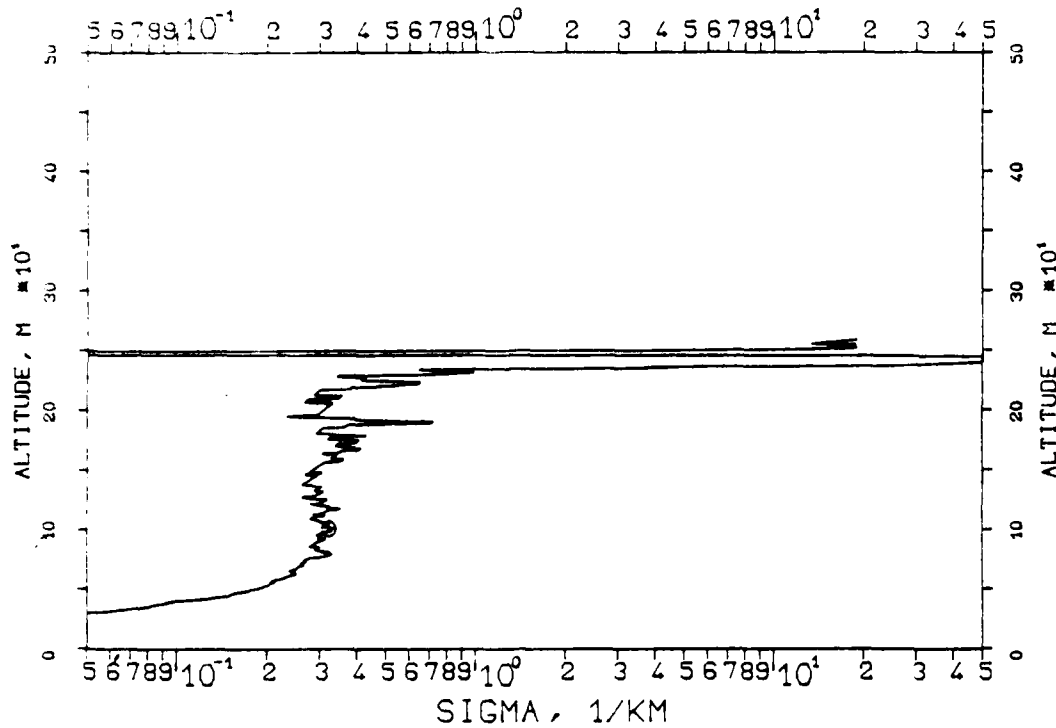


FIG. 7.184

KLETT-PROFILE, 1060NM, EL. 20DG00MN

840827, 11:03-11:03, CET

RM=0.856KM, SM=20.0000/KM, K=1.000

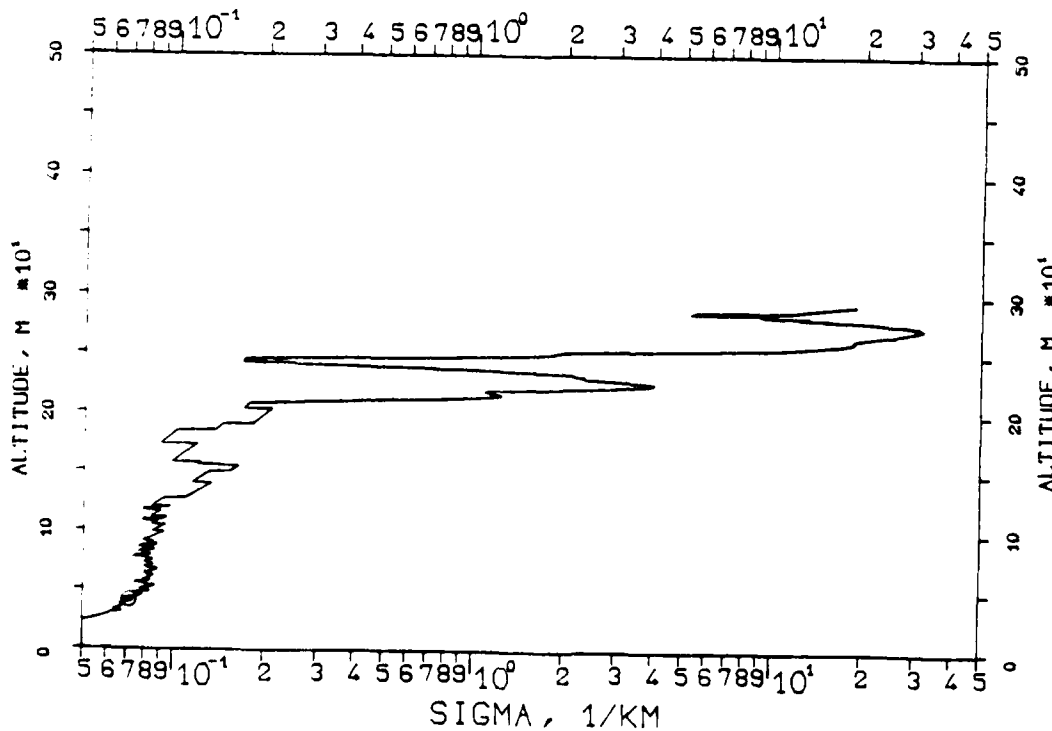


FIG. 7.185
 KLETT PROFILE, 1060NM, EL. 20DG00MN
 840827, 11:04~11:04, CET
 RM=0.774KM, SM=20.0000/KM, K=1.000

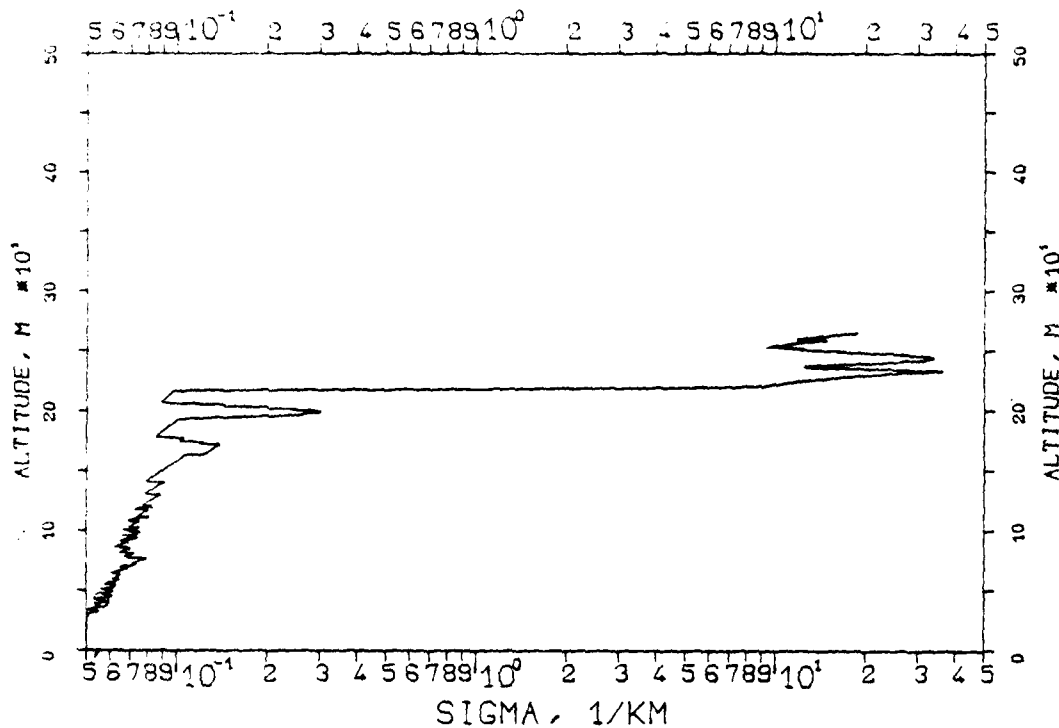


FIG. 7.186
 KLETT-PROFILE, 1060NM, EL. 20DG00MN
 840827, 13:25~13:25, CET
 RM=1.569KM, SM=20.0000/KM, K=1.000

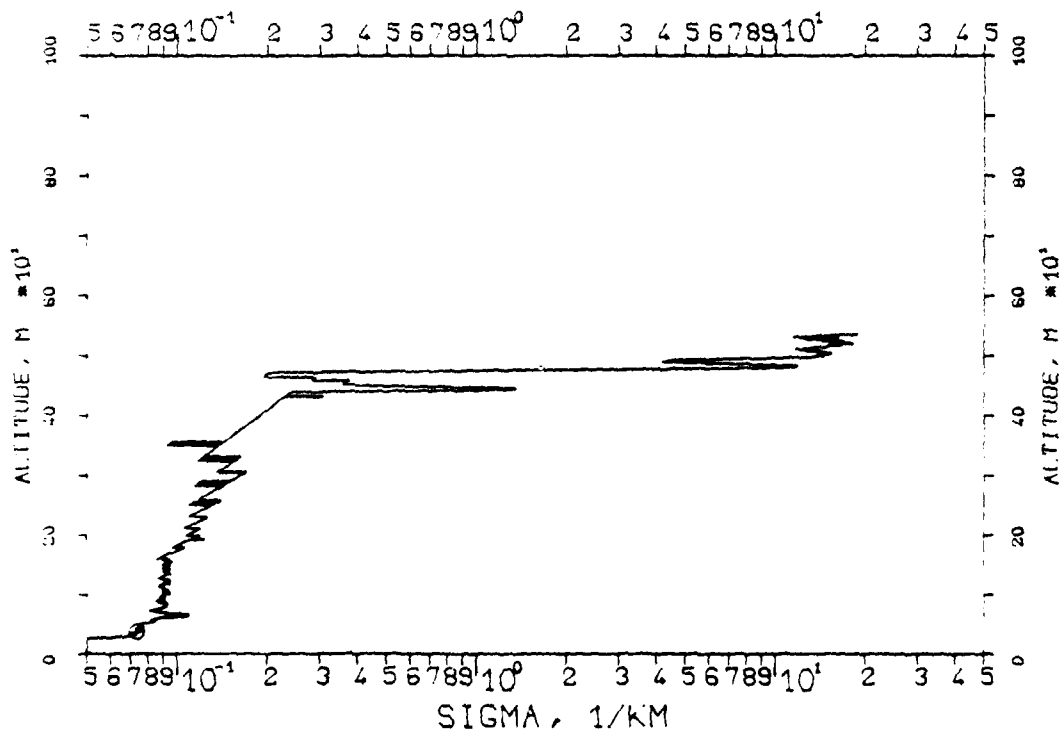


FIG. 7.187
KLETT PROFILE, 1060NM, EL. 20DG00MN
840827, 13:28-13:28, CET
RM=1.600KM, SM=20.0000/KM, K=1.000

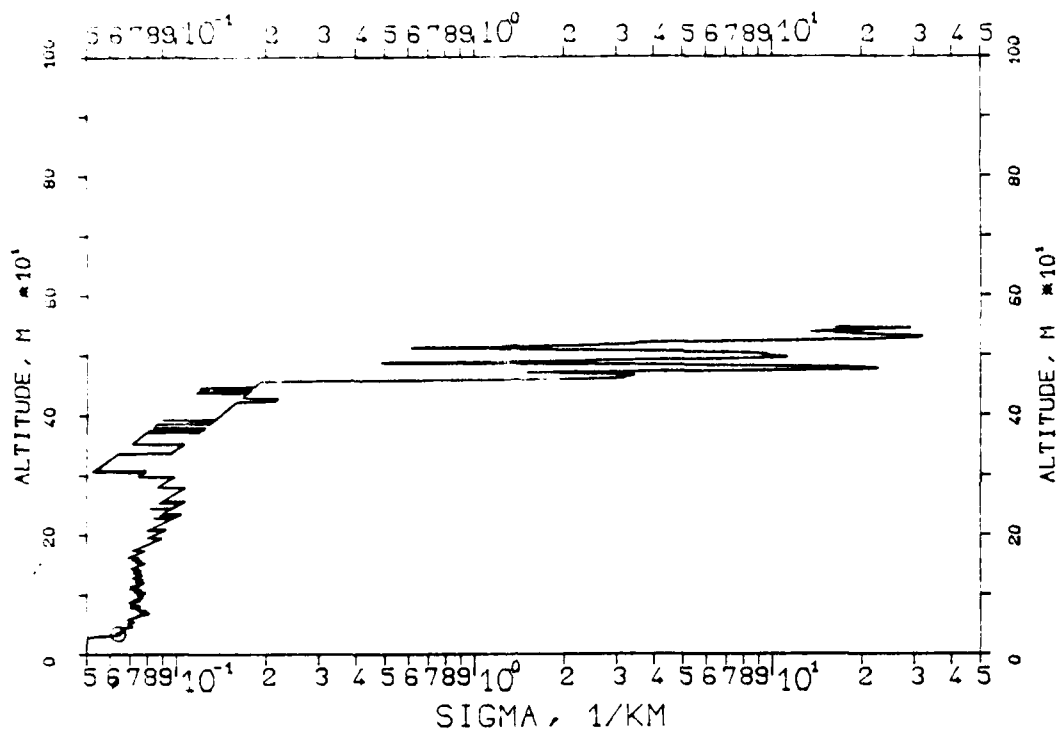


FIG. 7.188
KLETT-PROFILE, 1060NM, EL. 20DG00MN
840827, 13:29-13:29, CET
RM=1.617KM, SM=20.0000/KM, K=1.000

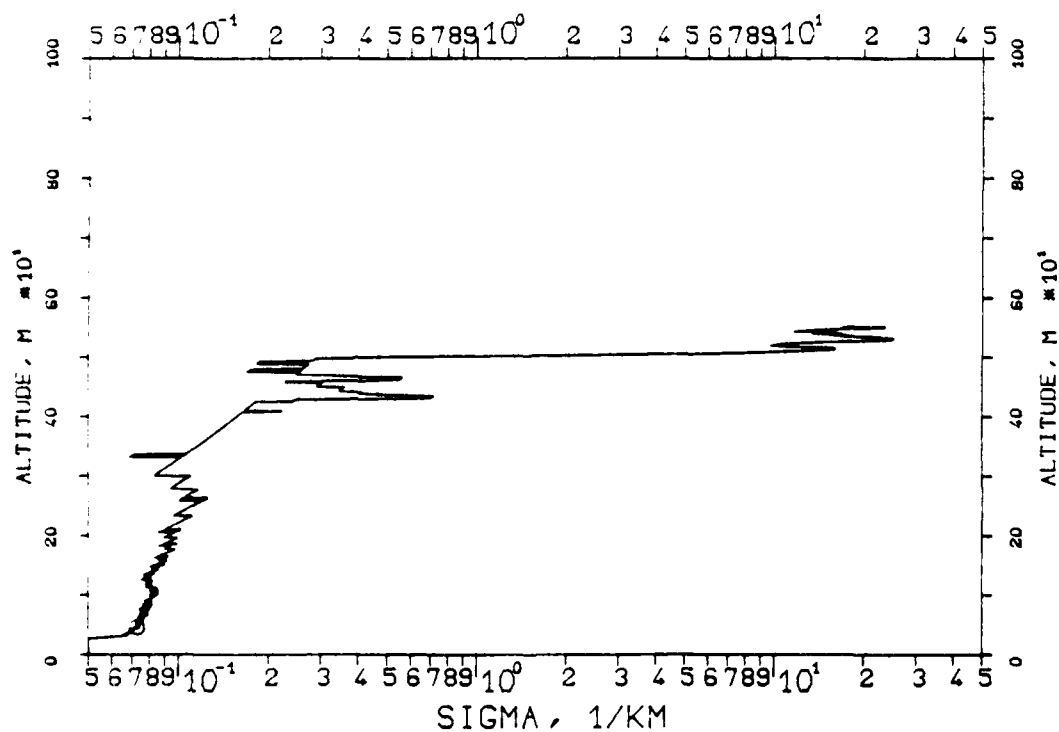


FIG. 7.189
KLETT-PROFILE, 1060NM, EL. 20DG00MN
840827, 13:30-13:31, CET
RM=1.555KM, SM=20.0000/KM, K=1.000

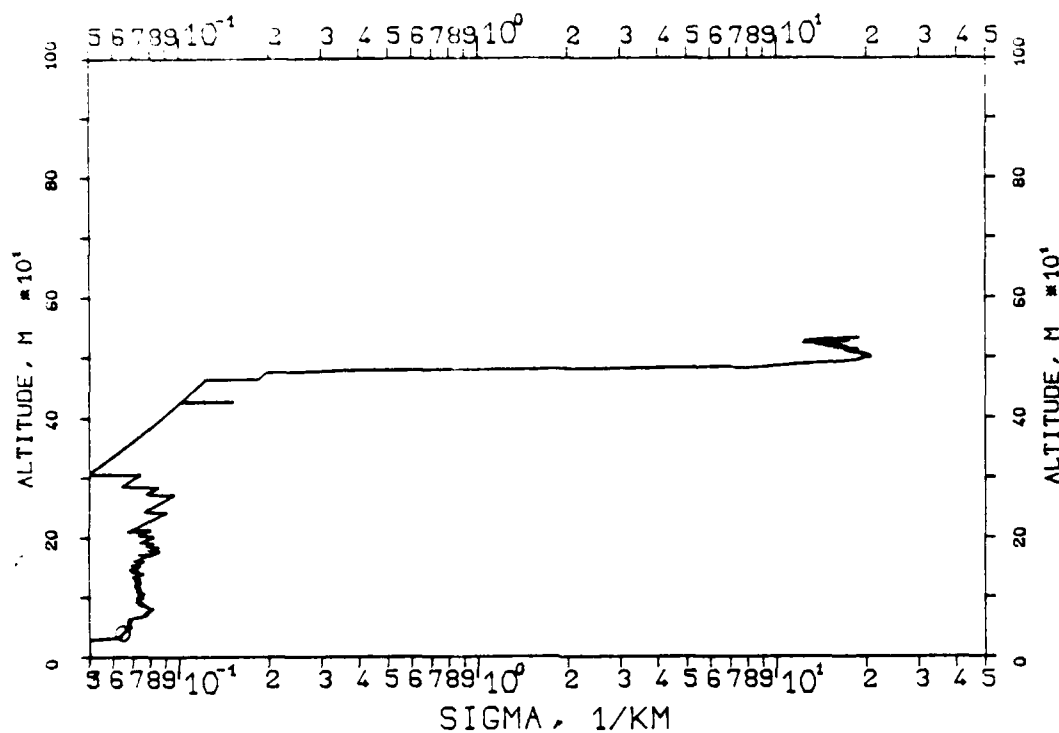


FIG. 7.190
KLETT-PROFILE, 1060NM, EL. 20DG00MN
840827, 13:32-13:33, CET
RM=1.860KM, SM=20.0000/KM, K=1.000

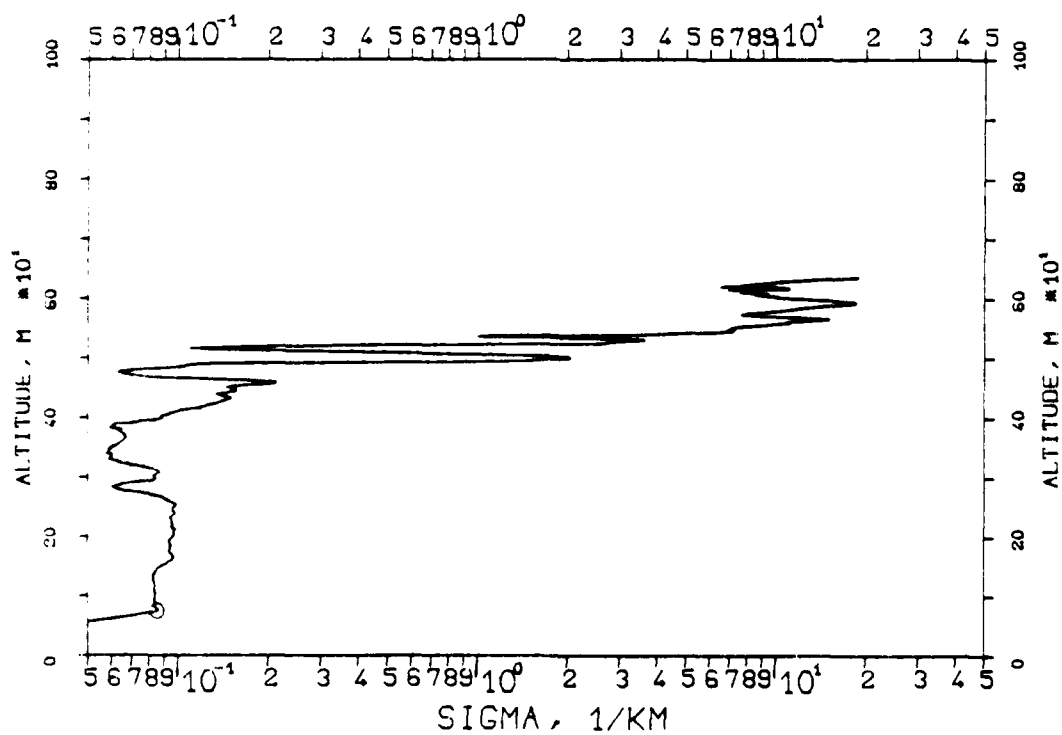


FIG. 7.191
 KLETT-PROFILE, 0530NM, EL. 20DG00MN
 840877, 13:35-13:36, CET
 RM=1.780KM, SM=20.0000/KM, K=1.000

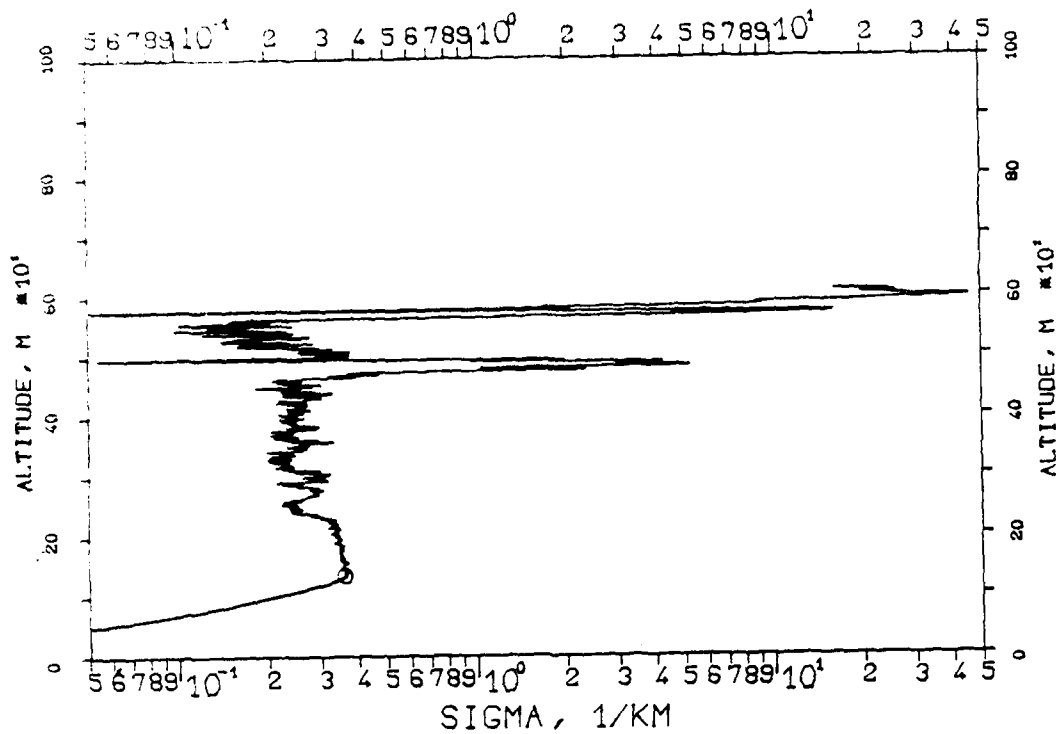


FIG. 7.192
 KLETT-PROFILE, 0694NM, EL. 20DG00MN
 840827, 13:39-13:40, CET
 RM=1.700KM, SM=20.0000/KM, K=1.000

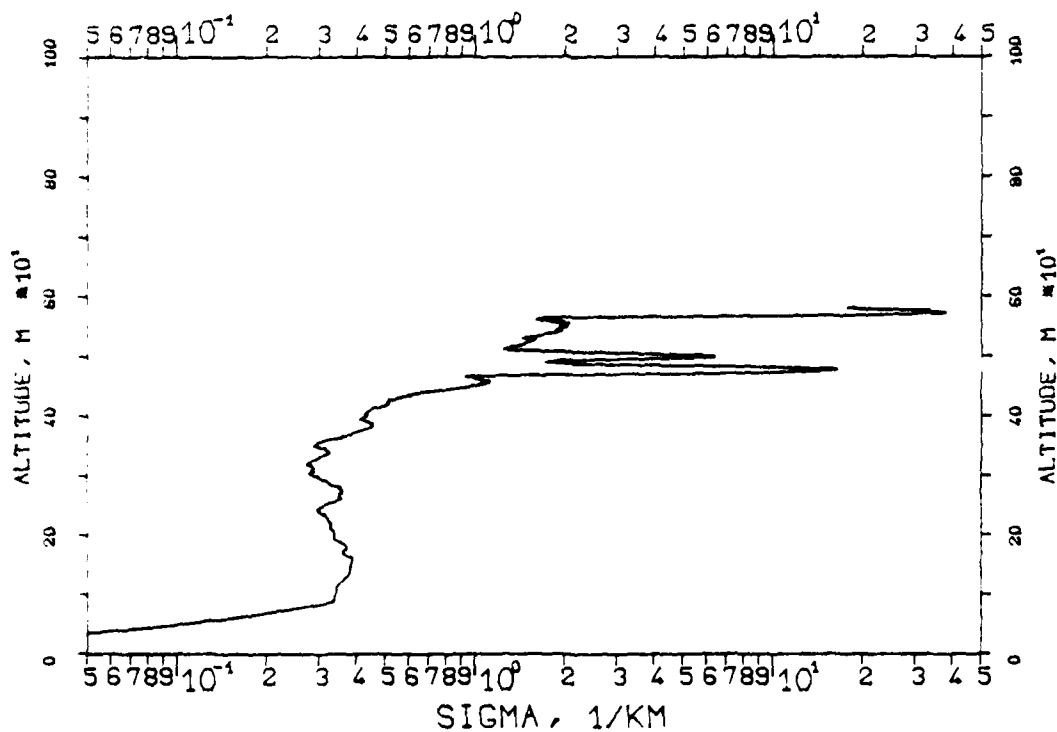


FIG. 7.193
KLETT PROFILE, 1060NM, EL. 20DG00MN
840829, 08:13-08:15, CET
RM=3.600KM, SM=20.0000/KM, K=1.000

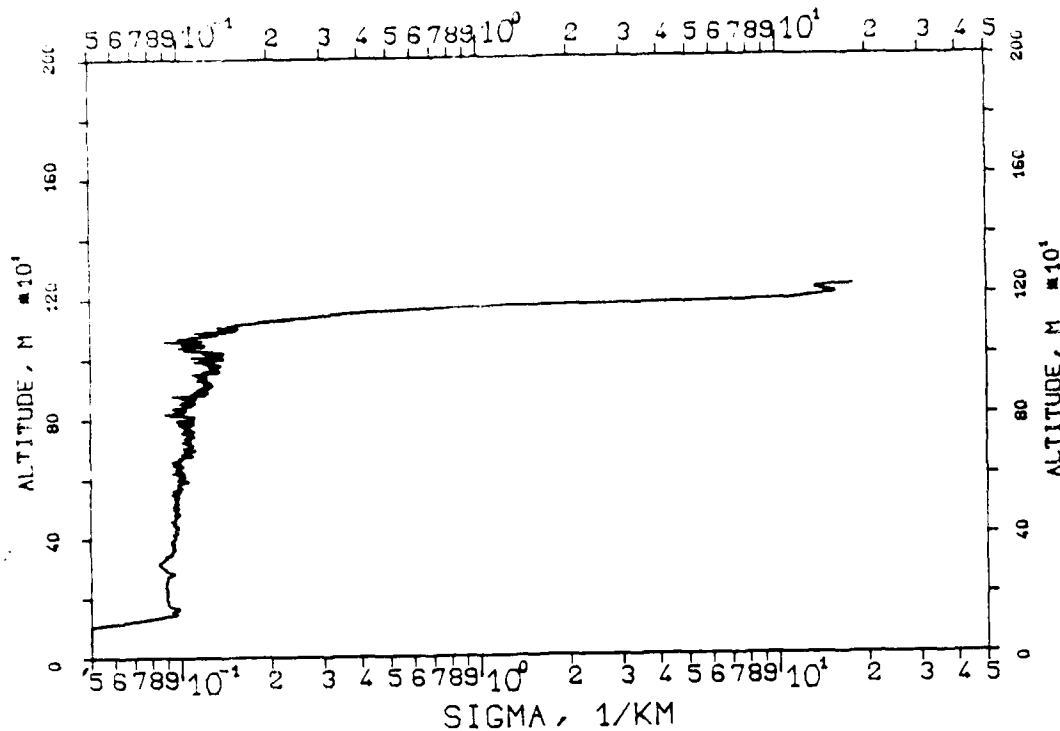


FIG. 7.194
KLETT-PROFILE, 0694NM, EL. 20DG00MN
840829, 08:22-08:23, CET
RM=3.975KM, SM=20.0000/KM, K=1.000

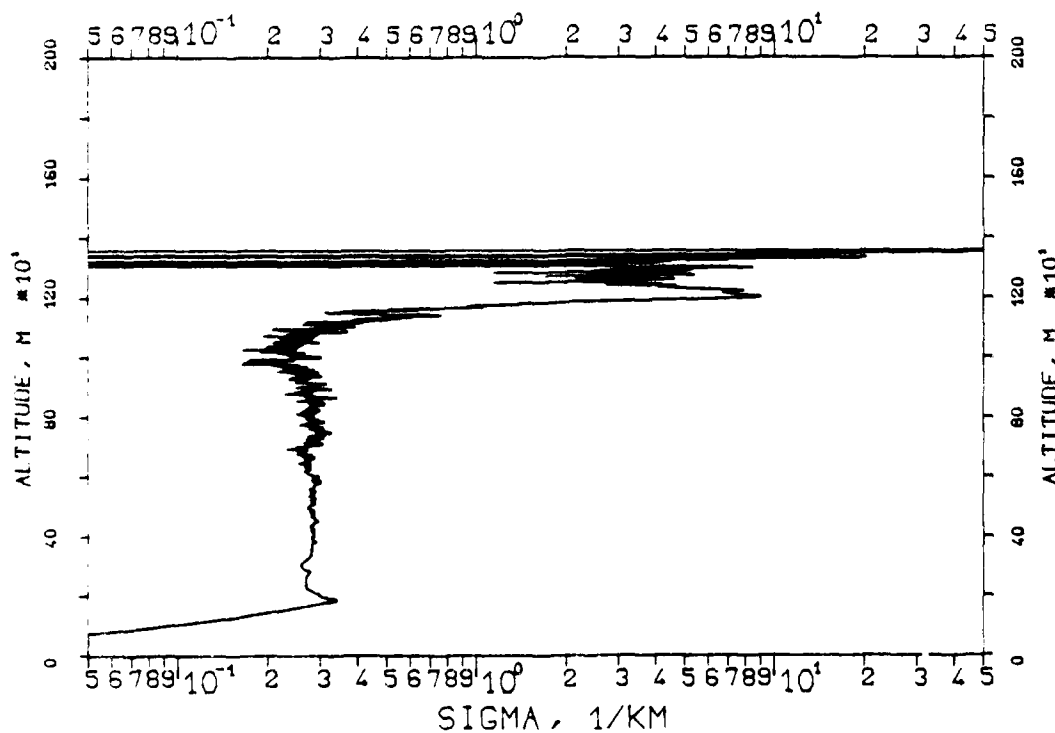


FIG. 7.195
KLETT-PROFILE, 1060NM, EL. 19DG20MN
841008, 09:19-09:20, CET
RM=0.319KM, SM=20.0000/KM, K=1.000

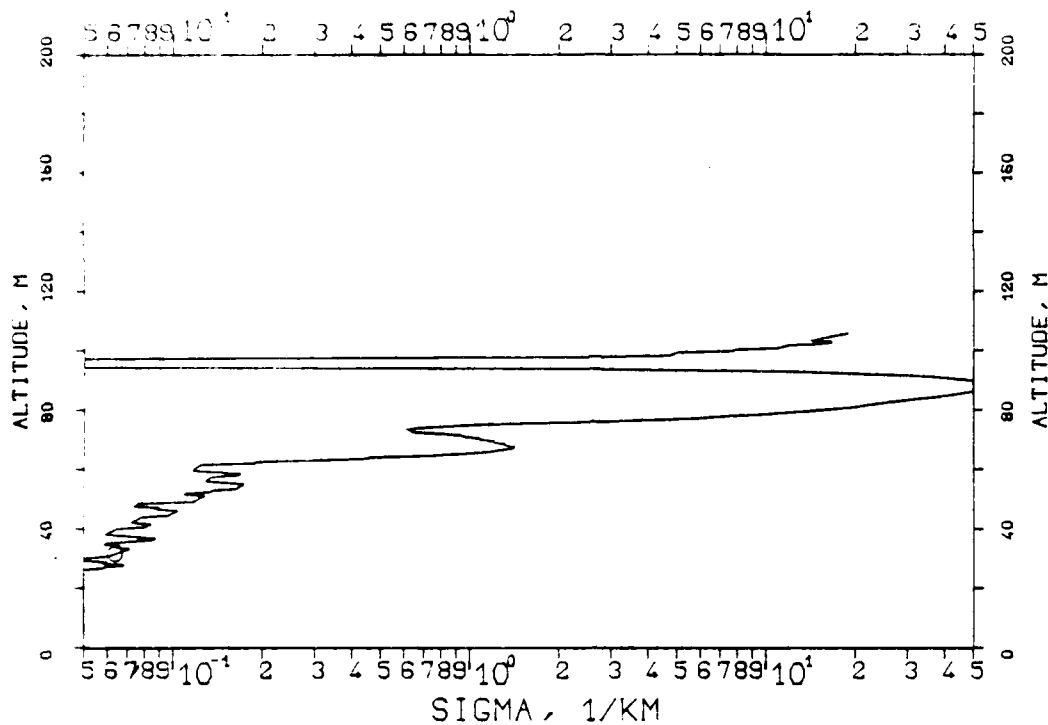
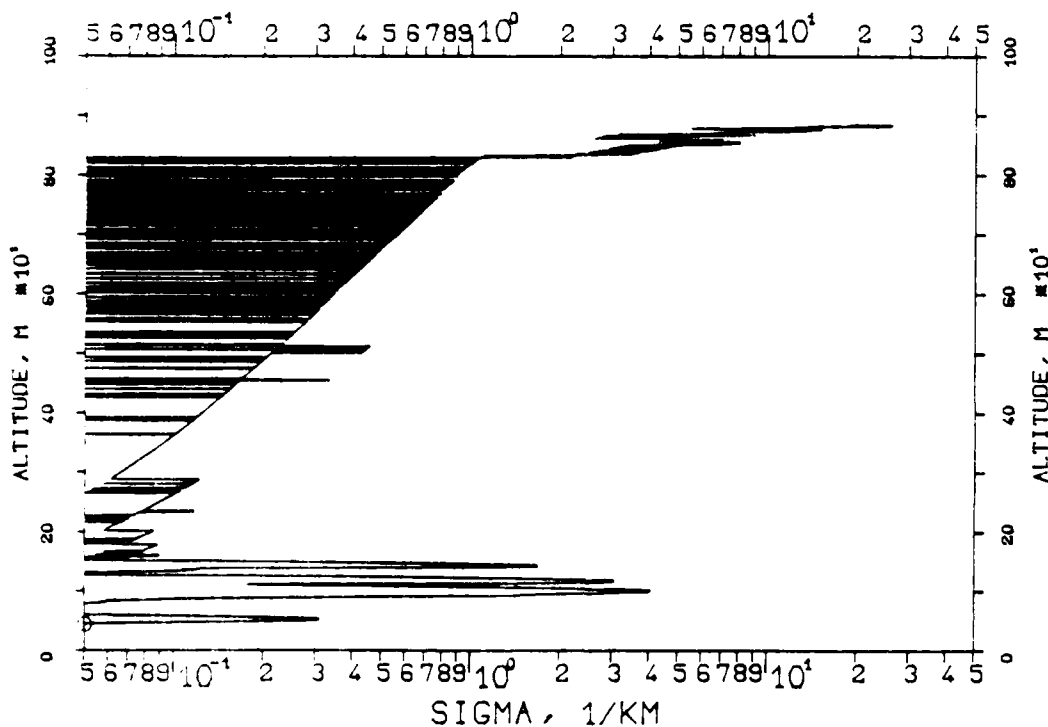
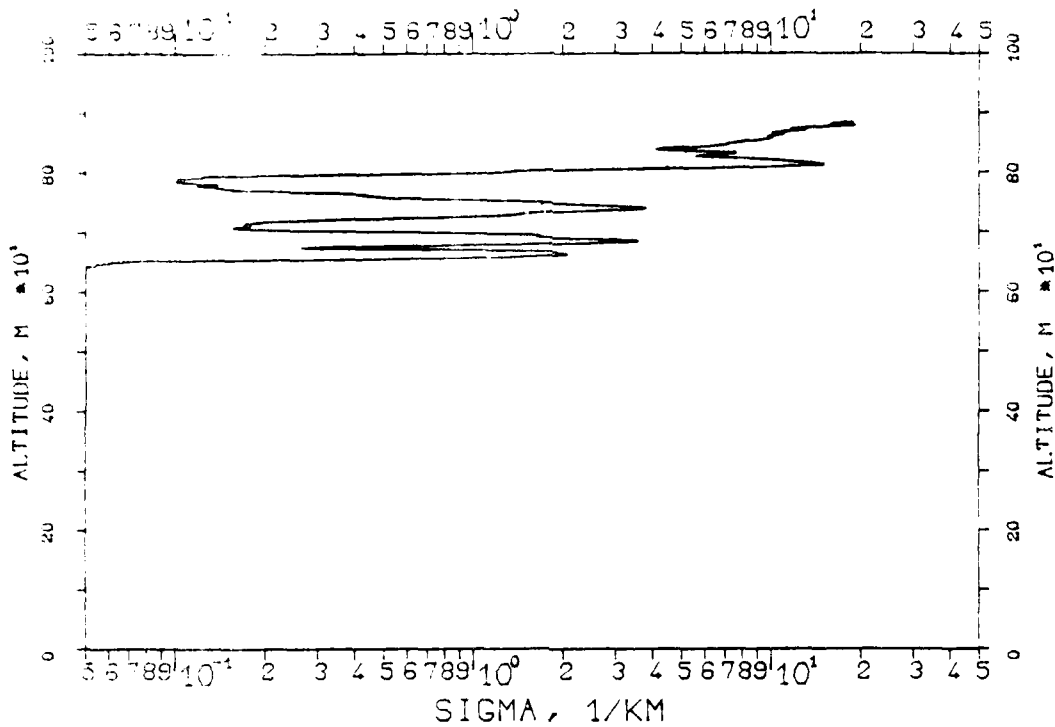


FIG. 7.196
KLETT-PROFILE, 1060NM, EL. 19DG20MN
841008, 09:22-09:23, CET
RM=2.670KM, SM=20.0000/KM, K=1.000



7.197
 KLETT-PROFILE, 1060NM, EL. 19DG20MN
 8.11.08, 11:19-11:20, CET
 RM=0.670KM, SM=20.0000/KM, K=1.000



7.208
 KLETT-PROFILE, 1060NM, EL. 05DG00MN
 841012, 08:10-08:10, CET
 RM=2.053KM, SM=20.0000/KM, K=1.000

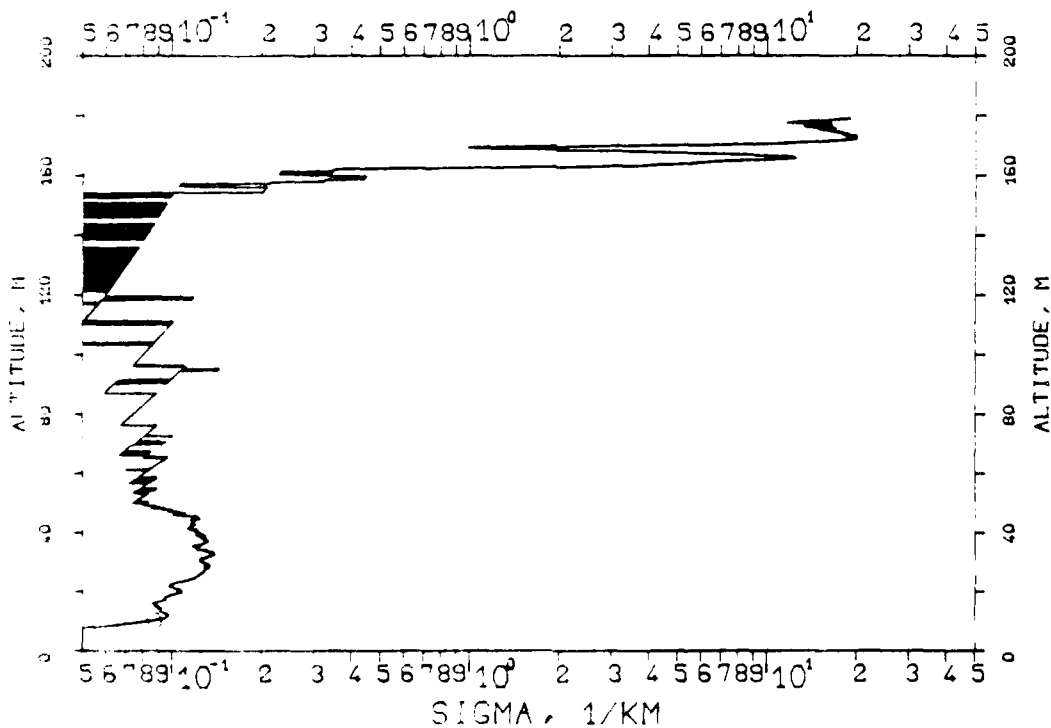


FIG. 7.240
KLETT PROFILE, 1060NM, EL. 300G00MN
8-1203, 12:21-12:21, CET
RM=1.231KM, SM=20.0000/KM, K=1.000

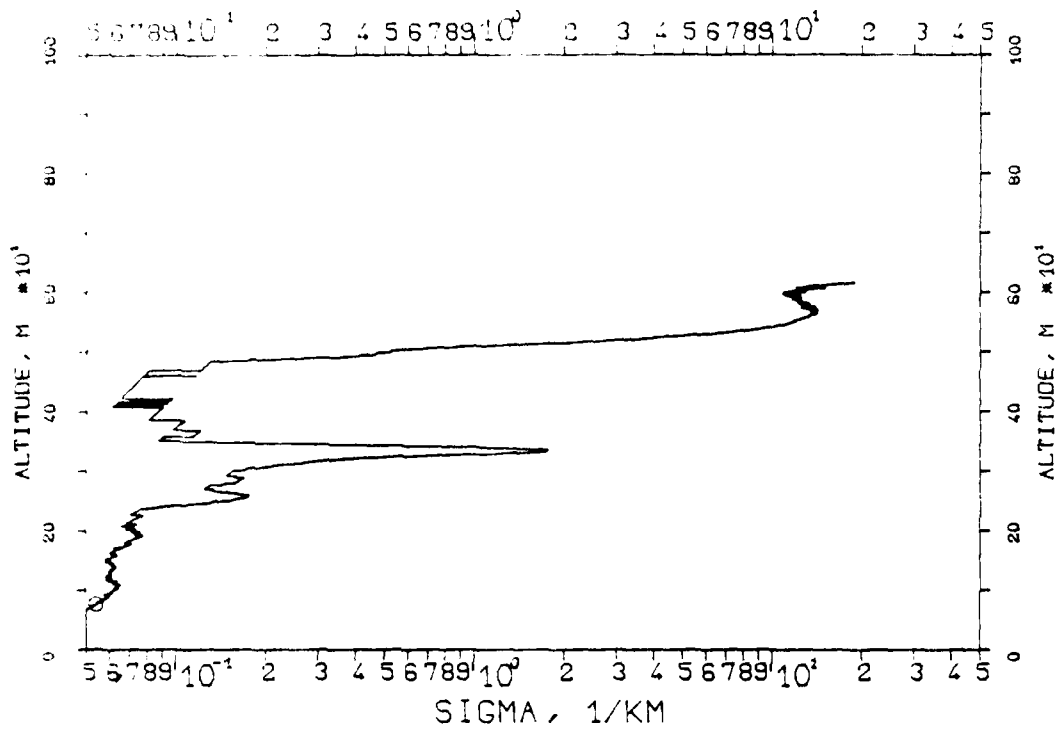


FIG. 7.241
KLETT-PROFILE, 1060NM, EL. 300G00MN
8-1203, 12:22-12:22, CET
RM=1.245KM, SM=20.0000/KM, K=1.000

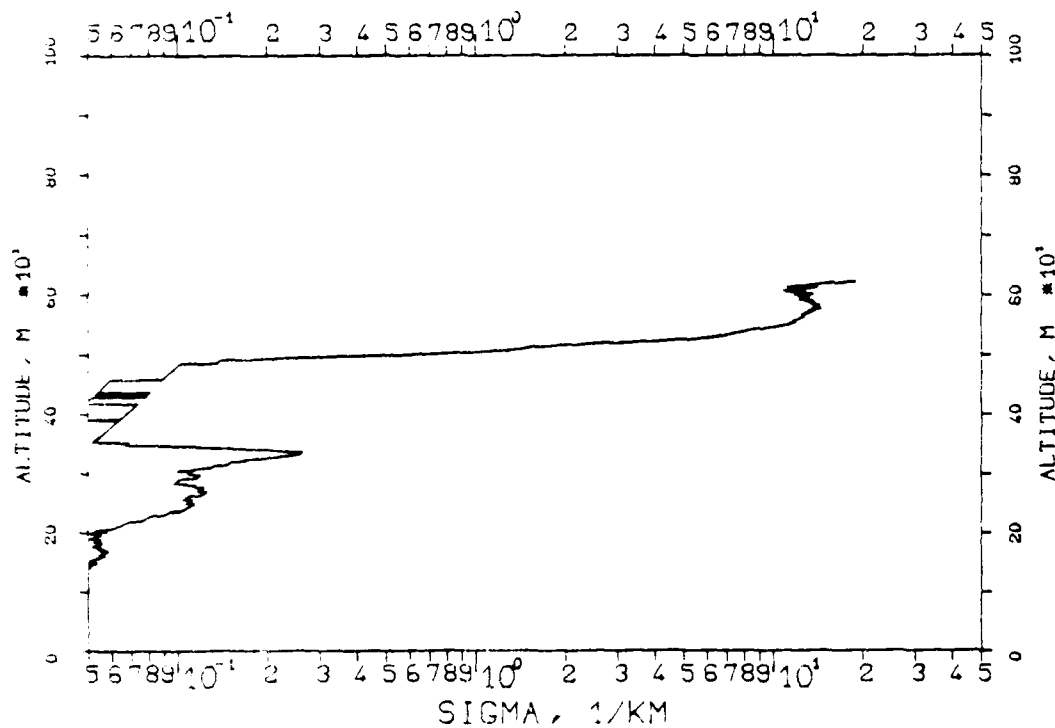


FIG. 7.238
KLETT-PROFILE, 1060NM, EL. 30DG00MN
841203, 12:19-12:19, CET
RM=1.236KM, SM=20.0000/KM, K=1.000

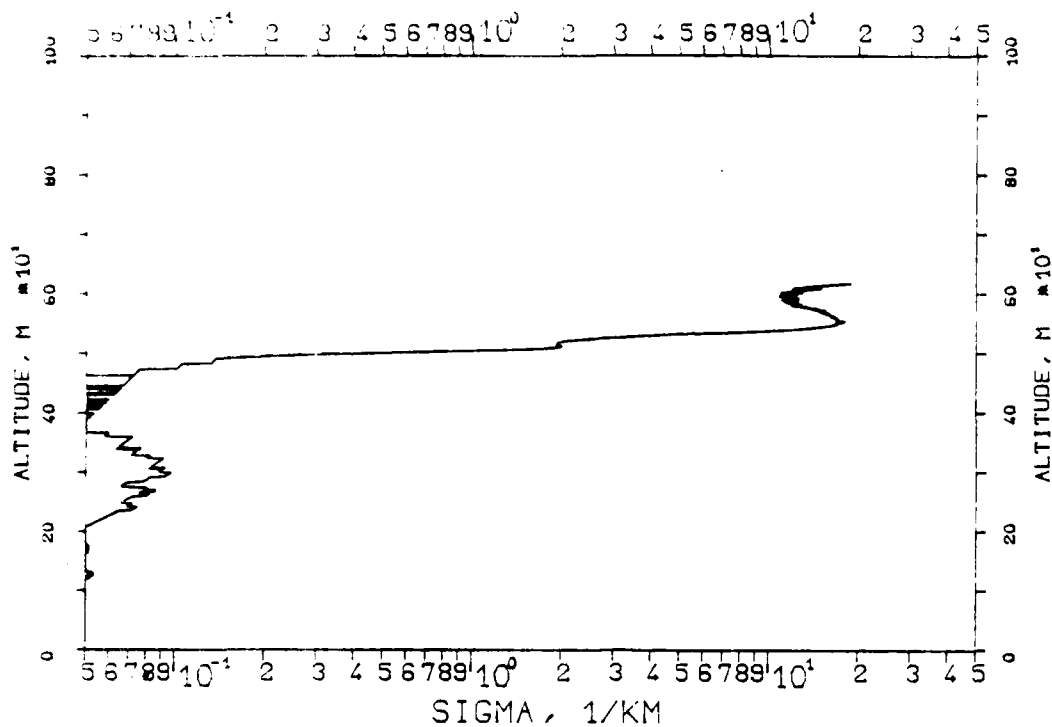


FIG. 7.239
KLETT-PROFILE, 1060NM, EL. 30DG00MN
841203, 12:20-12:20, CET
RM=1.234KM, SM=20.0000/KM, K=1.000

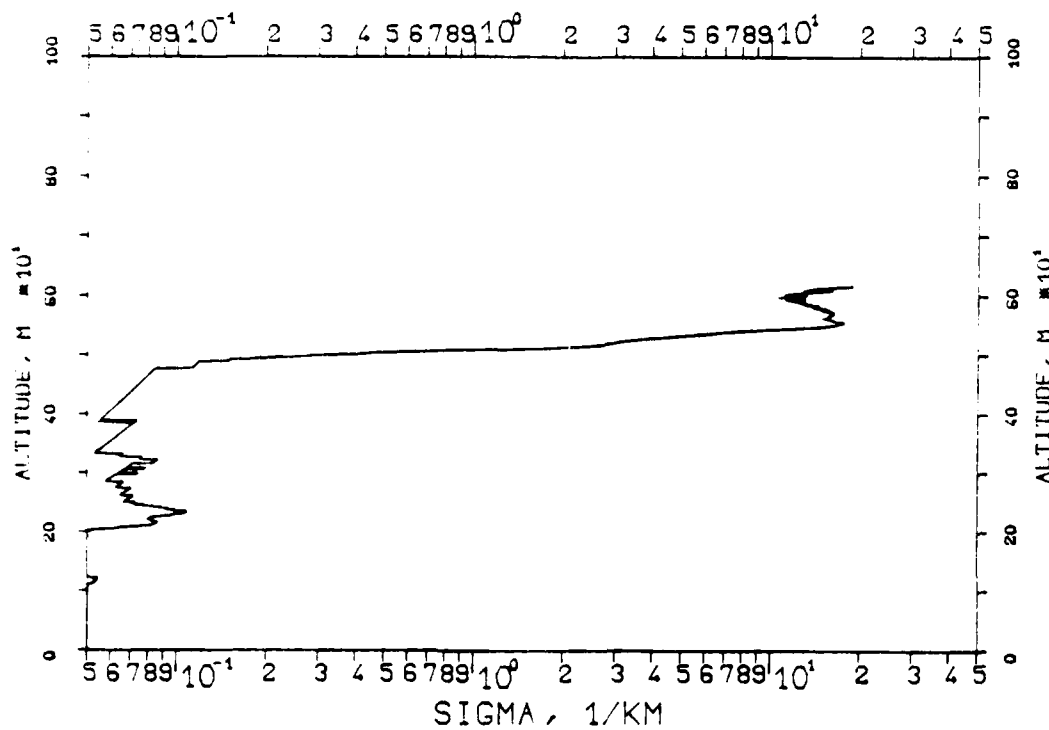


FIG. 7.236
 KLETT-PROFILE, 0694NM, EL. 30DG00MN
 841203, 11:46-11:46, CET
 RM=1.17KM, SM=20.0000/KM, K=1.000

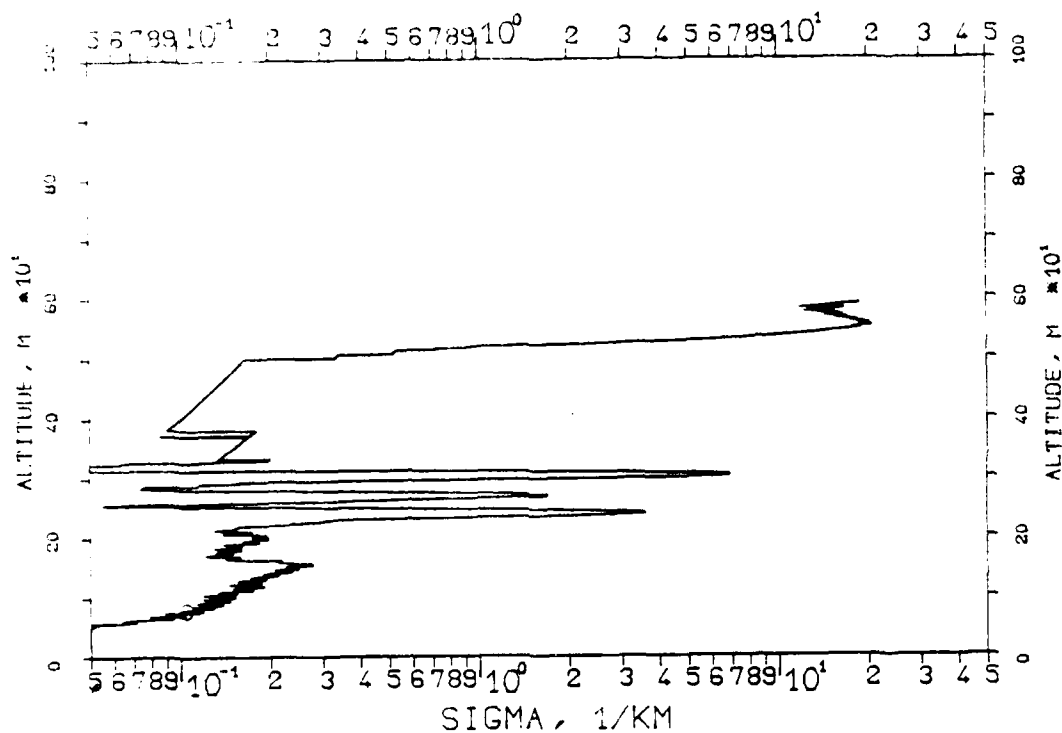


FIG. 7.237
 KLETT-PROFILE, 0694NM, EL. 20DG00MN
 841203, 11:56-11:57, CET
 RM=0.780KM, SM=20.0000/KM, K=1.000

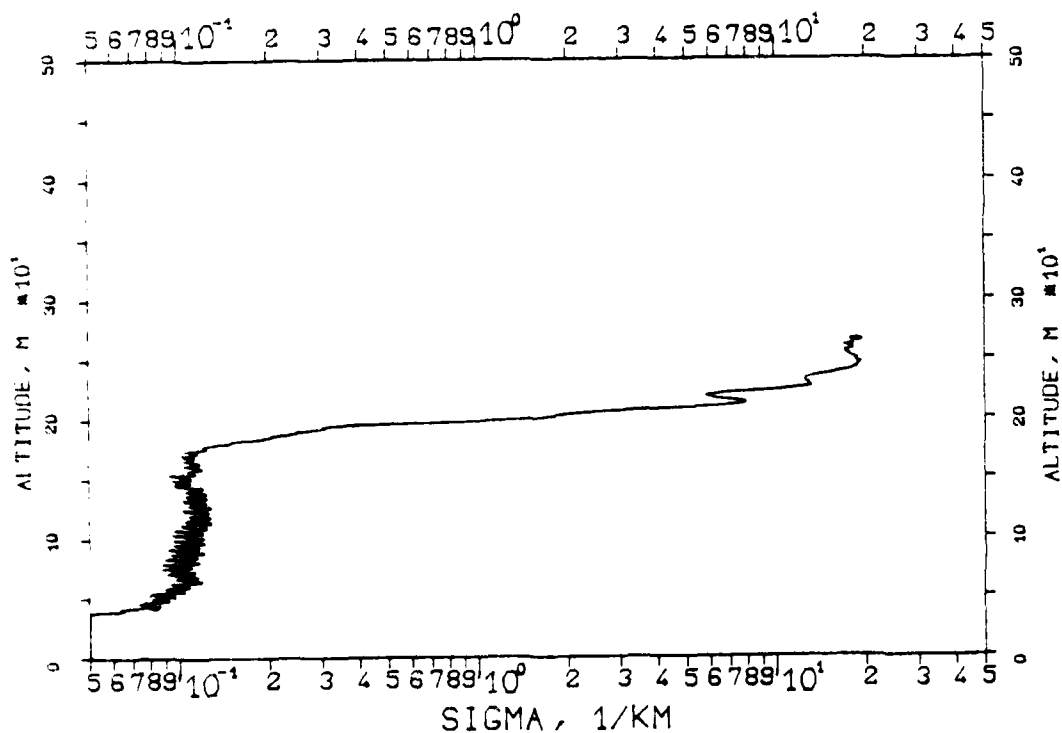


FIG. 7.234
KLETT-PROFILE, 0694NM, EL. 30DG00MN
841203, 11:43-11:43, CET
RM=0.762KM, SM=20.0000/KM, K=1.000

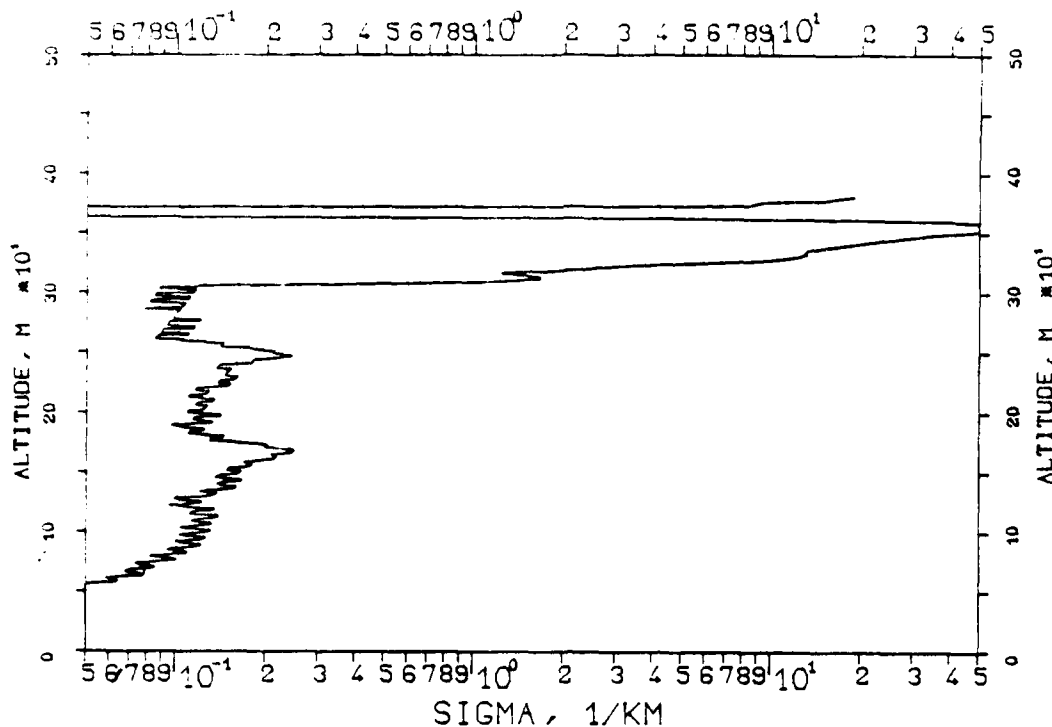


FIG. 7.235
KLETT-PROFILE, 0694NM, EL. 30DG00MN
841203, 11:44-11:44, CET
RM=1.209KM, SM=20.0000/KM, K=1.000

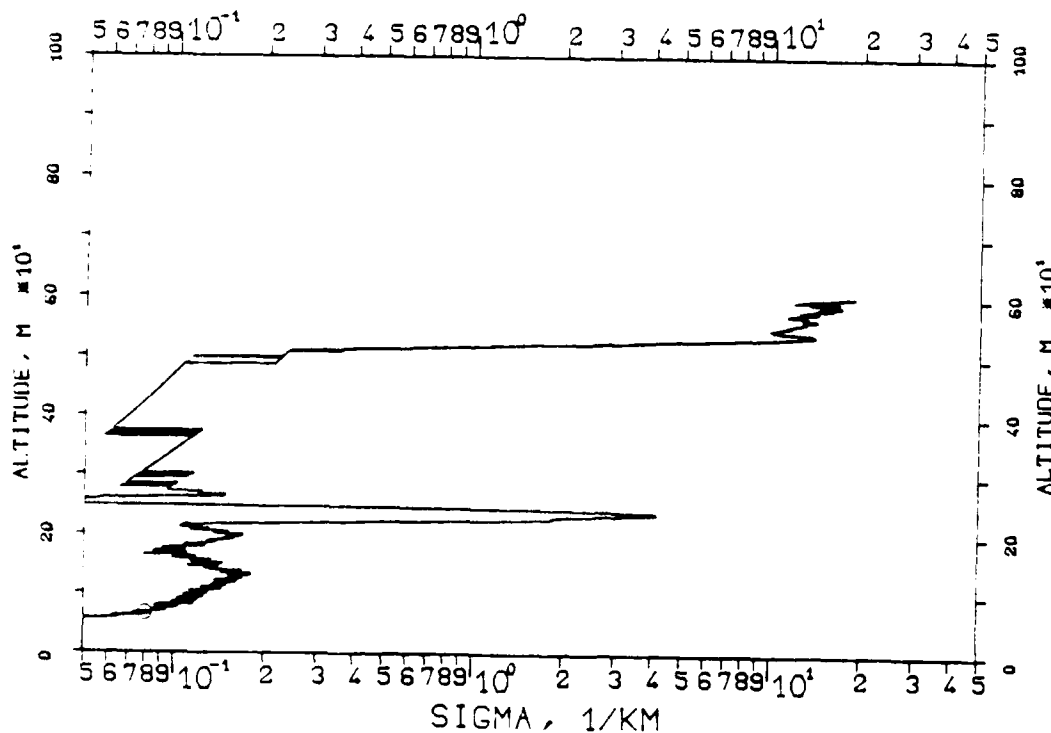


FIG. 7.232
KLETT-PROFILE, 1060NM, EL. 10DG00MN
841203, 11:00-11:00, CET
RM=1.483KM, SM=20.0000/KM, K=1.000

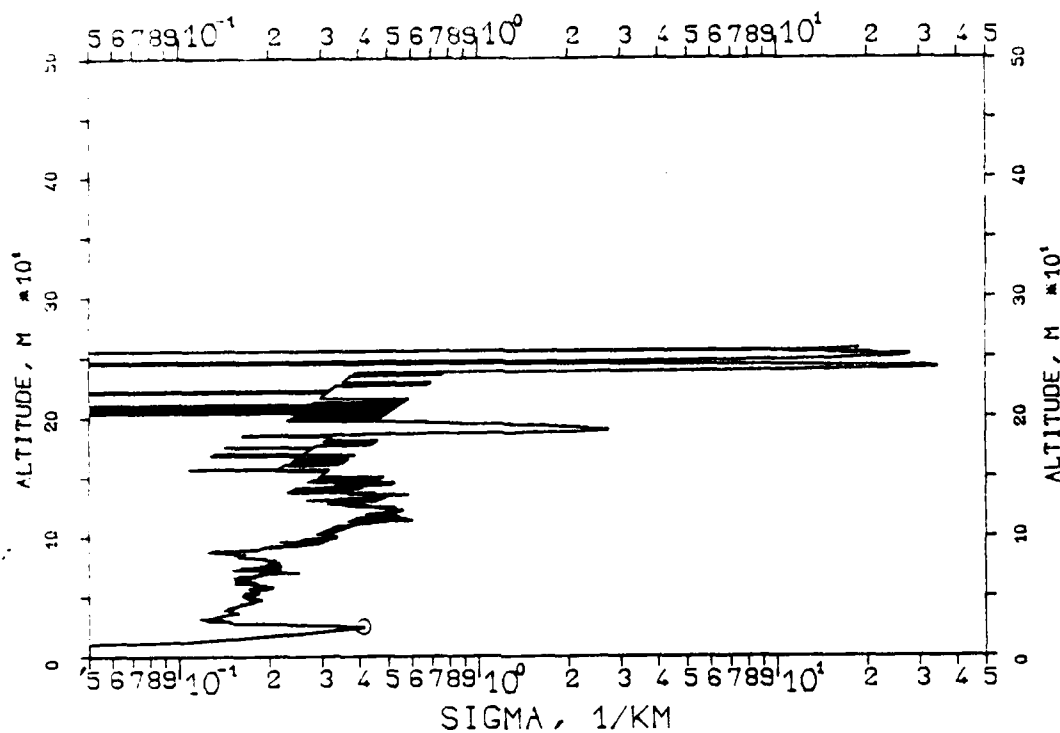


FIG. 7.233
KLETT-PROFILE, 0694NM, EL. 10DG00MN
841203, 11:40-11:40, CET
RM=1.564KM, SM=20.0000/KM, K=1.000

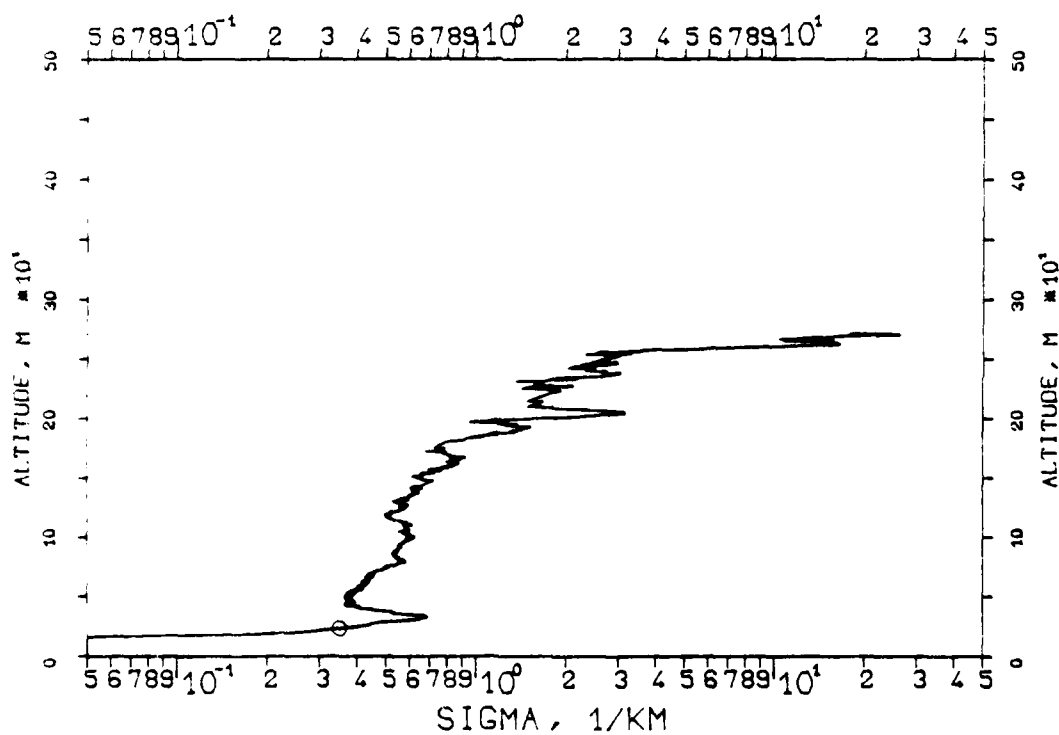


FIG. 7.226
KLETT-PROFILE, 1060NM, EL. 10DG00MN
841116, 12:34-12:35, CET
RM=0.717KM, SM=20.0000/KM, K=1.000

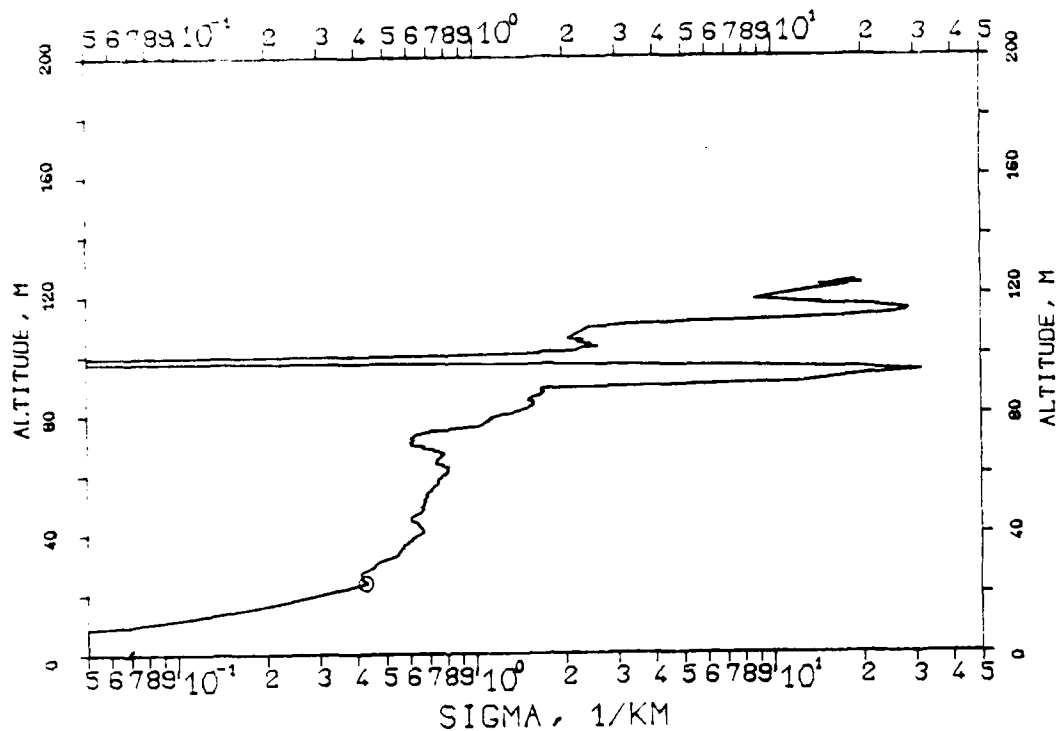


FIG. 7.227
KLETT-PROFILE, 1060NM, EL. 30DG00MN
841116, 12:38-12:38, CET
RM=0.297KM, SM=20.0000/KM, K=1.000

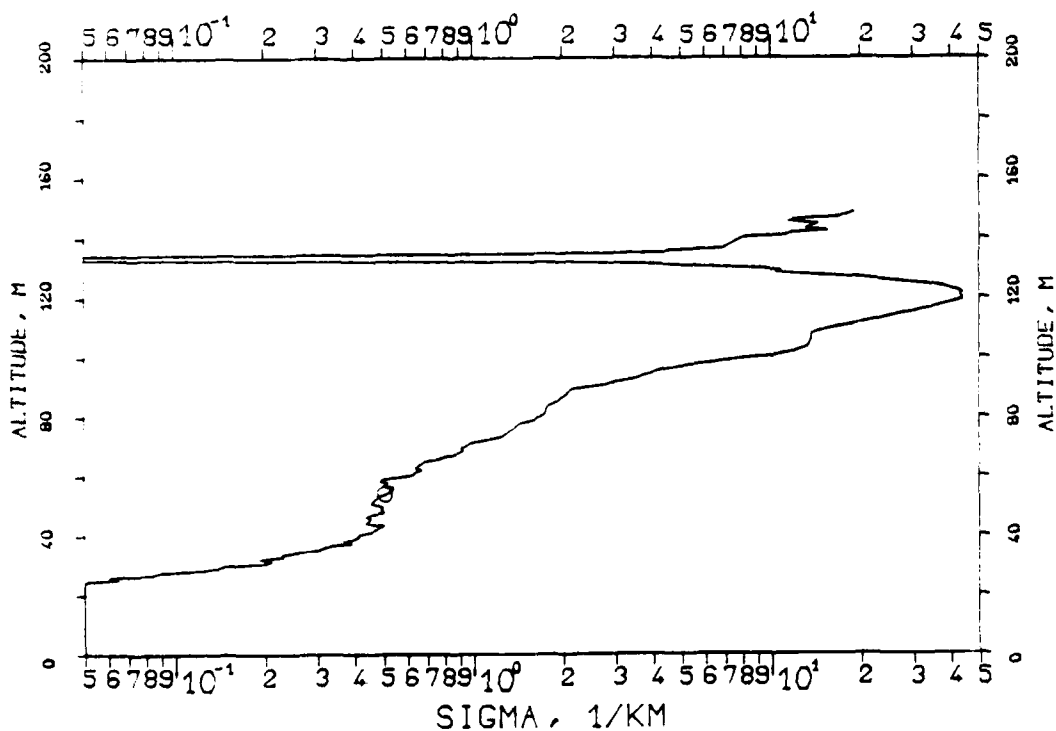


FIG. 7.224
KLETT-PROFILE, 1060NM, EL. 10DG00MN
841116, 12:32-12:33, CET
RM=0.627KM, SM=20.0000/KM, K=1.000

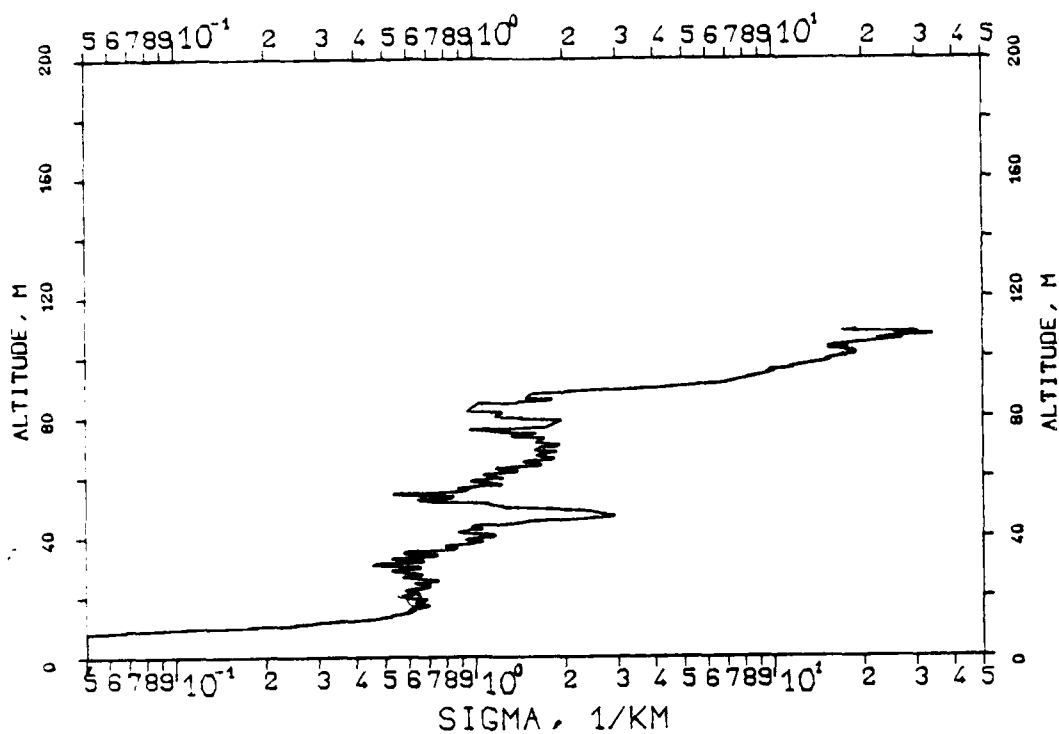


FIG. 7.225
KLETT-PROFILE, 1060NM, EL. 10DG00MN
841116, 12:33-12:34, CET
RM=0.729KM, SM=20.0000/KM, K=1.000

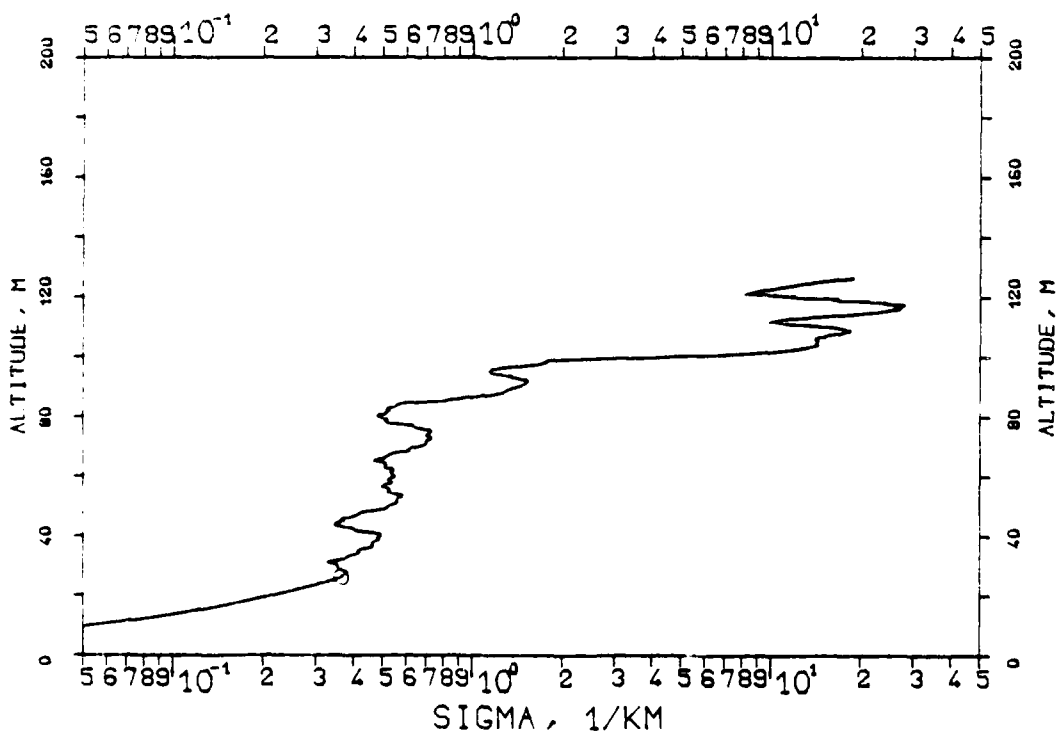


FIG. 7.222

KLETT-PROFILE, 0694NM, EL. 10DG00MN

841116, 12:28-12:28, CET

RM=0.529KM, SM=20.0000/KM, K=1.000

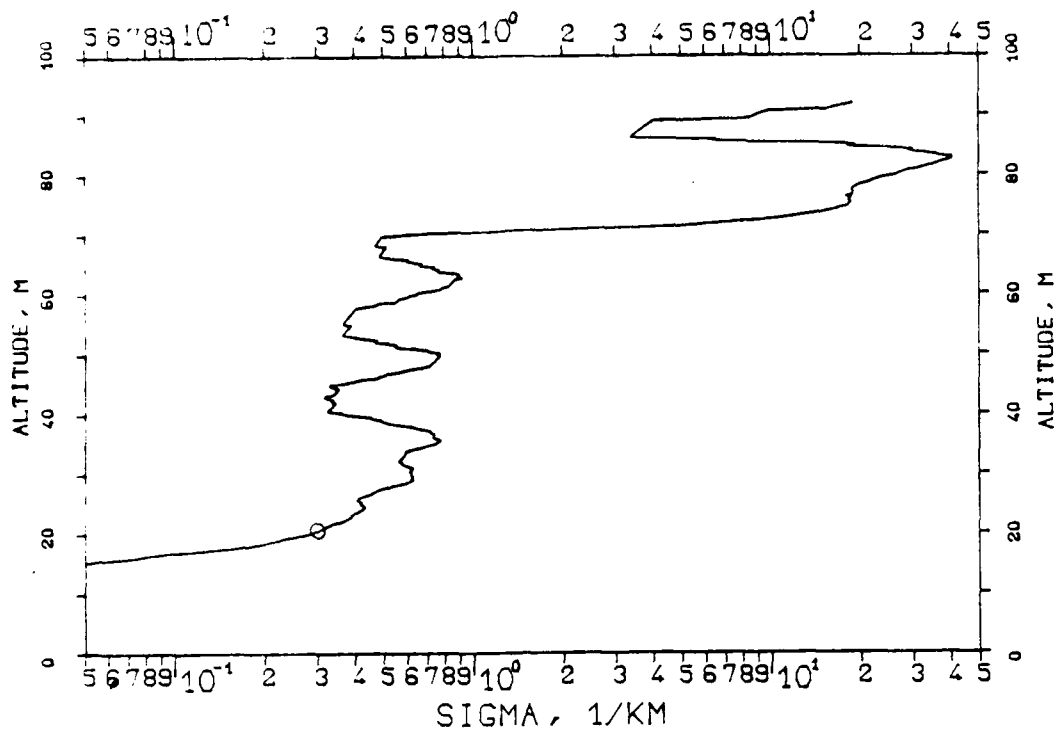


FIG. 7.223

KLETT-PROFILE, 0694NM, EL. 10DG00MN

841116, 12:29-12:29, CET

RM=0.528KM, SM=20.0000/KM, K=1.000

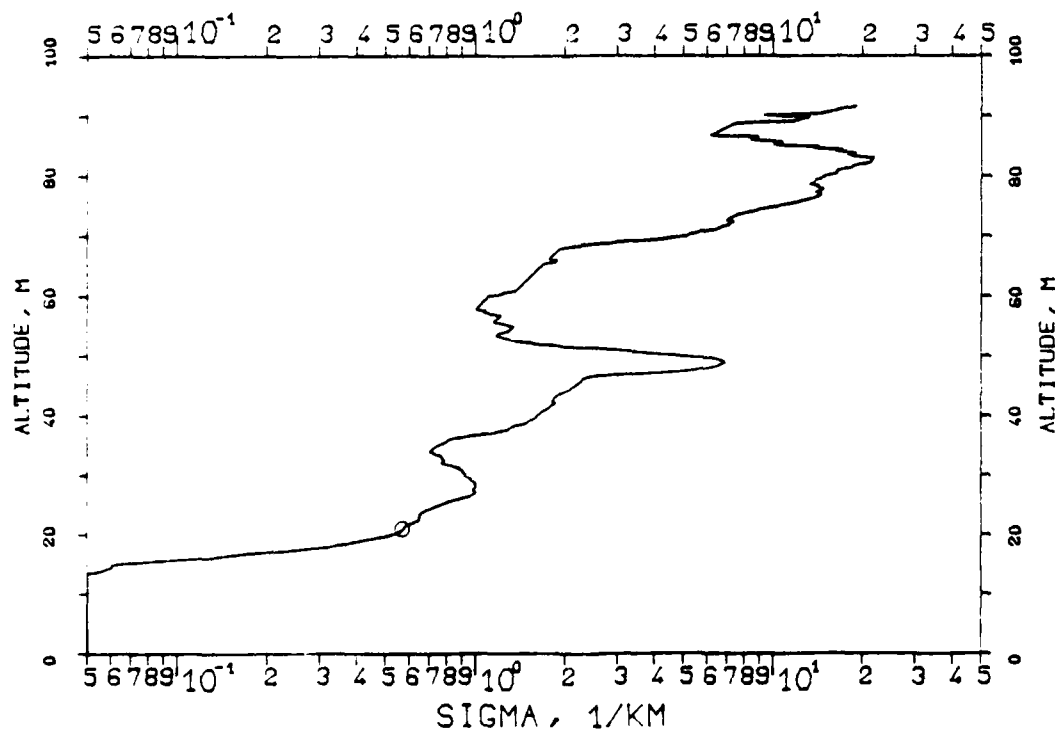


FIG. 7.220
 KLETT-PROFILE, 0694NM, EL. 10DG00MN
 841116, 12:26-12:26, CET
 RM=0.594KM, SM=20.0000/KM, K=1.000

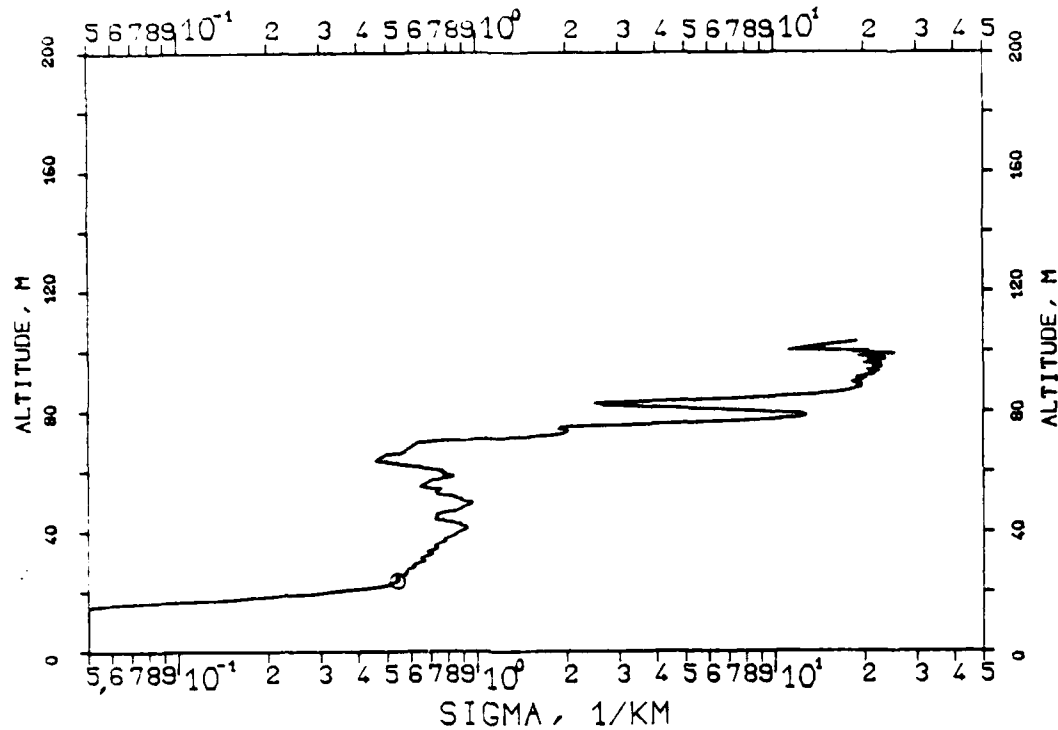


FIG. 7.221
 KLETT-PROFILE, 0694NM, EL. 10DG00MN
 841116, 12:27-12:27, CET
 RM=0.550KM, SM=20.0000/KM, K=1.000

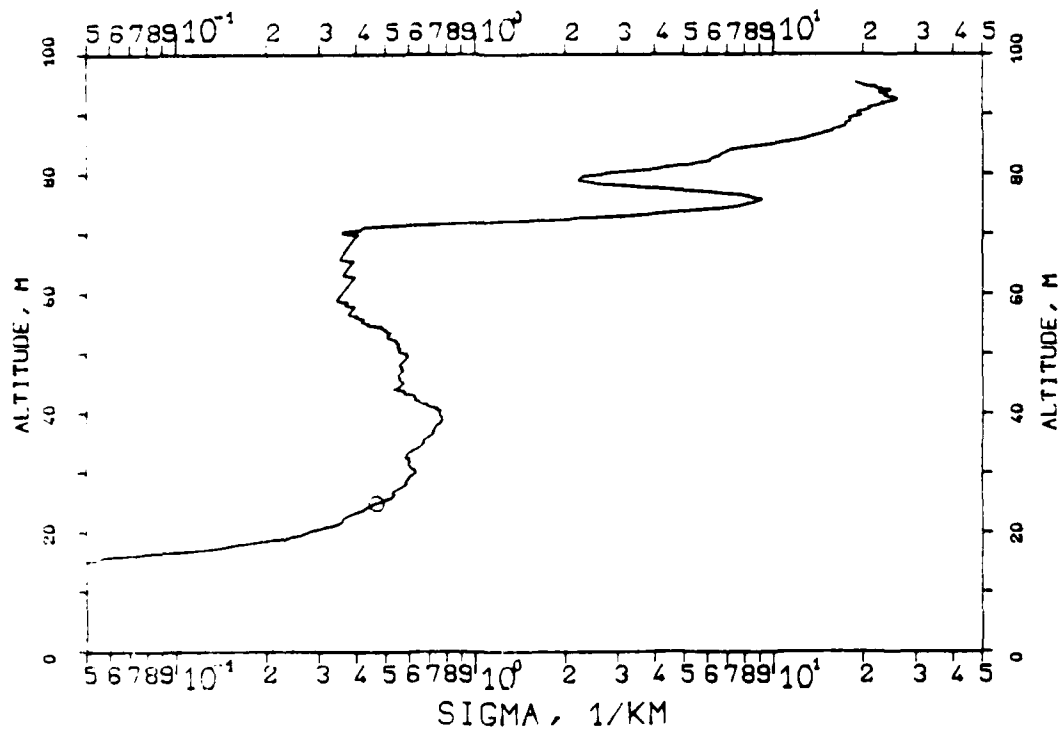


FIG. 7.218
 KLETT-PROFILE, 0694NM, EL. 10DG00MN
 841116, 12:20-12:21, CET
 RM=0.637KM, SM=20.0000/KM, K=1.000

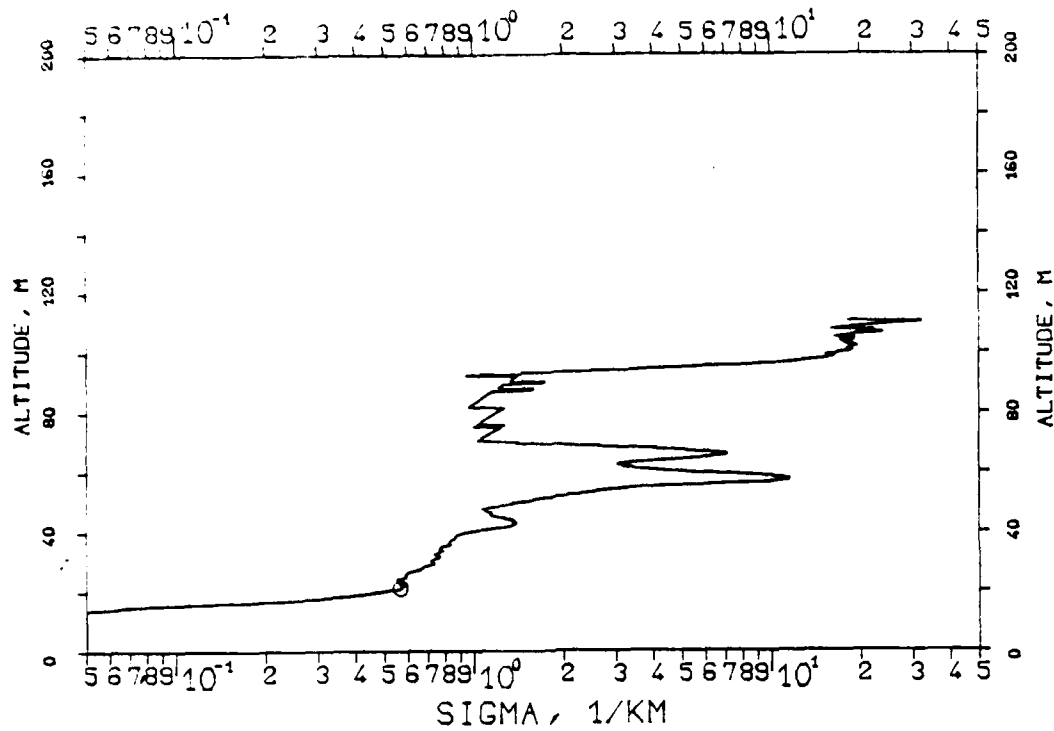


FIG. 7.219
 KLETT-PROFILE, 0694NM, EL. 10DG00MN
 841116, 12:24-12:25, CET
 RM=0.565KM, SM=20.0000/KM, K=1.000

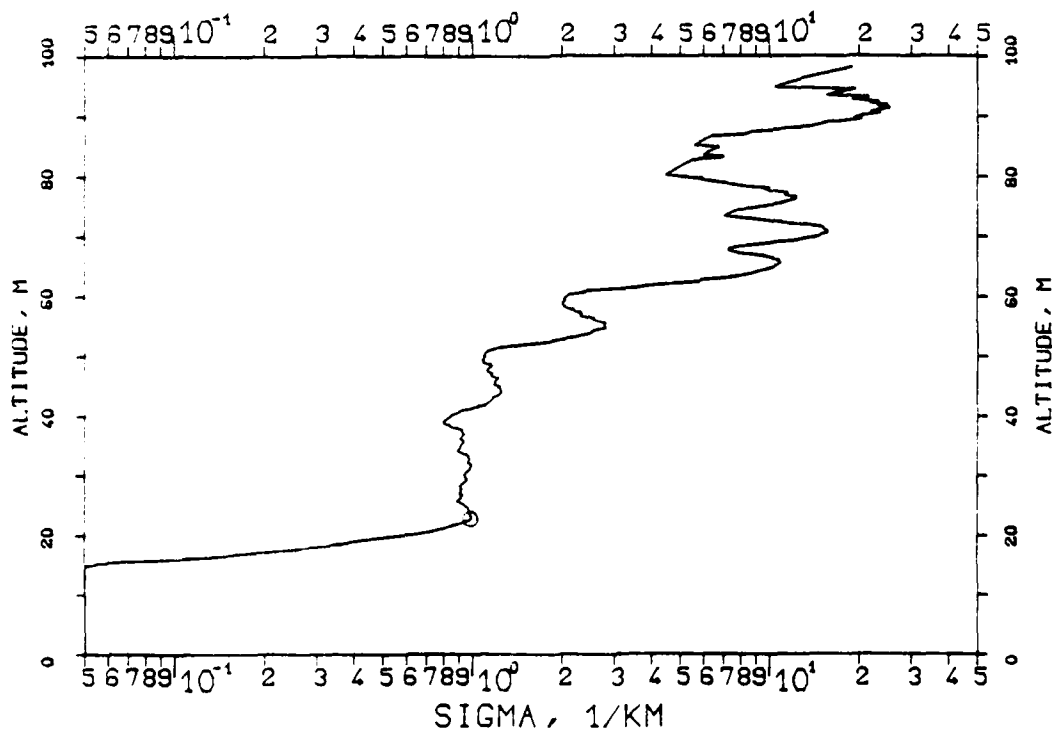


FIG. 7.215
KLETT-PROFILE, 1060NM, EL. 20DG00MN
841104, 09:11-09:11, CET
RM=1.000KM, SM=20.0000/KM, K=1.000

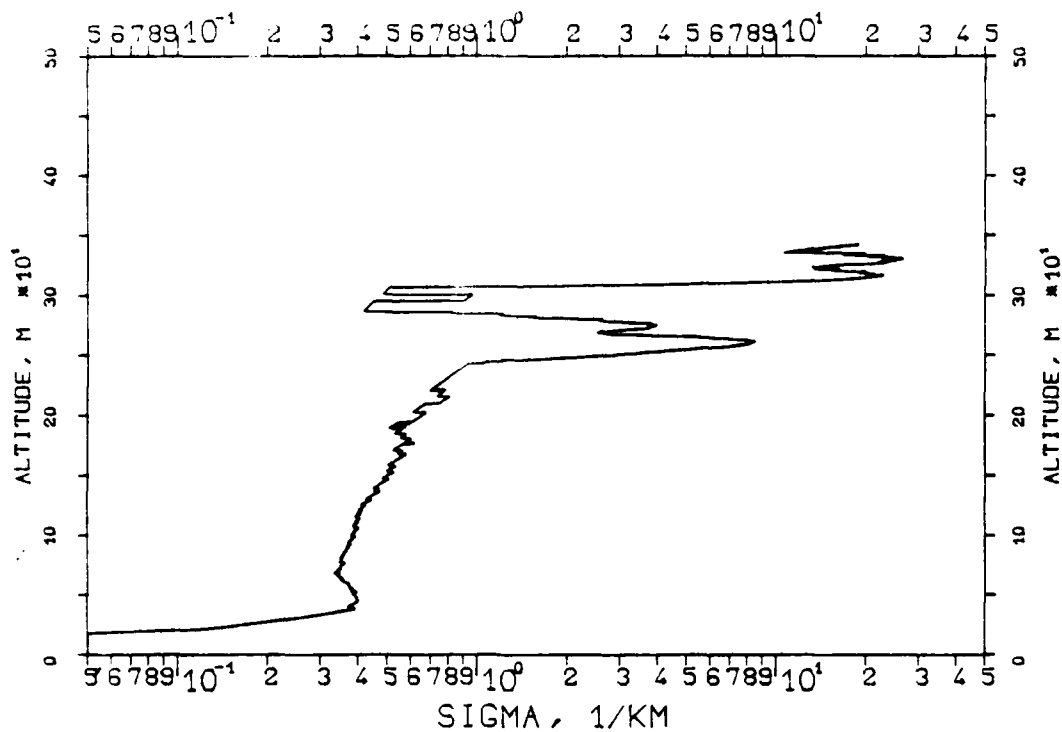
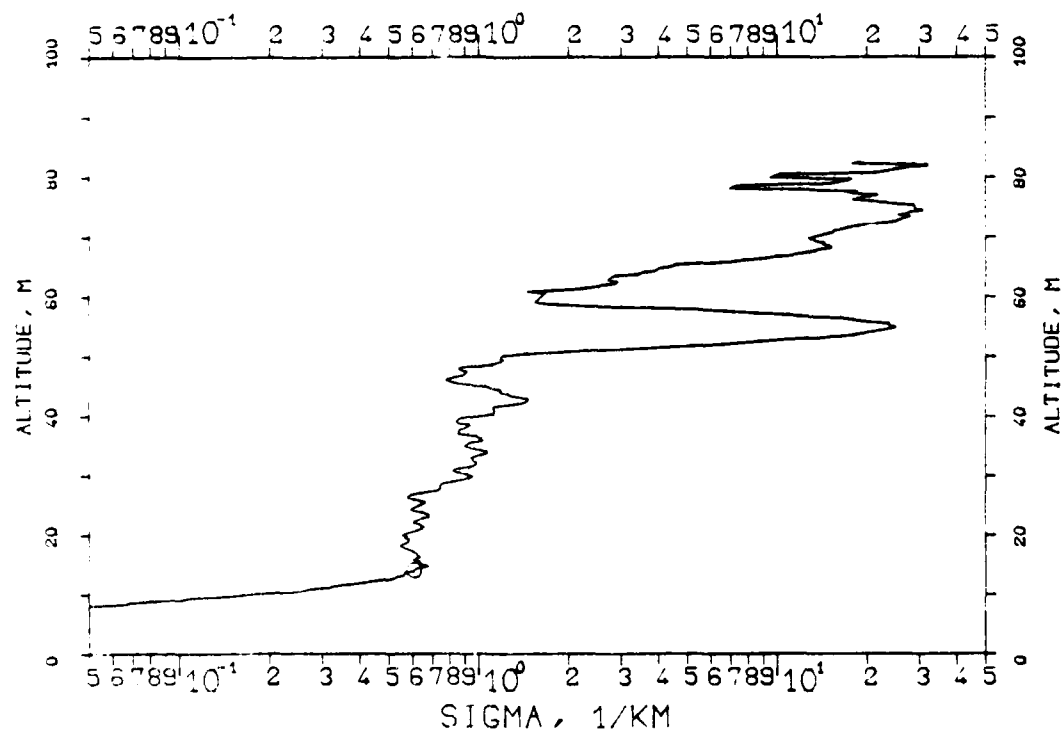


FIG. 7.217
KLETT-PROFILE, 1060NM, EL. 10DG00MN
841116, 12:19-12:19, CET
RM=0.475KM, SM=20.0000/KM, K=1.000



FILE: 7.213
 KLETT-PROFILE, 1060NM, EL. 20DG00MN
 841104, 09:09-09:09, CET
 RM=0.880KM, SM=20.0000/KM, K=1.000

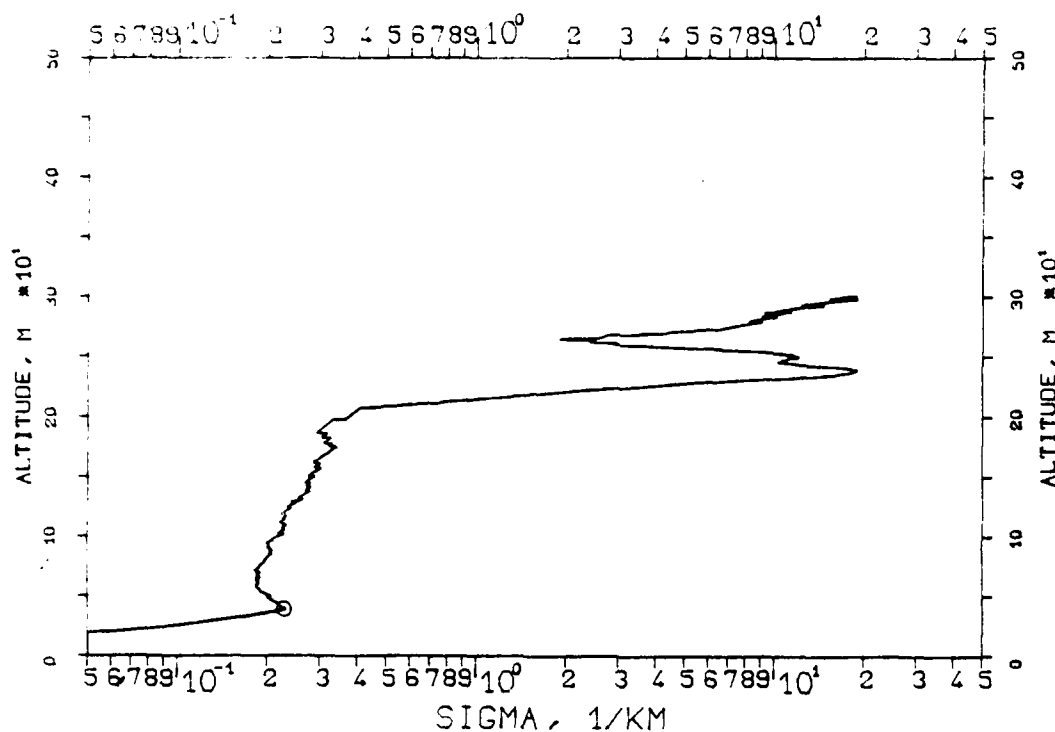


FIG. 7.214
 KLETT-PROFILE, 1060NM, EL. 20DG00MN
 841104, 09:10-09:10, CET
 RM=0.957KM, SM=20.0000/KM, K=1.000

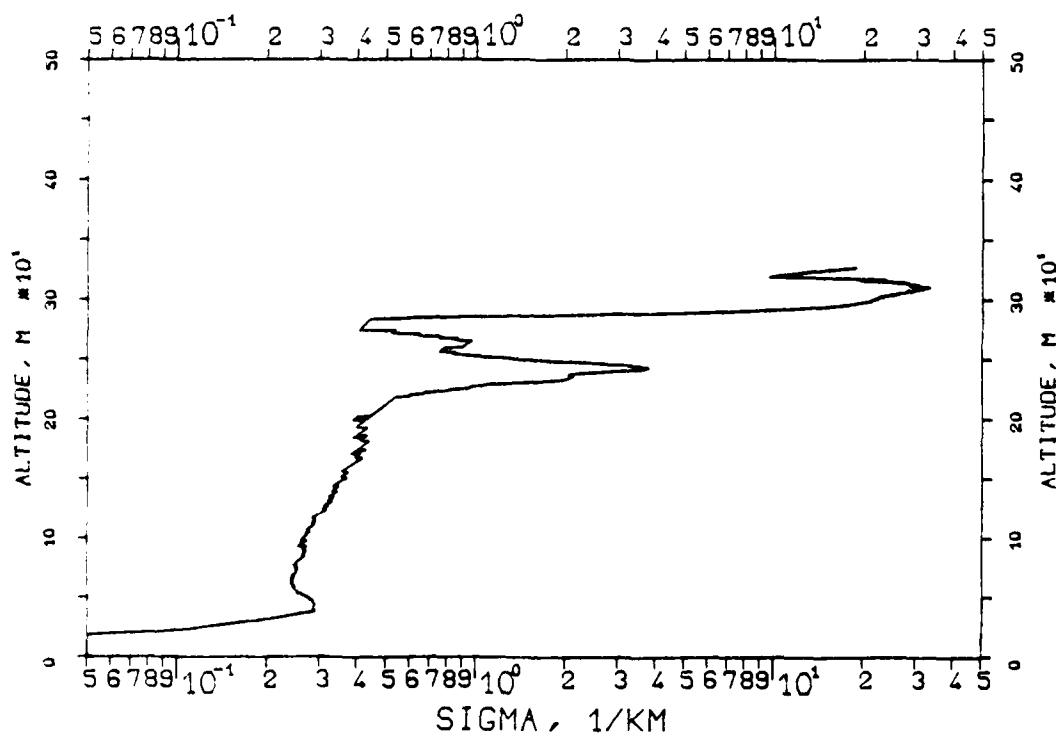


FIG. 7.211
 KLETT-PROFILE, 0530NM, EL. 20DG00MN
 841101, 09:07-09:07, CET
 RM=0.967KM, SM=20.0000/KM, K=1.000

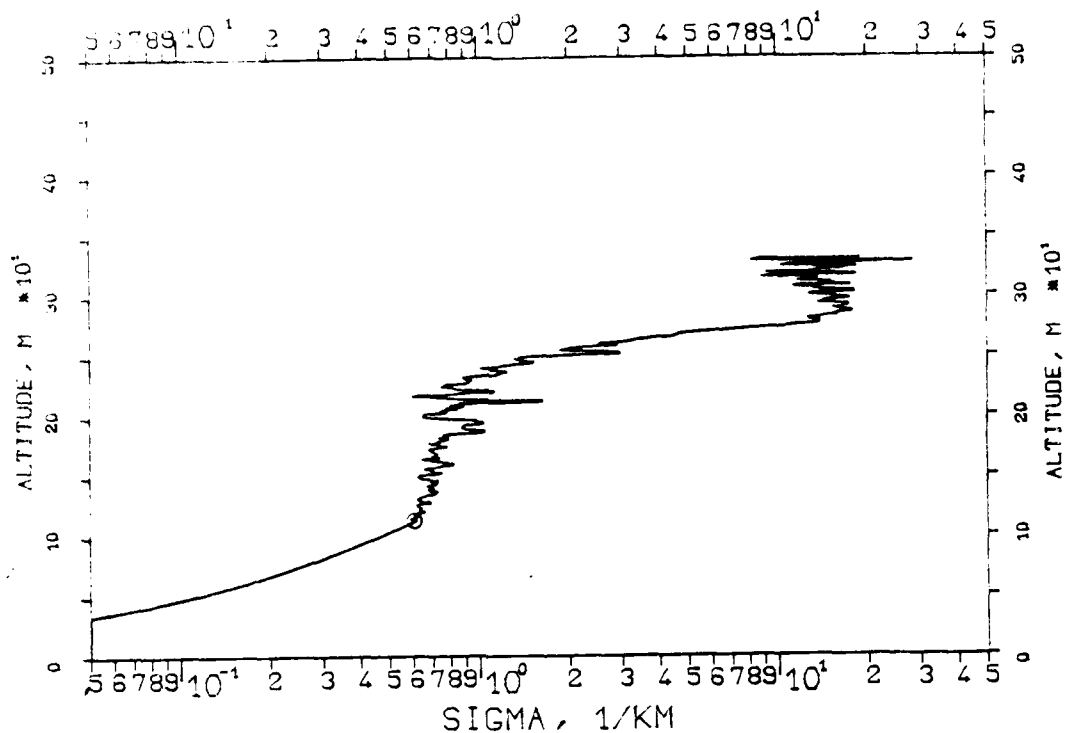


FIG. 7.212
 KLETT-PROFILE, 0530NM, EL. 20DG00MN
 841101, 09:08-09:08, CET
 RM=0.930KM, SM=20.0000/KM, K=1.000

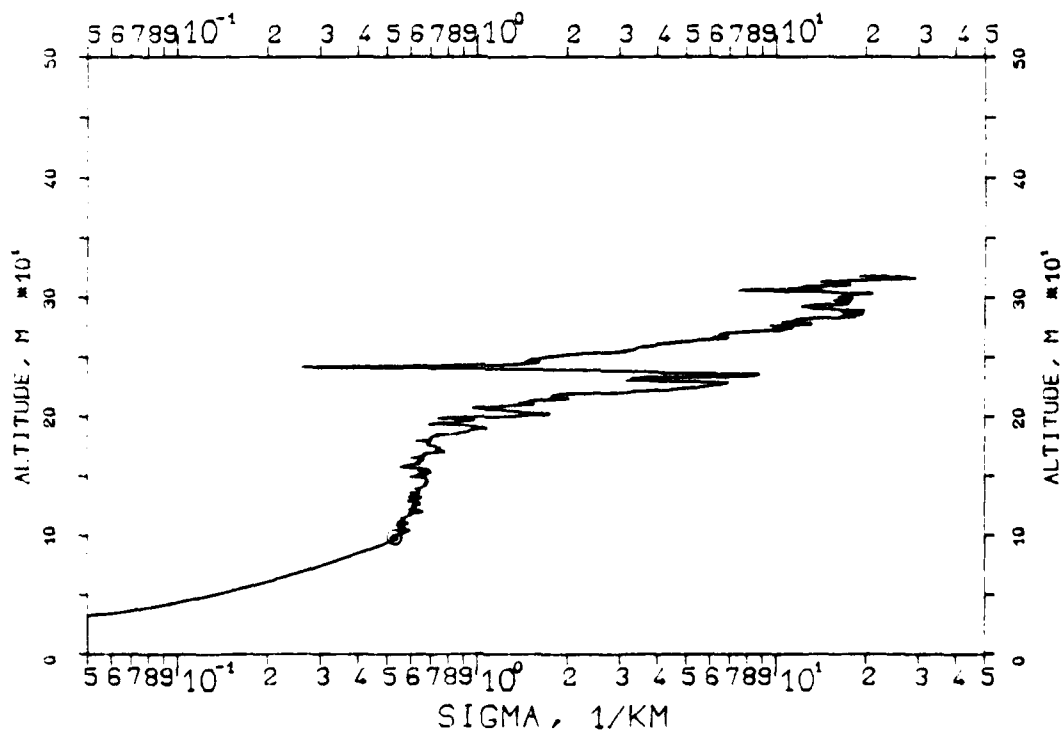


FIG. 7.200
KLETT-PROFILE, 1060NM, EL. 050G00MN
841012, 08:11-08:11, CET
RM=2.397KM, SM=20.0000/KM, K=1.000

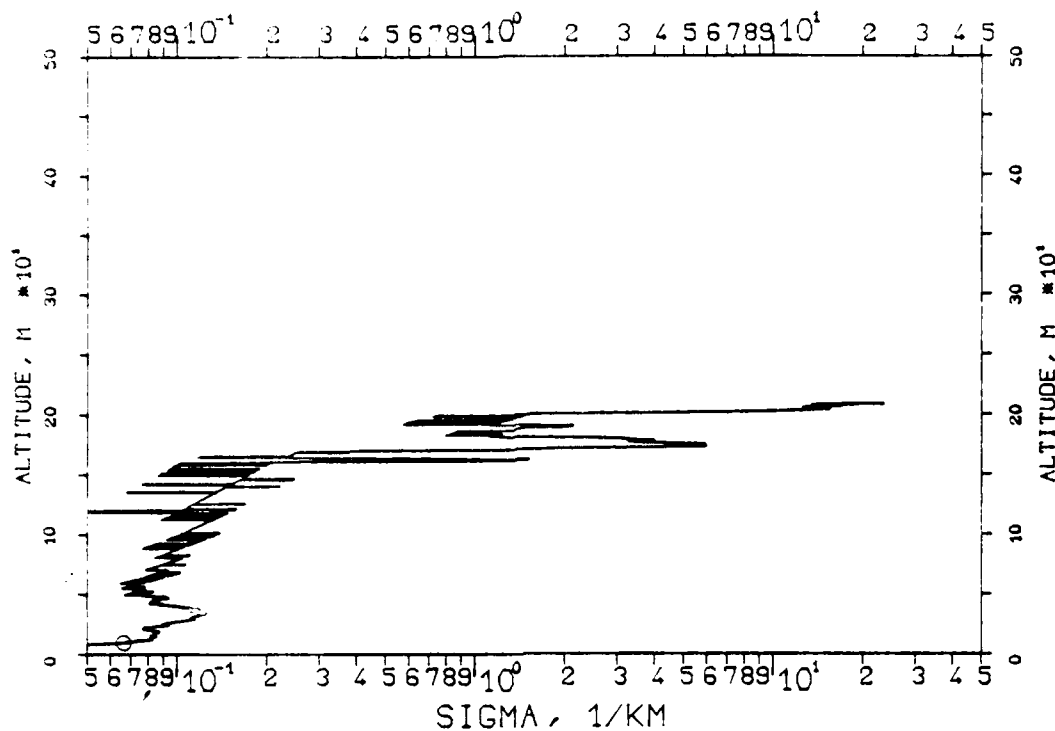
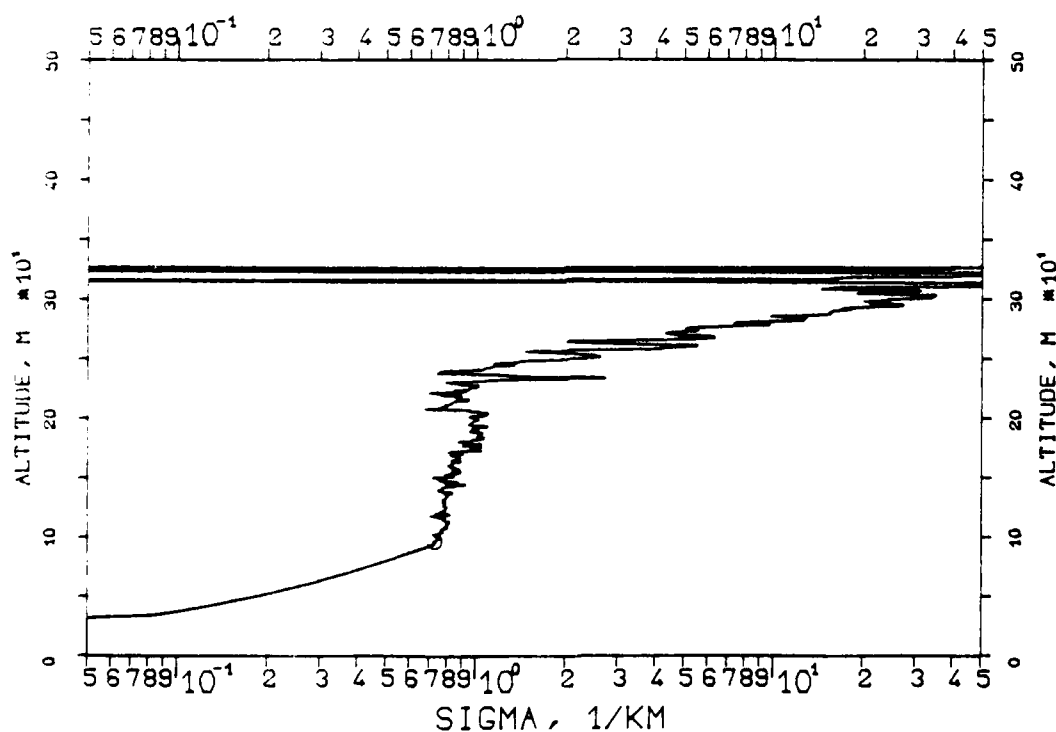


FIG. 7.210
KLETT-PROFILE, 0530NM, EL. 20DG00MN
841104, 09:06-09:06, CET
RM=0.958KM, SM=20.0000/KM, K=1.000



ALBERTA PROFILE, 1060NM, EL. 30DG00MN
 541203, 12:22-12:23, CET
 RM=1.255KM, SM=20.0000/KM, K=1.000

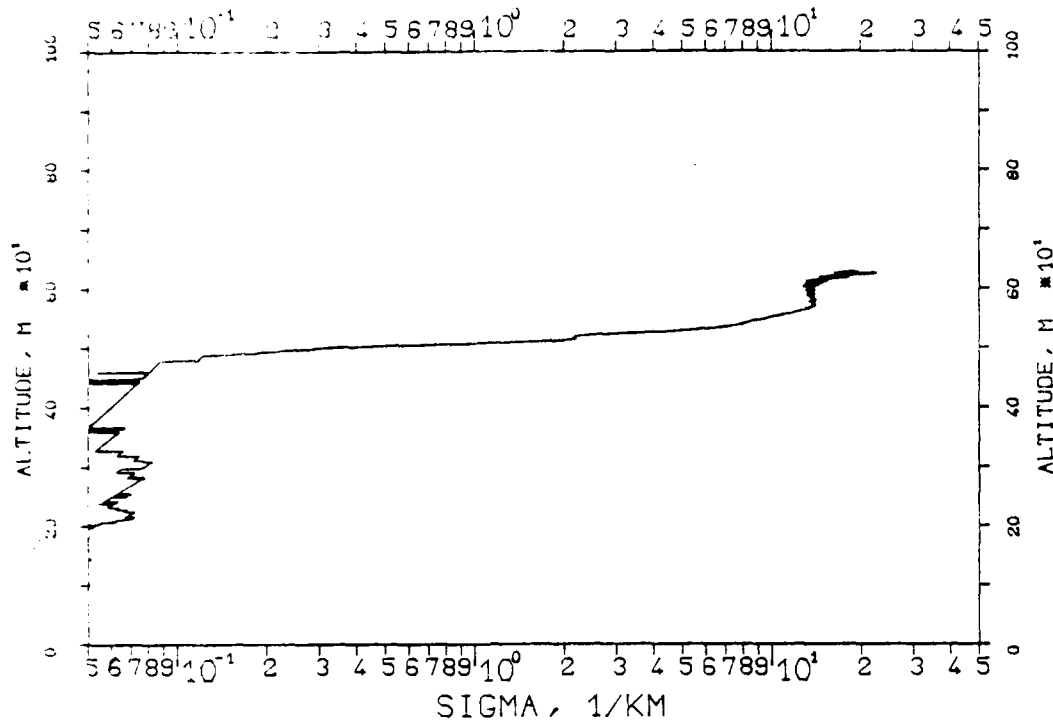


FIG. 7.243
 ALBERTA PROFILE, 1060NM, EL. 30DG00MN
 341203, 12:25-12:25, CET
 RM=1.257KM, SM=20.0000/KM, K=1.000

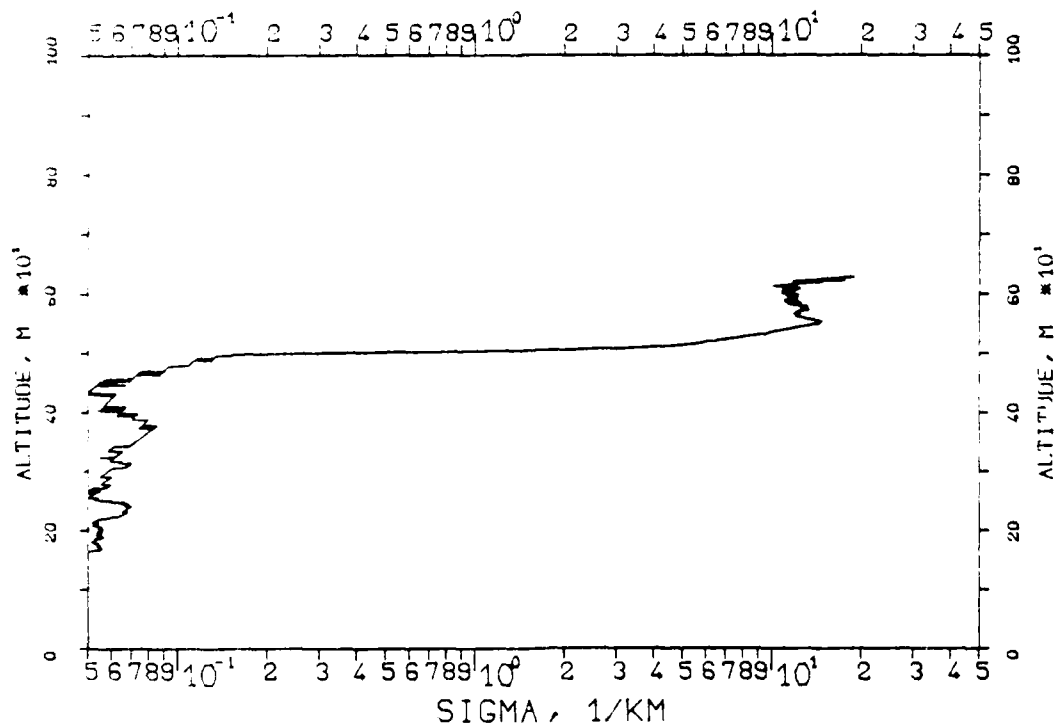


FIG. 7.2.5
KLETT-PROFILE, 0530NM, EL. 30DG00MN
841203, 12:45-12:45, CET
RM=1.128KM, SM=20.0000/KM, K=1.000

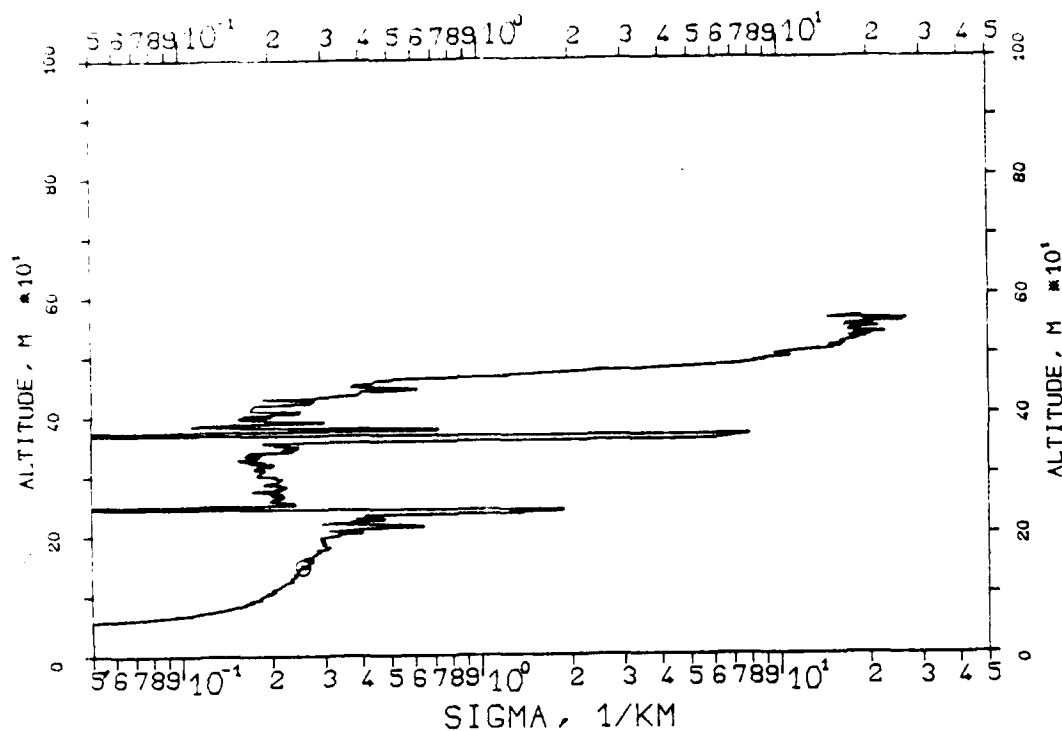
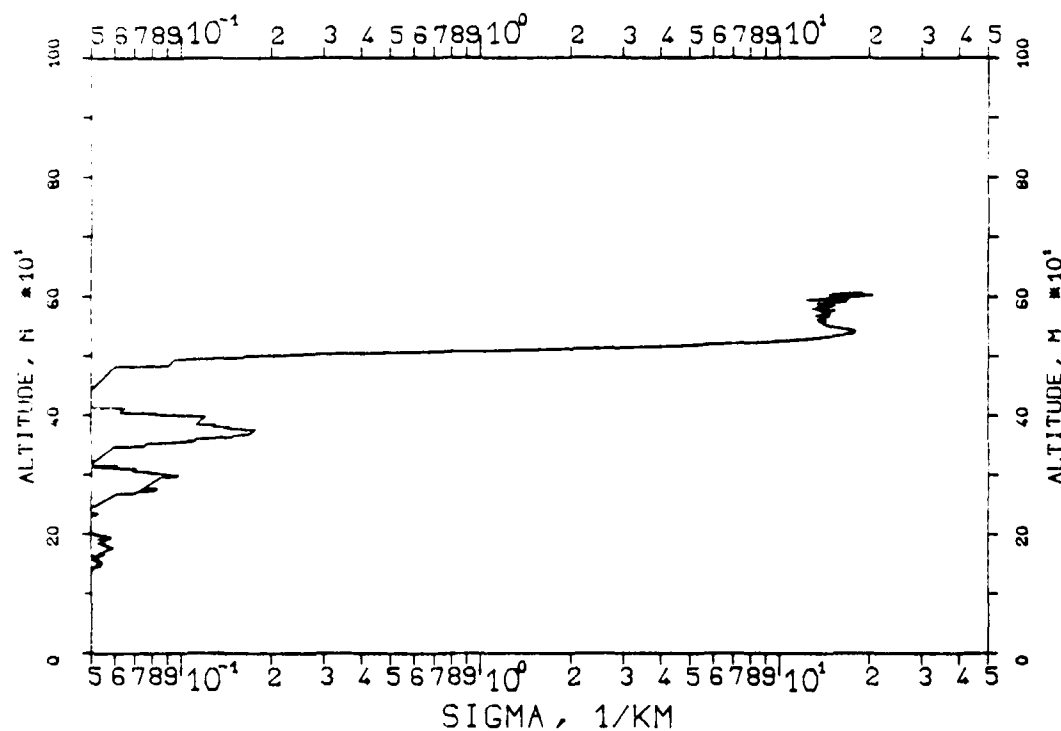


FIG. 7.244
KLETT-PROFILE, 1060NM, EL. 30DG00MN
841203, 12:26-12:26, CET
RM=1.215KM, SM=20.0000/KM, K=1.000



11.12.6
 KLETT-PROFILE, 0530NM, EL. 30DG00MN
 341203, 12:46-12:46, CET
 RM=0.888KM, SM=20.0000/KM, K=1.000

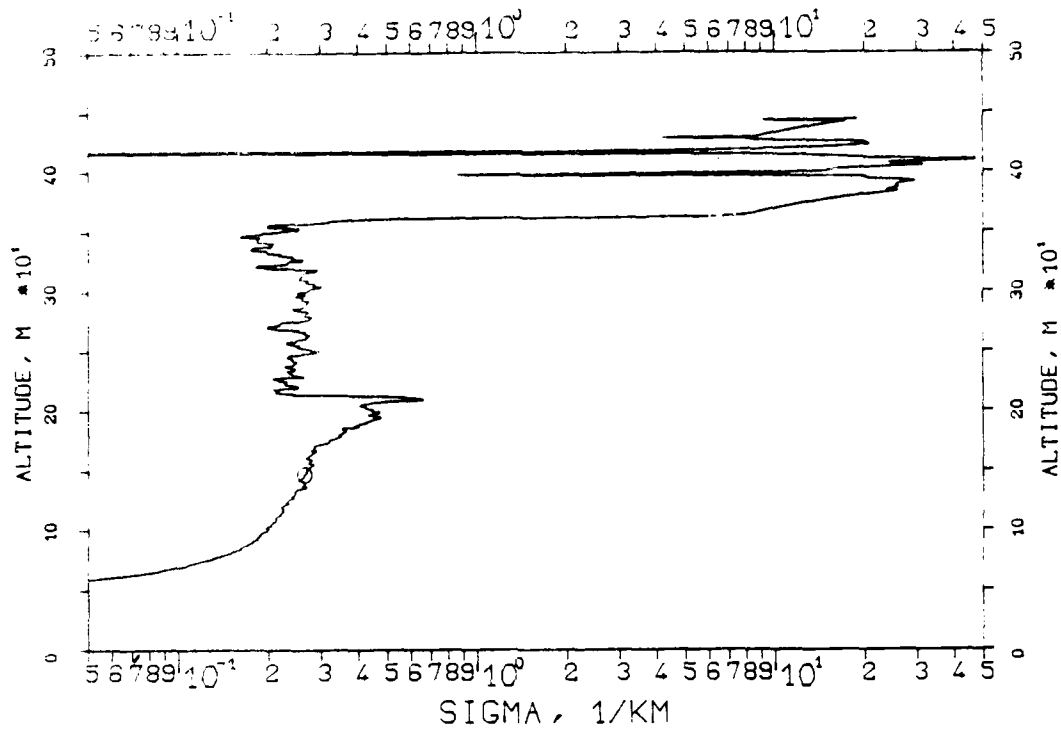


FIG. 7.247
 KLETT-PROFILE, 0530NM, EL. 30DG00MN
 341203, 12:47-12:47, CET
 RM=1.095KM, SM=20.0000/KM, K=1.000

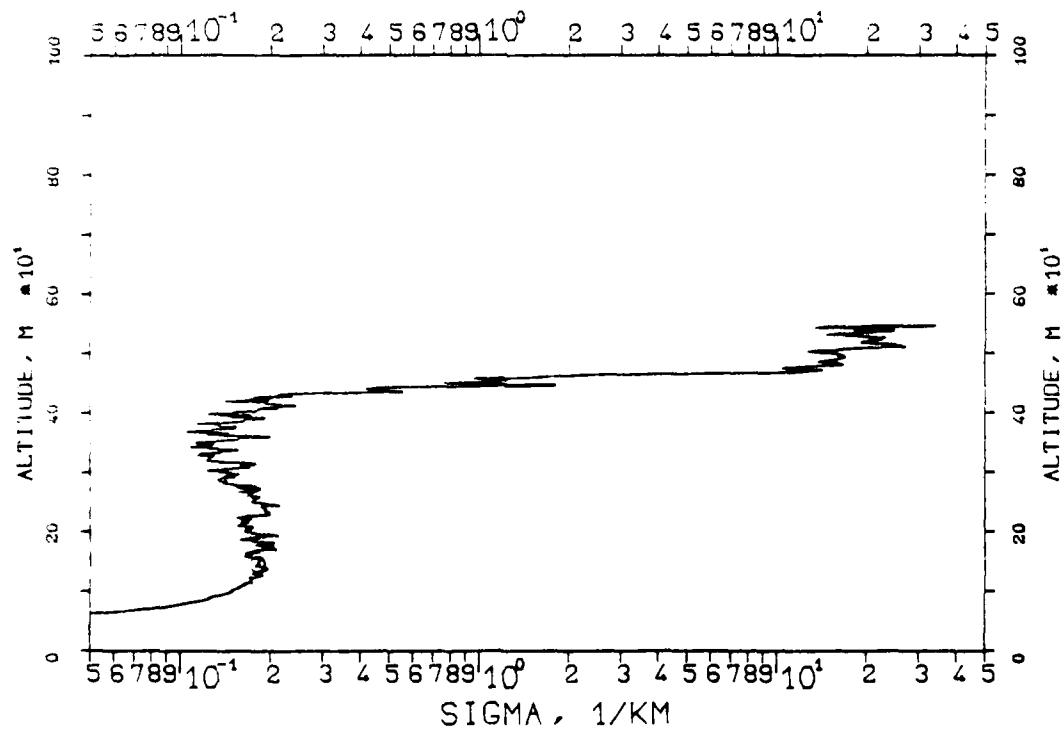


FIG. 7.248
KLETT-PROFILE ,0694NM,EL.30DG00MN
841203, 12:55-12:56,CET
RM=1.150KM,SM=20.0000/KM,K=1.000

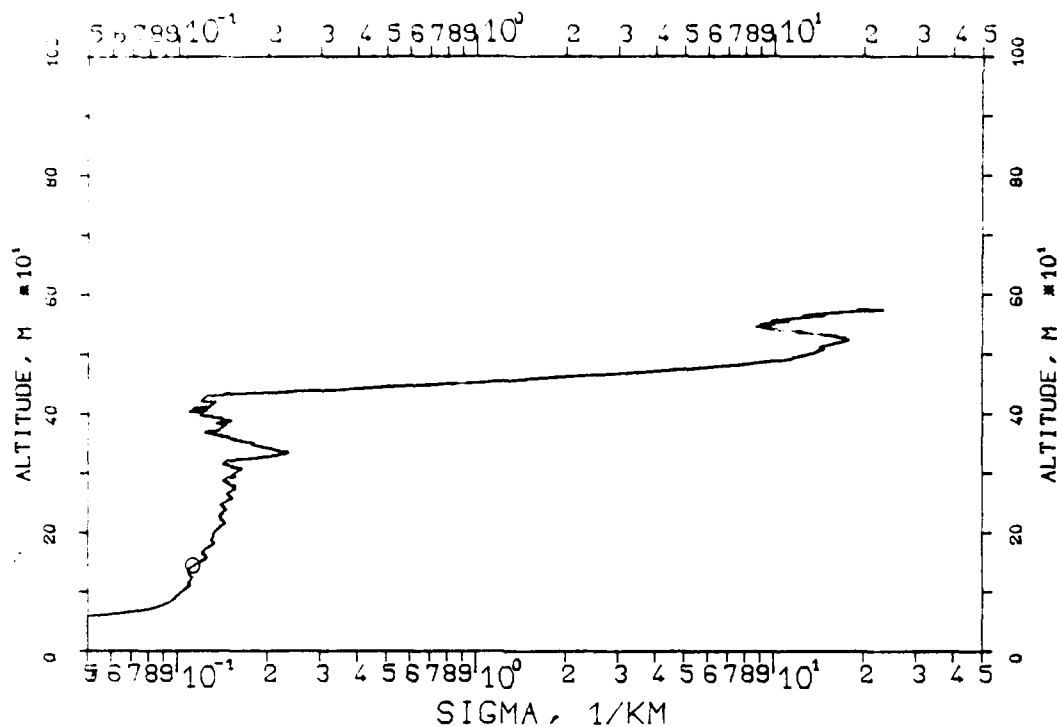


FIG. 7.249
KLETT-PROFILE ,0694NM,EL.30DG00MN
841203, 12:57-12:58,CET
RM=1.162KM,SM=20.0000/KM,K=1.000

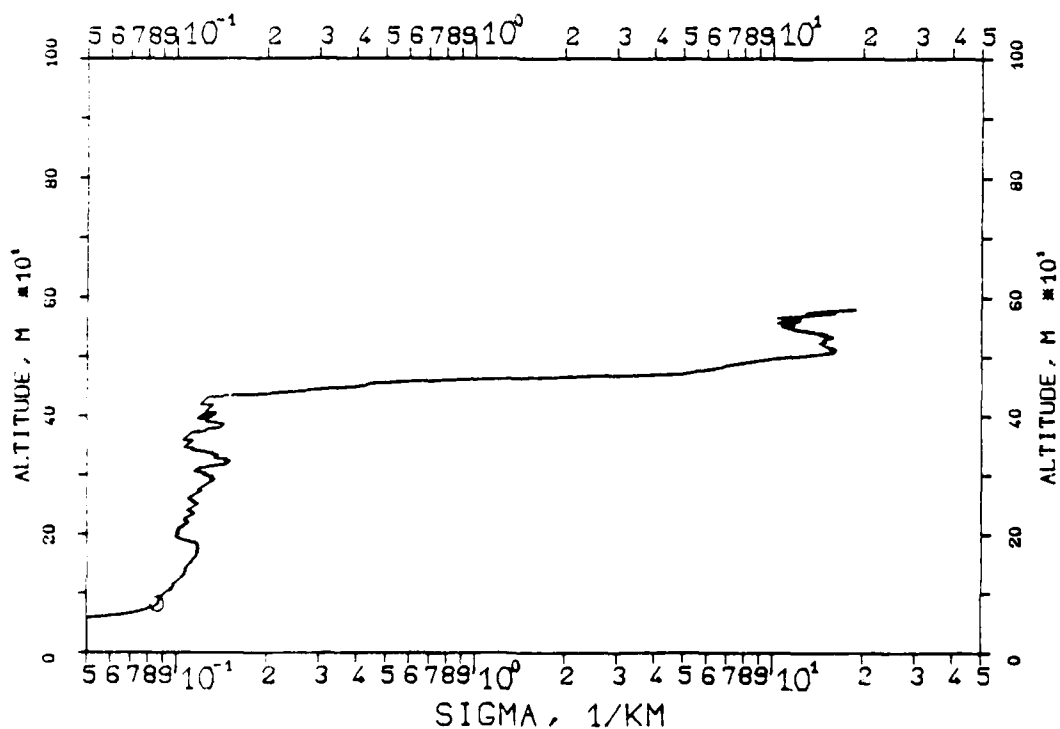


FIG. 7.250
 KLETT PROFILE, 0694NM, EL. 30DG00MN
 841203, 13:02-13:02, CET
 RM=0.829KM, SM=20.0000/KM, K=1.000

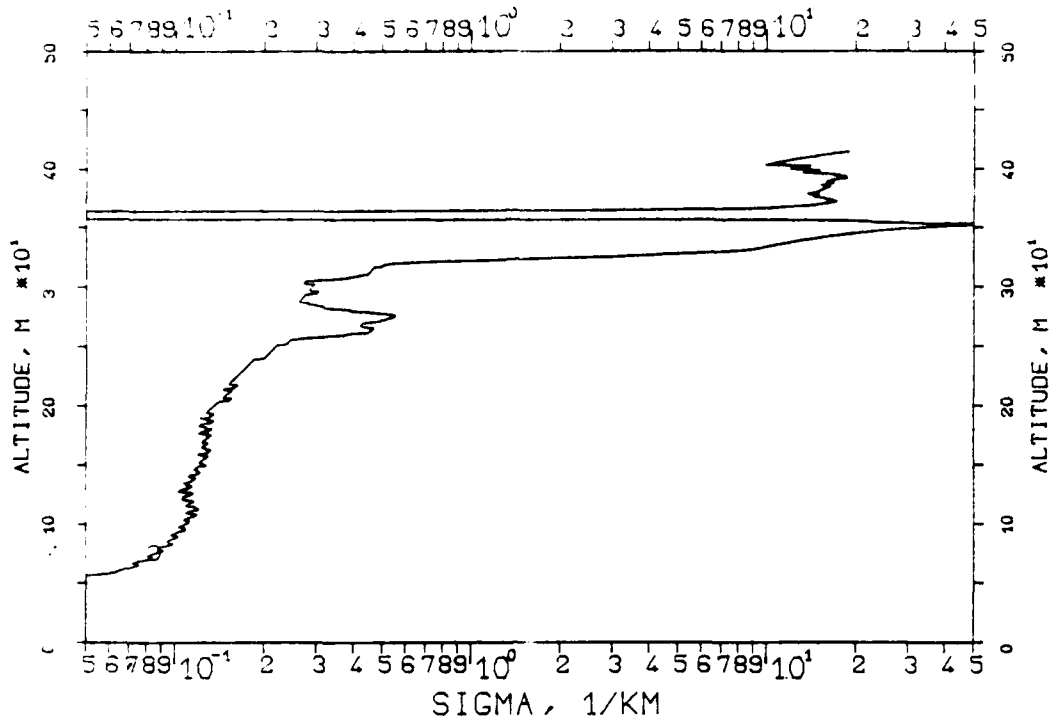


FIG. 7.251
 KLETT PROFILE, 0694NM, EL. 30DG00MN
 841203, 13:03-13:03, CET
 RM=0.862KM, SM=20.0000/KM, K=1.000

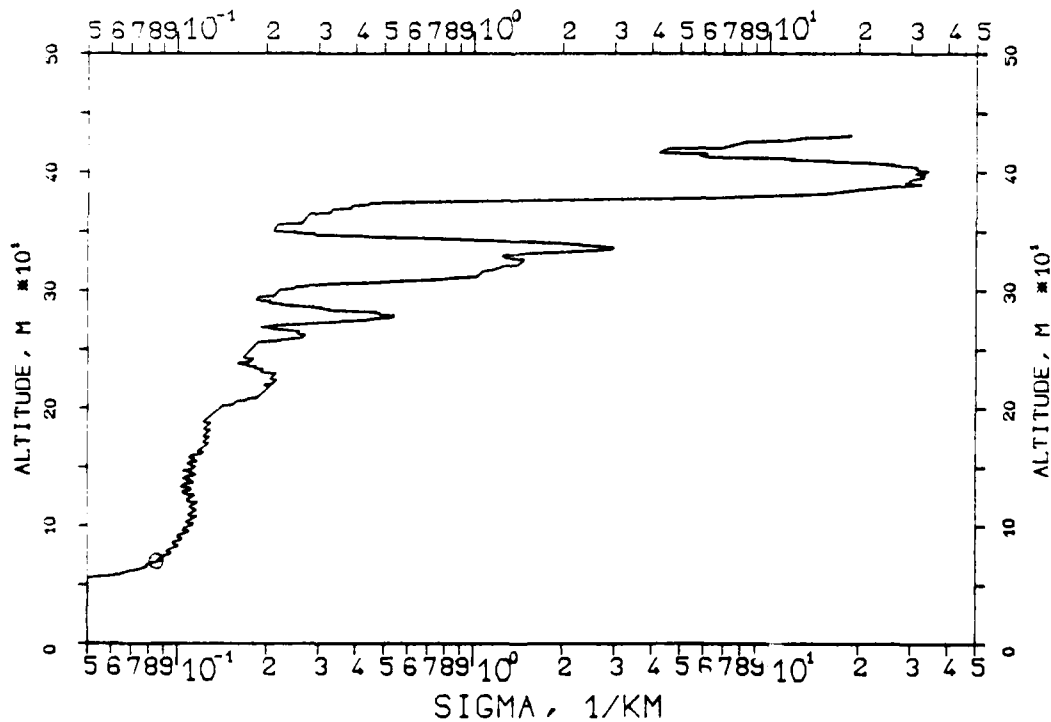


FIG. 7.252

KLETT-PROFILE, 0694NM, EL. 30DG00MN

841203, 13:04-13:05, CET

RM=0.744KM, SM=20.0000/KM, K=1.000

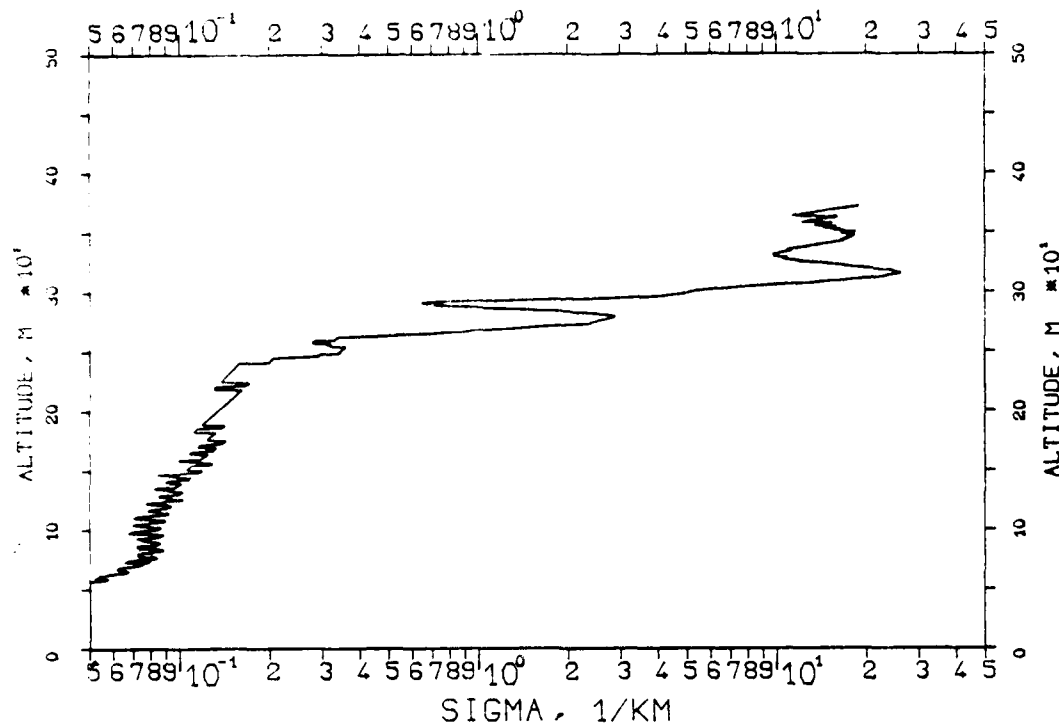


FIG. 7.253

KLETT-PROFILE, 0694NM, EL. 30DG00MN

841203, 13:05-13:06, CET

RM=0.688KM, SM=20.0000/KM, K=1.000

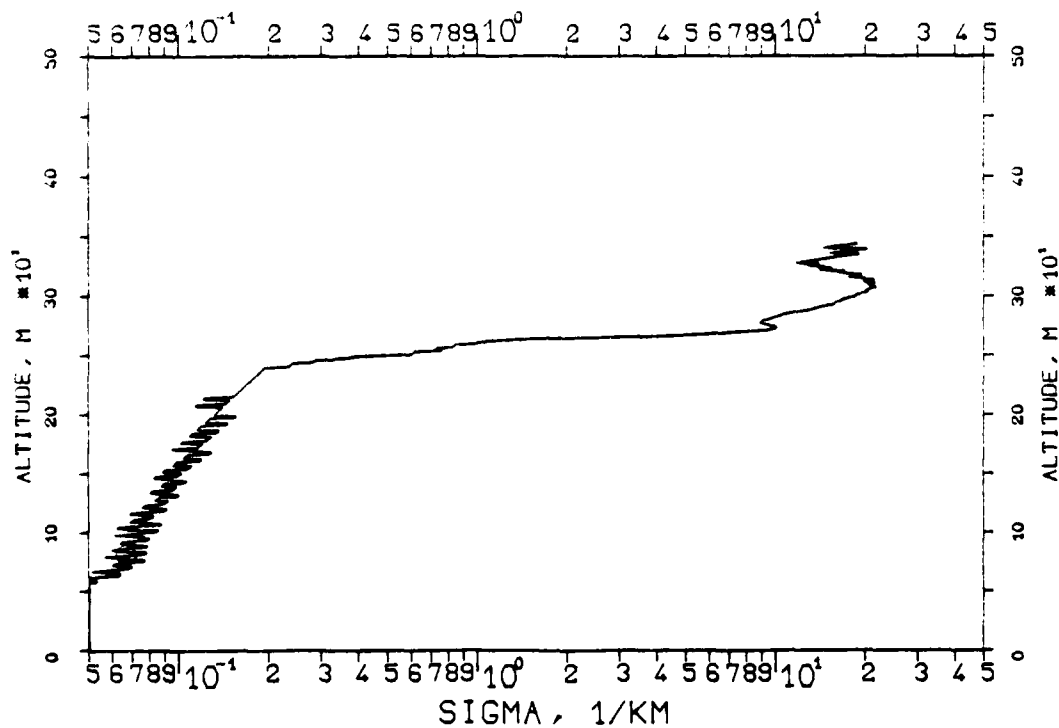


FIG. 7.254
 KLETT PROFILE, 0694NM, EL. 30DG00MN
 841203, 13:06-13:06, CET
 RM=0.678KM, SM=20.0000/KM, K=1.000

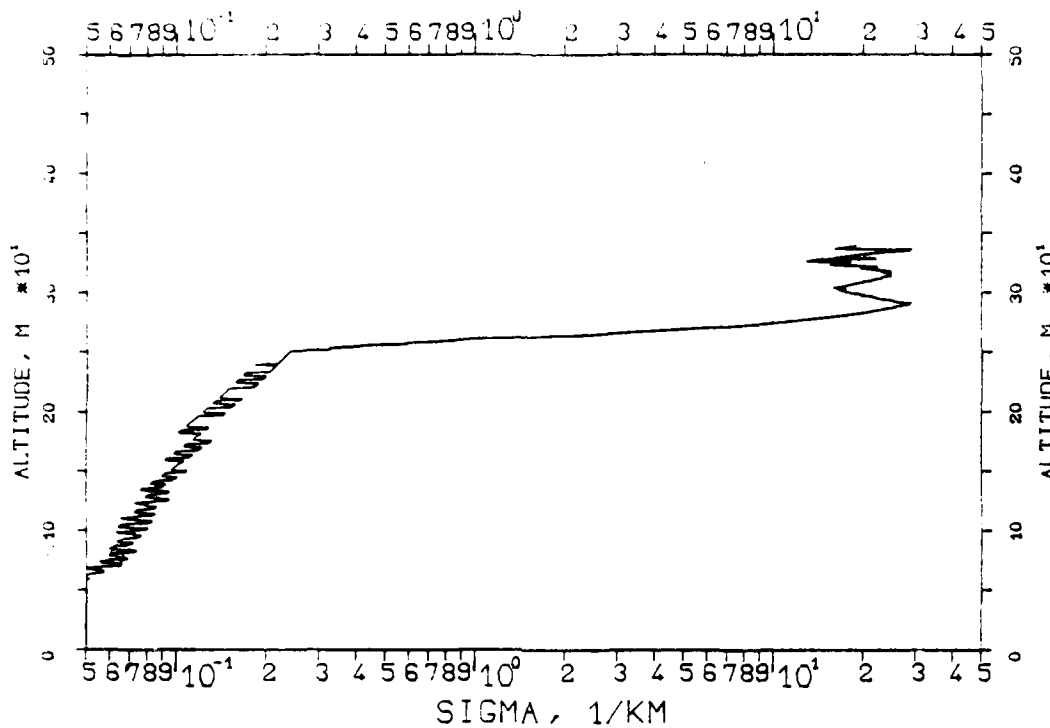


FIG. 7.255
 KLETT PROFILE, 0694NM, EL. 30DG00MN
 841203, 13:07-13:07, CET
 RM=0.600KM, SM=20.0000/KM, K=1.000

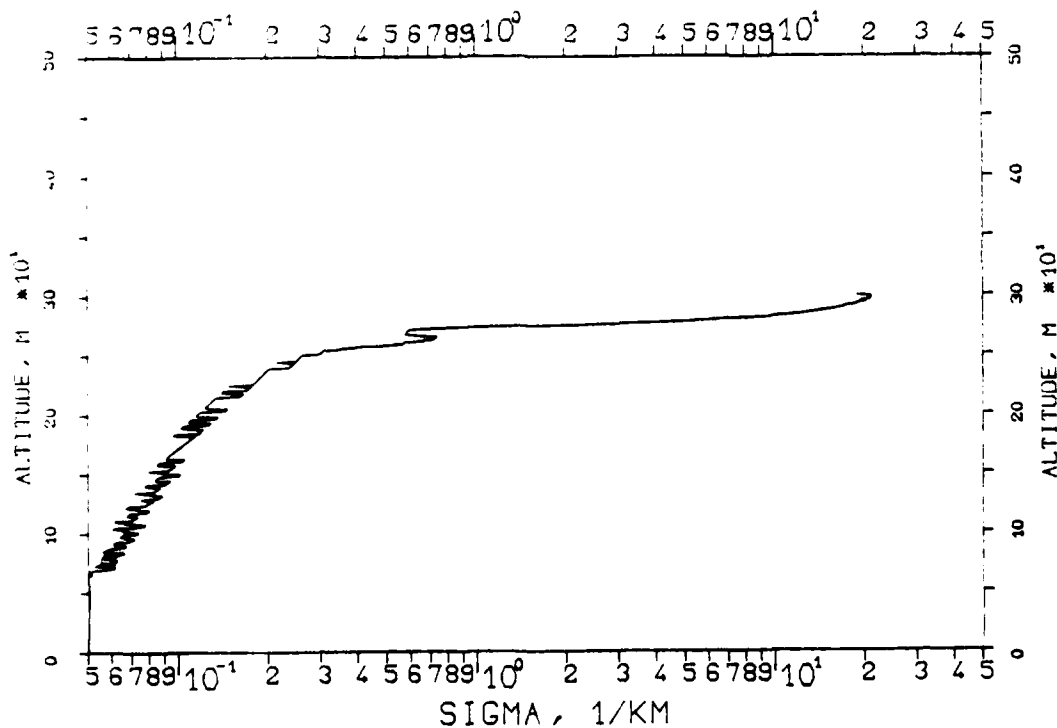


FIG. 7.256
KLETT-PROFILE, 0694NM, EL. 30CG00MN
841203, 13:08-13:08, CET
RM=0.84 KM, SM=20.0000/KM, K=1.000

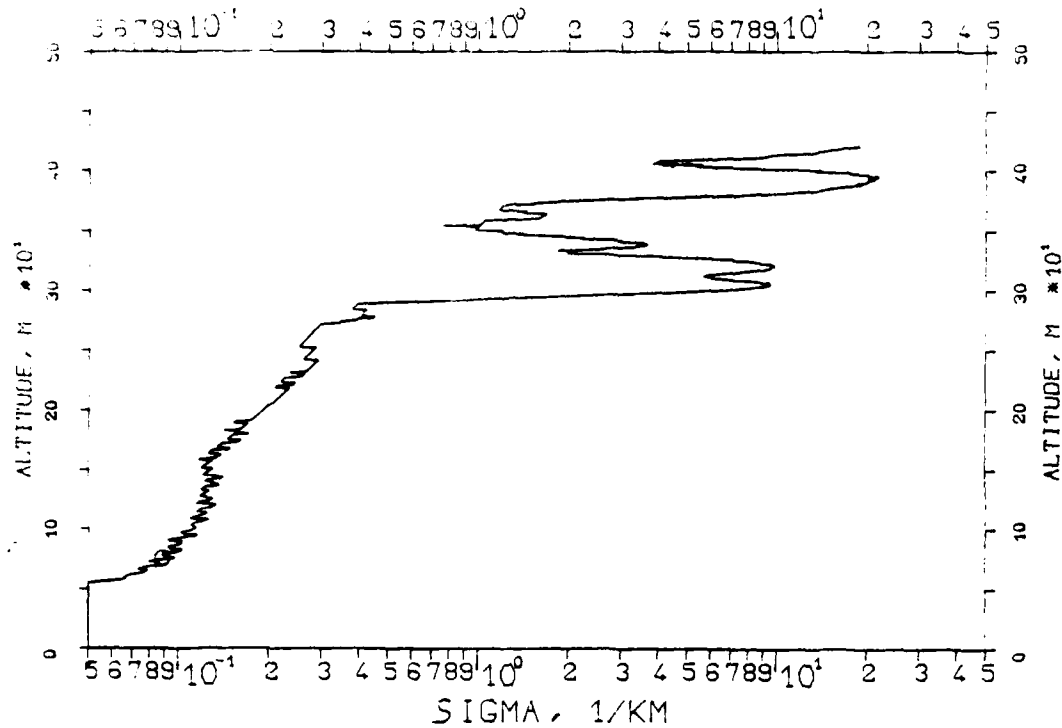


FIG. 7.257
KLETT-PROFILE, 0694NM, EL. 10DG00MN
841204, 11:04-11:04, CET
RM=0.720KM, SM=20.0000/KM, K=1.000

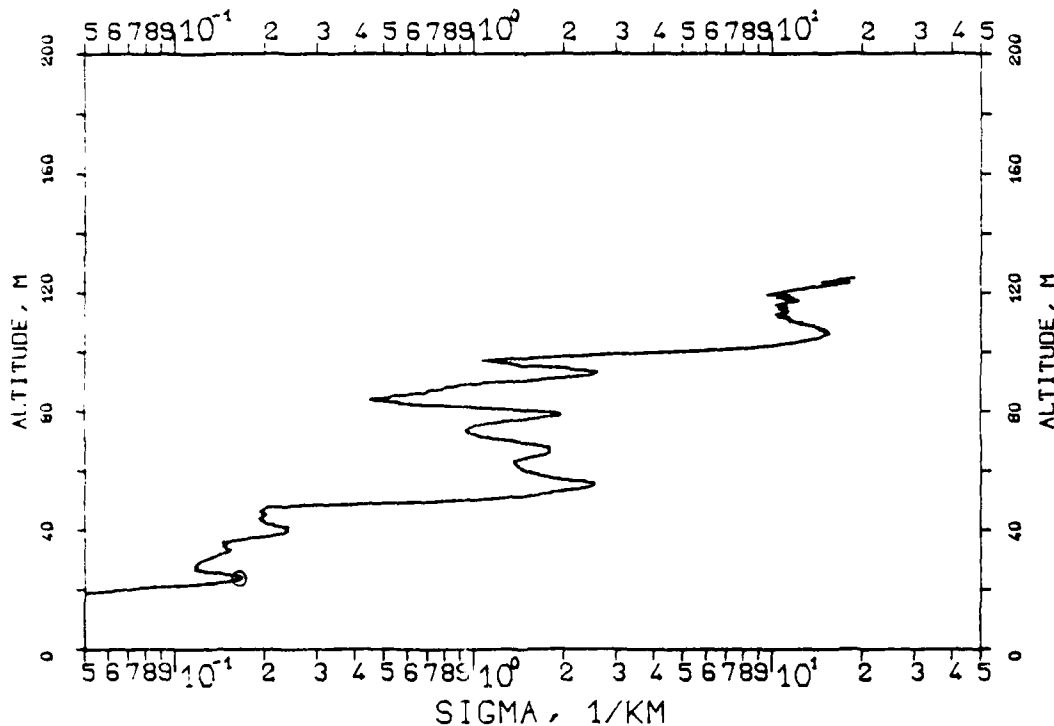


FIG. 7.258
KLETT-PROFILE, 0694NM, EL. 10DG00MN
841204, 11:04-11:05, CET
RM=0.747KM, SM=20.0000/KM, K=1.000

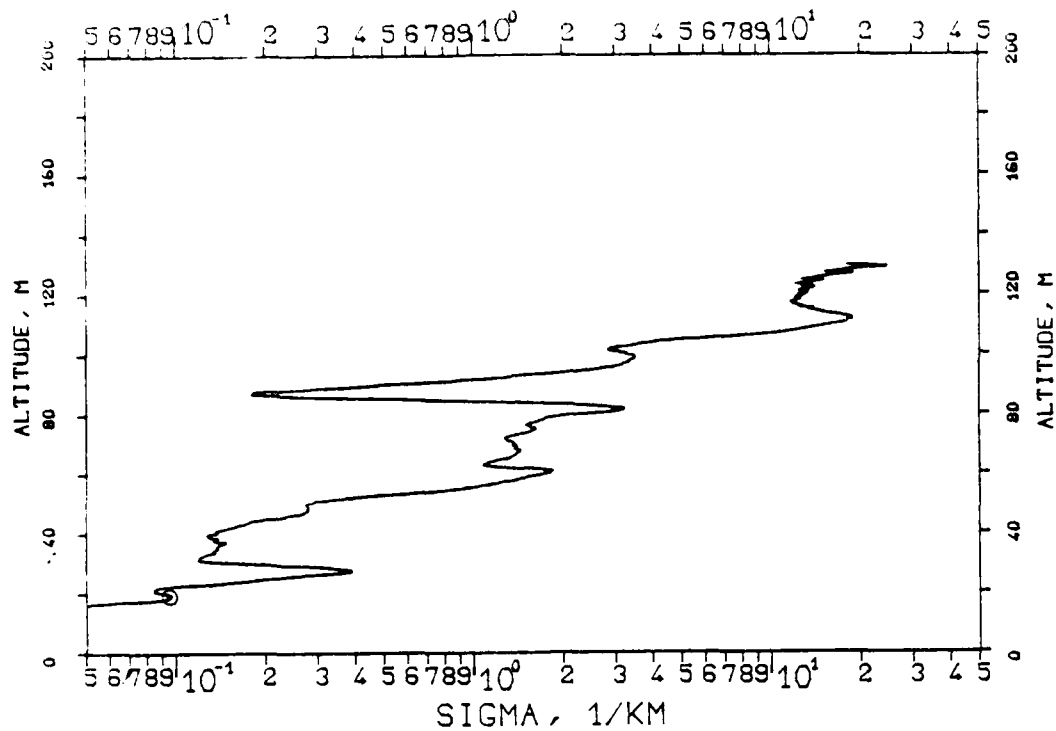


FIG. 7.259
KLETT-PROFILE, 0694NM, EL. 10DG00MN
841204, 11:05-11:06, CET
RM=0.724KM, SM=20.0000/KM, K=1.000

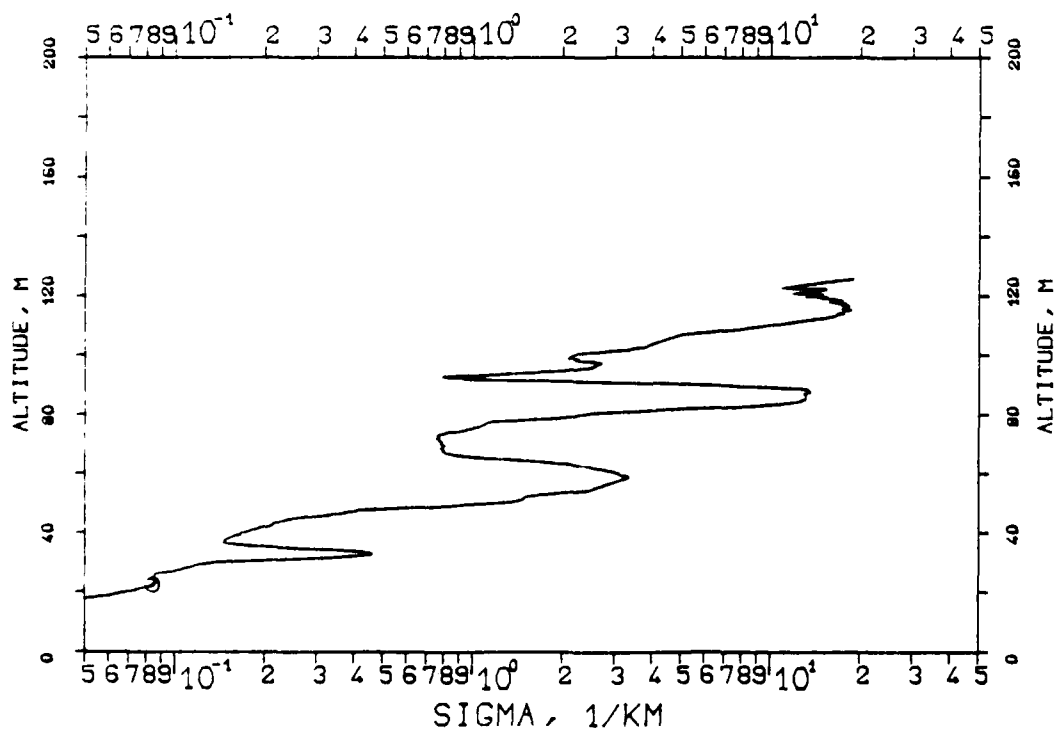


FIG. 7.260
KLETT-PROFILE ,0694NM,EL. 10DG00MN
841204, 11:06-11:07,CET
RM=0.655KM,SM=20.0000/KM,K=1.000

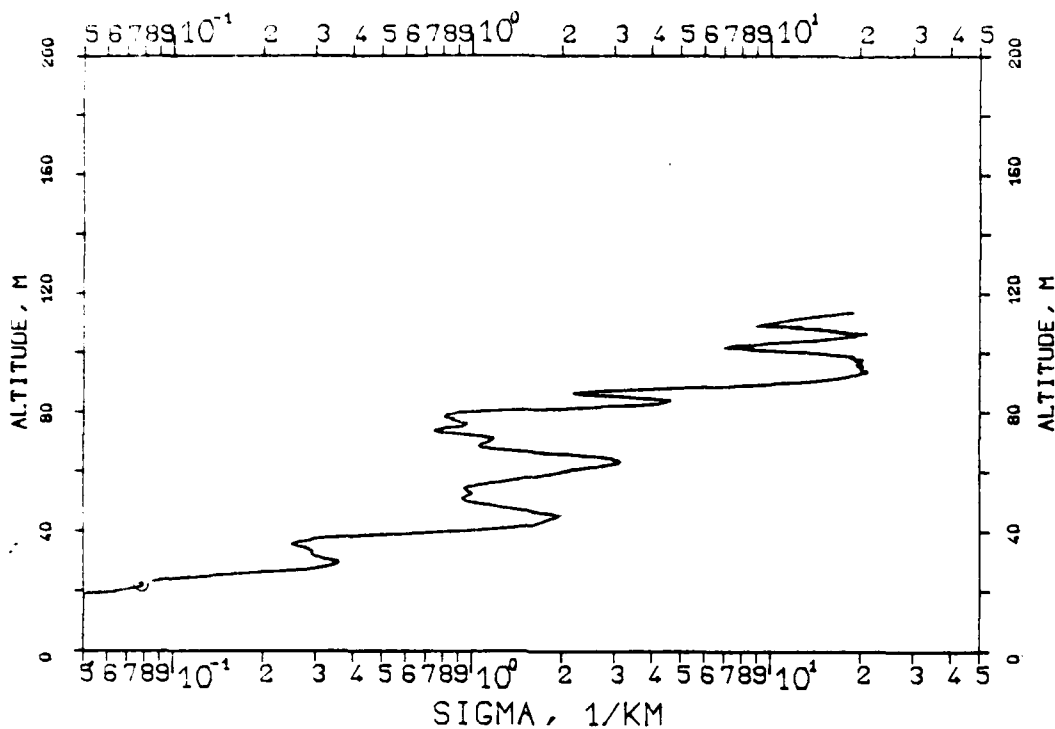


FIG. 7.261
KLETT-PROFILE ,0694NM,EL. 10DG00MN
841204, 11:08-11:08,CET
RM=0.718KM,SM=20.0000/KM,K=1.000

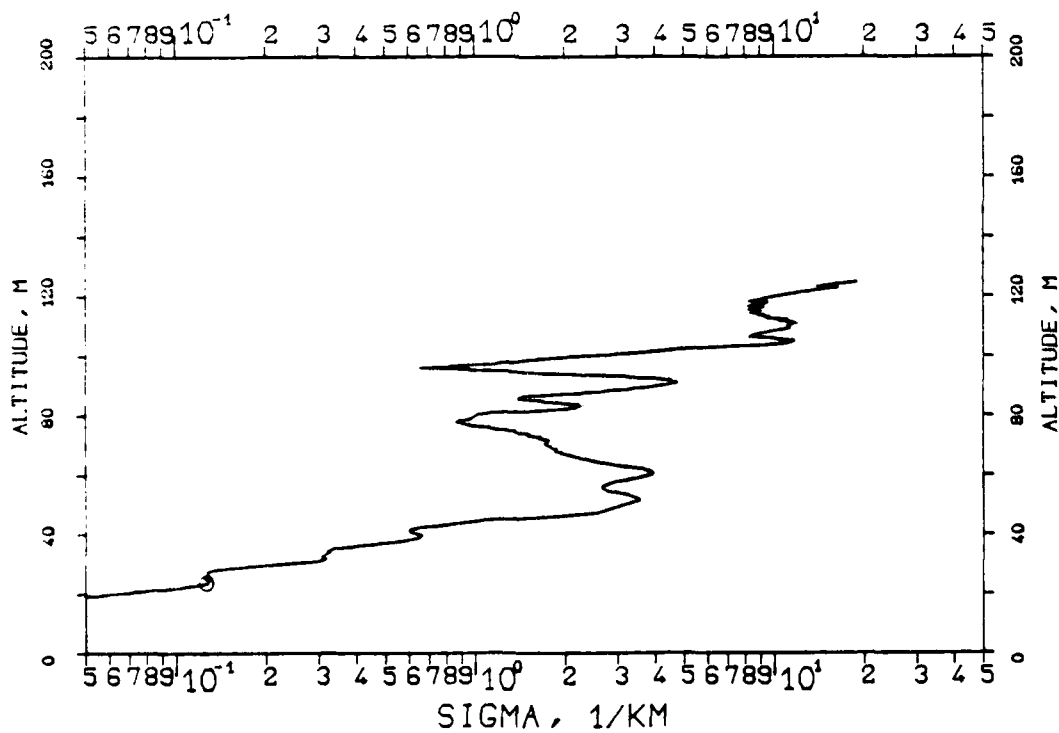


FIG. 7.262
KLETT-PROFILE, 0694NM, EL. 10DG00MN
841204, 11:21-11:22, CET
RM=0.753KM, SM=20.0000/KM, K=1.000

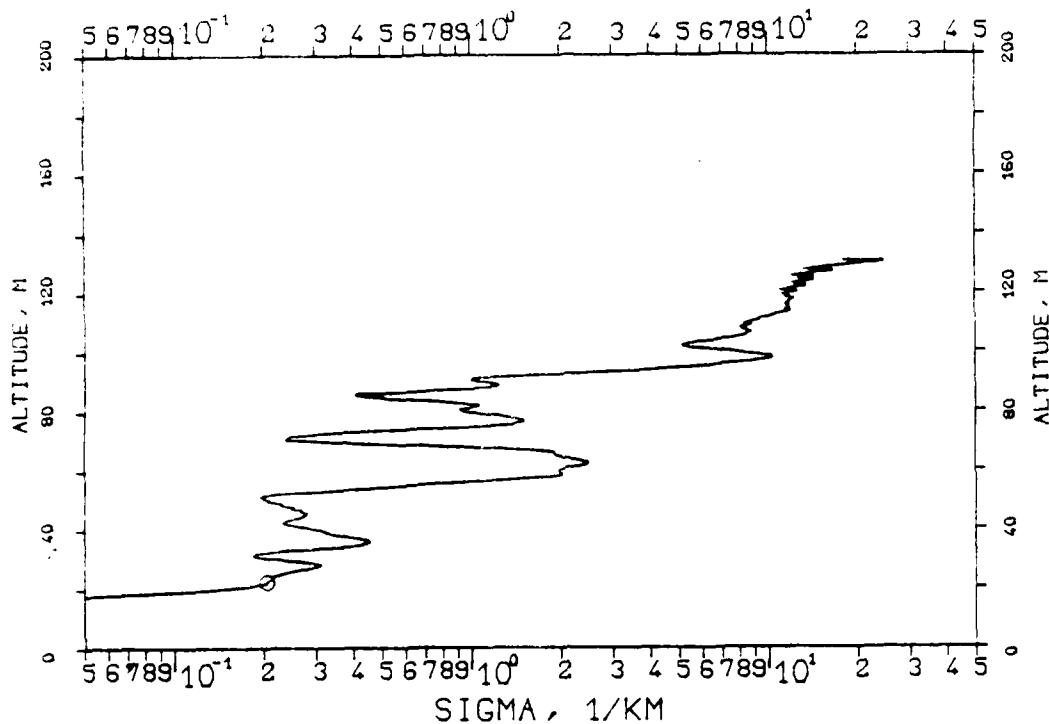


FIG. 7.263
KLETT-PROFILE, 0694NM, EL. 10DG00MN
841204, 11:23-11:23, CET
RM=0.733KM, SM=20.0000/KM, K=1.000

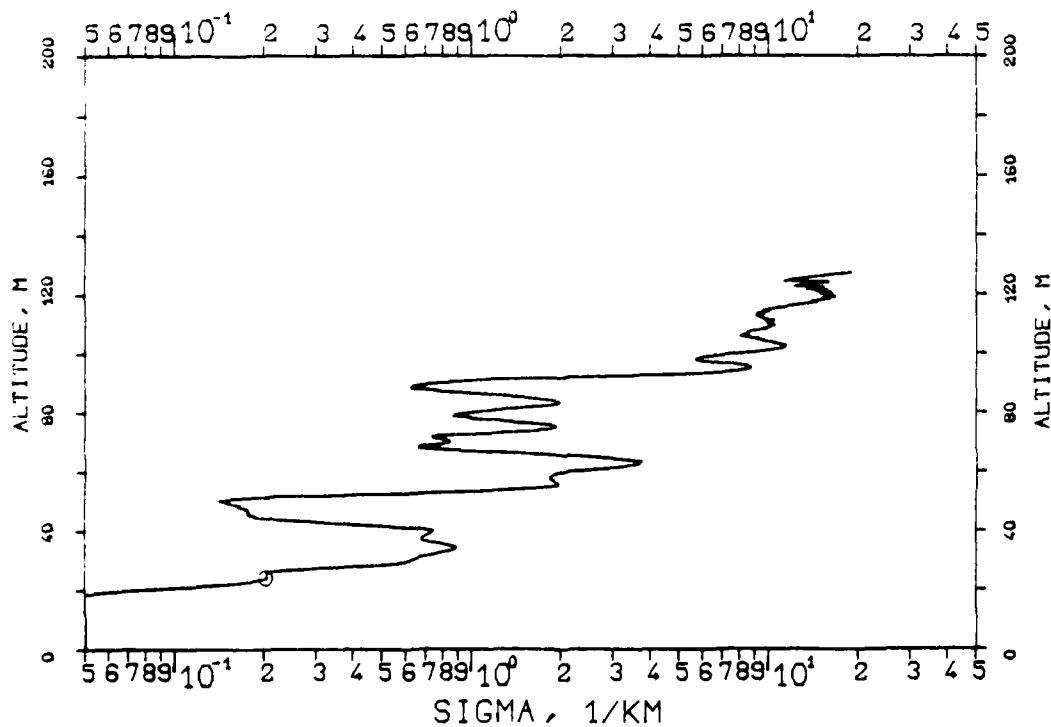


FIG. 7.264
KLETT-PROFILE, 0694NM, EL. 10DG00MN
841204, 11:24-11:24, CET
RM=0.703KM, SM=20.0000/KM, K=1.000

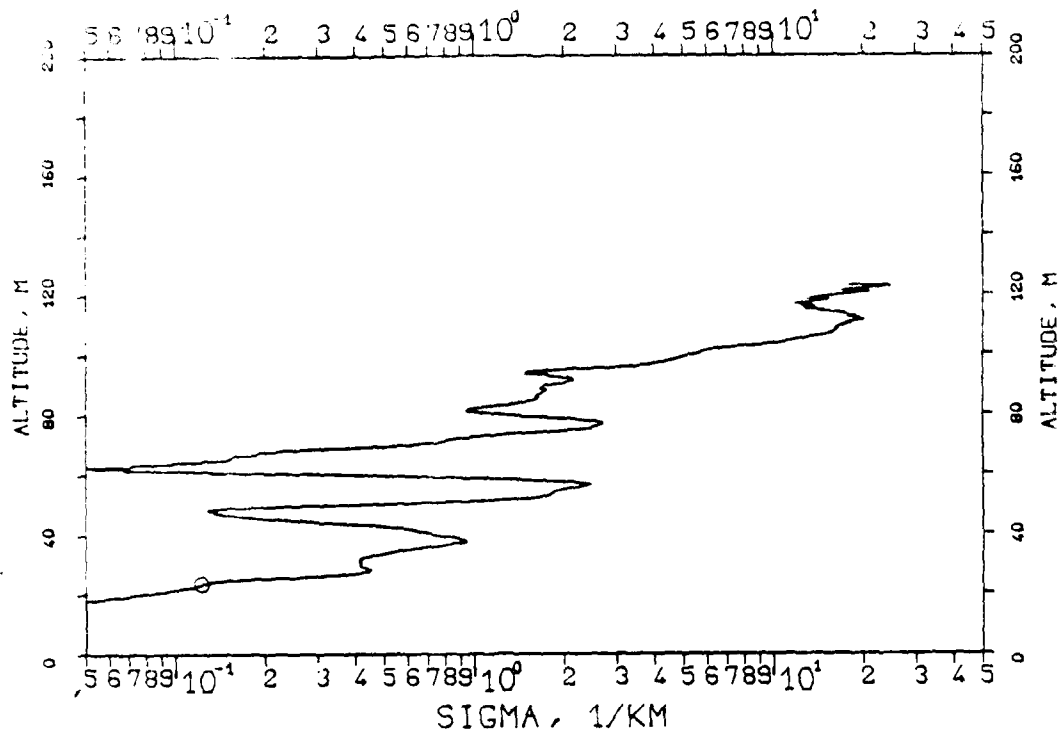


FIG. 7.265
KLETT-PROFILE, 0694NM, EL. 10DG00MN
841204, 11:25-11:25, CET
RM=0.702KM, SM=20.0000/KM, K=1.000

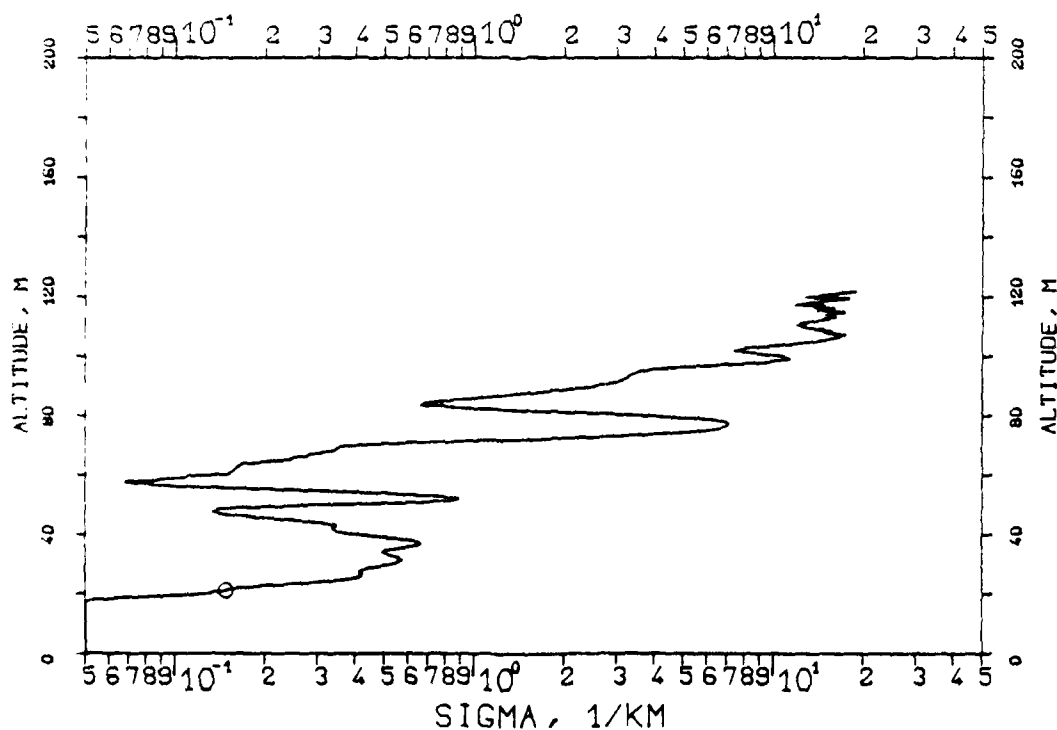


FIG. 7.266
 KLETT-PROFILE, 0694NM, FL. 10DG00MN
 8.1104, 11:26-11:26, CET
 RM=0.682KM, SM=20.0000/KM, K=1.000

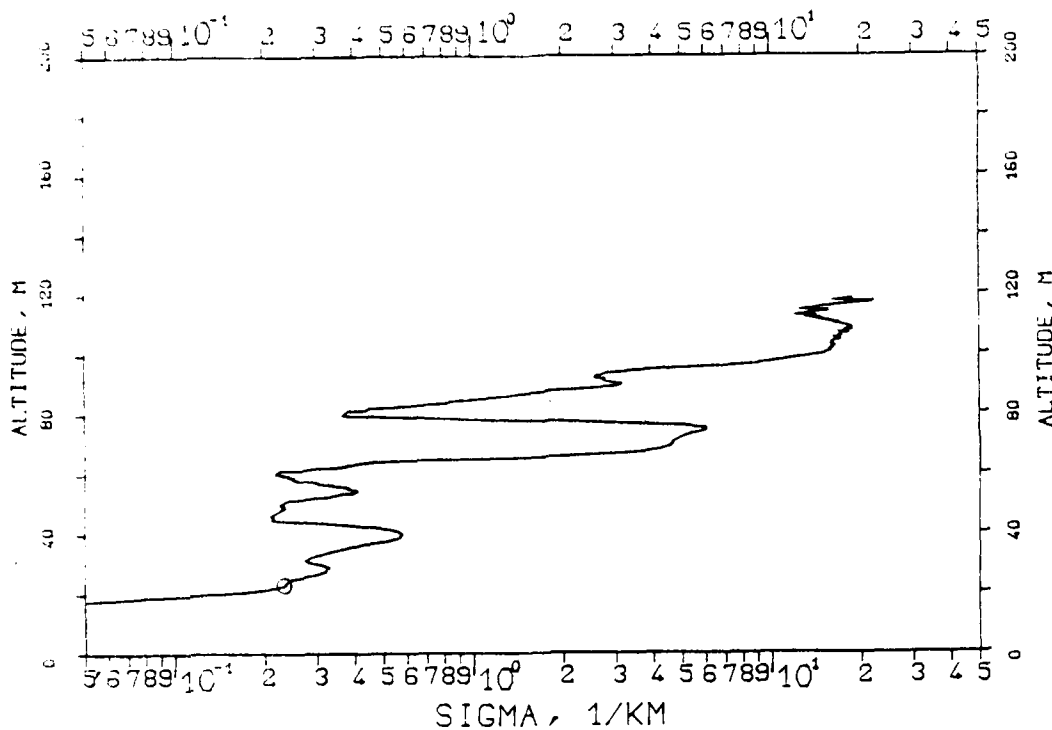


FIG. 7.267
 KLETT-PROFILE, 0694NM, EL. 10DG00MN
 8.1204, 11:51-11:52, CET
 RM=0.648KM, SM=20.0000/KM, K=1.000

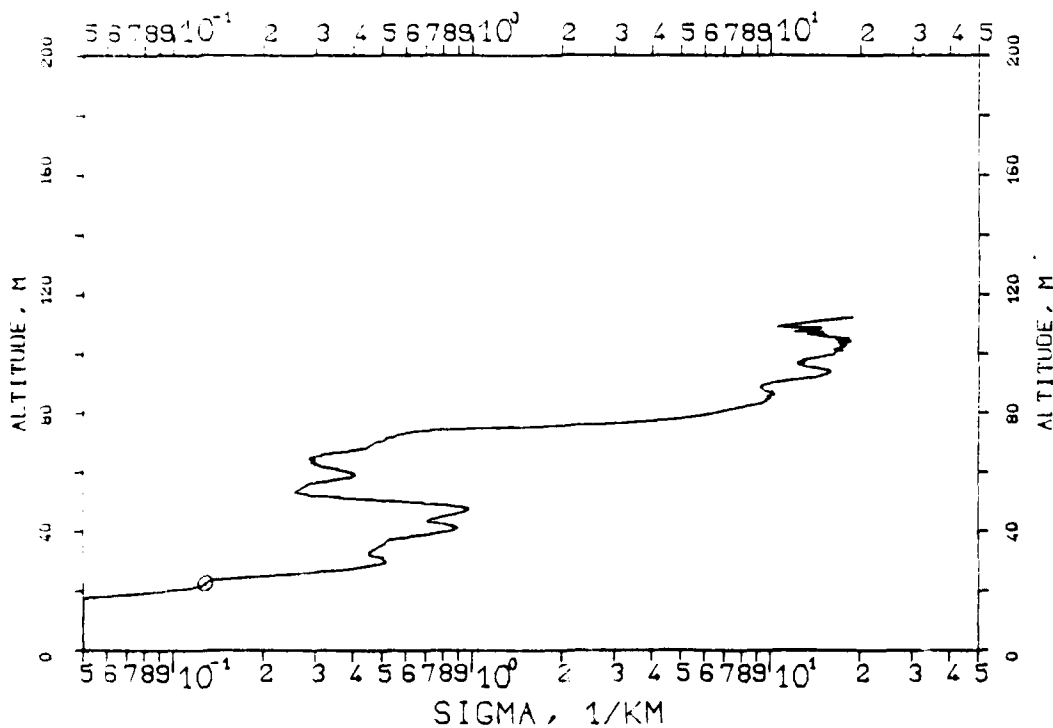


FIG. 7.268
 KLETT-PROFILE, 0694NM, EL. 10DG00MN
 841204, 11:53-11:53, CET
 RM=0.661KM, SM=20.0000/KM, K=1.000

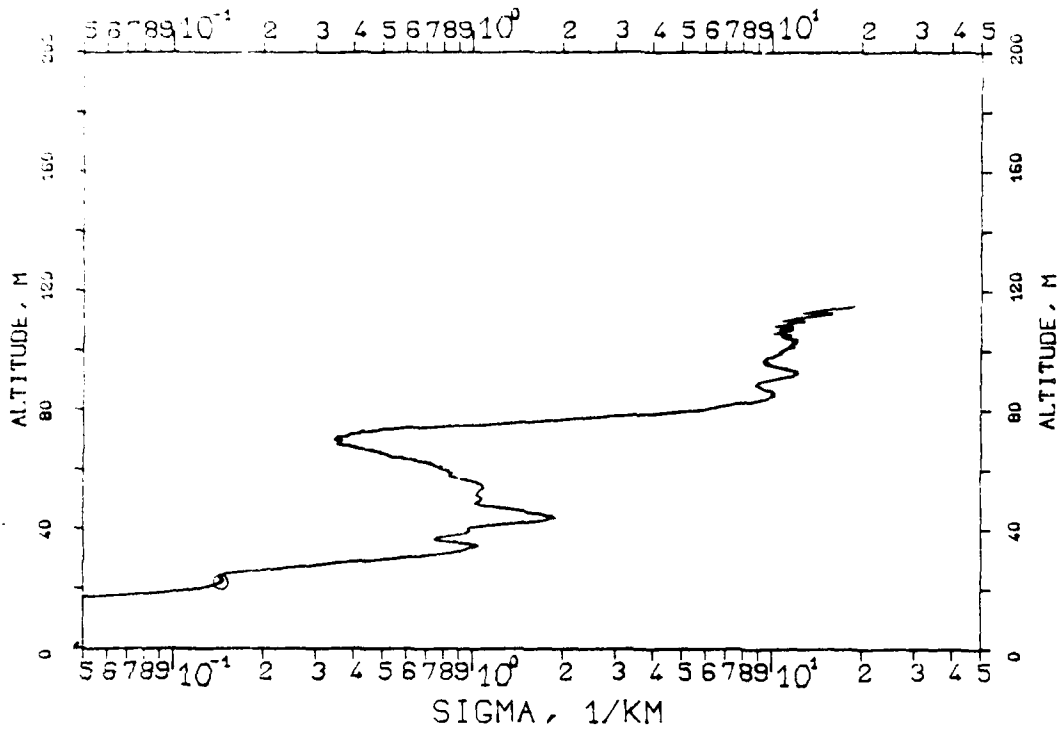
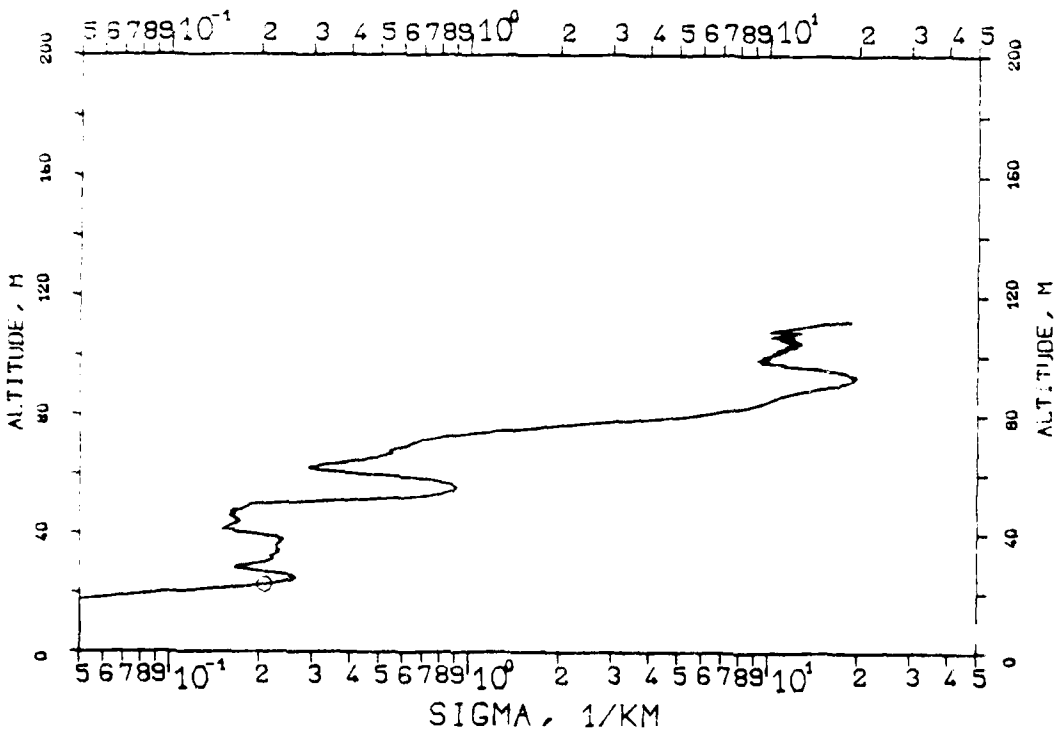


FIG. 7.269
 KLETT-PROFILE, 0694NM, EL. 10DG00MN
 841204, 11:56-11:57, CET
 RM=0.645KM, SM=20.0000/KM, K=1.000



AD-A154 714

VISIBILITY AND VERTICAL STRUCTURE MEASUREMENTS IN
SOUTHERN GERMANY(U) FRAUNHOFER-INST FUER
ATMOSPHAERISCHE UMWELTFORSCHUNG GARMISCH.

3/3

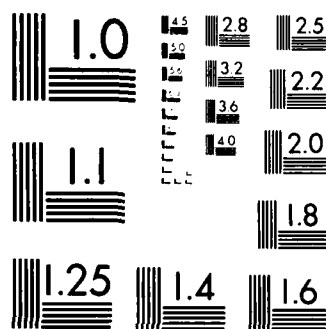
UNCLASSIFIED

R REITER ET AL. DEC 84 DAJA45-83-C-0023

F/G 4/2

NL





MICROCOPY RESOLUTION TEST CHART
NATIONAL BUREAU OF STANDARDS 1963-A

FIG. 7.270
 KLETT-PROFILE, 0694NM, EL. 10DG00MN
 841204, 11:57-11:57, CET
 RM=0.657KM, SM=20.0000/KM, K=1.000

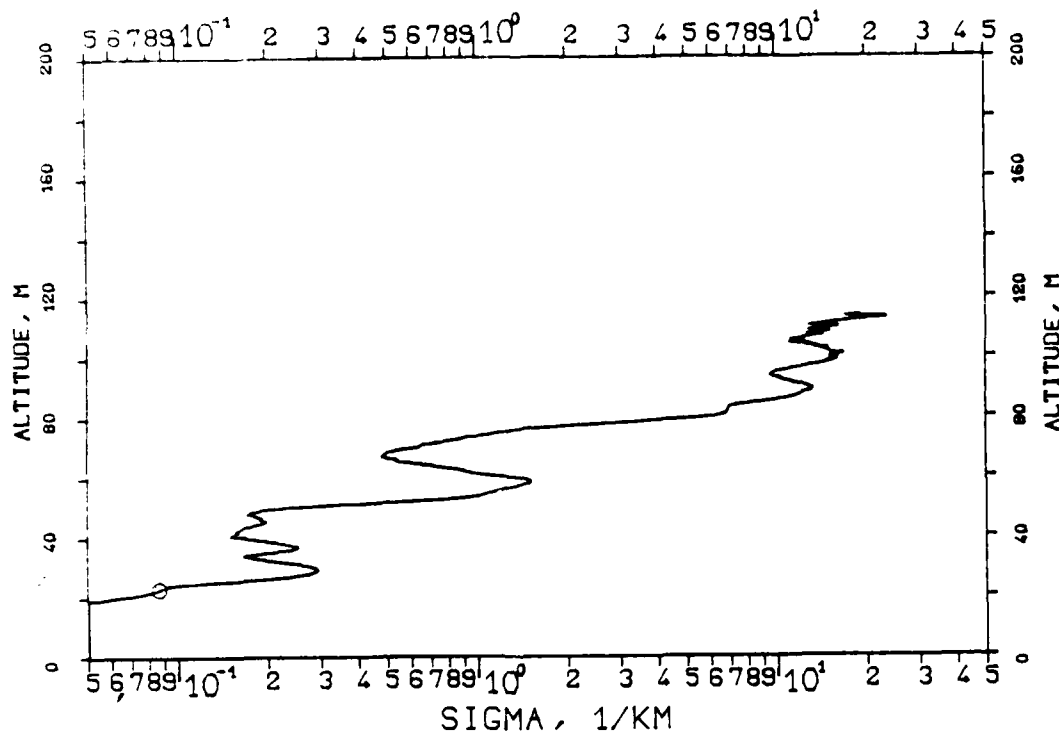


FIG. 7.271
 KLETT-PROFILE, 0694NM, EL. 10DG00MN
 841204, 11:58-11:58, CET
 RM=0.669KM, SM=20.0000/KM, K=1.000

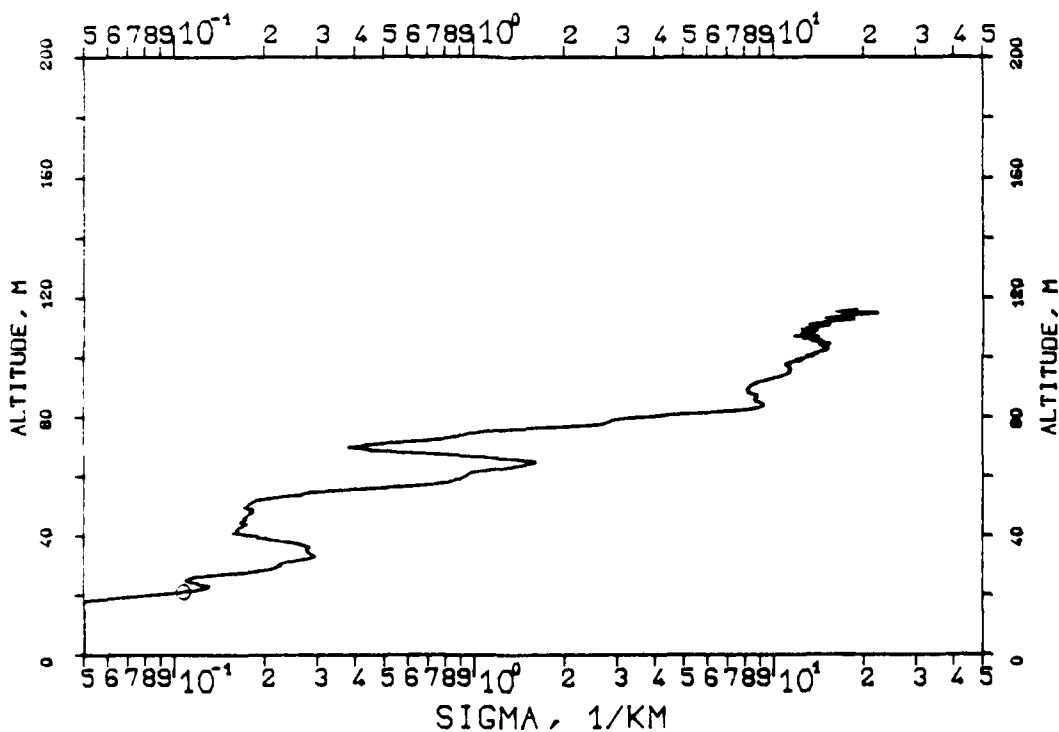


FIG. 7.272
 KLETT-PROFILE, 0694NM, EL. 10DG00MN
 841204, 12:36-12:36, CET
 RM=0.616KM, SM=20.0000/KM, K=1.000

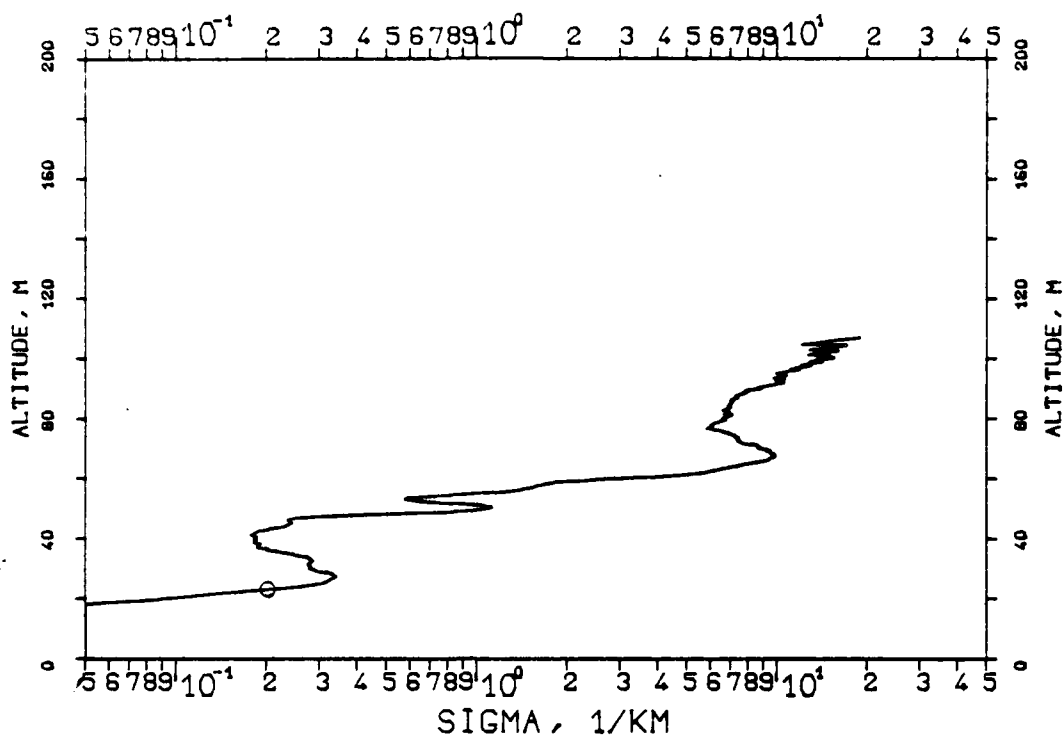


FIG. 7.273
 KLETT-PROFILE, 0694NM, EL. 10DG00MN
 841204, 12:39-12:39, CET
 RM=0.603KM, SM=20.0000/KM, K=1.000

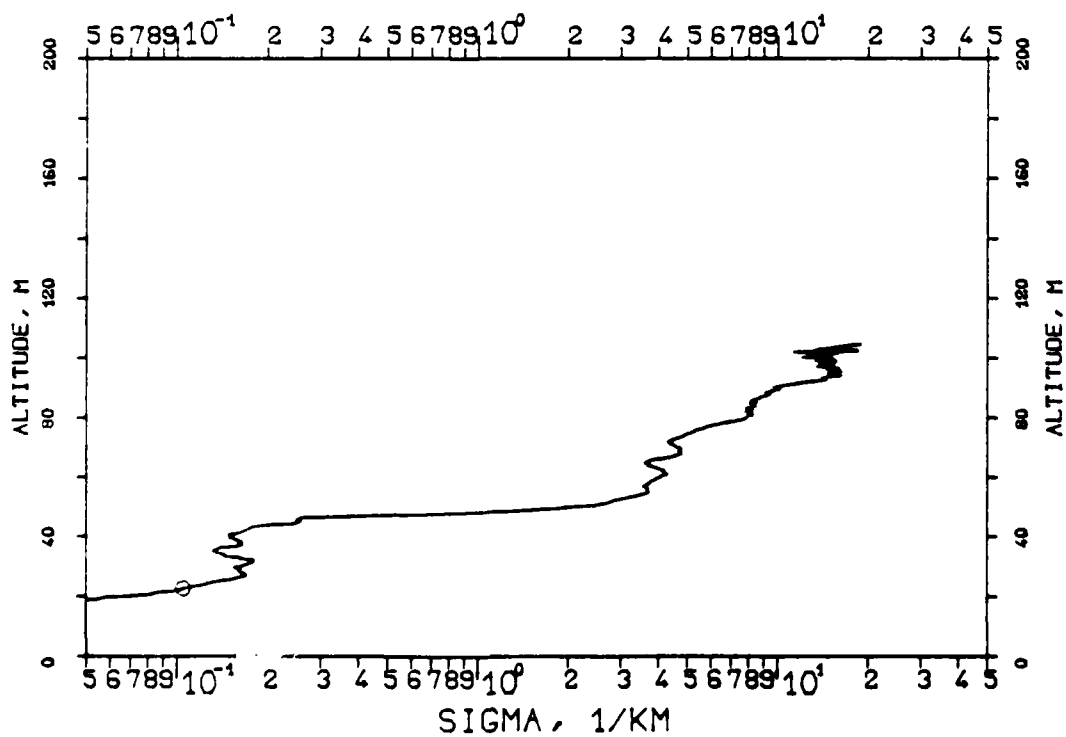


FIG. 7.274
KLETT-PROFILE, 0694NM, EL. 10DG00MN
841204, 12:40-12:40, CET
RM=0.610KM, SM=20.0000/KM, K=1.000

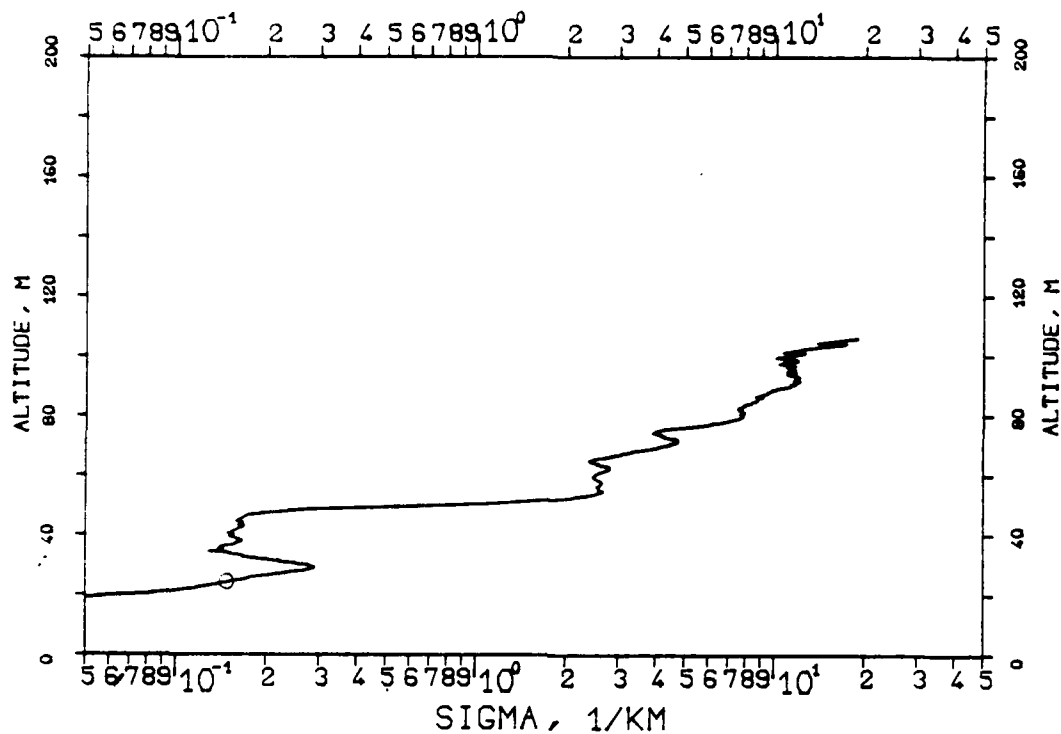


FIG. 7.275
KLETT-PROFILE, 0694NM, EL. 10DG00MN
841204, 12:41-12:41, CET
RM=0.636KM, SM=20.0000/KM, K=1.000

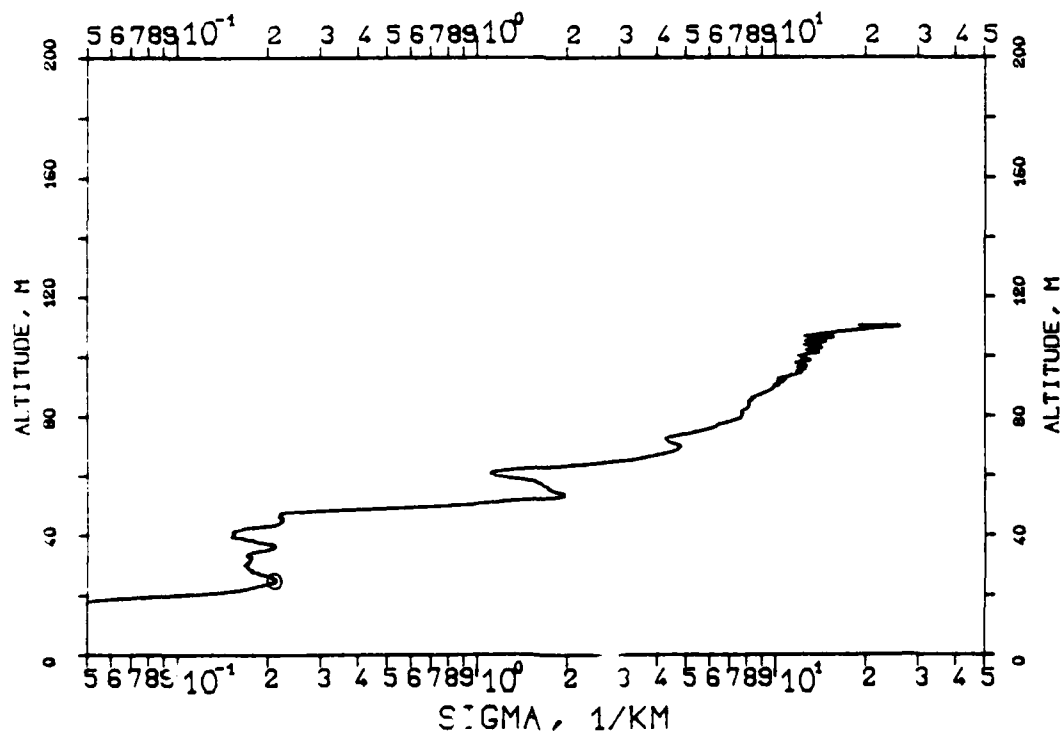


FIG. 7.276
KLETT-PROFILE, 0694NM, EL. 10DG00MN
841204, 13:06-13:07, CET
RM=0.690KM, SM=20.0000/KM, K=1.000

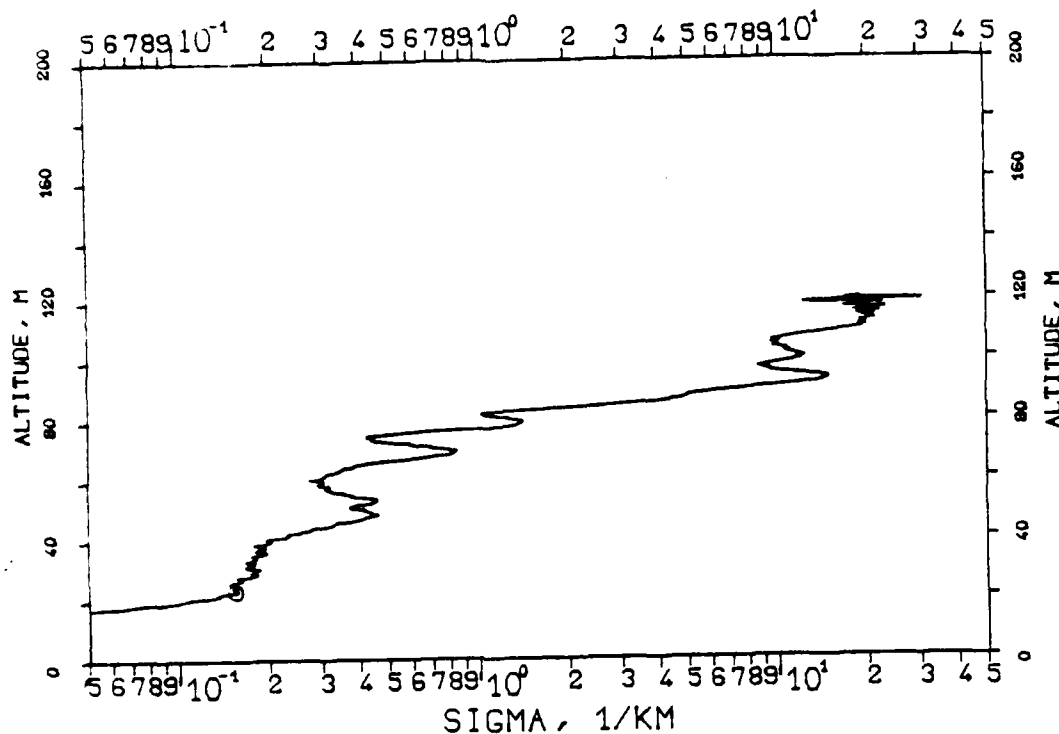


FIG. 7.277
KLETT-PROFILE, 0694NM, EL. 10DG00MN
841204, 13:07-13:08, CET
RM=0.690KM, SM=20.0000/KM, K=1.000

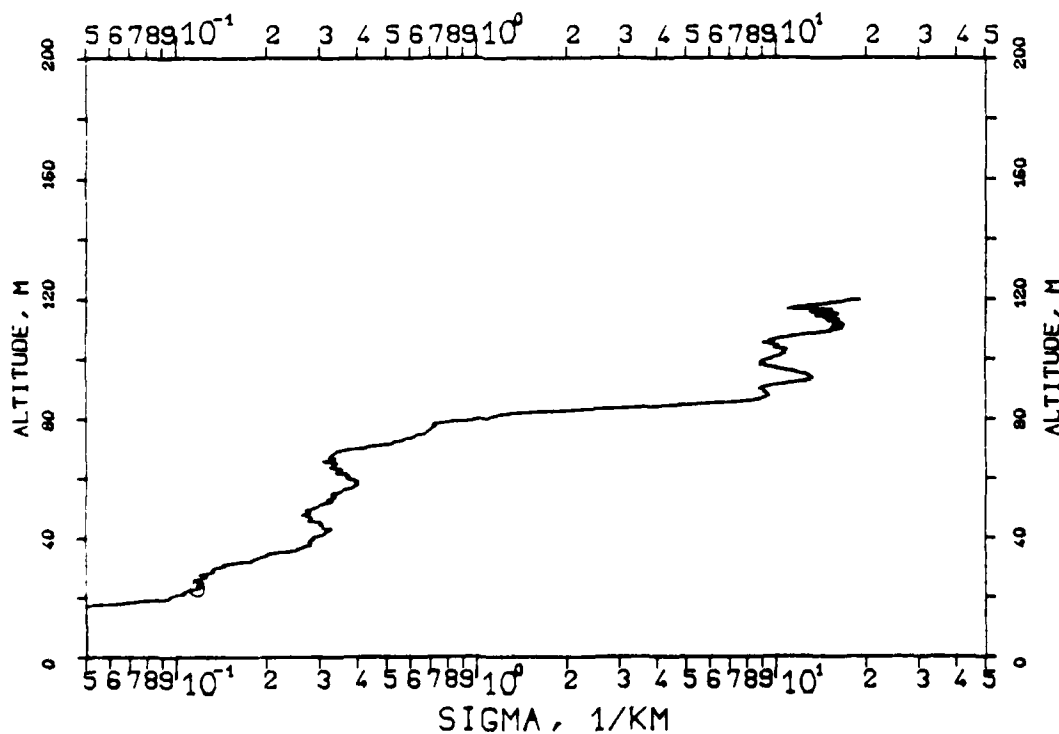


FIG. 7.278
KLETT-PROFILE, 0694NM, EL. 10DG00MN
841204, 13:08-13:08, CET
RM=0.663KM, SM=20.0000/KM, K=1.000

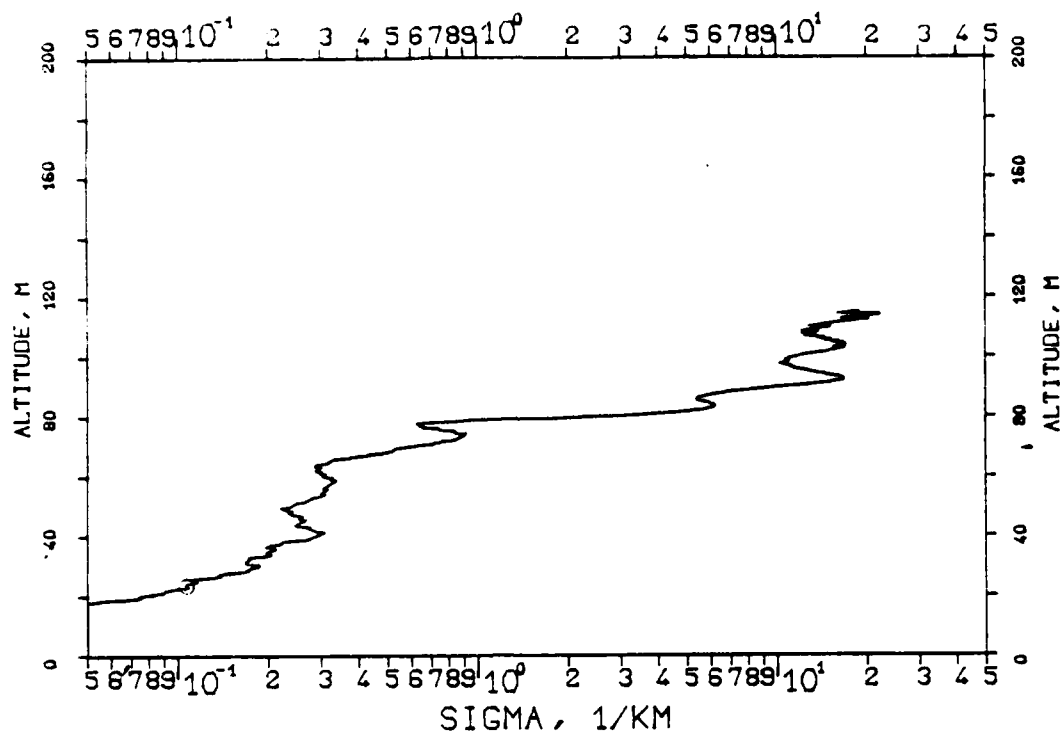


FIG. 7.279
KLETT-PROFILE, 0694NM, EL. 10DG00MN
841204, 13:09-13:09, CET
RM=0.660KM, SM=20.0000/KM, K=1.000

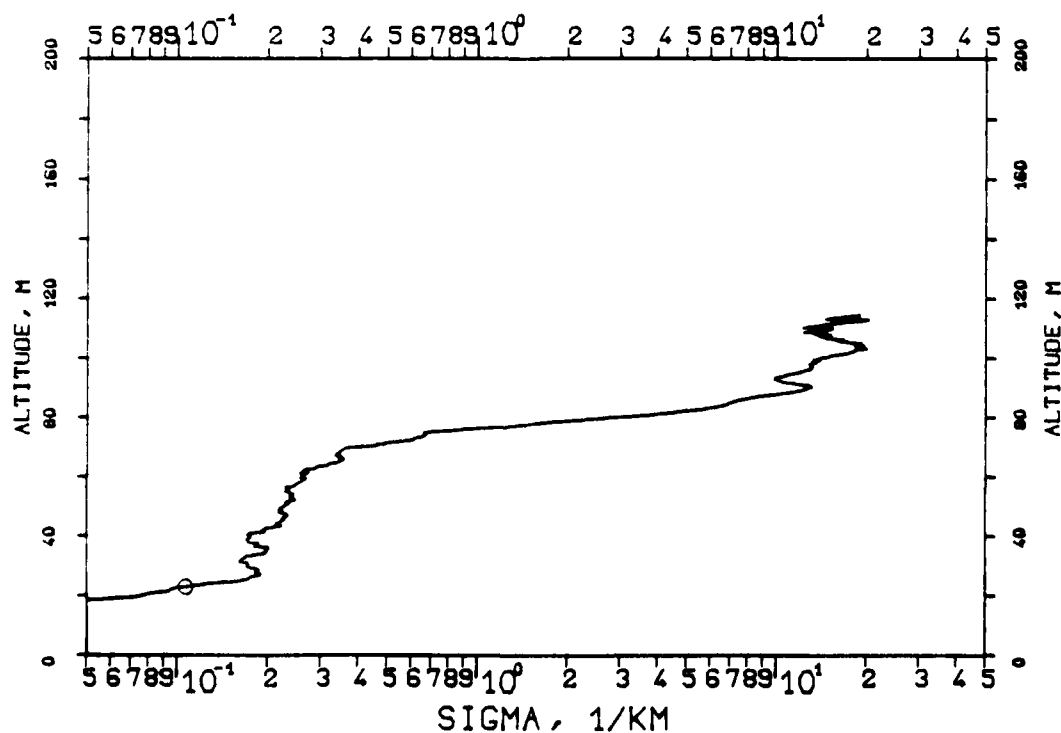


FIG. 7.280
KLETT-PROFILE, 0694NM, EL. 10DG00MN
841204, 13:10-13:10, CET
RM=0.654KM, SM=20.0000/KM, K=1.000

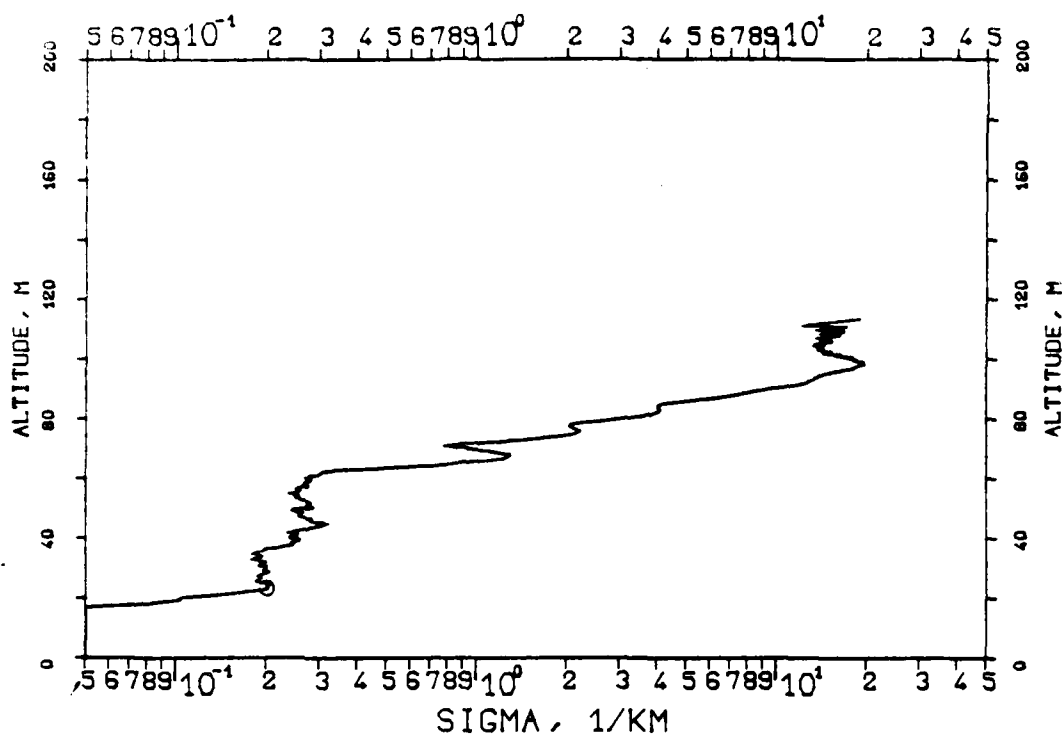


FIG. 7.281
KLETT-PROFILE, 0694NM, EL. 15DG00MN
841204, 13:12-13:12, CET
RM=0.510KM, SM=20.0000/KM, K=1.000

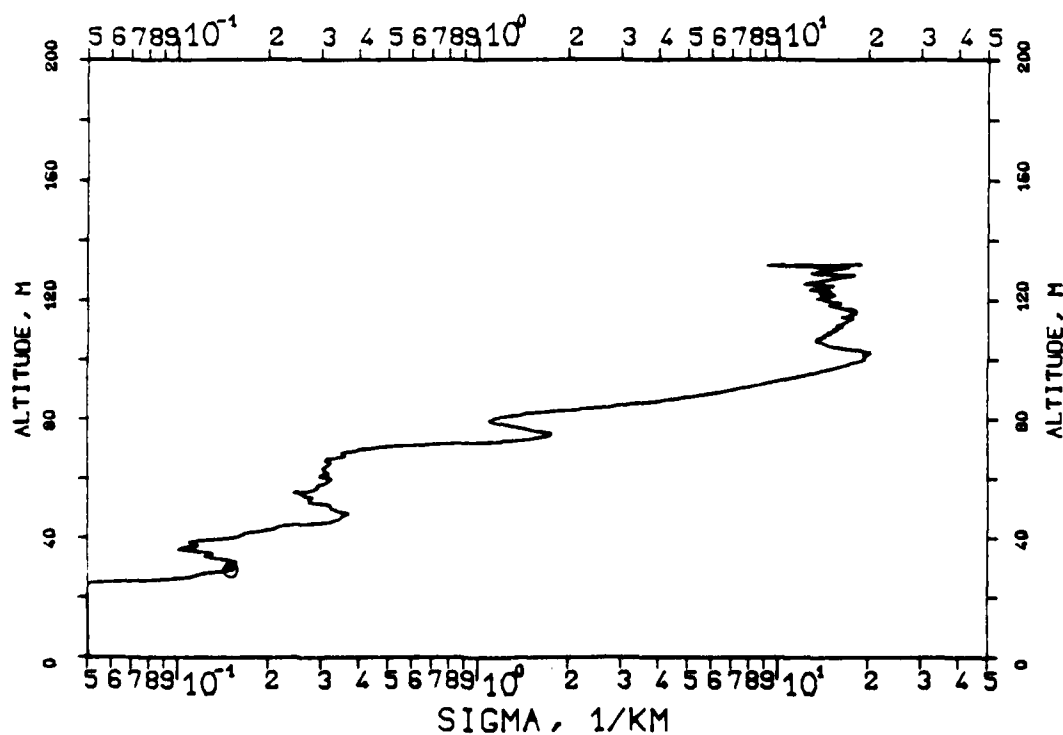


FIG. 7.282
KLETT-PROFILE, 0694NM, EL. 15DG00MN
841204, 13:15-13:15, CET
RM=0.511KM, SM=20.0000/KM, K=1.000

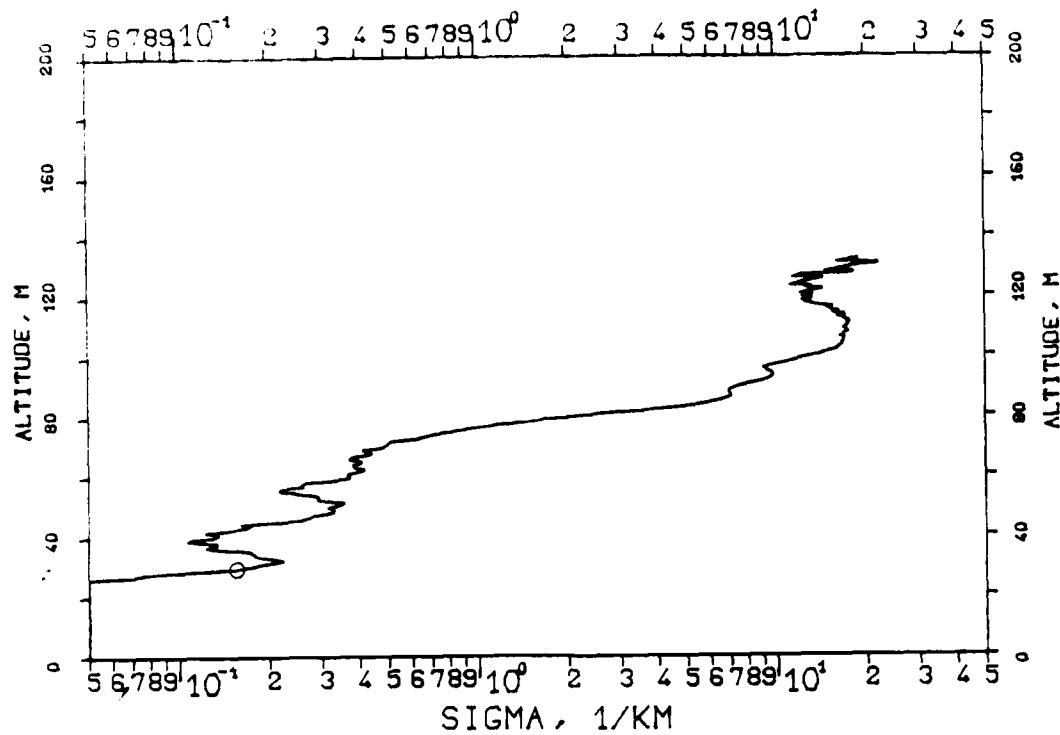


FIG. 7.283
KLETT-PROFILE, 0694NM, EL. 15DG00MN
841204, 13:18-13:18, CET
RM=0.519KM, SM=20.0000/KM, K=1.000

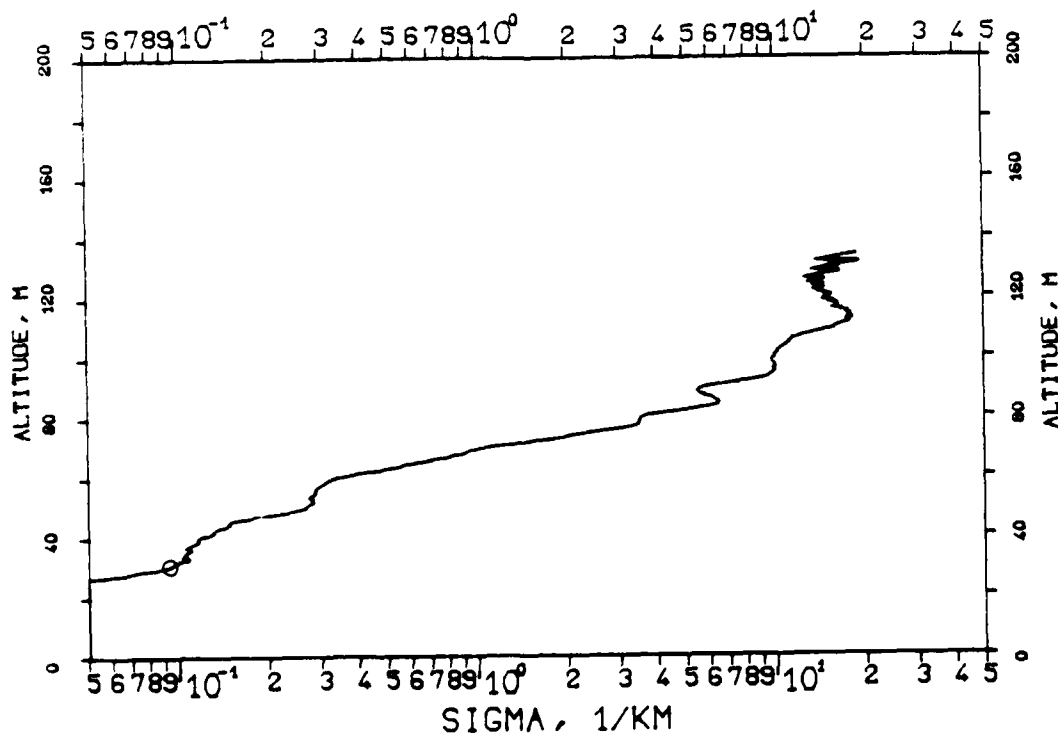


FIG. 7.284
 KLETT-PROFILE, 0694NM, EL. 150G00MN
 841204, 14:01-14:01, CET
 RM=0.538KM, SM=20.0000/KM, K=1.000

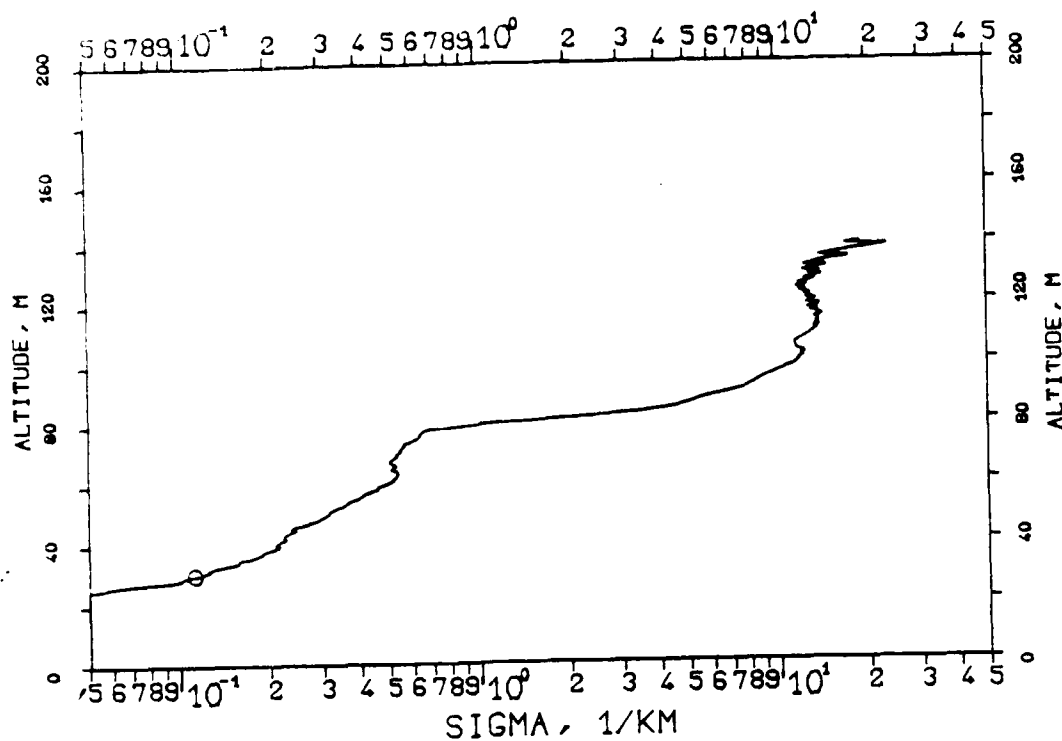


FIG. 7.285
 KLETT-PROFILE, 0694NM, EL. 150G00MN
 841204, 14:05-14:05, CET
 RM=0.516KM, SM=20.0000/KM, K=1.000

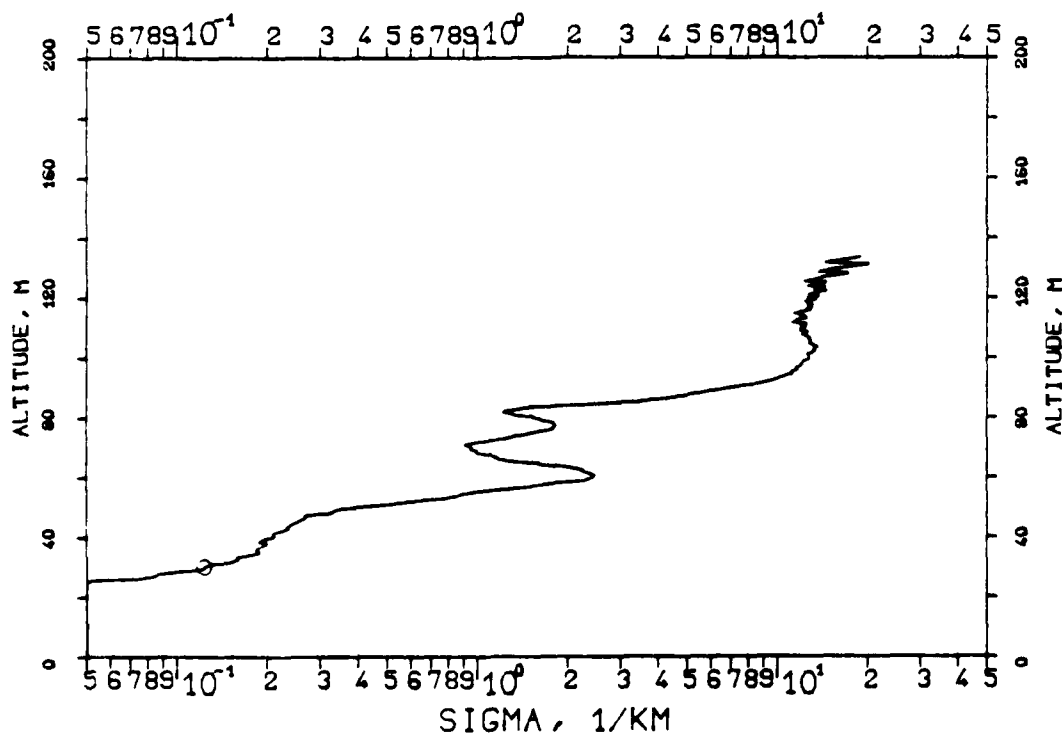


FIG. 7.286
 KLETT-PROFILE, 0694NM, EL. 15DG00MN
 8.120., 14:06-14:06, CET
 RM=0.517KM, SM=20.0000/KM, K=1.000

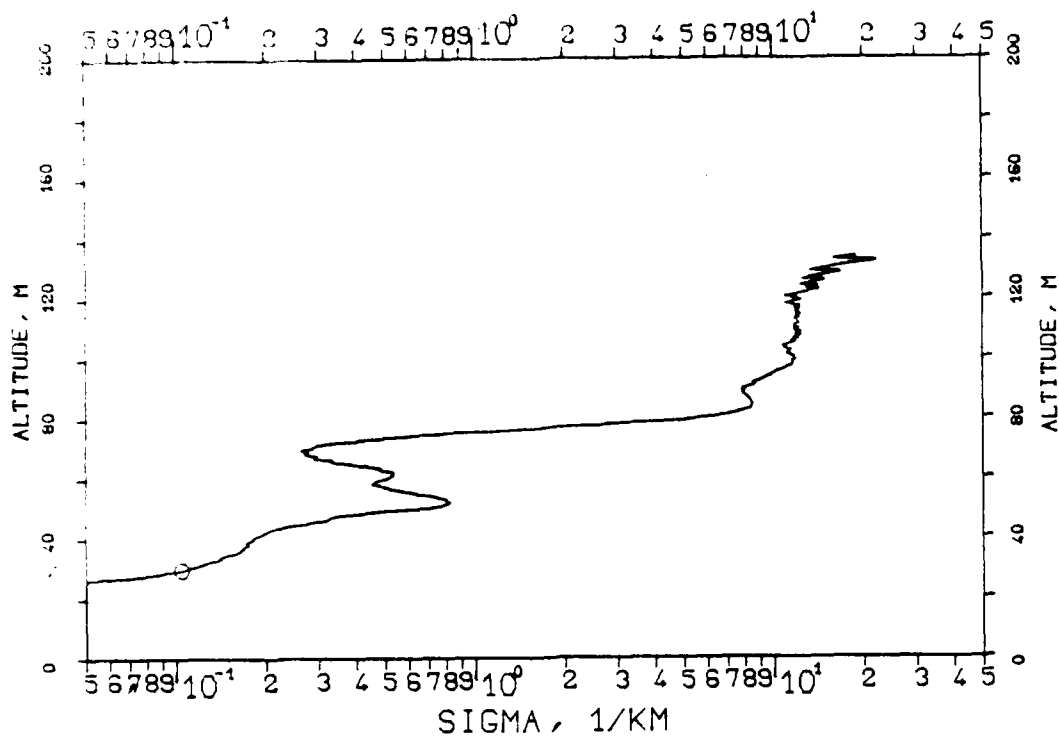


FIG. 7.287
 KLETT-PROFILE, 0694NM, EL. 15DG00MN
 841204, 14:07-14:07, CET
 RM=0.511KM, SM=20.0000/KM, K=1.000

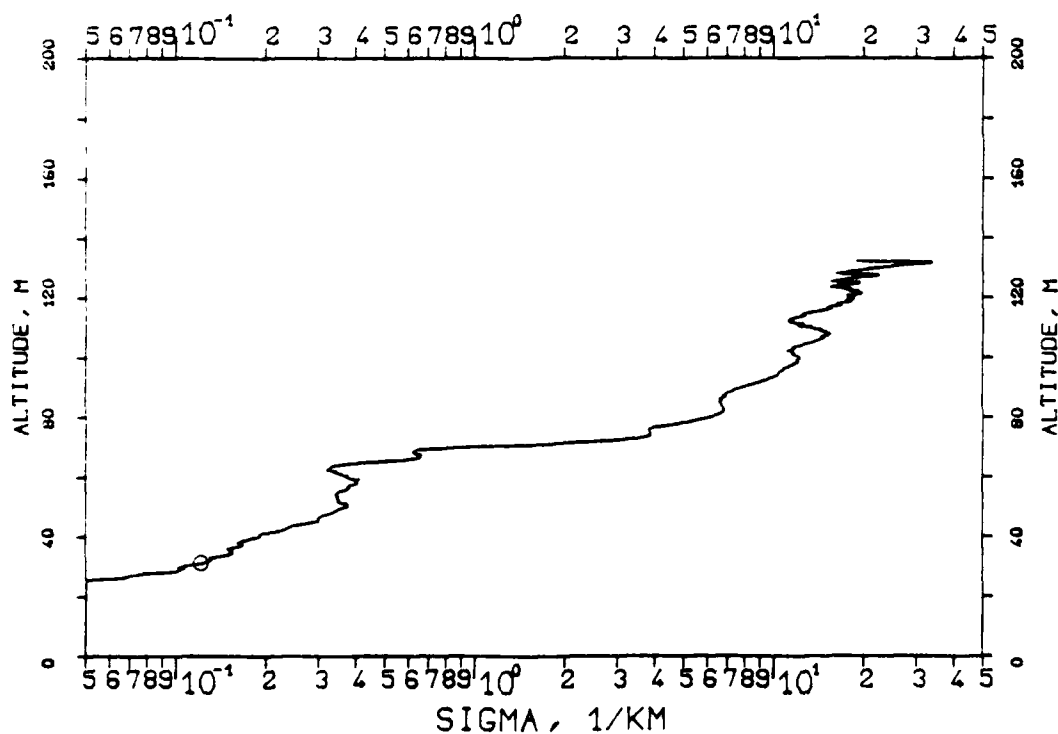


FIG. 7.288
 KLETT-PROFILE, 0694NM, EL. 15DG00MN
 841204, 14:07-14:07, CET
 RM=0.499KM, SM=20.0000/KM, K=1.000

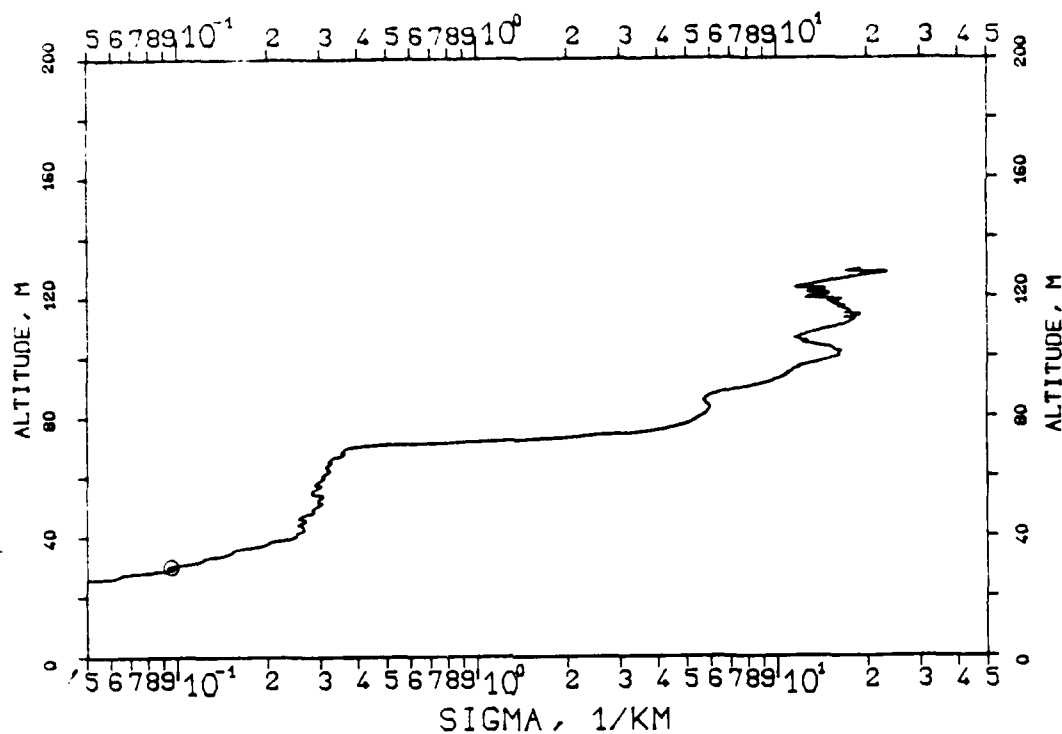


FIG. 7.289
 KLETT-PROFILE, 0694NM, EL. 15DG00MN
 841204, 14:08-14:08, CET
 RM=0.520KM, SM=20.0000/KM, K=1.000

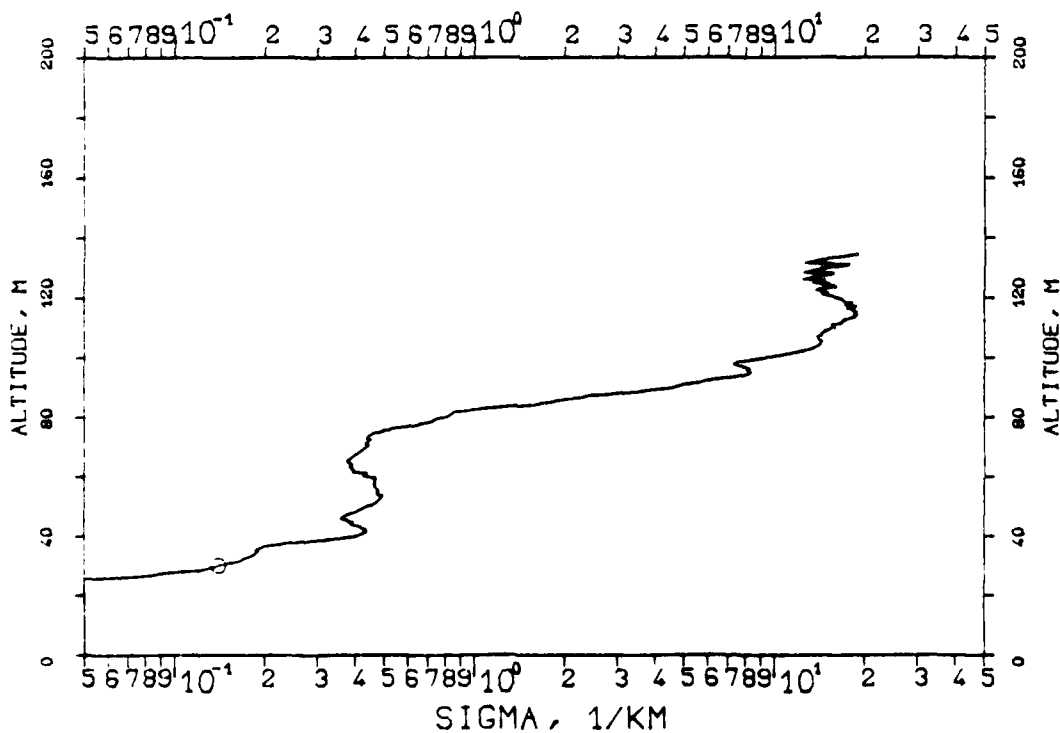


FIG. 7.290
KLETT-PROFILE, 0694NM, EL. 15DG00MN
841204, 14:30-14:30, CET
RM=0.537KM, SM=20.0000/KM, K=1.000

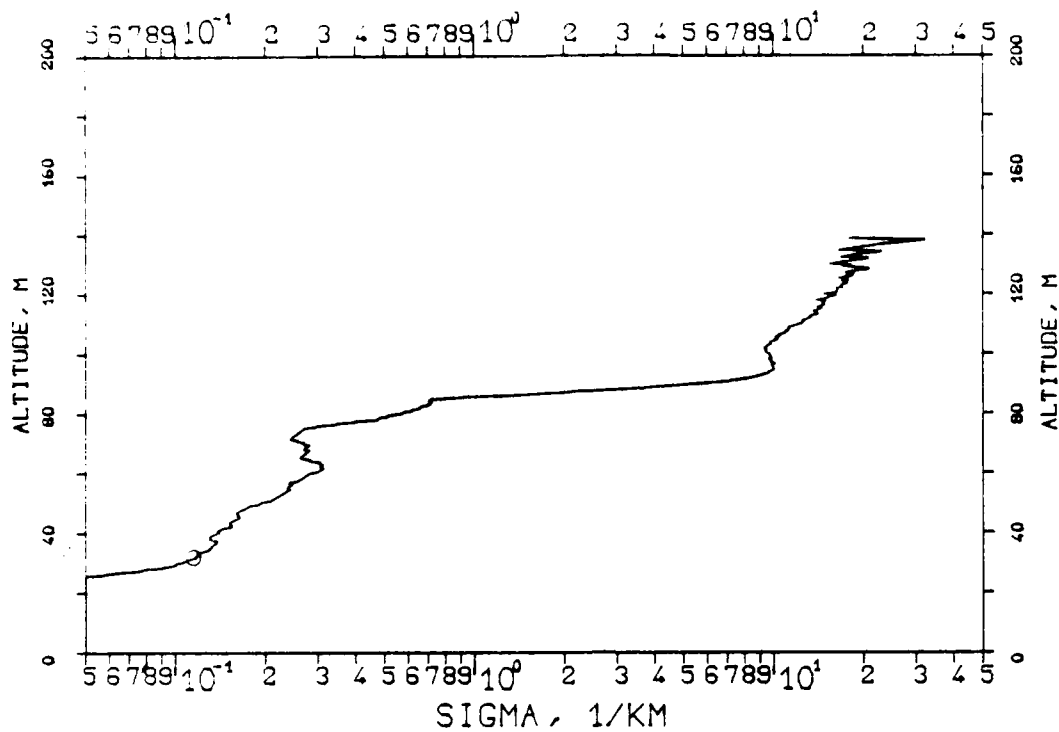


FIG. 7.291
KLETT-PROFILE, 0694NM, EL. 15DG00MN
841204, 14:32-14:32, CET
RM=0.520KM, SM=20.0000/KM, K=1.000

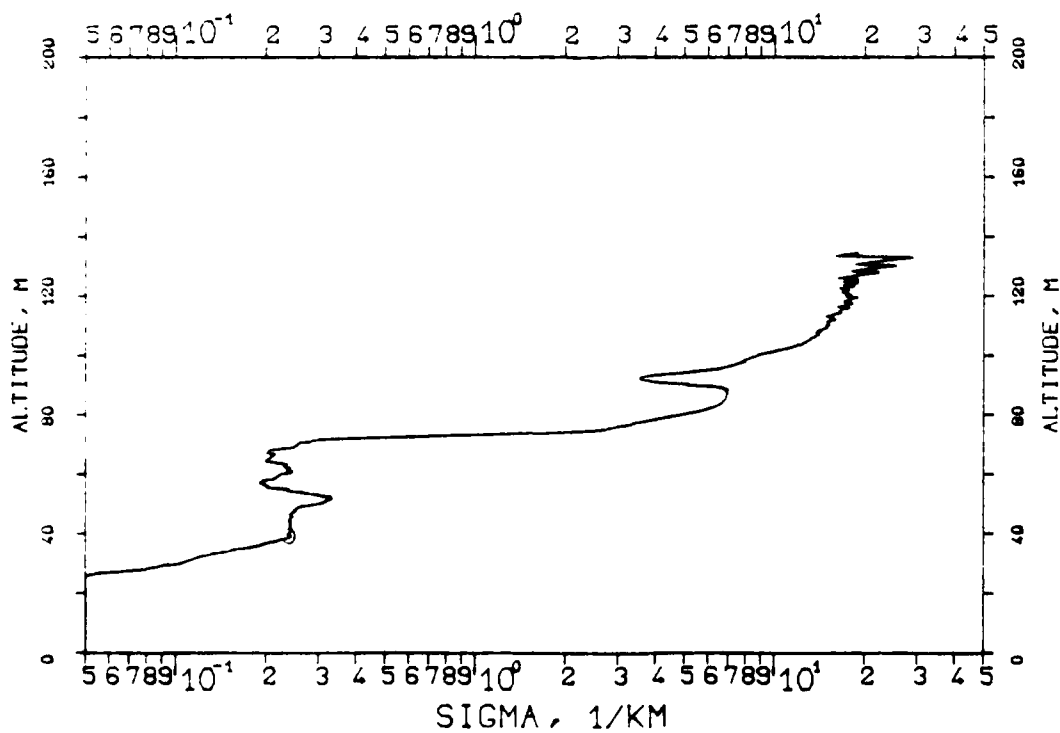


FIG. 7.292
 KLETT-PROFILE, 0694NM, EL. 15DG00MN
 8.1204, 14:32-14:33, CET
 RM=0.513KM, SM=20.0000/KM, K=1.000

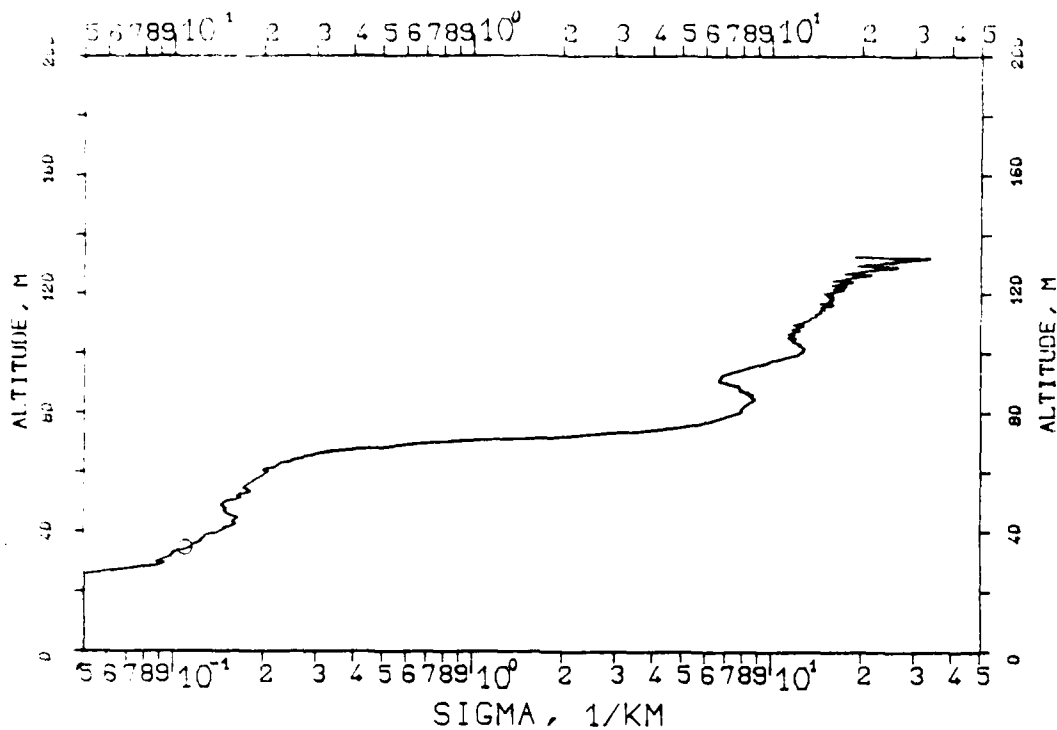


FIG. 7.293
 KLETT-PROFILE, 0694NM, EL. 15DG00MN
 841204, 14:33-14:33, CET
 RM=0.511KM, SM=20.0000/KM, K=1.000

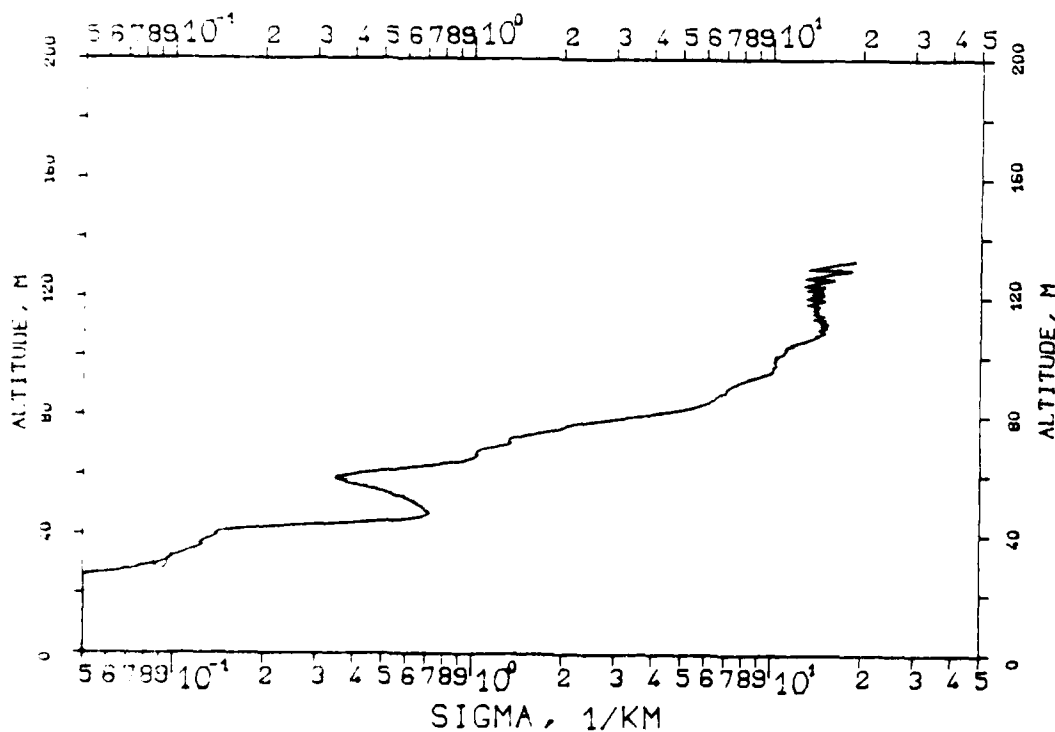


FIG. 7.294
 KLETT-PROFILE, 0694NM, EL. 15DG00MN
 841204, 15:02-15:03, CET
 RM=0.468KM, SM=20.0000/KM, K=1.000

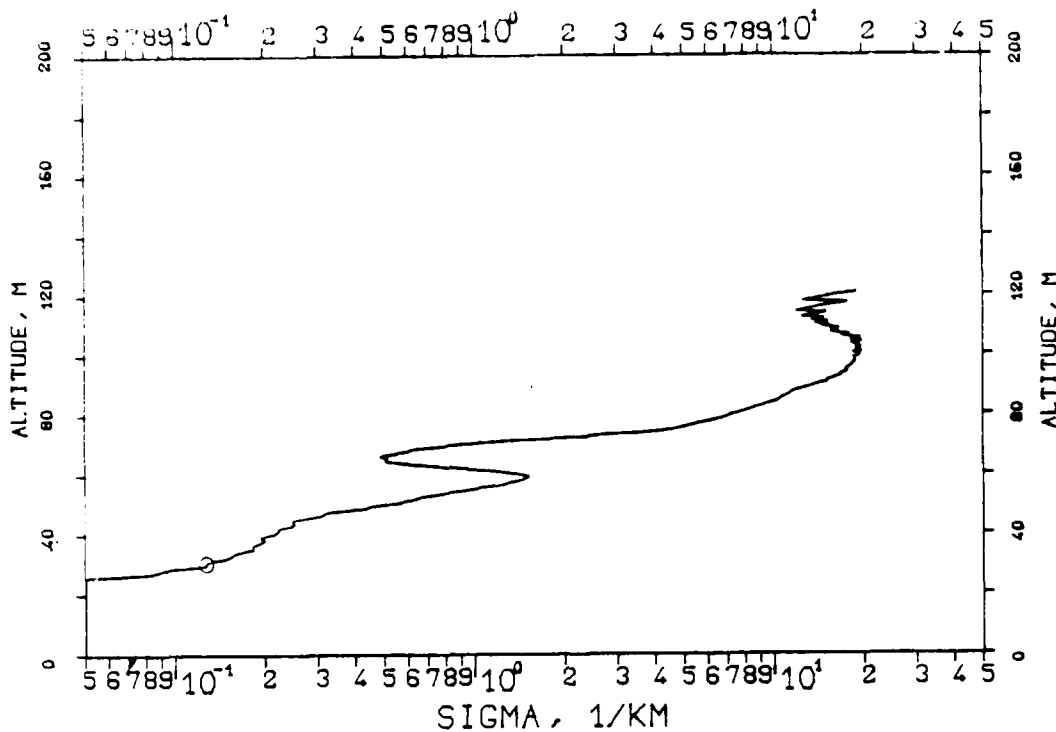


FIG. 7.295
 KLETT-PROFILE, 0694NM, EL. 15DG00MN
 841204, 15:03-15:03, CET
 RM=0.471KM, SM=20.0000/KM, K=1.000

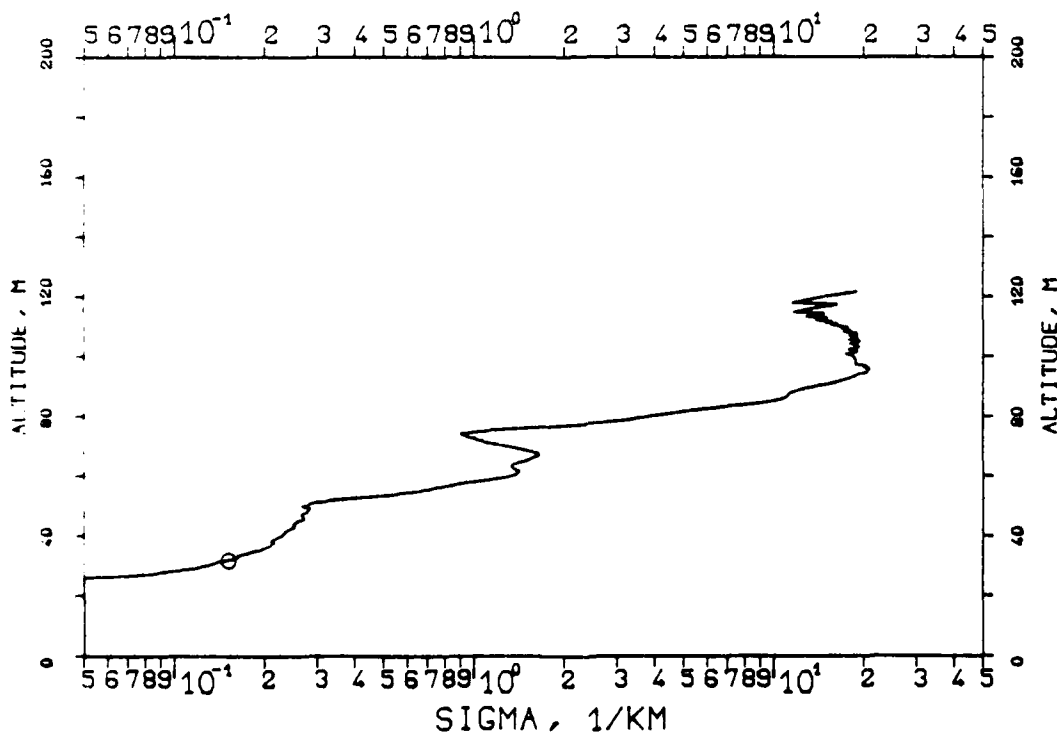


FIG. 7.296
 KLETT-PROFILE, 0694NM, EL. 15DG00MN
 841204, 15:04-15:04, CET
 RM=0.478KM, SM=20.0000/KM, K=1.000

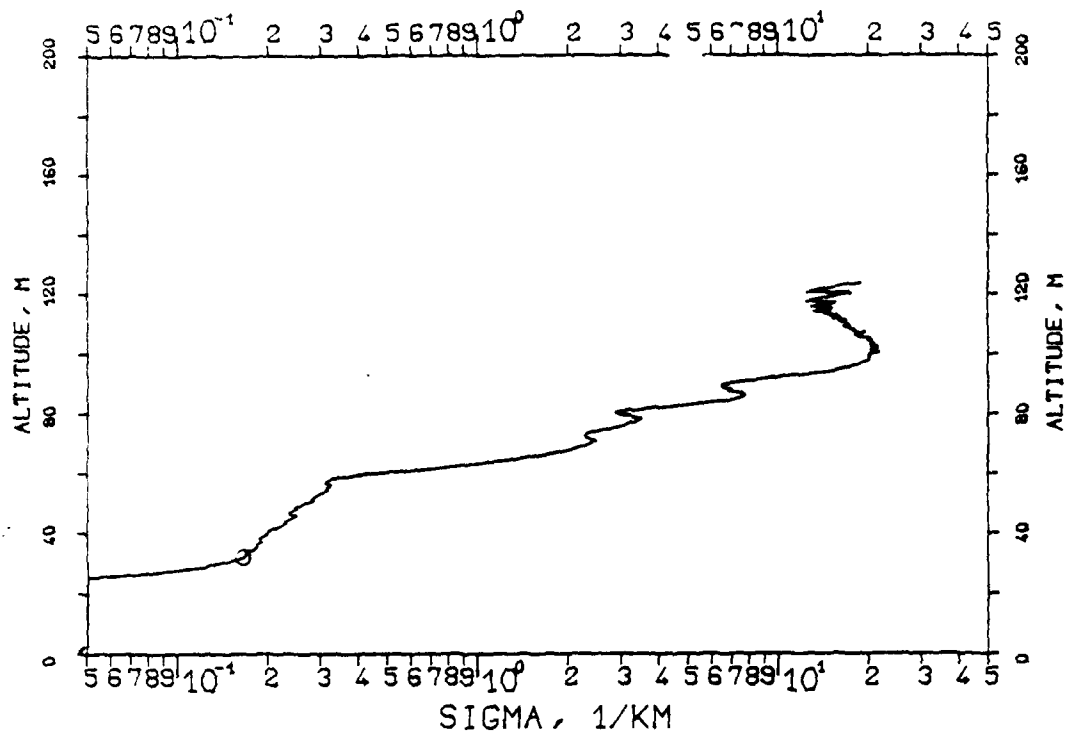


FIG. 7.297
 KLETT-PROFILE, 0694NM, EL. 15DG00MN
 841204, 15:05-15:05, CET
 RM=0.481KM, SM=20.0000/KM, K=1.000

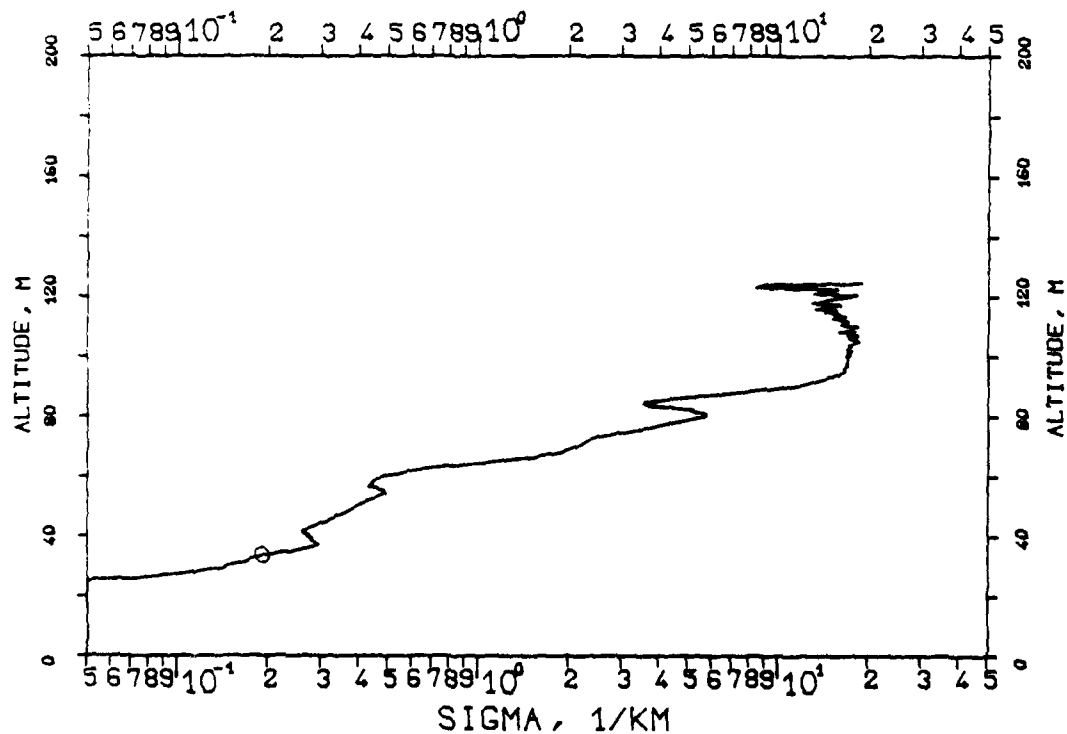


FIG. 7.298

KLETT-PROFILE, 0694NM, EL. 15DG00MN

841204, 15:06-15:06, CET

RM=0.481KM, SM=20.0000/KM, K=1.000

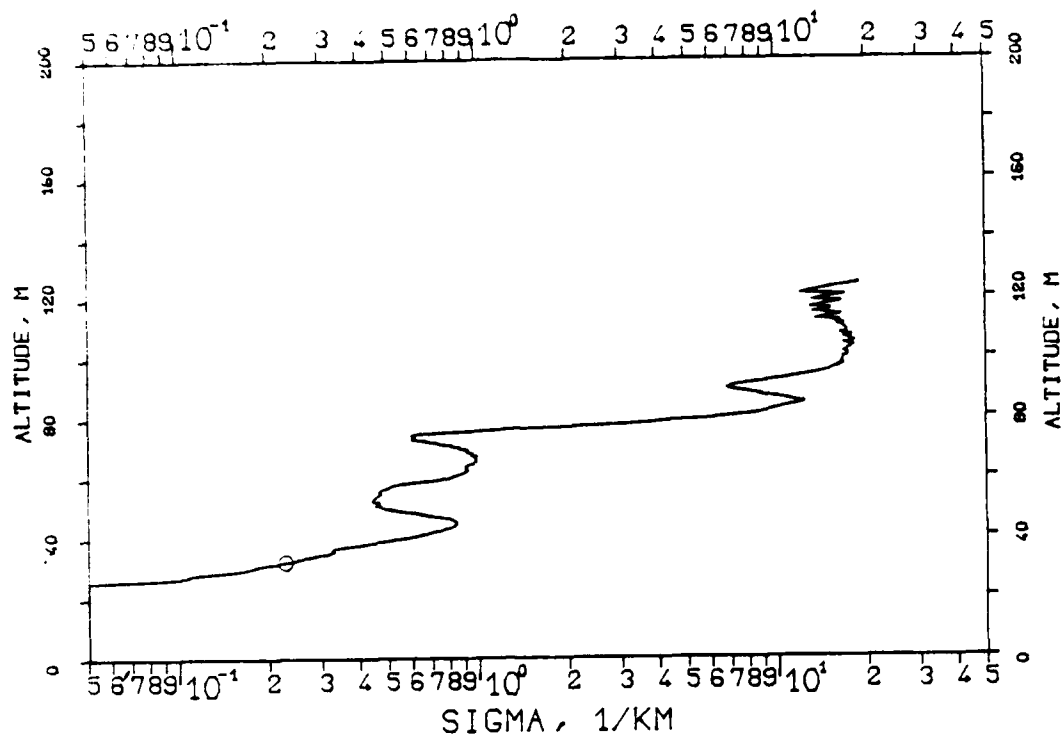


FIG. 7.299

KLETT-PROFILE, 0694NM, EL. 10DG00MN

841204, 15:35-15:35, CET

RM=0.500KM, SM=20.0000/KM, K=1.000

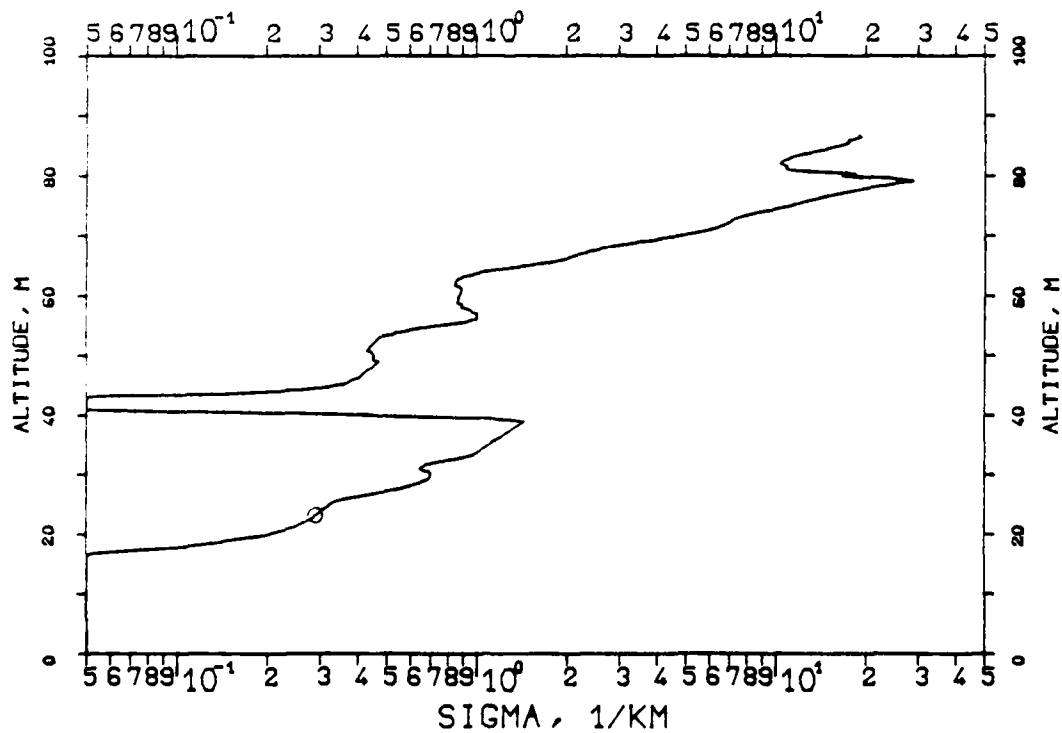


FIG. 7.300

KLETT-PROFILE, 0694NM, EL. 10DG00MN

841204, 15:36-15:36, CET

RM=0.592KM, SM=20.0000/KM, K=1.000

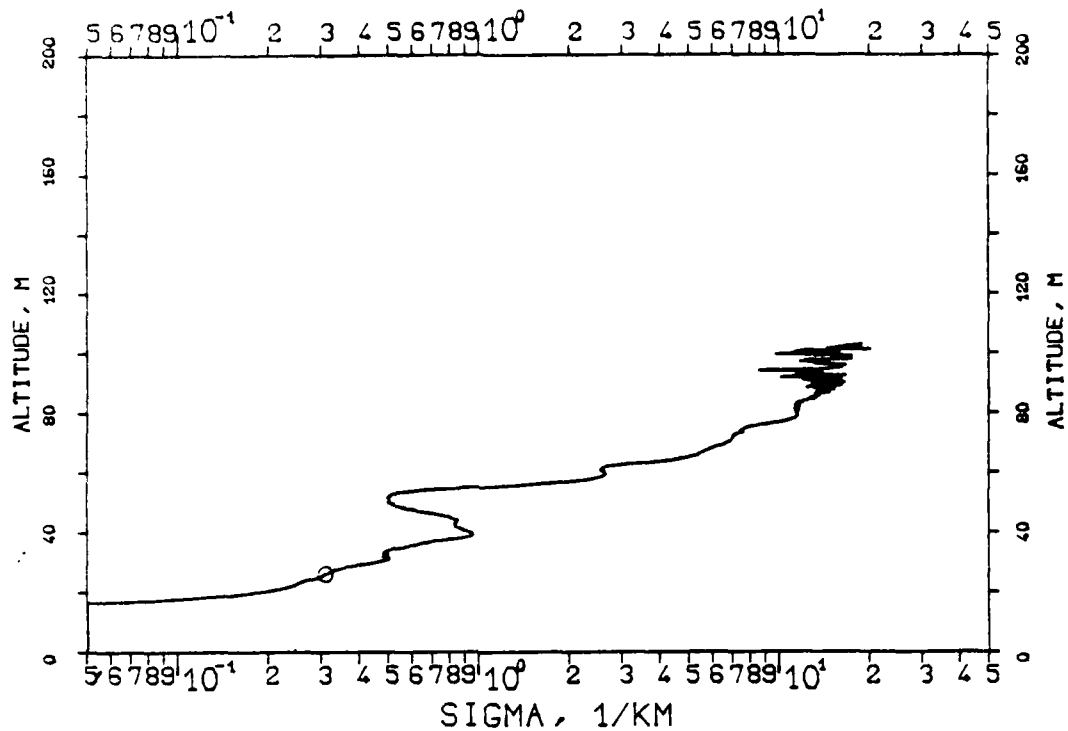


FIG. 7.301

KLETT-PROFILE, 0694NM, EL. 10DG00MN

841204, 15:38-15:38, CET

RM=0.607KM, SM=20.0000/KM, K=1.000

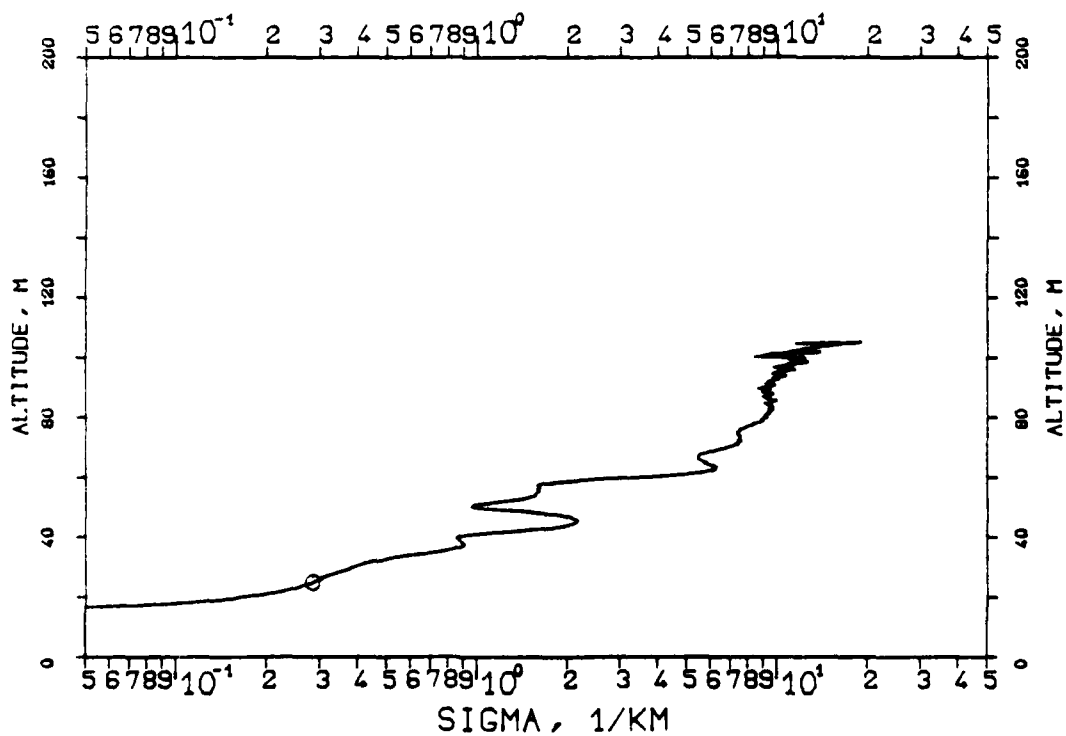


FIG. 7.302

KLETT-PROFILE, 0694NM, EL. 10DG00MN

841204, 15:39-15:39, CET

RM=0.609KM, SM=20.0000/KM, K=1.000

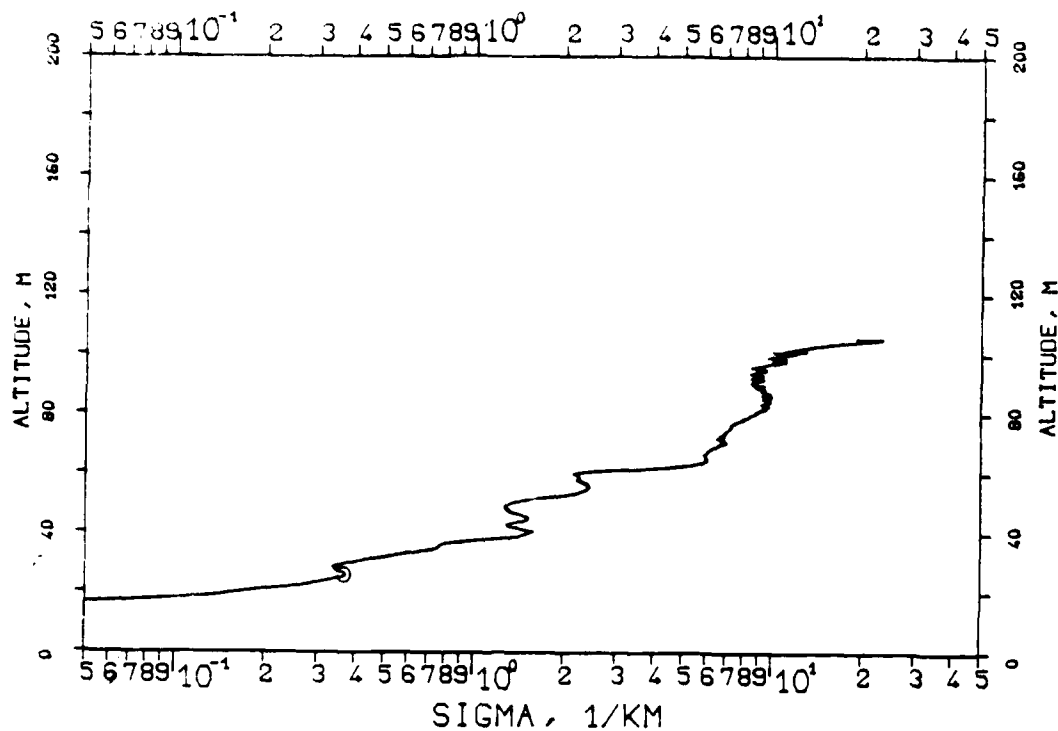
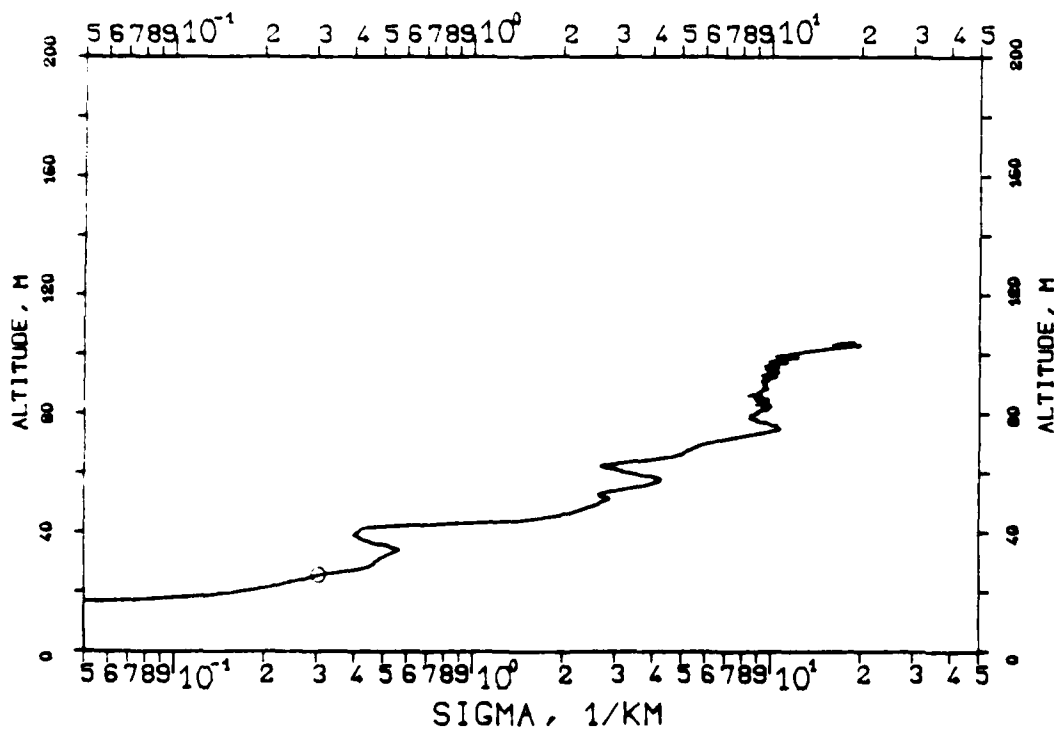


FIG. 7.303

KLETT-PROFILE, 0694NM, EL. 10DG00MN

841204, 15:39-15:39, CET

RM=0.600KM, SM=20.0000/KM, K=1.000



END

FILMED

7-85

DTIC